Structure and Bonding 163
Series Editor: D.M.P. Mingos

Peng Cheng *Editor*

Lanthanide Metal-Organic Frameworks

Springer

163
Structure and Bonding

Aims and Scope

The series *Structure and Bonding* publishes critical reviews on topics of research concerned with chemical structure and bonding. The scope of the series spans the entire Periodic Table and addresses structure and bonding issues associated with all of the elements. It also focuses attention on new and developing areas of modern structural and theoretical chemistry such as nanostructures, molecular electronics, designed molecular solids, surfaces, metal clusters and supramolecular structures. Physical and spectroscopic techniques used to determine, examine and model structures fall within the purview of *Structure and Bonding* to the extent that the focus is on the scientific results obtained and not on specialist information concerning the techniques themselves. Issues associated with the development of bonding models and generalizations that illuminate the reactivity pathways and rates of chemical processes are also relevant

The individual volumes in the series are thematic. The goal of each volume is to give the reader, whether at a university or in industry, a comprehensive overview of an area where new insights are emerging that are of interest to a larger scientific audience. Thus each review within the volume critically surveys one aspect of that topic and places it within the context of the volume as a whole. The most significant developments of the last 5 to 10 years should be presented using selected examples to illustrate the principles discussed. A description of the physical basis of the experimental techniques that have been used to provide the primary data may also be appropriate, if it has not been covered in detail elsewhere. The coverage need not be exhaustive in data, but should rather be conceptual, concentrating on the new principles being developed that will allow the reader, who is not a specialist in the area covered, to understand the data presented. Discussion of possible future research directions in the area is welcomed.

Review articles for the individual volumes are invited by the volume editors.

In references *Structure and Bonding* is abbreviated *Struct Bond* and is cited as a journal.

More information about this series at
http://www.springer.com/series/430

Peng Cheng
Editor

Lanthanide Metal-Organic Frameworks

With contributions by

M. Bosch · B. Chen · J. Chen · L. Chen · P. Cheng · F. Cimpoesu · M. Ferbinteanu · S. Fordham · M. Hong · F. Jiang · B. Li · K. Liu · W. Liu · W. Shi · S.-Y. Song · X.-Z. Song · J. Su · S. Tanase · X. Tang · X. Wang · M. Wu · H.-J. Zhang · Z. Zhang · Z. Zheng · H.-C. Zhou · K. Zhou

Springer

Editor
Peng Cheng
Department of Chemistry
Nankai University
Tianjin
China

ISSN 0081-5993 ISSN 1616-8550 (electronic)
ISBN 978-3-662-45772-6 ISBN 978-3-662-45773-3 (eBook)
DOI 10.1007/978-3-662-45773-3
Springer Heidelberg New York Dordrecht London

Library of Congress Control Number: 2014958293

Printed on acid-free paper

Springer is part of Springer Science+Business Media (www.springer.com)

Preface

The title of this volume consists of two keywords, "lanthanide" and "metal-organic frameworks", both of which are among the most active fields of research in chemistry and material science. In comparison with other types of metal ions, lanthanide ions exhibit a large atomic magnetic moment, strong spin-orbital coupling, high coordination number, and abundant coordination modes originating from their unique 4*f* electronic configurations, which endow lanthanide complexes with various structures and highly distinctive optical, electric, and magnetic properties as well as significant applications covering a vast range in daily living, laboratory research, industrial production, and high technology at present. Metal-organic frameworks, MOFs as the abbreviation, have been one of the most famous and active molecular materials in this century till now. MOFs are a kind of porous material and constructed from organic ligands and metal ions, which exhibit fascinating structural and chemical properties and attract considerable attention in vast areas including resource, environment, and materials. As a kind of organic–inorganic hybrid material, the structure of MOFs can be easily adjusted through altering the type of either organic ligand or metal ions, which subsequently leads to extensive properties meeting different application requests such as energy and pollution gas storage, luminescent detector, molecular magnets, catalysis, and so on.

As a constituent of the "Structure and Bonding" book series, this volume serves to provide the readers with some fundamentals of one specified family of MOFs, lanthanide metal-organic frameworks (Ln-MOFs), including the homo Ln-MOFs and hetero Ln-transition metal-organic frameworks. The volume comprises nine chapters covering general knowledge and the recent developments of Ln-MOFs, including synthetic strategies, the appropriate and representative functions, and potential applications.

The first chapter of this volume by Zhou illustrates a general picture of MOFs and then specifies Ln-MOFs out of MOF materials by the characteristic structures, properties, and applications attributing to the high coordination number, hard Lewis acidity, and strong magnetic anisotropy originating from the *f* block of lanthanides. Several well-known Ln-MOFs structures are presented to demonstrate the various synthetic strategies, interesting structural and chemical properties including

porosity, chirality, magnetism, and luminescence, as well as the overview of potential applications including gas storage, catalysis, and chemical sensing.

Chirality is one of the central elements for life on our earth and is important for most of the scientific areas. Chiral MOFs have drawn much attention as a kind of new low symmetric material based on their particular characters, such as high density of active catalytic centers, high level of porosity, regular and reliable crystalline nature, and relatively easy immobilization in comparison with other heterogeneous systems. In the second chapter by Liu, the synthetic approaches and structural features of chiral Ln-MOFs are summarized, and their applications in asymmetric catalysis, separation, and luminescence are revealed.

Gas storage and separation is one of the most widely studied and applied areas of MOFs. According to the unique electronic configuration, high coordination number, and flexible coordination environment of lanthanide ions, Ln-MOFs could exhibit high stability, high selectivity, and tunable pore sizes and shapes for the application of gas storage and separation. In the chapter by Chen, a comprehensive review is provided focusing on the synthesis and applications of Ln-MOFs in gas storage and separation including H_2 storage, selective CO_2 capture and separation as well as H_2 and CH_4 purification. Strategies for effectively enhancing gas storage capacities and selectivities of Ln-MOFs are presented as well.

Luminescence is one of the most representative features of lanthanide ions with sharp luminescent bands, large Stokes' shifts, and long luminescent lifetimes arising from the *f–f* transitions, leading to their diverse applications as chemical sensors, light-emitting devices, and biomedicine. The chapter by Zhang presents the luminescent Ln-MOFs containing the basic principles, recent research achievements and nanoscale Ln-MOFs as well as their applications in the field of cell imaging, drug delivery, and molecular sensing.

The assembly of the metal clusters into MOFs is another area of MOF-construction newly developed in recent years, which has led to series of unprecedented architectures and excellent properties by incorporating the particular characteristics of the clusters into the obtained frameworks. In comparison of the well-established research on transition metal clusters, construction of Ln-MOFs from lanthanide clusters is just at the beginning. Recent developments on the synthetic strategy and structures and properties of MOFs based on lanthanide clusters varying from di- to octatetraconta-nuclei are illustrated in the chapter by Hong, of which different fascinating topological networks and potential applications in a variety of fields are revealed.

Two chapters in this volume are about the hetero-MOFs (HMOFs), which are constructed by lanthanide ions together with transition metal ions. Since the chemical and physical properties originated from *d* and *f* electrons are totally different, it is difficult to synthesize HMOFs, while distinguishing characteristics with regard to structures and properties are endowed into HMOFs on the other hand by the combination of *d* and *f* electrons in a single framework. The chapter by myself presents an overview on HMOFs, covering the synthetic strategy and structures and properties of luminescence, magnetism, adsorption, etc. to help readers to have a general idea about HMOFs and to understand various aspects of

HMOFs. In the sixth chapter, Tanase reveals a specified branch of HMOFs, namely MOFs with *d–f* cyanide bridges, which are constituted from the unit of $Ln[M(CN)_n]$ (n =6, 8). Synthetic strategies and properties, especially the magnetic property, of this kind of HMOFs are reviewed in detail as well as the theoretical investigations.

As a complement, an individual series of MOFs from actinide elements with stepwise filled 5*f* orbitals are described in the chapter by Chen. The basic building units and the strategies to construct MOFs of uranium and other actinides are discussed. A comprehensive understanding of MOFs with actinide cations and valuable references for the development of novel MOF materials are provided.

Most of the chapters above are dealing with Ln-MOFs in single crystal or powder states, while in the last chapter by Zheng the scale of this volume is extended to the nanoscale. At first, a special series of Ln-MOFs, namely nanostructured Ln-MOFs, are thoroughly introduced, which are constructed from the subunits of nanosized lanthanide clusters or lanthanide–nonlanthanide metal clusters. Afterwards, Ln-MOFs in nano-crystal form are illustrated including synthetic methods, morphology, properties, and applications in imaging, luminescence, nanothermometry, sensing, and drug delivery.

Last but not least, I would like to extend my appreciation to the authors for their stupendous contributions to this book. I hope that the readers will get a satisfactory scene and find valuable information on the research and development of Ln-MOFs. I would also like to acknowledge Dr. J.G. Ma for the assistance in the preparation of this volume.

Tianjin, China Peng Cheng
October 2014

Contents

Struct Bond (2015) 163: 1–28
DOI: 10.1007/430_2014_162

Published online: 15 November 2014

Lanthanide Metal-Organic Frameworks: Syntheses, Properties, and Potential Applications

Stephen Fordham, Xuan Wang, Mathieu Bosch, and Hong-Cai Zhou

Abstract Metal-organic frameworks (MOFs) have emerged as a novel category of porous materials. Currently, rational design of MOFs provides a convenient method to design MOFs with desired properties. After a short introduction of traditional metal MOFs, this chapter discusses the development, properties, and applications of Lanthanide MOFs (Ln-MOFs). Ln-MOFs have garnered much interest due to a wide array of features from the marriage of lanthanide ions with traditional MOFs. An introduction to the Ln-MOF field is presented with several well-known structures to demonstrate various synthetic strategies. Furthermore, interesting structural and chemical properties including porosity, chirality, magnetism, and luminescence are highlighted from recent studies, as well as, a brief overview of potential applications including gas storage, catalysis, and chemical sensing.

Keywords Catalysis · Chemical sensing · Porous coordination networks · Coordination polymers · Gas storage · Lanthanide MOFs (Ln-MOFs) · Luminescence · Magnetism · Metal-organic frameworks (MOFs) · Porosity

Contents

The first two authors have equal contributions.

S. Fordham, X. Wang, M. Bosch, and H.-C. Zhou (✉)
Department of Chemistry, Texas A&M University, PO Box 30012, College Station, TX 77842, USA
e-mail: zhou@chem.tamu.edu

Abbreviations

bbc	4,4′,4″-(Benzene-1,3,5-triyl-tris(benzene-4,1-diyl))tribenzoate
bdc	1,4-Benzenedicarboxylate
BET	Brunauer–Emmett–Teller
btc	1,3,5-Benzenetricarboxylate
bpdc	4,4′-Biphenyldicarboxylate
COF	Covalent organic framework
DEF	*N*,*N*′-diethylformamide
DMA	Dimethylacetamide
DMF	*N*,*N*′-Dimethylformamide
DMSO	Dimethyl sulfoxide
dobdc	2,5-Dioxido-1,4-benzene-dicarboxylate
dpa	1,4-Phenylenediacetate
hfipbb	4,4′-(Hexafluoroisopropylidene)bis(benzoic acid)
HKUST	Hong Kong University of Science and Technology
htb	4,4′,4″-(1,3,4,6,7,9,9)-Heptaazaphenalene-2,5,8-triyl)tribenzoate
ina	Isonicotinic acid
ip	Isophthalic acid
LMCT	Ligand-to-metal charge transfer
Ln-MOF	Lanthanide MOF
Ln-TM MOF	Lanthanide-transition metal MOF
mdip	Methylenediisophthalate
mell	Mellitic acid
MIL	Materials of Institut Lavoisier
MLCT	Metal-ligand charge transfer
MOF	Metal-organic framework
NJU	Nanjing University
oda	Oxydiacetate
pam	4,4′-Methylenebis[3-hydroxy-2-naphthalenecarboxylate]
PCN	Porous coordination network
pdc	Pyridine-3,5-dicarboxylate
RPF	Rare earth polymeric frames
SBU	Secondary building unit

tatab	4,4′,4″-*s*-Triazine-1,3,5-triyltri-*p*-aminobenzoate
tatb	4,4′,4″-*s*-Triazine-2,4,6-triyltribenzoate
tda	1H-1,2,3-Triazole-4,5-dicarboxylate
TM	Transition metal
TOF	Turnover frequency
tpbtm	*N*,*N*′,*N*″-Tris(isophthalyl)-1,3,5,-benzenetricarboxamide
UMC	Unsaturated metal centers
UiO	University of Oslo
UTSA	University of Texas-San Antonio

1 Introduction to Metal-Organic Frameworks

Porous materials have attracted a significant amount of attention during the past few decades in scientific and technological research. Porous materials have significant surface area, which makes them capable of adsorbing and interacting with small molecules and ions on their inner surface. Classic inorganic porous materials contain activated carbon, silica gels, activated alumina, molecular sieve, zeolites, and mesoporous silica. Extensive studies have focused on the development of new classes of porous materials, such as covalent organic frameworks (COFs) and metal-organic frameworks (MOFs).

Traditional porous materials have limitations of either pore size or surface area. Silica gels, activated carbon, and activated alumina are all amorphous (irregular arrangement of pores) polymers containing micro- and mesopores (micropore is defined as pores smaller than 2 nm and mesopores between 2 and 50 nm) with a wide pore size distribution. From the perspective of materials, the wide pore size distribution, the micropores, and limited surface area hamper the utilization of those pores. Therefore, both COFs and MOFs have immerged as advanced class of porous materials. MOFs, also known as porous coordination polymers (PCPs), are defined as 1, 2, or 3 dimensional coordination networks with potential porosity [1–3]. Different from COFs, which are constructed from the linkage between light elements (H, B, C, N and O) by strong covalent bond [4], MOFs are connected by coordination bonds through self-assembly between inorganic metal-containing units (generally known as secondary building units SBUs) and organic linkers to form a rigid uniform crystalline hybrid materials [2, 5–7].

2 Synthesis of MOFs

2.1 Synthetic Routes

In general, MOFs are prepared via solvothermal or hydrothermal reactions, in which metal salts and organic linkers are heated in the presence of high boiling point and polar solvents (dialkyl formamides, dimethyl sulfoxide, or water) in a sealed vessel. In order to prepare a highly crystalline material in dilute liquid phase condition, a reaction time of hours to days is needed for the crystallization process [8]. The synthesis of MOFs can be quite delicate due to a variety of factors greatly impacting the formation of crystalline material that can be easily characterized through traditional techniques. In general, the main factors that contribute to MOF formation include temperature, pressure, reactant solubility, pH, and concentrations of metal salts and ligands. These Lewis acid–base reactions often lead to the formation of amorphous precipitate from the rapid deprotonation of the ligand [9]. Several reaction conditions can be modified to improve crystallinity including decreasing the reaction temperature or the addition of acid, such as hydrofluoroboric acid (HBF_4), to slow down ligand deprotonation rate. This often difficult trial-and-error process has led to the growth of combinatorial synthetic methods including high-throughput robotic screening [10].

MOF-5 [11], one of the most important representatives in the field of MOFs, was first reported by Yaghi et al. through diffusion of triethylamine into a solution of zinc (II) nitrate and H_2**bdc**(1,4-benzenedicarboxylic acid) in *N*,*N*′-dimethylformamide (DMF) and chlorobenzene. However, the yield of MOF-5 through the diffusion synthesis is low. Therefore, the method was further optimized to a high-yield solvothermal reaction of $Zn(NO_3)_2{\cdot}4H_2O$ and H_2**bdc** in *N*,*N*′-diethylformamide (DEF) at 120°C for 24 h [12]. The pore size of MOF-5 was further investigated to be controlled and functionalized by applying the isoreticular chemistry in the similar solvothermal conditions. After weak hydrothermal stability was revealed for MOF-5, attention shifted to other porous materials such as HKUST-1 [13], MIL-101 [14], and UiO-66 [15]. In the effort to shorten the synthesis time and produce high-quality crystals, alternative synthesis methods have been developed, such as microwave-assisted, sonochemical, electrochemical, and mechanochemical methods [8] (Fig. 1).

In microwave-assisted synthesis, the mixture of substrates (metals salts and organic ligands) and suitable solvent sealed in a Teflon vessel is placed under an applied oscillating electric field, which results in molecular rotation after coupling with the permanent dipole moment of substrate and consequently leads to rapid heating of the system [17, 18]. In terms of reaction time of Cr-MIL-100, the microwave-assisted reaction was significantly shortened to 4 h from 4 days in a conventional hydrothermal synthesis [8]. For the sonochemical synthesis, an adjustable powder output is introduced to sonicate the substrate mixture, providing very high local temperature and pressure resulting in the formation of relatively small but high-quality crystallites [16]. In the case of MOF-5, the crystals were obtained

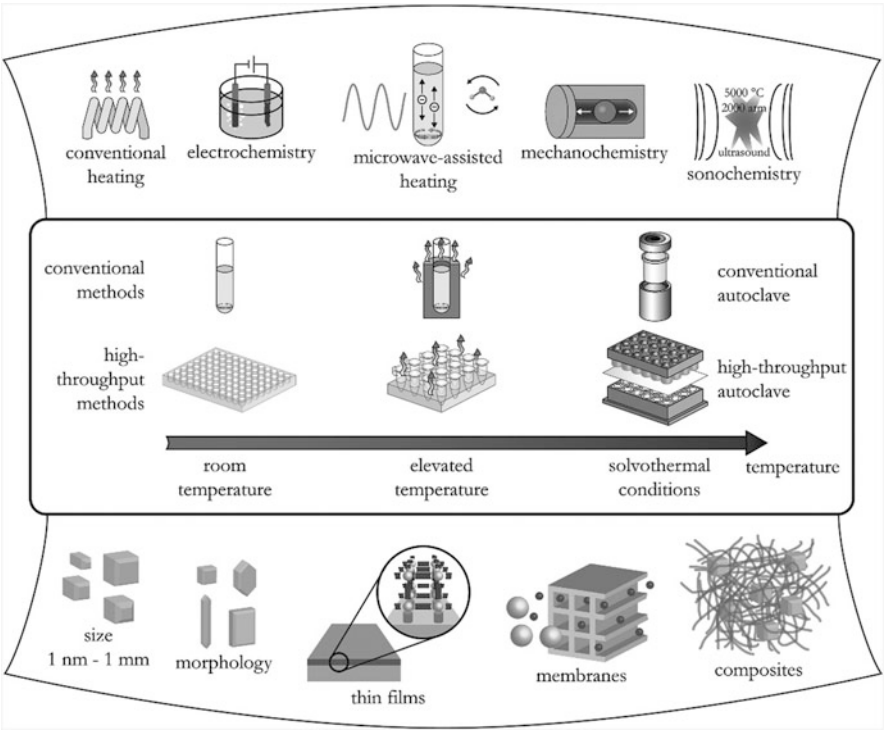

Fig. 1 Different synthesis methods of MOFs. (Reprinted with permission from Stock and Biswas [16], copyright © 2012 American Chemical Society)

within 30 min compared to 24 h in a solvothermal reaction [19]. In the electrochemical synthesis, the continuous anodic dissolution drives the metal ions to react with the dissolved polyprotic acids, forming highly crystalline powder MOF compared to the larger crystals in a batch reaction [16, 20]. The electrochemical method has demonstrated high efficiency with lower temperature requirements than conventional synthesis, high yield, and no need for metal salts [21]. In the mechanochemical synthesis, mechanical force is introduced not only to break the intramolecular bonds but also facilitate the chemical transformation, which usually occurs under solvent-free conditions at room temperature [16].

2.2 Key Structures in MOF

2.2.1 Traditional MOFs

For the aforementioned MOFs synthesis, a multitude of new MOFs have been developed and extended from several key structures that may be important for the

future development and applications of MOFs. The hallmark of those MOFs is their permanent porosity. The MOFs are constructed from the metal units or SBUs [22], formed in situ from pre-formed organic linkers through coordination bonds. The adjustment of the geometry, length, ratio, and functional group of the linkers will consequently tune the size and shape of the pores. Based on the number and geometry of carboxylates and elements in the linker, the pre-formed organic linkers could be categorized as ditopic, tritopic, tetratopic, hexatopic, octatopic, mixed, desymmetrized, metallo, and *N*-heterocyclic linkers [23]. In this chapter, the key discussion will focus mainly on metal units or SBUs with ditopic or tritopic linkers. For MOFs composed of other linkers including phosphonate and sulfonate, detailed reviews have been published [23–25].

In 1999, MOF-5 [11] and HKUST-1 [13] were synthesized and characterized to demonstrate their high crystallinity and porosity, the first major breakthrough of MOF chemistry. MOF-5 was constructed from a 6-connected octahedral $Zn_4O(CO_2)_6$ cluster and ditopic acid terephthalate (**bdc**) giving an extended 3D cubic framework with square opening of 8 and 12 Å. One of the unique benefits of MOFs is that the pore size and the internal pore surface functionalities can be tuned by using pre-designed organic linkers of the same symmetry, which, according to the theory of isoreticular chemistry, will not alter the underlying topology [12, 26]. MOF structure is predicable on the premise of forming SBUs with fixed linking geometries. Using MOF-5 as the prototype material, the 3D porous systems can be functionalized with the organic groups of bromo, amino, *n*-propyl, *n*-pentoxy, cyclobutyl, and fused benzene rings [12]. Their pore size can be further expanded with a stepwise expansion to biphenyl, tetrahydropyrene, pyrene, and terphenyl. This IRMOF-*n* series has open pores that range from 2.8 to 28.8 Å (Fig. 2).

Another archetypical MOF, HKUST-1 [13] consists of 4-connected square planar dicopper paddle-wheel units as nodes and tritopic 1, 3, 5-benzenetricarboxylates (**btc**) as linker. Each **btc** linker connects to three copper paddle-wheel SBUs forming a T_d-octahedron and occupies the alternating triangular faces of the octahedron. Along with the connection of other units, a cubic framework with **tbo** topology is formed. However, linking a 4-connected paddle-wheel unit with ditopic acid, such as **bdc**, results in a two dimensional (2D) sheet rather a three dimensional (3D) MOF material. The various combinations of different carboxylates and metal units would lead to a rich library of MOFs. The marriage of dicopper paddle-wheel units and extended tritopic organic linkers has been investigated to extend the networks and produces a variety of materials with the same network topology.

Combination of elongated tritopic linkers, such as 4,4′,4″-*s*-triazine-1,3,5-triyltri-*p*-aminobenzoate (**tatab**), 4,4′,4″-(1,3,4,6,7,9,9)-heptaazaphenalene-2,5,8-triyl)tribenzoate (**htb**), 4,4′,4″-*s*-triazine-2,4,6-triyltribenzoate (**tatb**), 4,4′,4″-(benzene-1,3,5-triyl-tris(benzene-4,1-diyl))tribenzoate (**bbc**), and paddle-wheel units yields a number of isoreticular MOFs (meso-MOF-1, PCN-htb, PCN-6′, and MOF-399, respectively) (PCN stands from Porous Coordination Network) (Fig. 3).

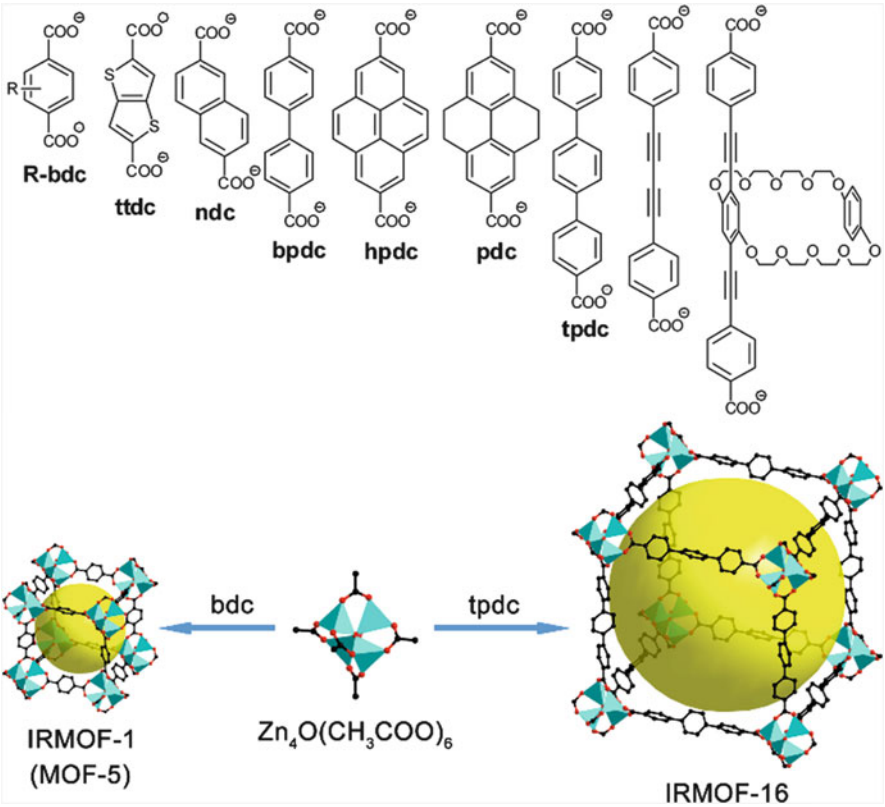

Fig. 2 Examples of IRMOF-*n* series. Color scheme: Zn (*turquoise polyhedral*); O (*red*); C (*black*). (Reprinted with permission from Lu et al. [23], copyright © 2014 Royal Society of Chemistry)

MOF-74 [27, 28], another well-known example, is the product of the coordination between tetraanionic 2,5-dioxido-1,4-benzene-dicarboxylate (**dobdc**) and an infinite metal chain, in which both the aryloxide and carboxylate moieties are bonded to the metal units. After applying the isoreticular chemistry of **dobdc** by the stepwise expansion of long molecular struts with phenylene units, a series of MOF-74 isoreticular materials was synthesized with pore apertures incrementally varied from 14 to 98 Å (Fig. 4) [29].

To date, IRMOF-74-XI with pore aperture of 98 Å is the record holder for the largest pore among all crystalline materials. Those large pores are capable of allowing natural protein to enter without folding, which demonstrate great potential for MOFs to serve as the matrix for enzyme immobilization.

Besides 6-connected octahedral metal units, another important SBUs is 6-connected trigonal prismatic metal units. MIL-101 [14] (MIL stands for Materials Institute Lavoisier) is a signature MOF, made from the linkage of **bdc** and metal trimmers, where three trivalent metals each coordinate with four oxygen atoms of

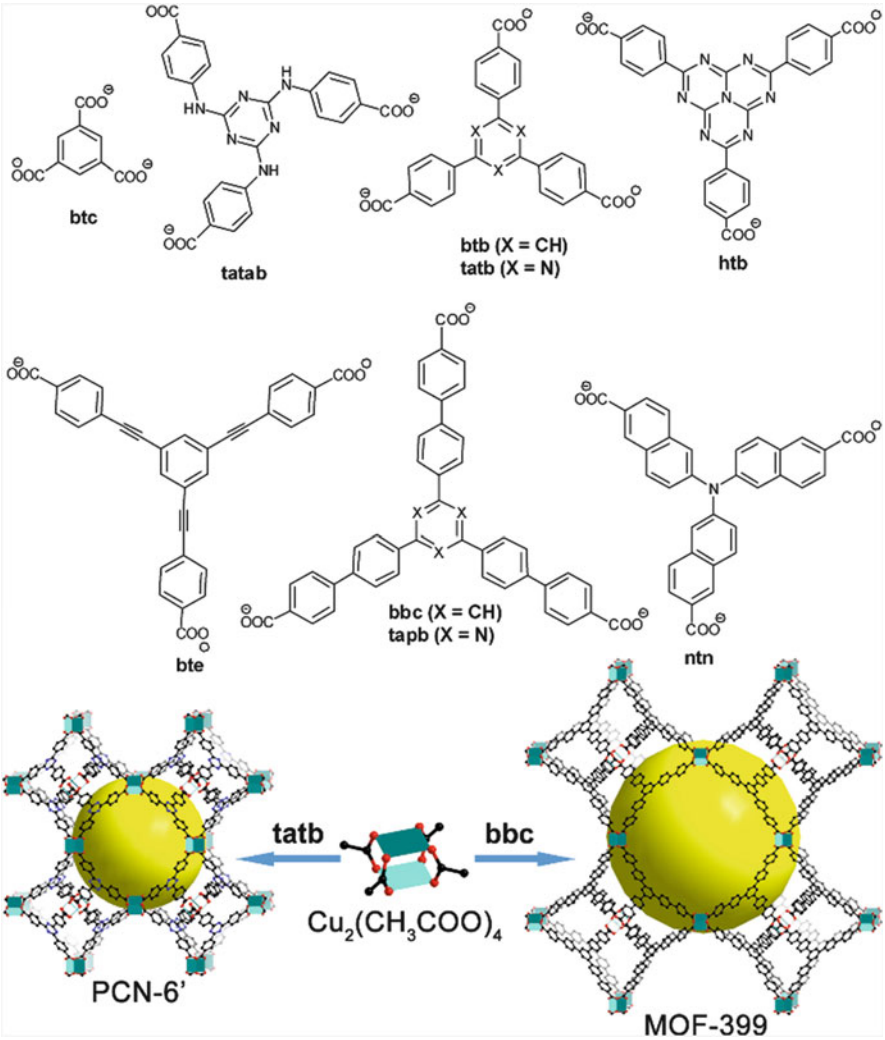

Fig. 3 Examples of MOFs constructed from tritopic carboxylate linkers and dicopper paddle-wheel SBUs. Color scheme: Cu (*turquoise*); O (*red*); C (*black*). (Reprinted with permission from Lu et al. [23], copyright © 2014 Royal Society of Chemistry)

bdc, one μ_3-O, and one oxygen from terminal water or fluorine group in an octahedral environment.

MIL-101 (Fig. 5) is a mesoporous MOF with a hexagonal window of 16 Å and a cage diameter of 34 Å. At the same time, MIL-101 is also acknowledged for enhanced hydrothermal stability through increasing the charge of the metals. Assembling the same trimeric SBUs with tritopic linker **btc**, MIL-100 [30] was successfully synthesized. A so-called "supertetrahedra" is formed with four

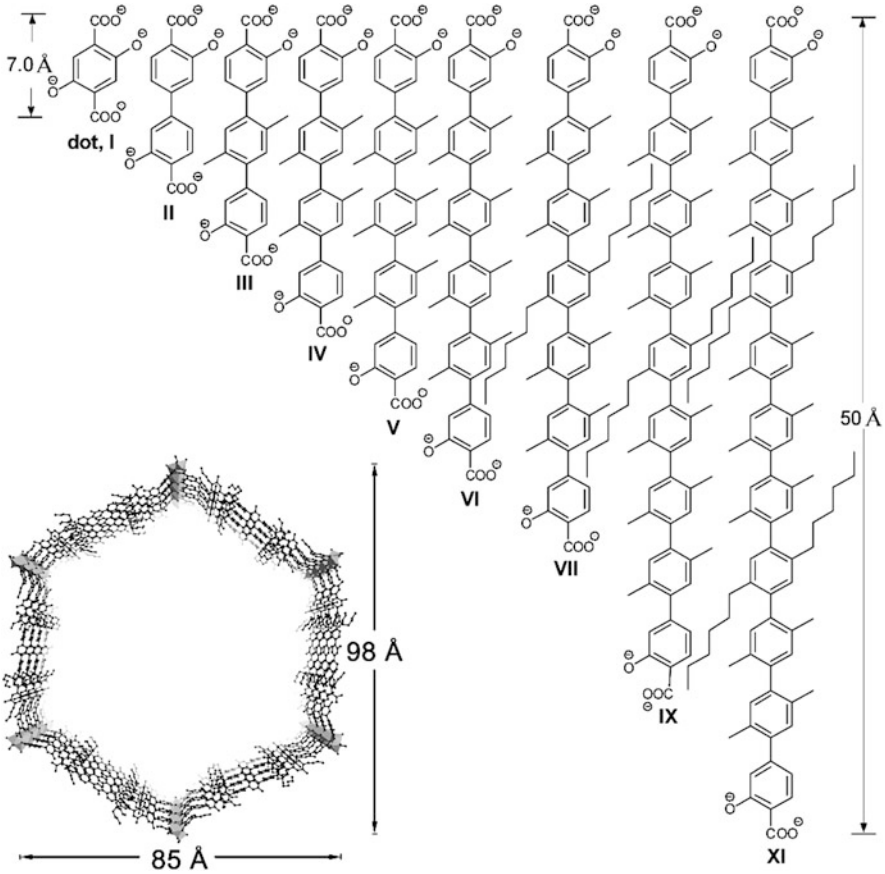

Fig. 4 List of organic linkers used in IRMOF-74 series with the one-dimensional channel with 98 Å for IRMOF-74-XI. (Reprinted with permission from Lu et al. [23], copyright © 2014 Royal Society of Chemistry)

trimeric metal units as vertices and four **btc** as the triangular faces. The further connection between these supertetrahedras gives rise to two mesoporous cages with accessible diameters of 25 and 29 Å.

In addition to the aforementioned 4- and 6-connected SBUs, a 12-connected SBU, $Zr_6O_4(OH)_4$ is identified as a new class of building units to be investigated and explored. In 2008, the first Zr-MOF, UiO-66 (UiO stands for University of Oslo) was synthesized under solvothermal condition using **bdc** as the organic struts [15]. In the framework of UiO-66, six Zr atoms in the square-antiprismatic coordination environment are linked by eight oxygen atoms from four **bdc** and four alternatives of μ_3-O and μ_3-OH on the triangle face to form the $Zr_6O_4(OH)_4$ core. In the UiO-66 structure, each $Zr_6O_4(OH)_4$ core is further connected by 12 **bdc**, consequently resulting in a 3D framework with triangular window of 6 Å in diameter. The $Zr_6O_4(OH)_4$ building units have been further applied to achieve

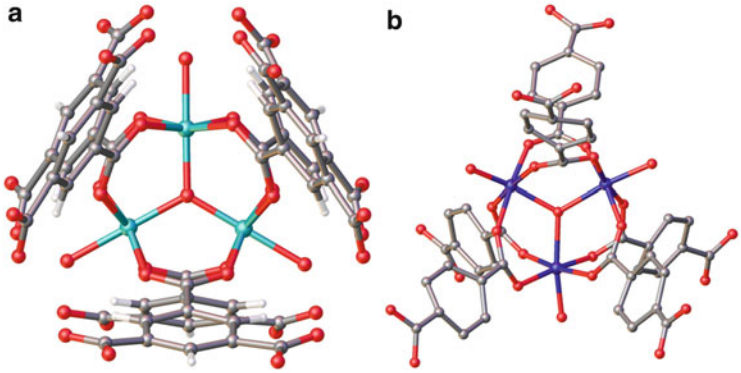

Fig. 5 (**a**) MIL-100, Al SBU with coordinated btc (bold) linker; (**b**) MIL-101, Al SBU coordinated **bdc** linker. Color scheme: Al (*blue*, *purple*); O (*red*); C (*gray*)

desired stable porous materials. Functional groups on **bdc** [31] and elongated benzene rings [15, 32] have been designed for gas storage and metal sensing. However, MOFs with 12-connected SBUs are still scarce.

As the study of MOFs is still a burgeoning field, new SBUs are expected to be identified in the future. With the knowledge of reticular chemistry, substantial development of MOFs with new structures is expected. Further discussions of MOF synthesis and characterization have been previously published in several review articles [9].

2.2.2 Lanthanide MOFs

Homonuclear Clusters

Different from the transition metals, the electrons in the *f* block of lanthanides make those elements capable of having a larger coordination sphere. Based on the hard-soft acid–base consideration [33], the lanthanides have affinity in relatively hard oxygen-containing linkers over other functional groups. A series of Ln-MOFs have been synthesized from **bdc** and Ln (Ln = La, Ce, Pr, Nd, Sm, Eu, Gd, Tb, Dy, Ho, Er, and Tm) in water, which adopts a general formula of $Ln_2(1,4\text{-}\mathbf{bdc})_3(H_2O)_4$ [34]. The Ln (III) ions are in the all 8-connected mode to six oxygen atoms from **bdc** and two oxygen atoms from water molecules (Fig. 6). Each **bdc** is further bound to four Ln ions to generate a 3D network. Upon dehydrating, the heavier lanthanide ions (Tb-Tm) demonstrated a phase transition by the linking of Ln ions through μ-carboxylate bridges, while the lighter lanthanide ions preserve their original structure. Further information on Ln-MOFs from lanthanide metal clusters can be found in Hong et al. [35].

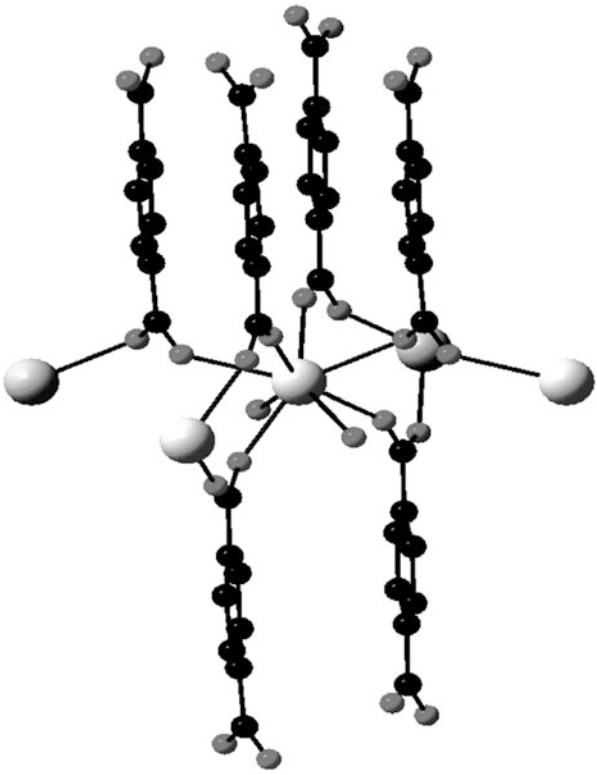

Fig. 6 Projection view of an extended asymmetric unit of $[Tb_2(\mathbf{bdc})_3(H_2O)_4]n$. Color scheme: Tb (*white*); O (*gray*); C (*black*). (Reprinted with permission from Daiguebonne et al. [34], copyright © 2008 American Chemical Society)

Heteronuclear Clusters

Recently, the combination between lanthanides and transition metals has also been employed to construct 3D lanthanide-transition metal MOFs (Ln-TM MOFs). Benzenecarboxylates are commonly rigid and suitable to coordinate with metal atoms in abundant coordination modes. Reactions between isophthalic acid, 2,2′-bipyridine, and copper and lanthanide salts produced a series of Ln-Cu MOF based on rod-shaped metal units and 2D sheets [36]. However, benzenecarboxylate oxygen has an affinity to coordinate to lanthanides over transition metals. Therefore, an addition of *N* donor-ligand will assist the introduction of transition metal into the final product [37]. One class of satisfactory ligands are the pyrazine carboxylic acids, which contain multiple *O*- and *N*-donors. More information on transition-lanthanide MOFs will be presented in Cheng et al. [38].

3 Properties of MOFs

The tunable nature of MOFs through rational design affords new materials which can be judiciously tailored toward a variety of applications [39]. The duality of inorganic metal nodes and organic linkers in the frameworks gives rise to functional materials with significant properties. Ln-MOFs benefit from the intrinsic properties of lanthanide metal ions that provide unique electronic and coordination properties. Further functionalization can be incorporated through the judicious selection of organic linkers, which contribute additional properties that can be tuned for different purposes. Ln-MOF properties such as porosity, magnetism, and luminescence provide a unique class of functional materials with potential in a wide array of applications.

3.1 Porosity

Perhaps one of the most widely studied properties of MOF materials is the existence of porosity. The porous nature of MOFs promotes favorable host–molecule interactions due to their high surface areas and tunable pore sizes [40]. As previously mentioned, MOFs are generally classified in two categories, microporous (<2 nm) and mesoporous (2–50 nm).

3.1.1 Microporous Ln-MOFs

High coordination environment and connectivity of lanthanide metal ions have led to a large number of reported Ln-MOFs. However, compared to traditional transition metal MOFs, Ln-MOF has been significantly less studied. The highly connective lanthanides usually lead to the formation of condensed frameworks in the microporous range. Microporous Ln-MOFs offer a distinct advantage in gas storage and separation applications in that they possess permanent porosity with tunable pore size. Due to the expanse of microporous Ln-MOFs, only a few simple examples composed with commercially available ligands will be discussed; however, a detailed review of microporous Ln-MOFs has been previously published [41]. The simplest linear ditopic carboxylate linker is the appropriate starting point for our discussion. A series of Ln-MOFs composed of **bdc** and Ln metal ions (Ln = La, Ce, Nd,) in DMF have been studied. In this study, a series of isostructural Ln-MOFs have been synthesized (Fig. 7) with the Ln ions having three different types of coordination numbers [42]. This framework features a 1D 4 × 7 Å channel. This rod-shaped chain SBU leads to MOFs with no interpenetration due to topological preference and provides an avenue for rational design of SBUs.

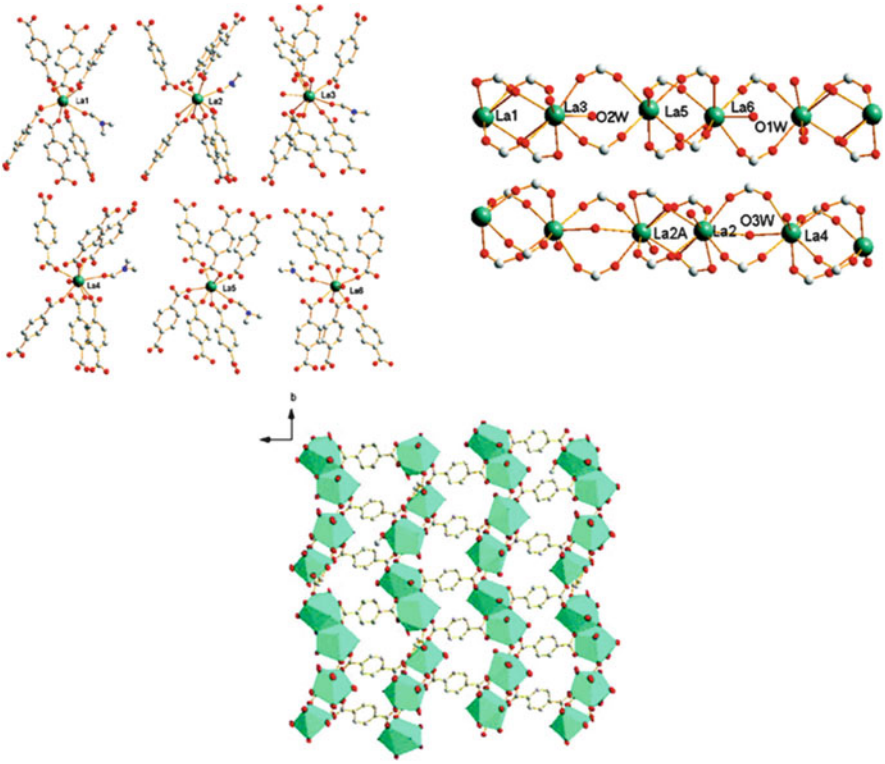

Fig. 7 (*Top left*) Coordination of Ln^{3+} ions; (*top right*) Lanthanide rod SBU; (*bottom*) Framework structure, [0 0 1] direction. Color scheme: C (*gray*); O (*red*); Ln (Ln = La, Ce, Nd) (*green*). (Reprinted with permission from Han et al. [42], copyright © 2010 American Chemical Society)

Ligand extension has been often used to enlarge the pore size in MOFs without effecting geometry of the framework; however, in some instances new frameworks are obtained. The Zhou group has synthesized PCN-71 from the trigonal planar **tatb** linker with Ln^{3+} metal ions (Ln = Dy, Er, Y, Yb) in DMSO yielding four isostructural microporous Ln-MOFs with observed interpenetration (Fig. 8) [43]. PCN-71 is composed of a square planar $Ln_4(\mu_4\text{-}H_2O)$ SBU connecting to eight **tatb** and four sulfates. Interestingly, two cages, a larger truncated octahedron, and a smaller cuboctahedron inscribed by eight truncated octahedron cages are formed. The extension of pore size in the mesoporous domain could provide the opportunity for new applications of Ln-MOFs. However, traditional methods through ligand extension have been mostly unsuccessful due to the lanthanide coordination environment. Detailed information on microporous Ln-MOFs will be further demonstrated in Chen et al. [44].

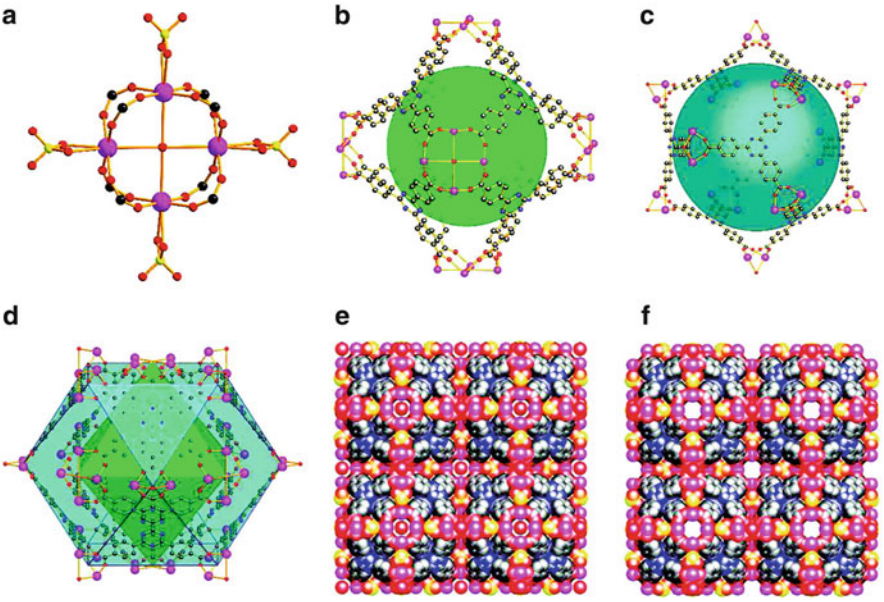

Fig. 8 Structures of PCN-17 (Dy, Er, Y, Yb): (**a**) $Ln_4(\mu_4\text{-}H_2O)$ SBUs; (**b**) octahedral cage; (**c**) cuboctahedral cage; (**d**) an octahedral cage enclosed by an cuboctahedral cage; (**e**) space-filling packing of unactivated [1 0 0] direction; (**f**) space-filling packing of framework [viewed from (1 0 0) direction]. Color scheme: Ln (Ln = Dy, Er, Y, Yb) (*pink*); C (*gray*); O (*red*); S (*yellow*). (Reprinted with permission from Ma et al. [43], copyright © 2009 American Chemical Society)

3.1.2 Mesoporous Ln-MOFs

A limited number of mesoporous robust Ln-MOFs have been reported; this is attributed to the coordination environments of the lanthanide SBUs which often have coordinated solvent molecules in the non-activated state that results in framework collapse upon activation. The first reported mesoporous Ln-MOF with permanent porosity was synthesized from the solvothermal reaction of **tatb** with $Tb(NO_3)_3{\cdot}5H_2O$ to yield a MOF with cages of 3.9 (S cage) and 4.7 nm (L cage), respectively (Fig. 9) [45]. Interestingly, the structure is composed of multiple Tb_4 units with four of these units forming the faces of a truncated square tetrahedron. The unique geometry of the Tb^{3+} with the carboxylate moiety affords a mesoporous structure due to the increased separation between the Tb^{3+} ions which is typically not observed with other lanthanide ions. Additionally, UTSA-61 (UTSA stand for University of Texas-San Antonio) has been reported, composed of Tb^{3+} ions with the elongated ligand 1,3,5-tris(3,5-di(4-carboxyphenyl)phenyl)benzene synthesized in DMA (Fig. 10) [46]. An induced chirality in the structure yields a novel topology that exhibits permanent porosity. The mesoporous nature of this framework is mostly attributed to the dendritic nature of the hexatopic carboxylate linker. This rod-shaped SBU leads to MOFs with no interpenetration and provides an

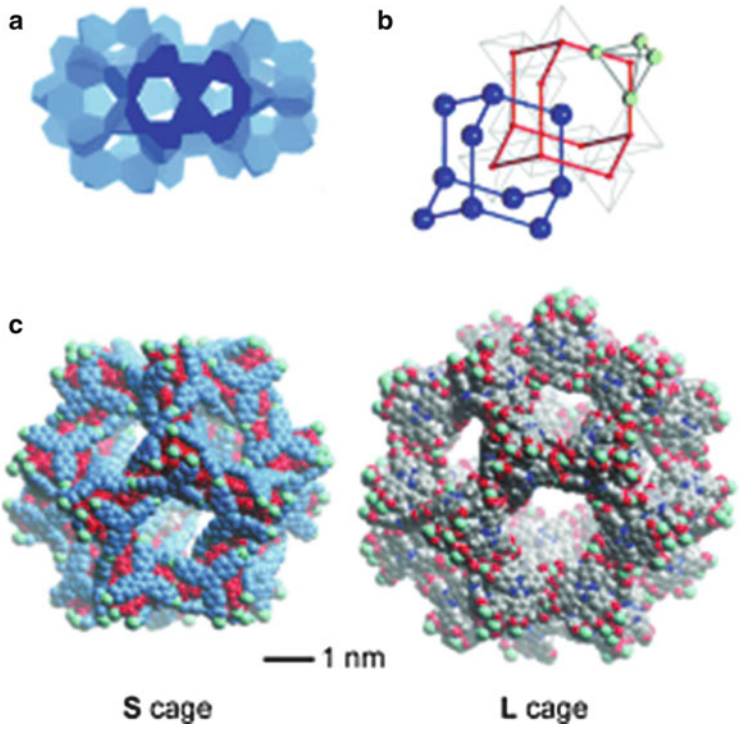

Fig. 9 (**a**) Fused S and L mesocages formed by truncated square tetrahedron. (**b**) Doubly interpenetrating diamond-like (**c**) The S and L mesocages. Color scheme: C (*gray*), H (*white*), N (*blue*), O (*red*), Tb (*light blue*). (Reprinted with permission from Park et al. [45], copyright © 2007 Wiley-VCH Verlag GmbH & Co. KGaA, Weinheim)

avenue for rational design of microporous frameworks. To the best of our knowledge, the two structures presented are the only examples of mesoporous Ln-MOFs in the literature; further investigation of these materials is needed to unleash their full potential.

3.2 Magnetism

One of the main reasons to incorporate Ln^{3+} metal ions into a framework is due to the fact that many of them have a large *J* value caused by unquenched orbital contribution, high easy-axis magnetic anisotropy, and interesting magnetic interactions between lanthanides and transition metals. A full discussion of the magnetic properties of lanthanides is beyond the scope of this introduction, but several interesting examples of magnetic Ln and Ln-TM MOFs have recently been reported and will be briefly described. The potential for porosity inherent in a stable 3D

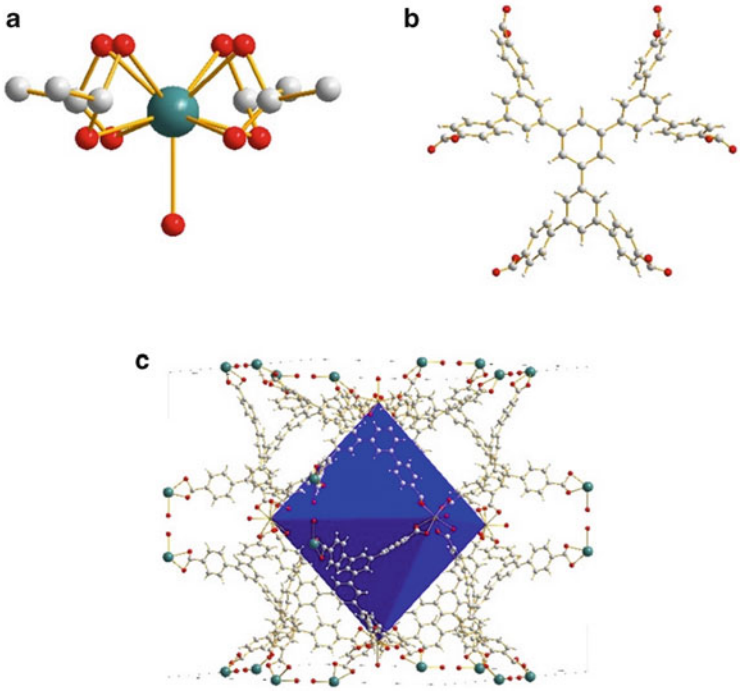

Fig. 10 (**a**) Tb^{3+} SBU; (**b**) 1,3,5-tris(3,5-di(4-carboxyphenyl)phenyl)benzene; (**c**) USTA-61 showing octahedral cavity. Color scheme: C (*white*), O (*black*), Tb (*gray*)

framework is required for many applications, though for magnetic study 1D and 2D coordination polymer networks are often as or more interesting.

3.2.1 Magnetic Ln-MOFs

Recent studies of magnetic MOFs have concentrated on those using transition metals, due to greater understanding of the magnetic properties of such ions. However, an overlap between the research communities studying the magnetic properties of lanthanide clusters and those studying magnetism in MOFs has emerged, due to the synthesis and magnetic characterization of a variety of Ln-MOFs. In $[NH_2Me_2][Ln(\mathbf{mdip})(H_2O)]$ (Ln = Pr, Nd, Sm, Eu, Gd, Tb, Dy; $H_4\mathbf{mdip}$ = methylenediisophthalic acid) and $[NH_2Me_2][Ln(\mathbf{mdip})(H_2O)] \cdot 0.5NHMe_2$ (Ln = Er, Tm, Yb), negative Weiss constants for the magnetic susceptibility measurements show very weak antiferromagnetic interactions between Gd^{3+} ions, coupled along a Gd^{3+}-carboxylate chain [47]. $[Ln_2(\mathbf{bpdc})(\mathbf{bdc})_2(H_2O)_2]_n$ (Ln = Gd, Dy, Ho, Er), a mixed-ligand lanthanide MOF, was reported to also show weak antiferromagnetic interaction between Gd^{3+} ions at very low temperatures [46]. $[Ln_2(\mathbf{pam})_3(DMF)_2(H_2O)_2]_n \cdot n$DMF {Ln = Gd, Dy;

H_2**pam** = 4, 4′-methylenebis[3-hydroxy-2-naphthalenecarboxylic acid]}also shows weak antiferromagnetic interactions between the Gd^{3+} centers, with a room temperature $\chi_M T$ value of 15.36 $cm^3\ mol^{-1}$ K, while no antiferromagnetic coupling is found in the Dy^{3+} framework [48].

3.2.2 Magnetic Ln-TM MOFs

Much effort has been contributed to the synthesis and characterization of heteronuclear compounds using both transition metal ions and lanthanides. An important reason for this was the findings of Kahn and Gatteschi that Gd^{3+} and Cu^{2+} ions bridged together in a metal complex interacted ferromagnetically [49]. This seemed unlikely, because any overlap between a 4*f* orbital on Gd^{3+} and a 3*d* orbital on Cu^{2+} should produce an antiferromagnetic interaction instead. However, because the 4*f* shell is shielded by the 5*s* and 5*p* orbitals, no orbital overlap between the 4*f* orbitals and the transitions metals is possible. Instead, the half-filled $d_{x^2-y^2}$ orbital of Cu^{2+} overlaps with an empty 5*d* orbital of Gd^{3+}, with the ferromagnetic exchange being energetically favored [50, 51]. This has led to the development of many other mixed-metal units with interactions between 3*d* transition metals and lanthanides, with theoretical work focused on coupling between Gd^{3+} and transition metals due to large orbital angular momentum contributions in other lanthanides [37].

Recently, several extended Ln-TM frameworks with magnetic interactions similar to those described above have been reported, in an attempt to synthesize materials with novel coupling pathways between the 3*d* and 4*f* metal ions. A representative example includes $[Cu_3Ln_2(\mathbf{ip})]$(Ln = Eu, Gd), which is also a rare example of a Ln-TM framework made purely from carboxylate bridging ligands, to cap the SBUs [36]. An example of a non-nitrogen based Ln-TM MOF is $[\{Cu_3Ln_2(\mathbf{oda}))_6(H_2O)_6\}\cdot 12H_2O]_n$ (Ln = Y, Gd, Eu, Nd, Pr, Dr, Er), where **oda** means oxydiacetate [52]. This MOF not only demonstrates porosity in its honeycomb of solvent-filled 3D channels but also features weak antiferromagnetic interaction. However, by far the most common category of Ln-TM MOFs found is ones using *N*-donor and carboxylate groups in the same ligand, such as pyridine-based carboxylic acids. A typical example of a Ln–Cu frameworks using isonicotinic acid as a linker is $[Ln_{14}(\mu_6\text{-}O)(\mu_3\text{-}OH)_{20}(\mathbf{ina})_{22}Cu_6Cl_4(H_2O)_8]\cdot 6H_2O$ (Ln = Y, Gd, Dy, **ina** = isonicotinic acid) [53]. In this framework, $Ln_{14}(\mu_6\text{-}O)(\mu_3\text{-}OH)_{20}$ clusters linked by isonicotinic acid show antiferromagnetism between the Gd^{3+} or Dy^{3+} ions.

More recently, $\{[Co(H_2O)_6]\cdot[Ln_2(\mathbf{oda})_6Co_2]\cdot 6H_2O\}o_n$ [1; Ln = Gd, Dy, and Er], $\{[Ln_2(\mathbf{oda})_6Cd_3(H_2O)_6]\cdot mH_2O\}_n$ [Ln = Pr, Nd, Sm, Eu, and Dy, *m* = 9, 6, or 3], and $\{[Cd(H_2O)_6]\cdot[Ln_2(\mathbf{oda})_6Cd_2]\cdot mH_2O\}_n$ [Ln = Dy, Ho, Er, Tm, and Lu, *m* = 6 or 12], three isoreticular series of Ln-Cd/Co frameworks starting from the Ln metalloligand $[Ln(\mathbf{oda})_3]^{3-}$, were synthesized and among which showed ferromagnetic interactions between lanthanide and Co metal centers through the bridging ligands at 1.8 K [54]. $\{[(CH_3)_2NH_2]_3[Co_3Ln(\mathbf{tda})_3(HCOO)_3]\cdot 2H_2O\cdot 0.75DMF\}_n$

[Ln = Eu, Gd, Tb, and Dy; H_3**tda** = 1H-1,2,3-triazole-4,5-dicarboxylic acid] MOFs were also recently synthesized, with antiferromagnetic ordering shown at very low temperatures [55].

In general, these frameworks can demonstrate both porosity and significant magnetic interactions between Ln and transition metals. However the large degree of physical separation between the Ln and TM ions prohibits direct ferromagnetic interactions shown between Gd^{3+} and Cu^{2+} which were the product of direct orbital overlap [50, 51]. As discussed above, Ln-TM interactions through the bridging ligands have been shown, but only at extremely low temperatures thus far.

3.3 Luminescence

Traditional luminescent materials have been extensively explored and employed for their applications in light, display, sensing, and optical devices. The unique luminescence is attributed to the narrow emission and high color purity from the rare earth ions [56]. Several electronic transitions contribute to the observed luminescent properties including inner shell 4*f*–4*f* transitions, 4*f*–5*d* charge transfer, and other charge-transfer transitions (e.g., ligand-to-metal charge transfer LMCT and metal-ligand charge transfer MLCT) [57]. The luminescent emissions of the several Ln^{3+} ions are well known with Eu^{3+} emitting red light, Tb^{3+} green, Sm^{3+} orange, Tm^{3+} blue; Yb^{3+}, Nd^{3+}, and Er^{3+} emitting near-infrared luminescence; and no emission from La^{3+} and Lu^{3+} [56]. In MOFs, all components of the framework and even guest molecules can contribute to luminescence. The ability to structurally tune these features in Ln-MOFs has led to the development of new materials for chemical sensors and light-emitting devices [41]. An abundance of luminescent Ln-MOFs have been reported; however, an in-depth discussion is beyond the scope of this introduction and a few representative samples will be discussed.

A series of luminescent frameworks have been synthesized from the reaction of Ln^{3+} metals salt with 4,4′-(hexafluoroisopropylidene)bis(benzoic acid) (H_2**hfipbb**) to form [Ln_2(**hfipbb**)$_3$] (Ln = Y, La, Ce, Pr, Nd, Sm, Eu, Gd, Tb, Dy, Ho, Er, Yb) (Fig. 11) [58]. Upon UV excitation, the bluish-white emission of the ligand is observed with most metals except Eu, Tb, and Gd, with red, green, white emission, respectively. The propensity for light emission is most likely due to the separation of Ln ions in the chain SBUs which prevent quenching.

The shielding of the 4*f* orbitals in lanthanide ions, in which optical transitions occur, by the 5*s* and 5*p* orbitals leads to sharp emissions; however, due to weak photon adsorption direct excitation is often inefficient. Ln-MOFs offer the ability to utilize optical active Ln metal ions with organic linkers that facilitate through emission sensitization. Recent studies have attempted to utilize the so-called "antenna effect" in which direct excitation of a sensitized ligand leads to nonradiative transfers of energy to excite a Ln ion which can release energy through the emission of a photon [59]. One such mixed-metal Ln-MOF, $Ba_2(H_2O)_4[LnL_3(H_2O)_2](H_2O)_nCl$ (Ln = Sm^{3+}, Eu^{3+}, Gd^{3+}, Tb^{3+}, Dy^{3+}), in which 4,4′-disulfo-2,2′-bipyridine-*N*′*N*′-dioxide was used to successfully sensitize all the Ln ions except

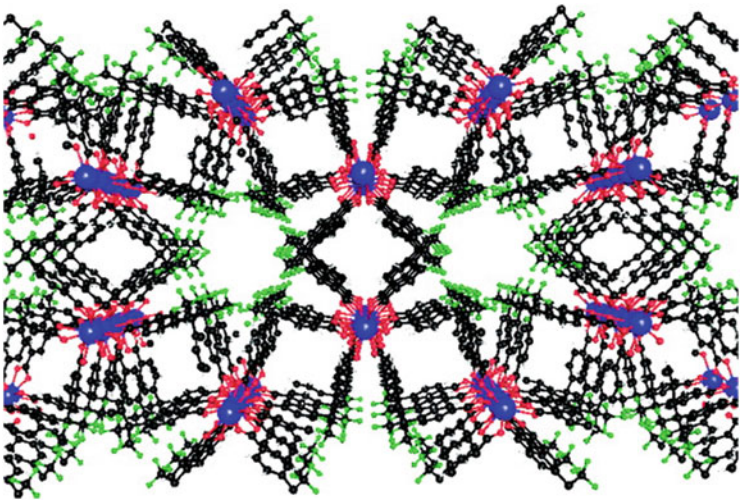

Fig. 11 Structure of a luminescent Ln-MOF [Ln_2(**hfipbb**)$_3$]. Color scheme: Ln (Ln = Y, La, Ce, Pr, Nd, Sm, Eu, Gd, Tb, Dy, Ho, Er, Yb) (*blue*); C (*black*); O (*red*); F (*green*). (Reprinted with permission from Gándara et al. [58], copyright © 2008 American Chemical Society)

Gd^{3+} [60]. Through the incorporation of luminescent Ln building blocks and photosensitizing organic linkers, many new Ln-MOFs may be obtained with interesting luminescent properties. Further analysis of luminescent Ln-MOFs will be provided in Zhang et al. [61].

4 Applications of Ln-MOFs

Through the judicious selection of metal-containing components and organic linkers, the structure and properties of MOFs can be systematically tuned and used for specific applications. The uniform and tunable pore size gives MOFs great potential be applied into a broad range of application, such as catalysis, small molecule sensing, drug delivery, gas storage/capture and separation, luminescence, and magnetic materials [62].

4.1 Gas Storage

Traditional MOFs based on transition metals have shown great potential for gas storage due to their highly porous nature and yield a large surface area for gas–host interactions. The ability to tune pore size and shape is advantageous for gas storage.

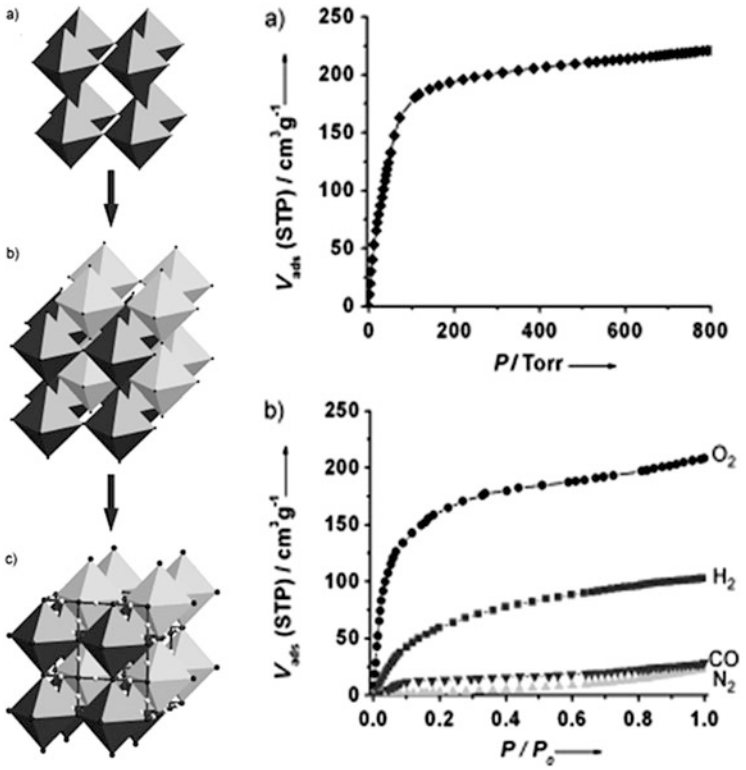

Fig. 12 Interpenetrated structure of PCN-17 (Yb) and gas uptake isotherms (*Top*: CO_2, 195 K; *Bottom*: gas uptake, 77 K). (Reprinted with permission from Ma et al. [63], copyright © 2008 Wiley-VCH Verlag GmbH & Co. KGaA, Weinheim)

Unfortunately, traditional MOFs, especially those composed of copper, zinc, and cobalt, often have limited chemical and thermal stability. The incorporation of lanthanide metal ions with carboxylate linkers improves stability due to the affinity to polarize the O atom causing strong metal-oxygen bonds. Although there are a multitude of useful gases for commercial storage applications, our discussion will be limited to H_2, N_2, CO, and CO_2. Several features can be incorporated into the framework to facilitate favorable gas interaction including framework interpenetration, functional channel walls, and coordinatively unsaturated metal centers (UMCs).

The aforementioned PCN-17 (Fig. 8), an interpenetrated Ln-MOF, exhibits high thermal stability and gas adsorption [63]. Although four isostructural PCN-71 MOFs (Dy, Er, Y, Yb) have been reported, PCN-17 (Yb) will be the focus of this discussion with the other isostructural frameworks having comparable uptake. The framework consists of doubly interpenetrated (8,3)-nets composed of octahedral cages (Fig. 12). The framework has pore size of approximately 3.5 Å and a Brunauer–Emmett–Teller (BET) surface area of 820 m^2 g^{-1} calculated from the

CO_2 adsorption at 195 K. Adsorption of H_2, N_2, O_2, and CO at 77 K demonstrates an apparent selectivity of O_2 over N_2 and a moderate uptake of hydrogen (105 cm^3 g^{-1}) (Fig. 12). These results are most likely due to size selection, with a pore opening of 3.5 Å, N_2 and CO were mostly excluded (kinetic diameter of 3.64 and 3.76 Å, respectively). Another Ln-MOF $[Y_2(\mathbf{tpbtm})(H_2O)_2]\cdot xG$, ($G$ = guest molecule) (NJU-Bai11) has been synthesized from an acylamide-functionalized ligand *N*,*N*′,*N*″-tris(isophthalyl)-1,3,5,-benzenetricarboxamide (**tpbtm**) [64]. The incorporation of nitrogen functionalities into the channel walls has led to increased CO_2 uptake due to the CO_2-philic interaction from the polarization of the gas molecules. NJU-Bai11 exhibits a BET surface area of 1,152.1 m^2 g^{-1} (N_2, 77 k) with high CO_2 and H_2 uptake of 130.0 cm^3 g^{-1} (1 bar, 273 K) and 160.0 cm^3 g^{-1} (1 bar, 77 K), respectively. However, low nitrogen uptake of 4.9 cm^3 g^{-1} (1 bar, 273 K) is observed, yielding framework with high CO_2/N_2 selectivity due to the affinity of the alkylamide chains to preferentially interact with CO_2 over N_2. Lastly, Ln(**btc**)$(H_20)\cdot(DMF)_{1.1}$ (Ln = Y, Tb, Dy, Er, Yb) have been prepared and exhibit moderate surface areas with exposed UMCs and high thermal stability. The BET surface areas of these isostructural Ln-MOFs range from 774 cm^3 g^{-1} (Er) to 1,080 cm^3 g^{-1} (Y) calculated from Ar isotherms (87 K). Moderate hydrogen uptakes (1 bar, 77 K) of 1.79 (Y), 1.45 (Tb), 1.40 (Dy), 1.51 (Er), and 1.41 (Yb) wt % were reported.

4.2 Catalysis

Ln-MOFs have considerable potential for catalytic applications, due to their similarity to other MOFs that form SBUs with UMCs, which can possess Lewis acidic sites that are easily functionalized with Lewis basic and other groups within the pores [65]. Furthermore, unlike many other metals, lanthanide metal ions can have wide variation and tunability in their coordination number and modes, producing novel catalytic centers [66]. Most importantly, it is common to see many different Ln^{3+} ions forming a single isostructural series of frameworks, and variation of the Ln^{3+} ion used can often tune the catalytic activity, as shown below. However, to function as catalysts, MOFs must be highly chemically and thermally stable [67]. Demonstration of high catalytic activity is encouraging, but promising MOF catalysts must also demonstrate that catalytic activity remains high over repeated trials and over time. Several recent studies of Ln-MOF catalysts will be described, some of which include encouraging further study of their high framework stability.

For example, $[Ln_2(\mathbf{dpa})_3(H_2O)]\cdot 2H_2O$ [Ln = La, Ce, Pr, Nd, Sm, Eu, Gd, Tb, Dy, Ho, Er, Tm, and Yb; H_2**dpa** = 1,4-phenylenediacetate] was synthesized in mixed water/dimethylacetamide solvent, and demonstrated stability to air, water, and other solvents. This Ln-MOF series demonstrates thermal stability to 450°C, and chemical stability to repeated hydration/dehydration cycles. $[Tb_2(\mathbf{dpa})_3]$ showed 78 % conversion of benzaldehyde to 1,1-dimethoxytoluene in methanol

in 10 h, unlike other isostructural Ln-MOFs, which have shown much lower catalytic activity for this reaction [65]. This demonstrates one of the main advantages of Ln-MOFs – since many Ln-MOFs show great variability in which Ln^{3+} ion can be used in their isostructural frameworks, many of them can easily be tried until a metal energetically suitable for a particular reaction is found. A detailed discussion of how the different energy levels of Lewis acidic catalysts render them suitable for different catalysis, and how they can be tuned, will not be discussed. However, the facile variation of which ligand and lanthanide is used in an isostructural framework provides a convenient platform for fast experimentation, allowing a wide variety of potentially novel catalysis to be explored. Ln-MOFs provide a good platform for the systematic study of how such variation in the catalytic environment changes catalytic behavior. For example, in Ln-sulfonate MOFs, catalysis requiring redox and acid sites, such as the sulfide oxidation, occurs only when the Ln coordination number is below 9, and so $[Ln_2(C_2H_4C_2O_4)_2(SO_4)(H_2O)_2]$, (RPF-16), (Ln = La, Pr, Nd, Sm) with a coordination number of 9 on the lanthanides demonstrated no activity for such reactions. High activity toward reduction of nitro groups with H_2 was demonstrated with high recyclability and stability of the catalyst [68].

A systematic study of three isostructural Ln-MOFs using 3,5-disulfobenzoic acid, RPF-21, −22, and −23 has shown thermal stability of 460–540°C with significantly higher catalytic activity for RPF-21 for the cyanosilation of several aldehydes. Notably, this difference remained regardless of what lanthanide was used. RPF-21 has a coordination number of 9, higher than RPF-22 and −23, and 5 of those positions by water, indicating aldehyde displacement of water was a necessary step in the reaction. In this case, the framework's structural differences were more important to the reaction than the tuning provided by changing the metal, which produced only small differences in turnover frequency (TOF) and yield [69]. Tuning the catalytic activity of a set of Ln-MOFs for reaction of trimethylsilyl cyanide with various aldehydes was also done for $[Ln_2(\textbf{mell})(H_2O)_6]$ by altering which Ln^{3+} ion and which solvent was used, with $[Eu_2(\textbf{mell})(H_2O)_6]$ in acetonitrile demonstrating high catalytic activity and recyclability [70].

4.3 Chemical Sensors

The interesting optical properties of Ln-MOFs have led to their use in a variety of chemical sensing applications including luminescent probes and sensors. Of particular interest is sensing of cations, anions, and small molecules that can easily be incorporated into the pores of the framework and reversibly released to provide a regenerable chemical sensor. Size selectivity due to pore size and the promotion of host–guest interactions from functional sites and UMCs make Ln-MOFs an attractive material with enhanced luminescence [56].

A Ln-MOF $[Eu(\textbf{pdc})_{1.5}(DMF)]$ (**pdc** = pyridine-3,5,dicarboxylate) has been reported, constructed with Lewis basic pyridyl sites for metal ion sensing

[71]. Luminescent quenching was observed upon incorporation of metal ions into the framework, with transition metal ions having variable effects on luminescence intensity. Alkali and alkaline-earth metals have no effect on luminescence due to the inability to coordinate to the pyridyl group. Quenching is observed for several transition metals (Co^{2+}, Mn^{2+}, Cu^{2+}); however, further investigation is needed for selective metal ion probes. Cu^{2+} ions contribute to noticeable quenching, with reduction of luminescent intensity corresponding proportionally to the metal ion concentration. Further investigation of immobilized Lewis basic site in the framework may lead to tunable metal sensing.

Another example MOF-76, Tb(**btc**)$(H_2O)_{1.5}$(DMF), has been synthesized from the trigonal tritopic linker, **btc** with Tb^{3+} ions in mixed solvent system of DMF, ethanol, and water [27]. MOF-76 is composed of seven-coordinated rod SBUs with each Tb^{3+} ion connected with six carboxyl groups and one water. The resulting framework has a 1-D 6.6 × 6.6 Å channel. Anion exchange within the framework has been studied in order to elucidate anion effects on luminescence [72]. The incorporation of F^- ions into the framework enhances the luminescence of the parent framework leading to the potential of anion sensing. The contributions to luminescence are ascribed to the decrease in quenching from guest solvent molecules (methanol).

Lastly, Eu(**btc**)$(H_2O)\cdot 1.5H_2O$, isostructural with MOF-76, has been prepared and studied for small molecule sensing applications [73]. Several common solvents including DMF, acetone, chloroform, methanol, ethanol, tetrahydrofuran, acetonitrile, 1-propanol, and 2-propanol were studied using photoluminescence spectroscopy. Using 1-propanol as a control, the effects of the addition of DMF and acetone to the system were observed contributing to luminescence enhancement and quenching, respectively. The effects on luminescence are due to the coordinating nature of the solvent and may lead to the potential for small molecule sensing applications based on sieving properties.

5 Summary

This chapter has provided a brief overview of the preparation, properties, and applications of Ln-MOFs. Insight from the synthesis of traditional MOFs can be translated to Ln-MOF synthesis; however, rational design is limited due to various coordination modes of the lanthanide metal ions. Ln-MOFs show great promise in photoluminescent, catalytic, and magnetic applications; however further exploration of Ln-MOFs may lead to other possible applications. Although a large number of Ln-MOFs have been reported, these materials have been far less studied than MOFs composed of transition metals. Further investigations are necessary to fully utilize the potential of these materials and to continue to build upon their existing applications.

Acknowledgements The authors would like to acknowledge Texas A&M University, and our financial sponsors the United States Department of Energy (DOE), the United States Office of Naval Research (ONR), and the Welch Foundation. We would also like to acknowledge Zachary Perry, Weigang Lu, Muwei Zhang, and Lizzie West for assistance in the preparation of this chapter.

References

1. Batten SR, Champness NR, Chen X-M et al (2013) Terminology of metal-organic frameworks and coordination polymers (IUPAC Recommendations 2013). Pure Appl Chem 85:1715–1724
2. Kitagawa S, Kitaura R, Noro S-I (2004) Functional porous coordination polymers. Angew Chem Int Ed 43(18):2334–2375
3. Zhang M, Chen Y-P, Bosch M et al (2014) Symmetry-guided synthesis of highly porous metal-organic frameworks with fluorite topology. Angew Chem Int Ed 53(3):815–818
4. Feng X, Ding X, Jiang D (2012) Covalent organic frameworks. Chem Soc Rev 41(18): 6010–6022
5. Lee J, Farha OK, Roberts J et al (2009) Metal-organic framework materials as catalysts. Chem Soc Rev 38(5):1450–1459
6. Murray LJ, Dinca M, Long JR (2009) Hydrogen storage in metal-organic frameworks. Chem Soc Rev 38(5):1294–1314
7. Zhou H-C, Long JR, Yaghi OM (2012) Introduction to metal-organic frameworks. Chem Rev 112(2):673–674 (Washington, DC, US)
8. Lee Y-R, Kim J, Ahn W-S (2013) Synthesis of metal-organic frameworks: a mini review. Korean J Chem Eng 30(9):1667–1680
9. Makal TA, Yuan D, Zhao D et al (2011) Metal-organic frameworks. In: Yang P (ed) The chemistry of nanostructured materials, vol II. World Scientific, Singapore, pp 37–64
10. Biemmi E, Christian S, Stock N et al (2009) High-throughput screening of synthesis parameters in the formation of the metal-organic frameworks MOF-5 and HKUST-1. Microporous Mesoporous Mater 117(1–2):111–117
11. Li H, Eddaoudi M, O'Keeffe M et al (1999) Design and synthesis of an exceptionally stable and highly porous metal-organic framework. Nature 402(6759):276–279
12. Eddaoudi M, Kim J, Rosi N et al (2002) Systematic design of pore size and functionality in isoreticular MOFs and their application in methane storage. Science 295(5554):469–472
13. Chui SS-Y, Lo SM-F, Charmant JPH et al (1999) A chemically functionalizable nanoporous material $[Cu_3(TMA)_2(H_2O)_3]n$. Science 283(5405):1148–1150
14. Férey G, Mellot-Draznieks C, Serre C et al (2005) A chromium terephthalate-based solid with unusually large pore volumes and surface area. Science 309(5743):2040–2042
15. Cavka JH, Jakobsen S, Olsbye U et al (2008) A new zirconium inorganic building brick forming metal organic frameworks with exceptional stability. J Am Chem Soc 130(42):13850–13851
16. Stock N, Biswas S (2012) Synthesis of metal-organic frameworks (MOFs): routes to various MOF topologies, morphologies, and composites. Chem Rev 112(2):933–969 (Washington, DC, US)
17. Jhung SH, Lee JH, Yoon JW et al (2007) Microwave synthesis of chromium terephthalate MIL-101 and its benzene sorption ability. Adv Mater 19(1):121–124 (Weinheim, Ger.)
18. Kerner R, Palchik O, Gedanken A (2001) Sonochemical and microwave-assisted preparations of PbTe and PbSe. A comparative study. Chem Mater 13(4):1413–1419
19. Son W-J, Kim J, Kim J et al (2008) Sonochemical synthesis of MOF-5. Chem Commun 47:6336–6338 (Cambridge, UK)

20. Mueller U, Schubert M, Teich F et al (2006) Metal-organic frameworks-prospective industrial applications. J Mater Chem 16(7):626–636
21. Martinez Joaristi A, Juan-Alcañiz J, Serra-Crespo P et al (2012) Electrochemical synthesis of some archetypical Zn^{2+}, Cu^{2+}, and Al^{3+} metal organic frameworks. Cryst Growth Des 12(7): 3489–3498
22. Tranchemontagne DJ, Mendoza-Cortes JL, O'Keeffe M et al (2009) Secondary building units, nets and bonding in the chemistry of metal-organic frameworks. Chem Soc Rev 38(5): 1257–1283
23. Lu W, Wei Z, Gu Z-Y et al (2014) Tuning the structure and function of metal-organic frameworks via linker design. Chem Soc Rev 43:5561–5593. doi:10.1039/C1034CS00003J
24. Gagnon KJ, Perry HP, Clearfield A (2011) Conventional and unconventional metal-organic frameworks based on phosphonate ligands: MOFs and UMOFs. Chem Rev 112(2):1034–1054 (Washington, DC, US)
25. Shimizu GKH, Vaidhyanathan R, Taylor JM (2009) Phosphonate and sulfonate metal organic frameworks. Chem Soc Rev 38(5):1430–1449
26. Yaghi OM, O'Keeffe M, Ockwig NW et al (2003) Reticular synthesis and the design of new materials. Nature 423(6941):705–714
27. Rosi NL, Kim J, Eddaoudi M et al (2005) Rod packings and metal-organic frameworks constructed from rod-shaped secondary building units. J Am Chem Soc 127(5):1504–1518
28. Caskey SR, Wong-Foy AG, Matzger AJ (2008) Dramatic tuning of carbon dioxide uptake via metal substitution in a coordination polymer with cylindrical pores. J Am Chem Soc 130(33): 10870–10871
29. Deng H, Grunder S, Cordova KE et al (2012) Large-pore apertures in a series of metal-organic frameworks. Science 336(6084):1018–1023
30. Férey G, Serre C, Mellot-Draznieks C et al (2004) Angew Chem Int Ed 436296
31. Kim M, Cahill JF, Su Y et al (2012) Postsynthetic ligand exchange as a route to functionalization of 'inert' metal-organic frameworks. Chem Sci 3(1):126
32. Wang C, Wang JL, Lin W (2012) Elucidating molecular iridium water oxidation catalysts using metal-organic frameworks: a comprehensive structural, catalytic, spectroscopic, and kinetic study. J Am Chem Soc 134(48):19895–19908
33. Pearson RG (1990) Hard and soft acids and bases—the evolution of a chemical concept. Coord Chem Rev 100:403–425
34. Daiguebonne C, Kerbellec N, Guillou O et al (2008) Structural and luminescent properties of micro- and nanosized particles of lanthanide terephthalate coordination polymers. Inorg Chem 47(9):3700–3708
35. Chen L, Jiang F, Zhou K, Wu M, Hong M (2014) Metal-organic frameworks based on lanthanide clusters. Struct Bond. doi:10.1007/430_2014_161
36. Luo F, Batten SR, Che Y et al (2007) Synthesis, structure, and characterization of three series of 3d–4f metal-organic frameworks based on rod-shaped and (6,3)-sheet metal carboxylate substructures. Chemistry 13(17):4948–4955
37. Huang Y-G, Jiang F-L, Hong M-C (2009) Magnetic lanthanide–transition-metal organic–inorganic hybrid materials: from discrete clusters to extended frameworks. Coord Chem Rev 253(23–24):2814–2834
38. Shi W, Liu K, Cheng P (2014) Transition-lanthanide heterometal-organic frameworks: synthesis, structures and properties. Struct Bond. doi:10.1007/430_2014_157
39. Zhang M, Bosch M, Gentle T III et al (2014) Rational design of metal-organic frameworks with anticipated porosities and functionalities. CrystEngComm 16(20):4069–4083
40. Ferey G (2008) Hybrid porous solids: past, present, future. Chem Soc Rev 37(1):191–214
41. Chen Y, Ma S (2012) Microporous lanthanide metal-organic frameworks. Rev Inorg Chem 32(2–4):81
42. Han Y, Li X, Li L et al (2010) Structures and properties of porous coordination polymers based on lanthanide carboxylate building units. Inorg Chem 49(23):10781–10787

43. Ma S, Yuan D, Wang X-S et al (2009) Microporous lanthanide metal-organic frameworks containing coordinatively linked interpenetration: syntheses, gas adsorption studies, thermal stability analysis, and photoluminescence investigation. Inorg Chem 48(5):2072–2077
44. Li B, Chen B (2014) Porous lanthanide metal-organic frameworks for gas storage and separation. Struct Bond. doi:10.1007/430_2014_159
45. Park YK, Choi SB, Kim H et al (2007) Crystal structure and guest uptake of a mesoporous metal-organic framework containing cages of 3.9 and 4.7 nm in diameter. Angew Chem Int Ed 46(43):8230–8233
46. Zhou J-M, Li H-M, Xu N et al (2013) Construction of lanthanide multi-functional metal–organic frameworks via mixed ligand approach: syntheses, structures, magnetic and luminescent properties. Inorg Chem Commun 37:30–33
47. Su S, Chen W, Qin C et al (2012) Lanthanide anionic metal–organic frameworks containing semirigid tetracarboxylate ligands: structure, photoluminescence, and magnetism. Cryst Growth Des 12(4):1808–1815
48. Biswas S, Jena HS, Goswami S et al (2014) Synthesis and characterization of two lanthanide (Gd^{3+} and Dy^{3+})-based three-dimensional metal organic frameworks with squashed metallomacrocycle type building blocks and their magnetic, sorption, and fluorescence properties study. Cryst Growth Des 14(3):1287–1295
49. Bencini A, Benelli C, Caneschi A et al (1985) Crystal and molecular-structure of and magnetic coupling in 2 complexes containing gadolinium(III) and copper(II) ions. J Am Chem Soc 107(26):8128–8136
50. Pei Y, Journaux Y, Kahn O et al (1986) A Mn-II-Cu-II-Mn-II trinuclear species with an S = 9/2 ground-state. J Chem Soc Chem Commun 16:1300–1301
51. Benelli C, Caneschi A, Gatteschi D et al (1990) Synthesis, crystal-structure, and magnetic-properties of tetranuclear complexes containing exchange-coupled Gd_2cu_2, Dy_2cu_2 species. Inorg Chem 29(9):1750–1755
52. Rizzi A, Baggio R, Calvo R et al (2001) Synthesis, crystal structure, and magnetic properties of the mixed-ligand complex [$Gd(CF_3CO_2)(3)(phen)(2)(H_2O)$]. Inorg Chem 40(14):3623–3625
53. Zhang M-B, Zhang J, Zheng S-T et al (2005) A 3D coordination framework based on linkages of nanosized hydroxo lanthanide clusters and copper centers by isonicotinate ligands. Angew Chem Int Ed 44(9):1385–1388
54. Huang X-F, Ma J-X, Liu W-S (2014) Lanthanide metalloligand strategy toward d–f heterometallic metal–organic frameworks: magnetism and symmetric-dependent luminescent properties. Inorg Chem 53(12):5922–5930
55. Zou J-Y, Shi W, Xu N et al (2014) Cobalt(II)–lanthanide(III) heterometallic metal–organic frameworks with unique (6,6)-connected Nia topologies with 1H-1,2,3-triazole-4,5-dicarboxylic acid: syntheses, structures and magnetic properties. Eur J Inorg Chem 2014(2):407–412
56. Cui Y, Yue Y, Qian G et al (2011) Luminescent functional metal–organic frameworks. Chem Rev 112(2):1126–1162 (Washington, DC, US)
57. Bünzli J-CG (2010) Lanthanide luminescence for biomedical analyses and imaging. Chem Rev 110(5):2729–2755 (Washington, DC, US)
58. Gándara F, Andrés AD, Gómez-Lor B et al (2008) A rare-earth MOF series: fascinating structure, efficient light emitters, and promising catalysts. Cryst Growth Des 8(2):378–380
59. Whan RE, Crosby GA (1962) Luminescence studies of rare earth complexes: benzoylacetonate and dibenzoylmethide chelates. J Mol Spectrosc 8(1–6):315–327
60. Chandler BD, Cramb DT, Shimizu GKH (2006) Microporous metal–organic frameworks formed in a stepwise manner from luminescent building blocks. J Am Chem Soc 128(32):10403–10412
61. Song X-Z, Song S-Y, Zhang H-J (2014) Luminescent lanthanide metal-organic frameworks. Struct Bond. doi:10.1007/430_2014_160
62. Horcajada P, Gref R, Baati T et al (2011) Metal–organic frameworks in biomedicine. Chem Rev 112(2):1232–1268 (Washington, DC, US)

63. Ma S, Wang X-S, Yuan D et al (2008) A coordinatively linked Yb metal–organic framework demonstrates high thermal stability and uncommon gas-adsorption selectivity. Angew Chem Int Ed 47(22):4130–4133
64. Tang K, Yun R, Lu Z et al (2013) High CO_2/N_2 selectivity and H_2 adsorption of a novel porous yttrium metal–organic framework based on N,N′,N″-tris(isophthalyl)-1,3,5-benzenetricarboxamide. Cryst Growth Des 13(4):1382–1385
65. Ren Y-W, Liang J-X, Lu J-X et al (2011) 1,4-Phenylenediacetate-based Ln MOFs – synthesis, structures, luminescence, and catalytic activity. Eur J Inorg Chem 2011(28):4369–4376
66. Shibasaki M, Yamada K-I, Yoshikawa N (2008) Lanthanide lewis acids catalysis, Lewis acids in organic synthesis. Wiley-VCH Verlag GmbH, Weinheim, pp 911–944
67. Gascon J, Corma A, Kapteijn F et al (2013) Metal organic framework catalysis: quo vadis? ACS Catal 4(2):361–378
68. D'Vries RF, Iglesias M, Snejko N et al (2012) Mixed lanthanide succinate-sulfate 3D MOFs: catalysts in nitroaromatic reduction reactions and emitting materials. J Mater Chem 22(3): 1191–1198
69. D'Vries RF, de la Peña-O'Shea VA, Snejko N et al (2012) Insight into the correlation between net topology and ligand coordination mode in new lanthanide MOFs heterogeneous catalysts: a theoretical and experimental approach. Cryst Growth Des 12(11):5535–5545
70. Batista PK, Alves DJM, Rodrigues MO et al (2013) Tuning the catalytic activity of lanthanide-organic framework for the cyanosilylation of aldehydes. J Mol Catal A Chem 379:68–71
71. Chen B, Wang L, Xiao Y et al (2009) A luminescent metal–organic framework with lewis basic pyridyl sites for the sensing of metal ions. Angew Chem Int Ed 48(3):500–503
72. Chen B, Wang L, Zapata F et al (2008) A luminescent microporous metal–organic framework for the recognition and sensing of anions. J Am Chem Soc 130(21):6718–6719
73. Chen B, Yang Y, Zapata F et al (2007) Luminescent open metal sites within a metal–organic framework for sensing small molecules. Adv Mater 19(13):1693–1696 (Weinheim, Ger.)

Struct Bond (2015) 163: 29–74
DOI: 10.1007/430_2014_163

Published online: 25 October 2014

Chiral Lanthanide Metal-Organic Frameworks

Weisheng Liu and Xiaoliang Tang

Abstract Chiral metal-organic frameworks (MOFs) have attracted much attention, not only due to their potential applications in enantioselective separation and catalysis, but also because of many advantages such as the high density of active catalytic centers, high level of porosity, regular and reliable crystalline nature, and relatively easy immobilization as compared to other heterogeneous systems. As metal-connecting nodes of MOFs, a large number of chemical synthetic strategies have focused on the transition metal ions which exhibit specific coordination geometries and restricted stereochemistry in the past two decades. However, the researches on chiral lanthanide MOFs are still limited up to now because of high coordination numbers, kinetic lability, weak stereochemical preference, and more variable nature of the coordination sphere for lanthanide ions. In this chapter, we would give a brief introduction to highlight the synthetic approaches reported and the structural features of chiral lanthanide MOFs or coordination polymer, which may be beneficial to explore structurally and functionally defined chiral solid materials.

Keywords Chiral metal-organic frameworks · Chirality · Lanthanide · Structures of MOFs · Synthesis of MOFs

Contents

W. Liu (✉) and X. Tang
College of Chemistry and Chemical Engineering, Lanzhou University, Lanzhou 730000, P. R. China
e-mail: liuws@lzu.edu.cn

1 The Status and Advantage of Chiral Solid Material

Chirality is "a signature of life," which is one of the intrinsic features of nature and is considered to play a decisive role in life sciences [1–3]. From the small molecule to the infinite universe, chirality exists in different levels of matter—configurational chirality, conformational chirality, phase chirality, and object chirality. Among them, the first level of chirality related to the chiral center is the most fundamental chiral source, and the higher levels of chirality are derived from chiral stacking or combination of the lower levels [4].

The chirality induction, inversion, and transfer occur at various levels. For example, at a molecular level, chirality represents an intrinsic property of the "building blocks of life," such as amino acids and sugars, and therefore, of peptides, proteins, and polysaccharides. And a higher level of DNA double helices is representative of effective chirality switches active in several biochemical processes. Almost all of important biological molecules with life activities and important physiological functions show chiral recognition and catalysts [5–8]. As a consequence, metabolic and regulatory processes mediated by biological systems are sensitive to stereochemistry and many biological receptors preferentially recognize a single enantiomeric form, whose biological activity is often drastically different from the other in some cases [9]. For instance, the drug thalidomide, prescribed to many pregnant women in the 1950s, was subsequently found to have an *R*-enantiomer with desirable sedative properties, whereas its *S*-enantiomer was shown to be teratogenic and induced fetal malformations [9, 10]. Therefore, the nature and origin of chirality need to be understood deeply at different levels, and the synthesis methods of enantiomerically pure (enantiopure) compounds with pharmacological values need to be sought and developed more effectively and rapidly.

Control of chirality is one of the most sophisticated processes in artificial and biological systems, in which chirality information controls structures and functions of various molecules and assemblies at the molecular, supramolecular, and macromolecular levels. Many research works have been carried out in control of chirality, and of particular note is that the Nobel Prize in Chemistry 2001 was divided, one half jointly to William S. Knowles and Ryoji Noyori "for their work on chirally catalysed hydrogenation reactions" and the other half to K. Barry Sharpless "for his work on chirally catalysed oxidation reactions" [11–14]. In order to develop practical chirotechnology in the preparation of the isolated enantiomers, two alternative approaches are often considered: (1) separation of one enantiomer

from racemic mixtures, and (2) enantioselective synthesis of the desired enantiomer by using chiral asymmetric catalysts [15–17].

Among all practical strategies, heterogeneous systems with chirality have significant advantages in enantioselective separation and catalysis, including easy separation, efficient recycling, minimization of catalyst traces in the product, and improved handling and process control [18, 19]. All kinds of zeolites, silica, alumina, and polymeric resins solid supports loading the homogeneous catalysts or compounds by covalent binding, electrostatic interaction, adsorption, or encapsulation are widely used heterogeneous materials [20]. With the development of material sciences, chiral metal-organic frameworks (MOFs) as microporous materials have attracted much attention due to their important superiorities in abundant catalytic centers, high void content, great specific surface area, crystalline nature enabling elucidation of structural details, and relatively easy immobilization as compared to other traditional heterogeneous systems. In addition, these chiral MOFs also can be applied in nonlinear optics, biomimetic chemistry, and magnetic materials [21–29]. However, the development of MOFs, after all, is only two decades old and the field is still in its infancy.

Notably, as metal-connecting nodes of MOFs, most of the works have mainly focused on the transition metal ions which exhibit specific coordination geometries and restricted stereochemistry in general, and the research of chiral lanthanide MOFs is still limited, although lanthanide complexes are ideal candidates for fascinating self-assembled structures and potential applications in materials science including superconductive, magnetic, optical, electronic, and catalytic processes. The reason is due to the inherent nature of lanthanide ions, such as their high coordination numbers, kinetic lability, weak stereochemical preference, and more variable nature of the coordination sphere, which often cause the design and preparation of lanthanide-based chiral materials to be very difficult [30]. Thus, the controllable preparation of chiral lanthanide MOFs and the relationships between structures and properties need to be recognized and summarized.

2 The Synthetic Strategies of Chiral Lanthanide MOFs

In recent years, in order to develop MOFs materials with various potential application, reasonable design and construction methods have attracted more and more attention [31, 32]. However, there are many difficulties and uncertainties for the controlled synthesis of chiral lanthanide MOFs, the reasons are mainly as follows: (1) The coordination number of the lanthanide ions is often more than eight and the nature of the coordination sphere is variable. Therefore, the coordinating bonds of lanthanide complexes are not directional and the coordination number varies from 3 to 12, which leads to more geometrical isomers but not optical isomerical MOFs for common achiral ligands. (2) Lanthanide ions are hard bases from a soft–hard acid–base point of view and the types of coordination atoms are usually limited, which make carboxylates excellent candidates for wide use as bridging ligands.

However, variable coordination modes of carboxylic group usually lead to the generation of geometrical isomers for lanthanide complexes. (3) Many interpenetrating structures and lower dimensional coordination polymers tend to be self-assembled because of more stable framework structures based on supramolecular interaction and the effect of solvent, which lead to fewer porous chiral lanthanide MOFs [33–38].

Generally speaking, chiral lanthanide MOFs as the same as common MOFs structures have two main components: the organic linkers and the metal centers. The organic linkers as organic secondary building unit (SBU), no doubt, are very important and play a critical role in the network structure [23, 31, 32]. For chiral lanthanide MOFs, there are three main synthetic strategies reported:

1. The most straightforward and effective method is to choose enantiopure organic ligand with rigid structure to bridge metal ions or SBUs, by which lanthanide center as inorganic SBU with absolute configuration can be achieved and the resulting framework would be homochiral [39–42].
2. The second effective method starts with achiral ligands and usually employs chiral catalysts, templates, or solvents that do not act as components ligands to induce a particular handedness in the assembly process of lanthanide MOFs [43–45].
3. The third approach to create chiral lanthanide MOFs is using an achiral ligand under spontaneous resolution. The spontaneous resolution of chiral complexes without any chiral auxiliary is a peculiar phenomenon and has been found only occasionally in self-assembly of the complexes or MOFs [46–50].

In addition, there are other ways to synthesize chiral MOFs. For example, post-synthesis is also an important method, which could obtain a homochiral MOFs from a chiral or achiral parent MOFs by synthetic modification of the organic struts or the metal nodes and by guest exchange [51]. But so far, the method is rarely applied and reported in preparation of chiral lanthanide MOFs.

2.1 Synthesis of Chiral Lanthanide MOFs with Chiral Ligands

Various chiral ligands have been applied to construct chiral lanthanide MOFs (Fig. 1). As a correspondingly inexpensive ligand source, D-camphoric acid, consisting of a rigid banding backbone based on a cyclopentane ring and two freely rotating carboxylate groups, has proved its effectiveness as a chiral building block for the syntheses of chiral MOFs materials with many transition metals [52–54]. It also can adopt a variety of coordination modes to participate in the formation of Ln cluster units due to the high affinity of lanthanide ions for oxygen donor atoms, resulting in diverse multidimensional structures. Meanwhile, the two carboxylates may allow a significant magnetic exchange pathway between the bridged paramagnetic centers.

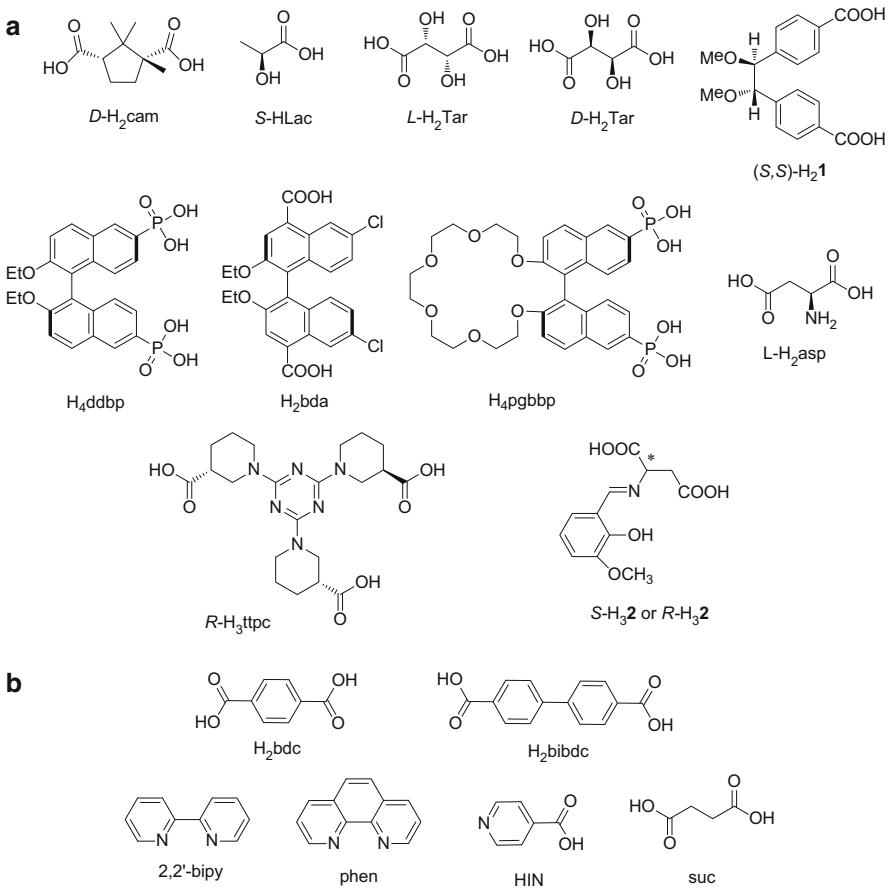

Fig. 1 (**a**) Various chiral ligands in chiral lanthanide MOFs reported; (**b**) Second ligands or co-ligands with multidentate coordination or bridging function in chiral lanthanide MOFs reported

Various chiral lanthanide MOFs with different structures can be synthesized by using pure chiral D-camphoric acid as ligand through different preparation methods or participation of different solvent. Song et al. [55] have first constructed homochiral lanthanide-based chiral MOFs, $[Ln(\mu\text{-}H_2O)(D\text{-}cam)(CH_3COO)]_n$ ($Ln = Gd$, Tb, Eu, Dy), by using enantiopure D-camphorate ligand (D-H_2cam) and $Ln(CH_3COO)_3$ under hydrothermal condition. These isomorphous Ln(III)–camphorate compounds with the $P6_5$ chiral space group. For $[Gd(\mu\text{-}H_2O)(D\text{-cam})(CH_3COO)]_n$, the Gd(III) ions are bridged by D-cam carboxylates, CH_3COO– carboxylates, and CH_3COO– oxygens to give rise to the neutral helical substructure $\{Gd(COO)_3\}_n$. The camphorate ligand adopts tridentate coordinated mode, whilst CH_3COO– adopts the μ_2:$\eta^1\eta^2$ coordinated fashion. Within the helical substructure of $\{Gd(COO)_3\}_n$, the CH_3COO– ligands orientate in six directions around one 6_5 axis. If one only takes into account the CH_3COO– oxygen bridges, then the helical

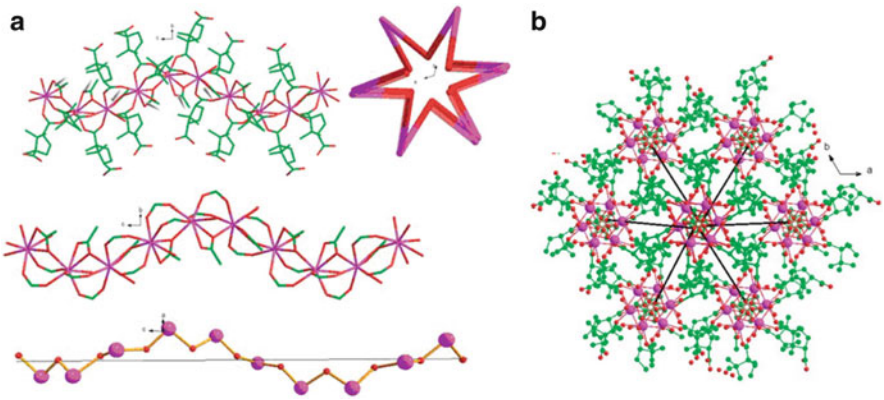

Fig. 2 (**a**) A view along the *c* direction of the helical substructure of $\{Gd(COO)_3\}_n$ and $\{Gd–O\}_n$; (**b**) A view of the special hex rod-packing architecture built on the helical $\{Ln–O\}_n$ rod substructure. (Reproduced from Song et al. [55] by permission of The Royal Society of Chemistry)

substructure becomes an inorganic helical tube of $\{Gd–O\}_n$ with a seemingly hexagram-like figuration. These $\{Gd(COO)_3\}_n$ substructures are combined together to generate the 3D hex rod-packing architecture via chiral D-camphorate ligands (Fig. 2).

Jhu et al. [56] obtained three isomorphous 3D homochiral rigid lanthanide frameworks $[Ln(D\text{-cam})(HCOO)]_n$ (Ln = Tb, Dy, Ho, Er) by mixing $Ln(NO_3)_3{\cdot}6H_2O$ and D-camphoric acid under DMF solvothermal conditions in 2013, and then Sun et al. [57] also obtained the same lanthanide MOFs (Ln = Dy, Ho, Er) by using rare earth oxide and DMF/H_2O solvothermal method in 2014. These chiral MOFs also crystallize in orthorhombic, chiral space group $P2_12_12_1$. For chiral Dy-MOF, the Dy(III) centers are bridged by the carboxylate groups of D-cam ligands and formate ligands produced from the hydrolysis of DMF into infinite 1D triple-strand helical rod-shaped SBUs. Then, each 1D helical $\{Dy–O\}_n$ rod SBU is further linked to four neighboring symmetry-related analogs via chiral D-cam spacers, giving rise to a 3D rod-packing architecture. The methyl groups on the ring of the D-cam ligands protrude into the void space of the 3D framework preventing the inclusion of any guest molecules. Structure analysis further suggests that the SBUs consisted of an infinite $\{Dy–O\}_n$ chain with DyO_7 pentagonal bipyramids are joined by these D-camphorate spacers as linker to get a 3D network with **sra** topology (Fig. 3).

In addition to using D-camphoric acid as the only ligand, the introduction of other transition metal ions and co-ligands with multidentate coordination or bridging function is also a common strategy to obtain functional chiral MOFs. Sun et al. [58] synthesized seven homochiral lanthanide MOFs by using D-H_2cam, $\{Ln_2(D\text{-cam})_2(bdc)(H_2O)_2\}{\cdot}DMF$ (Ln = Sm, Eu, Gd, Tb, Dy, Ho, Er) by solvothermal method. In these MOFs, achiral terephthalate ligand is mixed to obtain antenna effect and enhances the luminescent emissions of Ln(III) ions because there is no large π-conjugated system in D-cam group. Thus, the

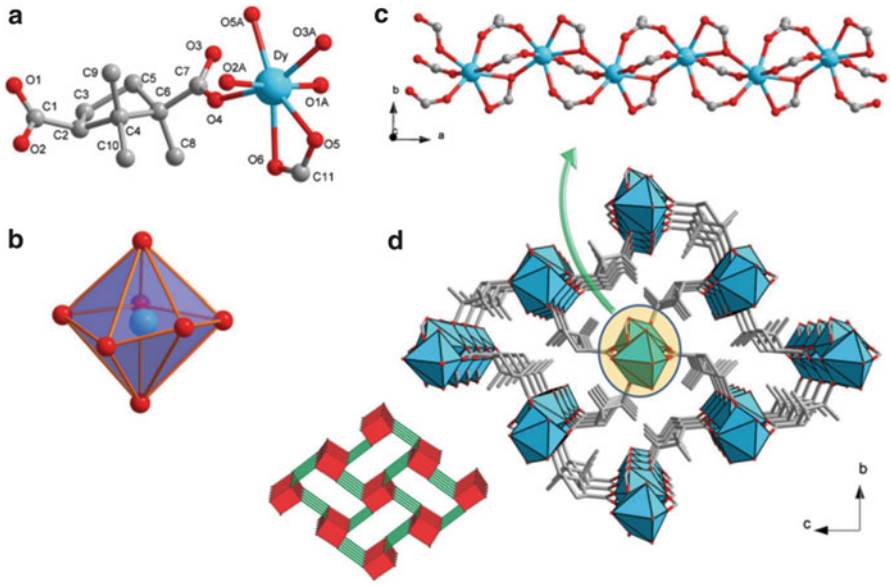

Fig. 3 (**a**) The asymmetric unit of Dy-MOF. The H atoms have been omitted for clarity; (**b**) The pentagonal bipyramid coordination polyhedron of DyO_7; (**c**) Perspective view of the Dy–carboxylate chain aligned along the *a* direction; (**d**) 3D rod-packing architecture of Dy-MOF and diagram of the sra topological network simplified from the 3D framework. (Reproduced from Jhu et al. [56] by permission of The Royal Society of Chemistry. Reproduced from Sun et al. [57] by permission of The Royal Society of Chemistry (RSC) on behalf of the Centre National de la Recherche Scientifique (CNRS) and the RSC)

combination of an enantiopure D-cam ligand with an achiral bdc ligand brings both homochirality and rigidity into the lanthanide MOFs materials. The crystal structures of these MOFs reveal that they are isostructural and crystallize in orthorhombic, chiral space group $P2_12_12_1$. Moreover, they also represent the first example of homochiral lanthanide camphorates adopting 3D open frameworks constructed from rod-shaped $[Ln_2(COO)_6(H_2O)_2]_n$ SBUs. The guest DMF molecules occupy the void space of the MOFs (Fig. 4).

Dang et al. [59] synthesized four 3D isostructural homochiral manganese–lanthanide frameworks $\{MnLn(D\text{-cam})_2(D\text{-Hcam})(2,2'\text{-bipy})\}_n$ (Ln = La, Nd, Dy, Eu) with chiral space group $P2_12_12_1$, by the reaction of $Ln(NO_3)_3{\cdot}6H_2O$, D-H_2cam, $MnCl_2$ $4H_2O$, and 2,2′-bipy via hydrothermal process, which are the first 3d–4f heterometallic features in the system of chiral camphoric acids. Taking Mn-Nd MOF as an example, heterometallic centers are linked by Mn–O–Nd rods and Mn–O–C–O–Nd rods with the Mn···Nd distance of 3.760(2) Å to form $\{MnNdO_{11}C_7N_2\}$ as the SBU. Each SBU is interconnected with six SBUs along multi-direction through the modes of SBU-cam-SBU. It is a breakthrough that D-cam serves as $\mu_2{-}\kappa^1,\kappa^1,\kappa^1,\kappa^1$ (cam-1), $\mu_5{-}\kappa^2,\kappa^1,\kappa^1,\kappa^1$ (cam-2), and $\mu_4{-}\kappa^1,\kappa^2,\kappa^1$ (cam-3) bridging ligands, respectively, which rarely unfold in three coordination modes in one

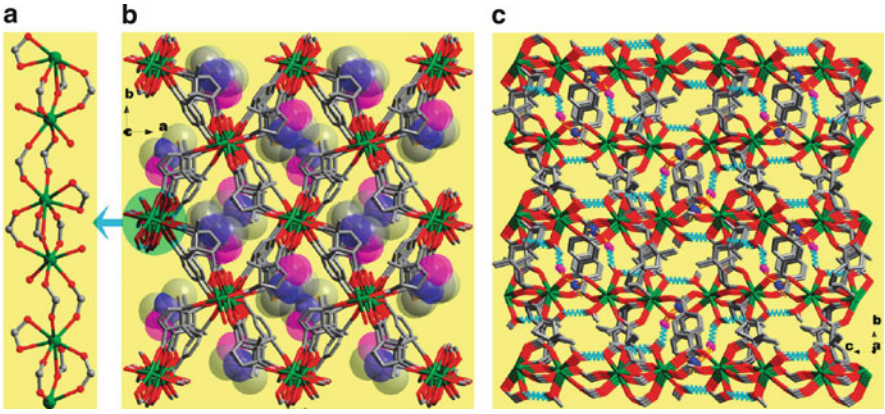

Fig. 4 (**a**) *Ball*-and-*stick* representation of a 1D inorganic rod-shaped chain of $\{Eu_2(COO)_6(H_2O)_2\}_n$. The H atoms have been omitted for clarity; (**b**) Schematic view of the 3D open framework along the *c* axis. DMF host molecules are trapped in the apertures; (**c**) 3D framework viewed along the *bc* plane. All of the hydrogen bonds are denoted with *dashed cyan lines*. (Reprinted with the permission from Sun et al. [58]. Copyright 2010 American Chemical Society)

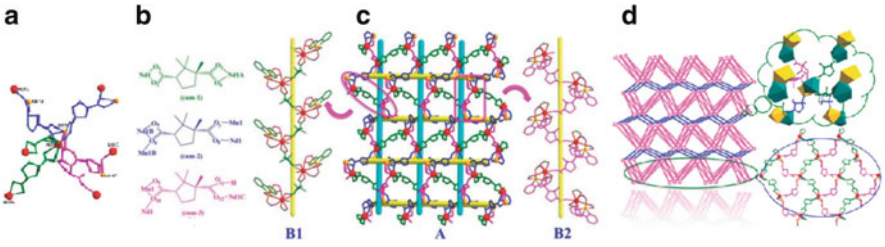

Fig. 5 (**a**) Crystallographic coordination modes of the D-cam ligands; (**b**) Three kinds of D-cam in SBU; (**c**) View of 2_1 helical chains in Mn-Nd MOF. A represents the *ac* layer; B1 and B2 represent different connection modes prolongation along *b* orientation; (**d**) The topological structure of Mn-Nd MOF viewed along *b* orientation. Each heterometallic center unit can be considered as a node connected to six others through six cam ligands along multi-direction, and the (4,4) layer is constructed by cam-1 and cam-3. (Reproduced from Dang et al. [59] by permission of The Royal Society of Chemistry)

structure. The four kinds of helices are joined together with the ratio 1:1:1:1 through the different connection ways of these ligands. Simultaneously, cam-1 and cam-3 interlink SBUs into undulating (4,4) *ac* layers, which are further pillared by cam-2 into a 3D structure. Topologically, if considering the SBU as a node, the overall framework can be represented as a six-connected net with a vertex symbol of $4{\cdot}4{\cdot}4^2{\cdot}4{\cdot}4{\cdot}4{\cdot}4{\cdot}4^2{\cdot}4^2{\cdot}6^4{\cdot}6^4{\cdot}6^4{\cdot}6^4{\cdot}6^4{\cdot}6^4$ and a short Schläfli symbol of $4^9{\cdot}6^6$ (Fig. 5).

Similar studies with similar results have been done by Tan et al. [60]. They also used the mixed ligands of D-H_2cam and phen/2,2′-bipy to give rise to 11 chiral 3d–4f heterometallic MOFs, $\{MDy(D\text{-}cam)_2(D\text{-}Hcam)(phen)\}_n$ (M = Ni, Cu), {CoLn

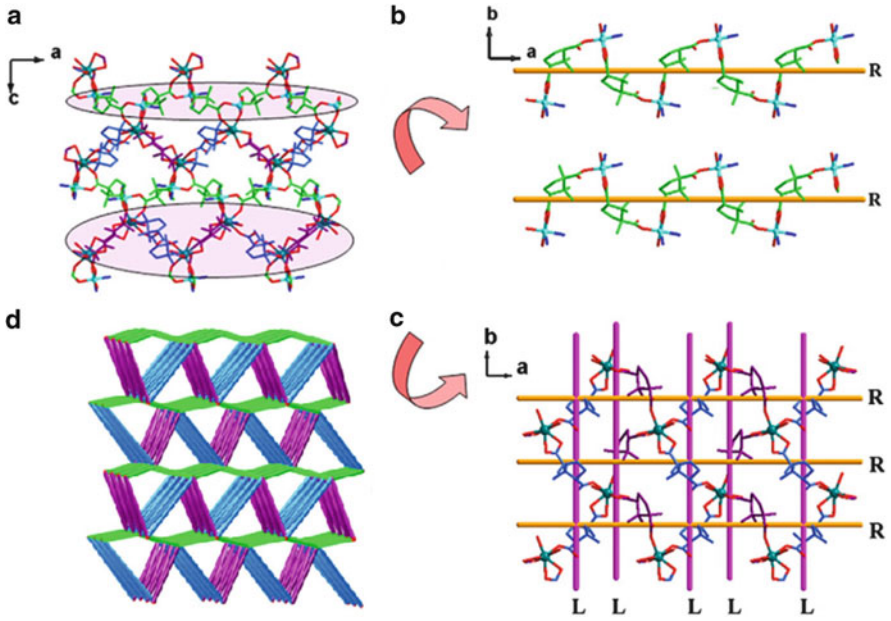

Fig. 6 (**a**) The 3D coordination network of Ni-Dy MOF along the *b* axes; (**b**) 1D Ni(II) zigzag chains along *a* direction (*right-handed helical chains*); (**c**) 2D Dy(III) wave-like layer along *c* orientation constructed by *right-handed* and *left-handed helical chains* in the intercrossed arrangement; (**d**) Topological representation for the 3D structure of Ni-Dy MOF. (Reprinted from Tan et al. [60], Copyright 2013, with permission from Elsevier)

$(\text{D-cam})_2(\text{D-Hcam})(2,2'\text{-bipy})\}_n$ (Ln = Sm, Eu, Gd, Tb, Dy), $\{\text{CuLn}(\text{D-cam})_2(\text{D-Hcam})(2,2'\text{-bipy})\}_n$ (Ln = Sm, Eu, Dy), $\{\text{ZnDy}(\text{D-cam})_2(\text{D-Hcam})(2,2'\text{-bipy})\}_n$. Single-crystal X-ray diffraction measurements reveal that the crystal structures are isostructural, crystallizing in the orthorhombic space group $P2_12_12_1$, and they exhibit unique three-dimensional chiral 6-connected frameworks involving 1D zigzag chains aligned parallel to the *a* axis and the 2D wave-like lanthanide layers, with the Schläfli symbol $(4^9 \cdot 6^6)$ (Fig. 6).

Qiu et al. [61] reported a Ln(III)–Ag(I) heterometallic chiral MOF based on (*S*)-lactic acid (*S*-HLac) as ligand, $[Eu_2Ag_3(S\text{-Lac})(IN)_6(H_2O)_4]\cdot 2(ClO_4)\cdot 4(H_2O)$, which crystallize in the triclinic space group *P*1. In the MOF structure, two europium ions are linked by one *S*-Lac ligand to form a chiral building block as in a knot with a Eu···Eu separation of 4.956(2) Å. These dinuclear chiral building units are connected by two pairs of $Ag(IN)_2$ units in an antiparallel orientation to form a zigzag chain in the *b* axis direction, in which two adjacent $Ag(IN)_2$ units are stacked atop each other. These 1D zigzag chains can be regarded as supramolecular second building units and are further cross-linked via pillared $Ag(IN)_2$ units into a 3D pillared coordination framework (Fig. 7).

For the preparation of MOFs by solvothermal or hydrothermal method at high pressure and high temperature, carboxylic acid esters often are applied as the source

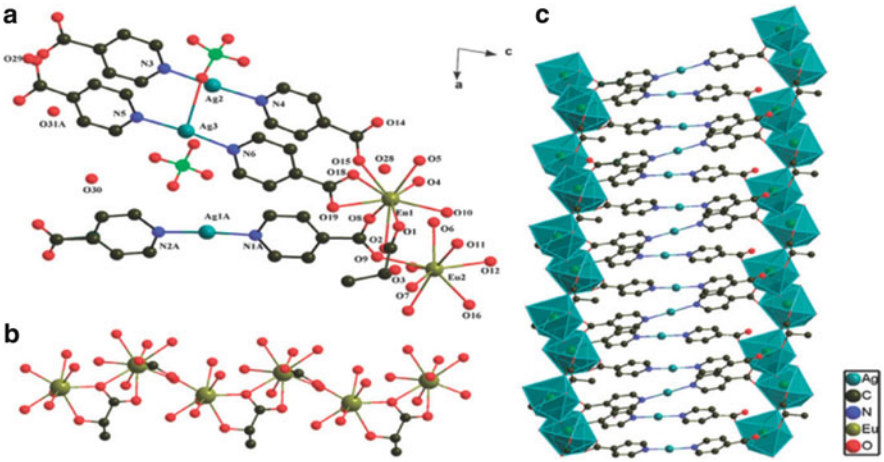

Fig. 7 (**a**) Perspective view of the asymmetric unit of heterometallic chiral MOF $[Eu_2Ag_3(S\text{-Lac})(IN)_6(H_2O)_4]\cdot 2(ClO_4)\cdot 4(H_2O)$; (**b**) View of a helical chain of Eu–Ag MOF constructed from the carboxylate groups of IN^- and *S*-Lac ligands and metal ions; (**c**) View of a 2D coordination network composed of 1D helical chains and pillared $Ag(IN)_2$ subunits. (Reproduced from Qiu et al. [61] by permission of The Royal Society of Chemistry)

of carboxylic ligands and the starting material. With the same synthesis strategy, Xiong group [62, 63] used chiral compound of L-ethyl lactate to react with $Eu(ClO_4)_3\cdot 6H_2O$ and $Tb(ClO_4)_3\cdot 6H_2O$ under hydrothermal (deuteratothermal) conditions, resulting into laminar crystals of $[Eu(S\text{-Lac})_2(X_2O)_2](ClO_4)$ (X = H, D) and $[Tb(S\text{-Lac})_2(X_2O)_2](ClO_4)$ (X = H, D) with space group *C*2, respectively. These compounds are isostructural, possessing a two-dimensional laminar homochiral framework. For $[Eu(S\text{-Lac})_2(H_2O)_2](ClO_4)$, the Eu ions were connected by the oxygen atoms of *S*-Lac ligands, leading to a two-dimensional homochiral layered framework. A cation laminar layer of $[Eu(S\text{-Lac})_2(H_2O)_2]^+$ acts as the sides of a sandwich to intercalate perchlorate ions, resulting in the formation 3D framework through hydrogen bonds. The dielectric constants parallel to the layer may be quite different from that is perpendicular to it. Thus, compounds $[Eu(S\text{-Lac})_2(X_2O)_2](ClO_4)$ (X = H, D) display a giant dielectric anisotropy approximately exceeding 100 and large isotopic effect with about 54% enhancement along the *a* axis (Fig. 8).

Thushari et al. [64] synthesized successfully isostructural enantiopure 3D open-framework $[Ln_2(L\text{-Tar})_3(H_2O)_2]\cdot 3H_2O$ (Ln = La–Yb, Y) by using a simple and readily available chiral source L-tartaric acid under hydrothermal conditions up to 160°C. For crystal of $[Er_2(L\text{-Tar})_3(H_2O)_2]\cdot 3H_2O$, it belongs to the triclinic system and crystallizes in space group *P*1. Three ligands in the asymmetric unit are crystallographically independent, two of them are chemically similar and may be classed as μ_4,κ^6, that is they bind to four Ln ions using all six oxygen atoms of the tartrate, which combine with metal ions to form a condensed 2D slab of $[Ln_2(\mu_4,\kappa^6\text{-}L\text{-Tar})_2]$ in the *ab* plane. The other tartrate bridges only two Ln(III) ions via two bidentate carboxylates described as μ_2,κ^4. These chiral ligands link lanthanide ions

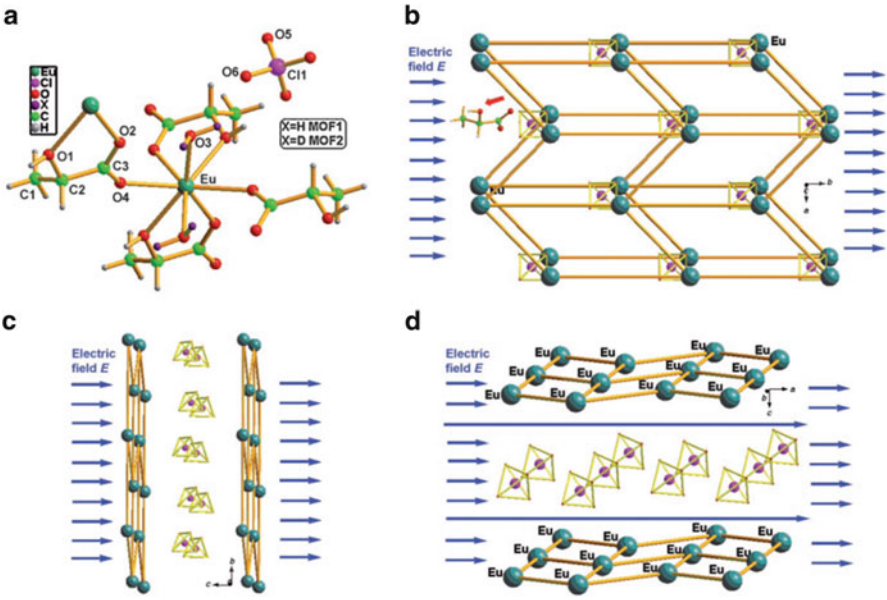

Fig. 8 (**a**) Asymmetric unit of $[Eu(S\text{-Lac})_2(X_2O)_2](ClO_4)$ (X = H, D) in which Eu anion has an eight-coordinate local coordination geometry; (**b**) Two-dimensional laminar framework along the *c* axis in which the ClO_4^- ions are intercalated between two layers and *long orange sticks* and *gray-green balls* stand for *S*-Lac and Eu atoms; (**c**) Two-dimensional layered representation of the coordination polymer along the *a* axis; (**d**) Two-dimensional layered representation of the coordination polymer along the *b* axis. The *blue arrows* indicate the electric field directions. (Reproduced from Qu et al. [62] by permission of John Wiley & Sons Ltd)

to form 3D framework, which has hydrophilic channels of ca. 5×7 Å dimension bounded by rings of four lanthanide ions and four L-Tar ligands. The channels have a polar chiral arrangement along the *a* axis. Furthermore, the substitution of the *R, R*-configuration L-tartaric acid with either racemic D/L-tartaric acid (*R,R*/*S,S*) or *meso*-tartaric acid (*R,S*) in the original reaction also is investigated. The result shows that racemic D/L-Tar gives the more condensed $[Ln_2(D/L\text{-Tar})_3(H_2O)_2]$ with non-centrosymmetric space group *Iba*2, and the extent of chiral racemization under the reaction conditions is minimal (Fig. 9).

They also showed enantiopure 3D open-framework $[Pr_2(L\text{-Tar})_2(suc)(H_2O)_2]\cdot 5.5H_2O$ in space group $P2_12_12$ with incorporation of the succinate in place of the μ_2-tartrate. The unit cell and crystal symmetry have changed compared to $[Ln_2(L\text{-Tar})_3(H_2O)_2]\cdot 3H_2O$. The retention of the strongly bonded $[Ln_2(\mu_4,\kappa^6\text{-L-Tar})_2]$ slabs can be seen and the effect of succinate incorporation on channel shape and functionality is also clear. The channels are now enlarged to ca. 6×9 Å and contain $5.5H_2O$ rather than $3H_2O$ per Ln_2 unit (Fig. 10).

Amghouz et al. [65, 66] obtained chiral metal-organic frameworks [NaLn(L-Tar)(bdc)$(H_2O)_2$] and [NaLn(L-Tart)(bibdc)$(H_2O)_2$] (Ln = Sm, Eu, Gd, Tb, Dy, Ho, Er, Yb, Y) by using mixed ligands under hydrothermal conditions. Both compounds are

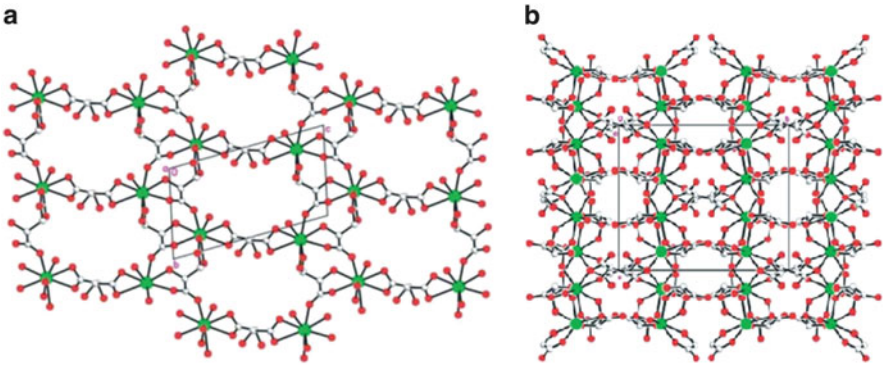

Fig. 9 Packing diagram for (**a**) $[Er_2(L\text{-}Tar)_3(H_2O)_2]\cdot 3H_2O$ along the *a* axis and (**b**) $[Er_2(D/L\text{-}Tar)_3(H_2O)_2]$ along the *c* axis. (Reproduced from Thushari et al. [64] by permission of The Royal Society of Chemistry)

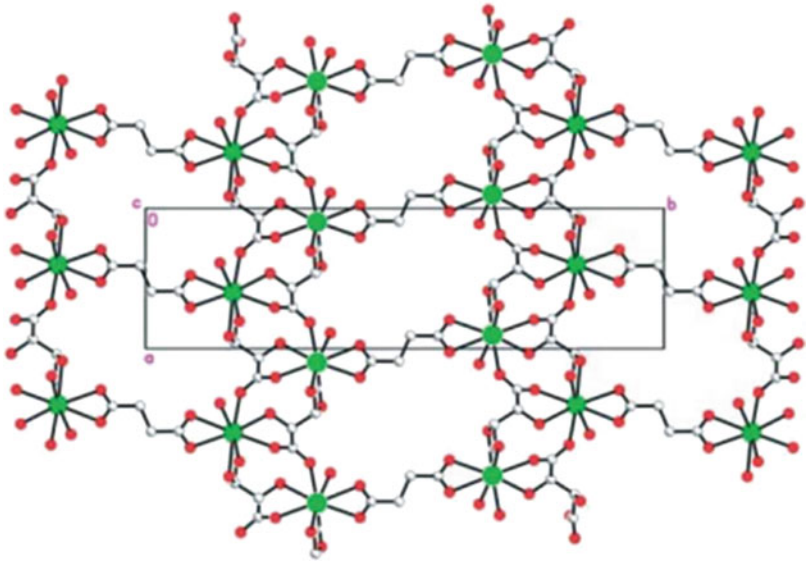

Fig. 10 Packing diagram for $[Pr_2(L\text{-}Tar)_2(suc)(H_2O)_2]\cdot 5.5H_2O$ along the *c* axis. (Reproduced from Thushari et al. [64] by permission of The Royal Society of Chemistry)

layered chiral structures built up by mixing Ln(III), Na(I), and chiral flexible-achiral rigid dicarboxylate ligands, and crystallize in the orthorhombic chiral space group $C222_1$. In each compound, the Ln(III) cation is bonded to eight oxygen atoms, six of them are from carboxylic groups and two are from hydroxyl groups. While the Na(I) cation is bonded to six oxygen atoms, four of them are from carboxylic and two are from coordinated water molecules. The Ln(III) and Na (I) polyhedra alternate in a chain edge-to-edge parallel to the *a* axis. These chains

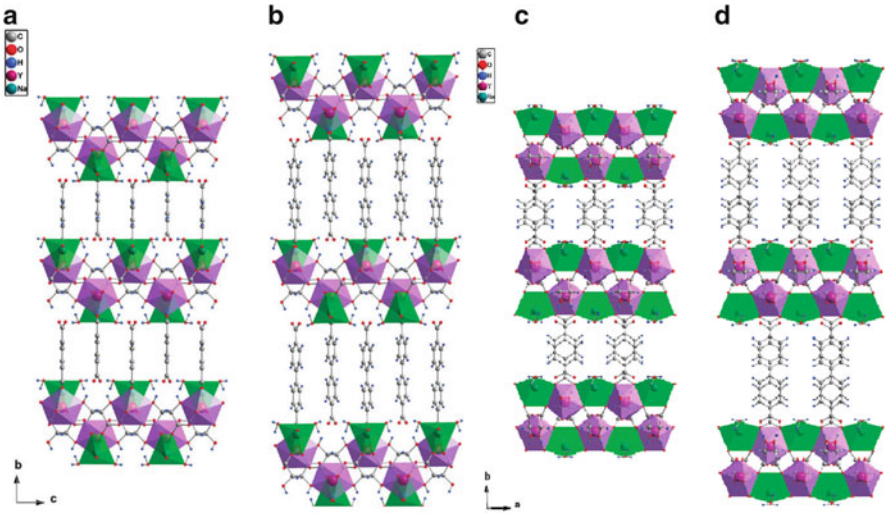

Fig. 11 Projection of the structure of [NaLn(L-Tar)(bdc)$(H_2O)_2$] along the *a* axis (**a**) and along the *c* axis (**c**); Projection of the structure of [NaLn(L-Tart)(bibdc)$(H_2O)_2$] along the *a* axis (**b**) and along the *c* axis (**d**). (Reprinted with the permission from Amghouz et al. [65]. Copyright 2010 American Chemical Society)

are in turn connected via L-Tar^{2-} bridges along *a* and *c* axis showing a zigzag arrangement, and forming a double layer. The resulting double layered network is then pillared by the rigid bdc^{2-} or $bibdc^{2-}$ to form channels. The three-dimensional stability is ensured by strong hydrogen bond interactions. For both of Y(III) compounds, the dehydration is accompanied by phase transformation, while the spontaneous rehydration process is characterized by different kinetics, fast in the case of [NaY(L-Tar)(bdc)$(H_2O)_2$] and slow for [NaY(L-Tart)(bibdc)$(H_2O)_2$] (Fig. 11).

Gao et al. [67] obtained a series of homochiral 2D compounds {[Ln$(H_2O)_5]_2[Sb_2$(L-$Tar)_2]_3$}·xH_2O (Ln = La, Ce, Pr, $x = 5$; Ln = La, $x = 6$) by utilizing a chiral dimer ligand Sb_2(L-$Tar)_2^{2-}$ as a SBU to react with lanthanide ions. For {[La$(H_2O)_5]_2[Sb_2$(L-$Tar)_2]_3$}·$5H_2O$, it crystallizes in space group $P2_1$. The La(III) ions were linked by two kinds of Sb_2(L-$Tar)_2^{2-}$ units, leading to two straight 1D helices along the [001] and [101] directions, respectively. The Sb_2(L-$Tar)_2^{2-}$ units link these two types of helices into infinite slabs, which then stack along the *b* axis. Lattice water molecules are located within and between the slabs. The structure of {[La$(H_2O)_5]_2[Sb_2$(L-$Tar)_2]_3$}·$6H_2O$ is almost the same as that of {[La$(H_2O)_5]_2[Sb_2$(L-$Tar)_2]_3$}·$5H_2O$, but it crystallizes in the higher symmetry space group *C*2 (Fig. 12).

By introducing the chiral ligand L-H_2asp, Li et al. [68] present four isostructural lanthanide MOFs formulated as {[$Ln_4(\mu_3$-OH)$_4$(L-Hasp)$_3(H_2O)_{10}$]·$(ClO_4)_5$·$10H_2O\}_n$ (Ln = Nd, Sm, Eu, Gd), which crystallized in chiral $P2_12_12_1$ space group. The coordination polyhedra of Ln(III) can be best depicted as a

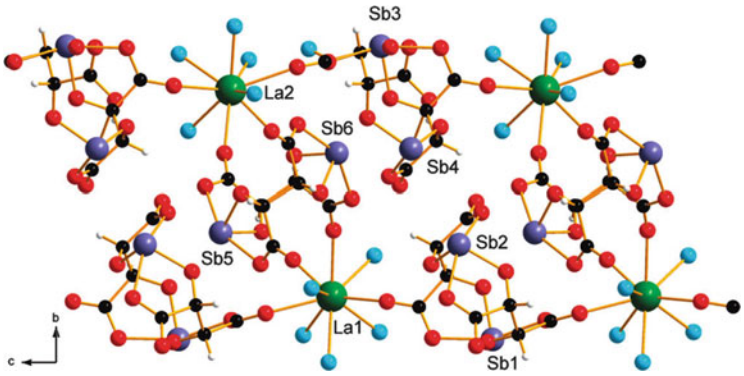

Fig. 12 *Ball*-and-*stick* representation of $\{[La(H_2O)_5]_2[Sb_2(L\text{-}Tar)_2]_3\}\cdot 5H_2O$. View of the layer along the *a* axis. (Reprinted with the permission from Gao et al. [67]. Copyright 2011 American Chemical Society)

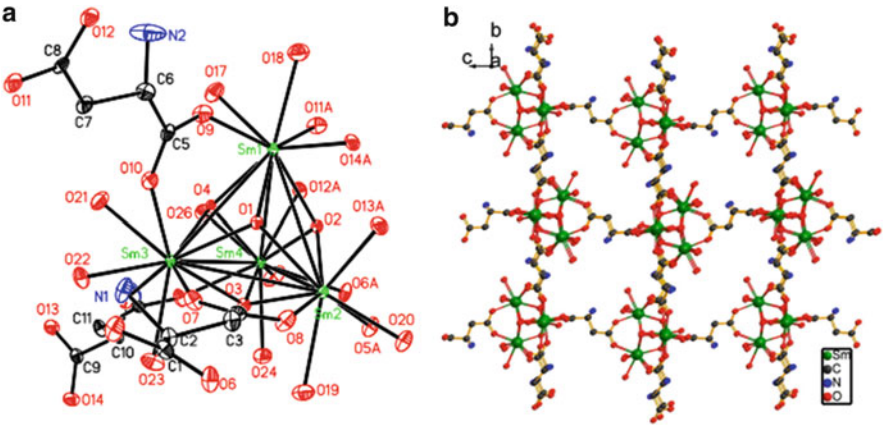

Fig. 13 (**a**) ORTEP drawing of $[Sm_4(\mu_3\text{-}OH)_4(L\text{-}Hasp)_3(H_2O)_{10}]^{5+}$ with 30% probability; (**b**) View of the 3D framework structure along the *a* axis, showing large channels. Lattice water molecules, perchlorate ions, and H atoms were omitted [68]

distorted mono capped square antiprism and four Ln(III) ions form a typical tetranuclear cubic $[Ln_4(\mu_3\text{-}OH)_4]^{8+}$ unit. Each tetranuclear unit is linked to six adjacent equivalents by six L-Hasp– ligands to generate a porous homochiral 3D framework structure (Fig. 13).

In addition to using natural chiral compounds as organic linkers, synthetic chiral ligands or modified natural compounds as linker are other important SBUs to construct chiral lanthanide MOFs.

Lin's team is devoting to designing and researching the structures and second-order nonlinear optical (NLO) effects of chiral MOFs, MOF-based asymmetric heterogeneous catalysis and enantioselective separation. They have designed a number of "privileged" chiral ligands based on BINOL derivatives [69]. Among

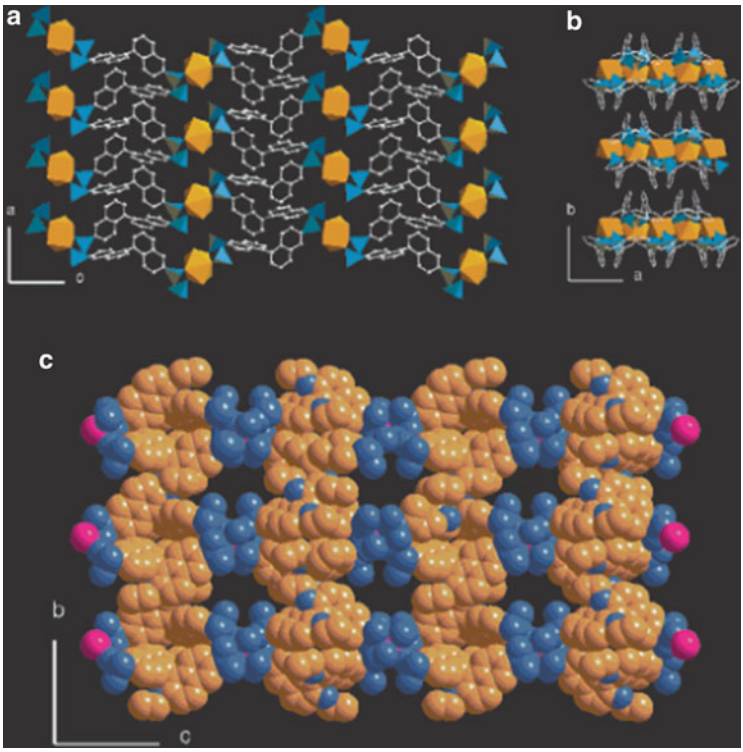

Fig. 14 A view of 2D framework of Gd coordination polymer along the *b* axis (**a**) and the *c* axis (**b**) Ethoxy groups have been omitted for clarity. The coordination environments of P atoms and Gd atoms are represented with *blue* and *orange* polyhedra, respectively; (**c**) A space-filling model viewed down the *a* axis. (Reprinted with the permission from Evans et al. [70]. Copyright 2001 American Chemical Society)

them, chiral lanthanide MOFs is one of the important research and exploration aspects. In 2001, Evans et al. [70] first synthesized homochiral lanthanide bisphosphonates 2D framework with the general formula of $[Ln(H_2ddbp)(H_3ddbp)(H_2O)_4]\cdot xH_2O$ (Ln = La, Ce, Pr, Nd, Sm, Gd, Tb, $x = 9$–14) by slow evaporation of an acidic mixture of nitrate or perchlorate salts of Ln(III) and optical pure chiral (*R*)-2,2′-diethoxy-1,1′-binaphthalene-6,6′-bisphosphonic acid (H_4ddbp) in methanol. A single-crystal structure reveals that $[Gd(H_2ddbp)(H_3ddbp)(H_2O)_4]\cdot 12H_2O$ crystallizes in the chiral space group $P2_12_12_1$ and is a 2D lamellar structure consisting of 8-coordinate Gd centers and bridging binaphthylbisphosphonate groups. Moreover, these lanthanide MOFs exhibited good framework stability and reversibility of the dehydration processes (Fig. 14).

Cui et al. [71] also demonstrated a 3D homochiral MOFs with the general formula of $[Ln_2(bda)_3(DEF)_2(py)_2]\cdot 2DEF\cdot 5H_2O$ (Ln = Gd, Er, Sm, DEF = *N*, *N*′-diethylformamide; py = pyridine) by using lanthanide metals and another enantiopure BINOL derivative. The MOFs are prepared in 30–45% yields by

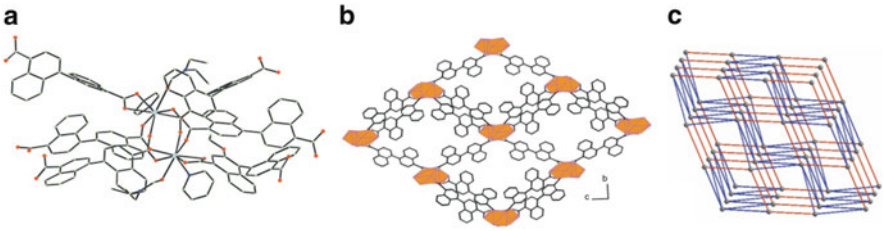

Fig. 15 (**a**) The digadolinium building unit of Gd-MOF. The DEF and water guest molecules are omitted; (**b**) Polyhedral presentation of the 3D network of Gd-MOF along the *a* axis; (**c**) Schematic illustrating the $4^9{\cdot}6^6$ topology of 3D network. The digadolinium SBUs are shown as *gray balls*, and the *blue* and *red lines* represent two kinds of bda^{2-} bridging ligands. (Reproduced from Cui et al. [71] by permission of The Royal Society of Chemistry)

treating hydrated lanthanide salts and H_2bda in a mixture of DEF, MeOH, and Py at 50°C. The basic building unit for Gd-MOF contains two crystallographically equivalent Gd centers that are quadruply bridged by four carboxylate groups of four bda^{2-} ligands. Each Gd center also coordinates to a chelating carboxylate group of a bda^{2-} anion, a DEF molecule, and a pyridine molecule to afford a distorted square antiprism geometry. Each digadolinum core in Gd-MOF is linked by six bda^{2-} ligands to six adjacent digadolinum cores to form two independent hexagonal 6^3 grids in the *ab* and *ac* planes, respectively, and result in a unique 3D neutral framework with a 1D channel running parallel to the *a* axis. The structure can be classified as a $4^9{\cdot}6^6$ topological type built upon six-connected nodes as defined by Wells. Both the ethoxy-protected BINOL functionalities and the chlorine atoms are pointing towards the channel, leading to an asymmetric 1D channel with a cross-section of $\sim 3.1 \times 6.2$ Å that is occupied by two DEF and five water guest molecules (Fig. 15).

In addition, they also incorporated a chiral crown ether moiety into the bridging bisphosphonate ligand to form homochiral porous lamellar lanthanide bisphosphonates $[Ln_2(Hpgbbp)_2(MeOH)_8]{\cdot}(H_4pgbbp){\cdot}(HCl)_3{\cdot}(H_2O)_6$ (Ln = Nd, Sm) [72]. The Nd centers in $[Nd_2(Hpgbbp)_2(MeOH)_8]$ adopt a square anti-prismatic geometry by coordinating to four methanol molecules and four phosphonate oxygen atoms of four different $Hpgbbp^{3-}$ ligands. Both phosphonate groups of the $Hpgbbp^{3-}$ ligand adopt a κ_2,μ_2 binding mode, and link adjacent Nd centers to form doubly bridged 1D lanthanide phosphonate chains along the *b* axis. The binaphthyl backbones of the $Hpgbbp^{3-}$ ligands link adjacent 1D lanthanide phosphonate chains to form a 2D coordination network lying in the *ab* plane. The lamellae of Nd complex are however intercalated with free H_4pgbbp molecules, and as a result, there is only enough void space to accommodate three hydrogen chloride and six water molecules per formula unit (Fig. 16).

Jeong et al. [73] researched the formation of cryptochiral MOF from homochiral ligand (*S*,*S*)-H_2**1** as an isomorphic MOF with that from a racemic mixture of H_2**1**. It could be one of the clues to explain how the chirality attenuation in chiral MOF occurred. Crystals, achiral La-(±)-**1** crystallized in $P\bar{1}$ space group, and chiral

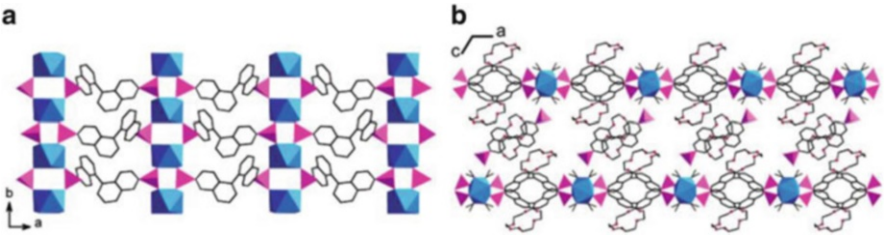

Fig. 16 (**a**) A view of the lamellar structure of $[Nd_2(Hpgbbp)_2(MeOH)_8]$ down the *c* axis. For clarity, the crown ether groups of $Hpgbbp^{3-}$ ligands and the carbon atoms of coordinated methanol molecules have been omitted; (**b**) A view showing chiral crown ether pillared lanthanide phosphonate lamellae as well as the intercalation of free H_4pgbbp molecules. (Reprinted with the permission from Ngo and Lin [72]. Copyright 2002 American Chemical Society)

La-(+)-(*S*,*S*)-**1** in *P*1 space group, were obtained from La^{3+} and a racemic mixture of (±)-H_2**1** and homochiral (+)-(*S*,*S*)-H_2**1**, respectively. Since ligand **1** has a flexible ethylene bridge between two aromatic carboxylates, they show structural similarity together with near identical unit cell parameters. There are three major conformers with a staggered arrangement. Among them, c2-(*S*,*S*)-**1** exhibited a close similarity to c1-(*R*,*R*)-**1**. Thus, c2-(*S*,*S*)-**1** disguised itself as c1-(*R*,*R*)-**1** and produced a near-centrosymmetric local asymmetric unit by pairing with c1-(*S*,*S*)-**1**. As a result, the coordination clusters formed a perfect local centrosymmetric arrangement, for La-(±)-**1**, but a near-centrosymmetric arrangement for La-(+)-(*S*,*S*)-**1**.

Besides this difference concerning the pairing of two ligands to form the unit cage, the remaining self-assembly details for the two crystals were near identical. These resultant 1D rods were further connected by c3-**1** to form a 2D layer. It is worth pointing out that while two mirror images of c3-**1** were found in La-(±)-**1** with equal abundance, only one enantiopure conformer, c3-(*S*,*S*)-**1**, was found in La-(+)-(*S*,*S*)-**1**. The 2D layers were connected to form a 3D network with 1D channel (Fig. 17).

Chiral amino acid ligands and their derivatives inherit chirality of chiral carbon. The functional groups with oxygen atoms allow extensive cross-linking between the metallic ions and organic moieties, but part of the methyl group and benzene ring are hindered in yielding high-dimensional architectures. Both helpful and hindering functions exist in one ligand, and that, in and of itself which have seemingly contradictory factors, providing the possible conditions to get unexpected crystal structures. Hao et al. [74] synthesized a pair of chiral lanthanide coordination polymers, $[Eu(S\text{-}\mathbf{2})_2]_2Na_6$ and $[Eu(R\text{-}\mathbf{2})_2]_2Na_6$, by using chiral Schiff bases ligands in enantiomeric, which not only retain the chirality of the amino acids but also have versatile coordination behaviors. X-ray crystallographic analysis reveals that enantiomeric complexes crystallize in the chiral space group $P2_1$. In each homochiral complex, two $\mathbf{2}^{3-}$ ligands and one Eu(III) ion form a $Eu\mathbf{2}_2^{3-}$ unit,

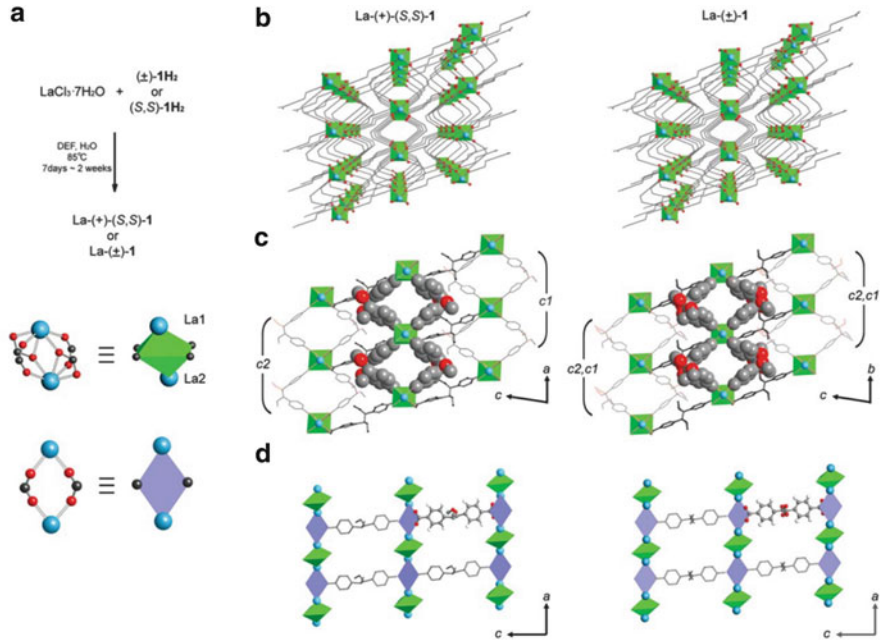

Fig. 17 (**a**) Synthesis of La-(+)-(*S*,*S*)-**1** and La-(±)-**1**, and their general SBUs; (**b**) Representative schematic 3D structures of La-(+)-(*S*,*S*)-**1** and La-(±)-**1**; (**c**) Two types of inorganic SBUs formed by two La ions and four carboxylates, M_2L_4 (*left*) or two carboxylates, M_2L_2 (*right*), and 1D chain of La-(+)-(S,*S*)-**1** (*bottom-left*) and La-(±)-**1** (*bottom-right*). The M_2L_4 are shown as *rectangles* from their top view; (**d**) 1D chains are further connected by **1** to form 2D layers parallel to the *ab* plane, and, in turn, linked along the *c* axis to form a 3D framework of La-(+)-(*S*,*S*)-**1** (*left*) and La-(±)-**1** (*right*). Selected conformers are shown in space filling model. (Reproduced from Jeong et al. [73] by permission of The Royal Society of Chemistry)

which is connected with Na^+ ion to produce 2D planes with the sandwich-like lamellar structure that is rarely reported in the literature (Fig. 18).

Liang et al. [75] have synthesized a chiral three-dimensional lanthanide MOF, $\{[Gd_4(R\text{-ttpc})_2(R\text{-Httpc})_2(HCOO)_2(H_2O)_8]\cdot 4H_2O\}_n$ by tripodal ligand *R*-H_3ttpc under solvothermal conditions. The structure of the MOF was solved by single-crystal X-ray diffraction in the chiral monoclinic space group $P2_1$. The fundamental subunit of the MOF structure is composed of two dimers with Gd···Gd distances of 4.131 and 4.117 Å. Each Gd dinuclear unit is linked by six different deprotonated *R*-H_3ttpc ligands, each of which bridges three different Gd dinuclear units, thus giving rise to a three-dimensional framework. From a topological perspective, if the deprotonated *R*-H_3ttpc ligand is considered to be a 3-connected node and the Gd dimer a 6-connected node, respectively, the structure of MOF can be simplified as a (3,6)-connected net with a Schläfli symbol of $(48^2)_2(4^6\cdot 8^7\cdot 10^2)$. In addition, the striking feature is the presence of a 1D O–H···O hydrogen-bonding chain among the oxygen atoms of lattice water molecules, coordinated aqua molecules and formate

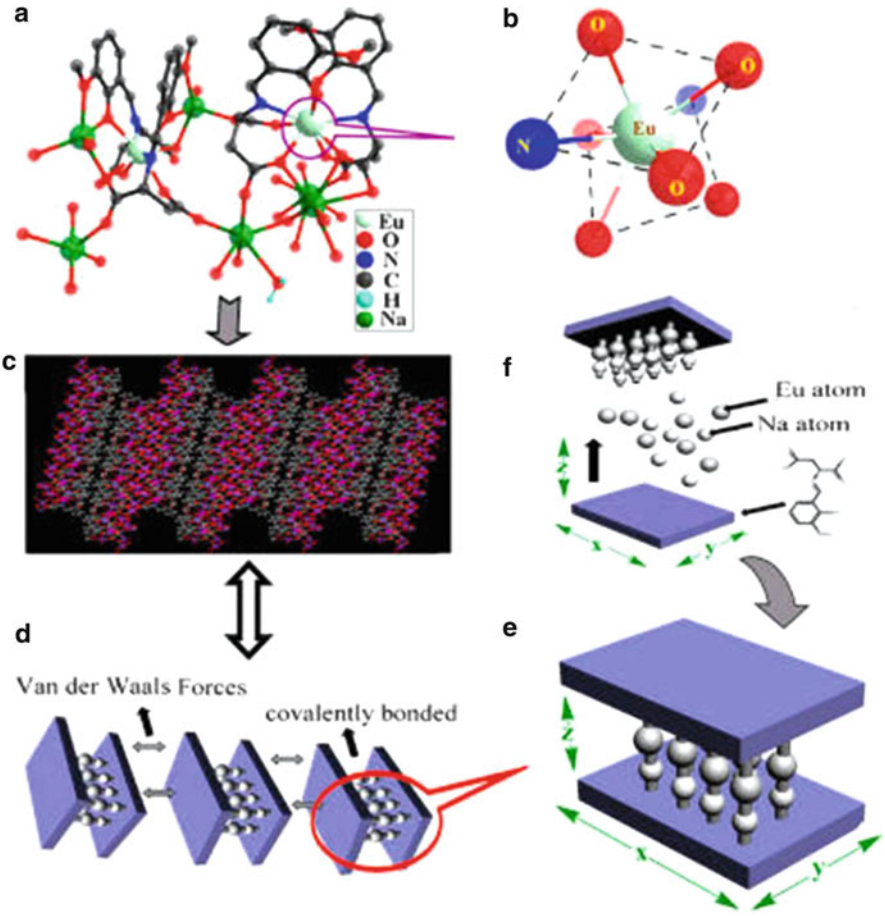

Fig. 18 (**a**) Representation of the molecular structure of complex $[Eu(S\text{-}\mathbf{2})_2]_2Na_6$. H atoms are omitted for clarity; (**b**) A distorted square antiprism which is formed by a Eu^{3+} ion; (**c**) The extended structure of complex viewed along the crystallographic *b* axis. (**d**) The schematic illustration of the extended structure. (**e**) The schematic presentation of the sandwich-like structure. (**f**) The vivid illustration of the basic components of the sandwich-like structure. (Reprinted with the permission from Hao et al. [74]. Copyright 2013 American Chemical Society)

ions in the 1D rectangular channel. The existence of hydrophilic channels, the carboxyl oxygen atoms as proton carriers, and hydrogen-bonding chains as proton-conducting pathways indicates that the chiral lanthanide MOF is likely a potential candidate for proton conduction (Fig. 19).

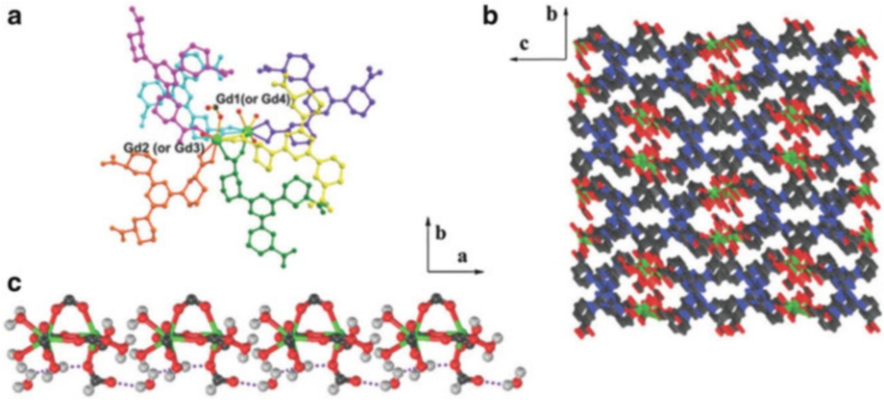

Fig. 19 (**a**) The fundamental subunit of $\{[Gd_4(R\text{-ttpc})_2(R\text{-Httpc})_2(HCOO)_2(H_2O)_8]\cdot 4H_2O\}_n$ is composed of two dimers. The bridging ligands are discriminated by color for clarity; (**b**) The three-dimensional framework of the MOF; (**c**) The 1D O–H···O hydrogen-bonding chain constructed from the oxygen atoms of the lattice water molecules, coordinated aqua molecules, and formate ions. (Reproduced from Liang et al. [75] by permission of The Royal Society of Chemistry)

2.2 *Synthesis of Chiral Lanthanide MOFs with Chiral Templates*

The way to construct chiral MOFs from achiral linkers could be achieved by employing chiral catalysts, templates, or solvents that do not act as components ligands. These chiral auxiliary materials can induce a particular enantiomeric form of the MOFs.

L-Proline and its derivatives are well-known asymmetric organocatalysts, accelerating a variety of enantioselective organic reactions. By using L- or D-*N*-*tert*-butoxy-carbonyl-2-(imidazole)-1-pyrrolidine (L- or D-BCIP) as chiral templates, Dang et al. [76] synthesized a pair of homochiral Ce-MOFs, Ce-MDIP-1, and Ce-MDIP-2, by solvothermal reaction of $Ce(NO_3)_3$ and achiral ligand methylene-diisophthalic acid (H_4MDIP) in 2010. Two enantiomers were crystallized in the chiral space group $P2_1$, but with opposite chirality to each other. Each cerium ion was coordinated by five oxygen atoms corresponding to five monodentate carboxyl groups, two oxygen atoms from one bidentate carboxyl group, and one water molecule. And the coordination geometry of the Ce metal node in two enantiomers was chiral, and both of them were mirror images of each other. The HMDIP ligands linked the metal ions through the carboxyl groups forming a non-interpenetrating 3D network containing chiral channels with a cross-section of 10.5×6.0 Å^2 along the *a* axis, in which the chiral inducer (L- or D-BCIP) was not included (Fig. 20).

Some bridging anion also could be used as linkers like the organic supporting ligands to form lanthanide MOF. In the presence of D-camphoric acid as chiral template, Wang et al. [77] successfully synthesized two novel chiral

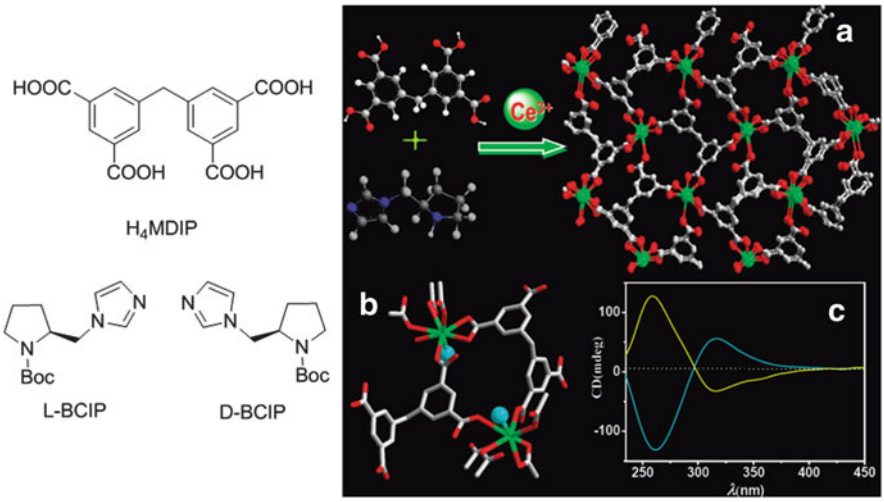

Fig. 20 (*Left*) The structures of H_4MDIP and chiral template L/D-BCIP; (*Right*) Crystal structure of Ce-MDIP-1 showing the positions of the removable coordinative molecules and the metal ions exposed within the 1D channels (*a*) and (*b*). The *cyan balls* show the removable coordinated water molecule. H atoms and lattice water molecules are omitted for clarity; (*c*) CD spectra of bulk crystals of Ce-MDIP-1 (*yellow line*) and Ce-MDIP-2 (*cyan line*), respectively, showing the opposite Cotton effects of the two compounds. (Reprinted with the permission from Dang et al. [76]. Copyright 2010 American Chemical Society)

lanthanide−sulfate MOFs, $Ln_4(OH)_4(SO_4)_4(H_2O)_3$ (Ln = Y, Er), by hydrothermal reactions of Ln_2O_3 and H_2SO_4 at pH 1. Two MOFs are isomorphous and crystallize in the orthorhombic space group $P2_12_12_1$. The Y(III) MOF structure exhibits that four μ_3-OH^- ions bridge four Y(III) ions to form $\{Y_4\}$ clusters as building blocks. Each SO_4^{2-} anion is linked to three $\{Y_4\}$ clusters, while each $\{Y_4\}$ cluster is linked to 12 nearest SO_4^{2-} ions. Therefore, the framework can be rationalized as a binodal (3,12)-connected net by assigning the SO_4^{2-} anion as a three-connected node and the $\{Y_4\}$ cluster as an 12-connected node with schläfli symbol of $(4^3)_4(4^{20}\cdot6^{28}\cdot8^{18})$. Moreover, the linkages between Y^{3+} and SO_4^{2-} ions form an unprecedented chiral 3D framework with helical tubes and channels. The helical tubes consist of double left-helical chains and double right-helical chains with a pitch of 16.57 Å running along the 2_1 axis; the double left-helical chains and double right-helical chains are interweaved to make the tubular walls with the same chirality. These adjacent tubular walls are further bridged together by SO_4^{2-} anions through their remaining μ-O atoms to form the helical channels. The coordinated water molecules are located in channels (Fig. 21).

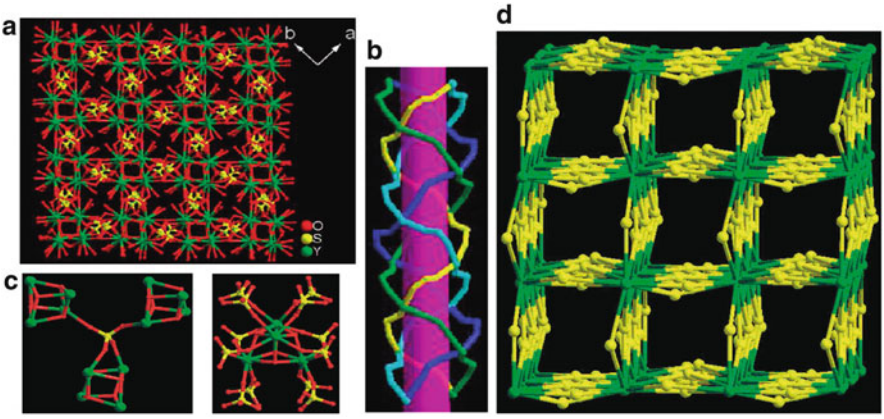

Fig. 21 (**a**) Framework of Y-MOF viewed along the *c* axis, showing helical tubes and channels arranged alternately, the coordinated water molecules are pointed to the channels; (**b**) View of the helical channels constructed from *double left-helical chains* weaved by *double right-helical chains* along the *c* axis; (**c**) Coordination environments of SO_4^{2-} and $\{Y_4\}$cluster in MOF; (**d**) Schematic representation of (3,12)-connected net. *Yellow*, SO_4^{2-}; *green*, $\{Y_4\}$ cluster. (Reprinted with the permission from Wang et al. [77]. Copyright 2012 American Chemical Society)

2.3 *Synthesis of Chiral Lanthanide MOFs with Spontaneous Resolution*

Homochiral MOFs are prepared from totally achiral components via spontaneous resolution during crystal growth. In this approach, a stereogenic center must be created in the complexation of the metal ions by more than two achiral ligands in the same coordination mode. And another option is to obtain the spatial arrangement of an achiral chain ligand around the metal ion. Both methods generally could result in the formation of helices by the wrapping of the components around a screw axis, which would further transfer chirality in the construction and crystallization of the MOF. If all the metal centers in the crystal keep the same L- or D-configuration the crystal will be chiral, the reaction yielding equivalent quantities of both crystal enantiomorphs (opposite handedness) of MOFs. Therefore, the helix, an attractive and evocative expression of chirality, exists as a secondary structure in a chiral framework and frequently interacts with each other by a specific interaction [78, 79] (Fig. 22).

In 2005, Rosi et al. [32] have synthesized 3D MOF-76, $[Tb(btc)(H_2O)_{1.5}]\cdot DMF$ in space group $P4_322$. In the structure, the Tb-O-C units are constructed from 7-coordinated Tb(III) centers. Six carboxyl groups as in mode A and a terminal water ligand bind each Tb. Each rod is connected to four neighboring rods through the benzene ring of the btc link. The rods pack in a tetragonal fashion, resulting in 6.6×6.6 Å^2 square channels in the *c* direction, which are filled with DMF molecules. Note, however, that the rods themselves are on 4_1 helices, but, because of the

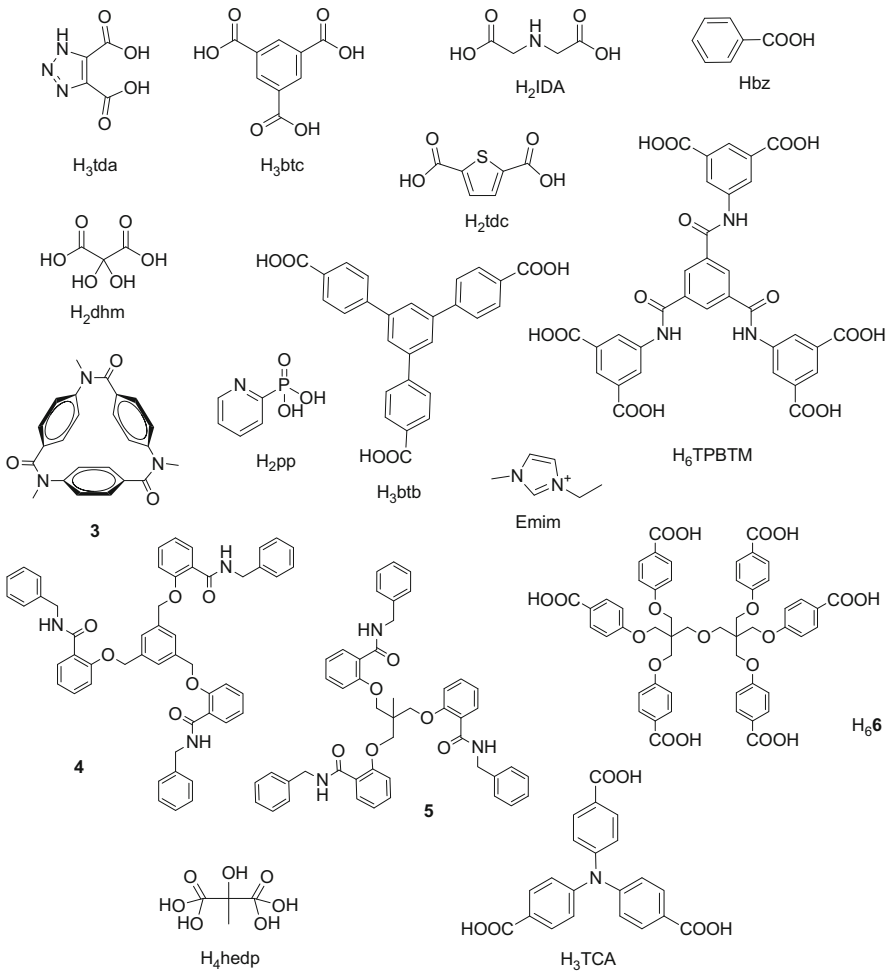

Fig. 22 Various achiral ligands in chiral lanthanide MOFs reported

tritopic nature of the organic SBU, result in a rather complicated overall topology (Fig. 23).

Guo et al. [80] reported a chiral lanthanide MOF, $[Dy(btc)(H_2O)]\cdot DMF$ in space group $P4_322$ in 2006, and they found the material had high surface area, 655 $m^2\ g^{-1}$, and high capacity for storage of hydrogen and carbon dioxide after removing the guest molecule and terminal coordinated molecule. Then, Gustafsson et al. [81] and Jiang et al. [82] have systematically synthesized and structurally characterized a series of enantiomerically pure chiral 3D lanthanide MOFs, $[Ln(btc)(H_2O)]\cdot x(solvent)$ (Ln = Nd, Eu, Tb, solvent = H_2O, DMF) in 2008 and $[Ln(btc)(H_2O)]\cdot 1.1(DMF)$ (Ln = Y, Tb, Dy, Er, Yb) in 2010, respectively, which are constructed from achiral ligands under spontaneous resolution without any chiral

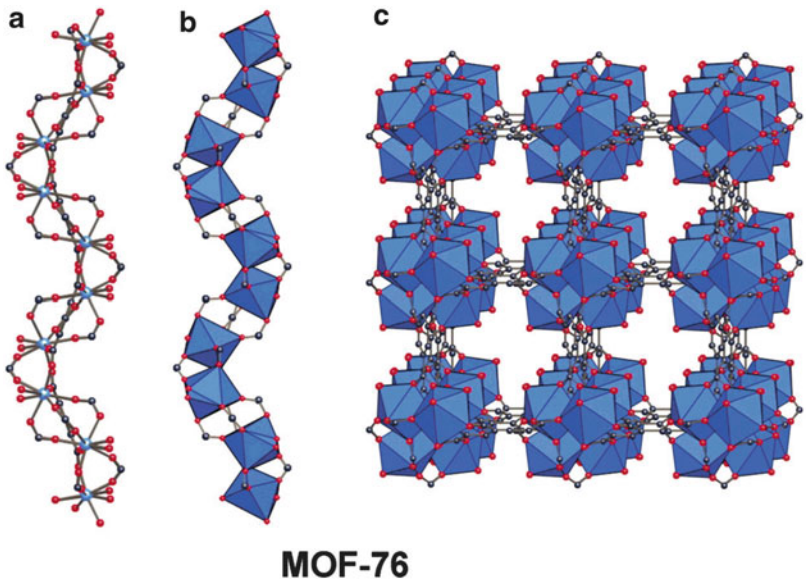

Fig. 23 (**a**) *Ball*-and-*stick* representation of SBU; (**b**) SBU with Tb shown as *polyhedra*; (**c**) view of crystalline framework with inorganic SBUs linked together via the benzene ring of 1,3,5-benzenetricarboxylate (DMF and H_2O guest molecules have been omitted for clarity). (Reprinted with the permission from Rosi et al. [32]. Copyright 2005 American Chemical Society)

auxiliary and the space group is $P4_322$ or $P4_122$. Although they provide slightly different formulae of MOFs, the frameworks of [Ln(btc)(H_2O)] are the same and the compounds are isostructural. The enantiopure counterparts of each compound can be separated manually. The btc^{3-} ligand bridges to six Ln(III) ions and each carboxylic oxygen connects one Ln(III). Such connection fashion of Ln(III) ion and btc^{3-} ligand leads to interesting 1D helical strands in the structure. Then, the carboxylic oxygen atoms of btc^{3-} ligands bridge adjacent Ln(III) ions to form three-stranded helical chains running along the crystallographic 4_3 axis. Both Ln (III) and btc^{3-} ligand can be regarded as six-connected nodes, and the whole network can be extended to an unusual 3D (6,6)-connected topology. In addition, these materials are highly thermostable and permanently porous with high surface areas and they show high potentials for H_2 storage (Fig. 24).

Majeed et al. [83] chose "parent" acid, benzoic acid (Hbz) as linker and obtained two 3D networks, [LnNa(bz)$_4$] (Ln = Ho, Dy), which also possesses the chiral srs-topology. Two compounds are isostructural and the single-crystal X-ray diffraction study of Ho-MOF shows an infinite 3D network, crystallizing in the chiral tetragonal space group $I4_1$. Within the structure, the Ho(III) cations are organized into dimers, which are linked via four benzoates with *syn*,*syn*-bridging mode. Each dimers cation is further ligated by two chelating benzoates. Na(I) ions are coordinated with oxygens from benzoates in metal dimers and these Ho···Na linkages are arranged as fourfold helices running parallel to the *c* axis as a result of the 4_1 screw

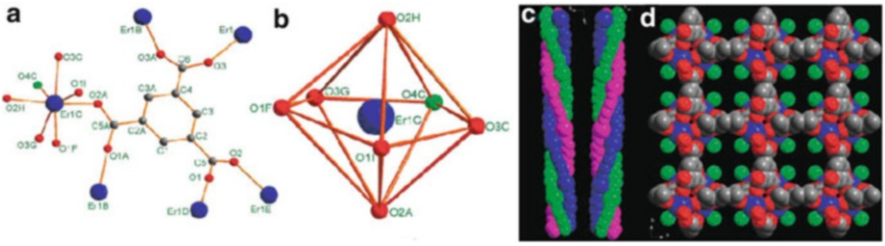

Fig. 24 (**a**) Coordination environment of Er(III) center and the binding fashion of btc^{3-} ligand; (**b**) the distorted pentagonal-bipyramidal coordination sphere of the Er(III) ion; (**c**) *Left-handed* (in structures with $P4_122$ space group) and *right-handed* (in structures with $P4_322$ space group) helical chains along the *c* axis in enantiomers; (**d**) View of the 3D structure with $P4_322$ space group along the *c* axis, exhibiting 1D helical channels for each side, and accessible Ln(III) sites can be obtained after removing the coordinated aqua molecules, which denoted as *green*. (Reprinted with the permission from Jiang et al. [82]. Copyright 2010 American Chemical Society)

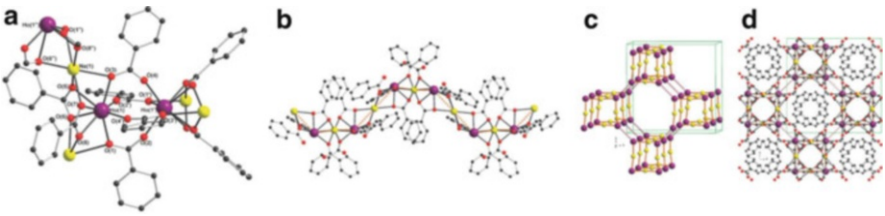

Fig. 25 (**a**) The $\{Ho_2(bz)_8\}^{2-}$ dimer, showing coordination of benzoate oxygens to the Na^+ cations, and the linkage to the Ho(III) of an adjacent dimer; (**b**) Ho···Na···Ho···Na helix in the structure; (**c**) Topology of the network of Ho ···Na ···Ho helices linked via the Ho_2 dimers viewed down the *c* axis; (**d**) Packing diagram for Ho-MOF, viewed down the *c* axis. (Reproduced from Majeed et al. [83] by permission of The Royal Society of Chemistry)

axes. These helices are linked by $\{Ho_2(bz)_8\}^{2-}$ dimers resulting in the complete 3D network (Fig. 25).

Yuan et al. [40] successfully synthesized seven isostructural coordination polymers by using achiral ligand H_3tda under hydrothermal conditions, $[Ln(tda)(H_2O)]_n{\cdot}2nH_2O$, (Ln = La, Ce, Pr, Nd, Sm, Eu, Gd). Single-crystal X-ray diffraction analyses reveal that compounds crystallize in the high-symmetry hexagonal space group $P3_221$ and possess a three-dimensional chiral coordination framework, which is an extremely successful strategy to obtain chirality of MOFs and transmit chiral information via the construction of helix. In the structure of the MOFs, the chiral unit can be considered as *a* chiral column built up from interweaving two different types of helices along the *c* axis. One is a right-handed double helix with the formula $[La\text{-}tda]_n$, which consists of two intertwined identical single helical chains formed by the tda^{3-} ligands bridging La(III) ions. The other is left-handed single helix with the formula $[La\text{-}OH_2]_n$ and it is formed by H_2O bridges between La(III) centers. Owing to the two kinds of helical chains possess different chiralities and

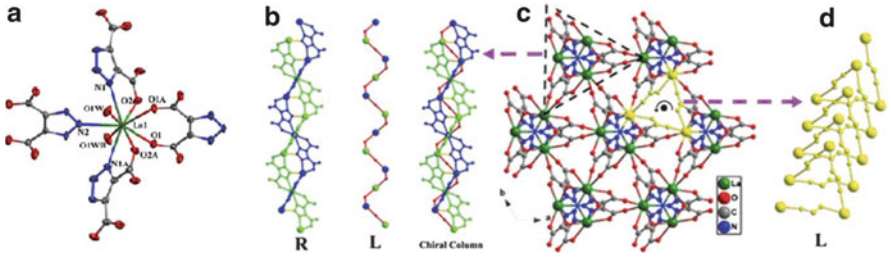

Fig. 26 (**a**) ORTEP plot of the coordination environment of the La atom in $[La(tda)(H_2O)]_n{\cdot}2nH_2O$; (**b**) View of the chiral column (*right*) formed by interweaving double helices (*left*) and single helix (*middle*); (**c**) Three-dimensional chiral framework; (**d**) View of the *left-handed* single helix constructed from carboxyl bridging metal atoms. (Reproduced from Yuan et al. [40] by permission of The Royal Society of Chemistry)

pitches, the column formed by them hold chirality. In addition, these helices have woven together to form interesting channels like labyrinth (Fig. 26).

Under ionothermal conditions, Wang et al. [84] synthesized two isomorphous chiral lanthanide MOFs $[Emim][Ln_{1.5}(tdc)_2Cl_{1.5-x}Br_x]$ (Ln = Nd, Eu) with orthorhombic space group $P2_12_12$, and two corresponding lanthanide MOFs [Emim] $[Ln(tdc)_2]$ (Ln = Nd, Eu) with space group $P2_1/c$, respectively. The structure of chiral MOF $[Emim][Nd_{1.5}(tdc)_2ClBr_{0.5}]$ shows that a trinuclear unit of $[Ln_3(tdc)_4Cl_2Br]^{2-}$ is formed by one independent Nd connecting two adjacent Nd centers through a series of carboxylate groups. Adjacent trinuclear units were further linked by one μ–Cl and two μ–O bridges to generate a 1D left-handed helical chain, which was connected with four adjacent ones with the same helicity to form a 3D structure. However, without halide ions in achiral $[Emim][Nd(tdc)_2]$, two Nd centers connected through bidentate carboxylate groups of four different tdc^{2-} ligands, forming a dinuclear unit. Such dinuclear units as 8-connected building blocks were linked to their respective neighbors, generating a 3D structure with a topology represented by the Schläfli symbol $(4^{24})(6^4)$.

A detailed structural analysis reveals that the coordination spheres of the lanthanide ions may be a key factor for the generation of a polar space group. The introduction of halide ions reduces the number of organic ligands necessary for the completion of the lanthanide coordination. As a result, the steric hindrance about the metal ion is significantly reduced, making it possible for the formation of the helical chain (Fig. 27).

Rossin et al. [85] have prepared anionic MOF $[(Fmd)Ln(HCOO)_4]_\infty$ ($Fmd^+ = NH_2–CH^+–NH_2$; Ln = Eu, Gd, Tb, Dy) through solvothermal methods. The compounds are isostructural and crystallize in the orthorhombic $C222_1$ chiral space group. Chirality is generated by the helicoidal packing of the bridging formate ions combined with square anti-prismatic coordination geometry around the lanthanide ion with coordination number eight. The resulting 3D network bears a negative charge that is balanced by the formamidinium cation lying inside the

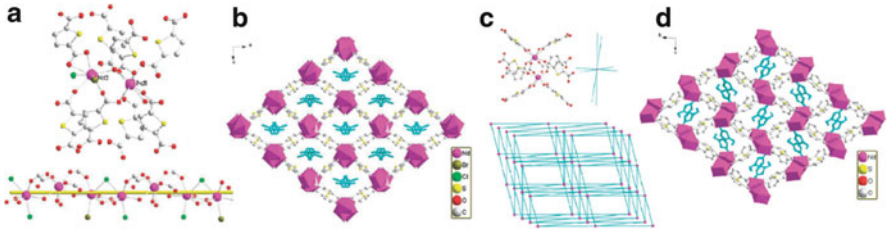

Fig. 27 (**a**) Coordination environments of Nd centers and the 1D helical chain in [Emim][$Nd_{1.5}(tdc)_2ClBr_{0.5}$]; (**b**) View of 3D MOF of [Emim][$Nd_{1.5}(tdc)_2ClBr_{0.5}$] along the *ac* plane; (**c**) The binuclear unit of {Nd_2} and schematic view of the 3D framework based on the {Nd_2} unit as a node for [Emim][$Nd(tdc)_2$]; (**d**) View of 3D MOF of [Emim][$Nd(tdc)_2$]. (Reproduced from Wang et al. [84] by permission of The Royal Society of Chemistry)

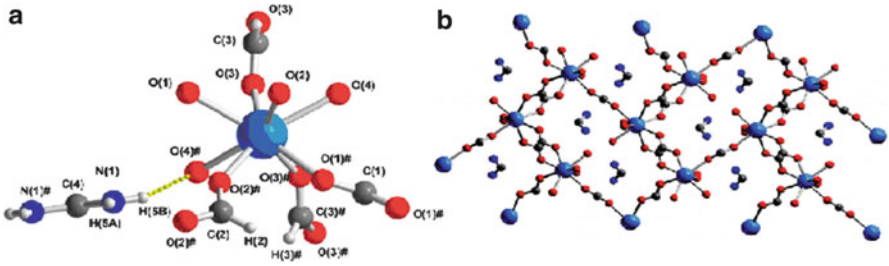

Fig. 28 (**a**) Unit cell of the crystal structure of Dy-MOF; (**b**) View of the polymer channels along the *a* axis. H atoms are omitted for clarity. (Reprinted with the permission from Rossin et al. [85]. Copyright 2012 American Chemical Society)

polymer channels. Their networks belong to the ecu ($3^6{\cdot}4^{15}{\cdot}5^7$) rare topology with Ln (III) nodes and $HCOO^-$ connections (Fig. 28).

The chiral MOFs having (6,3) and (10,3)-a topological frameworks can be targeted and constructed through direct assembly of triconnected inorganic and organic molecular building blocks, so the triconnected tripodal ligands are excellent candidates, which are labile and sensitive to the configuration environment including anions and solvent molecules. Masu et al. [86] obtained 2D chiral coordination network $\{[Yb(OTf)\mathbf{3}(H_2O)_3](OTf)_2(MeCN)\}_n$ (HOTf = Trifluoromethanesulfonic acid) constructed by tripodal rigid cyclic amide and lanthanide cations. This crystal has a *P*1 chiral space group, and each metal ion is coordinated by a counter anion and three H_2O molecules, except for three **3**. Every ligand also links three Yb(III) and a 2D infinite network is formed towards the *b* and *c* axes of a unit cell. Further, the layers of the coordination network of **3**-Yb are laminated along the *a* axis and form the channel structure. Free counter anions form hydrogen bonds between the coordinated H_2O molecules in different layers to link the layers together. The torsion angles of the three amide groups (CBz–N–C=O–CBz) in a crystal of **3**-Yb are 3.0(6), 3.4(7), and 24.2(6)°, respectively, and only the single-handed

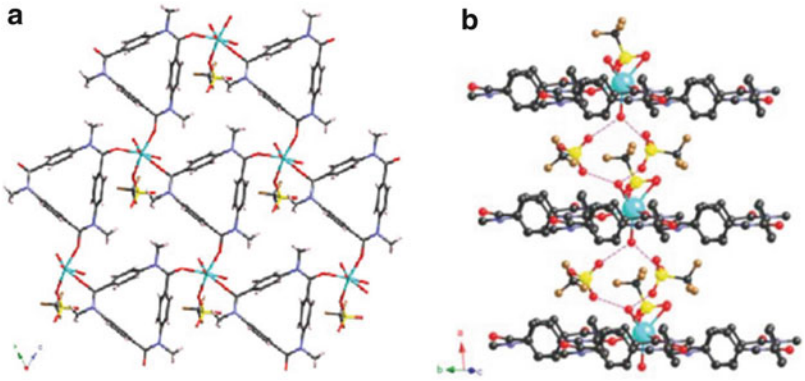

Fig. 29 (**a**) 2-D network of **3**-Yb. Non-coordinated triflate ions, water molecules, and solvent molecules are omitted for clarity; (**b**) Hydrogen bonding between counter anions and the coordinated H_2O molecules in the crystals of **3**-Yb. (Reproduced from Masu et al. [86] by permission of The Royal Society of Chemistry)

enantiomeric layers are laminated in the crystal. Therefore, this crystal forms an asymmetric space group, whereas the cyclic amide **3** is an achiral ligand (Fig. 29).

Tang and Liu et al. synthesized various achiral tripodal ligands and prepared a series of chiral lanthanide MOFs [87, 88]. In MOFs $[Ln\mathbf{4}(NO_3)_3]_n$ (Ln = Pr, Eu, Tb, Er) with orthorhombic chiral space group $P2_12_12_1$ and $\{[Eu\mathbf{5}(NO_3)_3]\cdot 1.5CHCl_3\}_n$ with hexagonal chiral space group $P6_3$ and $[Eu\mathbf{5}(pic)_3]_n$ with cubic chiral space group $P2_13$, each ligand binds to three Ln(III) ions using its three oxygen atoms of the amide groups, meanwhile, each Ln(III) connects with adjacent three ligands. However, the difference here is that $\{[Eu\mathbf{5}(NO_3)_3]\cdot 1.5CHCl_3\}_n$ demonstrates an chiral non-interpenetrated two-dimensional (2D) honeycomb-like (6,3) (hcb, Schläfli symbol 6^3) topological network, $[Ln\mathbf{4}(NO_3)_3]_n$ and $[Eu\mathbf{5}(pic)_3]_n$ are unusual chiral MOFs with three-dimensional (3D) (10,3)-a (srs, $SrSi_2$, Schläfli symbol 10^3) topological framework. The chirality of these frameworks results from the flexibility of the amide type tripodal ligands with three freely rotatable salicylamide moieties, which leads to the formation of propeller fashion or helical mode in complexes (Fig. 30).

Although the ligand H_6TPBTM used by Tang et al. [89] has no chirality, the introduction of Y(III) ions leads to the form of helical chains and the chiral character of the whole structure, $[Y_2(TPBTM)(H_2O)_2]\cdot x$G (G = guest molecule). The MOF possesses a chiral space group of $P2_12_12_1$ and a new topological net that contains left-helical rods constituted from edge-sharing pyramidal polyhedra with points of extension as carboxylic carbon atoms along the *a* axis. In accordance with the classification of the Reticular Chemistry Structure Resource and the simplification of rod MOFs, $TPBTM^{6-}$ can be simplified and the overall structure of MOF can be simplified to a new chiral 6-nodal net with a Schläfli symbol of $(3\cdot 9^2)(3^{10}\cdot 4^{11}\cdot 5^6\cdot 6)(3^2\cdot 4\cdot 9^3)(3^8\cdot 4^8\cdot 5^4\cdot 6)(9^3)$. Meanwhile, the MOF exhibits a high porosity, with the BET surface area of 1,152.1 $m^2\ g^{-1}$ and high CO_2 selectivity (Fig. 31).

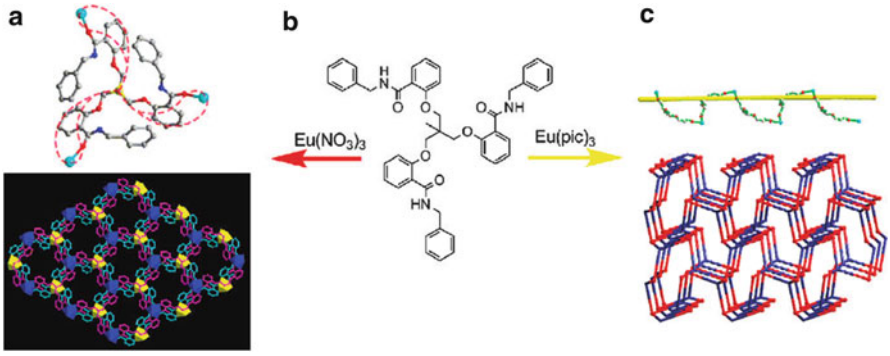

Fig. 30 (**a**) Chirality of the propeller-like structure and view of 3D non-interpenetrated honeycomb-like layers of (6,3) topology with 1D channels along the *c* axis in $\{[Eu\mathbf{5}(NO_3)_3]\cdot 1.5CHCl_3\}_n$; (**b**) The structure of the ligand; (**c**) Schematic illustration of the helical chain in $[Eu\mathbf{5}(pic)_3]_n$ propagating along the *a* axis and schematic representation of the (10,3)-a topological framework as viewed along the *a* axis. *Red nodes* represent the Eu(III) centers, and *blue nodes* represent the anchors of the ligands. (Reprinted with the permission from Yan et al. [88]. Copyright 2011 American Chemical Society)

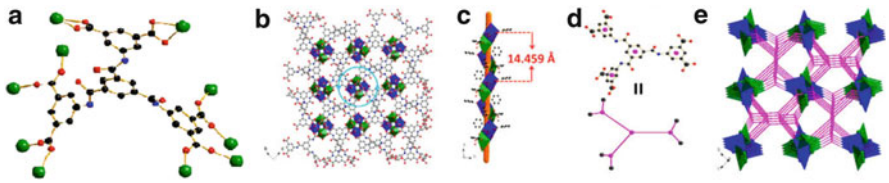

Fig. 31 (**a**) The coordination environment of $TPBTM^{6-}$ in Y-MOF; (**b**) 3D framework of MOF with a homochiral structure along the *a* axis (hydrogen atoms are removed for clarity); (**c**) *Left-helical chain* constituted from edge-sharing pyramidal polyhedra with points of extension as carboxylic carbon atoms along the *a* axis; (**d**) The simplification of $TPBTM^{6-}$; (**e**) The topology of MOF. (Reprinted with the permission from Tang et al. [89]. Copyright 2013 American Chemical Society)

Devic et al. [90] synthesized a series of porous lanthanides-based MOFs formulated $[Ln(btb)(H_2O)\cdot x(solv)]_n$ (Ln = La-Ho, Y; solv = H_2O, $C_6H_{11}OH$), among which only MOF $[Eu(btb)(H_2O)\cdot(C_6H_{11}OH)]_n$ was determined by single-crystal X-ray diffraction analysis. Structure analysis revealed that these solids crystallized in the chiral space group *R*32 with a slight contraction of the cell parameters according to the ionic radii of the rare-earth. Take Eu-MOF for example, it is built up from chains of corner-sharing $[EuO_9]$ polyhedra, connected through the btb^{3-} linkers to define a 3D honeycomb network. The Eu(III) ion adopts a tri-capped trigonal prismatic coordination arising from eight oxygen atoms of the carboxylates and one water molecule. The reversible character of the adsorption and desorption of free and coordinated solvent molecules reveals that dehydration is accompanied by a structural rearrangement of the lanthanide cations coordination shell. This rearrangement is reversible upon re-hydration, thus proving the presence

of accessible Lewis acid sites within the dehydrated forms, whose strength increases when the ionic radius of the metal decreases.

In 2012, Mu et al. [91] reported a new three-dimensional flexible lanthanide MOF $[La(btb)(H_2O)\cdot 3DMF]_n$ based on btb^{3-} ligand, which possesses a chiral space group $P6_522$, very high thermal stability (560°C), and high surface area (1,014 $m^2\ g^{-1}$). At about the same time, Lin et al. [92] prepared another isostructural three-dimensional lanthanide MOF $[Ce(btb)(H_2O)]$ with chiral space group $P6_122$, showing high surface area (1,091 $m^2\ g^{-1}$). Take the structure of $[La(btb)(H_2O)\cdot 3DMF]_n$ for example, the La(III) ions are linked by the bridging carboxyl groups from btb^{3-} ligands to generate an inorganic helical chain along the *c* axis. Three helices are linked by one btb^{3-} ligand, which lead to formation of a complicated 3D framework. The overall structure of La-MOF can be simplified as a binodal 6-connected nia net with a $(4^{12}\cdot 6^3)(4^9\cdot 6^6)$ Schläfli symbol, where La and btb^{3-} nodes possess $(4^{12}\cdot 6^3)$ and $(4^9\cdot 6^6)$ topology, respectively (Fig. 32).

Zhang et al. [79] have synthesized a series of homochiral lanthanide MOFs, $[Ln(IDA)(HIDA)]_n$ (Ln = Eu, Gd, Tb, Dy) under hydrothermally condition. These lanthanide MOFs are isomorphous with a chiral orthorhombic $P2_12_12_1$ space group. Notably, the enantiomers are obtained by spontaneous resolution during crystal growth in the absence of a chiral source and isolated the enantiomers based on their different morphologies. For example, the crystal morphologies of two Dy MOF enantiomers exhibit polyhedron and more acute triangular cone shape, respectively. For one of Dy MOF enantiomers, each Dy(III) ion is linked to its neighboring Dy(III) via the carboxyl groups of IDA^{2-} ligands, resulting in the

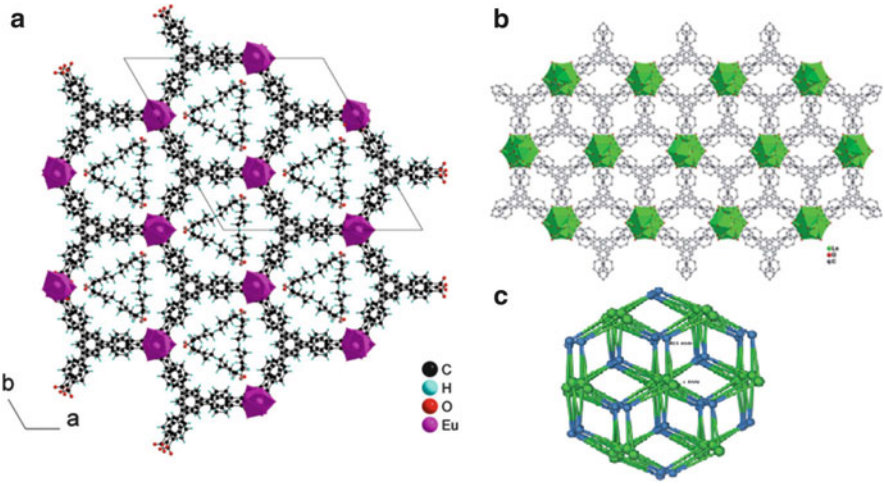

Fig. 32 (**a**) View of the structure of Eu-MOF as along the *c* axis. Note the *hexagonal pores* filled with free cyclohexanol molecules; (Reprinted from Devic et al. [90], Copyright 2011, with permission from Elsevier) (**b**) 3D framework of La-MOF along the *c* axis; (**c**) Three-periodic binodal nia net composed of btb^{3-} (*blue*) and La (*green*) nodes. (Reproduced from Mu et al. [91] by permission of The Royal Society of Chemistry)

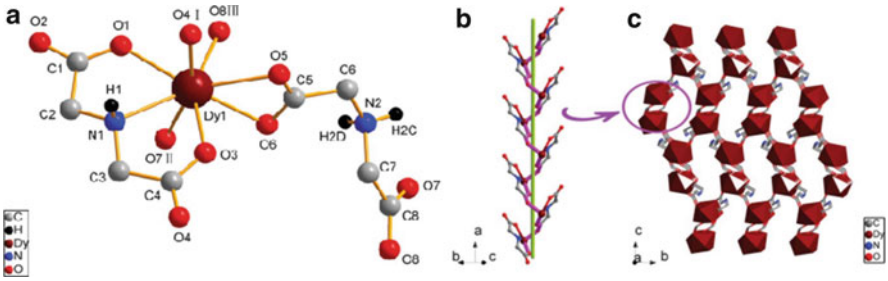

Fig. 33 (**a**) The asymmetric unit of Dy-MOF, showing the independent IDA^{2-} and $HIDA^{-}$ ligands; (**b**) *Left-handed* helix bridged by IDA^{2-} ligands, running parallel to the *a* direction with a 2_1 screw axis; (**c**) Perspective view of the 3D framework of Dy-MOF, showing one-dimensional helices are bridged by the $HIDA^{-}$ ligands to form a 3D framework. (Reproduced from Zhang et al. [79] by permission of The Royal Society of Chemistry)

formation of an infinite single chiral helix with a 2_1 screw axis passing through its center. The $HIDA^{-}$ ligands provide the remaining carboxyl groups as additional binding sites to assemble these single chiral helical chains into a 3D framework. When the IDA^{2-} ligand is represented simply as a linear linker between Dy(III) ions and the $HIDA^{-}$ ligand acts as a 3-connected node, each Dy(III) ion bridged by three $HIDA^{-}$ ligands and two IDA^{2-} ligands can be simplified as a 5-connected node. Therefore, topology analysis shows the overall framework can be described as a binodal (3,5)-connected *crs-d-3,5-Pnma* net with a short Schlafli symbol of $(4.6^2)(4^3.6^7)$. These compounds represent an intriguing example of helical and chiral MOFs based on iminodiacetic acid, demonstrating that this flexible ligand can lead to fascinating architectures (Fig. 33).

Isonicotinic acid (HNI) with both N and O donor atoms is a kind of special rigid molecule, which could work as a linker between the lanthanide and transition-metal ions to form novel structures with Ln-M heterometallic coordination frameworks. Gu and Xue [93] synthesized two isostructural homochiral 3D Ln-M MOFs $[LnAg(OAc)(IN)_3]$ (Ln = Nd, Eu) by hydrothermal process. They crystallize in the high-symmetry hexagonal space group $P6_122$. In the structure of $[NdAg(OAc)(IN)_3]$, a homochiral helical chain forms by introducing the second ligand, OAc^{-}, and a soft transition-metal ion, Ag(I). The OAc^{-} ligands connect to two types of metal centers in both chelating and bridging modes along different directions, which, therefore, lead to a non-centrosymmetric organization and a twist of the chain and the helical structure finally forms. Furthermore, the lack of a symmetry center of two types of metal centers also ensures the centricity of the chain and provides the possibility constructing a right-handed inorganic heterometallic helical chain with the alternate Nd(III) and Ag(I). In short, the occurrence of the helical structure may be attributed to the inducement of the Ag(I) ion and the coordination mode of OAc^{-}. These helical chains are connected together by IN^{-} spacers to form a homochiral 3D framework (Fig. 34).

By using HIN and displacing monovalent Ag(III), Peng et al. [94] also prepared a series of 3D isostructural chiral polymers, $[LnM(IN)_3(OAc)]$ (M = Li, Ln = Eu;

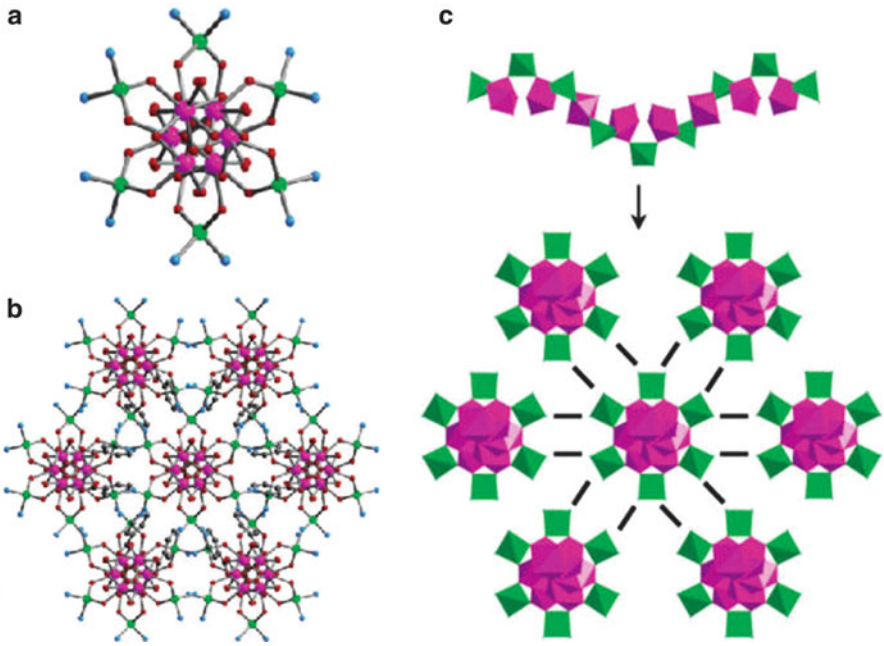

Fig. 34 (**a**) *Right-handed* heterometallic helicate with Nd-O-Ag connectivity along the *c* axis; (**b**) Perspective view of the 3D coordination framework along the *c* axis; (**c**) Polyhedral view of a helical chain interleaved with six other neighboring chains in $[NdAg(OAc)(IN)_3]$. The *bold line* represents the IN ligand. (Reprinted with the permission from Gu and Xue [93]. Copyright 2006 American Chemical Society)

M = Li, Ln = Tb; M = Na, Ln = Eu; M = Na, Ln = Tb). These coordination polymers were resolved spontaneously upon crystallization in hexagonal space group $P6_122$ ($[EuLi(IN)_3(OAc)]$ and $[TbNa(IN)_3(OAc)]$) or $P6_522$ ($[TbLi(IN)_3(OAc)]$ and $[EuNa(IN)_3(OAc)]$), displaying unique 3D chiral lanthanide-alkali heterometallic coordination frameworks built up by right-handed Eu/Tb-O-Li/Na chiral helicals and INA linkers. The right-handed chiral helical is constructed by the carboxylate oxygen atoms linking the adjacent Li(I) [or Na(I)] and Eu(III) [or Tb (III)] centers, which contribute to the chirality of the compound by chelation and linker effect of carboxyl groups around metal nodes. The 6_1 (or 6_5) screw axis passes down the center of the helical chain. Finally, the Eu/Tb-O-Li/Na helical chains are connected together by the INA linkers to form a 3D chiral heterometallic coordination framework. Topology analysis suggests that these compounds possess 3,3,4,7T2 topology.

And more notably, when alkali metal ions is K^+ ion, $[TbK(IN)_3(OAc)]$ shows a 3D pillared coordination polymer constructed from two-dimensional (2D) Tb-O-K layers with IN^- as connectivities possessing an alb-4,8-P21/c topology, which crystallize in the monoclinic space group $P2_1/n$. Authors think that the difference of chiral and achiral MOFs in those structures is generated from the size effect

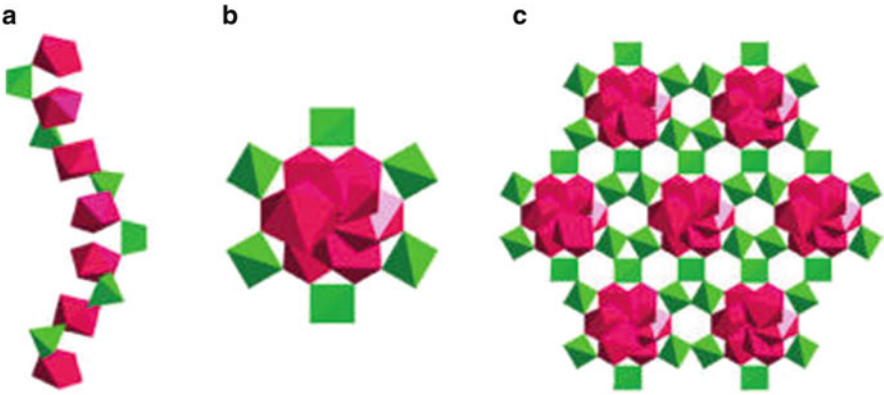

Fig. 35 (**a**) Polyhedral view of the 1D Eu–O–Li heterometallic helical chain in $[EuLi(IN)_3(OAc)]$ along the *b* axis; (**b**) View of 1D helical chain along the *c* axis; (**c**) View of the 3D coordination network of $[EuLi(IN)_3(OAc)]$ along the *c* axis (the IN linkers are omitted for clarity). (Reprinted with the permission from Peng et al. [94]. Copyright 2011 American Chemical Society)

of the alkali metal ions. Though the difference of the coordination mode of INA ligand does not change the structures of Ln-Li and Ln-Na compounds, the coordination number of alkali metal ions increases with the size of the ions: $LiN_2O_2 < NaN_2O_4 < KN_2O_5$ (Fig. 35).

Likewise, 2-pyridylphosphonate (pp^{2-}) is another bridging ligand containing phosphonate group similar to isonicotinic acid and could construct Ln-M complexes. Ma et al. [95] synthesized a series of Ln(III)–Cu(II) compounds with three-dimensional structures $Ln_2Cu_3(pp)_6{\cdot}4H_2O$ (Ln = La, Ce, Pr, Nd) by using H_2pp under hydrothermal conditions. These compounds are isostructural and crystallize in chiral cubic space group $I2_13$. In these structures, each Ln ion is nine-coordinate and has tri-capped triprismatic geometry, while each Cu center is six-coordinate with an octahedral environment. The $\{LnO_9\}$ polyhedra and $\{CuN_2O_4\}$ octahedra are connected by edge sharing to form an inorganic open-framework structure with a 3-connected 10-gon (10,3) topology in which the Ln and Cu atoms are alternately linked by the phosphonate oxygen atoms (Fig. 36).

Dong et al. [96] synthesized a series of isomorphous homochiral coordination frameworks of the general formula $[NH_4][Ln(hedp)(H_2O)]{\cdot}3H_2O$ (orthorhombic $P2_12_12_1$, Ln = La, Ce, Pr, Nd) by using the heptadentate ligand H_4hedp and lanthanide chloride under hydrothermal condition. Take $[NH_4][Ce(hedp)(H_2O)]{\cdot}3H_2O$ as examples, the Ce atoms are eight coordinated by six phosphonate oxygen atoms from four separate $hedp^{4-}$ ligands, one hydroxyl oxygen atom from one $hedp^{4-}$ ligand, and one oxygen atom from one coordinated water molecule. Each CeO_8 polyhedron is linked to each other through CPO_3 tetrahedra and thereby to form an infinite chain along the *b* axis. Such infinite chains are linked to form a three-dimensional framework structure via CPO_3 tetrahedra. The result of connections in this manner is formation of two types of 16-atom channels with dimensions of 9.5×8.5 Å^2 and 10×9 Å^2 along the crystallographic *a* and *b* axis, respectively.

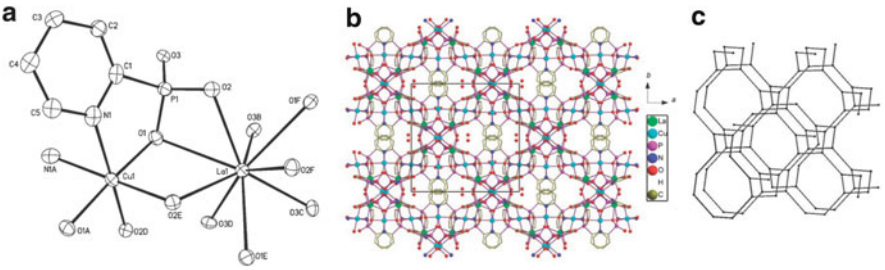

Fig. 36 (**a**) Building block of structure $La_2Cu_3(pp)_6{\cdot}4H_2O$ with atomic labeling scheme; (**b**) Three-dimensional structure of $La_2Cu_3(pp)_6{\cdot}4H_2O$. All H atoms are omitted for clarity; (**c**) Simplified view of the topology in which the $Cu(pp)_2$ units are regarded as linkers and the La atoms as nodes. (Reproduced from Ma et al. [95] by permission of John Wiley & Sons Ltd)

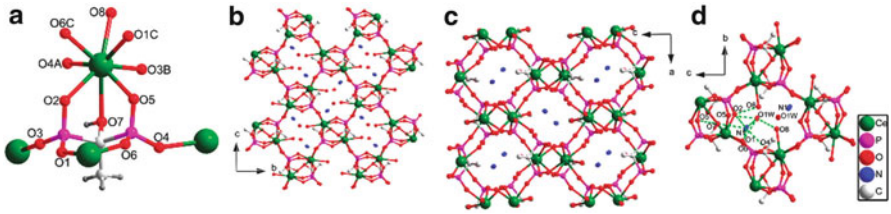

Fig. 37 (**a**) Fragment of the structure in Ce MOF; (**b**) View of the framework for Ce MOF along the *a* axis; (**c**) View of the framework along the *b* axis; (**d**) Perspective view of the 1D channels structure in Ce MOF showing the hydrogen bonds along the *a* axis. All H atoms are omitted for clarity. (Reprinted with the permission from Dong et al. [96]. Copyright 2011 American Chemical Society)

The lattice water molecules and charge compensating protonated NH_4^+ ions as templates being located inside this channel with extensive hydrogen-bonding interactions.

By comparing with other series of compounds, the chirality of Ce compound may originate from the extensive hydrogen-bonding interactions, such as crystal water molecule, which change the molecular steric orientation of protonated NH_4^+, and induce NH_4^+ as templates to form the chiral configuration. The interactions also influence the cerium coordination geometry, which exhibits a chiral configuration, and induce the distorted asymmetric framework, which transfers the chirality to three dimensions and generates the spontaneous (Fig. 37).

Gil-Hernandez et al. [78, 97] prepared the L/D-metal configured homochiral MOFs 2D-$[Ln_2(\mu\text{-dhm})_3(H_2O)_6]$ (Ln = La, Ce, Pr, Nd, Sm, Eu, Gd, Tb, Dy, Er, Yb) by using achiral chelating and bridging dhm^{2-} ligand through self-resolution during crystallization. All the compounds are all isostructural and crystallize in the space group *R*32. Three dhm^{2-} ligands chelate the Ln(III) atoms through one carboxylate oxygen atom and the hydroxyl oxygen atom. Three aqua ligands then complete the Ln coordination polyhedron to a tri-capped (slightly distorted)

trigonal prism. No significant amount of complexes with the opposite metal chirality (i.e., an enantiomer mixture) is present within one of the investigated crystals. Thus, the crystallization of a single crystal proceeds enantioselective to give either Λ- or Δ-metal-centered chirality within one single crystal. Although this enantioselectivity renders each single crystal homochiral (enantiopure), the batch most likely contains both enantiomorphs and the overall crystal mixture should be racemic. For example, there are overall 5 crystals with Λ-configuration and 6 with Δ-configuration for 11 selected MOFs with different metal centers. In other words, coordination geometry of lanthanide ion could induce the formation of one of MOF enantiomers but it is random. The structure analysis further exhibit the Ln(III) ions covalently connected by the mesoxalato ligands into a corrugated gray-arsenic type (6,3)-net (or layer) with chair-shaped six-membered rings (Fig. 38).

Dang et al. [98] reported a family of luminescent chiral lanthanide MOFs, Ln_2**6**·2DMF (Ln = La, Eu, Tb), based on a semi-rigid polycarboxylic acid (H_6**6**) under solvothermal conditions. The compounds with different metal centers are isostructural and crystallize in a chiral space group *C*2, displaying significant

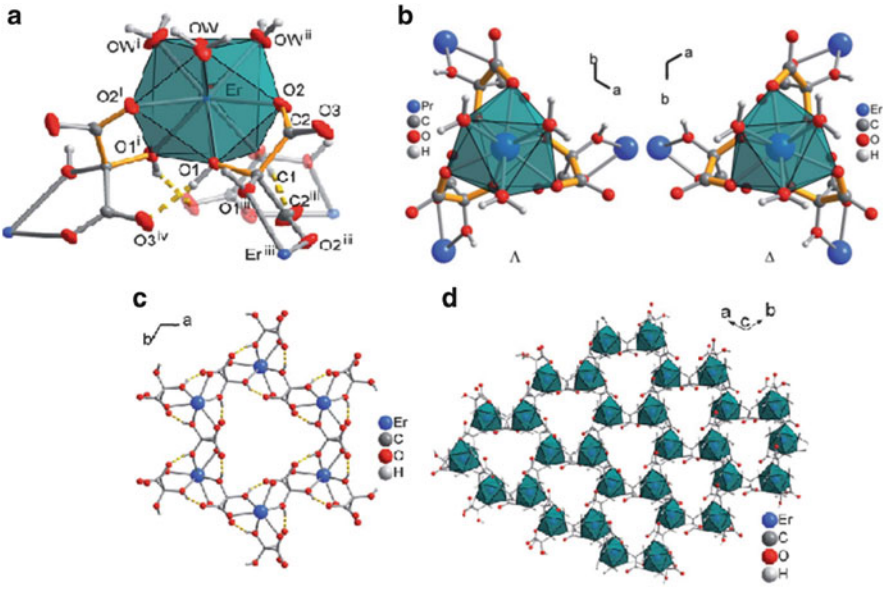

Fig. 38 (**a**) The ligand configuration around Er(III) in a polyhedral illustration to show the tri-capped trigonal prism. To highlight the Δ-configuration the chelating part of the ligand is presented with *orange bonds*; (**b**) The Λ-configuration around Pr(III) and the Δ-configuration around Er(III) (chosen as representative examples); (**c**) Chair-shaped six-membered rings through the ligand bridging action with the hydrogen bonds around the metal atom as *yellow dashed lines* (aqua ligands omitted for clarity); (**d**) A corrugated gray-arsenic type (6,3)-net for Er coordination polymer. (Reproduced from Gil-Hernandez et al. [78] by permission of The Royal Society of Chemistry)

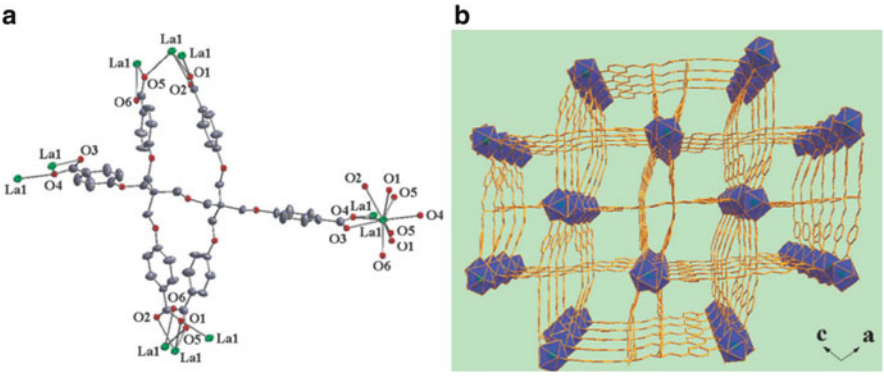

Fig. 39 (**a**) ORTEP representation of compound La**6**. Hydrogen atoms were omitted for clarity; (**b**) View of compound Ln**6** down the (010) direction, Ln(III) is represented as polyhedra. (Reproduced from Dang et al. [98] by permission of The Royal Society of Chemistry)

second-harmonic generation (SHG) activities. In the structures, each Ln atom is coordinated by nine oxygen atoms from five different ligands. The neighboring Ln (III) ions share three oxygen atoms leading to an infinite 1D chain along the *b* axis. These chains are further connected by the carboxylate groups to form a 3D framework with a pore size of around 8.0×6.0 Å^2 down the *b* axis. Free DMF molecules are located inside the pores (Fig. 39).

Zhang et al. [99] obtained a series of chiral two-dimensional lanthanide coordination polymers of $[Ln_2(dhm)_3(H_2O)_6]_n \cdot n/3H_2O$ (Ln = Nd, Sm, Eu, Tb, Dy, Ho, Er) by using dihydroxyfumaric acid under hydrothermal condition. All complexes are constructed from achiral ligands under spontaneous resolution without any chiral auxiliary and the space groups are *R*32. Though dhm^{2-} ion in coordination polymers is not the starting material, it can be formed by decomposition, rearrangement, and transformation of dihydroxyfumaric acid as a source of polydentate O-donor ligand under hydrothermal condition and in the presence of $CuCl_2$. For one of enantiomerically pure chiral Nd complexes, the dhm^{2-} adopts a bis-chelate coordination mode to bridge two Nd(III) centers through the carboxyl oxygen atom and hydroxyl group, a similar bridging and chelating behavior to oxalate. Each Nd center surrounded by three dhm^{2-} ligands presents a turbine blade structure with Δ-configuration, and alternatively connects adjacent centers with same Δ-configuration but with opposite orientation forming a chiral 2D framework on *ab* plane. If the $Nd(dhm)_3$ units are simplified as three-connect nodes, the 2D coordination framework form a wave-like (6,3) net of six-member topological ring (Fig. 40).

Lu et al. [100] reported the simple chiral lanthanide MOF, $Gd(IO_3)_3 \cdot H_2O$, which was synthesized hydrothermally from Gd_2O_3 and HIO_3 in the presence of Cu (II) ions and crystallizes in the chiral $P2_1$ space group. In this structure, each Gd (III) ion is ligated by eight O atoms from IO_3^- to give the GdO_8 bicapped trigonal-prism geometry with chiral symmetry, and a kind of IO_3^- polyhedra adopts the μ_3-

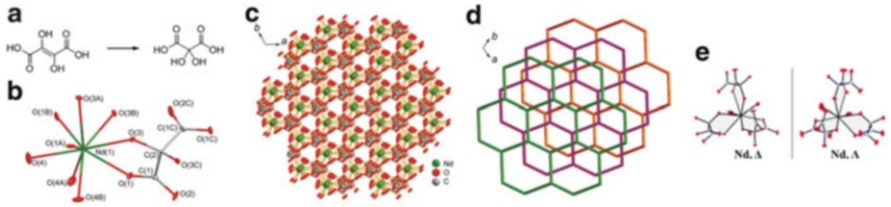

Fig. 40 (**a**) Decomposition reaction of dihydroxyfumaric acid in hydrothermal synthesis; (**b**) ORTEP views of Nd-MOF with 50% thermal ellipsoids; (**c**) View of the stacking mode of Nd-MOF; (**d**) Topological (6,3) net of MOF; (**e**) View of the configuration of $[Ln(dhm)_3]^{3-}$ units in compounds Δ-Nd-MOF and Λ-Nd-MOF. (Reproduced from Zhang et al. [99] by permission of John Wiley & Sons Ltd)

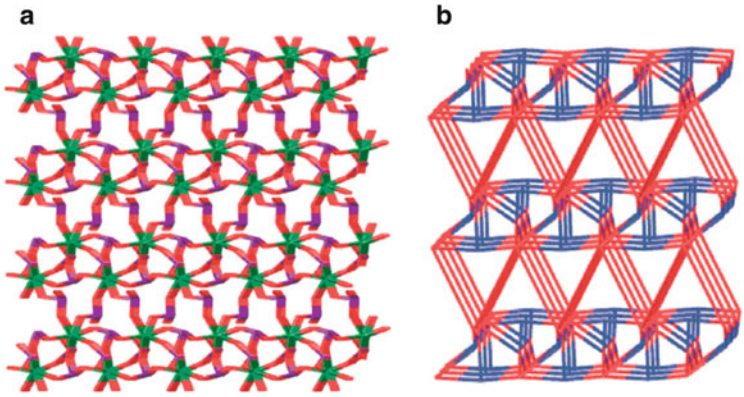

Fig. 41 (**a**) The pillared 3D frameworks of $Gd(IO_3)_3{\cdot}H_2O$; (**b**) schematic description of the $(4^3)(4{\cdot}6^2)(4^9{\cdot}6^{17}{\cdot}8^2)$ network built on (3,8)-connected nodes. (Reprinted from Lu et al. [100] by permission of Taylor & Francis Ltd)

bridging mode to link three neighboring Gd(III) ions to form 2D sheet structure. Further, these sheets are pillared by one μ_2-linkage of IO_3^- to construct the elegant 3D framework architecture presenting the (3, 8)-connected $(4^3)(4{\cdot}6^2)(4^9{\cdot}6^{17}{\cdot}8^2)$ topological network. The formation of the chiral MOF is analyzed by examining whether there is the inevitable relationship between the lanthanide iodate and the presence of $CuCl_2$ in preparation. The results show that anhydrous $Gd(IO_3)_3$ is the only product when $CuCl_2$ is absent, but $Gd(IO_3)_3{\cdot}H_2O$ could be generated by the introduction of various copper salts with different counter anions, such as $CuCl_2$, $Cu(NO_3)_2$, $Cu(SO_4)_2$, and $Cu(CH_3COO)_2$ (Fig. 41).

Ju et al. [101] reported ten chiral enantiomerically 3D architectures L- and D-$[Ln(HCO_2)(SO_4)(H_2O)]_n$ (Ln = La, Ce, Pr, Nd, Eu) without any chiral auxiliary under hydrothermal conditions. The addition of DMF not only acts as a solvent but also decomposes to a ligand of HCOOH. In all structures, the Ln atom is 9-coordinated by water molecule and bridging formyl group and sulfate group. Ln atoms are

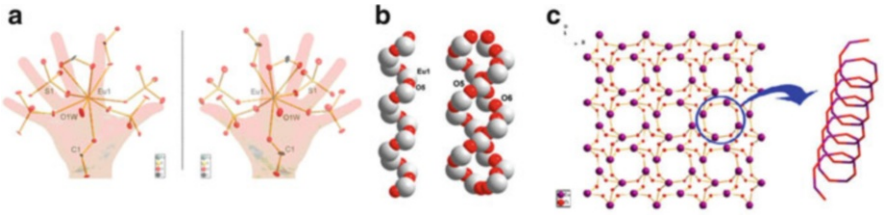

Fig. 42 (**a**) Coordination environment of Eu(III) in D- and L-$[Eu(HCO_2)(SO_4)(H_2O)]_n$; (**b**) D-Helical chain and chiral interpenetrating double-helix chain of D-MOF; (**c**) Chiral framework and D-chiral topological chain of D-$[Eu(HCO_2)(SO_4)(H_2O)]_n$. (Reprinted with the permission from Ju et al. [101]. Copyright 2012 American Chemical Society)

bonded by bridging O atoms to make a one-handed helical chain, while other bridging O atoms bond Ln atoms to generate other one-handed helical $[Ln{-}O]_n$ cluster chains. Adjacent helical $[Ln{-}O]_n$ chains are connected through O−Ln−O linkages to form chiral intertwined Ln−O double helices. The bridging formyl and sulfate groups connect the double helices to perform a topological framework. L-helical Ln–O cluster chains construct L-$[Ln(HCO_2)(SO_4)(H_2O)]_n$ with the space group $P4_3$ and D-helical Ln–O cluster chains construct D-$[Ln(HCO_2)(SO_4)(H_2O)]_n$ with the space group $P4_1$ (Fig. 42).

2.4 Synthesis of Chiral Lanthanide MOFs with Other Synthetic Strategies

Shi et al. [102] reported the synthesis strategy of chiral porous inorganic materials, lanthanide pyrophosphates, from chiral porous MOF precursors. First, the hydrothermal reaction of etidronic acid (H_5hedp) and lanthanide chlorides afforded a series of isotypical materials formulated as $[Ln_4(Hhedp)_3(H_2O)_2]$ (Ln = Er, Y, Tb, Dy, Ho; hedp = phosphonate). Take $[Er_4(Hhedp)_3(H_2O)_2]$ for example, it crystallizes in the chiral cubic $I2_13$ space group, with an asymmetric unit comprising two Er(III) centers plus one half of a $Hhedp^{4-}$ ligand, which has the central carbon atom on a twofold axis. These building blocks form a dinuclear trigonal bipyramidal SBU. Then, the structures of chiral porous lanthanide phosphonates may be transposed onto chiral lanthanide pyrophosphates via a suitable thermal treatment in air, with the pristine compound undergoing three stages of single-crystal-to-single-crystal transformation: (1) dehydration to remove bonded water ($\leq$300°C); (2) partial decomposition of the hedp ligand to $(PO_3{-}CH{=}PO_3)^{4-}$ (400–500°C); (3) oxidation of the $(PO_3{-}CH{=}PO_3)^{4-}$ ligand to inorganic pyrophosphate (600–700°C). This is one of those novel methods to synthesize chiral lanthanide MOFs by another chiral MOF template (Fig. 43).

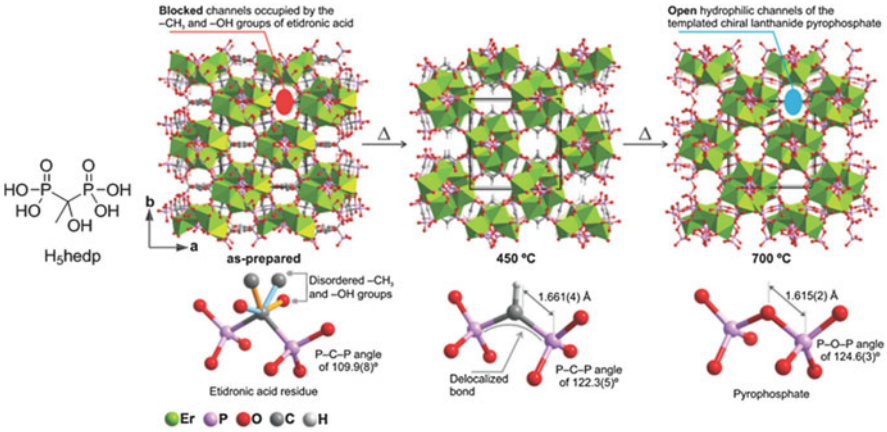

Fig. 43 Structural transformation of the frameworks and ligands, from room temperature to ca. 700°C: as-prepared MOF $[Er_4(Hhedp)_3(H_2O)_2]$ transforms into the hybrid $[Er_4(PO_3–CH=PO_3)_3]$ network at ca. 450°C, which upon further heating yields the purely inorganic $[Er_4(PO_3–O–PO_3)_3]$ network at ca. 700°C. (Reproduced from Shi et al. [102] by permission of The Royal Society of Chemistry)

3 The Application of Chiral Lanthanide MOFs

Although chiral lanthanide MOFs have been designed and prepared by various synthetic strategies, the research of their applications is still at an early stage and far behind the development of the synthesis technology. Only a few examples have been reported to utilize and explore the unique advantages of chiral lanthanide MOFs in asymmetric catalyst, separation, and luminescence.

Evans et al. [70] early explored the catalytic applications of chiral lanthanide MOFs in heterogeneous catalysis for different catalytic systems. The presence of both Lewis and Brönsted acid sites in chiral 2D framework $[Sm(H_2ddbp)(H_3ddbp)]$ has rendered them capable of catalyzing several organic transformations including cyanosilylation of aldehydes, ring opening of *meso*-carboxylic anhydrides, and Diels-Alder reactions.

Treatment of benzaldehyde, 1-naphthaldehyde or propionaldehyde, and cyanotrimethylsilane with a CH_2Cl_2 suspension of powdered and desolvated $[Sm(H_2ddbp)(H_3ddbp)]$ afforded the corresponding cyanohydrin products in 69, 55, and 61% yield, respectively, and all products were essentially racemic (ee < 5%). Treatment of *meso*-2,3-dimethylsuccinic anhydride with methanol in a dry THF suspension of powdered and desolvated catalyst afforded the corresponding hemiester in 81% yield with a disappointingly low ee of <5%. Although the catalysts could be recovered in quantitative yields (>98%) and used repeatedly without the loss of catalytic activity, these negligible ee illustrate the challenge in designing highly enantioselective MOF catalysts via remote influence by chiral environments of the open channels (Fig. 44).

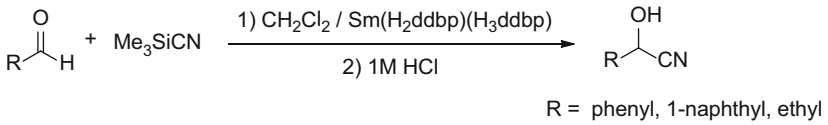

Fig. 44 Cyanosilylation of aldehydes in the presence of chiral [Sm(H_2ddbp)(H_3ddbp)]

In addition, they also attempted enantioselective separation of racemic *trans*-1,2-diaminocyclohexane with ammonia-treated *R*-[Sm(H_2ddbp)(H_3ddbp)] at a substrate/host ratio of 1.4, which gives an enantio-enrichment of 13.6% in *S*,*S*-1,2-diaminocyclohexane in the beginning fractions and an enantio-enrichment of 10.0% in *R*,*R*-1,2-diaminocyclohexane in the ending fractions.

For homochiral Ce-MOFs [76], the Ce metal nodes containing labile water molecules in the coordination sphere can serve as a Lewis acid catalyst, and the catalytic activities of two enantiomers Ce-MOFs in asymmetric cyanosilylation of aldehydes were examined. The asymmetric cyanosilylation experiments were employed with a 1:2.4 mol ratio of the selected aromatic aldehyde and cyanotrimethylsilane in CH_3CN at room temperature through a heterogeneous manner. Both MOFs showed excellent enantioselectivity (>91%) in the asymmetric cyanosilylation with high conversion (>95%). The result suggests that a chiral template is an important method to induce a particular enantiomeric form of the chiral framework with catalytic functional material. In addition, the solids of Ce-MDIP-1 can be easily isolated from the reaction suspension by simple filtration alone and can be reused at least three times with a slight decrease in the reactivity and enantioselectivity, which are valuable for heterogeneous asymmetric catalyst.

One important aspect for functions and applications of lanthanide elements in chiral MOFs is to study the luminescent properties and the relation between the structure and spectrum. The lanthanide ion most commonly used in sensing applications is Eu(III) due to their strong visible luminescence in the red regions. In Eu^{3+} complexes, the $^5D_0 \rightarrow {}^7F_2$ and $^5D_0 \rightarrow {}^7F_1$ transitions are the most readily observable transitions, which are the strongest and most useful for structural determination and sensing. The $^5D_0 \rightarrow {}^7F_1$ transition contains a prominent magnetic dipole and is nearly completely insensitive to the local environment. However, the $^5D_0 \rightarrow {}^7F_2$ transition with $\Delta J = \pm 2$ is hypersensitive to the coordination environment due to their strong electric-dipole character. This disparity allows the use of the ratio of relative intensities, ($^5D_0 \rightarrow {}^7F_2$):($^5D_0 \rightarrow {}^7F_1$) transitions, to probe the nature of the linker environment [34] and it is possible to discern some symmetry elements of a framework even in the absence of single-crystal X-ray data.

For homochiral lanthanide MOFs {Eu_2(D-cam)$_2$(bdc)(H_2O)$_2$}·DMF [58], the emission peaks occurred at 592, 616, 650, and 700 nm can be assigned to $^5D_0 \rightarrow {}^7F_J$ ($J = 1-4$) transitions, respectively. The symmetric forbidden emission $^5D_0 \rightarrow {}^7F_0$ at 580 nm is invisible. The most intense emission at 616 nm is attributed to the electric-dipole-induced $^5D_0 \rightarrow {}^7F_2$ transition, which is hypersensitive to the coordination environment of the Eu (III) ions and implies a red emission light. The

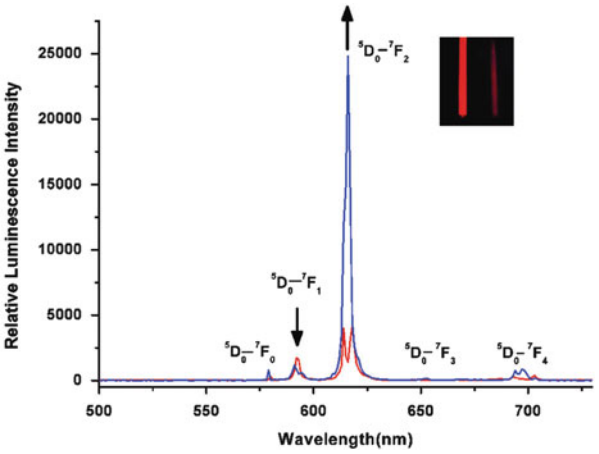

Fig. 45 Room-temperature emission spectra for the compounds $\{[Eu\mathbf{5}(NO_3)_3]_3{\cdot}1.5CHCl_3\}_n$ and $[Eu\mathbf{5}(pic)_3]_n$. (*inset*) Color changes for compounds $[Eu\mathbf{5}(pic)_3]_n$ (*left*) and $\{[Eu\mathbf{5}(NO_3)_3]_3{\cdot}1.5CHCl_3\}_n$ (*right*) under the excitation of UV light ($\lambda_{ex} = 365$ nm). (Reprinted with the permission from Yan et al. [88]. Copyright 2011 American Chemical Society)

medium-strong emission at 592 nm corresponds to the magnetic-dipole-induced $^5D_0 \rightarrow {}^7F_1$ transition, which is fairly insensitive to the environment of the Eu (III) ions. The intensity ratio of 3.63 for $I(^5D_0 \rightarrow {}^7F_2)$:$I(^5D_0 \rightarrow {}^7F_1)$ indicates that the symmetry of the Eu (III) ion site is low and Eu(III) ions in MOFs are not all located at the inversion center, which is in good agreement with the result of single-crystal X-ray analysis.

The luminescence properties of lanthanide MOFs could be improved by changing the coordination environment of Eu(III). For example, the emission intensity of the $^5D_0 \rightarrow {}^7F_2$ transition of $[Eu\mathbf{5}(pic)_3]_n$ is approximately six times stronger than that of $\{[Eu\mathbf{5}(NO_3)_3]_3{\cdot}1.5CHCl_3\}_n$ under the same conditions; however, the emission intensity of the $^5D_0 \rightarrow {}^7F_1$ transition is only an estimated 0.85 times [88]. Thus, replacement of the nitrate anion with the picrate anion not only resulted in chiral structural changes dramatically but also in luminescence of the MOFs enormously, which would lead to increasing monochrome of lanthanide MOFs or new luminous materials (Fig. 45).

The homochiral compounds should be good candidates for magnetic ferroelectrics, with residual dipole moments leading to ferroelectric properties where the layered structures with transition-metal or rare-earth ions may mimic a perovskite structure with magnetic properties because metal ions have unpaired electrons to result in the occurrence of magnetism while a homochiral ligand ensures that the MOF can crystallize in an acentric space group. For compound $[Tb(S\text{-}Lac)_2(H_2O)_2](ClO_4)$, ferroelectric and magnetic property measurements reveal that it probably is the first example of two "ferroic" MOFs. While for its analog $[Tb(S\text{-}Lac)_2(D_2O)_2](ClO_4)$, its ferroelectricity further confirms the presence of the ferroelectric deuterium effect. Therefore, the laminar and homochiral MOF will display larger permittivity anisotropy [63].

SHG is one of the most important NLO behaviors, which has been widely used in the laser industry, optoelectronic technologies, and optical microscopy in

biological and medical applications. The chiral lanthanide MOFs Ln_2**6**·2DMF crystallizing in a chiral space group *C*2 reported by Dang et al. [98] exhibited high SHG activities, which are nearly 6.0 times that of KDP (potassium dihydrogen phosphate, a commercially available NLO reference material). Furthermore, the measurements made on the powders with various particle sizes of the crystals of Eu**6**, ranging from 25 to 210 mm, reveal that the SHG signal relies on the particle sizes of the compound, in other words, the material exhibits a phase-matchable behavior. These studies are important for a deep understanding of the relationship between structure and property in order to explore more new NLO materials, which suggest these chiral lanthanide MOFs are considered as good candidates for the second-order NLO materials.

Liang et al. [75] also researched the NLO effect of chiral $\{[Gd_4(R\text{-ttpc})_2(R\text{-Httpc})_2(HCOO)_2(H_2O)_8]\cdot 4H_2O\}_n$ which crystallizes in the chiral space group $P2_1$ and theoretically exhibits the second-order NLO effect. The preliminary experimental result indicates that the MOF displays SHG activity with a value of approximately 0.5 times that of urea. The notable SHG efficiency is likely to result from the strength and number of intermolecular hydrogen bonds constructed from water molecules.

References

1. Gardner M (1990) The new ambidextrous universe, 3rd edn. W. H. Freeman & Co., New York
2. Heilbronner E, Dunitz JD (1993) Reflections on symmetry. VHCA, Basel
3. Aboul-Enein HY, Wainer IW (1997) The impact of stereochemistry on drug development and use. Wiley, New York
4. Li CY, Cheng SZ, Weng X et al (2001) Left or right, it is a matter of one methylene unit. J Am Chem Soc 123(10):2462–2463
5. Ariëns EJ (1986) Stereochemistry: a source of problems in medicinal chemistry. Med Res Rev 6(4):451–466
6. Maier NM, Franco P, Lindner W (2001) Separation of enantiomers: needs, challenges, perspectives. J Chromatogr A 906(1–2):3–33
7. Kuroda R, Endo B, Abe M et al (2009) Chiral blastomere arrangement dictates zygotic left-right asymmetry pathway in snails. Nature 462(7274):790–794
8. Capdevila J, Vogan KJ, Tabin CJ et al (2000) Mechanisms of left-right determination in vertebrates. Cell 101(1):9–21
9. Francotte E, Lindner W (2006) Chirality in drug research. Wiley-VCH, Weinheim
10. Blaschke G, Kraft HP, Fickentscher K et al (1979) Chromatographic separation of racemic thalidomide and teratogenic activity of its enantiomers. Drug Res 29(10):1640–1642
11. Nobel Prize homepage. http://nobelprize.org/nobel_prizes/chemistry/laureates/2001/
12. Noyori R (2002) Asymmetric catalysis: science and opportunities. Angew Chem Int Ed 41 (12):2008–2022
13. Sharpless BK (2002) Searching for new reactivity. Angew Chem Int Ed 41(12):2024–2032
14. Knowles WS (2002) Asymmetric hydrogenations. Angew Chem Int Ed 41(12):1998–2007
15. Morrison JD (1985) Asymmetric synthesis. Academic, New York
16. Subramanian G (2001) Chiral separation techniques. Wiley-VCH, Weinheim
17. Ward TJ (2006) Chiral separations. Anal Chem 78(12):3947–3956

18. Hattori H (1995) Heterogeneous basic catalysis. Chem Rev 95(3):537–558
19. Mizuno N, Misono M (1998) Heterogeneous catalysis. Chem Rev 98(1):199–218
20. Trindade AF, Gois PM, Afonso CA (2009) Recyclable stereoselective catalysts. Chem Rev 109(2):418–514
21. Kesanli B, Lin W (2003) Chiral porous coordination networks: rational design and applications in enantioselective processes. Coord Chem Rev 246(1–2):305–326
22. Ngo HL, Lin W (2005) Hybrid organic–inorganic solids for heterogeneous asymmetric catalysis. Top Catal 34:85–92
23. Ma L, Abney C, Lin W (2009) Enantioselective catalysis with homochiral metal-organic frameworks. Chem Soc Rev 38(5):1248–1256
24. Kim K, Banerjee M, Yoon M et al (2010) Chiral metal-organic porous materials: synthetic strategies and applications in chiral separation and catalysis. Top Curr Chem 293:115–153
25. Bradshaw D, Claridge JB, Cussen EJ et al (2005) Design, chirality, and flexibility in nanoporous molecule-based materials. Acc Chem Res 38(4):273–282
26. Song F, Zhang T, Wang C et al (2012) Chiral porous metal-organic frameworks with dual active sites for sequential asymmetric catalysis. Proc R Soc A 468(2143):2035–2052
27. Férey G (2008) Hybrid porous solids: past, present, future. Chem Soc Rev 37(1):191–214
28. Verbiest T, Elshocht SV, Kauranen M et al (1998) Strong enhancement of nonlinear optical properties through supramolecular chirality. Science 282(5390):913–915
29. Seo JS, Whang D, Lee H et al (2000) A homochiral metal-organic porous material for enantioselective separation and catalysis. Nature 404(6781):982–986
30. Huang CH (2010) Rare earth coordination chemistry: fundamentals and applications. Wiley, UK
31. Yaghi OM, O'Keeffe M, Ockwig NW et al (2003) Reticular synthesis and the design of new materials. Nature 423(6941):705–714
32. Rosi NL, Kim J, Eddaoudi M et al (2005) Rod packings and metal-organic frameworks constructed from rod-shaped secondary building units. J Am Chem Soc 127(5):1504–1518
33. Sabbatini N, Guardigli M, Lehn JM (1993) Luminescent lanthanide complexes as photochemical supramolecular devices. Coord Chem Rev 123(1–2):201–228
34. Allendorf MD, Bauer CA, Bhakta RK et al (2009) Luminescent metal-organic frameworks. Chem Soc Rev 38(5):1330–1352
35. Binnemans K (2009) Lanthanide-based luminescent hybrid materials. Chem Rev 109 (9):4283–4374
36. Carlos LD, Ferreira RA, Bermudez Vde Z et al (2009) Lanthanide-containing light-emitting organic-inorganic hybrids: a bet on the future. Adv Mater 21(5):509–534
37. Eliseeva SV, Bünzli JC (2010) Lanthanide luminescence for functional materials and bio-sciences. Chem Soc Rev 39(1):189–227
38. Bünzli JC, Piguet C (2005) Taking advantage of luminescent lanthanide ions. Chem Soc Rev 34(12):1048–1077
39. Zhou TH, Zhang J, Zhang HX et al (2011) A ligand-conformation driving chiral generation and symmetry-breaking crystallization of a zinc(II) organoarsonate. Chem Commun 47 (31):8862–8864
40. Yuan G, Shan KZ, Wang XL et al (2010) A series of novel chiral lanthanide coordination polymers with channels constructed from 16Ln-based cage-like building units. CrystEngComm 12(4):1147–1152
41. Crassous J (2009) Chiral transfer in coordination complexes: towards molecular materials. Chem Soc Rev 38(3):830–845
42. Lin X, Blake AJ, Wilson C et al (2006) A porous framework polymer based on a zinc (II) 4,4′-bipyridine-2,6,2′,6′-tetracarboxylate: synthesis, structure, and "zeolite-like" behaviors. J Am Chem Soc 128(33):10745–10753
43. Zhang J, Chen S, Wu T et al (2008) Homochiral crystallization of microporous framework materials from achiral precursors by chiral catalysis. J Am Chem Soc 130(39):12882–12883
44. Lin Z, Slawin AM, Morris RE (2007) Chiral induction in the ionothermal synthesis of a 3-D coordination polymer. J Am Chem Soc 129(16):4880–4881

45. Kang Y, Chen S, Wang F et al (2011) Induction in urothermal synthesis of chiral porous materials from achiral precursors. Chem Commun 47(17):4950–4952
46. Qiu S, Zhu G (2009) Molecular engineering for synthesizing novel structures of metal-organic frameworks with multifunctional properties. Coord Chem Rev 253(23–24):2891–2911
47. Pérez-García L, Amabilino DB (2002) Spontaneous resolution under supramolecular control. Chem Soc Rev 31(6):342–356
48. Pérez-García L, Amabilino DB (2007) Spontaneous resolution, whence and whither: from enantiomorphic solids to chiral liquid crystals, monolayers and macro- and supra-molecular polymers and assemblies. Chem Soc Rev 36(6):941–967
49. Ma Y, Han Z, He Y et al (2007) A 3D chiral Zn(II) coordination polymer with triple Zn-oba-Zn helical chains (oba = 4,4′-oxybis(benzoate)). Chem Commun 40:4107–4109
50. Yoon M, Srirambalaji R, Kim K (2012) Homochiral metal-organic frameworks for asymmetric heterogeneous catalysis. Chem Rev 112(2):1196–1231
51. Liu Y, Xuan W, Cui Y (2010) Engineering homochiral metal-organic frameworks for heterogeneous asymmetric catalysis and enantioselective separation. Adv Mater 22 (37):4112–4135
52. Zeng MH, Wang B, Wang XY et al (2006) Chiral magnetic metal-organic frameworks of dimetal subunits: magnetism tuning by mixed-metal compositions of the solid solutions. Inorg Chem 45(18):7069–7076
53. Dybtsev DN, Yutkin MP, Peresypkina EV et al (2007) Isoreticular homochiral porous metal-organic structures with tunable pore sizes. Inorg Chem 46(17):6843–6845
54. Zhang J, Yao YG, Bu XH (2007) Comparative study of homochiral and racemic chiral metal-organic frameworks built from camphoric acid. Chem Mater 19(21):5083–5089
55. Song YM, Huang HX, Sun GM et al (2011) Multi-functional magnetic, ferroelectric, and fluorescent homochiral lanthanide (Ln)-camphorate compounds built on helical $\{Ln\text{-}O\}_n$ inorganic substructures. CrystEngComm 13(22):6827–6830
56. Jhu ZR, Yang CI, Lee GH (2013) Two new series of rare-earth organic frameworks involving two structural architectures: syntheses, structures and magnetic properties. CrystEngComm 15(13):2456–2465
57. Sun ML, Zhang X, Huang YY et al (2014) Homochiral 3D lanthanide camphorates with high thermal stability. New J Chem 38(1):55–58
58. Sun ML, Zhang J, Lin QP et al (2010) Multifunctional homochiral lanthanide camphorates with mixed achiral terephthalate ligands. Inorg Chem 49(20):9257–9264
59. Dang DB, An B, Bai Y et al (2013) Three-dimensional homochiral manganese-lanthanide frameworks based on chiral camphorates with multi-coordination modes. Chem Commun 49 (22):2243–2245
60. Tan X, Du YZ, Che YX et al (2013) Syntheses, structures and magnetic properties of one family of 3d-4f chiral metal-organic frameworks (MOFs) based on D(+)-camphoric acid. Inorg Chem Commun 36:63–67
61. Qiu Y, Liu Z, Mou J et al (2010) Rationally designed and controlled syntheses of different series of 4d-4f heterometallic coordination frameworks based on lanthanide carboxylate and $Ag(IN)_2$ substructures. CrystEngComm 12(1):277–290
62. Qu ZR, Ye Q, Zhao H et al (2008) Homochiral laminar europium metal–organic framework with unprecedented giant dielectric anisotropy. Chem Eur J 14(11):3452–3456
63. Ye Q, Fu DW, Tian H et al (2008) Multiferroic homochiral metal−organic framework. Inorg Chem 47(3):772–774
64. Thushari S, Cha JAK, Sung HHY et al (2005) Microporous chiral metal coordination polymers: hydrothermal synthesis, channel engineering and stability of lanthanide tartrates. Chem Commun 44:5515–5517
65. Amghouz Z, Roces L, Garcia-Granda S et al (2010) Metal organic frameworks assembled from Y(III), Na(I), and chiral flexible-achiral rigid dicarboxylates. Inorg Chem 49(17):7917–7926

66. Amghouz Z, Garcia-Granda S, Garcia JR et al (2012) Series of metal organic frameworks assembled from Ln(III), Na(I), and chiral flexible-achiral rigid dicarboxylates exhibiting tunable UV-vis-IR light emission. Inorg Chem 51(3):1703–1716
67. Gao Q, Wang X, Jacobson AJ (2011) Homochiral frameworks formed by reactions of lanthanide ions with a chiral antimony tartrate secondary building unit. Inorg Chem 50 (18):9073–9082
68. Li XF, Liu TF, Gao ZX et al (2011) Syntheses and characterization of homochiral 3-dimensional lanthanide-organic frameworks based on Ln_4O_4 clusters and L-aspartic acid. Chin J Struct Chem 30(5):757–763
69. Lin W (2007) Metal-organic frameworks for asymmetric catalysis and chiral separations. Mrs Bull 32(7):544–548
70. Evans OR, Ngo HL, Lin W (2001) Chiral porous solids based on lamellar lanthanide phosphonates. J Am Chem Soc 123(42):10395–10396
71. Cui Y, Ngo HL, White PS et al (2002) Homochiral 3D lanthanide coordination networks with an unprecedented $4^9 6^6$ topology. Chem Commun 16:1666–1667
72. Ngo HL, Lin W (2002) Chiral crown ether pillared lamellar lanthanide phosphonates. J Am Chem Soc 124(48):14298–14299
73. Jeong KS, Lee BH, Li Q et al (2011) Near achiral metal-organic frameworks from conformationally flexible homochiral ligands resulted by the preferential formation of pseudo-inversion center in asymmetric unit. CrystEngComm 13(5):1277–1279
74. Hao Z, Song S, Su S et al (2013) Design and synthesis of enantiomerically pure chiral sandwichlike lamellar structure: new explorations from molecular building blocks to three-dimensional morphology. Cryst Growth Des 13(3):976–980
75. Liang X, Zhang F, Zhao H et al (2014) A proton-conducting lanthanide metal-organic framework integrated with a dielectric anomaly and second-order nonlinear optical effect. Chem Commun 50(49):6513–6516
76. Dang D, Wu P, He C et al (2010) Homochiral metal-organic frameworks for heterogeneous asymmetric catalysis. J Am Chem Soc 132(41):14321–14323
77. Wang WH, Tian HR, Zhou ZC et al (2012) Two unusual chiral lanthanide-sulfate frameworks with helical tubes and channels constructed from interweaving two double-helical chains. Cryst Growth Des 12(5):2567–2571
78. Gil-Hernandez B, Maclaren JK, Hoeppe HA et al (2012) Homochiral lanthanoid(III) mesoxalate metal-organic frameworks: synthesis, crystal growth, chirality, magnetic and luminescent properties. CrystEngComm 14(8):2635–2644
79. Zhang LM, Deng DY, Peng G et al (2012) A series of three-dimensional (3D) chiral lanthanide coordination polymers generated by spontaneous resolution. CrystEngComm 14 (23):8083–8089
80. Guo X, Zhu G, Li Z et al (2006) A lanthanide metal-organic framework with high thermal stability and available Lewis-acid metal sites. Chem Commun 30:3172–3174
81. Gustafsson M, Li Z, Zhu G et al (2008) A porous chiral lanthanide metal-organic framework with high thermal stability. Stud Surf Sci Catal 174A:451–454
82. Jiang HL, Tsumori N, Xu Q (2010) A series of (6,6)-connected porous lanthanide-organic framework enantiomers with high thermostability and exposed metal sites: scalable syntheses, structures, and sorption properties. Inorg Chem 49(21):10001–10006
83. Majeed Z, Mondal KC, Kostakis GE et al (2010) $LnNa(PhCO_2)_4$ (Ln = Ho, Dy): the first examples of chiral srs 3D networks constructed using the monotopic benzoate ligand. Chem Commun 46(15):2551–2553
84. Wang MX, Long LS, Huang RB et al (2011) Influence of halide ions on the chirality and luminescent property of ionothermally synthesized lanthanide-based metal-organic frameworks. Chem Commun 47(35):9834–9836
85. Rossin A, Giambastiani G, Peruzzini M et al (2012) Amine-templated polymeric lanthanide formates: synthesis, characterization, and applications in luminescence and magnetism. Inorg Chem 51(12):6962–6968

86. Masu H, Tominaga M, Katagiri K et al (2006) 2-D coordination network of a cyclic amide with a lanthanide metal cation and its columnar stacking. CrystEngComm 8(8):578–580
87. Tang Y, Tang K, Liu W et al (2008) Assembly, crystal structure, and luminescent properties of three-dimensional (10,3)-a netted rare earth coordination polymers. Sci China Chem 51 (7):614–622
88. Yan X, Cai Z, Yi C et al (2011) Anion-induced structures and luminescent properties of chiral lanthanide-organic frameworks assembled by an achiral tripodal ligand. Inorg Chem 50 (6):2346–2353
89. Tang K, Yun R, Lu Z et al (2013) High CO_2/N_2 selectivity and H_2 adsorption of a novel porous yttrium metal-organic framework based on N,N′,N″-tris(isophthalyl)-1,3,5-benzenetricarboxamide. Cryst Growth Des 13(4):1382–1385
90. Devic T, Wagner V, Guillou N et al (2011) Synthesis and characterization of a series of porous lanthanide tricarboxylates. Microporous Mesoporous Mater 140(1–3):25–33
91. Mu B, Li F, Huang Y et al (2012) Breathing effects of CO_2 adsorption on a flexible 3D lanthanide metal-organic framework. J Mater Chem 22(20):10172–10178
92. Lin Z, Zou R, Liang J et al (2012) Pore size-controlled gases and alcohols separation within ultramicroporous homochiral lanthanide-organic frameworks. J Mater Chem 22(16):7813–7818
93. Gu X, Xue D (2006) Spontaneously resolved homochiral 3D lanthanide–silver heterometallic coordination framework with extended helical Ln–O–Ag subunits. Inorg Chem 45(23):9257–9261
94. Peng G, Ma L, Cai J et al (2011) Influence of alkali metal cation (Li(I), Na(I), K(I)) on the construction of chiral and achiral heterometallic coordination polymers. Cryst Growth Des 11 (6):2485–2492
95. Ma YS, Li H, Wang JJ et al (2007) Three-dimensional lanthanide(III)–copper(II) compounds based on an unsymmetrical 2-pyridylphosphonate ligand: an experimental and theoretical study. Chem Eur J 13(17):4759–4769
96. Dong DP, Liu L, Sun ZG et al (2011) Synthesis, crystal structures, and luminescence and magnetic properties of 3D chiral and achiral lanthanide diphosphonates containing left- and right-handed helical chains. Cryst Growth Des 11(12):5346–5354
97. Gil-Hernandez B, Hoppe HA, Vieth JK et al (2010) Spontaneous resolution upon crystallization of chiral La(III) and Gd(III) MOFs from achiral dihydroxymalonate. Chem Commun 46(43):8270–8272
98. Dang S, Zhang JH, Sun ZM et al (2012) Luminescent lanthanide metal-organic frameworks with a large SHG response. Chem Commun 48(90):11139–11141
99. Zhang M, Lu J, Hu R (2012) Chiral (6,3) network assembled by lanthanide and changeful dihydroxyfumaric acid. Chin J Chem 30(2):228–232
100. Lu J, Mang D, Li L et al (2008) Hydrothermal synthesis of a chiral rare earth iodate ($Gd(IO_3)_3{\cdot}H_2O$) showing the rare (3,8)-connected $(4^3)(4{\cdot}6^2)$ $(4^9{\cdot}6^{17}{\cdot}8^2)$ topology. J Coord Chem 61(9):1406–1411
101. Ju W, Zhang D, Zhu D et al (2012) L- and D-$[Ln(HCO_2)(SO_4)(H_2O)]_n$ (Ln = La, Ce, Pr, Nd, and Eu): chiral enantiomerically 3D architectures constructed by double-$[Ln\text{-}O]_n$-helices. Inorg Chem 51(24):13373–13379
102. Shi FN, Paz FAA, Ribeiro-Claro P et al (2013) Transposition of chirality from diphosphonate metal-organic framework precursors onto porous lanthanide pyrophosphates. Chem Commun 49(99):11668–11670

Struct Bond (2015) 163: 75–108
DOI: 10.1007/430_2014_159

Published online: 13 September 2014

Porous Lanthanide Metal–Organic Frameworks for Gas Storage and Separation

Bin Li and Banglin Chen

Abstract Lanthanide metal–organic frameworks (Ln-MOFs) have attracted increasing attention as an emerging type of porous materials in the last decades due to their high porosities, adjustable pore sizes/sharps, ready functionalization, as well as high thermal/chemical stability. In this chapter, we seek to not only provide a comprehensive review focusing on porous Ln-MOF materials for a wide range of applications in gas storage and separation, such as H_2 storage, selective CO_2 capture and separation, and H_2 and CH_4 purification, but also highlight some strategies as a means of effectively enhancing their gas storage capacities and selectivities.

Keywords Framework interpenetration • Gas separation • Gas storage • Lanthanide metal–organic frameworks • Pore size/sharp exclusion

Contents

B. Li and B. Chen (✉)
Department of Chemistry, University of Texas at San Antonio, One UTSA Circle, San Antonio, TX 78249-0698, USA
e-mail: banglin.chen@utsa.edu

Abbreviations

btb	1,3,5-Benzenetrisbenzoic
H_2bdc	1,4-Benzenedicarboxylic acid
H_2bpdc	2,2′-Bipyridine-3,3′-dicarboxylic acid
$H_2C_2O_4$	Oxalic acid
H_2fda	Furan-2,5-dicarboxylic acid
H_2ftzb	2-Fluoro-4-(1H-tetrazol-5-yl)benzoic acid
H_2pam	4,4′-Methylenebis[3-hydroxy-2-naphthalenecarboxylic acid]
H_2pda	Pyridine-2,6-dicarboxylic acid
H_2tbdc	2,3,5,6-Tetramethyl-1,4-benzenedicarboxylic acid
H_3btc	1,3,5-Benzenetricarboxylate
H_3btn	1,3,5-Tri(6-hydroxycarbonylnaphthalen-2-yl)benzene
H_3CIP	5-(4-Carboxybenzylideneamino)isophthalic acid
H_3L^2	5,5′,5″-(Benzene-1,3,5-triyl)tris(1-naphthoic acid)
H_3L^2	5,5′,5″-(Benzene-1,3,5-triyl)tris(1-naphthoic acid)
H_3L^3	Tris((4-carboxyl)phenylduryl)amine acid
H_3L^3	Tris((4-carboxyl)phenylduryl)amine acid
H_3L^5	4,4′,4″-(Benzenetricarbonyltris-(azanediyl)) tribenzoic acid
H_3tpo	Tris-(4-carboxylphenyl)phosphineoxide
H_4L^4	2,6-Di(3′,5′-dicarboxylphenyl)pyridine
H_6L^1	5′,5‴-(4″-Carboxy-5′-(4-carboxyphenyl)-[1,1′:3′,1″-terphenyl]-3,5-diyl)bis(([1,1′:3′,1″-terphenyl]-4,4″-dicarboxylic acid))
H_6tpbtm	*N*,*N*′,N″-tris(isophthalyl)-1,3,5-benzenetricarboxamide
p-$CDCH_2$	1,12-Dihydroxycarbonyl-1,12-dicarba-*closo*-dodecaborane
tatb	4,4′,4″-S-triazine-2,4,6-triyl tribenzoate

1 Introduction

Metal–organic frameworks (MOFs), also termed coordination polymers, have been explosively growing as a new type of multifunctional materials over the last two decades for wide applications in gas storage and separation [1–27], luminescence [28–35], heterogeneous catalysis [36–42], chemical sensing [43–48], proton conducting [49–51], drug delivery, and biomedical imaging [52–55]. Such inorganic–organic hybrid materials can be readily self-assembled from a large number of metal ions/clusters with organic linkers in mild conditions. Owing to their high porosities, tunable pore sizes/shapes, and functionalizable pore walls, porous MOF materials are superior to those traditional porous materials such as zeolites and porous carbons in terms of porosities, making them a very promising potential as absorbent materials for gas storage and separation applications. Compared with transition-metal ions, the lanthanide ions hold unique electronic, optical, and magnetic properties arising from 4f electrons [56–62]. Taking advantage of the

permanent porosities, the utilization of lanthanide ions to construct lanthanide metal–organic frameworks (Ln-MOFs) has a great opportunity to develop multifunctional materials for chemical sensing, heterogeneous catalysis, and biomedical applications. In this case, the establishment of the permanent porosity is very important to pursue multifunctional Ln-MOF materials.

At the beginning, extensive research endeavor has been paid to stabilize Ln-MOFs and then to establish their permanent porosity; however, it basically failed. The breakthrough in porous Ln-MOFs was realized by Yaghi and coworkers in 1999 when two activated Ln-MOFs upon solvent removal were experimentally confirmed for their gas/vapor sorption isotherms [63–65]. From then on, a great deal of progress has been made on porous Ln-MOFs for their wide applications in gas storage and separation [66–97]. Relative to transition-metal ions, lanthanide ions have much higher coordination numbers and connectivities, in the range of 6–13, which facilitate to stabilize the frameworks if all these coordination sites are utilized and bridged by organic linkers. Thus, a lot of stable porous Ln-MOFs show not only high thermal stability up to 500°C but also high water and chemical stabilities, which are very important properties that need to be addressed for gas storage and separation in practical industrial applications. As a result of variable coordination numbers of lanthanide ions, the framework structures and pore sizes/sharps can be easily tuned by judicious selection of lanthanide ions/clusters and organic linkers [66, 80–82]. The exquisite control over framework interpenetration within Ln-MOFs is another powerful approach in this regard [83–90]. Owing to the molecular sieving effect, such tunable pore sizes/sharps can certainly induce highly selective gas storage and separation. Furthermore, some functional sites, such as open lanthanide sites (OLSs) [69–79], acylamide group, pyridyl site, and so on [89–92], can be readily incorporated into porous Ln-MOFs, which provide the favorable interactions between the frameworks and the quadrupole gas molecules, certainly leading to the enhanced gas storage capacities and separation selectivities. Some flexible Ln-MOFs have also been explored to be utilized for selective gas storage and separation due to the "gate-opening effect" [93–95]. In this chapter, we will provide a basic summarization on the development of porous Ln-MOF materials for gas storage and separation in the last two decades and also highlight some strategies for effectively improving their gas storage capacity and selectivity.

2 Gas Storage and Separation of Porous Ln-MOFs

Compared with transition-metal ions, lanthanide ions have the higher coordination number and more flexible coordination environment, which allow more small solvent molecules such as DMF, H_2O, etc., to easily occupy the coordination sites of lanthanide ions within Ln-MOFs. Once the terminally coordinated and free solvent molecules are removed to establish their permanent porosities during the thermal/vacuum activation, the organic donors from the neighboring organic linkers within Ln-MOFs readily occupy the in situ-formed open lanthanide sites

(OLSs), resulting in the condensed nonporous structures and even the collapse of the frameworks in some case. Therefore, it is more difficult and challenging to establish the permanent porosity of Ln-MOFs than that of transition-metal MOFs (TMOFs).

Initial efforts to stabilize Ln-MOFs and then to establish their permanent porosity basically failed. For example, Michaelides and coworkers developed a porous 3D Ln-MOF $[La_2(ad)_3(H_2O)_4]\cdot 6H_2O$ using a flexible ligand ad^{2-} as a bridging linker. Upon removal of two coordinated water molecules, this porous sample was reversibly transformed into the nonporous framework $La_2(ad)_3(H_2O)_2$ [63]. It is obvious that the activated framework lost the porous structure during the thermal/vacuum activation, as further supported by adsorption studies. The breakthrough in the establishment of porous Ln-MOFs was realized during 1999–2005 when a few porous Ln-MOFs were experimentally confirmed for gas/vapor uptakes. In 1999, Yaghi and coworkers reported the first example of using a porous Ln-MOF Tb(bdc)NO_3 to absorb CO_2 molecules [64]. Though the CO_2 uptakes are kind of low, the activated framework retained its porous structure and then exhibited its permanent porosity. Wang et al. reported an interesting porous Ln-MOF $Er_2(pda)_3$ in 2003 [66]. This framework kept its crystallinity up to 450°C after removal of the coordinated and guest water molecules. The activated sample shows a selective adsorption of CO_2 into its pores at 273 K. This observed adsorption behavior demonstrated the feasibility of achieving porous and stable Ln-MOFs. Subsequently in 2005, Yaghi and coworkers [67] reported a very famous Ln-MOF formulated as Tb(btc) (termed **MOF-76**), which shows a reversible type I N_2 uptake at 77 K with a Langmuir surface area of 334 $m^2\ g^{-1}$. It is worth noting that the evacuated **MOF-76** displays a molecular sieving toward different gases such as N_2, Ar, CH_2Cl_2, C_6H_6, and C_6H_{12}. At the same time, Férey and coauthors [68] realized another important 3D porous Ln-MOF Tb(btb)(H_2O) (**MIL-103**), presenting a permanent porosity and high Langmuir surface area over 1,000 $m^2\ g^{-1}$ once the guest solvents were removed under the temperature below 200°C (Fig. 1b). However, when the degassed temperature increases above 280°C, the coordinated water departure led to the collapse of crystallinity. The initial works discussed above suggest that the permanent porosities of some Ln-MOFs can be well established with suitable degassed conditions.

Despite a lot of challenges and difficulties in the construction of permanently porous Ln-MOFs, there has been considerable progress in this regard over the past decade. For example, some mesoporous Ln-MOFs with very high surface area up to 3,000 m^2/g have been realized [98, 99], which is already comparable with most of very promising TMOFs. A lot of porous Ln-MOFs with functional sites such as the OLSs and nitrogen-containing heterocycle or alkylamine groups have been developed and utilized for gas storage and separation applications. Tuning of pore size/sharp and control of interpenetration within Ln-MOFs have been demonstrated to be other strategies capable of enhancing the ability of selective gas storage and separation. A few flexible frameworks also exhibit excellent performance on gas storage and separation. Next we will seek to summarize the development of porous

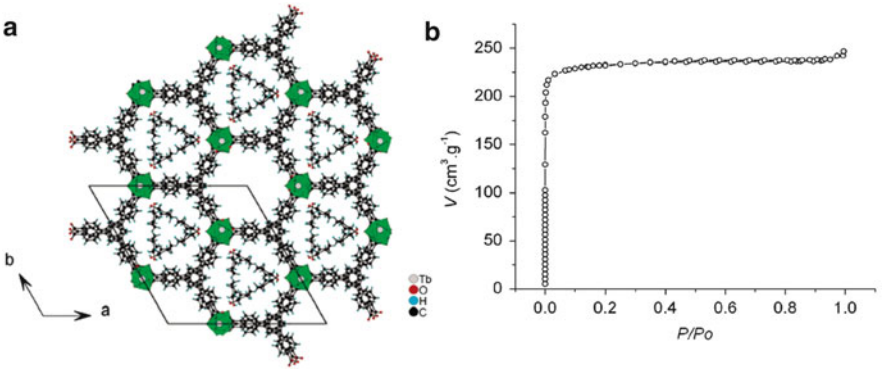

Fig. 1 (**a**) View of **MIL-103** along the *c* axis, showing the hexagonal pores filled with free solvent molecules (one pore is pictured empty for clarity). (**b**) Nitrogen gas adsorption isotherm at 77 K for **MIL-103** degassed overnight at 150°C Reprinted with permission from [68]. Copyright 2005 American Chemical Society

Ln-MOFs for gas storage and separation applications based on the following five strategies (Table 1).

2.1 Open Lanthanide Sites

Considering that the coordination sites of lanthanide ions can be easily occupied by some small solvent molecules, the available OLSs might be obtained if the terminally coordinated solvent molecules are carefully removed. Such OLSs can behave as Lewis acidic sites on the pore walls and then provide the favorable interactions with gas molecules. Thus, the formation of the OLSs in porous Ln-MOFs is considered to be beneficial for their gas adsorption and separation capacities. To date, a number of porous Ln-MOFs with the OLSs have shown excellent performance on H_2 storage, CO_2 capture and separation, and H_2 and CH_4 purification.

In 2006, Qiu and coworkers published a representative 3D Ln-MOF [Dy(btc)] with available open Dy^{3+} sites and evaluated its performance on H_2 and CO_2 adsorption [69]. This framework structure shows excellent thermal stability and keeps its crystallinity up to 350°C. After removal of all the guest and terminally coordinated solvates, the permanent porosity was characterized by N_2 sorption at 77 K with a Brunauer–Emmett–Teller (BET) surface area of 655 m^2/g. As a result of the presence of open Dy^{3+} sites, this Dy-MOF shows high H_2 uptake of 1.32 wt% at 77 K as well as excellent CO_2 capture capacity at 273 K and 1 atm. This work suggests that the effect of OLSs within Ln-MOFs can improve H_2 and CO_2 storage capacity.

To investigate the effect of the OLSs on hydrogen storage, Hong et al. explored a series of isostructural 3D Ln-MOFs [Ln(tpo)] with different lanthanide ions including Nd^{3+}, Sm^{3+}, Eu^{3+}, and Gd^{3+} (Fig. 2a,b) [70]. All these Ln-MOFs show

Table 1 Summary of porous Ln-MOFs for gas storage and separation categorized as (1) open lanthanide ions, (2) pore size/pore-exclusion effect, (3) control of interpenetration, (4) surface functionalization, and (5) flexible frameworks

Metal	Ln-MOFs	Category	Gas storage and separation applications	References
Y	$[(CH_3)_2NH_2]_2[Y_6(\mu_3\text{-}OH)_8(ftzb)_6(H_2O)_6]\cdot(H_2O)_{22}$	(1, 4)	CO_2 capture and separation	[75]
	$Y(btc)(H_2O)\cdot(DMF)_{1.1}$	(1)	H_2 storage	[73]
	$[Y_2(tpbtm)(H_2O)_2]\cdot xG$	(4)	CO_2 capture and separation, H_2 storage	[89]
	$[Y_2(tpo)_2(HCOO)]\cdot(Me_2NH_2)\cdot(DMF)_4\cdot(H_2O)_6$	(4)	CO_2 capture and separation	[92]
	$Y(btc)(H_2O)\cdot 4.3H_2O$	(2)	H_2 storage	[80]
	$Y_4(\mu_4\text{-}H_2O)(tatb)_{8/3}(SO_4)_2\cdot 3H_2O\cdot 10DMSO$	(2, 3)	O_2/N_2, H_2/CO, and H_2/N_2 separation	[88]
	$Y(L^5)DMF\cdot guest$	(4, 5)	CO_2/C_2H_4 and CO_2/C_2H_6 separation	[95]
La	$La(btb)(H_2O)$	(1, 2)	CO_2 capture and separation	[74]
	$[La(btb)H_2O]\cdot solvent$	(1)	CO_2/CH_4 and C_2s/CH_4 separation	[79]
	$[La(btn)DMF]\cdot solvent$	(2)	CO_2 capture and separation	[82]
	$La(btb)(H_2O)\cdot 3DMF$	(5)	CO_2 capture and separation	[93]
	$La(L^5)DMF\cdot guest$	(4, 5)	CO_2/C_2H_4 and CO_2/C_2H_6 separation	[95]
Ce	$Ce(btb)(H_2O)$	(1, 2)	CO_2 capture and separation	[74]
	$[Ce(L^3)]\cdot 1.5H_2O\cdot 0.5EtOH\cdot DMF$	(3)	H_2 storage, CH_4 purification	[85]
	$Ce_2(cip)_2(DMF)_4$	(5)	MeOH/EtOH separation	[94]
Nd	$[Nd(tpo)(DMF)](DMF)(H_2O)_2$	(1)	H_2 storage	[70]
	$Nd(btb)(H_2O)$	(1, 2)	CO_2 capture and separation	[74]
Sm	$[Sm(tpo)(DMF)](DMF)(H_2O)_{1.5}$	(1)	H_2 storage	[70]
	$Sm(btb)(H_2O)$	(1, 2)	CO_2 capture and separation	[74]
	$Sm(tbdc)_{1.5}(phen)(H_2O)\cdot DMF\cdot H_2O$	(3)	N_2 sorption	[86]
Eu	$[Eu(tpo)(DMF)](DMF)(H_2O)_{1.5}$	(1)	H_2 storage	[70]
	$Eu(btb)(H_2O)$	(1, 2)	CO_2 capture and separation	[74]
	$[Eu_2(tpo)_2(HCOO)]\cdot(Me_2NH_2)\cdot(DMF)_4\cdot(H_2O)_6$	(4)	CO_2 capture and separation	[92]
	$[H_2N(Me)_2][Eu_3(L^4)_2(HCOO)_2(DMF)_2(H_2O)]$	(4)	CO_2 capture and separation	[90]

Gd	$[Gd(tpo)(DMF)](DMF)(H_2O)_2$	(1)	H_2 storage	[70]
	$Gd(btb)(H_2O)$	(1, 2)	CO_2 capture and separation	[74]
	$Gd_2(pam)_3(DMF)_2(H_2O)_2$	(1)	CO_2 capture and separation, vapor sorption	[77]
	$\{(N_3\text{-ipa})_6(Gd)_4(DMF)_3(H_2O)_4\}(DMF)(H_2O)_2$	(4)	CO_2 capture and separation	[91]
Tb	$Tb(btc)(H_2O)_{1.5} \cdot (DMF)$	(2)	Gas sorption	[67]
	$Tb(btc)(H_2O) \cdot (DMF)_{1.1}$	(1)	H_2 storage	[73]
	$[Tb(fda)_{1.5}(DMF)] \cdot DMF$	(1)	CO_2/N_2 and CO_2/CH_4 separation	[72]
	$[(CH_3)_2NH_2]_2[Tb_6(\mu_3\text{-}OH)_8(ftzb)_6(H_2O)_6] \cdot (H_2O)_{22}$	(1, 4)	CO_2 capture and separation	[75]
	$Tb(btb)(H_2O)$	(1, 2)	CO_2 capture and separation	[74]
	$[Tb(tctpo)(OH_2)] \cdot 2DMF \cdot H_2O$	(1)	H_2 and CO_2 capture	[97]
	$(Me_2NH_2)_3[Tb_3(L)_2(H_2O)_3] \cdot 48DMA$	–	CO_2/CH_4 separation	[99]
	$[Tb_{16}(tatb)_{16}(DMA)_{24}] \cdot (DMA)_{91}(H_2O)_{108}$	–	CO_2 capture	[98]
Dy	$Dy(btc)(H_2O) \cdot DMF$	(1)	H_2 and CO_2 sorption	[69]
	$Dy(btc)(H_2O) \cdot (DMF)_{1.1}$	(1)	H_2 storage	[73]
	$Dy(btb)(H_2O)$	(1, 2)	CO_2 capture and separation	[74]
	$Dy_4(\mu_4\text{-}H_2O)(tatb)_{8/3}(SO_4)_2 \cdot 3H_2O \cdot 10DMSO$	(2, 3)	O_2/N_2 and H_2/CO separation	[88]
Ho	$KHo(C_2O_4)_2(H_2O)_4$	(1)	H_2 storage	[71]
	$Ho(btb)(H_2O)$	(1, 2)	CO_2 capture and separation	[74]
	$Ho(L^5)DMF \cdot guest$	(4)	CO_2/C_2H_4 and CO_2/C_2H_6 separation	[95]
Er	$[Er_2(pda)_3(H_2O)] \cdot 2H_2O$	(2)	CO_2/N_2 separation	[66]
	$Er(btc)(H_2O) \cdot (DMF)_{1.1}$	(1)	H_2 storage	[73]
	$Er(btb)(H_2O)$	(1, 2)	CO_2 capture and separation	[74]
	$Er_2(tbdc)_3(phen)_2 \cdot 4DMF \cdot 2H_2O$	(2, 3)	CO_2 capture and separation	[84]
	$Er_2(tbdc)_3(phen)_2 \cdot 4DMF \cdot 2H_2O$	(2, 3)	CO_2 capture and separation	[86]
	$Er_4(\mu_4\text{-}H_2O)(tatb)_{8/3}(SO_4)_2 \cdot 3H_2O \cdot 10DMSO$	(2, 3)	O_2/N_2 and H_2/CO separation	[88]
Tm	$Tm(bdc)_{1.5}(H_2O) \cdot 0.5DMF \cdot C_2H_5OH \cdot 2H_2O$	(3)	Gas sorption	[86]
	$Tm_4(bdc)_6(H_2O)_2(DMF)(C_2H_5OH) \cdot 2DMF \cdot 2H_2O$	(3)	Gas sorption	[86]

(continued)

Table 1 (continued)

Metal	Ln-MOFs	Category	Gas storage and separation applications	References
Yb	$Yb(btc)(H_2O)\cdot(DMF)_{1.1}$	(1)	H_2 storage	[73]
	$Yb(btb)(H_2O)$	(1, 2)	CO_2 capture and separation	[74]
	$Yb(bpt)(H_2O)\cdot(DMF)_{1.5}(H_2O)_{1.25}$	(1)	C_2H_2/CH_4 and CO_2/CH_4 separation	[76]
	$[Yb(L^2)]\cdot 3DMA$	(2)	CH_4 purification	[81]
	$Yb_3O(H_2O)_3(L^1)(NO_3)\cdot xG$	(1)	H_2 purification	[78]
	$Yb_4(\mu_4\text{-}H_2O)(tatb)_{8/3}(SO_4)_2\cdot 3H_2O\cdot 10DMSO$	(3)	O_2/N_2 and H_2/CO separation	[87]
	$Yb_2(p\text{-}CDC)_3(MeOH)_3(H_2O)(DMF)_2$	(1)	CO_2 capture and separation	[96]
Pr	$Pr(btb)(H_2O)$	(1, 2)	CO_2 capture and separation	[74]
	$\{(N_3\text{-}IPA)(N_3\text{-}HIPA)(H_2O)_2Pr\}(H_2O)_2$	(4)	CO_2 capture and separation	[91]

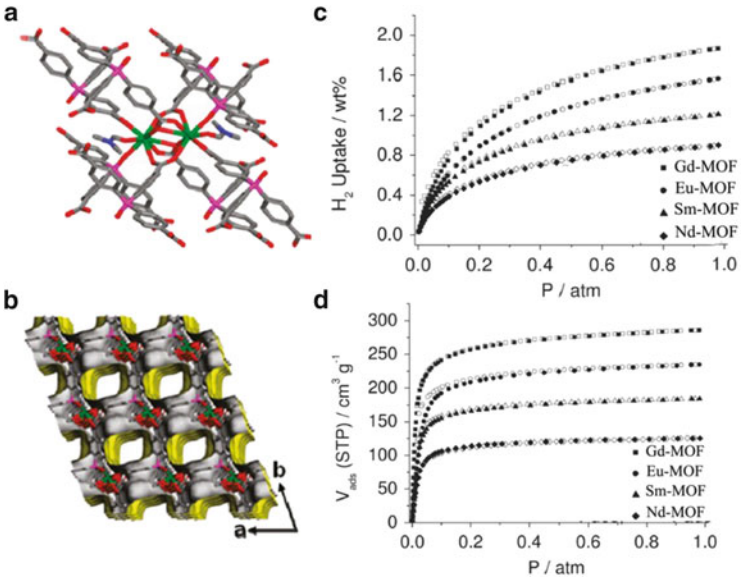

Fig. 2 (**a**) Molecular view of the secondary building unit (SBU) in Nd-MOF including coordinated DMF molecules; H atoms are omitted for clarity (Nd, *green*; C, *gray*; N, *blue*; O, *red*; P, *purple*). (**b**) Top view of 1D channels in the *ab* plane. (**c**) Gas sorption isotherms of H_2 at 1 atm and 77 K for the four porous Ln-MOFs. (**d**) Gas sorption isotherms of CO_2 at 1 atm and 195 K. Reprinted with permission from [70]. Copyright 2010 American Chemical Society

exceptionally high thermal stability up to 500°C. Under activation at 180°C, the terminal coordinated DMF molecules can be completely removed due to the absence of the characteristic C=O stretchings of DMF in the activated samples, as revealed by the IR spectra. The permanent porosities and OLSs for all the Ln-MOFs can be well established, exhibiting moderate BET surface areas between 793 and 1,163 m^2/g. At 1 atm and 77 K, the uptake of hydrogen by Nd-, Sm-, Eu-, and Gd-MOF reaches 0.89 wt% (100 cm^3/g), 1.02 wt % (134 cm^3/g), 1.52 wt% (170 cm^3/g), and 1.82 wt% (208 cm^3/g) (Fig. 2c), respectively. Since all the Ln-MOFs have identical structures and nearly the same pore sizes, the authors speculated that different OLSs are mainly responsible for the drastically different H_2 adsorption capacity. With the atomic radius of lanthanide ions progressively reduced from Nd^{3+} to Gd^{3+} ion, the charge density of the OLSs becomes pronounced. This behavior induces the gradually increased binding affinities toward H_2 molecules, which facilitates the enhancement of H_2 uptake. Similarly, the uptake of quadrupole CO_2 molecules at 195 K also progressively increases from Nd- to Gd-MOF (Fig. 2d), further indicating that the OLSs within Ln-MOFs play a vital role in gas storage.

Mohapatra and coworkers first demonstrated that the immobilization of K^+ ions into the surface of Ln-MOFs is capable of significantly enhancing H_2 storage capacity. Here a new lanthanide–alkali (Ho^{III}-K^I) bimetallic 3D framework KHo

$(C_2O_4)_2(H_2O)_4$ was designed and synthesized to study the effect of K^+ ions on H_2 storage [71]. The TGA studies found that the K^I-bound water molecules can be released in the temperature range of 45–120°C to generate the open K^+ sites, and the dehydrated sample is stable up to 380°C. The activated framework has two types of channels with a large one of 3.6 × 3.6 Å along the *c* axis and a small one of 2.0 × 1.2 Å perpendicular to the *a* axis. The permanent porosity of this dehydrated sample was well established by 195 K CO_2 adsorption isotherm with a Langmuir surface area of 324.35 m^2/g. High-pressure hydrogen uptake by this material was found to be 0.70 wt% at 77 K. Very interestingly, the H_2 uptake can steeply climb to near 0.70 wt% at very low pressure, indicating the strong interactions between the pore surfaces and H_2 molecules. It was believed that the presence of highly reactive unsaturated K^I sites can dramatically strengthen the gas-binding affinity toward H_2 molecules. This explanation was also confirmed by the high adsorption enthalpy of H_2 (ca. 9.21 kJ/mol) at the low-pressure region. To further understand the origin of the unique H_2 adsorption properties observed in this material, the first-principles DFT simulations were also performed. It was found that H_2 molecules preferentially stay near K sites over Ho sites. The distance between the H_2 molecule and K^+ site in a small pore is calculated to be 3.07 Å, which is much lower than 4.40 Å of H_2–Ho. These results unambiguously demonstrated that open K^+ ions are the favorable sites for H_2 adsorption rather than Ho sites in this Ho^{III}-K^I material.

With furan-2,5-dicarboxylic acid (H_2fda) as a bridging linker, Cheng and coworkers developed a new microporous Tb-MOF $[Tb(fda)_{1.5}(DMF)] \cdot DMF$ to evaluate its H_2 sorption capacity [72].This Tb-MOF shows a high thermal stability up to 450°C, and the available Tb^{3+} sites can be achieved after removal of the solvent DMF molecules. At 77 K and 1 bar, the H_2 uptake of the activated sample $Tb(fda)_{1.5}$ reaches 0.74 wt%. The adsorption enthalpy of H_2 was found to be 12.0 kJ mol^{-1} calculated by virial-type fitting, which is higher than most of the reported TMOFs. This high adsorption enthalpy indicates the strong affinity between open Tb^{3+} sites and H_2 molecules. Additionally, the remarkable effect of the OLSs on H_2 storage has also been demonstrated in a series of isostructural frameworks $Ln(btc)(H_2O) \cdot (DMF)_{1.1}$ (Ln=Y, Tb, Dy, Er, Yb) by Xu and coworkers [73].

Besides H_2 storage, the effect of OLSs on CO_2 capture and separation has also been widely investigated in porous Ln-MOFs. Given that the quadrupole moment of CO_2 molecule (13.4×10^{-40} cm^2) is higher than that of N_2 (4.7×10^{-40} cm^2) and CH_4 (nonpolar), the OLSs show much stronger binding affinities toward CO_2 molecules, leading to a greater influence on the CO_2 capture ability than that of CH_4 and N_2. To study the effect of OLSs on CO_2 adsorption capacity and selectivity, Zou et al. explored a large family of isostructural Ln-MOFs with different lanthanide ions, formulated as $Ln(btb)(H_2O)$ (Ln=Y, La, Ce, Pr, Nd, Sm, Eu, Gd, Tb, Dy, Ho, Er, and Yb) [74]. After removal of solvents at 300°C for 5 h, all the evacuated Ln-MOFs kept their crystal frameworks, and the permanent porosities were established by N_2 sorption isotherm at 77 K exhibiting a moderate BET surface area between 279.6 and 537.2 m^2 g^{-1}. At 273 K and 1 atm, all materials

show high CO_2 adsorption capacities, of which Nd-MOF shows the largest CO_2 uptake (10.7%). This value is comparable with one of most promising TMOFs. In terms of high-pressure CO_2 adsorption, Nd-MOF exhibits the highest CO_2 uptake among all these Ln-MOFs, which can reach 33.4 wt% at 32.8 atm and 273 K. The OLSs and ultramicroporous sizes with a size around 0.5 nm were considered to be the primary reasons for the remarkably high CO_2 capture. However, the difference of lanthanide ionic radius can result in a progressive decrease of pore sizes from Yb-MOF to La-MOF, making the diffusion of CO_2 molecules more difficult into the smaller pores. As a result, these Ln-MOFs show different CO_2 adsorption capacity. Moreover, all these Ln-MOFs preferentially adsorb much more CO_2 than CH_4 at 1 atm and 273 K, which was mainly attributed to the stronger interactions and smaller kinetic diameter of CO_2 relative to CH_4. Particularly, Pr-MOF shows the best adsorptive selectivity for CO_2 over CH_4 and N_2 with separation factors of 4.4 and 18.6 at 273 K, respectively.

Recently, Eddaoudi and coworkers further emphasized the importance of the OLSs to achieve the high CO_2 adsorption and separation capacity in Ln-MOFs [75]. Two isostructural Ln-MOFs $[(CH_3)_2NH_2]_2[Tb_6(\mu_3\text{-}OH)_8(ftzb)_6(H_2O)_6]\cdot(H_2O)_{22}$ and $[(CH_3)_2NH_2]_2[Y_6(\mu_3\text{-}OH)_8\text{-}(ftzb)_6(H_2O)_6]\cdot(H_2O)_{22}$ with face-centered cubic (fcu) topology were synthesized by making use of the linear fluorinated ligands H_2ftzb as a linker (Fig. 3a). The permanent porosity in both Ln-MOFs was confirmed by argon gas adsorption at 87 K with a moderate BET surface area of 1,220 $m^2\ g^{-1}$ for Tb-MOF and 1,310 $m^2\ g^{-1}$ for Y-MOF, respectively. The CO_2 uptakes by the activated Tb- and Y-MOF at ambient condition are found to be 3.5 (15.6%) and 4.1 mmol g^{-1} (18.1%), respectively (Fig. 3b). Particularly at low pressure (0.01 bar and 298 K), both Ln-MOFs show the highest CO_2 uptakes compared with all the reported MOFs except **Mg-MOF-74**. The high initial Q_{st} for CO_2 can be used to probably explain their high CO_2 adsorption, which was calculated to be 58.1 and 46.2 kJ mol^{-1} for Tb- and Y-MOF, respectively. To obtain a better insight into the unique CO_2 adsorption properties observed in both Ln-MOFs, an in-depth Q_{st} analysis was further carried out using a multiple-site Langmuir model (MSL). It was found that the effect of exposed lanthanide sites, combined with the proximal highly localized charge density from fluoro moieties and tetrazolate groups of the ftzb ligand, is believed to be the main reason for their high CO_2 adsorption properties. An exceptionally high adsorption selectivity of CO_2 over N_2 was also observed in the Tb-MOF with an evaluated selectivity of ca. 370. This selective adsorption was further confirmed using an experimental breakthrough test from a CO_2/N_2 0.10/99.90% mixture (Fig. 3c). Such high CO_2 adsorption selectivity over N_2 particularly at low pressure, as well as the favorable tolerance to water and high thermal stability, certainly makes both materials a very promising potential for carbon capture practical applications.

Selective CO_2 adsorption over CH_4 and N_2 was also observed in a 3D framework $Yb_2(p\text{-}CDC)_3(MeOH)_3(H_2O)(DMF)_2$ by Jin and coworkers [96]. The selectivity of CO_2/CH_4 and CO_2/N_2 at 298 K was calculated to be 3.4:1 and 8:1 at 1 atm, respectively. This high CO_2 selectivity was mainly attributed to the stronger interactions between CO_2 and coordinatively unsaturated Yb^{3+} sites of the surface

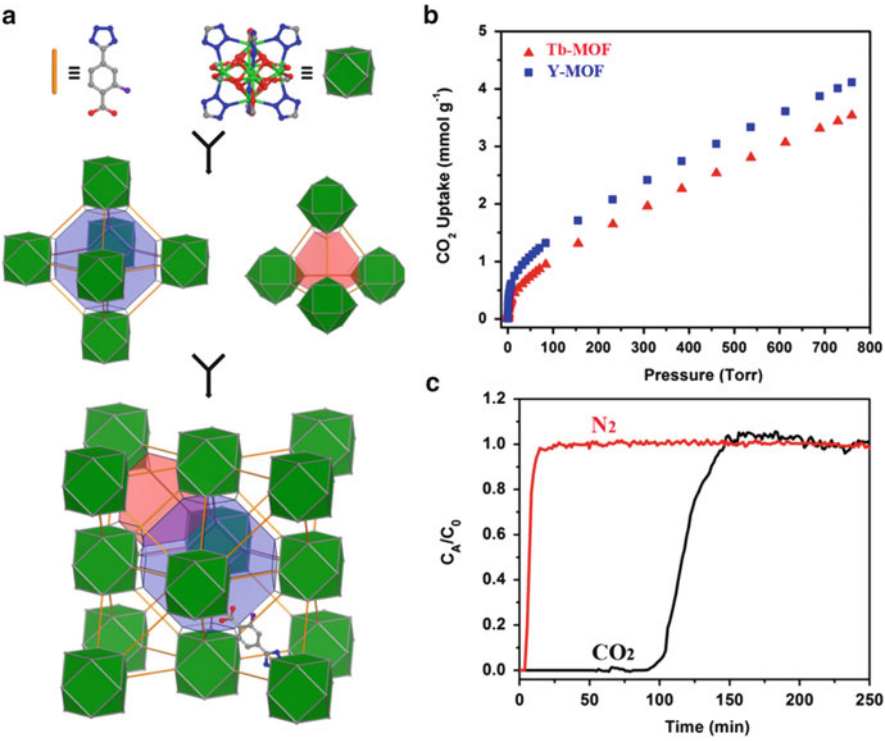

Fig. 3 (**a**) Ball-and-stick and schematic representation of $[(CH_3)_2NH_2]_2[Tb_6(\mu_3\text{-}OH)_8(ftzb)_6(H_2O)_6]\cdot(H_2O)_{22}$ (Tb-MOF): From *top* to *bottom*, organic and inorganic MBBs, $FTZB^{2-}$, and the 12-connected Tb-based cluster, respectively, which can be viewed as a linear connection and cuboctahedron node to afford the augmented fcu net, consisting of octahedral and tetrahedral cages shown as blue and pink truncated polyhedrons, respectively. H atoms and coordinated water molecules are omitted for clarity (Tb, *green*; C, *gray*; N, *blue*; O, *red*; F, *purple*). (**b**) CO_2 data for the Tb-MOF and Y-MOF at 298 K. (**c**) Experimental breakthrough test of traces (1,000 ppm) CO_2 in CO_2/N_2 mixture for the Tb-MOF. Reprinted with permission from [75]. Copyright 2013 American Chemical Society

walls. Cheng et al. [72] realized that a porous Ln-MOF $[Tb(fda)_{1.5}]$ with open Tb^{3+} sites exhibits highly selective capture and separation of CO_2 over N_2 and CH_4 from the equimolar CO_2/N_2 and CO_2/CH_4 binary gas mixtures with IAST separation selectivities of 36 and 10 at 273 K, respectively. Similarly, the preferential adsorption of CO_2 over CH_4 was also achieved in the activated frameworks $Gd_2(pam)_3$ with open Gd^{3+} sites [77].

Our research group first developed a novel microporous Ln-MOF $Yb_3O(H_2O)_3(L^1)(NO_3)$ (**UTSA-62**) for H_2 purification [78]. This 3D framework consists of $[Yb_3O(O_2C)_6]$ clusters and dendritic hexacarboxylate organic linkers, in which each Yb ion coordinates to six oxygen atoms from four carboxylate groups of L^1 ligands, one terminal water and μ_3-oxygen atom (Fig. 4a). Under a nitrogen atmosphere, **UTSA-62** can keep thermally stable up to 400°C. The open Yb^{3+}

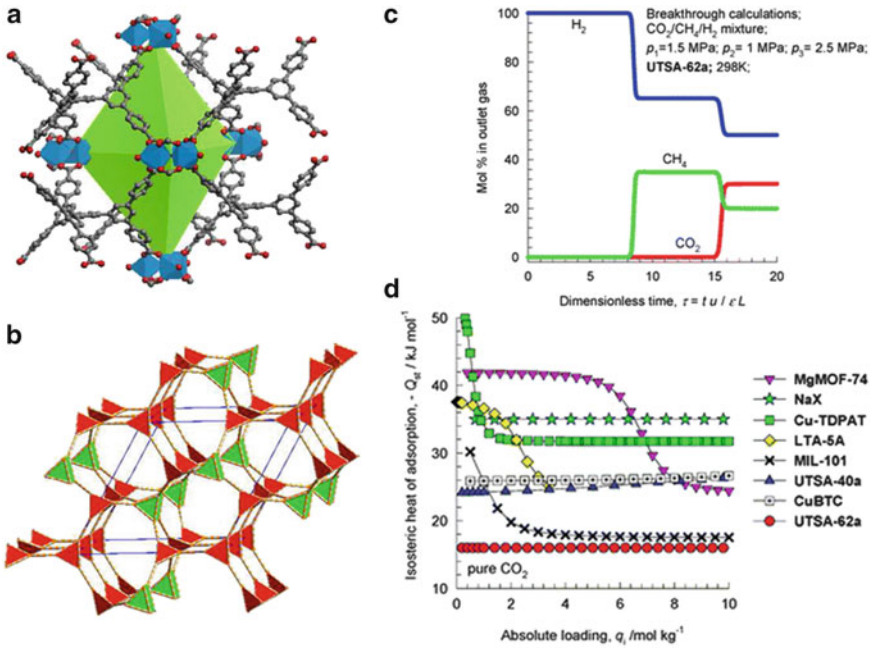

Fig. 4 (**a**) The coordination environment of the organic building block in **UTSA-62,** exhibiting one kind of polyhedral cages. (**b**) The framework topology of *jjt-a* for **UTSA-62**. (**c**) Transient breakthrough of a 30/20/50 $CO_2/CH_4/H_2$ mixture in an adsorber packed with **UTSA-62a**, maintained at isothermal 50 conditions at 298 K and 5.0 MPa. (**d**) Comparison of isosteric heats of CO_2 adsorption in **UTSA-62a** with the reported MOFs. The calculations are based on the Clausius Clapeyron equation. Reprinted with permission from [78]. Copyright 2013 Royal Society of Chemistry

sites can be obtained by carefully removing the terminal water molecules, and the permanent porosity of **UTSA-62a** was further characterized by 77 K N_2 sorption, exhibiting a very high BET surface area of 2,190 $m^2\ g^{-1}$. Given the high porosity and open Yb^{3+} sites of **UTSA-62a**, the high-pressure CO_2, CH_4, and H_2 adsorption up to 8 MPa was examined to evaluate the performance on $CO_2/CH_4/H_2$ separation (H_2 purification). The total CO_2 and CH_4 volumetric uptake by this material can reach 270 (8 MPa, 298 K) and 139 cm^3/cm^3 (3.5 MPa, 298 K), respectively, while a moderate H_2 uptake of 6.3 wt% at 77 K and 8 Mpa was observed. This much higher CO_2 and CH_4 adsorption over H_2 indicates that **UTSA-62a** can be utilized for high-pressure $CO_2/CH_4/H_2$ separation. As shown in Fig. 4c, simulated breakthrough experiments revealed that this material can separate H_2 of 99.95% purity from the ternary gas mixture of $CO_2/CH_4/H_2$ under the condition at 298 K and 5 MPa. Compared with the well-examined TMOFs such as **Mg-MOF-74**, **CuBTC,** and **CuTDPAT**, **UTSA-62a** shows the lowest isosteric heat of CO_2 adsorption and thus the lowest regeneration energy costs in H_2 purification despite its slightly lower H_2 productivities (Fig. 4d).

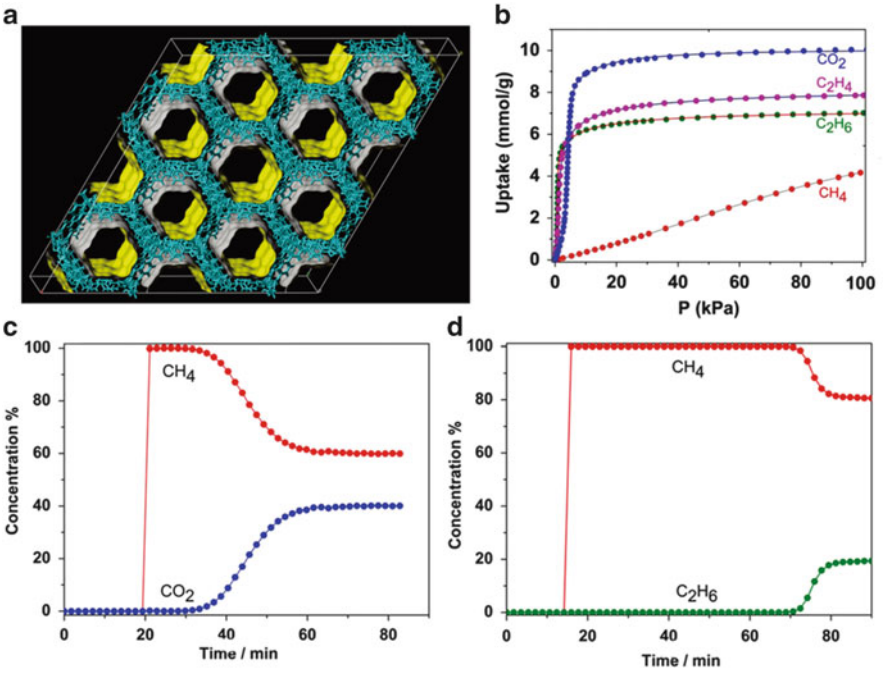

Fig. 5 (**a**) The Connolly surface diagram showing uniform1-D channel in La(btb)H_2O. (Inner surfaces: *yellow*, outer surfaces: *grey*). (**b**) Gas adsorption isotherms (circle points) for CO_2, CH_4, C_2H_4, and C_2H_6 in La(btb) at 195 K (100 kPa). (**c**) Breakthrough curves for a mixture CH_4/CO_2 (60:40 v/v) on La(btb) at 0.8 MPa with 6 min^{-1} space velocity at 273 K; (**d**) CH_4/C_2H_6 (80:20 v/v) on La(btb) at the same conditions with (**c**). Reprinted with permission from [79]. Copyright 2013 Wiley-VCH

Using a new porous La-MOF [La(btb)] with a large amount of open La^{3+} sites, the separation of methane from CO_2 and C_2 hydrocarbons (C_2s) has been achieved by Kitagawa and coworkers, which is still a very important and challenging industrial process in the chemical industry [79]. The overall structure of this La-MOF has 1D hexagonal channel (the size of the aperture window is about 10 Å) with an open La chain (Fig. 5a). Due to the combination of high coordination number, hydrophobic proton surface, and face-to-face assembly of the rigid ligand units in the structure, this framework shows exceptionally high water and chemical stability, as confirmed by the PXRD studies. The permanent porosity of the activated sample was further established by N_2 adsorption at 77 K to give a BET surface area of 1,024 $m^2\ g^{-1}$. These features make it a great promising potential for gas separation. Single-component adsorption isotherms revealed that this material preferentially absorbs more CO_2, C_2H_4, and C_2H_6 than CH_4 in the whole region of 100 kPa (Fig. 5b). Furthermore, the CO_2, C_2H_4, and C_2H_6 adsorption isotherms also show a steep initial increase and quick saturation around 10 kPa. However, the

uptake of CH_4 increases slowly following this pressure. This observed favorable adsorption of CO_2 and C_2 hydrocarbons relative to CH_4 suggests that this material can separate CH_4 from CO_2, C_1, and C_2s mixtures. According to the IAST simulation, the selectivity of C_2s relative to CH_4 is ca. 242 in the region of 100 kPa at 195 K. At 273 K, the calculated selectivity of C_2s to CH_4 also remains larger than 8. To investigate its methane separation capacity, the breakthrough experiments were performed in the CH_4/C_2H_6 (80/20) and CH_4/CO_2 (60/40) mixed gas at 273 K. It was found that this material shows good capacity to separate CH_4 of 100% purity from these CH_4 mixtures (Fig. 5c,d). The effect of the open La^{3+} site in this La-MOF was believed to be the primary reason for this high CH_4 separation ability because of the much stronger interactions between open La^{3+} sites and CO_2 and C_2s. To understand the effect of open La^{3+} sites in this framework, the in situ DRIFT spectra of CO_2 adsorption with increasing pressure was carried out at 273 K. The observed band around 2,300–2,380 cm^{-1} in the IR spectra indicates that CO_2 molecules could coordinate to the exposed La^{3+} site to form $La^{3+}\cdots O{=}C{=}O$ adducts with end-on configuration. In addition, C_2H_6 molecules may display the side-on binding modes to coordinate with the exposed La^{3+} cations. Their results directly demonstrated for the first time that the OLSs can be immobilized into porous Ln-MOFs as apparent adsorption sites to take up CO_2 and C_2s molecules, which can remarkably enhance the ability for selective gas separation. Most importantly, the CO_2 and C_2s adsorption capability of this material after humidity treatment at 80°C for 24 h shows a neglectable influence, strongly indicating the high water stability again. Such exceptionally high water and chemical stability of this La-MOF will make it a potential to be practically applied in methane purification.

2.2 *Pore Size/Sharp-Exclusion Effect*

Selective gas adsorption and separation based mainly on the pore size/sharp effect has been extensively investigated in a large number of TMOFs, also termed molecular sieving effect. It is well known that the pore sizes/sharps in this type of inorganic–organic hybrid materials can be exquisitely turned by judicious selection of metal ions/clusters and bridging organic linkers. Such tunable sizes/sharps of 1D channels in MOFs dominate that smaller molecules can go through, whereas larger substrates are blocked, thus leading to highly selective gas adsorption and separation. Given the fact that lanthanide ions have higher coordination numbers and more variable coordination environment than those of transition-metal ions, the modulation and control over pore sizes/shapes within Ln-MOFs should be more easily targeted. Therefore, porous Ln-MOFs have a fascinating opportunity to offer a tunable pore size/sharp for selective gas adsorption and separation based on molecular sieving effect.

The molecular sieving effect in Ln-MOFs was first observed in $Er_2(pda)_3$ by Wang and coworkers [66]. The effective pore window size in activated $Er_2(pda)_3$

was determined to be approximately 3.4 Å in diameter. Gas adsorption measurements revealed that this material can selectively adsorb CO_2 into its pores while showing no uptake toward Ar or N_2. This selective adsorption of CO_2 over Ar and N_2 can be explained by a molecular sieving effect, because the effective dimension of the channels shows a favorable size (3.4 Å) to preferentially absorb CO_2 molecules (3.3 Å) but exclude N_2 (3.4 Å) and Ar (3.64 Å). The open Er^{3+} sites were believed to further enhance CO_2 adsorption selectivity owing to the strong electrostatic interactions between the OLSs and quadrupole CO_2 molecules.

To study the molecular sieving effect on hydrogen storage, Luo and coworkers developed a highly stable Ln-MOF Y(btc)(H_2O) with an optimal pore size [80]. The activated Y(btc) exhibits an open channel of about 5.8 (Å) in diameter along the *c* axis. The permanent porosity was well established by both N_2 and H_2 gas sorption measurement at 77 K. Sorption studies show that the Y(btc) can take up a moderate amount of H_2 at 1 atm and 77 K, and a preferential adsorption of H_2 over N_2 was also observed. Using a virial equation, the adsorption enthalpy of H_2 for this material was determined to be about 7.3 kJ mol^{-1}, which is comparable with that of most TMOFs with open transitional metal sites. Most importantly, when the pressure increases to 10 bar, the uptake amount of H_2 is about 2.1 wt% at 77 K. This value is comparable to most of the very promising TMOFs. To pinpoint and understand the origin of the high H_2 storage capacity for the Y(btc), power neutron diffraction measurement was further carried out on this compound. It was clearly found that the strongest adsorption position (site I) for D_2 molecules is located nearby the aromatic btc linker rather than the open Y^{3+} site. As the D_2 loading increases to 2.11(7) D_2 molecules per formula unit, the adsorption at site I approaches saturation with a site occupancy of 92%. These observed behaviors indicate that the optimal small pores have much stronger interactions between pore walls with hydrogen molecules than that of open Y^{3+} sites. Therefore. this work first provides a direct evidence for the findings that the optimal small pores of slightly over twice than the kinetic diameter of H_2 molecule (6 Å) in porous Ln-MOFs can strengthen the interactions between the pore walls with H_2, leading to the remarkably enhanced hydrogen storage.

Using a novel porous Ln-MOF $[Yb(L^2)]\cdot 3DMA$ (**UTSA-30**), Chen and coworkers demonstrated for the first time the feasibility of the purification of natural gas from an equimolar 8-component mixture [81]. TGA studies revealed that **UTSA-30** is thermally stable up to 420°C. Under high vacuum at room temperature, the activated **UTSA-30a** shows a permanent porosity with a moderate BET surface area of 592 $m^2\ g^{-1}$. As shown in Fig. 6b, the uptake amount of each gas by **UTSA-30a** follows the hierarchy: C_3 hydrocarbons (C_3H_6 and C_3H_8) > C_2 hydrocarbons (C_2H_2, C_2H_4 and C_2H_6) > CO_2 > CH_4 > N_2. By making use of IAST calculations, high adsorption selectivities on C_2s/CH_4, C_3s/C_2s, CH_4/N_2, and CO_2/CH_4 separation all can be targeted in this material (Fig. 6c), which makes it capable of separating pure CH_4 from a 8-component gas mixture involving C_2H_2, C_2H_4, C_2H_6, C_3H_6, C_3H_8, CO_2, and N_2. To further demonstrate the feasibility of using **UTSA-30a** as an adsorbent material for natural gas purification, pulse

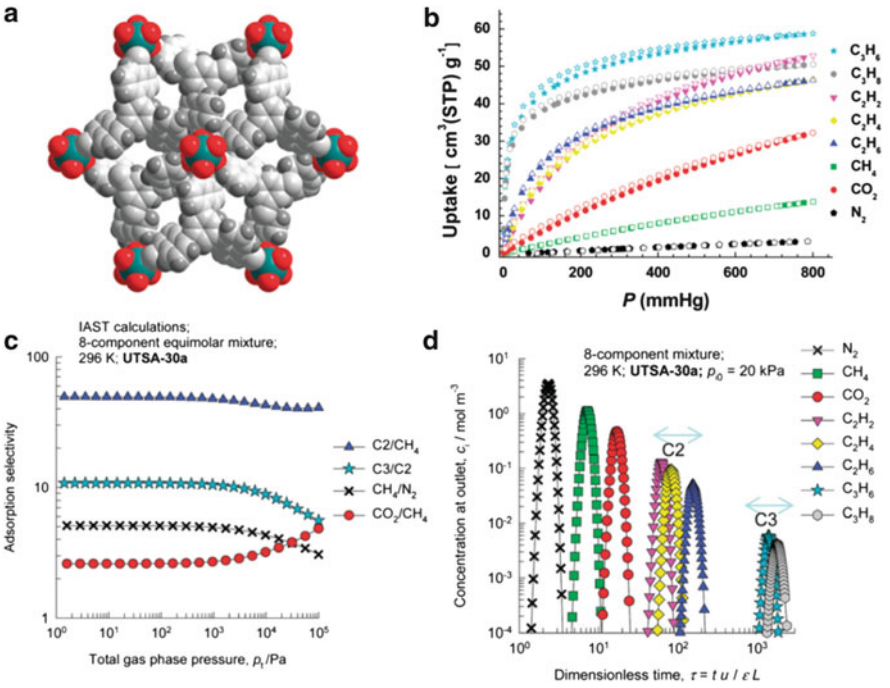

Fig. 6 (**a**) X-ray single-crystal structure of **UTSA-30** along *c* axis. (**b**) The pure-component sorption isotherms for **UTSA-30a** at 296 K. (**c**) The IAST calculations of C_3s/C_2s, C_2s/CH_4, CO_2/CH_4, and CH_4/N_2 adsorption selectivities as a function of the total bulk gas phase pressure at 296 K. (**d**) Pulse chromatographic separation of an equimolar 8-component mixture CH_4–CO_2–N_2–C_2H_2–C_2H_4–C_2H_6–C_3H_6–C_3H_8 using **UTSA-30a** at 296 K. The *x*-axis is the dimensionless time. The pulse of the equimolar mixture, with partial pressures of 20 kPa each, is injected for 10 s at the start of the process, and subsequently the adsorbed components are desorbed by the use of purge inert gas. Reprinted with permission from [81]. Copyright 2012 Royal Society of Chemistry

chromatographic simulations were performed on the 8-component gas mixture at 296 K. When such gas mixture goes through the packed beds of **UTSA-30a**, five fairly sharp fractions might be obtained in a different process (Fig. 6d). The breakthrough times follow the order $N_2 < CH_4 < CO_2 < C_2s < C_3s$, leading to the purification of natural gas from the 8-component gas mixture. It is worth noting that there are no strong binding sites such as the OLSs to interact with CO_2 and hydrocarbons, suggesting that the rational pore sizes in **UTSA-30a** may play a crucial role in hydrocarbon separation.

Kitagawa et al. developed a strategy for using a large organic linker (H_3btn) to construct a new robust Ln-MOF [La(btn)] (**PCP-1**), which can not only enhance the CO_2 capture and separation capacity but also remarkably reduce the adsorption enthalpy of CO_2 [82]. **PCP-1** shows a highly thermal stability up to 500°C and good water and chemical stability; in particular, it is stable from pH 2 to 12 at 100°C. In combination with the permanent porosity characterized by 77 K N_2 adsorption

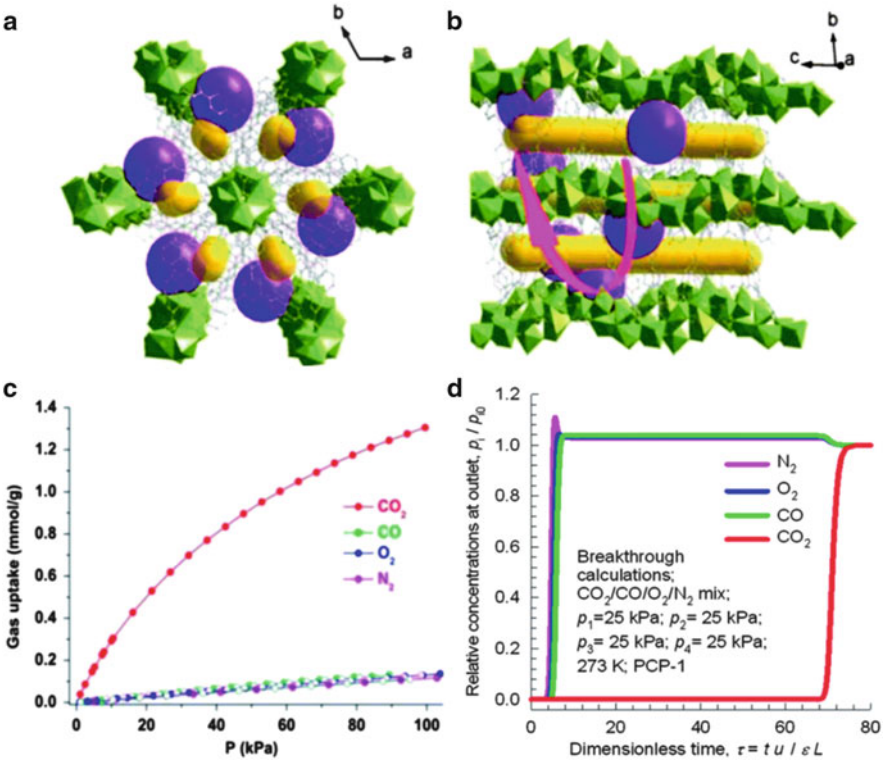

Fig. 7 (**a**) and (**b**) The structure of **PCP-1**. (**c**) The pure-component sorption isotherms for **PCP-1** at 273 K; (**d**) breakthrough characteristics of an adsorber packed with **PCP-1** and maintained at isothermal conditions at 273 K. The inlet gas is a quaternary mixture CO_2–CO–O_2–N_2 at 100 kPa, with partial pressures for each component of 25 kPa. Reprinted with permission from [82]. Copyright 2014 Royal Society of Chemistry

and pore sizes of about 5.5 Å in diameter (Fig. 7a,b), the activated **PCP-1** displays a well suitable potential for CO_2 sorption and separation. Single-component gas adsorption isotherms of CO_2, N_2, O_2, and CO found that **PCP-1** can preferentially take up CO_2 over CO, O_2, and N_2 at 195 K and 273 K. The predicted IAST adsorption selectivities of CO_2 over CO, O_2, and N_2 at 273 K exhibit high separation factors of 93–38 for CO_2/N_2, 78–20 for CO_2/O_2, and 68–18 for CO_2/CO separation, respectively. This indicates that **PCP-1** is a good candidate for selective capture of CO_2 from such four-gas mixtures similar to flue gases. To further evaluate the CO_2 separation ability of **PCP-1**, the breakthroughs of an equimolar four-component mixture including CO_2, N_2, O_2, and CO were tested at 195 K and 273 K using the pressure swing adsorption (PSA) process. As shown in Fig. 7d, the sequence of breakthroughs is N_2, O_2, CO, and CO_2 at both temperatures. Compared with other three-gas compositions, the breakthrough of CO_2 occurs at significantly later times. This significant time interval between the breakthroughs of CO, O_2, N_2,

and CO_2 suggests that the separation of CO_2 from a CO_2–CO–O_2–N_2 gas mixture can be achieved by **PCP-1**. In addition, the breakthrough of CO_2 in binary 25/75 mixtures of CO_2–CO, CO_2–O_2, and CO_2–N_2 at 100 kPa and 273 K has a similar dimensionless time, implying that the separation capability of **PCP-1** is not influenced by the gas composition. Most importantly, **PCP-1** displays a very low isosteric heat of CO_2 adsorption (26 kJ mol^{-1} by the virial method), which is lower than most of the promising TMOF materials with a high separation ability. Only the large aromatics site of **PCP-1** was believed to afford the binding energy to CO_2 molecules in the absence of the open La^{3+} sites, as supported by the temperature-programmed desorption (TPD) of NH_3 studies. As a result of its low isosteric heat of CO_2, the energy required for regeneration of the adsorbed CO_2 in fixed bed absorbers will be lower for **PCP-1** than most of TMOFs.

2.3 Control of Interpenetration

Besides tuning of the pore sizes/sharps by carefully choosing different lanthanide clusters or organic linkers, the framework interpenetration also plays important roles in the control of pore sizes/sharps in Ln-MOFs [83]. Though the pore sizes and volumes tend to be reduced by interpenetration, even leading to a nonporous framework [84–86], the porosities can be established, and the pore sizes/shapes of Ln-MOFs can be tuned if we rationally control the framework interpenetration of Ln-MOFs. Such porous materials can be used in selective gas sorption and separation via the molecular sieving effect [87, 88]. The interpenetration also can enhance the thermal stability by increasing the wall thickness of Ln-MOFs framework, which is favorable to establish their permanent porosities. The reasonable design of interpenetration or non-interpenetration in Ln-MOFs is a very important way to affect their adsorptive properties.

It is quite common that interpenetrated Ln-MOFs display no permanent porosities. The development of some strategies to avoid interpenetration and thus improve the porosities of Ln-MOFs is in great demand. Zhou and coworkers first systematically report the control of interpenetration in Ln-MOFs [84]. Two isostructural Ln-MOFs of $Ln(bdc)_{1.5}(DMF)(H_2O)$ (Ln=Er (**1**), Tm (**2**)) were synthesized, which show 3D nonporous frameworks because of double interpenetration. The existence of double interpenetration remarkably limits their porosities and applications in gas adsorption. It is necessary to avoid the coordinated H_2O and DMF molecules located at adjacent positions with O_{H2O}–Er–O_{DMF} angle of 78.56° in the Er-MOF structure. To control the framework interpenetration, the following strategies were employed: (1) a chelating ligand such as phen was used to replace the coordinated solvates and (2) modifying the bdc linker with a hindrance group. Based on complex **1**, the complex $Er_2(bdc)_3(phen)_2 \cdot 3H_2O$ (**3**) was synthesized by replacing the coordinated H_2O and DMF molecules with chelating phen ligand, leading to a non-interpenetrated framework. The linker tbdc with hindrance methyl groups was employed to construct a non-interpenetrated Tm-MOF

$Tm_2(tbdc)_3(DMF)_2(H_2O)_2 \cdot 3H_2O$ (**4**) framework instead of linker bdc, while the coordinated solvates keep unchanged compared to complex **2**. In complex $Er_2(tbdc)_3(phen)_2 \cdot 4DMF \cdot 2H_2O$ (**5**), both the coordinated solvates and the bdc were replaced by phen ligands and tbdc, respectively. As expected, complex **5** is a non-interpenetrating porous framework with the N–Er–N angle being 65.7°, which is smaller than O_{H2O}–Er–O_{DMF} angle of 78.56° in complex **1**. All three Ln-MOFs (**3**–**5**) have the same topology with complex **1**. The steric hindrance of the methyl groups in tbdc and large terminal phen ligand effectively control the interpenetration in **3**–**5** without changing the original topology, leading to porous Ln-MOFs. The activated **5** can absorb a moderate amount of CO_2 (51 $cm^3\ g^{-1}$) at 196 K and H_2 (56 $cm^3\ g^{-1}$) at 77 K but no N_2 and Ar sorption at 77 K. Considering the kinetic diameters of H_2 (2.89 Å), CO_2 (3.3 Å), Ar (3.54 Å), and N_2 (3.64 Å), the limited pore sizes of 3.3–3.54 Å for **5** make it selective uptake H_2 and CO_2 over N_2 and Ar due to molecular sieving effect.

Though interpenetration can be avoided by decorating hindrance groups in the linkers or chelating ligands, these bulky groups also reduce the pore sizes and volumes. Another feasible way to control the interpenetration of Ln-MOFs is to use in situ-generated rod-shaped secondary building units (SBUs). The rigid rod-shaped SBUs can efficiently prevent the formation of interpenetration. Meanwhile, the packing arrangements of such rods improve the porosity of the frameworks. Zhang and coworkers reported four isostructural non-interpenetrated Ln-MOFs with the infinite rod-shaped SBUs, named as $[Ln(L^3)] \cdot 1.5H_2O \cdot 0.5EtOH \cdot DMF$ (Ln=Ce (**FIR-8**), Pr (**FIR-9**), Nd (**FIR-10**), Sm (**FIR-11**)) (Fig. 8a,b) [85]. When the pH value was adjusted to 4.5 by adding five drops of HCOOH to the reaction system, eightfold interpenetrated dia type Ln-MOFs named as $(Me_2NH_2)[Ln(HL^3)_2(H_2O)_2] \cdot 1.5H_2O \cdot DMF$ (Ln=Ce (**FIR-12**), Pr (**FIR-13**), Nd (**FIR-14**), Sm (**FIR-15**)) were generated (Fig. 8c,d). The absorption properties of non-interpenetrated **FIR-8a-ht** and interpenetrated **FIR-12a-ht** were studied in detail. **FIR-8a-ht** displays a permanent porosity with a BET surface area of 457 $m^2\ g^{-1}$ and has a high H_2 uptake capacity. However, the interpenetrated **FIR-12a-ht** can hardly adsorb N_2 and H_2 even at 77 K. This indicates that **FIR-12a-ht** shows no porosity because of the high-fold interpenetration. In addition, **FIR-8a-ht** shows moderate CO_2 uptakes of 63 and 39 $cm_3 \cdot g^{-1}$ at 273 and 298 K under 1 atm, respectively. At 298 K and 1 atm, **FIR-8a-ht** can selectively adsorb C_2H_4, C_2H_6, and C_3H_8 over CH_4 based on the molecular sieving effect (Fig. 8e).

Sun and coworkers used both of the above ways to control the interpenetration of Ln-MOFs: one is to apply an organic ligand with large hindrance groups; the other one is to use in situ-generated rod-shaped secondary building units (SBUs). Firstly, two twofold interpenetrated lanthanide–organic frameworks, $Ln(bdc)_{1.5}(DMF)(H_2O)$ (Ln=Er (**6**), Tm (**7**)) with no porosities and no gas adsorptions, have been synthesized [86]. By using the hindrance methyl group tbdc or a chelating ligand phen to replace bdc and coordinated solvent molecules, three non-interpenetrated Ln-MOFs, $Er_2(bdc)_3(phen)_2 \cdot 3H_2O$ (**8**), $Tm(tbdc)_{1.5}(DMF)(H_2O) \cdot 2H_2O$ (**9**), and

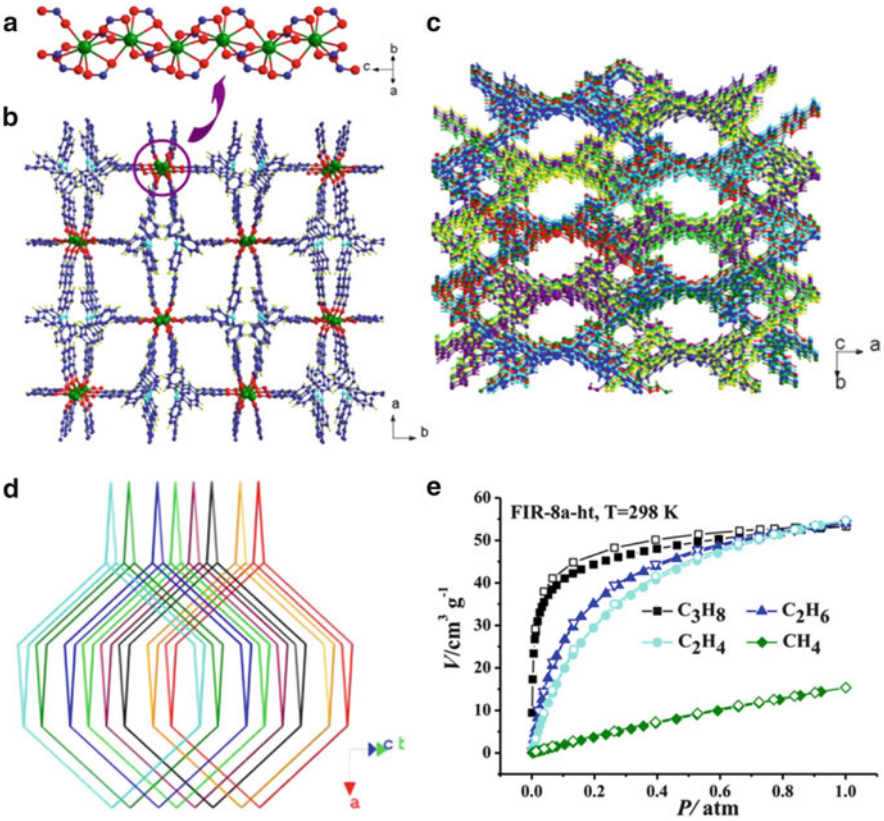

Fig. 8 (**a**) Metal–carboxylate chain and (**b**) 3D framework of **FIR-8**. (**c**) Eightfold interpenetrating 3D architecture of **FIR-12**. (**d**) View of the dia net in **FIR-12**. (**e**) C_3H_8, C_2H_6, C_2H_4, and CH_4 sorption isotherms of **FIR-8a-ht** at 298 K. Reprinted with permission from [85]. Copyright 2013 American Chemical Society

$Er_2(tbdc)_3(phen)_2 \cdot 3H_2O$ (**10**), have been constructed without changing the original topology of **6** and **7**. In addition, rigid rod-shaped SBUs were used to construct two non-interpenetrated Ln-MOFs: $Tm(bdc)1.5(H_2O) \cdot 0.5DMF \cdot C_2H_5OH \cdot 2H_2O$ (**11**) and $Tm_4(bdc)_6(H_2O)_2(DMF)(C_2H_5OH) \cdot 2DMF \cdot 2H_2O$ (**12**) by changing reaction conditions. Compared to interpenetrated **6** and **7**, all non-interpenetrated materials possess the permanent porosity and show adsorptive properties. The activated Er-MOF **10** exhibits a moderate CO_2 and H_2 adsorption of 51 and 56 $cm^3\ g^{-1}$, but no detectable absorption for N_2 and Ar. It is believed that the pore opening of activated **10** is limited to 3.3–3.54 Å, which only allows CO_2 and H_2 to enter the channels.

Though the interpenetration reduces the surface areas and porosities of an MOF, it also can increase the wall thickness, both of which lead to the significant enhancement of thermal stability and optimize the pore sizes for gas separation.

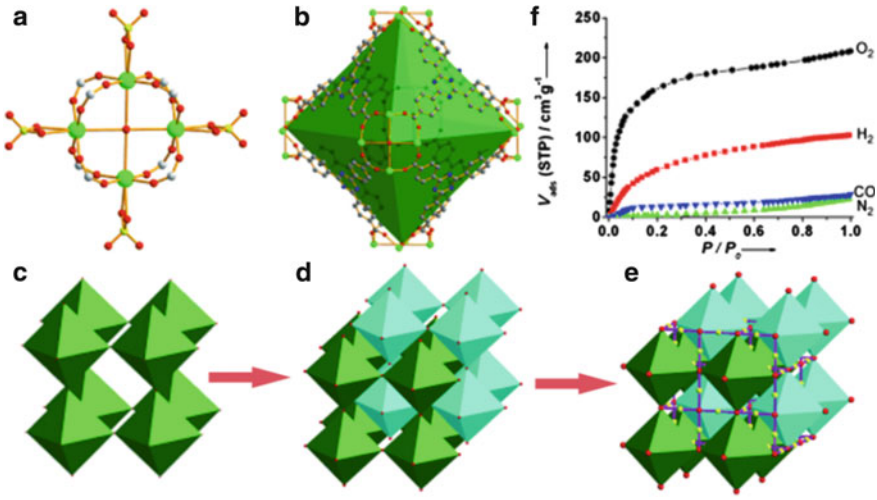

Fig. 9 (**a**) A $Yb_4(\mu_4\text{-}H_2O)$ SBU connecting four SO_4^{2-} anions in **PCN-17**. (**b**) The octahedral cage in **PCN-17**. Color scheme: C *gray*; N *blue*; O *red*; S *yellow*; Yb *green* (hydrogen atoms have been omitted for clarity). (**c**) Gas adsorption isotherms of the activated **PCN-17** for H_2, O_2, N_2, and CO at 77 K. (**d**) A single (8,3)-net. (**e**) Doubly interpenetrated nets. (**f**) Through sulfate bridges coordinatively linked interpenetrated framework (yellow spheres represent sulfur and red spheres represent the square-planar SBU). Reprinted with permission from [87]. Copyright 2009 Wiley-VCH

Ma et al. reported a doubly interpenetrated Yb-MOF $Yb_4(\mu_4\text{-}H_2O)(C_{24}H_{12}N_3O_6)_{8/3}(SO_4)_2$ (**PCN-17**) with improved thermal stability (up to 500°C) and high gas adsorption selectivity [87]. Bridging ligands SO_4^{2-} can chelate the two metal centers and function as the bridging ligand, which coordinatively link the two interpenetrated frameworks in **PCN-17** (Fig. 9c–e), leading to an exceptionally high thermal stability up to 500°C. The sulfate bridging ligands and double interpenetration reduce the pore size to approximately 3.5 Å, enabling this material to selectively adsorb O_2 over N_2, H_2 over CO, and H_2 over N_2 because of the molecular sieving effect (Fig. 9f). Four isostructural Ln-MOFs, **PCN-17** (Ln=Dy, Er, Y, and Yb) with similar coordinatively linked double interpenetration were further published by the same group [88]. The coordinatively linked interpenetration restricts the pore sizes of **PCN-17** (Yb) between 3.46 and 3.64 Å in diameter and those of **PCN-17** (Er), **PCN-17** (Dy), and **PCN-17** (Y) around 3.7 Å, enabling them to selectively adsorb O_2 and H_2 over N_2 and CO.

2.4 Surface-Functionalized Frameworks

The decoration of functional groups such as nitrogen-containing heterocycle or alkylamine onto the surface walls though predesigned or post-synthetic modification provides another important and effective route to enhance gas adsorption

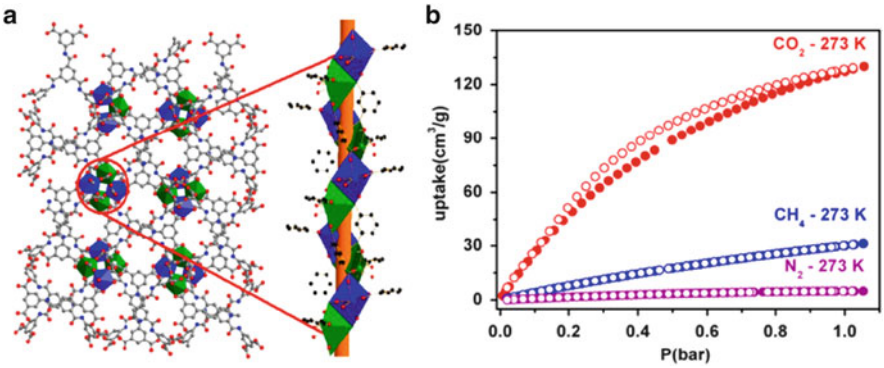

Fig. 10 (**a**) *Left*: Three-dimensional (3D) framework of **NJU-Bai11** with a homochiral structure along the *a* axis (hydrogen atoms are removed for clarity); *Right*: left helical chain constituted from edge-sharing pyramidal polyhedra with points of extension as carboxylic carbon atoms along the *a* axis. (**b**) CO_2, CH_4, and N_2 adsorption isotherms of **NJU-Bai11** at 273 K. Reprinted with permission from [89]. Copyright 2013 American Chemical Society

capacity and selectivity. These functional sites can form a large number of polarizing sites on the pore walls, which have strong interactions with the quadrupole gas molecules like CO_2, leading to a remarkable increase in selective adsorption of CO_2 over other gases. For example, Tang et al. successfully immobilized the bridging acylamide groups into a Ln-MOF to form a novel acylamide-functionalized framework $[Y_2(tpbtm)(H_2O)_2]\cdot xG$ (G=guest molecule) (**NJU-Bai11**) [89]. The framework structure of **NJU-Bai11** crystallizes a chiral orthorhombic $P2_12_12_1$ space group and shows a left helical chain constituted from the carboxyl groups tpbtm ligands bridging the Y^{3+} ions along the *a* axis (Fig. 10a). After desolvation, the activated **NJU-Bai11** exhibits a high porosity with a high BET surface area of ca. 1,152 $m^2\ g^{-1}$. At 273 K and 1 atm, the uptake amounts of CO_2, CH_4, and N_2 by **NJU-Bai11** are 130.0, 31.2, and 4.9 cm^3/g (Fig. 10b), respectively. The observed high CO_2 uptake for **NJU-Bai11** is higher than most of reported TMOFs. Due to the adsorption discrepancy between CO_2, CH_4, and N_2, this material shows a preferential adsorption of CO_2 over CH_4 and N_2 with an evaluated selectivity of about 6.4 and 30.2 at 1 atm and 273 K, respectively. It should be pointed out that the size of the open channel (8 Å) within **NJU-Bai11** is much larger than that of gas molecules, so a molecular sieving effect was not observed. Therefore, the high adsorption selectivity of CO_2 can probably be attributed to the inserted acylamide-functionalized groups, which was believed to have strong interactions with quadrupole CO_2 molecules rather than CH_4 and N_2. This explanation was further confirmed by the high zero-coverage adsorption enthalpy of CO_2 (30.3 kJ/mol) in **NJU-Bai11**.

Recently, by using a new 2,6-di(3′,5′-dicarboxylphenyl)pyridine (H_4L^4) ligand as a bridging linker, Hou and coworkers synthesized four isostructural Ln-MOFs, formulated as $[H_2N(Me)_2][Ln_3(L^4)_2(HCOO)_2(DMF)_2(H_2O)]$ (Ln=Eu, Tb, Gd and

Dy) [90]. As a result of the preferential binding of lanthanide ions to carboxylate oxygen atoms over pyridyl nitrogen atoms, the free pyridyl sites can be observed in these four Ln-MOFs. The presence of free Lewis basic pyridyl sites suggests the potential for the selective capture of CO_2. Among these four Ln-MOFs, the permanent porosity of Eu-MOF was confirmed by CO_2 sorption isotherm at 195 K with an uptake amount of 166.3 $cm^3\ g^{-1}$ at 1 atm. The uptake of CO_2 at 273 and 293 K can reach 51.7 and 33.2 $cm^3\ g^{-1}$, respectively. However, this material shows no uptake for N_2 and H_2 at 77 K. This selective adsorption of CO_2 was probably attributed to the certain interactions between the pyridine N atoms of the ligands and CO_2 molecules as well as the relatively narrow windows of cages within the Eu-MOF. The proposed explanation was further confirmed by the high zero-coverage adsorption enthalpy of CO_2 (23.1 kJ/mol), which is comparable with some TMOFs containing acylamide- or amine-functionalized groups. Moreover, this material shows good CO_2 sorption recurrence and complete regeneration, with no apparent decrease of the CO_2 sorption capacity upon repeating over at least six cycles.

Mondal and coworkers also demonstrated that the immobilization of the azide ($-N_3$) groups into two Ln-MOFs to form the azide-functionalized frameworks **SGR-Pr** and **SGR-Gd** can improve the adsorption selectivity of CO_2 over N_2. [91]. After removal of all the guest and coordinated solvents under degassed conditions at 110°C, both activated **SGR-Pr-110** and **SGR-Gd-110** exhibit typical type II N_2 sorption behavior with moderate surface area. At 273 K, **SGR-Pr-110** and **SGR-Gd-110** can adsorb more CO_2 than N_2 over the whole pressure to 1 atm. This selective adsorption of CO_2 over N_2 was mainly attributed to the immobilized functional azide groups along with the OLSs.

The development of some charged Ln-MOFs has also been utilized as a feasible strategy to improve CO_2 adsorption capacity and selectivity. This is because the charged pore walls and extra framework ions within charged Ln-MOFs show much higher affinity for CO_2 molecules because of the enhanced charge–quadrupole interactions. By making use of microwave-assisted solvothermal reaction, Lin et al. [92] synthesized a series of isostructural charged Ln-MOFs formulated as $[Ln(tpo)_2(HCOO)] \cdot (Me_2NH_2) \cdot (DMF)_4 \cdot (H_2O)_6$ [Ln=Y, Sm, Eu, Gd, Tb, Dy, Ho, Er, Tm, Yb, and Lu]. Compared with a conventional solvothermal reaction, microwave heating is more rapid and efficient to synthesize these Ln-MOFs within 30 min. All the Ln-MOFs have an anionic framework and extra framework $Me_2NH_2^+$ ions. Two fully activated Y-MOF and Eu-MOF exhibit the permanent porosities with the moderate BET surface area of 692 and 495.5 $m^2\ g^{-1}$, respectively. The H_2 uptake amount by two samples at 77 K and 40 bar can reach 2.66 and 1.58 wt%, respectively. At 298 K and 1 atm, the preferential adsorption of CO_2 over N_2 was also observed with an evaluated selectivity of about 28.2 for Y-MOF and 25.61 for Eu-MOF. The strong charge–quadrupole interaction between the charged pore walls of two Ln-MOFs with quadrupole CO_2 molecule was proposed to be the primary reason for the observed selective adsorption of CO_2 over N_2. Moreover, both materials also exhibit high CO_2 capture capacity at high pressure due to the strong charge–quadrupole interactions.

2.5 *Flexible Frameworks*

In contrast to the rigid frameworks mentioned above, selective gas adsorption and separation based on flexible MOFs has been demonstrated to have a remarkably different mechanism. The flexible MOFs usually exhibit extraordinary structure flexibility, whose pore sizes/shapes can be reversibly transformed between "open" and "close" forms by adsorption or release of gas molecules at a certain pressure. This unusual behavior is also termed the gate-opening effect. In most cases, the adsorption isotherms of flexible MOFs are typically characterized by distinct steps, in which almost no adsorption occurs below the "gate-opening" pressure for the closed structural phase, followed by an abrupt increase in adsorption beyond the gate-opening pressure. Such gate-opening effect in flexible MOFs at specific threshold pressures can also control the uptake or exclusion of specific gas molecules. Thus, with the flexibility of the framework, such MOFs often exhibit selective gas adsorption. To date, only a few examples of flexible Ln-MOFs have been developed for selective gas adsorption and separation [93–95].

Walton et al. developed a new 3D flexible porous Ln-MOF La(btb)$(H_2O)\cdot 3DMF$ that possesses a rare chiral space group (P_{6522}) (Fig. 11a,b) [93]. This framework exhibits very high thermal stability (up to 560°C) and high surface area (1014 $m^2\ g^{-1}$). Powder X-ray thermodiffraction experiments indicate that the reversible structural transformation occurs between the "open" form of as-synthesized sample to "close" form of the activated material upon removal of all guest molecules. The framework flexibility of this La-MOF was also confirmed by the N_2 adsorption isotherm at 77 K. As shown in Fig. 11c, the activated sample appears to be the "closed" form and displays an obviously breathing effect near $P/P_0 = 0.3$, indicating that the "close" pores open up at this pressure to allow more N_2 molecules to enter. The breathing effect with obvious two-step adsorption and hysteretic desorption was also observed in CO_2 adsorption isotherms at 278–298 K (Fig. 11d). These results demonstrated that gas sorption in this flexible material involves a pressure-dependent gate-opening and gate-closing process. Most importantly, this gate-opening effect can be only driven by adsorbing CO_2 molecules rather than CH_4 and N_2 at 278–298 K, leading to a sharp increase of CO_2 uptake and thus the enhanced selective adsorption of CO_2 over N_2 and CH_4. Adsorption kinetic studies revealed that the gate-opening/gate-closing behaviors of this La-MOF are dominated by the rate-determining step rather than molecular diffusion, and the equilibrium of the gate-opening process is much slower than the gate closing.

Another series of interesting flexible Ln-MOFs was realized by Tasiopoulos and coworkers [94]. They used a semirigid organic ligand H_3CIP to construct a series of new flexible Ln-MOFs, $[Ln_2(CIP)_2(DMF)_{4-x}(H_2O)_x]$ (Ln^{3+}=La^{3+}, Ce^{3+}, Pr^{3+}, Sm^{3+}, Eu^{3+}, Gd^{3+}, Tb^{3+}, Dy^{3+}, Ho^{3+}; $x = 0$–2). Among all these flexible Ln-MOFs, the coordinating terminal solvents can be exchanged by methanol or acetone molecules, resulting in a structural transformation using a single-crystal-to-single-crystal (SCSC) fashion. Such SCSC transformation was well demonstrated for the case of $Ce_2(CIP)_2(DMF)_4$ (**UCY-5**). It was found that the activated **UCY-5** exhibits

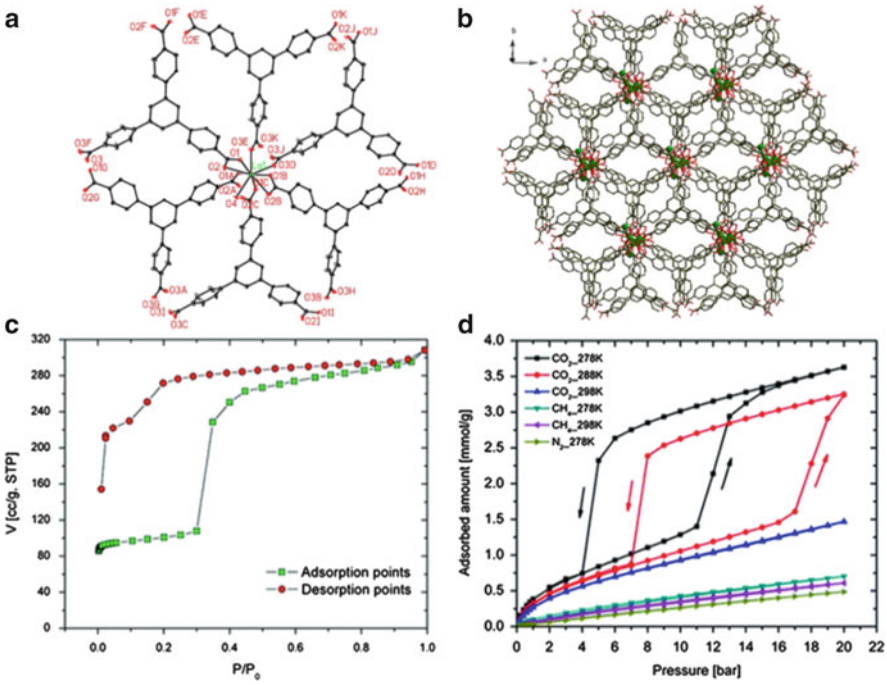

Fig. 11 (**a**) Coordination environment of La atom in compound La(btb). (**b**) 3D framework along the *c* axis. All hydrogen atoms removed for clarity (C, *black*; O, *red*; La atoms, *green*). (**c**) Nitrogen adsorption isotherm at 77 K for the activated La-MOF. (**d**) Gas adsorption isotherms for CO_2, CH_4, and N_2 in activated La-MOF. Reprinted with permission from [93]. Copyright 2012 Royal Society of Chemistry

an exceptional capacity to absorb liquid MeOH of ca. 96 mg g^{-1} due to the intrinsic weak connection of Ce^{3+} ions with methanol molecules. The X-ray diffraction data also indicates that the SCSC solvent exchange of **UCY-5** with MeOH indeed appears. However, the activated **UCY-5** shows no EtOH uptake. These results suggest a high preferential adsorption of MeOH over EtOH based on **UCY-5**. The excellent MeOH selectivity was considered to be a result of the narrow pores and channels of the activated **UCY-5** which facilitates the diffusion of the smaller MeOH. In addition, the change induced by the exchange of DMF with MeOH in this flexible crystal structure was believed to be larger than the corresponding exchange process with EtOH, which is also responsible for the high MeOH selectivity.

Kitagawa and coworkers developed another interesting flexible porous Ln-MOF. With a functional acylamide-modified ligand (H_3L^5) as a bridging linker, a series of porous Ln-MOFs $Ln(L^5)DMF \cdot guest$ was synthesized for the selective capture of CO_2 over C_2H_4 and C_2H_6 [95]. As exhibited in Fig 12a, two types of structural topologies are obtained; only La-MOF shows the unique and flexible structure,

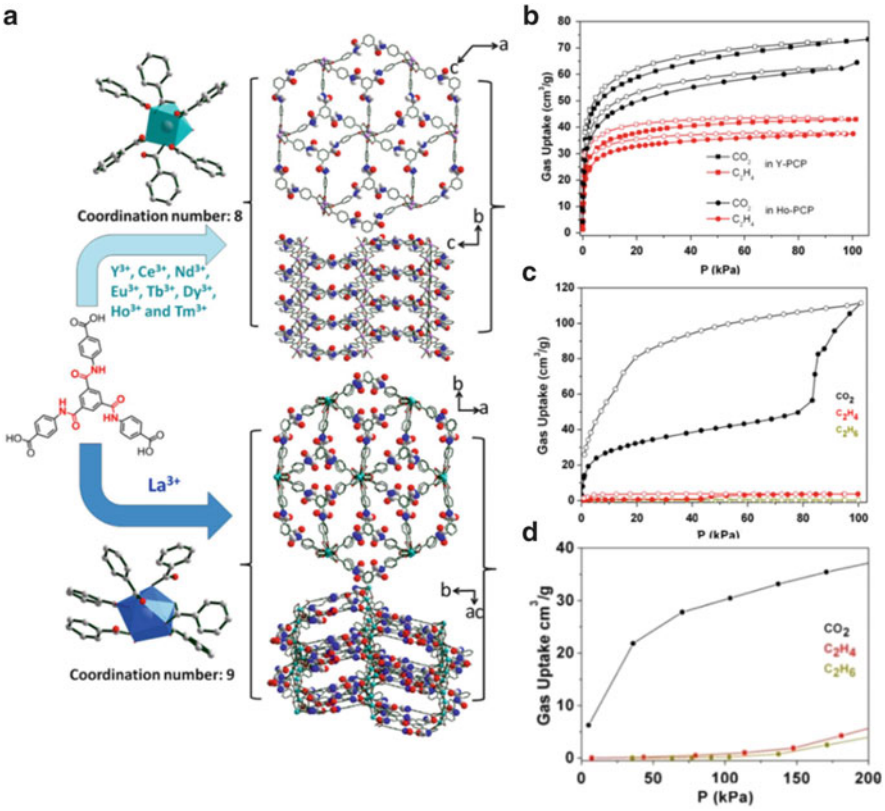

Fig. 12 (**a**) Scheme of the $Ln^{3+}L^4$ structures with different acylamide alignments. The right line shows the expected structural character of the samples before and after evacuation. (*Red spheres* represent oxygen, *blue spheres* represent nitrogen, and *gray spheres* represent carbon). (**b**) Adsorption isotherms of CO_2, C_2H_4, and C_2H_6 in Y-MOF and Ho-MOF at 195 K. (**c**) Adsorption isotherms of CO_2, C_2H_4, and C_2H_6 in La-MOF at 195 K. (**d**) Adsorption isotherms of CO_2, C_2H_4, and C_2H_6 in La-MOF at 273 K. Reprinted with permission from [95]. Copyright 2013 American Chemical Society

while the others give isomorphous rigid structures. The permanent porosities of two rigid frameworks Y-PMOF and Ho-PMOF are revealed by CO_2 adsorption at 195 K, where fully reversible type I isotherms are observed for both of them with apparent BET surface area of 273 and 243 m^2/g, respectively (Fig. 12b). However, the CO_2 adsorption isotherm of La-MOF at 195 K exhibits a distinct two-step adsorption and hysteretic desorption (Fig. 12c). Such observed CO_2 adsorption behavior is regarded as a "gate-opening" effect, demonstrating the flexible framework of La-MOF. This "gate-opening" effect for La-MOF can be only driven by CO_2 uptake rather than C_2H_4 and C_2H_6. With the pressure increased to the "open" value, the CO_2 uptake of La-MOF was significantly enhanced. In contrast, the gate-opening effect was not observed for C_2H_4 and C_2H_6 molecules. This phenomenon

suggests that this La-MOF can be used for selective capture of CO_2 over C_2H_4 and C_2H_6. Similarly, the preferential adsorption of CO_2 in CO_2/C_2H_4 and CO_2/C_2H_6 systems was also observed at 273 K, particularly at the ambient pressure area (0.1–1 bar) (Fig. 12d). Besides the flexible structure, the functional acylamide groups within La-MOF were proposed to be another main reason for the resulting highly selective capture of CO_2 over C_2H_4 and C_2H_6 owing to its strong interactions between acylamide groups and CO_2 molecules with the formation of La-BTB $\cdots$ CO_2 systems. Their results suggest a new promising approach to extend more sophisticated soft materials for important gas separation, incorporating functional groups into flexible frameworks to improve the capacity of gas separation.

Conclusions

In the past few years, much progress has been made in the design and synthesis of stable porous Ln-MOFs. Some of these porous materials have shown excellent performance on wide applications in gas storage and separation such as H_2 storage, selective CO_2 capture and separation, and H_2 and CH_4 purification. It is well demonstrated that incorporating functional sites and tuning of pore sizes and sharps as well as flexible structures within porous Ln-MOFs can certainly promote their gas storage and separation capacities. The fact that some stable Ln-MOFs exhibit extraordinarily high thermal and chemical stability in acidic/basic conditions indicates that a few porous Ln-MOFs will eventually be implemented in practical industrial applications in gas storage and separation in the near future. We can anticipate that with continued focus on the design and development of new materials as well as collaboration with industrial partners, porous Ln-MOFs have a bright future for their practical applications in gas storage and separation.

Acknowledgment This work was supported by grant AX-1730 from the Welch Foundation (BC).

References

1. Zhou H-C, Long JR, Yaghi OM (2012) Introduction to metal-organic frameworks. Chem Rev 112:673–674
2. Furukawa H, Cordova KE, O'Keeffe M, Yaghi OM (2013) The chemistry and applications of metal-organic frameworks. Science 341:6149–6160
3. Sumida K, Rogow DL, Mason JA, McDonald TM, Bloch ED, Herm ZR, Bae T-H, Long JR (2012) Carbon dioxide capture in metal-organic frameworks. Chem Rev 112:724–781
4. Suh MP, Park HJ, Prasad TK, Lim D-W (2012) Hydrogen storage in metal-organic frameworks. Chem Rev 112:782–835
5. He Y, Li B, O'Keeffec M, Chen B (2014) Multifunctional metal–organic frameworks constructed from *meta*-benzenedicarboxylate units. Chem Soc Rev 43:5618–5656
6. Férey G, Serre C (2009) Large breathing effects in three-dimensional porous hybrid matter: facts, analyses, rules and consequences. Chem Soc Rev 38:1380–1399

7. Wu H, Gong Q, Olson DH, Li J (2012) Commensurate adsorption of hydrocarbons and alcohols in microporous metal organic frameworks. Chem Rev 112:836–868
8. Li J-R, Sculley J, Zhou H-C (2012) Metal-organic frameworks for separations. Chem Rev 112:869–932
9. Furukawa H, Ko N, Go YB, Aratani N, Choi SB, Choi E, Yazaydin AÖ, Snurr RQ, O'Keeffe M, Kim J, Yaghi OM (2010) Ultrahigh porosity in metal-organic frameworks. Science 327:846–850
10. Zhang J-P, Zhang Y-B, Lin J-B, Chen X-M (2012) Metal azolate frameworks: from crystal engineering to functional materials. Chem Rev 112:1001–1033
11. Farha OK, Eryazici I, Jeong NC, Hauser BG, Wilmer CE, Sarjeant AA, Snurr RQ, Nguyen ST, Yazaydın AÖ, Hupp JT (2012) Metal-organic framework materials with ultrahigh surface areas: is the sky the limit? J Am Chem Soc 134:15016–15021
12. Kong G-Q, Han Z-D, He Y, Ou S, Zhou W, Yildirim T, Krishna R, Zou C, Chen B, Wu C-D (2013) Expanded organic building units for the construction of highly porous metal–organic frameworks. Chem Eur J 19:14886–14894
13. Li B, Wen H-M, Wang H, Wu H, Tyagi M, Yildirim T, Zhou W, Chen B (2014) A porous metal-organic framework with dynamic pyrimidine groups exhibiting record high methane storage working capacity. J Am Chem Soc 136:6207–6210
14. Xiang S-C, Zhang Z, Zhao C-G, Hong K, Zhao X, Ding D-R, Xie M-H, Wu C-D, Das MC, Gill R, Thomas KM, Chen B (2011) Rationally tuned micropores within enantiopure metal-organic frameworks for highly selective separation of acetylene and ethylene. Nat Commun 2:204–210
15. Xiang S, Zhou W, Gallegos JM, Liu Y, Chen B (2009) Exceptionally high acetylene uptake in a microporous metal-organic framework with open metal sites. J Am Chem Soc 131:12415–12419
16. Li T, Sullivan JE, Rosi NL (2013) Design and preparation of a core–shell metal-organic framework for selective CO_2 capture. J Am Chem Soc 135:9984–9987
17. Li B, Wang H, Chen B (2014) Microporous metal-organic frameworks for gas separation. Chem Asian J 9:1474–1498
18. Nugent P, Belmabkhout Y, Burd SD, Cairns AJ, Luebke R, Forrest K, Pham T, Ma S, Space B, Wojtas L, Eddaoudi M, Zaworotko MJ (2013) Porous materials with optimal adsorption thermodynamics and kinetics for CO_2 separation. Nature 495:80–84
19. He Y, Krishna R, Chen B (2012) Metal–organic frameworks with potential for energy-efficient adsorptive separation of light hydrocarbons. Energy Environ Sci 5:9107–9120
20. Li J-R, Kuppler RJ, Zhou H-C (2009) Selective gas adsorption and separation in metal-organic frameworks. Chem Soc Rev 38:1477–1504
21. Mason JA, Veenstra M, Long JR (2014) Evaluating metal-organic frameworks for natural gas storage. Chem Sci 5:32–51
22. Peng Y, Krungleviciute V, Eryazici I, Hupp JT, Farha OK, Yildirim T (2013) Methane storage in metal-organic frameworks: current records, surprise findings, and challenges. J Am Chem Soc 135:11887–11894
23. Getman RB, Bae Y-S, Wilmer CE, Snurr RQ (2012) Review and analysis of molecular simulations of methane, hydrogen, and acetylene storage in metal-organic frameworks. Chem Rev 112:703–723
24. Yan Y, Yang S, Blake AJ, Schröder M (2014) Studies on metal-organic frameworks of Cu (II) with isophthalate linkers for hydrogen storage. Acc Chem Res 47:296–307
25. Dincă M, Long JR (2008) Hydrogen storage in microporous metal-organic frameworks with exposed metal sites. Angew Chem Int Ed 47:6766–6779
26. Wilmer CE, Farha OK, Yildirim T, Eryazici I, Krungleviciute V, Sarjeant AA, Snurr RQ, Hupp JT (2013) Gram-scale, high-yield synthesis of a robust metal-organic framework for storing methane and other gases. Energy Environ Sci 6:1158–1163

27. Xiang S, He Y, Zhang Z, Wu H, Zhou W, Krishna R, Chen B (2012) Microporous metal-organic framework with potential for carbon dioxide capture at ambient conditions. Nat Commun 3:954–963
28. Cui Y, Yue Y, Qian G, Chen B (2012) Luminescent functional metal-organic frameworks. Chem Rev 112:1126–1162
29. Takashima Y, Martínez VM, Furukawa S, Kondo M, Shimomura S, Uehara H, Nakahama M, Sugimoto K, Kitagawa S (2011) Molecular decoding using luminescence from an entangled porous framework. Nat Commun 2:168–175
30. Almeida Paz FA, Klinowski J, Vilela SMF, Tomé JPC, Cavaleiro JAS, Rocha J (2012) Ligand design for functional metal-organic frameworks. Chem Soc Rev 41:1088–1110
31. Carlos LD, Ferreira RAS, Bermudez VZ, Julián-López B, Escribano P (2011) Progress on lanthanide-based organic–inorganic hybrid phosphors. Chem Soc Rev 40:536–549
32. Rocha J, Carlos LD, Paz FAA, Ananias D (2011) Luminescent multifunctional lanthanides-based metal-organic frameworks. Chem Soc Rev 40:926–940
33. Allendorf MD, Bauer CA, Bhakta RK, Houk RJT (2009) Luminescent metal-organic frameworks. Chem Soc Rev 38:1330–1352
34. Heine J, Müller-Buschbaum K (2013) Engineering metal-based luminescence in coordination polymers and metal-organic frameworks. Chem Soc Rev 42:9232–9242
35. Cui Y, Chen B, Qian G (2014) Lanthanide metal-organic frameworks for luminescent sensing and light-emitting applications. Coord Chem Rev 273:76–86
36. Song F, Wang C, Falkowski JM, Ma L, Lin W (2010) Isoreticular chiral metal-organic frameworks for asymmetric alkene epoxidation: tuning catalytic activity by controlling framework catenation and varying open channel sizes. J Am Chem Soc 132:15390–15398
37. Ma L, Abney C, Lin W (2009) Enantioselective catalysis with homochiral metal-organic frameworks. Chem Soc Rev 38:1248–1256
38. Lee J, Farha OK, Roberts J, Scheidt KA, Nguyen ST, Hupp JT (2009) Metal-organic framework materials as catalysts. Chem Soc Rev 38:1450–1459
39. Yoon M, Srirambalaji R, Kim K (2012) Homochiral metal-organic frameworks for asymmetric heterogeneous catalysis. Chem Rev 112:1196–1231
40. Gao W-Y, Chen Y, Niu Y, Williams K, Cash L, Perez PJ, Wojtas L, Cai J, Chen Y-S, Ma S (2014) Crystal engineering of an nbo topology metal-organic framework for chemical fixation of CO_2 under ambient conditions. Angew Chem Int Ed 53:2615–2619
41. Liu Y, Xuan W, Cui Y (2010) Engineering homochiral metal-organic frameworks for heterogeneous asymmetric catalysis and enantioselective separation. Adv Mater 22:4112–4135
42. Zhao M, Ou S, Wu C-D (2014) Porous metal-organic frameworks for heterogeneous biomimetic catalysis. Acc Chem Res 47:1199–1207
43. Chen B, Wang L, Zapata F, Qian G, Lobkovsky EB (2008) A luminescent microporous metal-organic framework for the recognition and sensing of anions. J Am Chem Soc 130:6718–6719
44. Chen B, Xiang S, Qian G (2010) Metal-organic frameworks with functional pores for recognition of small molecules. Acc Chem Res 43:1115–1124
45. Lan A, Li K, Wu H, Olson DH, Emge TJ, Ki W, Hong M, Li J (2009) A luminescent microporous metal-organic framework for the fast and reversible detection of high explosives. Angew Chem Int Ed 48:2334–2338
46. Shustova NB, Cozzolino AF, Reineke S, Baldo M, Dincă M (2013) Selective turn-on ammonia sensing enabled by high-temperature fluorescence in metal-organic frameworks with open metal sites. J Am Chem Soc 135:13326–13329
47. Kreno LE, Leong K, Farha OK, Allendorf M, Duyne RPV, Hupp JT (2012) Metal-organic framework materials as chemical sensors. Chem Rev 112:1105–1125
48. Wang C, Liu D, Lin W (2013) Metal-organic frameworks as a tunable platform for designing functional molecular materials. J Am Chem Soc 135:13222–13234
49. Horike S, Umeyama D, Kitagawa S (2013) Ion conductivity and transport by porous coordination polymers and metal-organic frameworks. Acc Chem Res 46:2376–2384

50. Shimizu GKH, Taylor JM, Kim S (2013) Proton conduction with metal-organic frameworks. Science 341:354–355
51. Yamada T, Otsubo K, Makiura R, Kitagawa H (2013) Designer coordination polymers: dimensional crossover architectures and proton conduction. Chem Soc Rev 42:6655–6669
52. Vivero-Escoto JL, Huxford-Phillips RC, Lin W (2012) Silica-based nanoprobes for biomedical imaging and theranostic applications. Chem Soc Rev 41:2673–2685
53. Horcajada P, Chalati T, Serre C, Gillet B, Sebrie C, Baati T, Eubank JF, Heurtaux D, Clayette P, Kreuz C, Chang J-S, Hwang YK, Marsaud V, Bories P-N, Cynober L, Gil S, Férey G, Couvreur P, Gref R (2010) Porous metal-organic-framework nanoscale carriers as a potential platform for drug delivery and imaging. Nat Mater 9:172–178
54. Rocca JD, Liu D, Lin W (2011) Nanoscale metal-organic frameworks for biomedical imaging and drug delivery. Acc Chem Res 44:957–968
55. Horcajada P, Gref R, Baati T, Allan PK, Maurin G, Couvreur P, Férey G, Morris RE, Serre C (2012) Metal-organic frameworks in biomedicine. Chem Rev 112:1232–1268
56. Kagan HB (2002) Introduction: frontiers in lanthanide chemistry. Chem Rev 102:1805–1806
57. Roy S, Chakraborty A, Maji TK (2014) Lanthanide-organic frameworks for gas storage and as magneto-luminescent materials. Coord Chem Rev 273:139–164
58. Huang Y-G, Jiang F-L, Hong M-C (2009) Magnetic lanthanide–transition metal organic–inorganic hybrid materials: from discrete clusters to extended frameworks. Coord Chem Rev 253:2814–2834
59. Chen Y, Ma S (2012) Microporous lanthanide metal-organic frameworks. Rev Inorg Chem 32:81–100
60. Bünzli J-C G (2010) Lanthanide luminescence for biomedical analyses and imaging. Chem Rev 110:2729–2755
61. Eliseeva SV, Bünzli J-C G (2010) Lanthanide luminescence for functional materials and bio-sciences. Chem Soc Rev 39:189–227
62. Meyer LV, Schönfeld F, Müller-Buschbaum K (2014) Lanthanide based tuning of luminescence in MOFs and dense frameworks- from mono- and multimetal systems to sensors and films. Chem Commun 50:8093–8108
63. Kiritsis V, Michaelides A, Skoulika S, Golhen S, Ouahab L (1998) Assembly of a porous three-dimensional coordination polymer: crystal structure of $\{[La_2(adipate)_3(H_2O)_4]_6H_2O\}_n$. Inorg Chem 37:3407–3410
64. Reineke TM, Eddaoudi MO, Keeffe M, Yaghi OM (1999) A microporous lanthanide-organic framework. Angew Chem Int Ed 38:2590–2594
65. Reineke TM, Eddaoudi M, Fehr M, Kelley D, Yaghi OM (1999) From condensed lanthanide coordination solids to microporous frameworks having accessible metal sites. J Am Chem Soc 121:1651–1657
66. Pan L, Adams KM, Hernandez HE, Wang X, Zheng C, Hattori Y, Kaneko K (2003) Porous lanthanide-organic frameworks: synthesis, characterization, and unprecedented gas adsorption properties. J Am Chem Soc 125:3062–3067
67. Rosi NL, Kim J, Eddaoudi M, Chen B, O'Keeffe M, Yaghi OM (2005) Rod packings and metal-organic frameworks constructed from rod-shaped secondary building units. J Am Chem Soc 127:1504–1518
68. Devic T, Serre C, Audebrand N, Marrot J, Férey G (2005) MIL-103, a 3-D lanthanide-based metal organic framework with large one-dimensional tunnels and a high surface area. J Am Chem Soc 127:12788–12789
69. Guo X, Zhu G, Li Z, Sun F, Yang Z, Qiu S (2006) A lanthanide metal–organic framework with high thermal stability and available Lewis-acid metal sites. Chem Commun 3172–3174
70. Lee WR, Ryu DW, Lee JW, Yoon JH, Koh EK, Hong CS (2010) Microporous lanthanide-organic frameworks with open metal sites: unexpected sorption propensity and multifunctional properties. Inorg Chem 49:4723–4725

71. Mohapatra S, Hembram KPSS, Waghmare U, Maji TK (2009) Immobilization of alkali metal ions in a 3D lanthanide-organic framework: selective sorption and H_2 storage characteristics. Chem Mater 21:5406–5412
72. Li H, Shi W, Zhao K, Niu Z, Li H, Cheng P (2013) Highly selective sorption and luminescent sensing of small molecules demonstrated in a multifunctional lanthanide microporous metal-organic framework containing 1D honeycomb-type channels. Chem Eur J 19:3358–3365
73. Jiang H-L, Tsumori N, Xu Q (2010) A series of (6,6)-connected porous lanthanide-organic framework enantiomers with high thermostability and exposed metal sites: scalable syntheses, structures, and sorption properties. Inorg Chem 49:10001–10006
74. Lin Z, Zou R, Xia W, Chen L, Wang X, Liao F, Wang Y, Lin J, Burrel AK (2012) Ultrasensitive sorption behavior of isostructural lanthanide–organic frameworks induced by lanthanide contraction. J Mater Chem 22:21076–21084
75. Xue D-X, Cairns AJ, Belmabkhout Y, Wojtas L, Liu Y, Alkordi MH, Eddaoudi M (2013) Tunable rare-earth fcu-MOFs: a platform for systematic enhancement of CO_2 adsorption energetics and uptake. J Am Chem Soc 135:7660–7667
76. Guo Z, Xu H, Su S, Cai J, Dang S, Xiang S, Qian G, Zhang H, O'Keeffed M, Chen B (2011) A robust near infrared luminescent ytterbium metal-organic framework for sensing of small molecules. Chem Commun 47:5551–5553
77. Biswas S, Jena HS, Goswami S, Sanda S, Konar S (2014) Synthesis and characterization of two lanthanide (Gd^{3+} and Dy^{3+})-based three-dimensional metal organic frameworks with squashed metallomacrocycle type building blocks and their magnetic, sorption, and fluorescence properties study. Cryst Growth Des 14:1287–1295
78. He Y, Furukawa H, Wu C, O'Keeffe M, Krishna R, Chen B (2013) Low-energy regeneration and high productivity in a lanthanide-hexacarboxylate framework for high-pressure CO_2/CH_4/H_2 separation. Chem Commun 49:6773–6775
79. Duan J, Higuchi M, Horike S, Foo ML, Rao KP, Inubushi Y, Fukushima T, Kitagawa S (2013) High CO_2/CH_4 and C_2 hydrocarbons/CH_4 selectivity in a chemically robust porous coordination polymer. Adv Funct Mater 23:3525–3530
80. Luo J, Xu H, Liu Y, Zhao Y, Daemen LL, Brown C, Timofeeva TV, Ma S, Zhou H-C (2008) Hydrogen adsorption in a highly stable porous rare-earth metal-organic framework: sorption properties and neutron diffraction studies. J Am Chem Soc 130:9626–9627
81. He Y, Xiang S, Zhang Z, Xiong S, Fronczek FR, Krishna R, O'Keeffee M, Chen B (2012) A microporous lanthanide-tricarboxylate framework with the potential for purification of natural gas. Chem Commun 48:10856–10858
82. Duan J, Higuchi M, Krishna R, Kiyonaga T, Tsutsumi Y, Sato Y, Kubota Y, Takatae M, Kitagawa S (2014) High $CO_2/N_2/O_2$/CO separation in a chemically robust porous coordination polymer with low binding energy. Chem Sci 5:660–666
83. Jiang H-L, Makal TA, Zhou H-C (2013) Interpenetration control in metal-organic frameworks for functional applications. Coord Chem Rev 257:2232–2249
84. He H, Yuan D, Ma H, Sun D, Zhang G, Zhou H-C (2010) Control over interpenetration in lanthanide-organic frameworks: synthetic strategy and gas-adsorption properties. Inorg Chem 49:7605–7607
85. He Y-P, Tan Y-X, Zhang J (2013) Gas sorption, second-order nonlinear optics, and luminescence properties of a series of lanthanide-organic frameworks based on nanosized tris((4-carboxyl)phenylduryl)amine ligand. Inorg Chem 52:12758–12762
86. He H, Ma H, Sun D, Zhang L, Wang R, Sun D (2013) Porous lanthanide-organic frameworks: control over interpenetration, gas adsorption, and catalyst properties. Cryst Growth Des 13:3154–3161
87. Ma S, Wang X-S, Yuan D, Zhou H-CA (2008) Coordinatively linked Yb metal–organic framework demonstrates high thermal stability and uncommon gas-adsorption selectivity. Angew Chem Int Ed 47:4130–4133

88. Ma S, Yuan D, Wang X-S, Zhou H-C (2009) Microporous lanthanide metal-organic frameworks containing coordinatively linked interpenetration: syntheses, gas adsorption studies, thermal stability analysis, and photoluminescence investigation. Inorg Chem 48:2072–2077
89. Tang K, Yun R, Lu Z, Du L, Zhang M, Wang Q, Liu H (2013) High CO_2/N_2 selectivity and H_2 adsorption of a novel porous yttrium metal-organic framework based on *N*,*N*′,*N*″-Tris (isophthalyl)-1,3,5-benzenetricarboxamide. Cryst Growth Des 13:1382–1385
90. Liu B, Wu W-P, Hou L, Wang Y-Y (2014) Four uncommon nanocage-based Ln-MOFs: highly selective luminescent sensing for Cu^{2+} ion and selective CO_2 capture. Chem Commun 50:8731–8734
91. Ganguly S, Pachfule P, Bala S, Goswami A, Bhattacharya S, Mondal R (2013) Azide-functionalized lanthanide-based metal-organic frameworks showing selective CO_2 gas adsorption and postsynthetic cavity expansion. Inorg Chem 52:3588–3590
92. Lin Z-J, Yang Z, Liu T-F, Huang Y-B, Cao R (2012) Microwave-assisted synthesis of a series of lanthanide metal-organic frameworks and gas sorption properties. Inorg Chem 51:1813–1820
93. Mu B, Li F, Huanga Y, Walton KS (2012) Breathing effects of CO_2 adsorption on a flexible 3D lanthanide metal-organic framework. J Mater Chem 22:10172–10178
94. Efthymiou CG, Kyprianidou EJ, Milios CJ, Manos MJ, Tasiopoulos AJ (2013) Flexible lanthanide MOFs as highly selective and reusable liquid MeOH sorbents. J Mater Chem A 1:5061–5069
95. Duan J, Higuchi M, Foo ML, Horike S, Rao KP, Kitagawa S (2013) A family of rare earth porous coordination polymers with different flexibility for CO_2/C_2H_4 and CO_2/C_2H_6 separation. Inorg Chem 52:8244–8249
96. Huang S-L, Lin Y-J, Yu W-B, Jin G-X (2012) Porous frameworks based on carborane–$Ln_2(CO_2)_6$: architecture influenced by lanthanide contraction and selective CO_2 capture. ChemPlusChem 77:141–147
97. Ibarra IA, Hesterberg TW, Holliday BJ, Lynch VM, Humphrey SM (2012) Gas sorption and luminescence properties of a terbium(III)-phosphine oxide coordination material with two-dimensional pore topology. Dalton Trans 41:8003–8009
98. Park YK, Choi SB, Kim H, Kim K, Won B-H, Choi K, Choi J-S, Ahn W-S, Won N, Kim S, Jung DH, Choi S-H, Kim G-H, Cha S-S, Jhon YH, Yang JK, Kim J (2007) Crystal structure and guest uptake of a mesoporous metal-organic framework containing cages of 3.9 and 4.7 nm in diameter. Angew Chem Int Ed 46:8230–8233
99. He Y, Furukawa H, Wu C, O'Keeffed M, Chen B (2013) A mesoporous lanthanide-organic framework constructed from a dendritic hexacarboxylate with cages of 2.4 nm. CrystEngComm 15:9328–9331

Struct Bond (2015) 163: 109–144
DOI: 10.1007/430_2014_160

Published online: 16 October 2014

Luminescent Lanthanide Metal–Organic Frameworks

Xue-Zhi Song, Shu-Yan Song, and Hong-Jie Zhang

Abstract More and more attention has been paid to the design and synthesis of the lanthanide metal–organic frameworks (LnMOFs). Their physicochemical properties were investigated deeply, especially in terms of the luminescent properties. Lanthanide ions, used as luminescence centers, in MOFs enable tuning options that exceed all other metals of the periodic table of the elements. This chapter explains the basic principles of lanthanide luminescence in advance, which will help the readers to understand the luminescent properties of the subsequent LnMOFs. Single-Ln^{3+} LnMOFs show fundamental luminescent phenomenon and law. Furthermore, mixed-Ln^{3+} LnMOFs exhibit significant ability of tunable white light emission and temperature measurement. Representative publication of LnMOFs with NIR luminescence and upconversion luminescence is also important to discuss here. Furthermore, bulk LnMOFs have been scaled down to the nanoregime to form nanoscale LnMOFs, which will enable their use in a broad range of applications, including drug delivery, bioimaging, and molecular sense.

Keywords Lanthanide metal–organic frameworks • NIR luminescence • Upconversion luminescence • Visible luminescence • White light emission

X.-Z. Song
State Key Laboratory of Rare Earth Resource Utilization, Changchun Institute of Applied Chemistry, Chinese Academy of Sciences, 5625 Renmin Street, Changchun 130022, P.R. China

University of Chinese Academy of Sciences, Beijing 100049, China
e-mail: songxz@ciac.ac.cn

S.-Y. Song (✉) and H.-J. Zhang (✉)
State Key Laboratory of Rare Earth Resource Utilization, Changchun Institute of Applied Chemistry, Chinese Academy of Sciences, 5625 Renmin Street, Changchun 130022, P.R. China
e-mail: songsy@ciac.ac.cn; hongjie@ciac.ac.cn

Contents

Abbreviations

1,3,5-BTC	1,3,5-Benzenetricarboxylate
1,4-NDC	1,4-Naphthalenedicarboxylate
ad	Adeninate
BPDC	Biphenyldicarboxylate
BTB	1,3,5-Tris(4-carboxyphenyl)benzene
BTPCA	1,1′,1″-(Benzene-1,3,5-triyl)tripiperidine-4-carboxylate
CPs	Coordination polymers
CTAB	Cetyltrimethylammonium bromide
DEF	*N*,*N*′-Diethylformamide
DMA	Dimethylammonium
DMAc	*N*,*N*′-Dimethylacetamide
DMBDC	2,5-Dimethoxy-1,4-benzenedicarboxylate
DMF	*N*,*N*′-Dimethylformamide
DPA	Dipicolinic acid
dpdc	2,2′-Diphenyldicarboxylate
H_2bidc	Benzimidazole-5,6-dicarboxylic acid
H_2L4	3,3′-(4-Amino-4*H*-1,2,4-triazole-3,5-diyl)dibenzoic acid
H_2oba	4,4′-Oxybis(benzoic acid)
H_2ox	Oxalic acid
H_2PIA	5-(Pyridin-4-yl)isophthalic acid
H_2PVDC	4,4′-[(2,5-Dimethoxy-1,4-phenylene)di-2,1-ethenediyl]bisbenzoic acid
H_3BPT	Biphenyl-3,4′,5-tricarboxylic acid
H_3cpda	5-(4-Carboxyphenyl)-2,6-pyridinedicarboxylic acid
H_3DSB	3,5-Disulfobenzoic acid
H_3L2	4,4′-((2-((4-Carboxyphenoxy)methyl)-2-methylpropane-1,3-diyl)bis(oxy))dibenzoic acid

H_4L3	*N*-phenyl-*N*′-phenyl bicyclo[2,2,2]-oct-7-ene-2,3,5,6-tetracarboxdiimide tetracarboxylic acid
H_4MDIP	Methylenediisophthalic acid
H_4pdca	Pyridine-2,3-dicarboxylic acid
H_4ptptc	*p*-Terphenyl-3,3″,5,5″-tetracarboxylic acid
H_4tpabn	*N*,*N*′,*N*′-Tetrakis[(6-carboxypyridin-2-yl)methyl]butylenediamine
H_5L5	3,5-Bis(1-methoxy-3,5-benzene dicarboxylic acid)benzoic acid
HL1	4-(Dipyridin-2-yl)aminobenzoic acid
IP	1*H*-imidazo[4,5-*f*][1,10]-phenanthroline
LnMOFs	Lanthanide metal–organic frameworks
m-bdc	1,3-Benzenedicarboxylate
MOFs	Metal–organic frameworks
MRI	Magnetic resonance imaging
NIR	Near infrared
NMOFs	Nanoscale metal–organic frameworks
p-BDC	1,4-Benzenedicarboxylate
p-BDC-F_4	Tetrafluoroterephthalate or 2,3,5,6-tetrafluoro-1,4-benzenedicarboxylate
phen	1,10-Phenanthroline
PVP	Polyvinylpyrrolidone
UC	Upconversion

1 Introduction

Metal–organic frameworks (MOFs), also termed as coordination polymers (CPs), are a class of crystalline organic–inorganic hybrid materials formed by the self-assembly of polydentate bridging linkers and inorganic connectors of metal ions or clusters via coordination bonds [1–3]. The availability of various building blocks of metal ions and organic linkers allows for the access to fascinating structures, novel topologies, and the direct manipulation of their physical and chemical properties. Because of the porous, periodic, and ordered and easily tailored structure, MOFs provide a splendid platform for deep investigation of the structure–property relationship and have shown promise for a number of diverse applications including gas storage [4, 5], catalysis [6, 7], nonlinear optics [8], separations [9, 10], sensing [11, 12], and light harvesting [13], drug delivery [14, 15], and so forth [16–18]. In contrast to the large branch of transition metal ion-based MOFs, the lanthanide ions have been introduced to the MOFs to form LnMOFs material, which have been reported relatively scarcely. However, the lanthanide ions with unique 4f electrons buried beneath their 6s, 5p, and 5d orbitals impart the materials with interesting, special photophysical, catalytic, and magnetic properties. Especially, the lanthanide ions have numerous energy levels arising from the f–f transitions, which may make the luminescent spectra usually spanning from ultraviolet (UV) to visible and near-infrared (NIR) region. Lanthanide complexes, as luminescent materials, exhibit

unique photoluminescent features, such as sharp absorption and luminescence bands (pure emission lines arising from characteristic 4f electron transitions), large Stokes' shifts (>200 nm), and long luminescence lifetimes (~ms) and are not affected by the environment. Compared with the traditional molecular approach, by use of molecular organic and coordination compounds to explore functional luminescent materials, the MOF approach also has the advantage to collaboratively interact with each other among the periodically located luminescent centers to direct new functionalities. In fact, a variety of luminescent LnMOFs have been realized for their diverse applications on chemical sensing, light-emitting devices, and biomedicine over the past two decades.

This chapter focuses on the brief presentation of basic principles of lanthanide-based luminescence, recent research achievement on single-color luminescence from visible region to near-infrared (NIR) region, well-tuned multicolor luminescence, and upconversion luminescence of LnMOFs materials. Furthermore, the nanoscale LnMOFs material are also overviewed, showing applied perspective in the field of cell imaging, drug delivery and molecular sensor.

2 Basic Principles of Lanthanide Luminescence

2.1 Electronic Structure and Spectra Term

Lanthanide elements (denoted as Ln) have atomic numbers ranging from 57 to 71 with electronic configurations of neutral atoms being $[Xe]4f^n6s^2$ or $[Xe]4f^{n-1}5d^16s^2$ according to the principle of lowest energy. They possess characteristic 4f open-shell configurations and exhibit similar chemical properties, particularly oxidation states [19–21]. Their most stable oxidation state is +3, giving rise to the electronic configuration $[Xe]4f^n$ ($n = 0$ to 14). These electronic configurations indeed generate a rich multiplicity (or degeneracy), with the number of $14!/n!(14\text{-}n)!$. Because the 4f shells of lanthanide elements are unfilled, different arrangements of 4f electrons generate different energy levels. Generally, the following quantum numbers can be used to describe the energy levels, and the relationships between the quantum number of electrons are as follows:

1. Total spin quantum number $M_s = \Sigma m_s$.
2. Total orbital quantum number $L = \Sigma l_i$.
3. Total magnetic quantum number $M_L = \Sigma m_l$.
4. Total angular momentum quantum number J, which takes $L+S$, $L+S-1$,... $L-S$ when $L \geq$ S and can take $S+L$, $S+L-1$,... $S-L$ when $L \leq S$. M_J is the total magnetic angular quantum number J along the magnetic field. In a multi-electronic ion, a given association of the electrons with the 4f wave functions is called a micro state. A set of micro states can be described by the spectral term. The spectral term is a symbol which combines the total magnetic quantum number M_L (its maximum is the total orbital angular quantum number L) and

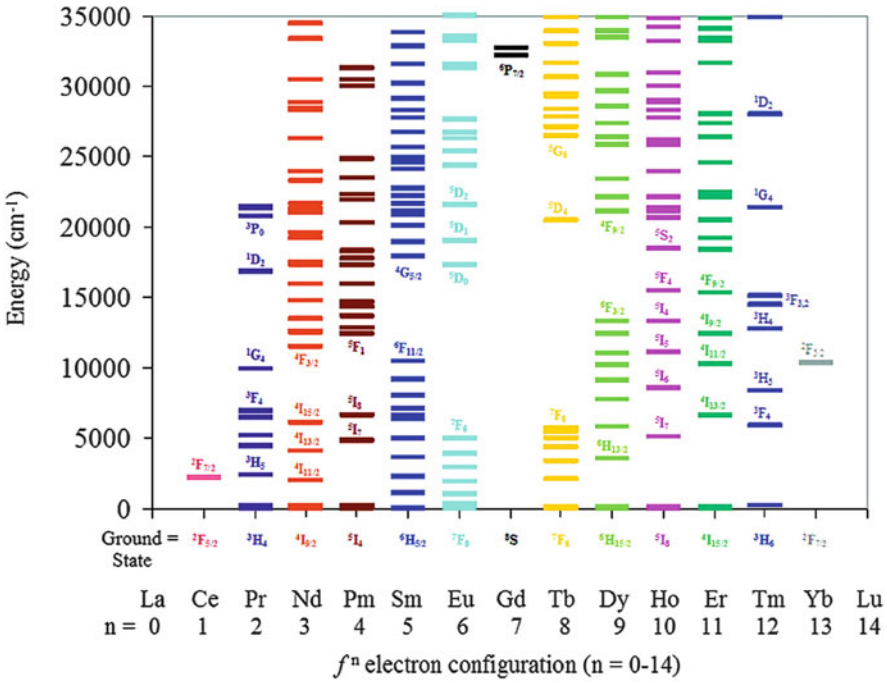

Fig. 1 Energy diagrams for Ln^{3+} in a $LaCl_3$ lattice. Reprinted with permission from [22]. Copyright 2009 American Chemical Society

total spin quantum number M_S (its maximum is the total spin quantum number S), written as ^{2S+1}L, where L is a capital letter S, P, D, F, G, H, and I with the L value of 0, 1, 2, 3, 4, 5, and 6, respectively. As the two movements of the electrons (spin and orbital movement) are not independent and couple with each other, Russell–Saunders spin–orbit coupling scheme (L–S couple) has been proposed to consider this coupling at the level of the overall angular momenta and not for each individual electron. As a consequence, the above spectral term is further split into a series of spectroscopic levels as $^{2S+1}L_J$ each with a $(2J+1)$ multiplicity, where J is the total angular momentum quantum number ($\vec{J} = \vec{L} + \vec{S}$). The different arrangements of 4f electrons generate different energy levels or micro states, corresponding to the definite spectroscopic levels. The 4f electron transitions, between the various energy levels, could generate numerous absorption and emission spectra. However, it is a big tedious and intricate procedure to find all of them out, barring the ground spectral term according to the Hund's rules. The partial energy diagrams of Ln^{3+} in a $LaCl_3$ lattice are shown in Fig. 1 [22].

Table 1 Selection rules for f–f transitions between spectroscopic levels

Operator	ΔS	ΔL	ΔJ^a
ED	0	≤ 6	≤ 6 (2, 4, 6 if J or $J' = 0$)
MD	0	0	0, ± 1
EQ	0	0, ± 1, ± 2	0, ± 1, ± 2

[a] $J = 0$ to $J' = 0$ transitions are always forbidden

2.2 *f–f Absorption Spectra*

Lanthanide ions display three types of electronic transitions, broad charge-transfer transitions (LMCT or MLCT), broad 4f–5d transitions, and intraconfigurational 4f–4f transitions. The former two, parity allowed transitions, usually occur with high energies, so that they are rarely observed in coordination compounds, except for Ce^{3+}, Pr^{3+}, and Tb^{3+} in 4f–5d and Eu^{3+}, Yb^{3+}, and possibly Sm^{3+} and Tm^{3+} in LMCT [23]. The latter, a main type of transitions, are quite narrow and not depend much on the chemical environment of the central ion. The f–f transitions are divided into electric dipole transitions (ED), magnetic dipole transitions (MD), and electric quadrupole transitions (EQ). Not all transitions are permitted since they must obey some selection rules. The first *Laporte's parity selection rule* requires that for ED transitions the parity must change from the initial to final states. As a corollary, the f–f electric dipole transition is forbidden and faint, with low absorption coefficients (usually $<1\ M^{-1}\ cm^{-1}$) [24]. While as for the MD, they are parity allowed, but have intensity of the same order of magnitude as ED. EQ transitions are not easily observed with much weaker intensity than MD and ED transitions, although they are also parity allowed. In addition, the other selection rules by S, L, and J quantum numbers for f–f transitions between spectroscopic states are listed in Table 1.

The forbidden ED can often be identified when the free Ln^{3+} ion is inserted into a chemical environment, because the selection rules may be relaxed by several mechanisms: the coupling between vibrational and electronic parts temporarily changing the symmetry of the ions, J-mixing, and the mixing with charge-transfer states [25]. They are termed induced (or forced) ED transitions, and their intensities can be evaluated by Judd–Ofelt (JO) theory [26, 27]. The intensity of some induced ED transitions has been verified to be particularly sensitive to the change in Ln^{3+} environment, and they are so-called hypersensitive, a typical example is Eu^{3+} ($^5D_0 \rightarrow {}^7F_2$).

To summarize the absorption spectra briefly, the absorption spectra of lanthanide ions are line-like due to the shield effect by outer $5p^6 5s^2$ subshells, but with low absorption efficiency. While in the lanthanide complexes, the absorption spectra are mainly contributed by the absorption ability of organic ligands.

2.3 Emission Spectra, Energy Transfer, and Antenna Effect

One of the most significant features of lanthanide ions is their photoluminescent properties arising from the f–f intraconfigurational transitions. Similar to the absorption spectra, these optical bands are sharply line-like and characteristic, due to the insensitivity to the ligand environments. With the exception of La^{3+} ($4f^0$) and Lu^{3+} ($4f^{14}$), all Ln^{3+} ions show emission lines, almost covering the entire spectrum. For instance, Eu^{3+}, Tb^{3+}, Sm^{3+}, and Tm^{3+} emit red, green, orange, and blue light, respectively, in the visible region. Additionally, Dy^{3+} is luminescent with white or near white light, while Ln^{3+} ions, such as Pr^{3+}, Nd^{3+}, Sm^{3+}, Dy^{3+}, Ho^{3+}, Er^{3+}, Tm^{3+}, and Yb^{3+}, show emissions in the near-infrared (NIR) region. Therefore, some Ln^{3+} ions show single visible or NIR emission, some can emit both visible and NIR light. Ce^{3+} ion emits a broad-band spectrum in the range 370–410 nm due to the allowed 5d–4f transition [21]. Due to the absence of sufficient intermediate energy level, the radiation of Gd^{3+} locates in the ultraviolet region, which can be only observed in the absence of organic ligands with low-lying singlet and triplet levels [28].

Although photoluminescence of Ln^{3+} ions is intriguing, as mentioned above, the low absorption efficiency of f–f transitions making direct photoexcitation of lanthanide ions is difficult. To circumvent this problem, the commonly accepted method in luminescent lanthanide–organic compounds is the incorporation of a strongly absorbing chromophore to sensitize Ln^{3+} emission through *antenna effect*. The groundbreaking work reported by Weissman in 1942 [29] disclosed that the metal(Eu)-centered luminescence can be easily triggered through light absorption by organic ligands and subsequent energy transfer in Eu-based β-diketonate, phenolate, or salicylate complexes. About twenty years later, Crosby and Whan proposed the detailed mechanism of energy transfer from organic ligands to the Ln^{3+} ion [30–32], well documented and widely used by the subsequent researchers (Fig. 2). Briefly, the overall process of energy transfer is complicated and involves the following main four steps: (1) the excited step is accomplished due to the Laporte- and spin-allowed ligand-centered absorptions upon the UV light illumination; (2) the energy of S_1 excited state is transferred to the triplet excited state T_1 of the ligands via nonradiative *intersystem crossing* (ISC); (3) the intramolecular energy transfer from T_1 to Ln^{3+} ions, concomitant with the population of the excited 4f states; and (4) the radiative process undergoes with its characteristic line emission.

In principle, the energy transfer process from T_1 of organic ligands to Ln^{3+} ions is quite intricate, since several mechanisms may be invoked: (1) exchange or Dexter's mechanism, (2) dipole–dipole or Förster's mechanism, and (3) dipole–multipolar interaction mechanism [34]. As proposed by Dexter, the energy transfer efficiency is sensitive to the energy gap (ΔE) between the triplet state of the organic ligand and the resonance level of the Ln^{3+} ion [35]. When the energy levels of the organic ligands are below the resonance level of the Ln^{3+} ion, no metal-based luminescence is observed. The energy transfer efficiency decreases due to the

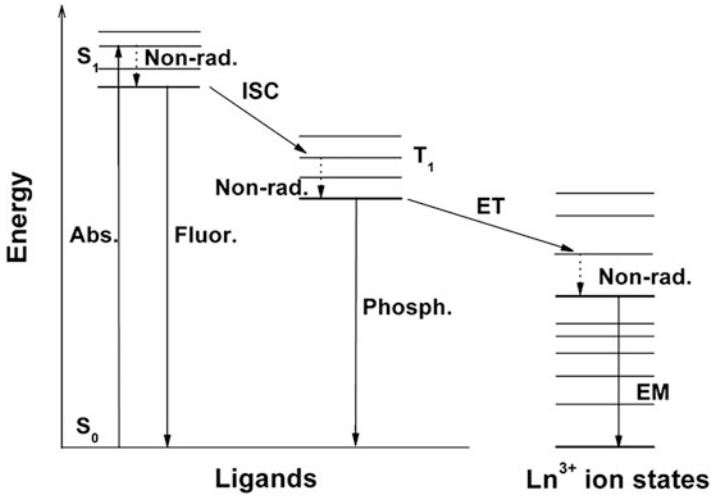

Fig. 2 Simplified energy diagram showing the energy migration path in a lanthanide–organic complex system. *Abs.* absorption, *Fluor.* fluorescence, *Phosph.* phosphorescence, *EM* Ln^{3+} ion emission, *ISC* intersystem crossing, *ET* energy transfer, *S* singlet, *T* triplet, *Non-rad.* nonradiative transitions. Reproduced from [33] by permission of The Royal Society of Chemistry (RSC)

diminution in the overlap between the donor and the acceptor when the energy difference is too big. And another aspect, energy back transfer will occur and repopulate the T_1 state of organic ligands when the reverse conditions are satisfied; at least $10\,k_BT$ (2,000 cm^{-1}) is needed for efficient population of the lanthanide excited state [36]. The triplet-state level of organic ligands could be calculated and evaluated by measuring the phosphorescence spectra of the corresponding Gd complex at cryogenic temperatures (usually at 77 K).

Similar to absorption spectra, light emission is due to two main types of transitions, MD and ED. The two important parameters characterizing the light emission from a given Ln^{3+} ion are the lifetime of the excited state and the quantum yield (Φ), with the following definition:

$$\tau_{obs} = 1/A_{obs} \tag{1}$$

$$\Phi = \frac{\text{Number of emitted photos}}{\text{Number of absorbed photos}}. \tag{2}$$

For luminescent lanthanide compounds, the *overall luminescence quantum yield*, $\Phi_{overall}$, could be calculated by Eq. (3), where η_{sens} is sensitization efficiency of organic ligands and Φ_{Ln} is called *intrinsic quantum yield*, that is, the Ln-centered luminescence yield upon direct excitation into the 4f levels:

$$\Phi_{\text{overall}} = \eta_{\text{sens}} \Phi_{\text{Ln}}. \tag{3}$$

However, determination of *intrinsic quantum yield* from experimental data is difficult in view of the faint f–f transition absorbance. It can be calculated from Eq. (4), in which A is the rate constant and τ is lifetime. Its value reflects the extent of nonradiative deactivation processes. The rate constant A_{obs} is the sum of the rates of the various deactivation processes (Eq. (5)), where A_{rad} and A_{nrad} are the radiative and nonradiative rate constants, respectively. The nonradiative process refers to vibration-induced process, photoinduced electron transfer process, and other remaining deactivation paths. In the equations, the values of Φ_{overall}, τ_{obs} can be experimentally measured, and τ_{rad} could be theoretically calculated, although they all involve with complicated processes. To keep the lanthanide-containing edifices with high *intrinsic quantum yield*, one has to design them with minimal nonradiative deactivation pathways. The high-energy OH, NH, and CH oscillations are the chief factors contributing to the deactivation process, particularly when the energy gap between the emissive state of Ln^{3+} ion and the highest sublevel of its ground, or receiving, multiplet is smaller enough closer to the nonradiative process:

$$\Phi_{\text{Ln}} = \frac{A_{\text{rad}}}{A_{\text{obs}}} = \frac{\tau_{\text{obs}}}{\tau_{\text{rad}}}, \tag{4}$$

$$A_{\text{obs}} = A_{\text{rad}} + \sum A_{\text{nrad}}. \tag{5}$$

3 Lanthanide MOFs with Visible Luminescence

3.1 *Single-Ln^{3+} MOFs with Visible Luminescence*

Up to now, a plethora of lanthanide MOFs have been synthesized, and most of them exhibit interesting photophysical properties. However, the design and synthesis of multidimensional LnMOFs is challenging due to the high coordination number and flexible coordination geometry of lanthanide ions. Thus the judicious choice of the organic linker plays a key role in the structural assembly. On the other hand, the high affinity of lanthanide ions for oxygen donor atoms makes ligands with carboxylate groups excellent candidates as bridging ligands for preparing stable architectures. The ligands not only act as structural components but also act as sensitizers to overcome the weak absorption of the Ln-centered forbidden transitions. In addition, the introduction of the carboxyl groups with sufficiently strong binding capacity would preclude the coordination of water molecules to metal centers in the first coordination sphere, therefore reducing the activation of nonradiative decay processes. As a consequence, a number of different carboxylic acids, such as aliphatic acids, aromatic multicarboxylic acids, and heterocyclic acids have been investigated widely to achieve bright single-color lanthanide luminescence in the intriguing, various architectures [37–43]. A few examples

would be enumerated to expatiate the fundamental luminescent phenomenon and some advice to enhance the luminescent intensity and efficiency.

A novel carboxylate ligand *p*-terphenyl-3,3″,5,5″-tetracarboxylic acid (H_4ptptc), a strong absorbing sensitizer, was exploited for the first time to explore the luminescent properties of the Eu(III) complexes owing to its highly delocalized π-electron system [44]. Additionally, its robustness and a certain degree of rigidity are also useful in accessing a rigid and protective coordination shell to minimize nonradiative deactivation. Three different europium–tetracarboxylate frameworks were successfully synthesized from identical raw reactants by subtly changing the solvothermal conditions, in order to systematically investigate the structure-related photophysical properties in detail. The formulas of these compounds are $\{[Eu(ptptc)_{0.75}(H_2O)_2]\cdot 0.5DMF\cdot 1.5H_2O\}_n$ (**1**), $\{[Me_2H_2N]_2[Eu_2(ptptc)_2(H_2O)(DMF)_{0.5}]\cdot 1.5DMF\cdot 7H_2O\}_n$ (**2**), and $\{[Eu(Hptptc)(H_2O)_4]\cdot 0.5DMF\cdot H_2O\}_n$ (**3**). The former two compounds feature three-dimensional (3D) frameworks constructed by $\{Eu_2(\mu_2\text{-}COO)_2(COO)_4\}_n$ chains and $[Eu_2(\mu_2\text{-}COO)_2(COO)_6]^{2-}$ dimetallic subunits, respectively. The last complex exhibits a 2D layer architecture assembling to 3D framework.

As discussed in the "Basic principles of lanthanide luminescence" part of this chapter, the energy migration process involves ligand-centered absorptions followed by the $^1S^* \rightarrow {}^3T^*$ intersystem crossing, $^3T^* \rightarrow Ln^*$ transfer, and Ln*-centered emission. The triplet energy of ligand H_4ptptc ($^3T^*$) was calculated by referring to the lower wavelength emission edge of the phosphorescence spectrum of the corresponding Gd(III) analogue $\{[Me_2H_2N]_2[Gd_2(ptptc)_2(H_2O)(DMF)_{0.5}]\cdot x DMF\cdot y H_2O\}_n$ to be 21,230 cm^{-1}. This energy level is lying ~4,000 cm^{-1} above the $^5D_0$ emitting level (17,500 cm^{-1}) of the Eu(III) ion, sufficiently suitable to sensitize the Eu-centered luminescence and prevent quenching via the back energy transfer. Therefore, all of the complexes display bright red luminescence.

The room-temperature excitation and emission spectra of the free ligand and Eu(III) complexes in the solid state are shown in Fig. 3. Broad excitation bands between 260 and 380 nm exist in the free ligand and Eu(III) complexes, attributed to the $n \rightarrow \pi^*$ or $\pi \rightarrow \pi^*$ electronic transitions of ligand H_4ptptc. The similarity of the excitation profiles demonstrates that energy transfer occurs from the ligand H_4ptptc to the Eu(III) center. A series of sharp lines are also observed in the excitation spectra of all complexes, which can be assigned to the transitions between $^7F_0$ and $^5L_6$ states and transitions between $^7F_{0,1}$ and $^5D_{2,1}$ states. Under ligand excitation (350 nm), the emission spectra of all three compounds reveals well-resolved peaks centered at 578, 592, 614, 650, and 702 nm, corresponding to the f–f electronic transitions ($^5D_0 \rightarrow {}^7F_J$, $J = 0$–4) of the Eu^{3+} ion, with the hypersensitive $^5D_0 \rightarrow {}^7F_2$ transition dominating the spectra. No broad and strong emission band resulting from the ligand is observed, demonstrating the ligand transfers the absorbed energy very effectively to the emitting level of the Eu^{3+} center. The observed luminescence decays for **1** and **3** could be fitted with a monoexponential function, while the decay for **2** was a biexponential, all of which are consistent with the presence of one and two crystallographically independent Eu sites. Analyses of

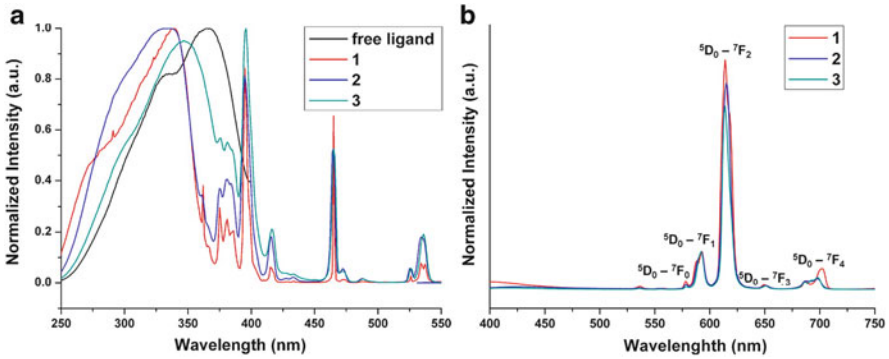

Fig. 3 (**a**) Excitation spectra of the free ligand and compounds **1**–**3**. (**b**) Emission spectra of the compounds **1**–**3** excited at 350 nm. The spectra were normalized with respect to the magnetic dipole transition ($^5D_0 \rightarrow {}^7F_1$). Reprinted with permission from [44]. Copyright 2013 American Chemical Society

the ligand-sensitized overall quantum yield ($\Phi_{overall}$), intrinsic quantum yield (Φ_{Ln}), and the efficiency of the ligand-to-metal energy transfer (η_{sens}) will help the readers to qualify the sensitizing ability of the ligand H_4ptptc and to get information on the relationship between the structures and photoluminescence properties. The radiative lifetime of Eu($^5D_0$) τ_{rad} can be determined by Eq. (6) to further calculate the intrinsic quantum yield Φ_{Ln} (Eq. (4)), in which $A_{MD,0}$ is the deactivation rate associated with the spontaneous emission probability for the $^5D_0 \rightarrow {}^7F_1$ transition in vacuo, equal to 14.65 s^{-1}; I_{tot}/I_{MD} is the ratio between the total integrated $^5D_0 \rightarrow {}^7F_J$ emissions ($J = 0$–4) and the magnetic dipole $^5D_0 \rightarrow {}^7F_1$ transition; and the refractive index of the medium (n) is taken to be equal to 1.5 in the solid sample:

$$\frac{1}{\tau_{rad}} = A_{MD,0} \times n^3 \times \left(\frac{I_{tot}}{I_{MD}}\right). \tag{6}$$

The pertinent values of $\Phi_{overall}$, τ_{obs} and other photophysical parameters are summarized in Table 2. Generally, this ligand does not occupy the entire coordination sphere of the Eu^{3+} ion, leaving some binding sites for solvent DMF or water molecules. The deactivation process arising from vibronic coupling between Eu and OH oscillators leads to the small luminescence quantum yields and lifetimes, which is also proven by the large nonradiative rates. The $^5D_0 \rightarrow {}^7F_2$ hypersensitive transition is allowed by symmetry-related selection rules and becomes sizable due to the distorted 8-coordinate dodecahedron environment of the Eu(III) ion in compound **1**, therefore resulting in a relatively large quantum yield and radiative decay rate constant. With respect to **1**, the nonradiative rate constant of **2** decreases by ~17% which are attributed to the presence of only one water molecule in the inner coordination sphere, compared to two. Finally, due to four bond water molecules in **3**, the nonradiative rate constant is 60% larger than for **2**, resulting

Table 2 $\Phi_{overall}$, τ_{obs}, τ_{rad}, radiative (A_{rad}), and nonradiative (A_{nrad}) decay rates, Φ_{Ln} η_{sens} for compounds **1–3**

Compound	$\Phi_{overall}$ (%)	τ_{obs} (ms)	τ_{rad} (ms)	A_{rad} (s^{-1})	A_{nrad} (s^{-1})	Φ_{Ln} (%)	η_{sens} (%)
1	22	0.46	2.41	415	1,759	19	100
2	16	0.55[a]	2.77	361	1,457	20	80
3	11	0.37	2.86	350	2,353	13	85

[a]This value corresponds to τ_{av}, given by $\tau_{av} = (A_1\tau_1^2 + A_2\tau_2^2)/(A_1\tau_1 + A_2\tau_2)$; $\tau_1 = 0.57$ ms (94%),$\tau_2 = 0.30$ ms (6%)

Reprinted with permission from [44]. Copyright 2013 American Chemical Society

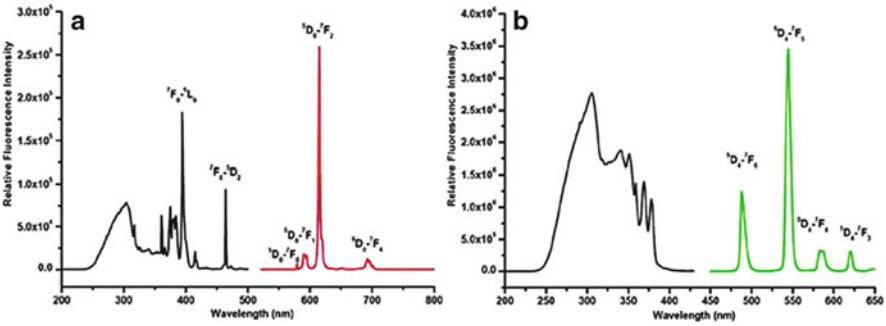

Fig. 4 Room-temperature excitation and emission spectra for (**a**) the Eu^{3+} complex and (**b**) the Tb^{3+} complex. Reprinted with permission from [45]. Copyright 2012 American Chemical Society

in a concomitant decrease in the overall quantum yield. So that the removal of aqua ligands from the inner coordination sphere would increase the luminescent intensity and quantum yield of the EuMOFs.

Methylenediisophthalic acid (H_4MDIP), a V-shaped tetracarboxylate ligand with relative rotation freedom around $-CH_2-$ spacer, can possess a variety of connection modes and give rise to structural peculiarity. One of the two structural types of LnMOFs was obtained by assembly of Ln ions and H_4MDIP, manifesting infinite metal-carboxylate oxygen chain-shaped building blocks. The luminescent properties of the corresponding Eu and Tb complexes were investigated in detail [45]. As shown in Fig. 4, the intensity ratio $^5D_0 \rightarrow {}^7F_2/{}^5D_0 \rightarrow {}^7F_1$ in the spectrum of the Eu^{3+} complex is very high, which signifies that the Eu^{3+} ion is not located at the inversion center with low symmetry. This is further proved by the presence of the weak symmetry-forbidden $^5D_0 \rightarrow {}^7F_0$ emission, consistent with the result of X-ray structural analysis. For the Tb^{3+} complex, a broad band between 230 and 325 nm overlapped by the absorption spectrum of the ligand in the excitation spectrum reveals that energy transfer from the ligand to the metal ion is operative. The sharp lines assigned to transitions between the $^7F_6$ and the $^6L_9$ and ^5D_J ($J = 2, 3$) levels are much weaker than that of broad excitation band, demonstrating that luminescence sensitization via excitation of the ligand is much more efficient than the direct excitation of the Tb^{3+} ion absorption level. Its room-temperature emission spectrum

shows peculiar emission bands ($\lambda_{ex} = 300$ nm) at 488, 544, 582, and 620 nm ($^5D_4 \rightarrow {}^7F_J$, $J = 6, 5, 4, 3$). The decay curve is well fitted with a monoexponential function, indicative of the presence of one distinct emitting species. The energy transfer efficiency from the organic ligands to Tb^{3+} is higher than that to Eu^{3+} according to the luminescent intensity trend $Tb^{3+} \gg Eu^{3+}$, which is confirmed by the longer fluorescence lifetime of Tb^{3+} (0.85 ms) than that of Eu^{3+} (0.42 ms). The visible emission was also observed in the Sm^{3+} and Dy^{3+} corresponding frameworks.

In another related work, one-dimensional metal–organic frameworks were obtained by reaction of lanthanide salts and 4-(dipyridin-2-yl)aminobenzoic acid (HL1) [46]. The singlet energy level and triplet energy level of the ligand were estimated by the UV–vis absorption and the low-temperature phosphorescence spectra of the Gd^{3+} complex to be 28,900 and 23,697 cm^{-1}. The energy difference 5,203 cm^{-1}, close to ideal 5,000 cm^{-1}, reveals that this newly developed ligand has a good intersystem crossing efficiency [47]. A lower quantum yield has been observed in the Eu^{3+} complex ($\Phi_{overall} = 7\%$) than that of Tb^{3+} complex ($\Phi_{overall} = 64\%$) because of the larger energy gap between the triplet-state and the $^5D_0$ level of Eu^{3+} (6,447 cm^{-1}) and superior match of the triplet energy level of HL1 to the Tb^{3+} emitting level (3,197 cm^{-1}).

An appropriate organic ligand will impart structural novelty and enhance the stability of the final LnMOFs. The tunable energy level of the ligand will improve their luminescent properties, in terms of intensity, lifetime, and quantum yield.

3.2 White Light Emission in LnMOFs

White light generation is required on a daily basis, e.g., for room lighting, lasers, monitors, panel displays, and other optical devices [48, 49]. In general, three main types of principles are commonly considered to realize white light emission in light-emitting materials: (1) monochromatic emitters that emit in the entire visible spectrum, (2) dichromatic emitters that blend blue and yellow light, and (3) trichromatic emitters that combine red, green, and blue components. In LnMOFs, the lanthanide ions display emission in the primary color range (red, green, and blue) that fully spans almost the entire visible spectrum. The organic ligands play the roles as linkers, sensitizers for the Ln^{3+} ions, and even sometimes light emitters. The intrinsic tunability and modularity of organic ligand structures and the highly ordered LnMOF structures may systematically control luminescent properties. Furthermore, the mutual separation of lanthanide ions by ligands in LnMOFs will prevent self-quenching, and the isostructural behavior of LnMOFs may allow for the incorporation of different lanthanide ions into the same host material. So far, tremendous efforts have been dedicated toward the synthesis of LnMOFs with white light emission. Now, some examples are presented in the following paragraph to clarify how to produce white light in LnMOFs, according to the kinds of Ln^{3+} ion species.

3.2.1 Mono-Kind of Ln^{3+} Species

A novel one-dimensional lanthanide–organic framework, with the formula of $[Sm(dpdc)_{1.5}(IP)(H_2O)]_n$ (dpdc = 2,2′-diphenyldicarboxylate and IP = 1*H*-imidazo[4,5-*f*][1,10]-phenanthroline), was synthesized [50]. The emission spectrum of this compound consists of narrow bands and an additional broad band when excited at 330 nm. The broad emission band in the region 400–540 nm ($\lambda_{max} = 470$ nm) arises from the ligand-based $\pi^* \rightarrow \pi$ transition. And the narrow emission bands at 563, 598, and 642 nm are corresponding to $^4G_{5/2} \rightarrow {}^6H_{5/2}$, $^4G_{5/2} \rightarrow {}^6H_{7/2}$, and $^4G_{5/2} \rightarrow {}^6H_{9/2}$ transitions of the Sm(III) ion, respectively. The quantum yield (Φ) and luminescence lifetime (τ) are $\Phi = 1.76\%$ and $\tau_1 = 6.695$ μs, $\tau_2 = 10.64$ μs.

A suitable intensity ratio of green (563 nm), orange (598 nm), and red (642 nm) emissions from Sm^{3+} ion and ligand-centered blue luminescence is the sufficient condition to obtain white light emission. The intensity of the Sm-centered emission remains almost constant upon excitation at certain wavelength range (310–390 nm). As expected, the CIE coordinates change from (0.341, 0.347) to (0.312, 0.310), all of which fall exactly in the white region (Fig. 5). Summarily, this work provides a promising approach for preparation of single component white light-emitting materials.

An indium-based metal–organic $In(BTB)_{2/3}(ox)(DEF)_{3/2}$ BTB = 1,3,5-tris(4-carboxyphenyl)benzene, H_2ox=oxalic acid, and DEF = *N*,*N*′- diethylformamide was synthesized under solvothermal condition [51]. The broad-band emission with intrinsic overall white light emission observed when exciting the material between 350 and 380 nm can be associated with the ligand-to-metal charge-transfer (LMCT) $BTB \rightarrow M^{3+}$ transition. The intrinsic color properties of the pristine material could be improved by introduction of a narrow-band, red emission component into this system via Eu^{3+} doping. This result represented reliable new paths for the rational design of alternative materials for solid-state lighting applications with enhanced color properties.

3.2.2 Two Kinds of Ln^{3+} Species

Tang et al. reported the preparation of isostructural 3D LnMOFs (Ln=La^{3+}, Eu^{3+}, and Tb^{3+}) of the general formula $[Ln(BTPCA)H_2O] \cdot 2DMF \cdot 3H_2O$, where the ligand BTPCA is 1,1′,1″-(benzene-1,3,5-triyl)tripiperidine-4-carboxylate [52, 53]. Eu^{3+} ion was doped into a host of Tb-BTPCA to afford Eu_zTb_{1-z}-BTPCA, a mixed-lanthanide MOF. Upon excitation at 365 nm, the dominant emission of Tb^{3+} at 545 nm is more intense than that of Eu^{3+} at 618 nm in the case of $Eu_{0.0001}Tb_{0.9999}$-BTPCA. More interestingly, the relative intensity of these two emission peaks is reversed when $z = 0.75\%$ ($Eu_{0.0075}Tb_{0.9925}$-BTPCA). Careful optimization the relative concentration of Tb^{3+} and Eu^{3+}, with maintenance of the blue emission from BTPCA ligand, producing the comparable emission intensities at 450, 545, and 618 nm, would realize overall white light emission. It was

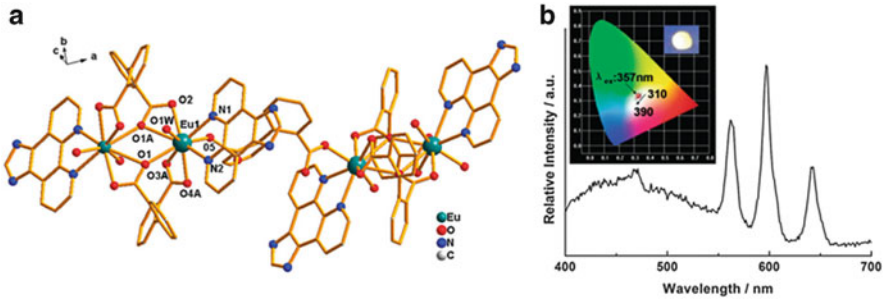

Fig. 5 (**a**) 1D chain structure of the Eu^{3+} analogue, symmetry code: A: 0.5-*x*,1.5-*y*,2-*z*. (**b**) Emission spectrum of $[Sm(dpdc)_{1.5}(IP)(H_2O)]_n$ excited at 330 nm. Inset: the CIE chromaticity diagram and image by 365 nm light. Reproduced from [50] by permission of The Royal Society of Chemistry (RSC)

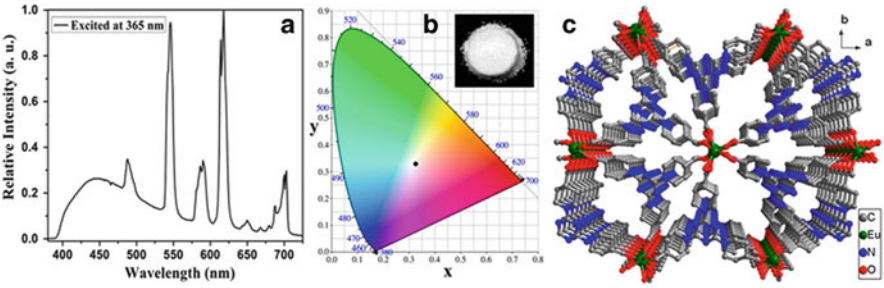

Fig. 6 (**a**) Emission spectrum and (**b**) the CIE chromaticity diagram of $Eu_{0.005}Tb_{0.995}$-BTPCA under excitation at 365 nm. (**c**) 3D structure of $[Eu(BTPCA)H_2O] \cdot 2DMF \cdot 3H_2O$ as viewed slightly off the *c* axis. Reprinted with the permission from [53]. Copyright 2014 American Chemical Society

found that in the case of $Eu_{0.005}Tb_{0.995}$-BTPCA ($z = 0.5\%$), nearly pure white light emission was indeed achieved with its CIE coordinate of (0.3264, 0.3308), very close to the optical coordinate (0.3333, 0.3333), depicted in Fig. 6.

3.2.3 Three Kinds of Ln^{3+} Species

In this part, the examples with white light emission were obtained according to the blue, green, and red trichromatic principle. Ligand-based and Ln^{3+}-based luminescence make contributions to blue emission, respectively.

Three novel chiral isostructural one-dimensional LnMOFs, $\{[Ln_3(bidc)_4(phen)_2(NO_3)] \cdot 2H_2O\}_n$ (Ln=Gd, Eu, and Tb; H_2bidc = benzimidazole-5,6-dicarboxylic acid; and phen = 1,10-phenanthroline), were synthesized via hydrothermal reaction [54]. The Gd-centered compound presented a blue emission band centered at 440 nm, which originates from the $\pi^* \rightarrow \pi$ transition of the ligands under

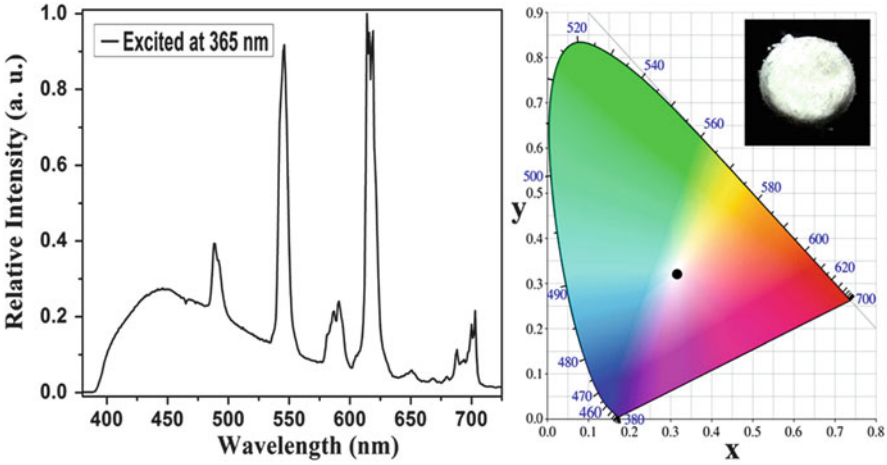

Fig. 7 Emission spectrum (*left*) and the CIE chromaticity diagram (*right*) of $La_{0.6}Eu_{0.1}Tb_{0.3}$-BTPCA under excitation at 365 nm. The inset is the optical photograph excited under 365 nm UV lamp. Reprinted with permission from [53]. Copyright 2014 American Chemical Society

excitation at 376 nm. Narrow and characteristic luminescent bands ($^5D_0 \rightarrow {}^7F_J$ ($J = 0$–4) transitions for Eu^{3+}, $^5D_4 \rightarrow {}^7F_J$ ($J = 3$–6) transitions for Tb^{3+}) dominated the emission spectra of the Eu- and Tb-centered compounds without ligand-based luminescence, indicating the efficient ligand-to-Ln(III) ion energy transfer in these two compounds under excitation at 350 nm. When the doping ratios of Gd(III), Eu (III), and Tb(III) changed, variations in the relative blue, red, and green emission intensities were obtained. The results revealed that white light emission of the doped material was achievable ($\lambda_{ex} = 376$ nm) as the molar ratio of $Gd^{3+}/Eu^{3+}/Tb^{3+}$ was 98.5:0.5:1 with the CIE chromaticity coordinate value of (0.322, 0.328). In the abovementioned literature [53], the sample of $La_{0.6}Eu_{0.1}Tb_{0.3}$-BTPCA displays white light emission upon excitation at 365 nm with the corresponding CIE coordinate (0.3161, 0.3212) and the CCT value of 6,370 K (Fig. 7). The reason is that La-BTPCA emits in blue region, and codoped with both Tb^{3+} and Eu^{3+} would result in green and red emission.

Considering the high energy (32,150 cm^{-1}) of the Gd^{3+} ion lowest-lying emission level, and the absence of 4f electron of the La^{3+} ion, one may anticipate that Gd^{3+}- and La^{3+}-centered MOFs can act as host material with blue ligand-centered emission. Thus, codoped Eu^{3+} and Tb^{3+} ions in appropriate concentration and ratio would generate white light emission according to the trichromatic principle.

Dang and coworkers aimed to develop novel white light emission LnMOFs, using a semirigid trivalent carboxylic acid 4,4′-((2-((4-carboxyphenoxy)methyl)-2-methylpropane-1,3-diyl)bis(oxy))dibenzoic acid (H_3L2) as organic building block [55]. Then a new family of LnMOFs, denoted as $LnL2 \cdot DMF$, was obtained (Ln=Y, La–Yb, except Pm). Compared with pure $LnL2 \cdot DMF$ (Ln=Sm and Dy) with no detectable emissions, the doped material $Sm_xGd_{1-x}L2$ and $Dy_xGd_{1-x}L2$ reveals characteristic 4f electrons transitions, indicating that enhanced visible

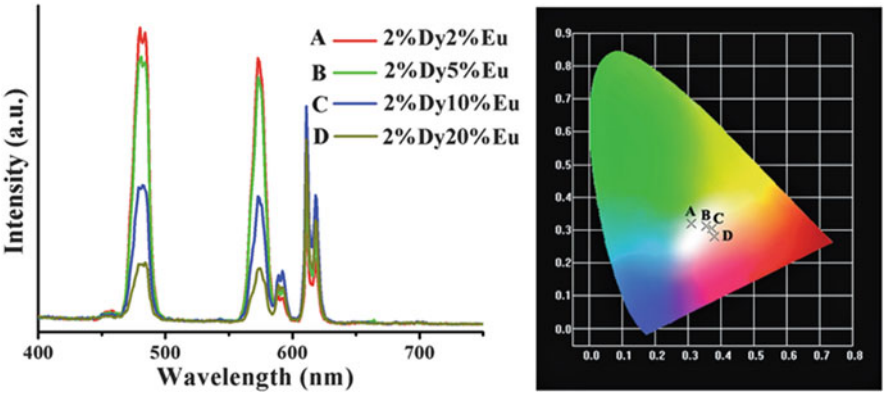

Fig. 8 *Left*: PL emission spectra of the Dy/Eu-doped Gd compounds ($\lambda_{ex} = 290$ nm). *Right*: CIE chromaticity diagram for the $Dy_xEu_yGd_{1-x-y}L2$: (*A*) $x = y = 0.02$; (*B*) $x = 0.02$, $y = 0.05$, (*C*) $x = 0.02$, $y = 0.10$, (D) $x = 0.02$, $y = 0.20$. Reproduced from [55] by permission of The Royal Society of Chemistry (RSC)

optical properties could be obtained by doping methods. Taking Dy-doped compound as an example, emissions at 480 and 573 nm, corresponding to the $^4F_{9/2} \rightarrow {}^6H_{15/2}$ (480 nm) and $^4F_{9/2} \rightarrow {}^6H_{13/2}$ (573 nm) transitions of Dy^{3+} ion, are comparable in intensity under the excitation at 290 nm. Due to almost the same intensity of blue emission (480 nm) and green emission (573 nm) from the Dy-doped materials, it is anticipated that other further doped Ln^{3+} ions with red emission can be applied to realize white light emission. By precise control of the proportion of Dy/Eu or Dy/Sm in Gd analogue, the white light emission was observed in the many cases, for example, $Dy_{0.02}Eu_{0.05}Gd_{0.93}L2$ and $Dy_{0.01}Sm_{0.10}Gd_{0.89}L2$ with the CIE coordinates of (0.355, 0.313) and (0.328, 0.320) (Fig. 8). Notably, no ligand-based emission implied that a highly efficient energy transfer from ligand-to-Ln^{3+} ions occurred in codoped samples. This work was declared to be the first example to achieve white light emission in LnMOFs without involving any emission of the organic ligands.

Then, our group utilized a tetracarboxylate ligand, *N*-phenyl-*N*′-phenyl bicyclo [2,2,2]-oct-7-ene-2,3,5,6-tetracarboxdiimide tetracarboxylic acid (H_4L3), to construct a new type of double-chain-based 3D LnMOF [56]. Following the above concept, by judicious control of the Ln^{3+} proportions, we also successfully obtained tunable white light emission in codoped materials $Dy_xEu_yGd_{1-x-y}L3$ and $Sm_xDy_yGd_{1-x-y}L3$ ($\lambda_{ex} = 293$ nm).

3.3 *Mixed-Ln^{3+} MOFs as Luminescent Thermometer*

Temperature is a fundamental thermodynamic parameter, the measurement of which is crucial in countless scientific investigations and technological

developments. In contrast to the conventional temperature sensors (so-called contact thermometers), luminescence-based method is an alternative noninvasive and accurate technique, because of its rapid response ability, high spatial resolution characteristics, and strong resistance to electric or magnetic fields [57–59]. A series of pioneering examples reported by Chen, Cui, and coworkers are the mixed LnMOFs, showing special temperature-dependent luminescence behavior and highlighting their potential application as luminescent thermometers.

First, they synthesized two novel LnMOFs (Ln=Tb^{3+} or Eu^{3+}) based on one organic sensitizer DMBDC (2,5-dimethoxy-1,4-benzenedicarboxylate), leading to isostructural frameworks, $[Tb_2(DMBDC)_3]_n$ and $[Eu_2(DMBDC)_3]_n$ [60]. As expected, a series of mixed LnMOFs Eu_xTb_{1-x}DMBDC ($x = 0.0011$, 0.0046, and 0.0069) were acquired and were isostructural to the parent structures, confirmed by the powder X-ray diffraction patterns. The parent 3D Tb-DMBDC and Eu-DMBDC exhibit characteristic lanthanide fluorescence upon excitation at 381 nm, attributed to the $\pi \rightarrow \pi^*$ electron transition of DMBDC linkers, indicating the strong sensitizing ability of DMBDC as an excellent antenna chromophore. By increasing the temperature from 10 to 300 K, the luminescent intensity of both Tb^{3+} and Eu^{3+} in Tb-DMBDC and Eu-DMBDC gradually decreases owing to the thermal activation of nonradiative decay pathways. Significantly different from the luminescent behavior of the mono-lanthanide ion MOF, the mixed-lanthanide MOF $Eu_{0.0069}Tb_{0.9931}$-DMBDC exhibits an interesting temperature-dependent luminescent property. The emission intensity of the Tb^{3+} ions decreases, while that of the Eu^{3+} ions increases upon heating (Fig. 9). The different temperature-dependent metal-centered emission behaviors within the same material enable itself to be an ideal candidate for self-referencing luminescent thermometers, as no additional calibration of luminescence intensity is required. The absolute temperature can be linearly correlated to I_{Tb}/I_{Eu} (I_{Tb} and I_{Eu} are the integrated intensities of the $^5D_4 \rightarrow {}^7F_5$ (Tb^{3+} at 546 nm) and the $^5D_0 \rightarrow {}^7F_2$ (Eu^{3+} at 615 nm) transitions, respectively, at different temperatures), by the equation $T = 287.09 - 263.85 I_{Tb}/I_{Eu}$ from 50 to 200 K with the sensitivity value of $1/263.85 = 0.38\%$, suggesting that $Eu_{0.0069}Tb_{0.9931}$-DMBDC is an excellent luminescent thermometer at this

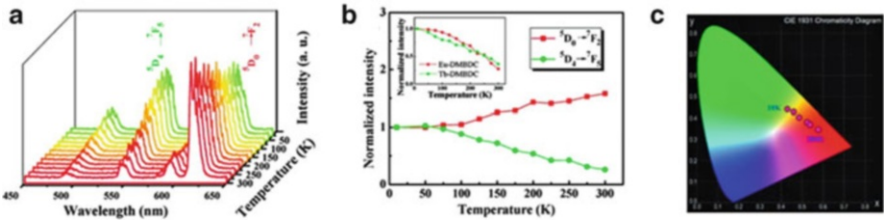

Fig. 9 (**a**) Emission spectra of $Eu_{0.0069}Tb_{0.9931}$-DMBDC recorded between 10 K and 300 K (excited at 355 nm). (**b**) Temperature-dependent PL intensities from different transitions for $Eu_{0.0069}Tb_{0.9931}$-DMBDC. *Inserted figure* shows temperature-dependent PL intensities from different transitions for Tb-DMBDC and Eu-DMBDC. (**c**) CIE chromaticity diagram showing the luminescence color of $Eu_{0.0069}Tb_{0.9931}$-DMBDC at different temperature. Reprinted with permission from [60]. Copyright 2012 American Chemical Society

temperature range. This unique behavior in the mixed LnMOF is attributed to the fact that the energy transfer efficiency from the Tb^{3+} to Eu^{3+} displays stable enhancement with increasing temperature, which might be mainly controlled by the phonon-assisted Förster transfer mechanism. Furthermore, the changing red–green emission intensity ratios at different temperatures result in systematically tunable colors from green–yellow to red from 10 to 300 K, allowing us to utilize it for directly visualizing the temperature change instantly and mapping the temperature distribution.

Utilizing the same strategy, they subsequently reported another two examples of Eu–Tb mixed LnMOF: $Eu_{0.1}Tb_{0.9}$-PIA ($H_2PIA = 5$-(pyridin-4-yl)isophthalic acid) and $Eu_{0.043}Tb_{0.957}$-cpda ($H_3cpda = 5$-(4-carboxyphenyl)-2,6-pyridinedicarboxylic acid), both of which were also evaluated as fluorescent thermometers [61, 62]. By varying the triplet excited state energy level of the organic ligands, constructing diverse MOF structures, changing the Eu–Tb ratios, and optimizing the energy transfer among the lanthanide ions, the final sensitivity and temperature response range of the luminescence-based thermometers could be improved. Almost at the same time, D'Vries and coworkers took advantage of the phosphorescence of a ligand, H_3DSB (3,5-disulfobenzoic acid), in the construction of mixed LnMOFs: $Eu_{0.02}Gd_{0.98}$-DSB, $Tb_{0.02}Gd_{0.98}$-DSB, and $Eu_{0.05}Tb_{0.09}Gd_{0.86}$-DSB, as color changed luminescent thermometers [63]. It is anticipated that the accessible preparation of MOF-based nanoparticles will provide the possibility that these novel luminescent thermometers can be further applied in intracellular sensing and thermal mapping with nanospatial resolution in the near future.

4 Lanthanide MOFs with NIR Luminescence

Recently, research toward NIR-emitting lanthanide materials has become increasingly popular for their highlighted value in the applications of fiber-optic communications, laser systems, biosensing and bioimaging analysis, etc. For instance, one of the emissions from Nd^{3+} ion at 1,300 nm and the emissions around 1,500 nm from Ho^{3+}, Er^{3+}, and Tm^{3+} match the two telecommunication windows for amplification, where the loss in silica-based fibers is low and the chromatic dispersion of the fibers is weak. The Yb^{3+} ion emission at about 1,000 nm shows advantage in bioimaging and various analytical applications, since biological tissues and fluids (e.g., blood) are relatively transparent. Compared with the LnMOFs with visible emissions, emissive NIR LnMOFs (usually $Ln^{3+} = Yb^{3+}$, Nd^{3+}, and Er^{3+}) are rarely studied. That is because (1) most organic ligands possess low efficiency to sensitize Yb^{3+}, Nd^{3+}, and Er^{3+} ions and (2) the energy gap between the emissive state and the ground level is quite small, easily matched by the CH, OH, and NH overtones, reducing the emission intensity and efficiency. Organic ligands with careful designable structure can be used to overcome such limitations [64].

Two related erbium–organic frameworks, $Er_2(p\text{-BDC})_3(DMF)_2(H_2O)_2 \cdot H_2O$ and $Er_2(p\text{-BDC-}F_4)_3(DMF)(H_2O) \cdot DMF$ (p-BDC = 1,4-benzenedicarboxylate;

p-BDC-F_4 = tetrafluoroterephthalate or 2,3,5,6-tetrafluoro-1,4-benzenedicarboxylate), have been synthesized by Chen [65]. After treatment at 140°C under vacuum overnight, the completely desolvated Er-*p*-BDC showed NIR emission at 1,450–1,650 nm ($^4I_{13/2} \rightarrow {}^4I_{15/2}$) under the excitation of a laser diode source (808 nm). The intensity of partially desolvated Er-*p*-BDC-F_4 was further enhanced and was about 3 times higher than that of Er-*p*-BDC because that fluorination could reduce the quenching effect of the C–H vibration. After the removal of lattice water molecules from $H_3O[Nd(tpabn)] \cdot 6H_2O$ and $[Er(Htpabn)] \cdot 14H_2O$ (H_4tpabn = *N*, *N*′,*N*′-tetrakis[(6-carboxypyridin-2-yl)methyl]butylenediamine), an important increase of the NIR luminescence efficiency was observed, due to the absence of deactivation by OH oscillators [66].

In 2009, White et al. firstly utilized 4,4′-[(2,5-dimethoxy-1,4-phenylene) di-2,1-ethenediyl]bisbenzoic acid (H_2PVDC) as sensitizer and organic strut to construct two NIR luminescent ytterbium–organic frameworks, $[Yb_2(PVDC)_3(H_2O)_2] \cdot (DMF)_6(H_2O)_{8.5}$ (**Yb-PVDC-1**) and $[Yb_2(PVDC)_3(H_2O)_2] \cdot (DMF)_{12}(H_2O)_{10}$ (**Yb-PVDC-2**). These MOFs display typical Yb^{3+} emission at 980 nm with tunable excitation properties controlled by the structural changes of three-dimensional MOFs. Interestingly, the lowest-energy excitation band of **Yb-PVDC-2** is further red-shifted to 500 nm from 470 nm in **Yb-PVDC-1**, and it was proposed that the close π–π interactions between the PVDC linkers decrease the energy of the $\pi \rightarrow \pi^*$ transition, resulting in a lowered excitation energy [67].

Furthermore, they chose **Yb-PVDC-1** as parent prototype to create a new barcode system by codoping multiple Ln^{3+} ions, which provided characteristic and independent NIR signals [68]. They described Er_xYb_{1-x}-PVDC-1 ($x = 0.32$, 0.58, 0.70, and 0.81) MOFs with different Er^{3+}–Yb^{3+} ratios, determined by energy-dispersive X-ray spectroscopy (EDS) and inductively coupled plasma (ICP) analysis. The ratio of the integrated intensities of Yb^{3+} (980 nm) and Er^{3+} (1,530 nm) emissions is linearly correlated with respect to the Er^{3+}/Yb^{3+} ratio, under either excitation band (370 or 470 nm) (Fig. 10). This feature provides the validity of their usage as encryption tags. In addition, the number and diversity of barcodes could, thus, be increased by using a large number of Ln–Ln ratios or by incorporating additional lanthanide cations into the material. The latter concept was demonstrated by the as-synthesized sample $Nd_{0.09}Er_{0.55}Yb_{0.36}$-PVDC-1. The NIR emission of the MOFs-barcoded materials was also easily detected when coated in superglue, demonstrating the possibility for practical application.

The lanthanide–organic frameworks with NIR emission were extended to the sense function of small organic molecules by our group for the first time [69]. We chose biphenyl-3,4′,5-tricarboxylic acid (H_3BPT) as antenna to construct a ytterbium MOF $Yb(BPT)(H_2O) \cdot (DMF)_{1.5}(H_2O)_{1.25}$. This MOF crystallizes in a chiral tetragonal space group $P4_3$. Yb^{3+} ions are bridged by BPT organic linkers to form a 3D rod-packing architecture, in which there exist fourfold helical rod SBUs and one-dimensional square channels. The activated Yb(BPT) with open Yb^{3+} sites exhibits typical NIR emission at 980 nm arising from the $^2F_{5/2} \rightarrow {}^2F_{7/2}$ transition of the Yb^{3+} ion, when excited at 326 nm. The luminescent intensity is largely dependent on the solvent molecules, significant enhancing by DMF, and quenching

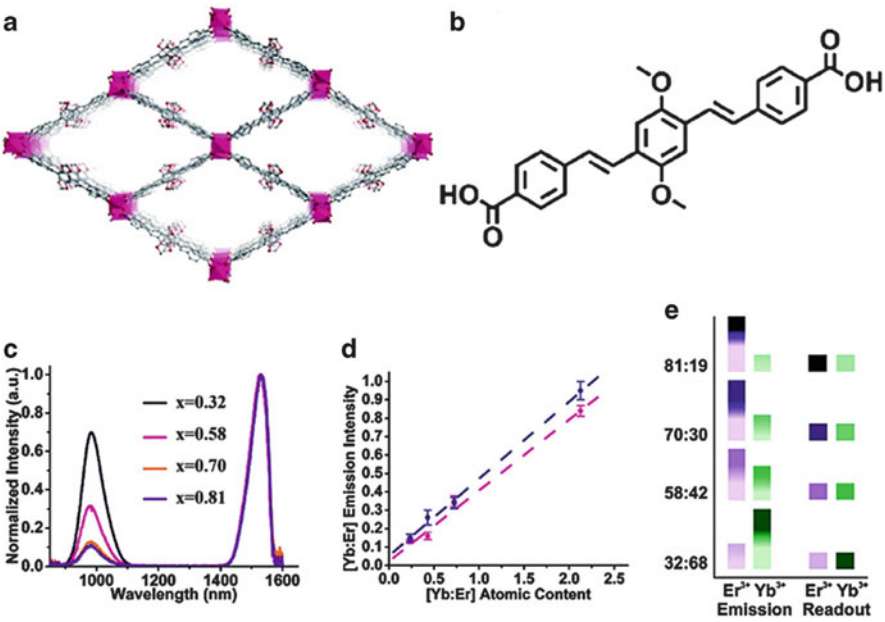

Fig. 10 (**a**) Crystal structure of **Yb-PVDC-1** viewed along the crystallographic *c* axis. (**b**) Structure of H_2PVDC. (**c**) Yb^{3+} (980 nm) and Er^{3+} (1,530 nm) emission spectra of Er_xYb_{1-x}-PVDC-1 normalized to the Er^{3+} signal upon 490 nm excitation. (**d**) Plot of the ratio of integrated emission intensities versus their atomic ratio. (**e**) Color-coded schematic of the barcode readout. Reprinted with permission from [68]. Copyright 2009 American Chemical Society

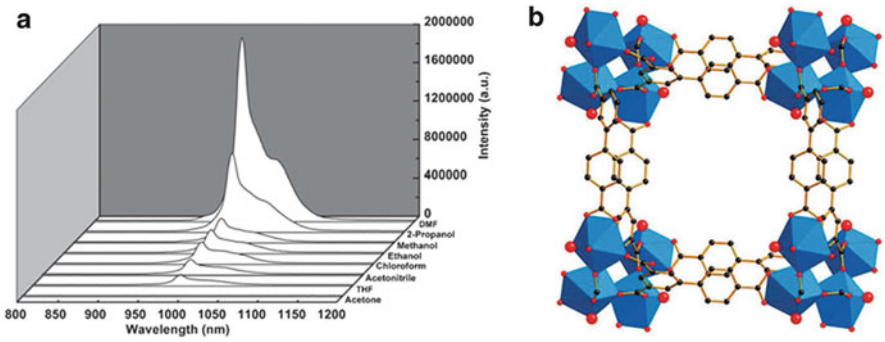

Fig. 11 (**a**) The PL spectra of activated Yb(BPT) introduced into various pure solvent emulsions when excited at 304 nm. (**b**) 1D micropore in the 3D framework along *c* axis. Reproduced from [69] by permission of The Royal Society of Chemistry (RSC)

by acetone, respectively (Fig. 11). The decreasing trend of the fluorescence intensity at 980 nm versus the volume ratio of acetone could be well fitted with a first-order exponential decay, indicating that fluorescence quenching of Yb(BPT) by

acetone is diffusion controlled. This work reveals the promise of NIR luminescent MOF materials for the sensing of substrates in biological systems.

Stimulated by our abovementioned work, another MOF-based sensor with NIR emission was manufactured by Sun and coworkers in our institute [70]. They explored LnL2 (Ln=Y, La–Yb, except Pm) and Yb/Gd codoped MOFs. Compared with those of YbL2, the emission intensity of the peak at 983 nm and the emission lifetime of $Yb_{0.10}Gd_{0.90}$ L2 were increased 10.5- and 18.4-fold, respectively, under excitation at 290 nm. The PL spectra of $Yb_{0.10}Gd_{0.90}$ L2 were dependent on the solvents, especially for acetone, which exerted a significant quenching effect on the Yb luminescence with undetectable luminescence lifetime. UV–vis absorption spectra were measured to investigate the mechanism of the quenching effect. Acetone exhibits a wider absorption band from 230 to 325 nm, which covers the whole range of that of the ligand H_3L2 (250–300 nm). It means that most of the excitation energy was absorbed by acetone in the emulsion, resulting in less energy absorbed by the ligand to sensitize the metal-centered NIR luminescence. The quenching effect by various other ketones, namely, acetophenone, benzophenone, and cyclohexanone, can also be rationalized in terms of spectral overlap, referring to the UV absorption spectra of the various ketones in *n*-hexane.

5 Lanthanide MOFs with Upconversion Luminescence

The upconversion (UC) process refers to the nonlinear optical process, in which higher-energy photons were emitted after the absorption of two or more lower-energy photons. Thulium (Tm) is the first Ln^{III} ion for which upconversion has been discovered with blue emission [71]. Upconversion luminescent materials have been extensively investigated for their potential applications in the realm of laser, display, bioassay, and bioimaging. The use of NIR light as excitation will minimize photobleaching and photodamage to biological specimens and enhance the signal-to-noise ratio and light penetration depth in biological tissues. Up to now, most of the reported UC Ln^{3+}-based materials are mainly based on inorganic nanomaterials by doping rare-earth ions into host lattices; however, only a handful of upconversion luminescent LnMOFs have also been reported due to the existence of effective multiphonon relaxation which decreases the efficiency of the UC process.

Yang et al. synthesized a two-dimensional MOF $[Nd_2(1,4\text{-NDC})_3(DMF)_4 \cdot H_2O]$ (1,4-NDC = 1,4-naphthalenedicarboxylate) with visible-to-visible UC luminescence upon pulse laser excitation at 580 nm, corresponding to the transition $^4I_{9/2} \rightarrow {}^4G_{5/2}$ of the Nd^{3+} ions [72]. It exhibits a weak UV upconversion emission at about 391.6 nm and a much stronger blue emission at about 449.5 nm. The distance between the dinuclear Nd^{3+} ions is 4.101 Å, which enables facile energy transfer between two optically active Nd^{3+} centers, resulting in an efficient UC blue emission through ground-state absorption (GSA) and energy transfer process.

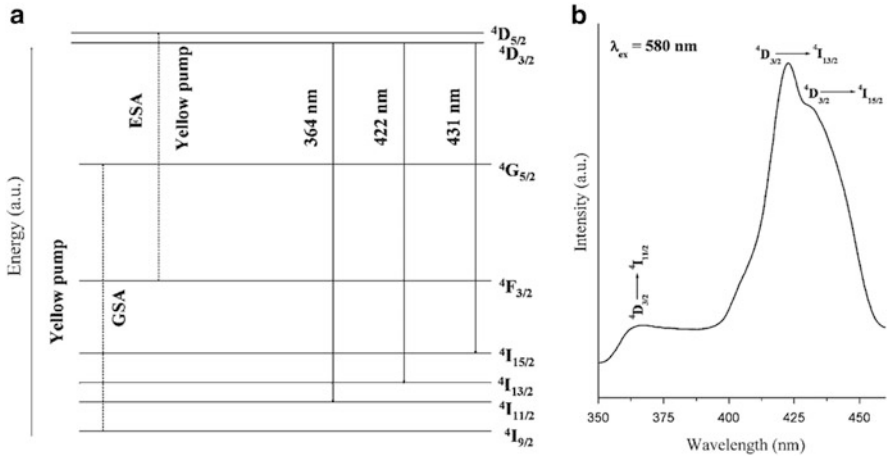

Fig. 12 (**a**) Energy-level diagram for the Nd^{3+} ion. The *dotted and solid lines* indicate yellow pumping (580 nm) and the transitions related to the observed emissions, respectively. (**b**) Upconverted luminescence spectrum at room temperature ($\lambda_{ex} = 580$ nm). Reproduced from [74] by permission of John Wiley & Sons Ltd

Subsequently, Natarajan's group reported another two Nd-based MOFs with the formulas of $Nd_2(H_2O)(m\text{-bdc})_2(m\text{-Hbdc})_2] \cdot H_2O$ (m-bdc = 1,3-benzenedicarboxylate) and $[Nd_2(H_2O)_4(pdca)_2(p\text{-BDC})]$ (H_4pdca=pyridine-2,3-dicarboxylic acid) [73, 74]. They also show UC luminescent properties with emission peaks around 364, 422, and 431 nm, which correspond to the $^4D_{3/2} \rightarrow {}^4I_{11/2}$, $^4D_{3/2} \rightarrow {}^4I_{13/2}$, and $^4D_{3/2} \rightarrow {}^4I_{15/2}$ transitions, respectively. The possible UC excitation was achieved by the ground-state absorption to the $^4G_{5/2}$ level, followed by a rapid nonradiative relaxation to the $^4F_{3/2}$ level, and an excited state absorption from this level to the $^4D_{5/2}$ state which also relaxes nonradiatively to the $^4D_{3/2}$ level, emitting one photon (Fig. 12). The linear fit of the log–log plot for the luminescence intensity *versus* excitation intensity indicated that all three emissions are two-photon process.

Another strategy was proposed by Jin's group, who reported two examples: Er^{3+}/Yb^{3+} codoped MOFs $[(Y{:}Er,Yb)_3(p\text{-BDC})_{3.5}(OH)_2(H_2O)_2] \cdot H_2O$ and [(Y:Er,Yb)(oba)$(ox)_{0.5}(H_2O)_2$] (H_2oba = 4,4′-oxybis(benzoic acid), H_2ox = oxalic acid) [75, 76]. The UC emission spectrum of the Y:Er–Yb codoped coordination polymers shows four major emission bands arising from Er^{3+} upon excitation at 980 nm or 975 nm. The red ($^4F_{9/2} \rightarrow {}^4I_{15/2}$ at ca. 655 nm) and green ($^2S_{3/2}$, $^2H_{11/2} \rightarrow {}^4I_{15/2}$, at ca. 540 and 520 nm, respectively) emissions were achieved by two-photon upconversion mechanism, while the seldom observed short-wavelength emissions of the two compounds centered at 455 nm ($^4F_{5/2} \rightarrow {}^4I_{15/2}$) and 407 nm ($^2H_{9/2} \rightarrow {}^4I_{15/2}$) could be explained by the three-photon mechanism. The energy levels and overall upconversion scheme of Er^{3+} are shown in Fig. 13. The upconversion emission intensity can be enhanced due to the introduction of the oxalate anion without high-energy vibrational groups.

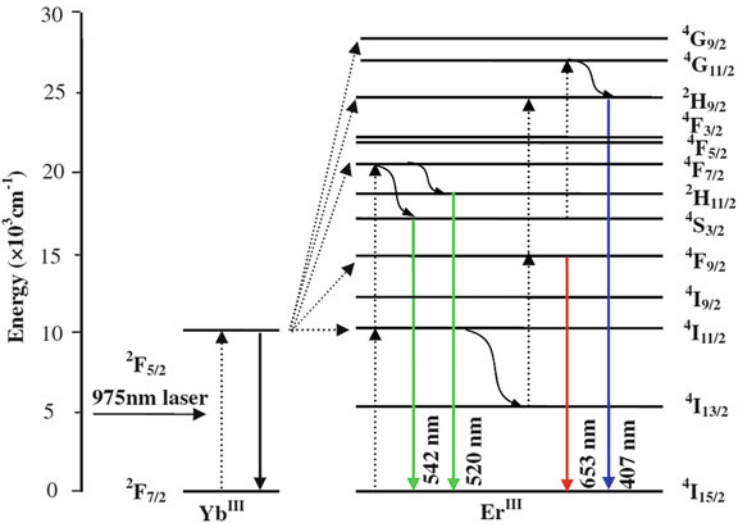

Fig. 13 Energy-level diagram for the upconversion mechanism of $[(Y:Er,Yb)(oba)(ox)_{0.5}(H_2O)_2]$ under 975 nm excitation. Full, dotted, and curved arrows indicate radiative emission, energy transfer, and nonradiative decay processes, respectively. Reprinted from [76], Copyright 2009, with permission from Elsevier

6 Guest Ln^{3+} Species-Induced Luminescence

The above paragraphs summarize the examples about the MOFs with lanthanide ions or clusters as nodes. Because of the highly regular channels with tunable pore size, the MOFs can also serve as versatile hosts and accommodate various guest species, such as gas molecules, fluorescent dyes, drug, and metal–organic coordination compound. During the last decade, Ln^{3+}-based guest species have been introduced into the MOF host to obtain multimodal luminescence.

Motivated by their own pioneering work about molecular lantern [77], Dong's group employed a ligand-directed approach to synthesize one-dimensional polymeric frameworks consisting of nanosized $Ln_2(L4)_4$ cagelike units, which encapsulate hydrated metallic cations ($H_2L4 = 3,3'$-(4-amino-4*H*-1,2,4-triazole-3,5-diyl) dibenzoic acid) [78]. Firstly, the $[Mn(H_2O)_6]^{2+}$ cations were enclosed in tetragonal prismatic cages to form the final neutral compounds $\{[(Ln_2(L4)_4)Mn(H_2O)_6] \cdot x(H_2O)\}_n$ (Ln=La, Gd, Eu, and Tb). The MOF $\{[(Gd_2(L4)_4)Mn(H_2O)_6] \cdot 0.5(H_2O)\}_n$ exhibits one emission maximum at 428 nm, blue shift compared to the ligand due to ligand-to-metal charge transfer (LMCT). The encapsulated $[Mn(H_2O)_6]^{2+}$ species are readily replaced reversibly by the $[Ln(H_2O)_8]^{3+}$ (Ln=Tb, Eu) cations with retention of structural integrity, leading to the formation of $\{[(Gd_2(L4)_4)Ln(H_2O)_8ClO_4] \cdot 0.5(H_2O)\}_n$ (Ln=Eu, Tb). After ion exchange, the typical emission intensities of Eu^{3+} or Tb^{3+} increased, while the intensity at 428 nm decreased, resulting in tunable luminescent properties (Fig. 14). Their other work

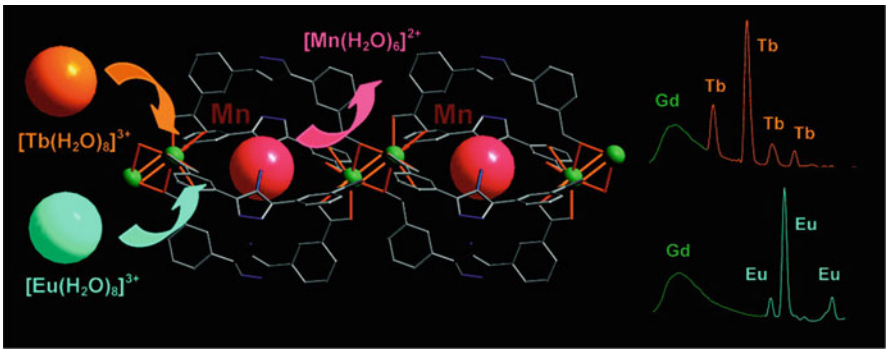

Fig. 14 Tunable luminescence based on reversible ion exchange in $\{[(Gd_2(L4)_4)Mn(H_2O)_6] \cdot 0.5(H_2O)\}_n$ MOF. Reprinted with permission from [78]. Copyright 2007 American Chemical Society

involved with the one-dimensional polymeric framework $\{[\{Nd(H_2O)_8@(Nd_2(L4)_4)]ClO_4\}_n$, in which $Nd(H_2O)_8^{3+}$ was trapped inside the cage by hydrogen-bonded interactions. The reversible ion exchange between Nd^{3+} and Eu^{3+} in this NIR host framework may afford opportunity to tune emission between the visible and the NIR regions, consequently to bimodal emission [79]. Thus, the guest-driven emission spectra not only provide a promising approach to access the tunable luminescent materials but also offer a diagnostic technique for monitoring the solid-state guest-exchange process.

As a matter of fact, the anionic frameworks have drawn more and more attention due to the presence of cations, providing the driving force for cation-exchange experiments. An et al. prepared a series of lanthanide ion-doped MOFs Ln^{3+}@bio-MOF-1 (Ln^{3+}=Tb^{3+}, Sm^{3+}, Eu^{3+}, or Yb^{3+}) via cation-exchange process [80]. The dimethylammonium (DMA) cations in the one-dimensional channels of bio-MOF-1 ($[Zn_8(ad)_4(BPDC)_6O(2Me_2NH_2) \cdot 8DMF \cdot 11H_2O]$ (ad=adeninate, BPDC=biphenyldicarboxylate) could be exchanged by lanthanide ions by soaking the as-synthesized bio-MOF-1 samples in DMF solution of $Ln(NO_3)_3$. When excited at 340 nm, the doped MOFs showed their characteristic sharp emissions corresponding to the respective encapsulated lanthanide cations (Tb^{3+}, 545 nm; Sm^{3+}, 640 nm; Eu^{3+}, 614 nm; Yb^{3+}, 970 nm). And their distinctive colors of the former three doped materials (Eu^{3+}, red; Tb^{3+}, green; Sm^{3+}, orange–pink) could be readily observed with the naked eye as a qualitative indication of lanthanide sensitization even under the excitation by a standard laboratory UV lamp (365 nm), as shown in Fig. 15. Notably, the similar lanthanide-centered excitation spectra with a consistent maximum at 340 nm suggested that energy migrates through the same electronic levels located in the MOF chromophoric structure for all four compounds. It is worthy to be mentioned that the characteristic luminescent signals can even be easily detected in aqueous environments with considerably high quantum yields despite the strong quenching effect of water molecules. This work highlighted that the MOF scaffold can not only effectively serve as an antenna for

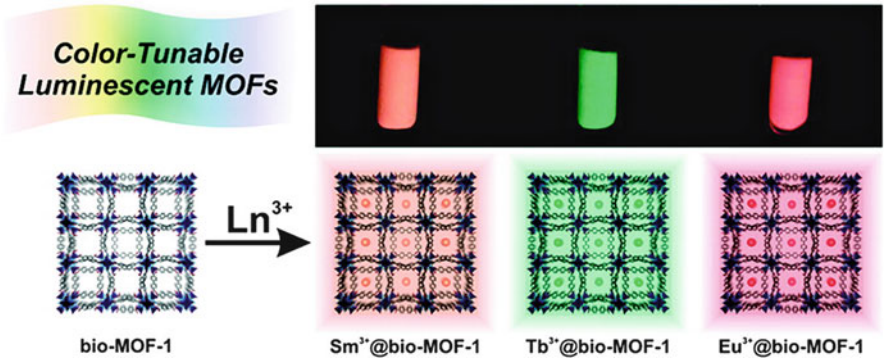

Fig. 15 Color-tunable luminescence of lanthanide ions exchanged in bio-MOF-1. Reprinted with permission from [80]. Copyright 2011 American Chemical Society

sensitizing three different visible-emitting and one NIR-emitting lanthanide cations but also can protect lanthanide cations from solvent quenching.

Subsequently, Ma et al. synthesized a novel porous metal–organic framework, $\{[Zn_2(L5)H_2O] \cdot 3H_2O \cdot 3DMAc \cdot NH_2(CH_3)_2\}_n$ ($H_5L5 = 3,5$-bis(1-methoxy-3,5-benzene dicarboxylic acid)benzoic acid, DMAc = *N*,*N*′-dimethylacetamide), containing 1D nanotubular channels of 13.8×16.4 Å and possessing a rare 5-connected *vbk* topology [81]. This Zn-MOF exhibits more enhanced blue light emission at 424 nm under the excitation at 359 nm. The dimethylammonium cations residing in its channels are possibly exchanging with Ln^{3+} cationic species, which can be trapped into the host framework to form mono- or hetero-metallic host–guest systems. With the increase of immersion time, the obvious increase of the emission intensity suggested that more Eu^{3+} or Tb^{3+} ions are trapped into the MOF scaffold, finally leading to the formation of $0.470Ln^{3+}$@Zn(II)-MOF after 24 h. By adjusting different amounts of the doped Eu^{3+} and Tb^{3+} ions, and compensating the blue color from Zn(II)-MOF, green color from Tb^{3+}, and red color from Eu^{3+} in the co-exchanged $x Eu^{3+}/y Tb^{3+}$@Zn(II)-MOF, the tunable luminescent properties would be obtained. Successfully, white light emission can be readily produced in the case of $0.127Eu^{3+}/0.432Tb^{3+}$@Zn(II)-MOF and $0.183Eu^{3+}/0.408Tb^{3+}$@Zn(II)-MOF. This ion-exchange approach has also been applied in other literatures, with $NH_2(CH_3)_2^+$ and NH_4^+ enclosed as counterions, respectively [82, 83].

The permanent porosity with large aperture of the neutral MOFs makes them suitable as given hosts for encapsulating extra-framework lanthanide cations to exhibit mono- or bimodal luminescence. A neutral porous MOF with corundum topology has been rationally designed and constructed by classical Zn_4O clusters and pre-designed tetratopic ligands by Xu and coworkers [84]. Lanthanide ions have been encapsulated into the pores of the MOF by simple soaking method. The Eu^{3+}- and Tb^{3+}-introduced samples emitted their respective red and green colors, the Eu^{3+}/Tb^{3+}-co-encapsulated MOF with various percentages of Eu^{3+}/Tb^{3+} displayed intermediate colors, all of which can also be observed by the naked eye

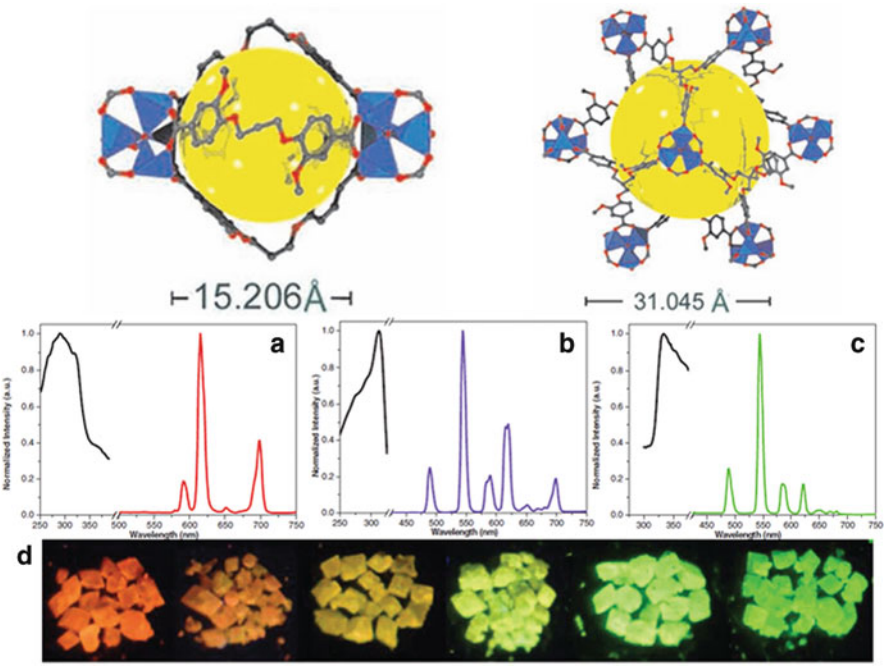

Fig. 16 *Top:* Two types of microporous and mesoporous cages within the framework. *Bottom*: Excitation and emission spectra of (*a*) Eu^{3+}-encapsulated, (*b*) Eu^{3+}/Tb^{3+}-co-encapsulated, and (*c*) Tb^{3+}-encapsulated MOF, (*d*) optical images of single/co-encapsulated MOFs illuminated with 365 nm laboratory UV light. Reproduced from [84] by permission of John Wiley & Sons Ltd

(Fig. 16). Other related reports have emerged during the subsequent years, bulk crystals as well as nanocrystals as hosts [85–88].

7 Luminescent Nano-LnMOFs and Their Applications

Scaling down the MOF materials to the nanoregime, forming nanoscale metal–organic frameworks (NMOFs), will offer many opportunities to integrate multi-functions into the materials, enabling their use in a broad range of applications. NMOFs possess some potential advantages over conventional nanomaterials: first, the structural and compositional diversity allows for the production of NMOFs of different compositions, shapes, sizes, and physicochemical properties. Second, NMOFs are intrinsically biodegradable owing to relatively labile metal–ligand bonds, making it a possible application in the biological field and possibly rapidly degrade and clear the nanocarriers after the intended task is completed [89]. Third, MOFs with nanoscale size are often the requirements for practical applications, such as optical devices, luminophores bound to the MOF surface. Successfully,

nanoscale LnMOFs have been applied in biomedical imaging, biosensing, and drug delivery.

In two seminal papers, Rieter et al. developed a general water-in-oil microemulsion-based methodology for the synthesis of nanoscale LnMOFs for the first time. Taking Gd(*p*-BDC)$_{1.5}$(H_2O)$_2$, for example, the nanorods were prepared by stirring an optically transparent microemulsion of $GdCl_3$ and bis (methylammonium)benzene-1,4-dicarboxylate (in a 2:3 molar ratio) in the cationic cetyltrimethylammonium bromide (CTAB)/isooctane/1-hexanol/water system for 2 h with a yield of 84%. The morphologies and sizes of the nanorods were influenced by the *w* value (defined as the water–surfactant molar ratio) of the microemulsion systems. The particle size was also affected by the reactant concentration and the reactant ratio. The presence of a large number of Gd^{3+} centers in the as-synthesized nanorods would therefore give very large relaxivities on a per particle basis for magnetic resonance imaging (MRI). Doping of luminescent lanthanide ions (Eu^{3+} or Tb^{3+}), nanorods of similar sizes, and morphologies were obtained with the compositions of $Gd_{0.95}$(*p*-BDC)$_{1.5}$(H_2O)$_2$:$Eu_{0.05}$ and $Gd_{0.95}$(*p*-BDC)$_{1.5}$(H_2O)$_2$:$Tb_{0.05}$. Their dispersions in ethanol are highly luminescent with characteristic luminescence upon UV excitation (red from Eu^{3+}, green from Tb^{3+}). These results demonstrated the ability of nanoscale LnMOF as potential contrast agents for multimodal imaging [90]. Furthermore, the abovementioned nanorods could be modified with polyvinylpyrrolidone (PVP) and then deposited with silica, leading to the formation of the NMOF@SiO_2 core-shell structure with controllable shell thickness by tuning the concentration and reaction time [91]. Silica coatings on NMOF would improve water dispersibility, biocompatibility, and the ability to further functionalize the shell via the co-condensation of siloxy-derived molecules. It was shown that the silica shell enhanced the NMOF core stability and retarded the release of Gd^{3+} ions from the core, presumably as a result of the slow diffusion rate of metal and organic constituents through the silica shell. To illustrate the utility and advantage of the core-shell nanostructures, Eu-doped Gd(*p*-BDC)$_{1.5}$(H_2O)$_2$@SiO_2 was prepared and further functionalized with a silylated Tb-EDTA monoamide derivative on the silica surface. The Tb luminescence signals serve as a sensitive probe for dipicolinic acid (DPA) detection by binding interaction between DPA and Tb^{3+} ions, while the Eu emission from the core serves as noninterfering internal calibration; thus, it showed excellent ratiometric luminescence sensing function of DPA, a chemical marker in spore-producing bacteria, with a detection of limit as low as 48 nM (Fig. 17).

Very recently, unique NIR-emitting nanoscale LnMOFs, incorporating Yb^{3+} cations and sensitizers derived from phenylene, have been designed as imaging agents for living cells [92]. In this work, a unique crystalline framework **Yb-PVDC-3**, bulk phase, and nanoscale version were synthesized by solvothermal strategy and a reverse microemulsion methodology, respectively. The nano-MOFs exhibit a blocklike morphology with average dimensions of 0.5 (±0.3) μm in length, 316 (±156) nm in width, and 176 (±52) nm in thickness. Nanoscale **Yb-PVDC-3** exhibits Yb^{3+} luminescence centered at 970 nm upon excitation of the PVDC sensitizer. The stability of nanoscale **Yb-PVDC-3** is the prerequisite to

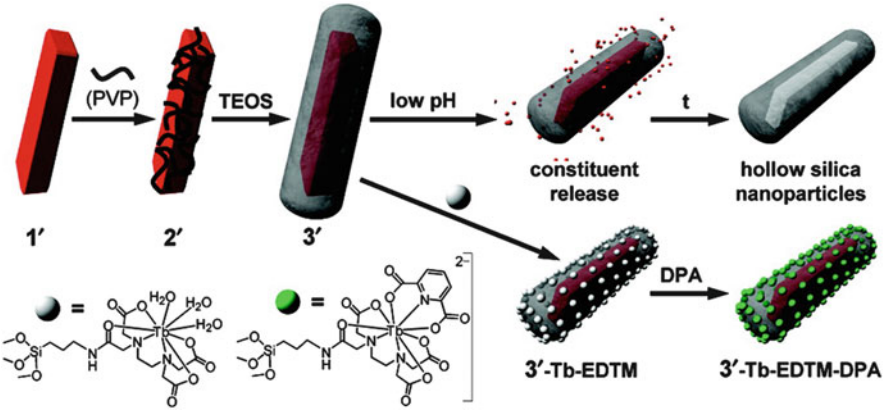

Fig. 17 Schematic representation of the surface modification with silica sell and functionalization with silylated Tb-EDTA monoamide derivative for the retarded release of Gd^{3+} ions and ratiometric luminescence sensing function of DPA of the nano-LnMOFs. Reprinted with permission from [91]. Copyright 2007 American Chemical Society

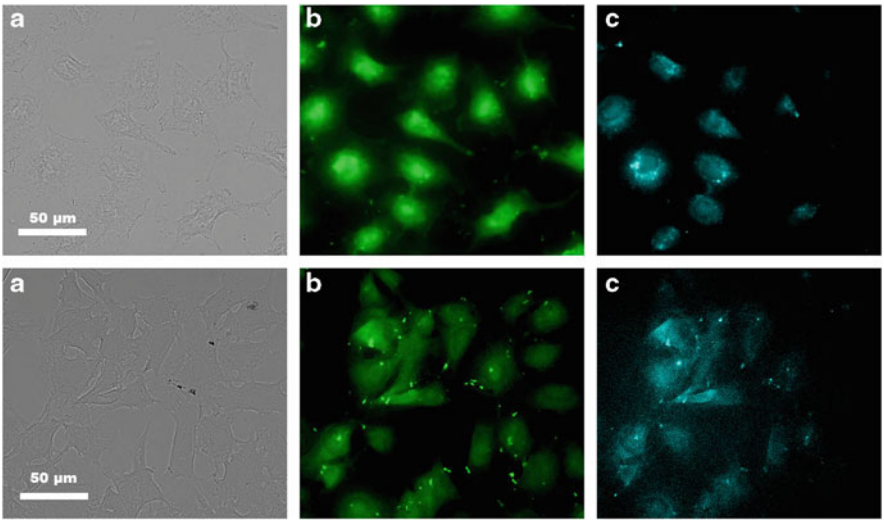

Fig. 18 Visible and NIR microscopy images of nano-**Yb-PVDC-3** in HeLa cells (*Upper*) and NIH 3 T3 cells (*Lower*) ($\lambda_{ex} = 340$ nm). Bright-field (*A*), H_2-PVDC emission ($\lambda_{ex} = 377/50$ nm, $\lambda_{em} = 445/50$ nm) (*B*), and Yb^{3+} emission ($\lambda_{ex} = 377/50$ nm, $\lambda_{em} =$ long pass 770 nm) (*C*) images are shown. Reproduced from [92] by permission of Proceedings of the National Academy of Sciences of the United States of America

preserve the constant luminescence intensity and to prevent the release of free lanthanide cations in cellular media. The nano-MOF material is found to have relatively low toxicity, which is meaningful to allow for live cell imaging. Despite its relatively low quantum yield, the specific Yb^{3+} emission signal of

nano-**Yb-PVDC-3** in HeLa cells and NIH 3 T3 cells was collected with good sensitivity as the result of the discrimination of the NIR signal from the visible autofluorescence arising from the biological material (high signal-to-noise ratio). The images by NIR microscopy were presented in Fig. 18, using a conventional excitation source.

A famous LnMOF prototype with the compositions of Tb(1,3,5-BTC)$(H_2O)\cdot 3H_2O$ (MOF-76 [93], 1,3,5-BTC = 1,3,5-benzenetricarboxylate) was innovatively and deeply investigated by our Zhang's group to construct their corresponding nanomaterials with various morphology. A convenient one-step approach, direct precipitation method, has been developed for the large-scale synthesis of the metal–organic framework Tb(1,3,5-BTC)$(H_2O)\cdot 3H_2O$ uniform nanobelts under mild conditions without the addition of any surfactant or template [94]. The final morphologies and sizes of the nanobelts were also affected by the reaction environment, including reaction temperature, concentration, molar ratio of reactants, and solvent. It was clearly found that the as-obtained 1D Tb(1,3,5-BTC)$(H_2O)\cdot 3H_2O$ nanobelt materials showed size-dependent luminescent intensity and more bigger, more greater intensity, owing to fewer defects with particle size increase. Moreover, the luminescent properties of the Eu^{3+}-doped nanobelts Tb(1,3,5-BTC)$(H_2O)\cdot 3H_2O$:$x$$Eu^{3+}$ ($x = 0.1$–10 mol%) with similar phase and morphology were deeply investigated under excitation at 304 nm. With the increase of Eu^{3+} ion concentration, the luminescence intensity of the Tb^{3+} ions decreases, while that of the Eu^{3+} increases. When the Eu^{3+} concentration is 1%, the luminescence intensity of the Eu^{3+} reaches the maximum and then begins to decrease due to the concentration quenching effect. Finally, the characteristic emissions of the Tb^{3+} ions disappear when the Eu^{3+} concentration increases to 10%, suggesting the existence of highly efficient energy transfer process from Tb^{3+} to Eu^{3+} ions. Therefore, the color of Eu^{3+}-doped host nanomaterials can be easily modulated from green to green–yellow, yellow, orange, and red-orange, and the corresponding CIE chromaticity coordinates change from (0.264, 0.62) to (0.596, 0.37) by changing the doping concentration of the Eu^{3+} ions (Fig. 19). This innovative work may open a new and convenient pathway for tuning luminescence properties of MOFs

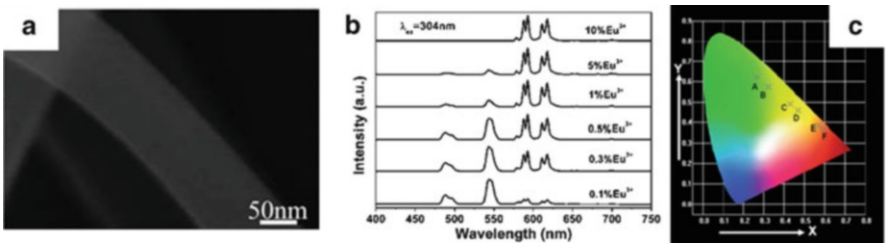

Fig. 19 (**a**) SEM image of nanobelt Tb(1,3,5-BTC)$(H_2O)\cdot 3H_2O$ material. (**b**) Emission spectra of the Tb(1,3,5-BTC)$(H_2O)\cdot 3H_2O$:$x$$Eu^{3+}$ ($x = 0.1$–10 mol%) nanobelts under 304 nm excitation. (**c**) CIE chromaticity diagram for the Tb(1,3,5-BTC)$(H_2O)\cdot 3H_2O$:$x$$Eu^{3+}$ ($x = 0$ for A, 0.1% for B, 0.3% for C, 0.5% for D, 5% for E, and 10% for F) nanobelts. Reproduced from [94] by permission of The Royal Society of Chemistry (RSC)

by selecting the appropriate MOFs host and lanthanide ions. Another approach, coordination modulation method, was applied for the synthesis of nanosized LnMOFs (the above famous host material MOF-76, Ln=Dy^{3+}, Eu^{3+}, or Tb^{3+}) nanocrystals with the assistance of capping reagent [95]. In the absence of a capping reagent, LnMOFs are pillar-like rods with a length of 60 ± 10 μm. After the addition of different capping agents, both the morphology and size of LnMOFs are drastically changed, which is attributed to modulating effect on the coordinating interactions between the metal ions and organic linkers. Different sodium salts were used as capping agents to obtain nano-LnMOFs with different morphology and tunable size. Sodium oxalate leads to the needle-shaped crystals with the length of 30–60 μm; sodium formate results in fairly uniform bean-shaped nanocrystals with a length and width of 125 ± 25 nm and 100 ± 15 nm; and sodium acetate as additive result in the formation of smaller crystals, 90 ± 15 nm in length and 75 ± 10 nm in width. Using sodium acetate as capping reagent, a mixture of $Tb(NO_3)_3 \cdot 6H_2O$ and $Eu(NO_3)_3 \cdot 6H_2O$ as reaction material, bimetallic $Eu_{1-x}Tb_x$-MOF nanocrystals were also successfully obtained, which could be used to prepare smooth, continuous, and defect-free luminescent films with high mechanical stability via spin-coating deposition. Similar tunable luminescent properties to the previous work were observed. The easy preparation approaches and the strong luminescent properties of the NMOFs films recommended them as potential candidates for applications in the field of color displays, luminescence sensors, and structural probes. Then rodlike monodisperse nanocrystals of Tb-MOF-76 are fabricated rapidly by means of microwave-assisted methods with amino acid (proline) as capping agent. These materials exhibited a green emission corresponding to the transition $^5D_4 \rightarrow {}^7F_J$ of Tb^{3+} ions under UV light excitation, which is a sensitive sensor for acetone molecules in solution [96].

Concluding Remarks

This chapter has summarized recent developments in the rational design of optical active LnMOFs. The basic principles of lanthanide luminescence have been introduced in brief, which will help the chemists obtain targeted materials with desirable luminescent properties. The designable structure and energy level of organic ligands leads to diverse supramolecular structures and systematic study of the luminescent properties of the final LnMOFs. The LnMOFs show visible, NIR, and upconversion luminescence owing to the feature of Ln^{3+} ions. Metal tuning by means of codoping different even multiple lanthanide ions is used to measure temperature and tune the chromaticity up to the creation of white light emission. As well as the bulk materials, the nanoscale materials of LnMOFs have also been overviewed in this chapter, showing applied perspective in the field of cell imaging, drug delivery, and molecular sensor. Fast and further development as well as new applications can be expected in the coming years. And some of the promising LnMOFs will be implemented in our daily life in the near future.

Acknowledgements The authors are grateful to the financial aid from the National Natural Science Foundation of China (Grant Nos. 91122030, 21210001, 21221061, and 51372242) and the National Key Basic Research Program of China (No. 2014CB643802).

References

1. Halder GJ, Kepert CJ, Moubaraki B, Murray KS, Cashion JD (2002) Guest-dependent spin crossover in a nanoporous molecular framework material. Science 298:1762–1765
2. Férey G (2008) Hybrid porous solids: past, present, future. Chem Soc Rev 37:191–214
3. Kitagawa S, Kitaura R, S-i N (2004) Functional porous coordination polymers. Angew Chem Int Ed 43:2334–2375
4. Dincă M, Long JR (2008) Hydrogen storage in microporous metal-organic frameworks with exposed metal sites. Angew Chem Int Ed 47:6766–6779
5. Rowsell JL, Yaghi OM (2005) Strategies for hydrogen storage in metal-organic frameworks. Angew Chem Int Ed 44:4670–4679
6. Ma L, Abney C, Lin W (2009) Enantioselective catalysis with homochiral metal-organic frameworks. Chem Soc Rev 38:1248–1256
7. Lee J, Farha OK, Roberts J, Scheidt KA, Nguyen ST, Hupp JT (2009) Metal-organic framework materials as catalysts. Chem Soc Rev 38:1450–1459
8. Evans OR, Lin W (2002) Crystal engineering of NLO materials based on metal-organic coordination networks. Acc Chem Res 35:511–522
9. Liu Y, Xuan W, Cui Y (2010) Engineering homochiral metal-organic frameworks for heterogeneous asymmetric catalysis and enantioselective separation. Adv Mater 22:4112–4135
10. Li JR, Kuppler RJ, Zhou HC (2009) Selective gas adsorption and separation in metal-organic frameworks. Chem Soc Rev 38:1477–1504
11. Chen B, Xiang S, Qian G (2010) Metal-organic frameworks with functional pores for recognition of small molecules. Acc Chem Res 43:1115–1124
12. Xie Z, Ma L, deKrafft KE, Jin A, Lin W (2010) Porous phosphorescent coordination polymers for oxygen sensing. J Am Chem Soc 132:922–923
13. Kent CA, Mehl BP, Ma L, Papanikolas JM, Meyer TJ, Lin W (2010) Energy transfer dynamics in metal-organic frameworks. J Am Chem Soc 132:12767–12769
14. Rieter WJ, Pott KM, Taylor KML, Lin W (2008) Nanoscale coordination polymers for platinum-based anticancer drug delivery. J Am Chem Soc 130:11584–11585
15. Huxford RC, Dekrafft KE, Boyle WS, Liu D, Lin W (2012) Lipid-coated nanoscale coordination polymers for targeted delivery of antifolates to cancer cells. Chem Sci 3:198–204
16. Meek ST, Greathouse JA, Allendorf MD (2011) Metal-organic frameworks: a rapidly growing class of versatile nanoporous materials. Adv Mater 23:249–267
17. Das MC, Xiang S, Zhang Z, Chen B (2011) Functional mixed metal-organic frameworks with metalloligands. Angew Chem Int Ed 50:10510–10520
18. Zhu QL, Li J, Xu Q (2013) Immobilizing metal nanoparticles to metal-organic frameworks with size and location control for optimizing catalytic performance. J Am Chem Soc 135:10210–10213
19. Kaltsoyannis N, Scott P (1999) The f elements. In: Evans J (ed) Oxford chemistry primers. Oxford Science Publications, Oxford
20. Cotton S (1991) Lanthanides and actinides, MacMillan Physical Science Series. MacMillan Education, London
21. Bünzli J-CG, Piguet C (2005) Taking advantage of luminescent lanthanide ions. Chem Soc Rev 34:1048–1077
22. Moore EG, Samuel APS, Raymond KN (2009) From antenna to assay: lessons learned in lanthanide luminescence. Acc Chem Res 42:542–552

23. Bünzli J-CG (2006) Benefiting from the unique properties of lanthanide ions. Acc Chem Res 39:53–61
24. Carnall WT (1979) The absorption and fluorescence spectra of rare earth ions in solution. In: Gschneidner Jr KA, Eyring L (eds) Handbook on the physics and chemistry of rare earths, vol 3. Elsevier, Amsterdam, pp 171–208
25. Bünzli J-CG (2005) Rare earth luminescent centers in organic and biochemical compounds. In: Liu G, Jacquier B (eds) Spectroscopic properties of rare earths in optical materials. Springer-Verlag, Berlin Heidelberg, pp 462–499
26. Judd BR (1962) Optical absorption intensities of rare-earth ions. Phys Rev 127:750–761
27. Ofelt GS (1962) Intensities of crystal spectra of rare-earth ions. J Chem Phys 37:511–520
28. Binnemans K (2009) Lanthanide-based luminescent hybrid materials. Chem Rev 109:4283–4374
29. Weissman SI (1942) Intramolecular energy transfer the fluorescence of complexes of europium. J Chem Phys 10:214–217
30. Whan RE, Crosby GA (1962) Luminescence studies of rare earth complexes: benzoylacetonate and dibenzoylmethide chelates. J Mol Spectrosc 8:315–327
31. Crosby GA, Whan RE, Alire RM (1961) Intramolecular energy transfer in rare earth chelates. role of the triplet state. J Chem Phys 34:743–748
32. Crosby GA, Whan RE, Freeman JJ (1962) Spectroscopic studies of rare earth chelates. J Phys Chem 66:2493–2499
33. Feng J, Zhang H (2013) Hybrid materials based on lanthanide organic complexes: a review. Chem Soc Rev 42:387–410
34. Eliseeva SV, Bünzli J-CG (2010) Lanthanide luminescence for functional materials and bio-sciences. Chem Soc Rev 39:189–227
35. Dexter DL (1953) A theory of sensitized luminescence in solids. J Chem Phys 21:836–850
36. Beeby A, Faulkner S, Parker D, Williams JAG (2001) Sensitised luminescence from phenanthridine appended lanthanide complexes: analysis of triplet mediated energy transfer processes in terbium, europium and neodymium complexes. J Chem Soc Perkin Trans (2) 1268–1273
37. Guo X, Zhu G, Sun F, Li Z, Zhao X, Li X, Wang H, Qiu S (2006) Synthesis, structure, and luminescent properties of microporous lanthanide metal-organic frameworks with inorganic rod-shaped building units. Inorg Chem 45:2581–2587
38. Li Z, Zhu G, Guo X, Zhao X, Jin Z, Qiu S (2007) Synthesis, structure, and luminescent and magnetic properties of novel lanthanide metal-organic frameworks with zeolite-like topology. Inorg Chem 46:5174–5178
39. Xia J, Zhao B, Wang H-S, Shi W, Ma Y, Song H-B, Cheng P, Liao D-Z, Yan S-P (2007) Two- and three-dimensional lanthanide complexes structures, and properties. Inorg Chem 46:3450–3458
40. Black CA, Costa JS, Fu WT, Massera C, Roubeau O, Teat SJ, Aromı´ G, Gamez P, Reedijk J (2009) 3-D lanthanide metal-organic frameworks structure, photoluminescence, and magnetism. Inorg Chem 48:1062–1068
41. Reineke TM, Eddaoudi M, Fehr M, Kelley D, Yaghi OM (1999) From condensed lanthanide coordination solids to microporous frameworks having accessible metal sites. J Am Chem Soc 121:1651–1657
42. Cepeda J, Balda R, Beobide G, Castillo O, Fernandez J, Luque A, Perez-Yanez S, Roman P, Vallejo-Sanchez D (2011) Lanthanide(III)/pyrimidine-4,6-dicarboxylate/oxalate extended frameworks: a detailed study based on the lanthanide contraction and temperature effects. Inorg Chem 50:8437–8451
43. Harbuzaru BV, Corma A, Rey F, Atienzar P, Jorda JL, Garcia H, Ananias D, Carlos LD, Rocha J (2008) Metal-organic nanoporous structures with anisotropic photoluminescence and magnetic properties and their use as sensors. Angew Chem Int Ed 47:1080–1083

44. Gai Y-L, Jiang F-L, Chen L, Bu Y, Su K-Z, Al-Thabaiti SA, Hong M-C (2013) Photophysical studies of europium coordination polymers based on a tetracarboxylate ligand. Inorg Chem 52:7658–7665
45. Su S, Chen W, Qin C, Song S, Guo Z, Li G, Song X, Zhu M, Wang S, Hao Z, Zhang H (2012) Lanthanide anionic metal-organic frameworks containing semirigid tetracarboxylate ligands: structure, photoluminescence, and magnetism. Cryst Growth Des 12:1808–1815
46. Ramya AR, Sharma D, Natarajan S, Reddy ML (2012) Highly luminescent and thermally stable lanthanide coordination polymers designed from 4-(dipyridin-2-yl)aminobenzoate: efficient energy transfer from Tb^{3+} to Eu^{3+} in a mixed lanthanide coordination compound. Inorg Chem 51:8818–8826
47. Steemers FJ, Verboom W, Reinhoudt DN, van der Tol EB, Verhoeven JW (1995) New sensitizer-modified calix[4]arenes enabling near-UV excitation of complexed luminescent lanthanide ions. J Am Chem Soc 117:9408–9414
48. Li X, Budai JD, Liu F, Howe JY, Zhang J, Wang X-J, Gu Z, Sun C, Meltzer RS, Pan Z (2013) New yellow $Ba_{0.93}Eu_{0.07}Al_2O_4$ phosphor for warm-white light-emitting diodes through single-emitting-center conversion. Light Sci Appl 2:e50
49. Hye Oh J, Ji Yang S, Rag Do Y (2014) Healthy, natural, efficient and tunable lighting: four-package white leds for optimizing the circadian effect, color quality and vision performance. Light Sci Appl 3:e141
50. Zhang Y-H, Li X, Song S (2013) White light emission based on a single component Sm(III) framework and a two component Eu(III)-doped Gd(III) framework constructed from 2,2'-diphenyl dicarboxylate and 1 h-imidazo[4,5-f][1,10]-phenanthroline. Chem Commun 49:10397–10399
51. Sava DF, Rohwer LES, Rodriguez MA, Nenoff TM (2012) Intrinsic broad-band white-light emission by a tuned, corrugated metal-organic framework. J Am Chem Soc 134:3983–3986
52. Tang Q, Liu S, Liu Y, Miao J, Li S, Zhang L, Shi Z, Zheng Z (2013) Cation sensing by a luminescent metal-organic framework with multiple lewis basic sites. Inorg Chem 52:2799–2801
53. Tang Q, Liu S, Liu Y, He D, Miao J, Wang X, Ji Y, Zheng Z (2014) Color tuning and white light emission via in situ doping of luminescent lanthanide metal-organic frameworks. Inorg Chem 53:289–293
54. Ma X, Li X, Cha Y-E, Jin L-P (2012) Highly thermostable one-dimensional lanthanide(III) coordination polymers constructed from benzimidazole-5,6-dicarboxylic acid and 1,10-phenanthroline: synthesis, structure, and tunable white-light emission. Cryst Growth Des 12:5227–5232
55. Dang S, Zhang J-H, Sun Z-M (2012) Tunable emission based on lanthanide(III) metal-organic frameworks: an alternative approach to white light. J Mater Chem 22:8868–8873
56. Zhu M, Hao Z-M, Song X-Z, Meng X, Zhao S-N, Song S-Y, Zhang H-J (2014) A new type of double-chain based 3D lanthanide(III) metal-organic framework demonstrating proton conduction and tunable emission. Chem Commun 50:1912–1914
57. Brites CDS, Lima PP, Silva NJO, Millán A, Amaral VS, Palacio F, Carlos LD (2011) Lanthanide-based luminescent molecular thermometers. New J Chem 35:1177–1183
58. Carlos LD, Ferreira RAS, de Zea Bermudez V, Julián-Lopez B, Escribano P (2011) Progress on lanthanide-based organic–inorganic hybrid phosphors. Chem Soc Rev 40:536–549
59. Feng J, Tian K, Hu D, Wang S, Li S, Zeng Y, Li Y, Yang G (2011) A triarylboron-based fluorescent thermometer: sensitive over a wide temperature range. Angew Chem Int Ed 50:8072–8076
60. Cui Y, Xu H, Yue Y, Guo Z, Yu J, Chen Z, Gao J, Yang Y, Qian G, Chen B (2012) A luminescent mixed-lanthanide metal-organic framework thermometer. J Am Chem Soc 134:3979–3982
61. Rao X, Song T, Gao J, Cui Y, Yang Y, Wu C, Chen B, Qian G (2013) A highly sensitive mixed lanthanide metal-organic framework self-calibrated luminescent thermometer. J Am Chem Soc 135:15559–15564

62. Cui Y, Zou W, Song R, Yu J, Zhang W, Yang Y, Qian G (2014) A ratiometric and colorimetric luminescent thermometer over a wide temperature range based on a lanthanide coordination polymer. Chem Commun 50:719–721
63. D'Vries RF, Álvarez-García S, Snejko N, Bausá LE, Gutiérrez-Puebla E, de Andrés A, Monge MÁ (2013) Multimetal rare earth MOFs for lighting and thermometry: tailoring color and optimal temperature range through enhanced disulfobenzoic triplet phosphorescence. J Mater Chem C 1:6316–6324
64. Rocha J, Carlos LD, Paz FAA, Ananias D (2011) Luminescent multifunctional lanthanides-based metal-organic frameworks. Chem Soc Rev 40:926–940
65. Chen B, Yang Y, Zapata F, Qian G, Luo Y, Zhang J, Lobkovsky EB (2006) Enhanced near-infrared–luminescence in an erbium tetrafluoroterephthalate framework. Inorg Chem 45:8882–8886
66. Marchal C, Filinchuk Y, Chen X-Y, Imbert D, Mazzanti M (2009) Lanthanide-based coordination polymers assembled by a flexible multidentate linker: design, structure, photophysical properties, and dynamic solid-state behavior. Chem Eur J 15:5273–5288
67. White KA, Chengelis DA, Zeller M, Geib SJ, Szakos J, Petoud S, Rosi NL (2009) Near-infrared emitting ytterbium metal-organic frameworks with tunable excitation properties. Chem Commun 4506–4508
68. White KA, Chengelis DA, Gogick KA, Stehman J, Rosi NL, Petoud S (2009) Near-infrared luminescent lanthanide MOF barcodes. J Am Chem Soc 131:18069–18071
69. Guo Z, Xu H, Su S, Cai J, Dang S, Xiang S, Qian G, Zhang H, O'Keeffe M, Chen B (2011) A robust near infrared luminescent ytterbium metal-organic framework for sensing of small molecules. Chem Commun 47:5551–5553
70. Dang S, Min X, Yang W, Yi F-Y, You H, Sun Z-M (2013) Lanthanide metal-organic frameworks showing luminescence in the visible and near-infrared regions with potential for acetone sensing. Chem Eur J 19:17172–17179
71. Auzel F (2004) Upconversion and anti-stokes processes with f and d ions in solids. Chem Rev 104:139–173
72. Yang J, Yue Q, Li G-D, Cao J-J, Li G-H, Chen J-S (2006) Structures, photoluminescence, up-conversion, and magnetism of 2D and 3D rare-earth coordination polymers with multicarboxylate linkages. Inorg Chem 45:2857–2865
73. Mahata P, Ramya KV, Natarajan S (2007) Synthesis, structure and optical properties of rare-earth benzene carboxylates. Dalton Trans 4017–4026
74. Mahata P, Ramya KV, Natarajan S (2008) Pillaring of $CdCl_2$-like layers in lanthanide metal-organic frameworks: synthesis, structure, and photophysical properties. Chem Eur J 14:5839–5850
75. Weng D, Zheng X, Jin L (2006) Assembly and upconversion properties of lanthanide coordination polymers based on hexanuclear building blocks with (μ_3-OH) bridges. Eur J Inorg Chem 2006:4184–4190
76. Sun C-Y, Zheng X-J, Chen X-B, Li L-C, Jin L-P (2009) Assembly and upconversion luminescence of lanthanide-organic frameworks with mixed acid ligands. Inorg Chim Acta 362:325–330
77. Dong Y-B, Wang P, Ma J-P, Zhao X-X, Wang H-Y, Tang B, Huang R-Q (2007) Coordination-driven nanosized lanthanide "molecular lantern" with tunable luminescent properties. J Am Chem Soc 129:4872–4873
78. Wang P, Ma J-P, Dong Y-B, Huang R-Q (2007) Tunable luminescent lanthanide coordination polymers based on reversible solid-state ion-exchange monitored by ion-dependent photoinduced emission spectra. J Am Chem Soc 129:10620–10621
79. Wang P, Ma J-P, Dong Y-B (2009) Guest-driven luminescence: lanthanide-based host-guest systems with bimodal emissive properties based on a guest-driven approach. Chem Eur J 15:10432–10445

80. An J, Shade CM, Chengelis-Czegan DA, Petoud S, Rosi NL (2011) Zinc-adeninate metal-organic framework for aqueous encapsulation and sensitization of near-infrared and visible emitting lanthanide cations. J Am Chem Soc 133:1220–1223
81. Ma M-L, Qin J-H, Ji C, Xu H, Wang R, Li B-J, Zang S-Q, Hou H-W, Batten SR (2014) Anionic porous metal-organic framework with novel 5-connected vbk topology for rapid adsorption of dyes and tunable white light emission. J Mater Chem C 2:1085–1093
82. Qin J-S, Zhang S-R, Du D-Y, Shen P, Bao S-J, Lan Y-Q, Su Z-M (2014) A microporous anionic metal-organic framework for sensing luminescence of lanthanide(III) ions and selective absorption of dyes by ionic exchange. Chem Eur J 20:5625–5630
83. Luo F, Batten SR (2010) Metal-organic framework (MOF): lanthanide(III)-doped approach for luminescence modulation and luminescent sensing. Dalton Trans 39:4485–4488
84. Lan Y-Q, Jiang H-L, Li S-L, Xu Q (2011) Mesoporous metal-organic frameworks with size-tunable cages: selective CO_2 uptake, encapsulation of Ln^{3+} cations for luminescence, and column-chromatographic dye separation. Adv Mater 23:5015–5020
85. Wang Y, Yang J, Liu Y-Y, Ma J-F (2013) Controllable syntheses of porous metal-organic frameworks: encapsulation of Ln(III) cations for tunable luminescence and small drug molecules for efficient delivery. Chem Eur J 19:14591–14599
86. He W-W, Li S-L, Yang G-S, Lan Y-Q, Su Z-M, Fu Q (2012) Controllable synthesis of a non-interpenetrating microporous metal-organic framework based on octahedral cage-like building units for highly efficient reversible adsorption of iodine. Chem Commun 48:10001–10003
87. Li Y-A, Ren S-K, Liu Q-K, Ma J-P, Chen X, Zhu H, Dong Y-B (2012) Encapsulation and sensitization of UV–vis and near infrared lanthanide hydrate emitters for dual- and bimodal-emissions in both air and aqueous media based on a porous heteroatom-rich Cd(II)-framework. Inorg Chem 51:9629–9635
88. Zhou Y, Yan B (2014) Imparting tunable and white-light luminescence to a nanosized metal-organic framework by controlled encapsulation of lanthanide cations. Inorg Chem 53:3456–3463
89. Della Rocca J, Liu D, Lin W (2011) Nanoscale metal-organic frameworks for biomedical imaging and drug delivery. Acc Chem Res 44:957–968
90. Rieter WJ, Taylor KML, An H, Lin W, Lin W (2006) Nanoscale metal-organic frameworks as potential multimodal contrast enhancing agents. J Am Chem Soc 128:9024–9025
91. Rieter WJ, Taylor KML, Lin W (2007) Surface modification and functionalization of nanoscale metal-organic frameworks for controlled release and luminescence sensing. J Am Chem Soc 129:9852–9853
92. Foucault-Collet A, Gogick KA, White KA, Villettea S, Pallier A, Collet G, Kieda C, Li T, Geib SJ, Rosi NL, Petoud S (2013) Lanthanide near infrared imaging in living cells with Yb^{3+} nano metal organic frameworks. Proc Natl Acad Sci U S A 110:17199–17204
93. Rosi NL, Kim J, Eddaoudi M, Chen B, O'Keeffe M, Yaghi OM (2005) Rod packings and metal-organic frameworks constructed from rod-shaped secondary building units. J Am Chem Soc 127:1504–1518
94. Liu K, You H, Zheng Y, Jia G, Song Y, Huang Y, Yang M, Jia J, Guo N, Zhang H (2010) Facile and rapid fabrication of metal-organic framework nanobelts and color-tunable photoluminescence properties. J Mater Chem 20:3272–3279
95. Guo H, Zhu Y, Qiu S, Lercher JA, Zhang H (2010) Coordination modulation induced synthesis of nanoscale $Eu_{1-x}Tb_x$-metal-organic frameworks for luminescent thin films. Adv Mater 22:4190–4192
96. Yang W, Feng J, Song S, Zhang H (2012) Microwave-assisted modular fabrication of nanoscale luminescent metal-organic framework for molecular sensing. ChemPhysChem 13:2734–2738

Struct Bond (2015) 163: 145–184
DOI: 10.1007/430_2014_161

Published online: 20 September 2014

Metal–Organic Frameworks Based on Lanthanide Clusters

Lian Chen, Feilong Jiang, Kang Zhou, Mingyan Wu, and Maochun Hong

Abstract The assembly of the metal clusters to multidimensional metal–organic frameworks remains one of the most attractive research frontiers due to its attractive architectures and excellent properties. Compared with transition metals, the cluster chemistry of lanthanide ions is less developed. The chapter mainly highlights recent research progress on the synthetic strategy, structures, and properties of metal–organic frameworks based on lanthanide clusters. Varying from di- to octatetraconta-nuclei, lanthanide clusters can act as versatile nodes to construct different fascinating topological networks by the linkage of the ligands. The cluster formations and the topologies of these compounds as well as the influence factors on them are described in detail. Potential applications in a variety of fields, especially in luminescence, magnetism, and catalysis, are shown in these materials.

Keywords Lanthanide ions • Luminescent properties • Magnet properties • Metal clusters • Metal–organic frameworks

Contents

L. Chen, F. Jiang, K. Zhou, M. Wu, and M. Hong (✉)
State Key Laboratory of Structure Chemistry, Fujian Institute of Research on the Structure of Matter, Chinese Academy of Sciences, Fuzhou 350002, China
e-mail: hmc@fjirsm.ac.cn

1 Introduction

Over the past decades, considerable experimental and theoretical efforts have been devoted to the chemistry of metal–organic frameworks (MOFs) owing to their intriguing structural topology and potential applications in a diverse range of fields, such as magnetism, adsorption, catalysis, ion exchange, luminescence materials, semiconductor, nonlinear optics, and so on [1–21]. Particularly, the metal–organic frameworks based on partially 4f shell filled lanthanide ions exhibit unique chemical and physical properties associated with their unusual electronic structures, resulting in rich applications especially in photoluminescence and magnetism [22–24]. In contrast to d-block metal ions, lanthanide ions possess the high and flexible coordination numbers as well as the versatile coordination modes, which leads the design and construction of lanthanide–organic frameworks (LOFs) to a challenging task. Many ligands such as carboxylate acids, pyridine carboxylic acids, Schiff bases, amino acids, alkoxide, disulfoxide, and cyclopentadienyl have been employed for the synthesis of LOFs [25–34].

On the other hand, the assembly of the metal clusters to metal–organic frameworks or coordination polymers attracts ever-growing attention in recent years, because the particular characteristics of the clusters can be incorporated into the obtained frameworks, resulting in unprecedented architectures and excellent properties related to the structures formed. Yaghi et al. proposed that the different types of metal clusters could self-assembly into extended networks; however, some of them were not realized [35]. Many 3D open metal–organic frameworks based on huge clusters of manganese, copper, nickel, molybdenum, and silver have been synthesized successfully [35–38]. Compared with the well-established cluster chemistry of transition metals, the chemistry of the counterpart of rare-earth ions is less developed. The lanthanide ions often undergo extensive interactions with oxygen-containing groups due to their special oxophilicity, which could result in inflexible precipitates of lanthanide hydroxides. Hydrophilic groups such as oxo, hydroxo, and carboxylate can bridge the metal ions inducing the core aggregation and take up the positions in the periphery, preventing the cores from further aggregation. By the strategy of controlled hydrolysis of lanthanide salts in the presence of supporting ligands, several examples of different nuclearity lanthanide clusters such as $\{Ln\}_3$, $\{Ln\}_4$, $\{Ln\}_5$, $\{Ln\}_6$, $\{Ln\}_7$, $\{Ln\}_8$, $\{Ln\}_9$, $\{Ln\}_{10}$, $\{Ln\}_{12}$, $\{Ln\}_{13}$, $\{Ln\}_{14}$, $\{Ln\}_{15}$, $\{Ln\}_{22}$, $\{Ln\}_{24}$, $\{Ln\}_{26}$, $\{Ln\}_{36}$, and $\{Ln\}_{60}$ were synthesized [39–50]. However, most examples of them are discrete cluster cores since the hydrophobic groups in the periphery of the cluster cores prevent the further aggregation. The extended metal–organic frameworks based on these lanthanide clusters are really unusual. The investigation on the synthetic strategy, structures, and properties of MOFs based on lanthanide clusters as well as the relationship among them is of great importance. This chapter mainly focuses on the recent development of the fascinating structures of metal–organic frameworks constituted by lanthanide clusters and their prominent properties in ion exchange, photoluminescence, magnetism, and so on.

2 Metal–Organic Frameworks Based on Low-Nuclearity Lanthanide Clusters

2.1 Dinuclear-Based Lanthanide MOFs

A zeolite-like metal–organic framework $[Nd(2,5\text{-pydc})(Ac)(H_2O)]_n \cdot 2nH_2O$ (**1**) [51] with nanotubular structure based on dinuclear lanthanide cluster was obtained by hydrothermal reaction of $Nd(NO_3)_3 \cdot 6H_2O$, $Mn(Ac)_2 \cdot 4H_2O$, and $H_2$2,5-pydc (pyridine-2,5-dicarboxylate acid) in a molar ratio of 2:1:2 at 160°C for 3 days. In the framework, two Nd^{3+} ions are first linked together through one acetate anion to generate a dinuclear cluster (Fig. 1a), which is further linked via 2-carboxylate groups of 2,5-$pydc^{2-}$ ligands to form a (4,4) grid layer in the [100] plane (Fig. 1b). Nd^{3+} ions in the neighboring layers are then bridged via 5-carboxylate groups of 2,5-$pydc^{2-}$ ligands, pillaring above (4,4) layer together to generate the final 3D framework, showing 1D channels along the *a*-axis with the dimensions of

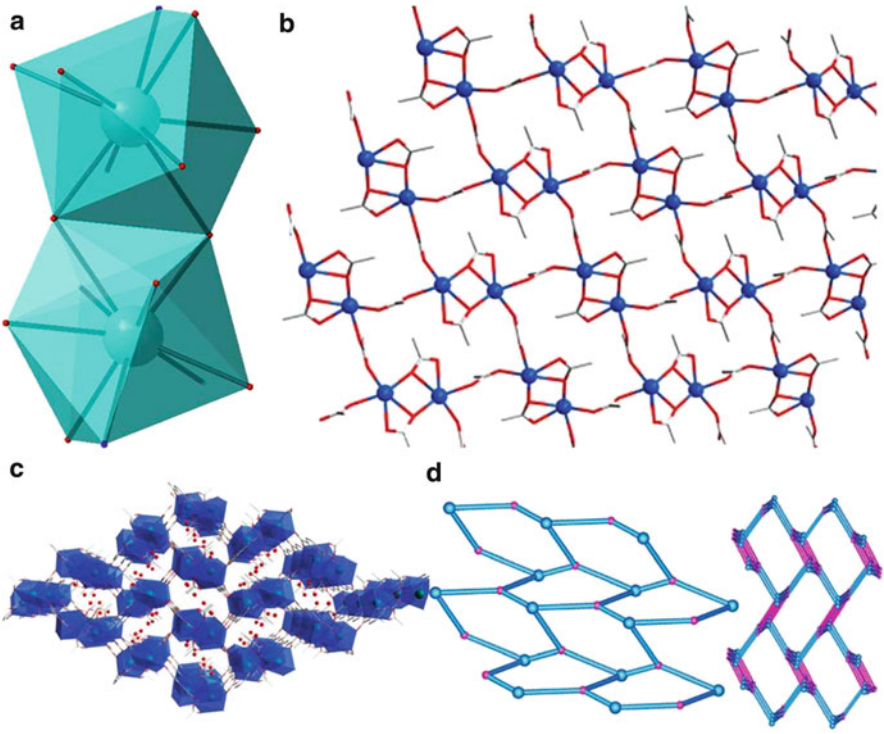

Fig. 1 (**a**) Dinuclear unit linked through acetate anion; (**b**) the ordered (4,4) layer formed by acetate linked helical chains, (**c**) perspective view of the three-dimensional prototypical zeolitic framework with nanotubular structure, (**d**) topological view of the 3D network of **1** with zeolite ABW topology

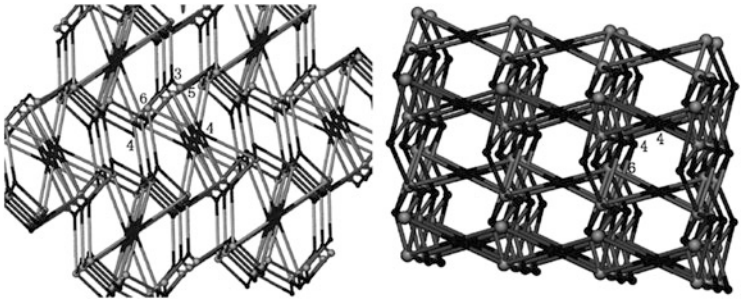

Fig. 2 A $CdSO_4$ net with $(4.8^2)(4.8^5)$ Schläfli symbol and a (4,4,6)-connected net with $(4^2.\ 8^4)(4^4.\ 6^2)_2(4^9.\ 6^6)_2$ circuit symbol based on the dinuclear lanthanide cluster compounds

6.4×12.0 Å^2 (Fig. 1c). The Nd^{3+} ions and 2,5-$pydc^{2-}$ ligands act as walls of the channels, while the acetate anions, the coordinated water molecules, and lattice water molecules are located in the channels. The topological analysis indicates that **1** can be considered as the lanthanide–organic analogue of the zeolite Li-A (Barrer and White) (ABW) [52, 53] with the Schläfli symbol of $(4^2\ 6^3\ 8)$ (Fig. 1d). By replacing the four-connected nodes Si and Al in zeolite ABW with the Nd^{3+} ions and 2,5-$pydc^{2-}$ ligands, the 3.4×3.8 Å eight-membered channels can be replicated and expanded to approximately 6.4×12.0 Å^2. When removing the guest molecules of **1**, it shows a microporous structure with a solvent-accessible volume of 20.7% calculated by PLATON [54]. After activation at 260°C, **1** has a good H_2 uptake capacity of 132 cm^3 g^{-1} at 77 K and 1.0 bar, which is compared to those of microporous zeolites and aluminophosphates [55, 56]. Temperature-dependent magnetic susceptibility measurements show that the μ_{eff} values for **1** are continuously decreased, which may be due to the depopulation of the stark levels for a single Nd^{3+} ion and/or possible antiferromagnetic interactions between lanthanide ions in the acetate bridged dinuclear units [57]. Following on this investigation, a (3,4)-connected $CdSO_4$ net with $(4.\ 8^2)(4.\ 8^5)$ Schläfli symbol and a (4,4,6)-connected net with $(4^2.\ 8^4)(4^4.\ 6^2)_2(4^9.\ 6^6)_2$ circuit symbol based on the dinuclear lanthanide cluster are further reported (Fig. 2) [58].

Introducing 2-hydroxyquinoline-4-carboxylic acid (Hhqc) as ligand, a series of luminescent lanthanide compounds were synthesized in organic solution at room temperature: $[Eu_2(hqc)_6(H_2O)_4] \cdot 8H_2O$ (**2**), $[Ln_2(hqc)_6(H_2O)_2(DMF)_2] \cdot 2H_2O$ (Ln=Eu (**3**), Dy (**4**), Ho (**5**)), and $[Ln_2(hqc)_6(H_2O)_4] \cdot 2H_2O \cdot 2DMF$ (Ln=Ce (**6**), La (**7**), Pr (**8**); DMF=*N*,*N*-dimethylformamide) [59]. The single-crystal X-ray analyses reveal that they all exhibit lanthanide dinuclear cluster linked by hqc ligand. These dinuclear units form a 2D square network and further extend to a supramolecular 3D network by strong hydrogen bonding interactions and the π–π interactions. Investigation on luminescent properties shows hqc ligand can effectively sensitize Ln^{3+} ions in **2** and **3.** On illuminating with a 365 nm excitation light provided by a 16 W ultraviolet lamp, compounds **2** and **3** show the strong red emissions, which can be clearly seen as revealed in the microscopic images (Fig. 3). Complexes **4**–**8** mainly show the characteristic blue luminescence ascribed to the

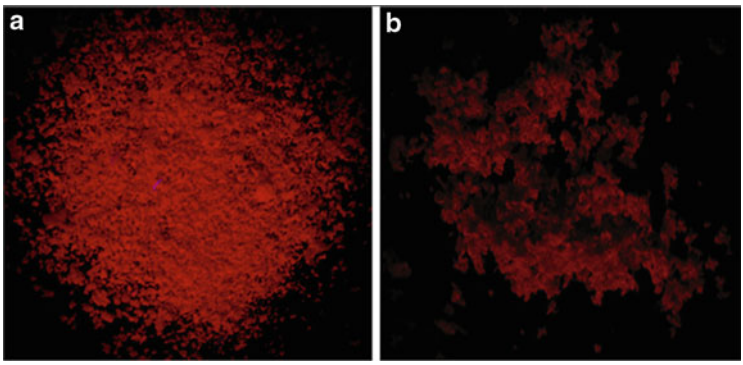

Fig. 3 Microscopic images of red luminescent complexes **2** (**a**) and **3** (**b**) under excitation at 365 nm

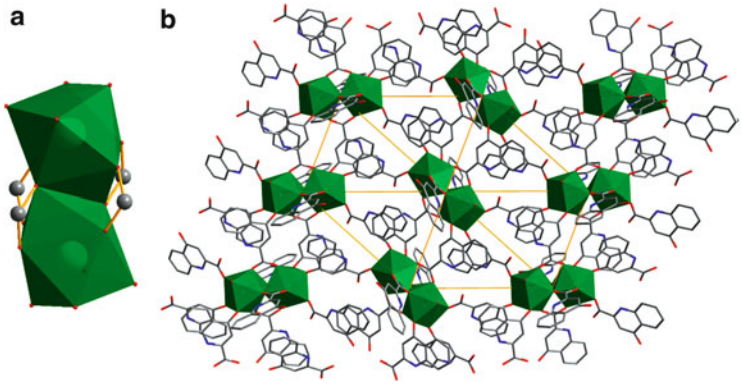

Fig. 4 (**a**) The structure of paddle-wheel unit for **9**. (**b**) The 2D layer of **9** running along the *bc* plane

intra-ligand transition (π–π*) of hqc ligand. An interesting self-absorption phenomenon occurred in Ho complex (**5**), which might be owing to the overlap between the emission wavelength of ligand and the absorption wavelength of Ho^{3+} located at 456 nm corresponding to the hypersensitive $^5I_8 \rightarrow {}^5G_6$ ($\Delta J = 2$) transition [60]. Ongoing investigation of lanthanoid–hydroxyquinoline metal–organic frameworks, another series of binuclear-based lanthanide networks with visible and NIR photoluminescence, $[Ln(Hhqc)_3(H_2O)]_n \cdot 3nH_2O$ (Ln=Eu (**9**), Tb (**10**), Sm (**11**), Nd (**12**), and Gd (**13**)), were reported [61]. Complexes **9**–**13** are isomorphous. Using compound **9** as a representative, two Eu^{3+} ions are joined by four μ_2-O atoms of carboxylate groups to form a binuclear paddle-wheel unit $Eu_2(COO)_4$ with the separation of Eu. . .Eu being 4.392 Å (Fig. 4a). Each $Eu_2(COO)_4$ unit is connected with six adjacent units through six $Hhqc^-$ ligands sustaining a 2D sheet along the *bc* plane (Fig. 4b). From the view of network topology, **9** shows a uninodal 2D hxl/Shubnikov (3, 6) lane net with the point symbol being $\{3^6.4^6.5^3\}$ by considering

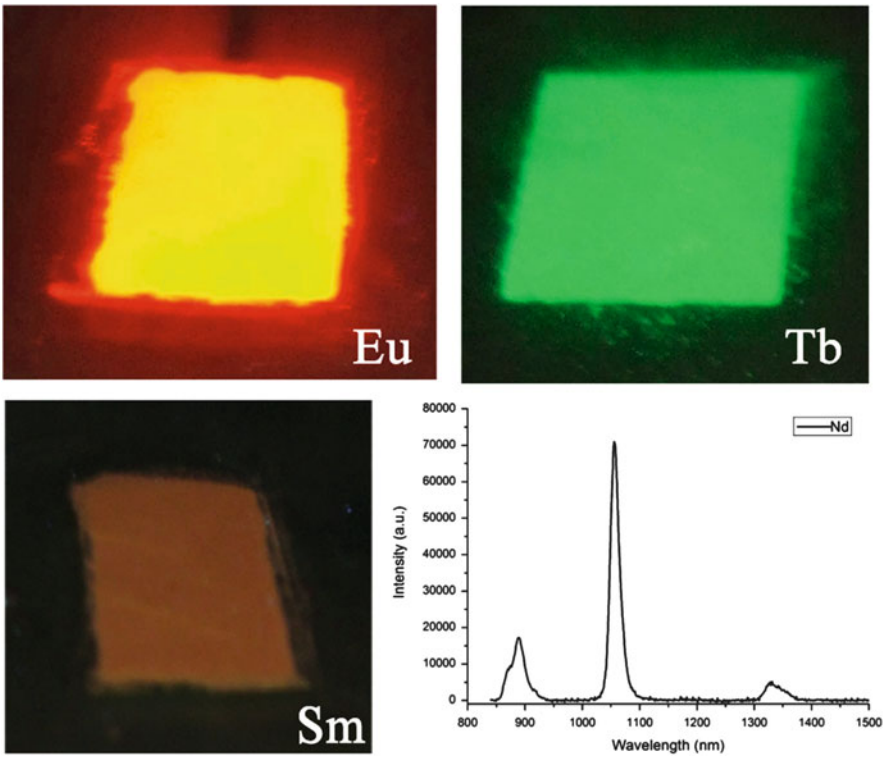

Fig. 5 Images of complexes **9–11** under UV lamp at 365 nm and NIR emission spectra of complex **12** at room temperature

the $Eu_2(COO)_4$ unit as a 6-connected node. Efficiently sensitized by hqc ligand, complexes **9** (Eu), **10** (Tb), and **11**(Sm) can emit strong luminescence in the visible region on UV excitation at room temperature in solid state (Fig. 5), in which Tb complex possesses longer excited state lifetimes than the others. Upon excitation at 397 nm at room temperature, luminescence spectra of Nd^{3+} complex (**12**) in solid state display typical narrow band emissions in the NIR region with three bands at 888, 1,055 and 1,329 nm (Fig. 5), which are attributed to the $^4F_{3/2} \rightarrow {}^4I_{9/2}$, $^4F_{3/2} \rightarrow {}^4I_{11/2}$, and $^4F_{3/2} \rightarrow {}^4I_{13/2}$ transitions of Nd^{3+} ions, respectively. The above study demonstrates that the H_2hqc can be as an efficient UV light sensitizer for visible and NIR emissions in lanthanide cluster-based system.

Besides hydroxyquinoline carboxylate ligand, multi-carboxylate ligands are often used to construct lanthanide metal–organic frameworks [62]. By using tetracarboxylate ligand H_4adip (5-aminodiacetic isophthalic acid) and H_4adtp (2-aminodiacetic terephthalic acid), two-dimensional layer assemblies $\{Me_2NH_2[Ln(adip)(H_2O)]\}_n$ (Ln=Eu (**14**), Tb (**15**), Sm (**16**)) and three-dimensional (3D) frameworks $\{[Ln_2(Hadtp)_2] \cdot 3H_2O\}_n$ (Ln=Eu (**17**), Tb (**18**), Sm (**19**)) were obtained under solvothermal condition [63]. Linking dinuclear

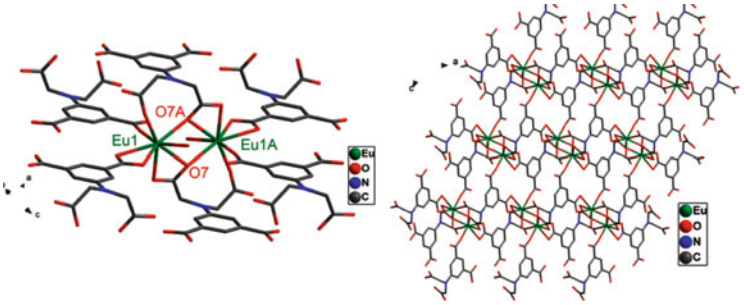

Fig. 6 The dinuclear unit and layer structure of **14**. Reprinted with permission from [63]. © 2012 The Royal Society of Chemistry

clusters by the isophthalic moieties of $adip^{4-}$ ligands, complexes **14–16** show the negatively charged layer structures (Fig. 6). Different from **14–16**, Hadtp ligands link the dinuclear clusters in complexes **17–19** to generate left- and right-handed helical chains, which further alternatively arrange along crystallographic *a*- and *b*-axis to form a 3D achiral architecture with two different channels A and B (6.1×6.1 Å^2) (Fig. 7). The topological analysis shows the structures of **17–19** can be simplified as a new uninodal 7-connected topological net with a Schläfli symbol of ($3^3.4^9.5^7.6^2$). On illuminating under 365 nm UV light, the strong red emissions of solid complex **17** and intense turquoise fluorescence of complexes **15** and **18** can be visible to the naked eyes (Fig. 8).

Another tetracarboxylate ligand *p*-terphenyl-3,3″,5,5″-tetracarboxylic acid (H_4ptptc),which possesses diverse coordination modes and strong ability to interact with the oxophilic lanthanide ions, has been introduced. This ligand has delocalized π-electron system and can provide a strong absorbing sensitizer. In addition, robustness and rigidity from the aromaticity of the terphenyl moiety are also helpful in accessing a rigid and protective coordination shell to minimize non-radiative deactivation. A new 3D metal–organic frameworks formulated as $\{[Me_2H_2N]_2[Eu_2(ptptc)_2(H_2O)(DMF)]\cdot 1.5DMF\cdot 7H_2O\}_n$ (**20**)[64] were synthesized by solvothermal reaction of europium ions with H_4ptptc in a mixed solvent DMF/H_2O system. In **20**, every two nine-coordinated Eu^{3+} ions are linked by a pair of *syn–syn* carboxylate bridges of $ptptc^{4-}$ to generate the $[Eu_2(\mu_2\text{-}COO)_2(COO)_6]^{2-}$ units, which are surrounded by four μ_6-coordination mode $ptptc^{4-}$ ligands forming a 2D network lying on (001) plane (Fig. 9a). The neighboring 2D layers are further pillared by μ_4-coordination mode $ptptc^{4-}$ ligands to form a 3D pillar-layer structure (Fig. 9b), showing one-dimensional tetragonal channels with the counterionic dimethylammonium, coordinated and lattice solvent molecules located in them. The energy level of the triplet state of the H_4ptptc ligand determined from the phosphorescence at 77 K of the Gd^{3+} complex is 21,230 cm^{-1}, lying above the $^5D_0$ emitting state of the Eu^{3+} ion, demonstrating H_4ptptc can act as an UV light sensitizer for europium-based red emission [65–67]. The speculation is supported by the bright red luminescence of **20** corresponding to the characteristic

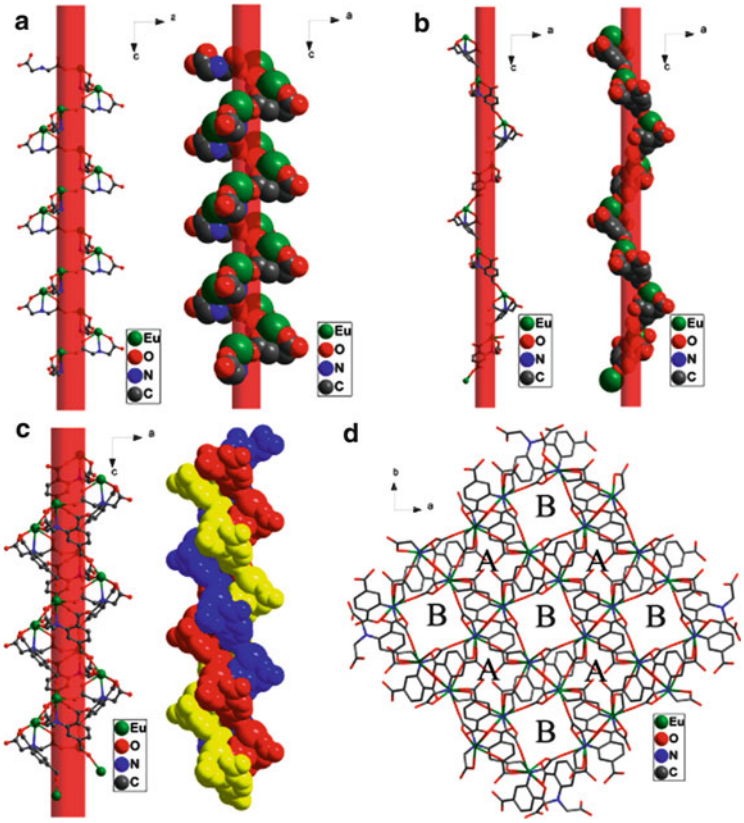

Fig. 7 (**a**) Right-handed 4_1 helical chain. (**b**) Single-stranded left-handed 4_3 helical chain. (**c**) Triple-stranded left-handed 4_3 helical chain. (**d**) The 3D framework of **17**. Reprinted with permission from [63]. © 2012 The Royal Society of Chemistry

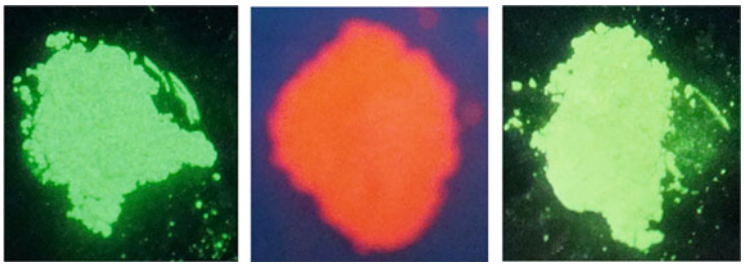

Fig. 8 Images of complexes **15**, **17,** and **18** under 365 nm UV lamp

$^5D_0$–^7F_J ($J = 0$–4) transitions in the solid state. When terphenyl hexacarboxylate ligand *p*-terphenyl-2,2″,2‴,5,5″,5‴-hexacarboxylate acid (H_6tphc) is employed, $[Ln(tphc)_{0.5}(H_2O)_2]\cdot 2H_2O$ (Ln=Eu (**21**), Tb (**22**), Gd (**23**)) were solvothermally

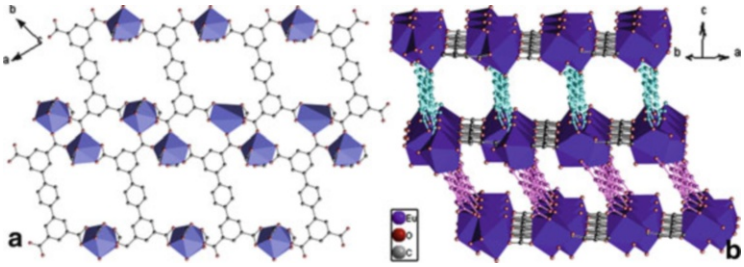

Fig. 9 (**a**) The 2D layer of **20** propagating along (0 0 1) plane; (**b**) the projection of 3D framework of **20**

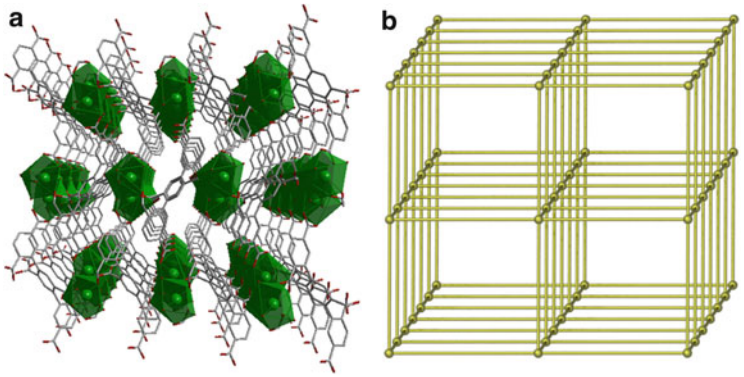

Fig. 10 (**a**) The projection of 3D framework in **21** at the (1 0 0) plane; (**b**) representation view of the 6-connected uninodal alpha-Po network with topology ($4^{12}.6^3$) in **21**

synthesized [68]. Every two Ln (III) generate a binuclear unit bridged by bidentate carboxylate groups from two independent $tphc^{6-}$ ligands. If both the binuclear unit and ligand $tphc^{6-}$ are considered as 6-connected nodes, the whole structure of **21**–**23** can be simplified as a 6-connected uninodal alpha-Po cubic network with topology ($4^{12}.6^3$), as shown in Fig. 10. The triplet state energies of the ligands H_6tphc determined from the phosphorescence at 77 K of the Gd^{3+} complex (**23**) are 24,000 cm^{-1} (416 nm), lying in an ideal range for sensitizing the luminescence of Tb^{3+} or Eu^{3+} luminescence, leading to the characteristic red emission of Eu^{3+} due to $^5D_0 \rightarrow {}^7F_J$ ($J = 0$–4) transitions and green emission of Tb^{3+} due to $^5D_4 \rightarrow {}^7F_J$ ($J = 6$–3) transitions, respectively (Fig. 11).

2.2 *Lanthanide Metal–Organic Frameworks Based on 3–10 Nuclearity Clusters*

The hydrothermal hydrolysis of $Ln(NO_3)_3$ directed by H_2Pra_2biim (H_2Pra_2biim = 10-di(propionic acid)-2,20-biimidazole) in the presence of NaOH

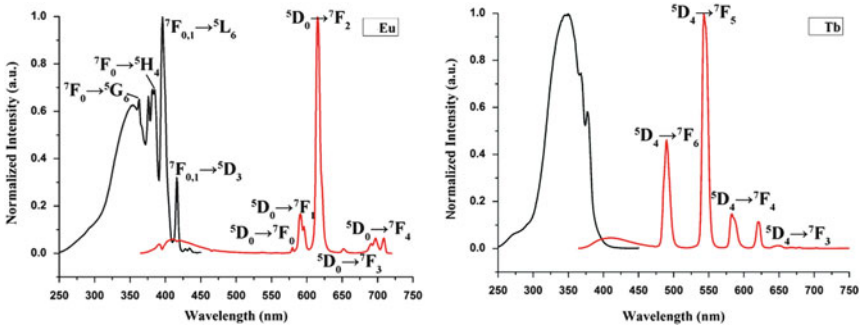

Fig. 11 Excitation spectra and emission spectra for **21** and **22** at room temperature

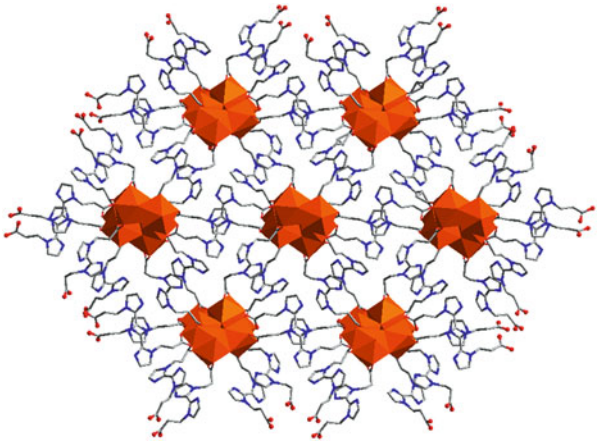

Fig. 12 The open framework structure of **24**–**26**

produced the crystals of 3D structures formulated as $\{[Ln_3(\mu_3\text{-}OH)_3(Pra_2biim)_3(H_2O)_2]_n \cdot 4nH_2O\}_n$ (Ln=Nd (**24**), Pr (**25**), and La (**26**)) [69]. Single-crystal X-ray diffraction analysis reveals that the asymmetric unit of **24**–**26** consists of three independent Ln^{3+} ions, which form Nd_3 triangle capped by a single μ_3-OH group to form the triangular $[Nd_3(\mu_3\text{-}OH)]^{8+}$ unit. Such triangular lanthanide cluster units have been recognized to account for the toroidal arrangement of local magnetization vectors, responsible for the magnetic relaxation phenomena such as single-molecule magnets (SMMs) and single-chain magnets (SCMs) [70–75]. By sharing vertexes, the triangular lanthanide clusters form infinite $[Nd_3(\mu_3\text{-}OH)_3]_n^{6+}$ ribbons, which are interconnected by Pra_2biim leading an open framework (Fig. 12). Ln. . .Ln antiferromagnetic coupling with magnetic anisotropy is observed in complexes **24** and **25**. The similar μ_3-OH capped triangular lanthanide clusters are found in another 3D framework by introducing 3,3′-dimethoxy-4,4′-biphenyldicarboxylic acid as ligand, in which Eu complex shows the strong red luminescence upon 343 nm excitation, Gd^{3+} complex exhibits antiferromagnetic

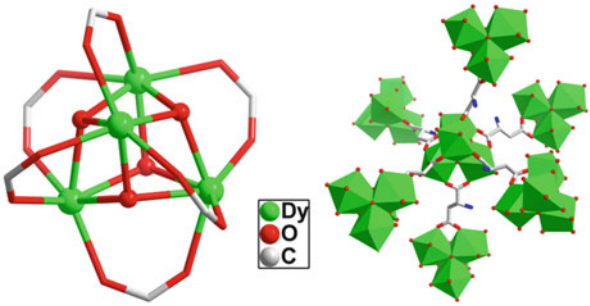

Fig. 13 The tetranuclear lanthanide cluster (*left*) and the linkage between the Dy_4 clusters (*right*) in **27**

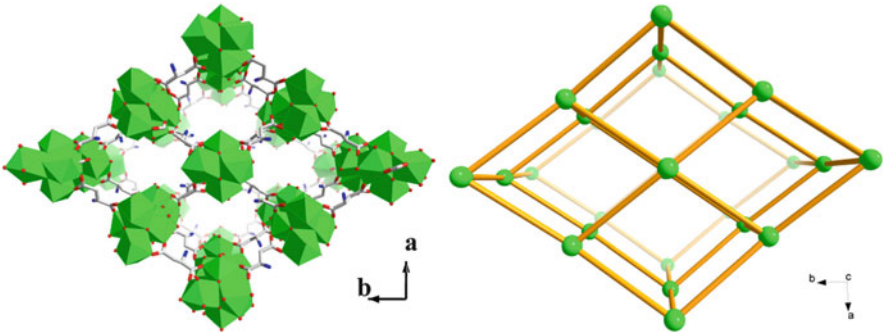

Fig. 14 The 3D framework of **27** showing large channels and the representation view of the **pcu** topology in **27**

coupling, and Dy^{3+} complex possesses ferromagnetic coupling between lanthanide ions [76].

Reacting $Ln(ClO_4)_3$ with L-aspartic acid yielded a tetranuclear lanthanide cluster-based three-dimensional open framework $\{[Dy_4(\mu\text{-}OH)(asp)_3(H_2O)_8](ClO_4)_2 \cdot 10H_2O\}_n$ (**27**) (H_2asp=L-aspartic acid) [77]. The X-ray structure analysis shows that compound **27** possesses a tetranuclear lanthanide cluster. The tetranuclear unit is based on a Dy_4 trigonal pyramid, in which Dy1 locates on a threefold axis and occupies the apical position, while the remaining Dy^{3+} ions lie in the basal plane with Dy…Dy separation ranges between 3.7211(5) and 3.8526 (6) Å. The edges of Dy_4 tetragon are linked by the dicarboxylate ligands to form the $\{Dy_4(OH)_4(COO)_4\}$ clusters (Fig. 13). Each cluster is linked with six neighboring clusters by asp^{2-} ligands to form a 3D open framework showing an interesting parallelepiped-shaped pore. By considering the $\{Dy_4(OH)_4(COO)_4\}$ unit as a 6-connected node, the 3D network can be simplified as a 6-connected *alpha*-Po network (Fig. 14).

Hydrothermal reaction of lanthanide nitrates with 3-sulfobenzoic acid obtained another example of the 3D lanthanide–organic constructed by tetradinuclear

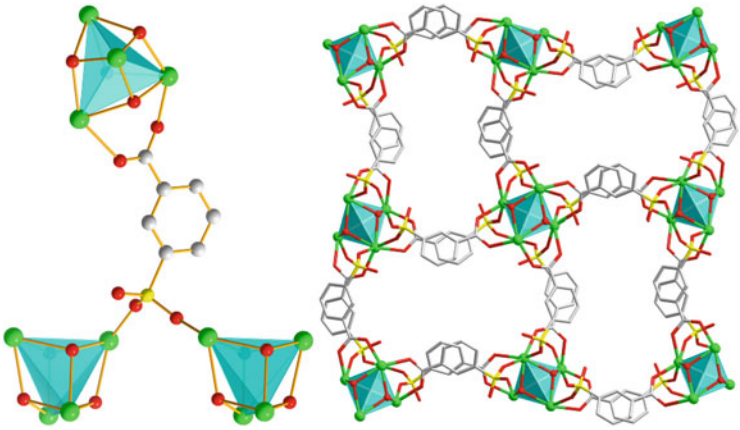

Fig. 15 The μ_3-bridging mode of 3-SBA and the 3D $\{Ln\}_4$ cluster-based network showing 1D channels in **28–30**

clusters, $\{[Ln_4(OH)_4(3\text{-SBA})_4(H_2O)_4]\cdot nH_2O\}_n$ (Ln=Eu (**28**), $n = 10$; Gd (**29**), $n = 10$; and Tb (**30**), $n = 8$, 3-SBA = 3-sulfobenzoate)) [78]. The structure contains cubane-like $\{Ln\}_4$ tetranuclear clusters supported by hydroxyl ions. Each μ_3-bridging mode 3-SBA ligand acts as the three-connected node by linking one $\{Ln\}_4$ unit through the carboxylate group and the other two through sulfonate species, while each $\{Ln\}_4$ SBU (second building unit) is connected with twelve 3-SBA ligands. Thus, a 3D porous lanthanide–organic framework is formed, showing two different kinds of 1D channels located with the unique T8(3) water tapes or zigzag water chains (Fig. 15). The resulting 3D network can be assigned to an unusual binodal (3, 12)-connected topology with the Schläfli symbol of $(4^3)_4(4^{20}.6^{28}.8^{18})$. This kind of high-connected topology is equivalent to that of the Au_4Ho crystalline lattice [79] which is first observed in metal–organic coordination frameworks.

Recently, Cheng et al. reported a chiral lanthanide–sulfate framework formulated as $[Ln_4(OH)_4(SO_4)_4(H_2O)_3]_n$ (Ln=Y (**31**) and Er (**32**))by hydrothermal reactions of Ln_2O_3, H_2SO_4, and D-camphoric acid at 170°C [80]. Four Ln^{3+} ions are linked by hydroxo bridges to give cubane-like $[Ln_4(OH)_4]^{8+}$ ($\{Ln\}_4$) clusters. Each sulfate anion is connected with three $\{Ln\}_4$ clusters, while each $\{Ln\}_4$ cluster is linked to 12 sulfate anions. By considering the sulfate anions as a three-connected node and the $\{Ln\}_4$ core as a 12-connected node, the structure can be rationalized as a binodal (3, 12)-connected net similar with those of **28–30**. The interesting feature of **31** and **32** is that the chiral framework contains helical tubes and channels constructed from double left- and right-handed helical chains. Rocha et al. also reported a 3D eight-connected **bct** network with the Schäfli symbol of $(3^6.4^{14}.5^8)$ based on cubane-like tetranuclear $[Er_4(\mu_3\text{-}OH)_6]$ cores [81].

By solvothermal reaction in the mixed solvent of H_2O/EtOH, Cheng et al. synthesized two 3D MOFs based on Ln_5 clusters as nodes, $\{[Ln_5Zn(pbdc)(H_2O)_{10}(\mu_3\text{-}OH)_6](CO_3)_{0.5}(NO_3)_4\cdot mH_2O\}_n$ (H_2bpdc = 4,4′-dicarboxylate-2,2′-dipyridine, Ln=Gd (**33**), $m = 12$; Dy (**34**), $m = 10$) [82]. The compound contains pentanuclear clusters $[Ln_5(OH)_6]^{9+}$ with distorted trigonal bipyramidal geometry.

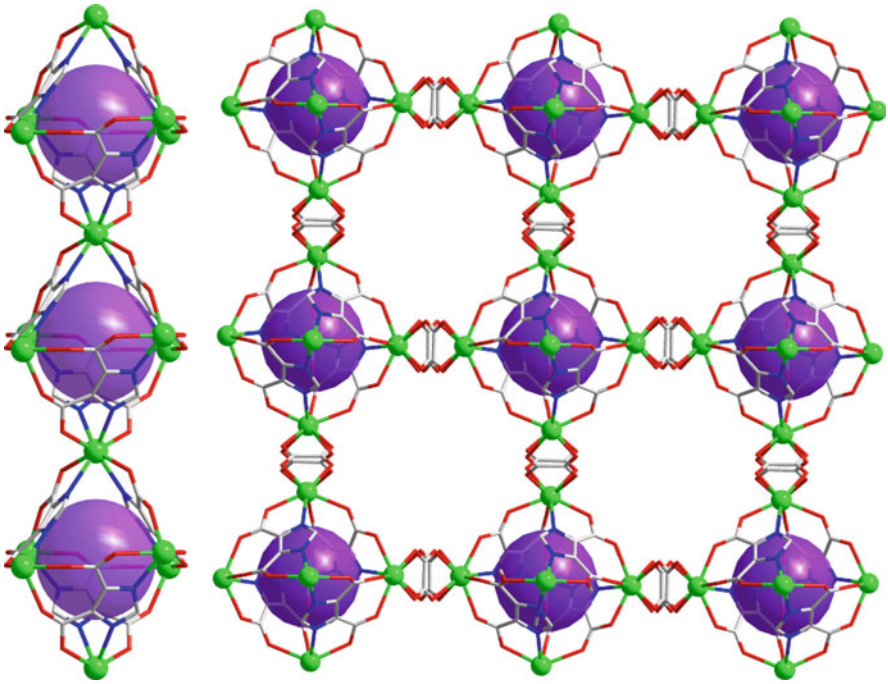

Fig. 16 The 1D chain constructed by Ln_6L_4 octahedra sharing the vertexes and the 3D framework showing 1D channels in **35–37**

The Ln. . .Ln separations range from 3.791 to 3.905 Å. These pentanuclear clusters are further linked by [Zn(pbdc)] units to form a 3D framework with a 6,6-connected topology. The compounds exhibit the good thermal stability and are stable in air as well as various common organic solvents. Magnetic investigation reveals that Gd^{3+} compound exhibits the large magnetocaloric effect (MCE) of up to 30.7 J kg^{-1} K^{-1} and Dy^{3+} compound shows the slow magnetic relaxation behavior.

By the hydrothermal reactions of $Ln(NO_3)_3 \cdot 6H_2O$, H_3idc, H_2ox, and KOH, Lu et al. presented a unique 3D hexanuclear lanthanide cluster-based anionic MOF, $\{K_5[Ln_5(idc)_4(ox)_4]\}n \cdot 20H_2O\}_n$ (Ln=Gd (**35**), Tb (**36**), and Dy (**37**), H_3idc=imidazole-4,5-dicarboxylate, H_2ox=oxalate acid) [83]. Six Ln^{3+} ions are bridged by four μ_3-idc^{3-} to generate a slightly distorted Ln_6L_4 octahedron units, with the equatorial and axial Ln. . .Ln distances of ca. 9.249 and 10.022 Å, respectively. These Ln_6L_4 octahedra are linked via sharing of the vertexes into the 1D chains which are further connected by oxalates to generate a 3D framework showing 1D channels along the *c*-axis (Fig. 16). The size of the channel is ca. 6.9×7.8 Å, in which the K^+ ions locate on the surfaces of the channels and weakly interact with idc^{3-}, oxalate, and water molecules. The results of PXRD and energy-dispersive X-ray spectroscopy (EDS) analysis show that the K^+ ions can be easily exchanged with various cations. The emission intensity is significantly increased by adding 1–3 equiv. of Ca^{2+} cations in the emulsion of compound **36**

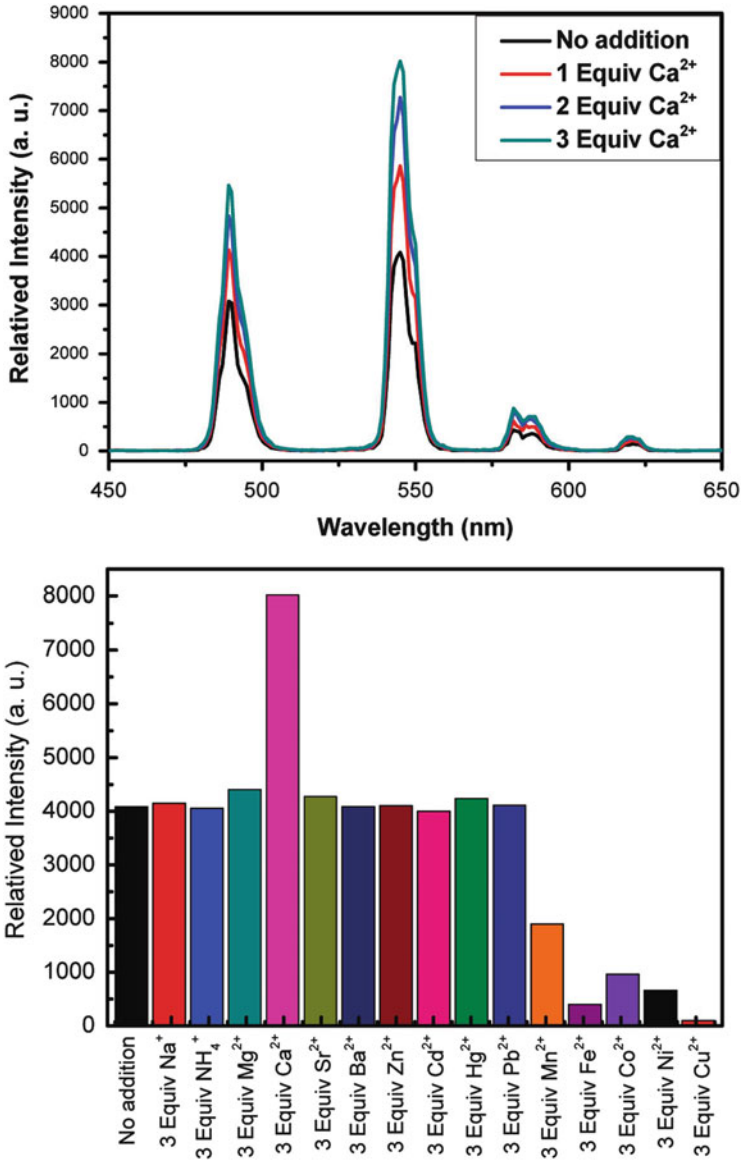

Fig. 17 Emission spectra of an emulsion of **36** in DMF in the presence of ~0–3 equiv. of Ca^{2+} ions (*top*) ; luminescent intensities at 545 nm for an emulsion of **36** in DMF upon the addition of various cations (*bottom*). Reprinted with permission from [83]. © 2009 American Chemical Society

in DMF while weakened or quenched upon the addition of transition metal ions Mn^{2+}, Fe^{2+}, Co^{2+}, Ni^{2+}, and Cu^{2+} (Fig. 17). The interesting tunable luminescence of **36** indicates that the compound can act as a promising Ca^{2+} ion-selective luminescent probe.

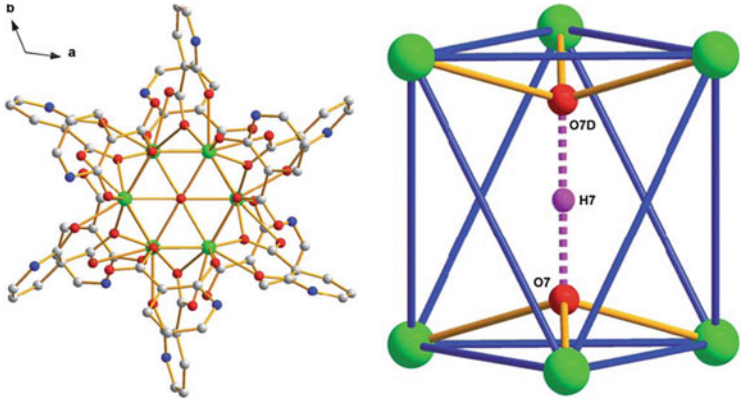

Fig. 18 View of the hexanuclear $\{Gd\}_6$ cluster (*left*) and the trigonal anti-prism formed by six Gd1 ions (*right*) in **39**. Reprinted with permission from [84]. © 2011 The Royal Society of Chemistry

Rocha et al. reported another 3D lanthanide–organic frameworks based on octahedron hexanuclear units, $[Pr^{3+}{}_2Pr^{4+}{}_{1.25}O(OH)_3(pydc)_3]_n$ (**38**) [81]. Different from compounds **35–37** in which the octahedron $\{Ln\}_6$ cluster is constructed by Ln^{3+} ions and idc ligands, the hexametric cluster in **38** is assembled by Pr^{3+} ions and oxo/hydroxyl groups, in which Pr^{3+}/Pr^{4+} ions locate in the vertexes while two μ_3-bridging oxo and six μ_3-OH groups occupy the eight triangular faces of the metallic octahedron. The topological structure of compound **38** can be viewed as 14-connected **bcu-x** network with the Schäfli symbol of $3^{36}.4^{48}.5^7$. The thermal analysis of compound **38** shows a significant weight increase (ca. 2.7%) between ambient temperature and 450 °C, which may be correlated with the uptake of oxygen from the surrounding environment by the praseodymium oxide inorganic core.

Comparing with octahedron hexanuclear clusters, lanthanide clusters with trigonal antiprismatic configurations are rare. Wu et al. reported two 3D lanthanide compounds with primitive cubic network featuring an ideal trigonal antiprismatic hexanuclear cluster [84]. The three-dimensional lanthanide–organic frameworks $\{[Ln_9(HNA)_{12}(O_2H)] \cdot 6H_2O\}_n$ (Ln=Gd (**39**), Eu (**40**); HNA = 2-hydroxylnicotinic anion) were obtained from the reactions of Ln_2O_3 with 2-mercaptonicotinic acid (MNA) under hydrothermal conditions. Single X-ray diffraction analysis reveals that there are two crystallographically independent Gd^{3+} ions in the structure of complex **39**. Six Gd1 ions are linked by 12 completely deprotonated ligands and one $[O_2H]^{3-}$ group to form hexangular $\{Gd\}_6$ cluster with the six gadolinium ions displaying in an ideal trigonal antiprismatic arrangement (Fig. 18). Each hexanuclear $\{Gd\}_6$ cluster is bridged to its six neighboring nodes by ten-coordinated Gd2 ions, generating a three-dimensional lanthanide–organic framework based on hexanuclear cluster with a distorted primitive cubic topology (Fig. 19). Compound **40** shows red luminescence with characteristic Eu^{3+} emission,

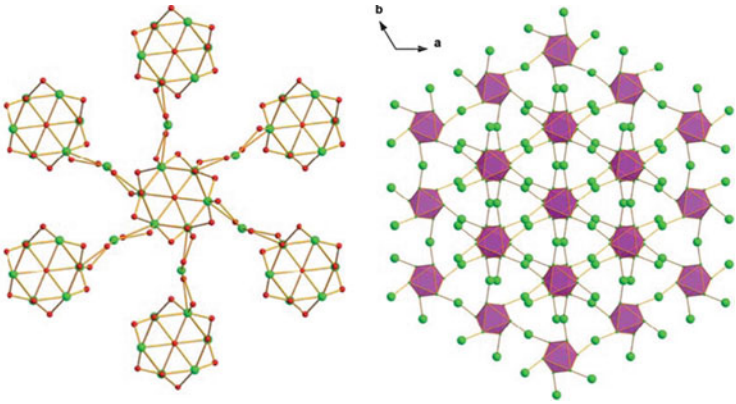

Fig. 19 The metal–oxygen framework of the six-connected hexanuclear cluster via the bridging Gd2 ions (*left*) and the metal framework of the three-dimensional cubic network constructed by the hexanuclear lanthanide clusters (*right*) in **39**. Reprinted with permission from [84]. © 2011 The Royal Society of Chemistry

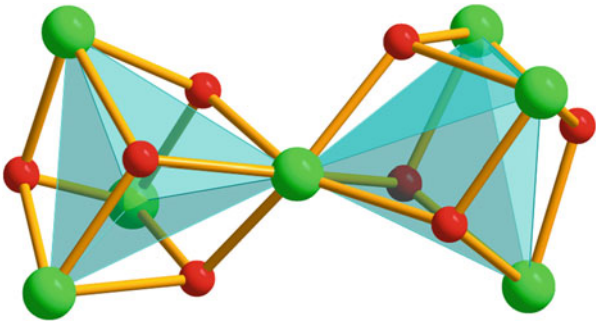

Fig. 20 The vertex-sharing dicubane-like structure of $[Yb_7(\mu_3\text{-}OH)_8]^{13+}$ in **42**

and **39** and **40** possess different magnetic behaviors though with the same constructions.

Although several examples of heptanuclear lanthanide cluster have been reported [43, 85–87], the extended metal–organic frameworks architectured by $\{Ln\}_7$ cores are extremely rare. By hydrothermal reaction at 120°C, Jin et al. obtained the first example of 3D porous frameworks constructed by heptanuclear lanthanide hydroxo clusters, $\{[Ln_7(\mu_3\text{-}OH)_8(NDA)_6(OH)_{0.5}(Ac)_{0.5}(H_2O)_7]\cdot 4H_2O\}_n$ (Ln=Ho (**41**), Yb (**42**), $H_2NDA = 1,4$-naphthalenedicarboxylic acid) [88]. The two compounds are isomorphous. Taking compound **42** as a representative, the metal skeleton of the heptanuclear Yb^{3+} cluster $[Yb_7(\mu_3\text{-}OH)_8]^{13+}$ can be regarded as two vertex-sharing tetrahedral tetranuclear units assembled via a Yb^{3+} ion. When considering the μ_3-OH groups as vertices of the polyhedron, $[Yb_7(\mu_3\text{-}OH)_8]^{13+}$ can also be viewed as a distorted vertex-sharing dicubane-like structure as shown in Fig. 20. Each heptanuclear core is surrounded

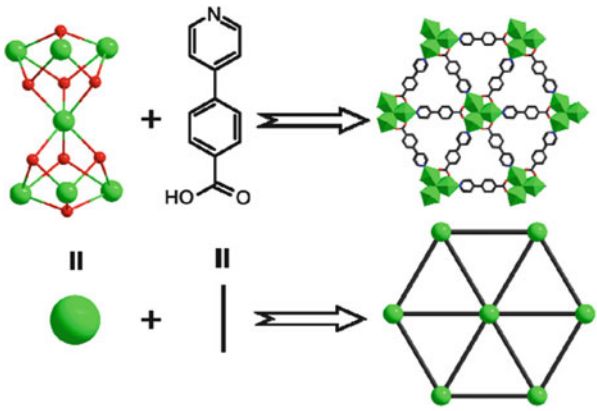

Fig. 21 The structure presentation of **43.** Reprinted with permission from [89]. © 2012 American Chemical Society

by six adjacent clusters with the distance of the centers of the heptanuclear cores ranging from 12.7 to 15.6 Å. By considering heptanuclear core as a 6-connected node, the 3D framework of **41/42** can be simplified as α-Po-related topology. Besides the vertex-sharing dicubane shape heptanuclear cluster, the trigonal–prismatic lanthanide core can also be employed to extended structure. Yang et al. reported a series of isostructural lanthanide-based cluster organic framework different from **41/42** in cluster shape and linkage mode [89]. The compounds formulated as $[Ln_7(\mu_3\text{-}OH)_8L_9(H_2O)_6]\cdot 4ClO_4\cdot 3HL\cdot nH_2O$ (HL = 4-pyridin-4-ylbenzoic acid; Ln=Y (**43**), La (**44**), Gd (**45**), Yb (**48**), $n = 6$; Ln = Dy (**46**), Er (**47**), $n = 4$) are synthesized under hydrothermal condition at 190°C in the presence of $HClO_4$. In compound **43** seven Y^{3+} are joined by eight μ_3-OH groups to form a cationic heptanuclear cluster core $[Y_7(\mu_3\text{-}OH)_8]^{13+}$. The metal skeleton of the $\{Y\}_7$ core can be viewed as a well regular trigonal prism with six Y^{3+} ions locating in the vertex and one Y^{3+} ions occupying the body center (Fig. 21). The comparison of the metal skeleton of **41/42** and **43–48** is illustrated in Fig. 22. Each $\{Y\}_7$ core connects six of the same ones through the linking of the ligand with a distance of 16.955 Å, producing a Ln cluster-based organic layer along the *b*-axis. From a topological point of view, the layer can be regarded as a six-connected uninodal $h \times l$ net with Schläfli symbol $(3^6.4^6.5^3)$ by considering the $\{Y\}_7$ core as a six-connected node (Fig. 21) [90]. A PLATON program analysis based on the crystal structure shows that the accessible volume of the compound is approximately 18.1% [91].

3 Metal–Organic Frameworks Based on High-Nuclearity Lanthanide Clusters

Choosing isonicotinic acid (HIN) as the multifunctional bridging ligand, three isostructural MOFs, $\{[Ln_{14}(\mu_6\text{-}O)(\mu_3\text{-}OH)_{20}(IN)_{22}Cu_6Cl_4(H_2O)_8]\cdot 6H_2O\}_n$ (Ln=Y (**49**), Gd (**50**), Dy (**51**)), were hydrothermal synthesized in the presence of the

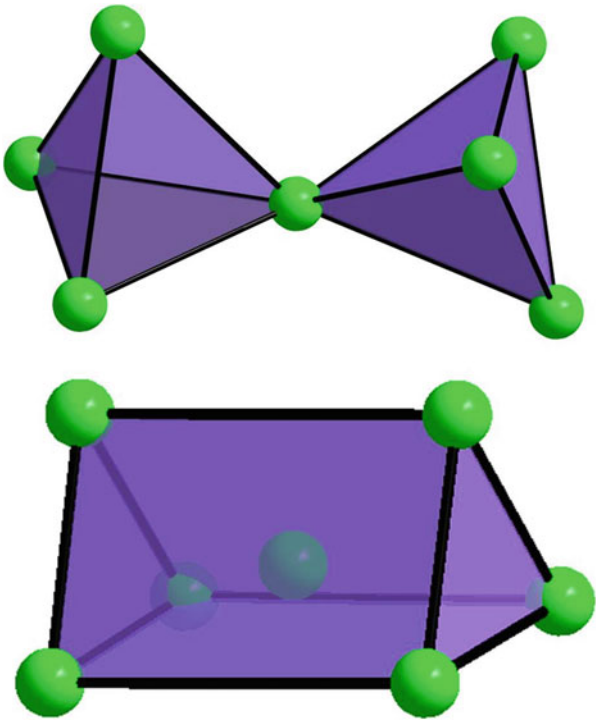

Fig. 22 The comparison of different metal skeletons of the heptanuclear clusters in **41/42** and **43–48**

perchloric acid [92]. The asymmetric unit of **50** contains four crystallographically unique Gd ions, of which two are nine coordinated and the others are eight coordinated. The fourteen Gd^{3+} ions are connected by hydrophilic hydroxo and oxo bridges to give the unusual nanosized tetradecanuclear $[Gd_{14}(\mu_6\text{-}O)(\mu_3\text{-}OH)_{20}]^{20+}$ cluster. The $\{Gd\}_{14}$ core can be described as one octahedral $\{Gd\}_6$ unit sharing two opposing Gd apexes with two novel trigonal bipyramid $\{Gd\}_5$ cores as shown in Fig. 23. The Cu^{2+} ions in the raw materials are reduced to Cu^{+} ions in the resulting structure. Two crystallographic unique Cu^{+} ions exhibit different coordination environments and form two kinds of four-connected linkers with monomer and $\{Cu_2Cl_2\}$ dimer. The $\{Gd\}_{14}$ cores, $\{Cu_2Cl_2\}$ dimers, and Cu ions are then bridged by IN ligands to generate an extremely complicated 3D framework exhibiting 1D channels with dimensions of about 7×7.5 Å along the *c*-axis (Fig. 23). Temperature-dependent molar susceptibility measurements reveal that there are antiferromagnetic interactions between the lanthanide ions.

Hydrothermal reaction of Ln_2O_3, $Zn(OAC)_2$, isonicotinic acid, and HCOOH in pH 2 at 170°C yielded two Ln_{26}-based 3D metal–organic framework with similar topological structures, $\{Zn_{1.5}Dy_{26}(IN)_{25}(CH_3OO)_8(CO_3)_{11}(OH)_{26}(H_2O)_{29}\}_n$ (**52**) and $Zn_{1.5}Gd_{26}(IN)_{26}(CH_3OO)_7(CO_3)_{11}(OH)_{26}(H_2O)_{28}$ (**53**) [93]. The single-crystal X-ray structural analysis reveals the asymmetric unit of **52** consists of 26 crystallographically independent Dy^{3+} ions, of which four are nine coordinated and the

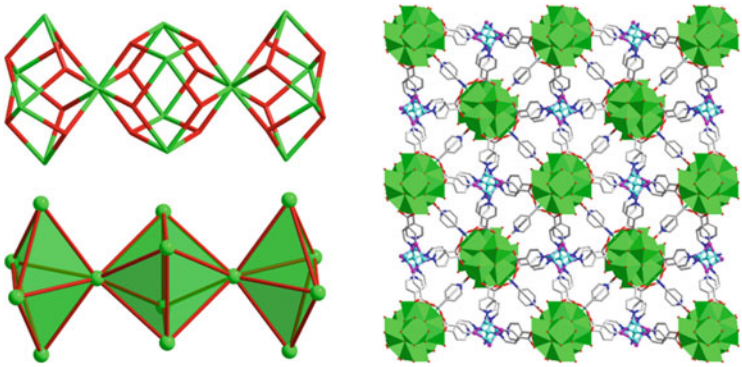

Fig. 23 The structure of the $[Gd_{14}(\mu_6\text{-}O)(\mu_3\text{-}OH)_{20}]^{20+}$ cluster and its metal skeleton (*left*); the overall 3D structure of **50** showing the unusual framework along the *c*-axis. The lattice water molecules are omitted for clarity (*right*)

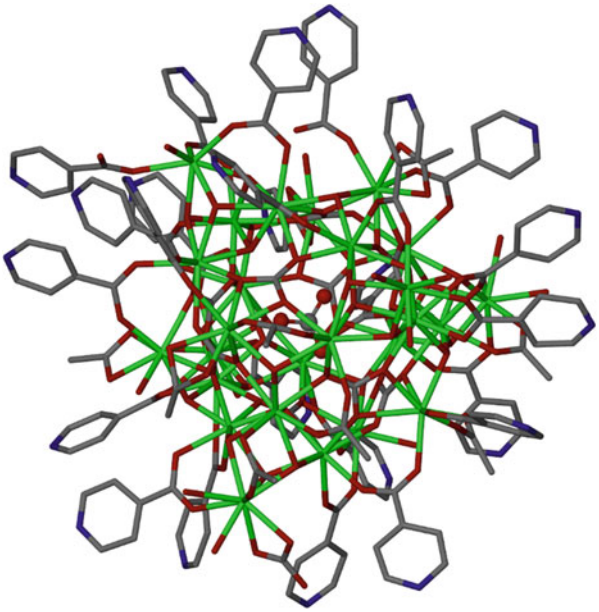

Fig. 24 The nanosized spherical $\{Dy\}_{26}$ cluster with a CO_3^{2-} anion located at the center in **52**

remaining are eight coordinated. Four DyO_x ($X = 8$ or 9) polyhedra are connected to each other to form a $\{Dy\}_4$ building unit by sharing four μ_3-OH groups, while three DyO_x polyhedra share a μ_3-OH to make another building unit of $\{Dy\}_3$. Then, five $\{Dy\}_4$ cluster are linked with six $\{Dy\}_3$ rings, giving rise to a nanosized spherical $\{Dy\}_{26}$ clusters with one free CO_3^{2-} anion located at the center (Fig. 24). The $\{Dy\}_{26}$ clusters are then stabilized via CO_3^{2-}, IN ligands, CH_3COO^-, and water molecules by completing the coordination of Dy^{3+} ions

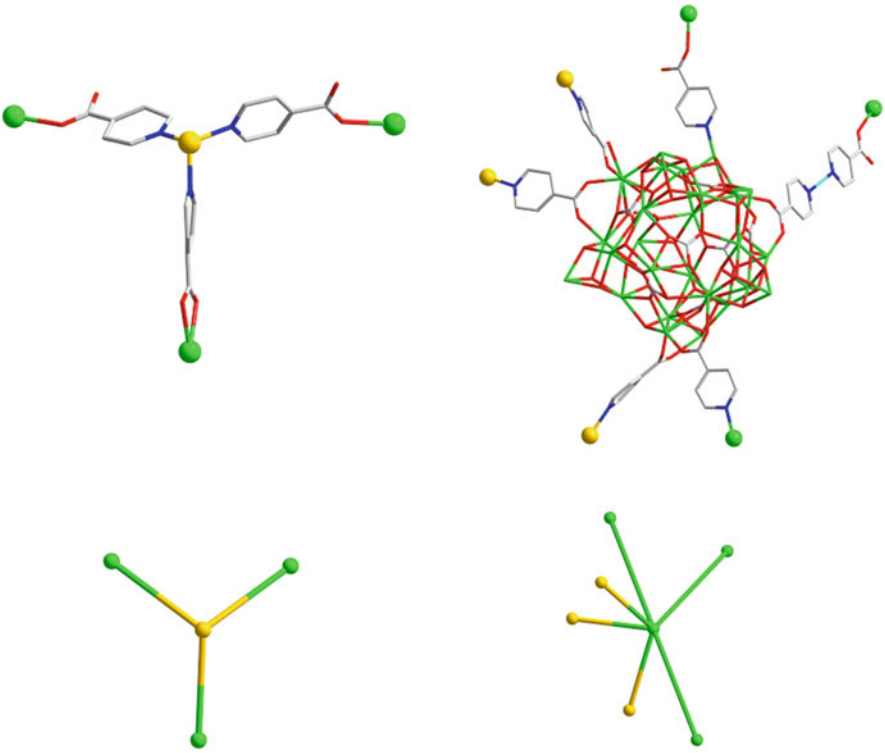

Fig. 25 The three-connected Zn^{2+} and six-connected $\{Dy\}_{26}$ cluster in **52**

with the diameter of the spherical cluster shell including organic ligands ca. 2.1 nm. Two Zn^{2+} centers are six and four coordinated, acting as two-connected linker and three-connected nodes, respectively. Each $\{Dy\}_{26}$ cluster is extended in six directions by the linkage of the IN^- ligands to Zn^{2+} centers and the Dy^{3+} ions from the neighboring clusters (Fig. 25). Considering the $\{Dy\}_{26}$ clusters and tetrahedral Zn^{2+} centers as six-connected and three-connected nodes, the topological structure of **52** can be described as a 3D (3, 6)-connected binodal net with Schläfli symbol of $\{4^2.6\}\{4^4.6^{10}.8\}$ (Fig. 26). Compound **53** possesses similar $\{Ln\}_{26}$ cluster and topological structure with **52** in spite of the slightly differences in the details. Three ligands are used and play the different roles in the final product: CO_3^{2-} ions play a very important role in the formation of the spherical Ln_{26} cluster, CH_3COO^- ions stabilize the Ln_{26} cluster and reduce the steric restriction, and isonicotinate (IN) further strengthens the stability of the cluster and acts as the linker to the neighboring nanosized Ln_{26} clusters and the Zn centers.

The above-mentioned three examples are multidimensional high-nuclearity lanthanide cluster frameworks connected by d-block elements. Isonicotinic acid in them is employed as a multifunctional ligand based on the following considerations: (1) the isonicotinic ligand can act as a rigid linear bridge with oxygen and

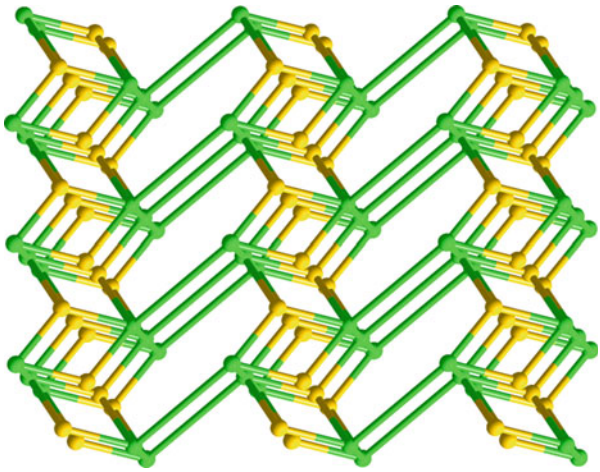

Fig. 26 The topological view of the three-dimensional framework in **52**

nitrogen donors occupying on opposite sides, and (2) the carboxyl group may induce the oxophilic lanthanide ions to hydroxo–lanthanide cluster aggregation while the nitrogen donors can coordinate to transition metal ions to form the extended networks. Construction of metal–organic frameworks built from high-nuclearity lanthanide-based building blocks and organic linker in the absence of d-block elements continues a challenge. Suitable ligands need to be elaborately selected to form and link the lanthanide clusters. Besides, the small anions are also proved to be of importance in core aggregation. By replacing Gd_2O_3 with $Gd(NO)_3$ and introducing sodium azide as weak base, another Gd_{26} cluster-based metal–organic framework without transition ions, $\{[Gd_{26}(\mu_6\text{-}CO_3)_9\ (NA)_{32}(\mu_3\text{-}OH)_{26}](NO_3)_2 \cdot 3(H_2O)\}_n$ (**54**, HNA=nicotinic acid), was obtained [94]. The metal skeleton of Gd_{26} in **54** is quite similar with that of **52** despite the slightly difference in the coordination environments of Gd^{3+} centers. The diameter of the spherical cluster shell including organic ligands is about 2.32(4) nm. The Gd_{26} cluster units are then connected to each other by the organic linker to form an extended framework, in which the N-donor of the NA^- ligand is coordinated to lanthanide ions. The coordination mode of lanthanide ions with monodentate N-donor of the ligand is rare in lanthanide chemistry [32, 95]. Further investigation reveals that the compound has good catalytic performance in epoxidation reactions of various olefinic substrates including α,β-unsaturated ketones in heterogeneous media (Fig. 27). It is worth to note that lanthanide compounds have rarely been explored as heterogeneous catalysts for olefin epoxidation [96, 97].

The high-nuclearity pure lanthanide clusters over thirty nuclei are especially difficult to be obtained. Recently, two isostructural coordination polymers based on huge 36-nuclearity lanthanide clusters, $\{[Ln_{36}(NA)_{36}(OH)_{49}(O)_6(NO_3)_6(N_3)_3(H_2O)_{20}]\ Cl_2{\cdot}28H_2O\}_n$ (Ln=Gd (**55**), Dy (**56**)), were synthesized [98]. Different from previous reports, $LnCl_3$ was used as lanthanide source to construct the lanthanide clusters. The nanosized Gd_{36} cluster in **55** can be viewed as the aggregation of two types of cluster units: wheel-like Gd_{24}

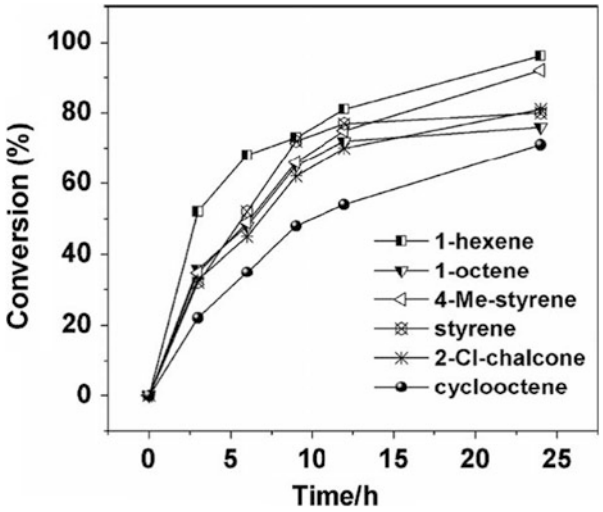

Fig. 27 Reaction profile for the epoxidation of olefins with *t*BuOOH catalyzed by compound **54** in acetonitrile media. Reprinted with permission from [94]. © 2011 Wiley-VCH Verlag 2826 GmbH & Co. KGaA, Weinheim

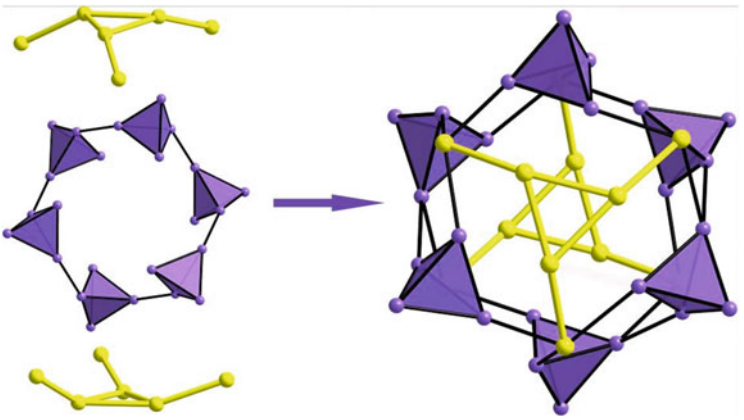

Fig. 28 Illustration of the structure of the Gd_{36} cluster constructed by one wheel-like Gd_{24} units and two tripod-like Gd_6 units in **55**

unit and tripod-like Gd_6 unit. The detailed assembly can be described as follows: firstly, six tetrahedral Gd_4 are jointed together adopting the up and down arrangement to generate a wheel-like Gd_{24} unit with cyclohexane chair-like structure; secondly, six Gd^{3+} ions form a noncoplanar tripod-like Gd_6 unit as Fig. 28 shown; and finally, two tripod-like Gd_6 units cap the wheel-like Gd_{24} unit from top and bottom to form the huge Gd_{36} cluster hosting two Cl^- guests inside the cavity (Fig. 28). Estimated by the Gd···Gd separations, the size of this huge Gd_{36} cluster is ca. $1.0 \times 1.7 \times 1.7$ nm. In the skeleton of this Gd_{36} cluster, there are six

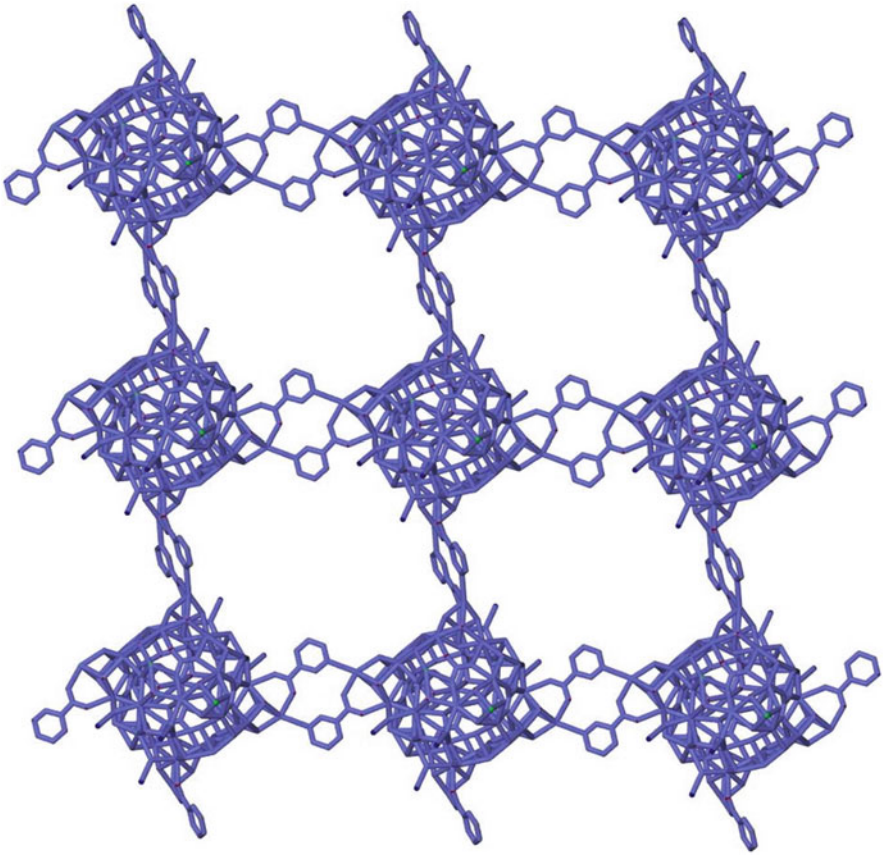

Fig. 29 The square layer of compound **55**

pentagonal windows occupied by the NO_3^- anions, which adopt a rare μ_5-η^2(O, O′):η^1(O):η^1(O′):η^1(O″):η^1(O″) coordination model to bridge five nonplanar Gd^{3+} cations [99]. This Gd_{36} unit is in D_{3d}-symmetry with six topologically non-equivalent Gd^{3+} vertexes: four Gd^{3+} ions in the tetrahedral Gd_4 unit and two Gd^{3+} ions in a tripod-like Gd_6 unit. According to the method for topological analysis of high-nuclearity d-block metal clusters suggested by Kostakis Blatov, and Proserpio [100, 101], it can be denoted as **3,4,5,6,6,6M36-1**. In **55**, every two Gd_{36} cluster are linked by a pair of NA^- ligand adopting a bridging bidentate coordination mode via its N-donor and carboxylic groups. Each cluster is four connected with its neighboring ones to form a two-dimensional square layer as shown in Fig. 29. The magnetic entropy change ΔS_m was calculated from the experimental magnetization data according to the Maxwell equation $\Delta S_m(T)_{\Delta H} = \int [\partial M(T,H)/\partial T]_H dH$. The result shows that compound **55** possesses a large magnetocaloric effect of 39.66 J kg^{-1} K^{-1} ($\Delta H = 7\,T$ at 2.5 K), indicating it may be a good candidate for molecular refrigerants (Fig. 30). This large MCE may

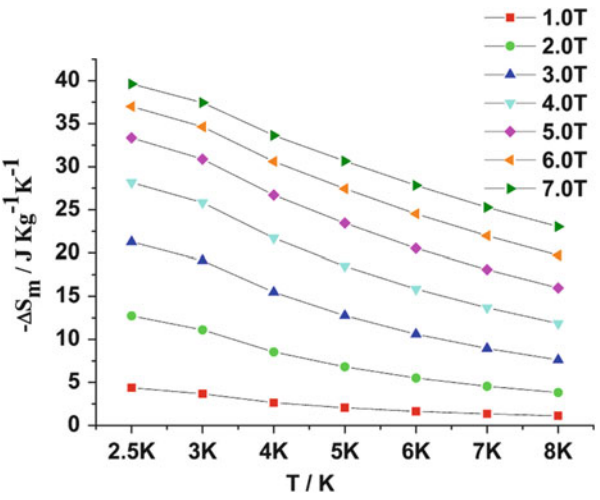

Fig. 30 Values of $-\Delta S_m$ calculated from the magnetization data using the Maxwell equation for **55** at various fields (1–7*T*) and temperatures (2.5-8 K). Reprinted with permission from [98]. © 2013 The Royal Society of Chemistry

be attributed to the high spin density in **55**. Alternating-current (AC) magnetic susceptibility measurements reveal that frequency-dependent out-of-phase signals are observed in Dy^{3+} compound (**56**), suggesting slow relaxation of the magnetization.

Previous research suggests that electronegative guest species act can not only to stabilize the highly positive charge clusters as the balance ions but also to induce the formation of the cluster skeletons as the templates. The size and the geometry of these anions will make a great impact on the ultimate nuclearity and structures. Several large lanthanide clusters have been successfully isolated by using single anionic species as templates [46, 73]. The investigation on double- or multiple-anion templated clusters is still underway. Using this strategy, an Er_{48} cluster-based LOF, $\{[Cl_2\&(NO_3)]@[Er_{48}(NA)_{44}(OH)_{90}(N_3)(H_2O)_{24}]\}\cdot 6nCl\cdot 35nH_2O$ (**57**), was synthesized [102]. The huge Er_{48} cluster in **57** can be viewed as the aggregation of two types of cluster units: one ringlike Er_{12} unit and 2 equiv. wheel-like Er_{18} units. The Er_{12} ring is constructed by 12 Er^{3+} ions showing a star shape, while the Er_{18} wheel-like is built by six tetrahedral Er_4 unit through a corner-sharing mode (Fig. 31). Different from the abovementioned cyclohexane chair-like Gd_{24} unit in **55**, six tetrahedral Er_4 clusters herein adopt the parallel arrangement. Two wheel-like Er_{18} units sandwich one ringlike Er_{12} unit to form the ultimate barrel-like Er_{48} nanotube (Fig. 32). The size of this tube is ca. $1.3 \times 1.3 \times 1.0$ nm^3 (evaluated from the Er···Er separations). It's interesting that the barrel-like Er_{48} cluster traps a NO_3^- and two Cl^- anions in the belly. The formation of Er_{48} core can be described as a double-anion-induced self-assembly of the lanthanide ions through hydrogen bonding reactions between the anion templates and the hydroxyl groups of the host cluster. The details are shown in Fig. 33. This Er_{48} tube is in D_{6h} symmetry with five topologically non-equivalent Er^{3+} vertexes: three Er^{3+} ions in one tetrahedral Er_4 unit and two Er^{3+} ions of a Er_{12} ring. Based on the method for topological analysis of high-nuclearity 3d metal clusters suggested by Kostakis, Blatov, and Proserpio [100, 101], it can be signed as **3,4,6,6,6 M48-1**. Outside the inner Er_{48} cluster, the

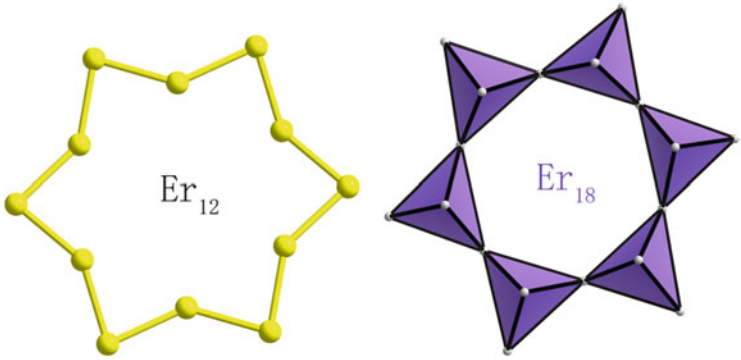

Fig. 31 Illustration of ringlike Er_{12} unit and wheel-like Er_{18} unit in **57**

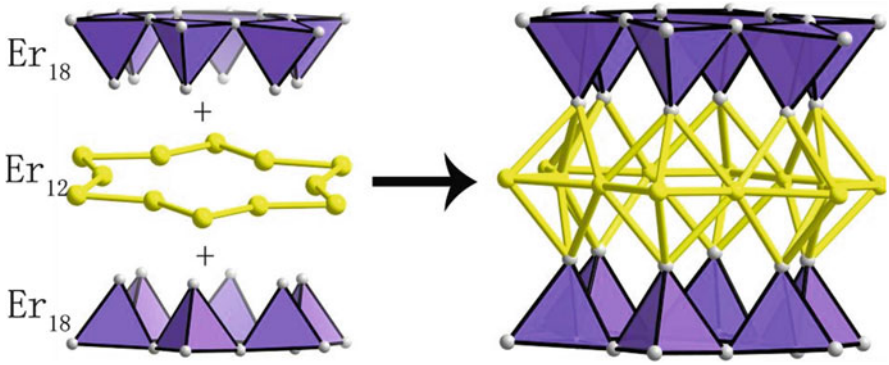

Fig. 32 Construction of the Er_{48} cluster in **57**

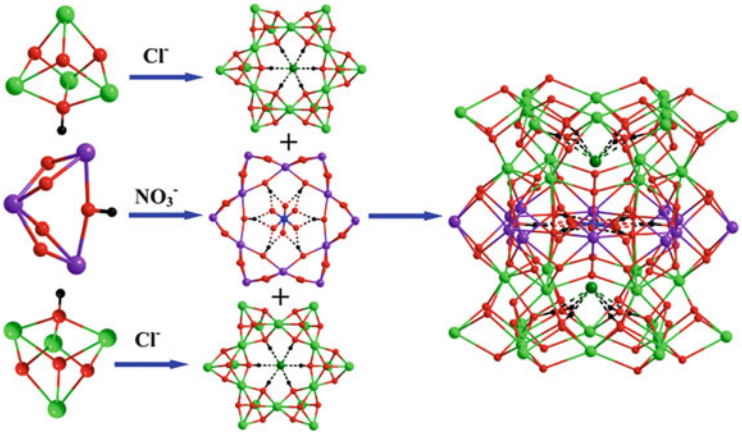

Fig. 33 The sketch map of the Cl^- and NO_3^- anions templating the formation of the nanosized Er_{48} tube through hydrogen bonding in **57**. Reprinted with permission from [102]. © 2014 The Royal Society of Chemistry

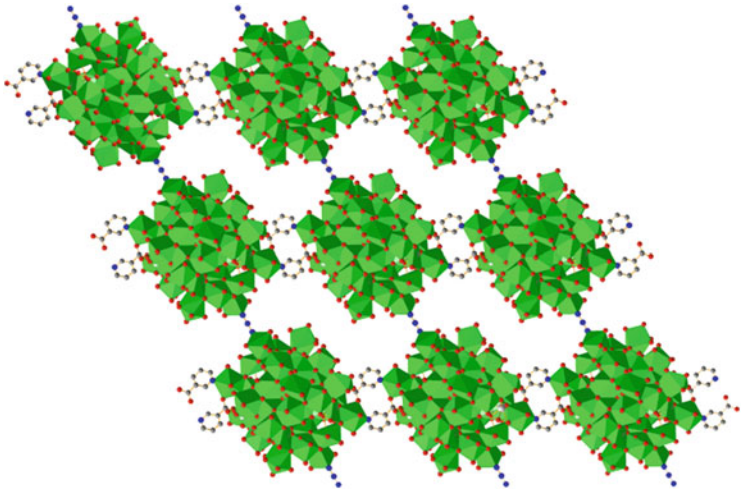

Fig. 34 The square layer in **57** based on the Er_{48} units via the coordination of the NA^- ligands and the N_3^- anions to the Er^{3+}cations. Reprinted with permission from [102]. © 2014 The Royal Society of Chemistry

NA^- ligands adopt their N-donor and carboxylate groups in monodentate, bidentate chelating, and bidentate bridging modes to coordinate with the inner Er^{3+} cations. The N_3^- ligand bridges two Er^{3+} ions from two neighboring Er_{48} clusters with the end–end mode (μ_2-1,3-N_3). By the connection of these two bridging ligands, Er_{48} clusters are linked together to form a layer structure as shown in Fig. 34. From this case, it can be seen that double- or multiple-anion templates can not only effectively increase the nuclearity of the clusters but also donate much more novelty to the final structures. In the absence of NaN_3, Xu et al. also reported a layered structure based on Ho_{48} cluster with similar Ln_{48} aggregation but different linkage between clusters [103].

4 Lanthanide Clusters Constructed by Calixarenes

Appropriate ligands are most pivotal in the construction of lanthanide cluster-based metal–organic frameworks. Calixarenes and their derivatives, a class of cyclic oligomers composed of phenoxy groups and alkyl, sulfur, nitrogen, or oxygen bridging atoms, are versatile multidentate ligands for constructing polynuclear compounds. Many efforts have been devoted to constructing polynuclear compounds based on calixarenes [104–110]. However, most of them are involving transition metals while multinuclear lanthanide complexes are rare [50, 111–113]. Herein, some examples are presented.

By introducing *p*-sulfonatocalix[4]arenes, three lanthanide polymeric frameworks based on hexanuclear hydroxo–lanthanide clusters and *p*-sulfonatocalix[4]

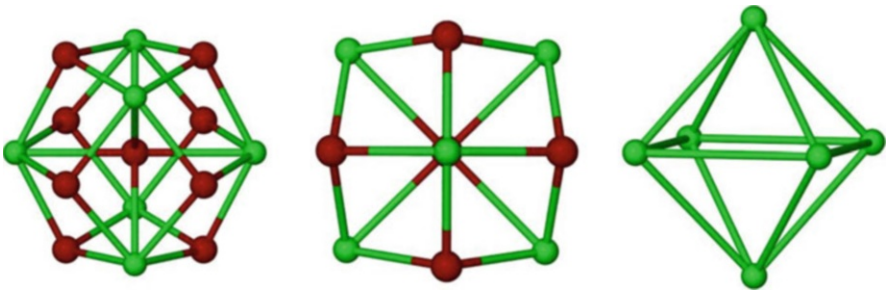

Fig. 35 The $[Ln_6(OH)_9]$ cluster seen from *a*-axis (*left*), *c*-axis (*middle*), and its metal skeleton (*right*) in **58–60**

arene, Ln-RPF9 (Ln=La (**58**), Pr (**59**), Nd (**60**)), were synthesized under hydrothermal conditions by adjusting pH value to 8 [114]. In the frameworks, six lanthanide ions are joined through eight μ_3-OH groups to give rise to a rhombic dodecahedron with a μ_6-OH group located in the center. The metal skeleton of the rhombic dodecahedral cluster $[Ln_6(OH)_9]$ can be described as a slightly compressed octahedron as shown in Fig. 35. The water molecules and sulfonate groups of *p*-sulfonatocalix[4]arene ligand complete the coordination of Ln^{3+} ions to further stabilize the $[Ln_6(OH)_9]$ cluster. Each SO_3^- group of the *p*-sulfonatocalix[4]arene ligand connects to one Ln_6 cluster by chelating coordination of its two oxygen atoms, remaining the third one uncoordinated. By this kind of linkage, every ligand joints four Ln_6 clusters while each Ln_6 cluster is connected with eight calixarene molecules. The calixarene molecules adopt a usual up–down "bilayer" arrangement to generate an interesting double layer structure, showing one-dimensional channels with a maximum height of ca.11.87 Å (Fig. 36). Considering calixarene anions as four-connected nodes and Ln_6 clusters as eight-connected nodes, the topology of the layer can be rationalized as a binodal (4, 8)-connected Al_2Os net with Schläfli symbol of $(4^{20}\,3\,6^8)(4^6)_2$. Ln-RPF9 shows a high adsorption of hydrogen compared with CO_2 or and CH_4, indicating it may be used as a H_2 absorber due to its high selectivity for this gas. Catalytic activity experiments show that Ln-RPF9 can also act as redox heterogeneous catalyst for the oxidation of methyl phenyl sulfide with a high ratio of substrate to metal (1,000:1).

More recently, two lanthanide compounds with nanosized decanuclear clusters, $[Ln_{10}(TBC8A)_2(PhPO_3)_4(\mu\text{-}H_2O)(\mu_3\text{-}OH)_4(\mu_4\text{-}OH)_2(DMF)_{14}] \cdot TBC8A \cdot x DMF \cdot y CH_3OH$ (for **61**, Ln=Pr, $x = 2$, $y = 2$; for **62**, Ln=Nd, $x = 0$, $y = 8$), were obtained by utilizing *p*-tert-butylcalix[8]arene (H_8TBC8A) (Su et al., unpublished work). The two compounds are isostructural. Taking compound **61** as a representative, four Pr^{3+} ions coordinate to eight lower-rim phenolic oxygen atoms from one fully deprotonated $TBC8A^{8-}$ ligand and one central μ_4-OH in the basal plane to form a double-cone tetranuclear Pr-calixarene entity. Then, two of the abovementioned double-cone entities are connected in a head-to-head style by one μ_2-H_2O, two Pr^{3+} ions, four μ_3-OH, and four $PhPO_3^{2-}$ ligands, forming a dumbbell-like cluster (Fig. 37). The distance between the two planes formed by

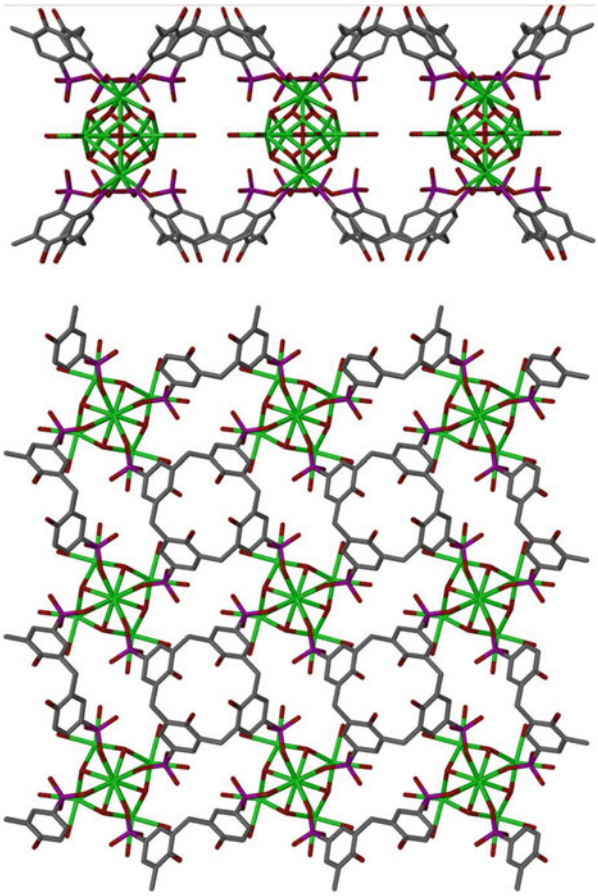

Fig. 36 The 2D layer constructed by hexanuclear lanthanide cluster and *p*-sulfonatocalix[4]arene ligand viewed from *a*-axis (top) and *c*-axis (*bottom*) in **58–60**

four Pr^{3+} ions from the upper and bottom of the dumbbell-like entity is about 5.05 Å. Each auxiliary phosphonate ligand binds to four Pr^{3+} ions adopting [4.112] coordination mode according to Harris notation to stabilize the cluster. Interestingly, the crystal structure of **61** contains an uncoordinated H_8TBC8A ligand, displaying a 2D layer constructed by them. Different from those in Pr_{10} cluster with double-cone conformations, the cocrystal uncoordinated H_8TBC8A molecules adopt pleated-loop conformations. Thus, the extended structure of compound contains two different kinds of layers: the Pr_{10} cluster layer and cocrystal H_8TBC8A layer (Fig. 38). These two different layers are separated by each other leading to sandwich-like arrays via weak interactions. The solid-state emission spectra at room temperature reveal compound **62** exhibiting the characteristic emissions of Nd^{3+} ion at the near-infrared region.

Besides pure lanthanide clusters, calixarenes can also help to construct 3d–4f heterometallic cluster. Two high-nuclearity 3d–4f heterometallic cluster-based compounds, $[Na_2Ni_{12}Ln_2(BTC4A)_3(\mu_7\text{-}CO_3)_3(\mu_3\text{-}OH)_4(\mu_3\text{-}Cl)_2(OAc)_6(dma)_4]\cdot 2OAc\cdot 0.5dma\cdot 3CH_3CN\cdot 8DMA$ (Ln=Dy for **63** and Tb for

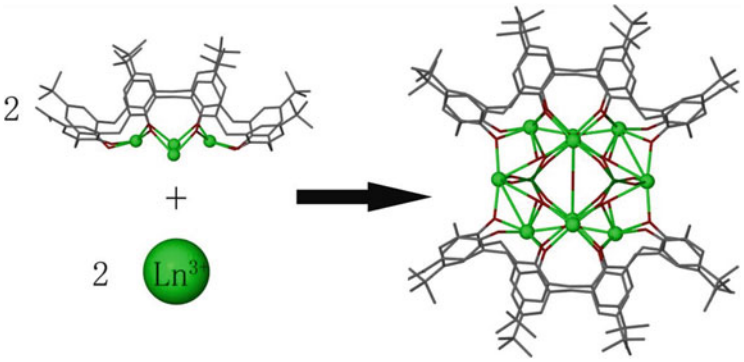

Fig. 37 The schematic map of formation of Ln_{10} cluster in **61**

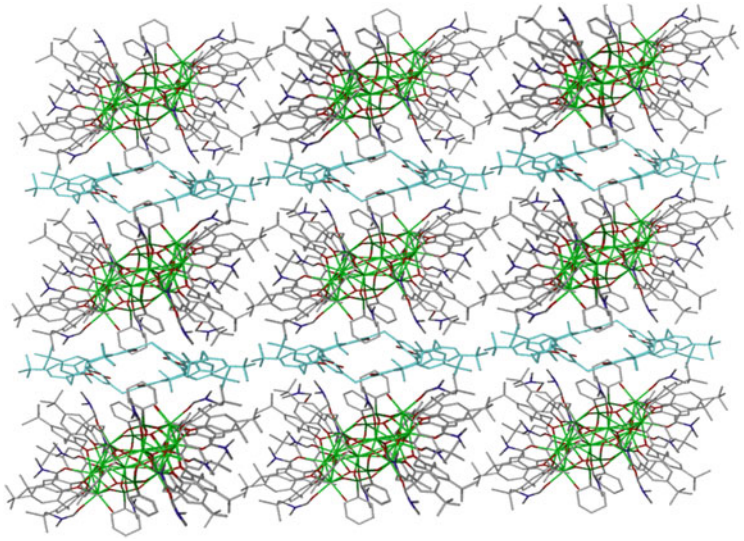

Fig. 38 The extended structure of **61**

64; H_4BTC4A = *p-tert*-butylthiacalix[4]arene, dma=dimethylamine, and DMA=*N*,*N*′-dimethylacetamide), were synthesized [115]. Every four Ni^{2+} ions bond to the lower-rim phenoxy oxygens and bridge sulfur atoms of one fully deprotonated $BTC4A^{4-}$ ligand leading to a shuttlecock-like building block of Ni^{II}_4-BTC4A, in which one carbonate anion acts as the cork base. Three subunits are linked together in an up-to-up fashion through four cations (two sodium ions and two Ln^{3+} ions) along with other anions (including two chloride anions, four hydroxide anions, and three acetate anions), leading to a pseudo-trigonal planar entity with heterometallic $Na_2Ni_{12}Ln_2$ cluster (Fig. 39). The formation of $Na_2Ni_{12}Ln_2$ can also be described as follows: (1) one Na^+, one Ln^{3+}, and two Ni^{2+} ions are connected by three oxygen and one chloride ions to form a cubane-like unit [$NaNi_2Ln$];

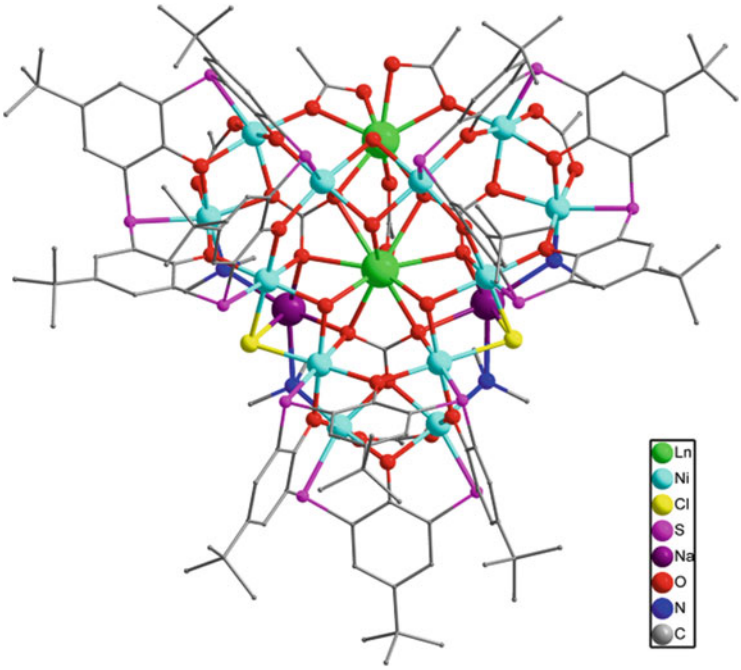

Fig. 39 Molecular structure of complexes **63** (Ln=Dy) and **64** (Ln=Tb). Reprinted with permission from [115]. © 2012 The Royal Society of Chemistry

(2) similarly, two Ln^{3+} and two Ni^{2+} are linked by two oxygen and two chloride ions to generate another cubane-like unit $[Ni_2Ln_2]$; (3) one $[Ni_2Ln_2]$ core and two $[NaNi_2Ln]$ units are further joint together by sharing one Ln^{3+} ion at the center to construct an unprecedented trinary–cubane cluster; and (4) the tricubane unit connects to six peripheral Ni^{2+} ions through three μ_7-carbonate anions, leading to the final $Na_2Ni_{12}Ln_2$ cluster (Fig. 40). Three $BTC4A^{4-}$ ligands are located on the trigonal plane of the tricubane core. It is worth to note that such vertex-fused tricubane unit possessing more than one metal elements has not been reported before. Upon crystal packing, the complex exhibits a bilayer structure with the pseudo-trigonal planar entities sitting in an up–down fashion. The frequency-dependent AC susceptibilities under zero DC field were also measured for the compounds. The results show that only Dy^{3+} complex exhibits slow magnetic relaxation behavior of single-molecule magnet nature. The possible reason might be the fact that the ground state of the Kramers ion Dy^{3+} is always degenerated while it is not the case for Tb^{3+} ion.

A hydrothermal reaction of $H_4BTC4A{\cdot}CHCl_3$, $Zn(OAc)_2{\cdot}2H_2O$, and $Ln(OAc)_3{\cdot}6H_2O$ in mixed solvent of DMF/CH_3OH at 120°C yielded four isomorphous colorless prismatic crystals, namely, $[Zn^{II}Ln^{III}{}_3(\mu_4\text{-}OH)(BTC4A)_2(OAc)_2(CH_3OH)(H_2O)(DMA)_2]{\cdot}3H_2O$ (Ln=Gd (**65**), Tb (**66**), Dy (**67**), Ho (**68**)) [116]. The single-crystal X-ray diffraction reveals that **65** contains four

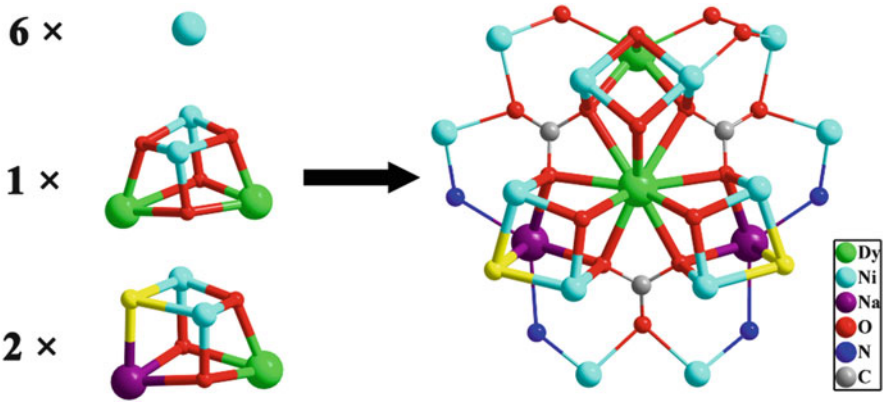

Fig. 40 The schematic map of formation of vertex-fused tricubane cluster in **63**

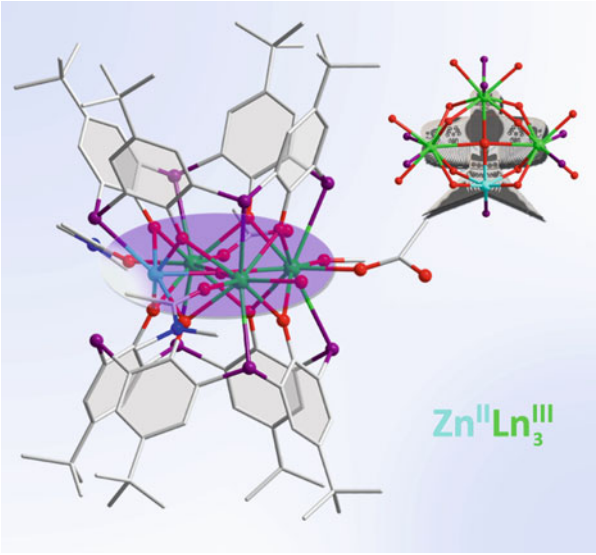

Fig. 41 The kite-like heterometallic tetranuclear $Zn^{II}Ln^{III}$ cluster. Reprinted with permission from [116]. © 2013 American Chemical Society

crystallographic unique metal ions, in which one Zn^{II} ion adopts six-coordinated mode while three Gd^{III} ions are eight coordinated. These four metal ions are bridged and complete the coordination environments by oxygen species, forming a kite-like tetranuclear core as shown in Fig. 41. All phenoxyl oxygen atoms are linked to two metal ions to stabilize the tetragonal $Zn^{II}Ln^{III}_3$ arrangement. In contrast to those formed in the routine antiparallel arrangements of the monometallic $BTC4A^{4-}$ sandwiches [117, 118], the heterometallic $Zn^{II}Ln^{III}_3$ square is surrounded by two tail-to-tail thiacalix[4]arene ligands to form a bent sandwich-like unit. The

formation of the bent sandwich-like unit can be ascribed as follows: (1) thiacalix[4]arene with four bridging sulfur atoms is more flexible than calix[4]arene, which can easily bind up to different metal ions simultaneously forming metal–thiacalix[4]arene clusters, and (2) the radius of zinc atom is smaller than the radius of gadolinium atom in the tetragonal $Zn^{II}Ln^{III}_3$ unit, which would lead the thiacalixarene molecules to be more inclined to zinc side. It is proposed that the degree of bent sandwich-like units can be modulated by changing composition and the radius ratio of metal ions, which further influences the properties of the cluster. The photoluminescent analyses reveal that the H_4BTC4A is an efficient sensitizer for Tb^{3+} ions in **66** and the magnetic properties show that complex **67** exhibits slow magnetization relaxation typical for single-molecule magnet nature.

5 Summary

In summary, the syntheses, structures, and the properties of metal–organic frameworks based on lanthanide clusters are reviewed. Based on lanthanide clusters, versatile metal–organic frameworks with intriguing topological structure can be obtained. The number of the nuclearity of lanthanide clusters as the secondary building units can vary from di- to octatetraconta-nuclei. The control of the hydrolysis of the lanthanide salts in the presence of supporting ligands is approved to be an efficient strategy for the synthesis of hydroxo–lanthanide clusters, in which electronegative guest anions can act as templates and induce the formation of the clusters. The size and the geometry of these anions will play a great role in the ultimate nuclearity and structures. On the other hand, the networks can also be modulated by the linkages between lanthanide clusters and the ligands. Appropriate ligands need to be elaborated selected, since they are most pivotal not only in the construction of lanthanide clusters but also in linking them to the extended metal–organic frameworks. The unusual bonding of lanthanide ions with monodentate N-donors can be realized under hydrothermal conditions. These lanthanide cluster-based metal–organic frameworks exhibit fascinating properties and may act as promising candidates especially in the fields of luminescence, magnetism, and catalysis. Despite with similar structures, the compounds containing different lanthanide ions usually show distinct chemical and physical properties, which may be due to the nature characteristic of the lanthanide ions.

Acknowledgements We thank the 973 Program (2011CBA00507, 2011CB932504, 2014CB932101) and National Natural Science Foundation of China (21131006, 21371169, 21390392).

Reference

1. Zhang QC, Bu XH, Lin Z, Biasini M, Beyermann WP, Feng PY (2007) Metal-complex-decorated homochiral heterobimetallic telluride single-stranded helix. Inorg Chem 46:7262–7264
2. Kitagawa S, Kitaura R, Noro S (2004) Functional porous coordination polymers. Angew Chem Int Ed 43:2334–2375
3. Meng XR, Song YL, Hou HW, Fan YT, Li G, Zhu Y (2003) Novel Pb and Zn coordination polymers: synthesis, molecular structures, and third-order nonlinear optical properties. Inorg Chem 42:1306–1315
4. Kondo M, Miyazawa M, Irie Y, Shinagawa R, Horiba T, Nakamura A, Naito T, Maeda K, Utsuno S, Uchida F (2002) A new Zn(II) coordination polymer with 4-pyridylthioacetate: assemblies of homo-chiral helices with sulfide sites. Chem Commun 2156–2157
5. Lee SJ, Hu AG, Lin WB (2002) First chiral organometallic triangle for asymmetric catalysis. J Am Chem Soc 124:12948–12949
6. Zhang J, Chen SM, Wu T, Feng PY, Bu XH (2008) Homochiral crystallization of microporous framework materials from achiral precursors by chiral catalysis. J Am Chem Soc 130:12882–12883
7. Seo JS, Whang D, Lee H, Jun SI, Oh J, Jeon YJ, Kim K (2000) A homochiral metal-organic porous material for enantioselective separation and catalysis. Nature 404:982–986
8. Prins LJ, Huskens J, de Jong F, Timmerman P, Reinhoudt DN (1999) Complete asymmetric induction of supramolecular chirality in a hydrogen-bonded assembly. Nature 398:498–502
9. Chin J, Lee SS, Lee KJ, Park S, Kim DH (1999) A metal complex that binds alpha-amino acids with high and predictable stereospecificity. Nature 401:254–257
10. Bu XH, Liu H, Du M, Zhang L, Guo YM, Shionoya M, Ribas J (2002) New mononuclear, cyclic tetranuclear, and 1-D helical-chain Cu(II) complexes formed by metal-assisted hydrolysis of 3,6-di-2-pyridyl-1,2,4,5-tetrazine (DPTZ): crystal structures and magnetic properties. Inorg Chem 41:1855–1861
11. Wang XL, Chao Q, Wang EB, Lin X, Su ZM, Hu CW (2004) Interlocked and interdigitated architectures from self-assembly of long flexible ligands and cadmium salts. Angew Chem Int Ed 43:5036–5040
12. Cui Y, Ngo HL, White PS, Lin WB (2002) Homochiral 3D lanthanide coordination networks with an unprecedented $4^9 6^6$ topology. Chem Commun 1666–1667
13. Chen XM, Liu GF (2002) Double-stranded helices and molecular zippers assembled from single-stranded coordination polymers directed by supramolecular interactions. Chem Eur J 8:4811–4817
14. Xiong RG, You XZ, Abrahams BF, Xue ZL, Che CM (2001) Enantioseparation of racemic organic molecules by a zeolite analogue. Angew Chem Int Ed 40:4422–4425
15. Wang HY, Cheng JY, Ma JP, Dong YB, Huang RQ (2010) Synthesis and characterization of new coordination polymers with tunable luminescent properties generated from bent 1,2,4-triazole-bridged N, N′-dioxides and Ln(III) salts. Inorg Chem 49:2416–2426
16. Liu QK, Ma JP, Dong YB (2010) Adsorption and separation of reactive aromatic isomers and generation and stabilization of their radicals within cadmium(II)-triazole metal-organic confined space in a single-crystal-to-single-crystal fashion. J Am Chem Soc 132:7005–7017
17. Leroux YR, Lacroix JC, Chane-Ching KI, Fave C, Felidj N, Levi G, Aubard J, Krenn JR, Hohenau A (2005) conducting polymer electrochemical switching as an easy means for designing active plasmonic devices. J Am Chem Soc 127:16022–16023
18. Seminario JM, De La Cruz C, Derosa PA, Yan LM (2004) Nanometer-size conducting and insulating molecular devices. J Phys Chem B 108:17879–17885
19. Lan AJ, Li KH, Wu HH, Olson DH, Emge TJ, Ki W, Hong MC, Li J (2009) A luminescent microporous metal-organic framework for the fast and reversible detection of high explosives. Angew Chem Int Ed 48:2334–2338

20. Li KH, Olson DH, Seidel J, Emge TJ, Gong HW, Zeng HP, Li J (2009) Zeolitic imidazolate frameworks for kinetic separation of propane and propene. J Am Chem Soc 131:10368–10369
21. Li KH, Lee J, Olson DH, Emge TJ, Bi WH, Eibling MJ, Li J (2008) Unique gas and hydrocarbon adsorption in a highly porous metal-organic framework made of extended aliphatic ligands. Chem Commun 6123–6125
22. Cui YJ, Yue YF, Qian GD, Chen BL (2012) Luminescent functional metal-organic frameworks. Chem Rev 112:1126–1162
23. Allendorf MD, Bauer CA, Bhakta RK, Houk RJT (2009) Luminescent metal-organic frameworks. Chem Soc Rev 38:1330–1352
24. Rocha J, Carlos LD, Almeida Paz FA, Ananias D (2011) Luminescent multifunctional lanthanides-based metal-organic frameworks. Chem Soc Rev 40:926–940
25. Bhunia A, Gotthardt MA, Yadav M, Gamer MT, Eichhöfer A, Kleist W, Roesky PW (2013) Salen-based coordination polymers of manganese and the rare-earth elements: synthesis and catalytic aerobic epoxidation of olefins. Chem Eur J 19:1986–1995
26. Qiu Y, Liu H, Ling Y, Deng H, Zeng R, Zhou G, Zeller M (2007) 3D Ln-Ag (Ln=Nd; Eu) coordination polymers based on N- and O-donor ligands: synthesis, crystal structures and luminescence. Inorg Chem Commun 10:1399–1403
27. Qiu YC, Liu ZH, Mou JX, Deng H, Zeller M (2010) Rationally designed and controlled syntheses of different series of 4d-4f heterometallic coordination frameworks based on lanthanide carboxylate and $Ag(IN)_2$ substructures. CrystEngComm 12:277–290
28. Bu XH, Weng W, Du M, Chen W, Li JR, Zhang RH, Zhao LJ (2002) Novel lanthanide(III) coordination polymers with 1,4-bis(phenyl-sulfinyl)butane forming unique lamellar square array: syntheses, crystal structures, and properties. Inorg Chem 41:1007–1010
29. Li JR, Bu XH, Zhang RH (2004) Novel lanthanide coordination polymers with a flexible disulfoxide ligand, 1,2-bis(ethylsulfinyl)ethane: structures, stereochemistry, and the influences of counteranions on the framework formations. Inorg Chem 43:237–244
30. Li JR, Bu XH, Zhang RH, Duan CY, Wong KMC, Yam VWW (2004) Lanthanide perchlorate complexes with 1,4-bis(phenylsulfinyl)butane: structures and luminescent properties. New J Chem 28:261–265
31. Sun YQ, Zhang J, Chen YM, Yang GY (2005) Porous lanthanide-organic open frameworks with helical tubes constructed from interweaving triple-helical and double-helical chains. Angew Chem Int Ed 44:5814–5817
32. Sun YQ, Zhang J, Yang GY (2006) Two novel luminescent lanthanide sulfate-carboxylates with an unusual 2-D bamboo-raft-like structure based on the linkages of left- and right-handed helical tubes involving in situ decarboxylation. Chem Commun 1947–1949
33. Huang YG, Wu BL, Yuan DQ, Xu YQ, Jiang FL, Hong MC (2007) New lanthanide hybrid as clustered infinite nanotunnel with 3D Ln-O-Ln framework and (3,4)-connected net. Inorg Chem 46:1171–1176
34. Deng ZP, Huo LH, Wang HY, Gao S, Zhao H (2010) A series of three-dimensional lanthanide metal-organic frameworks with biphenylethene-4,4′-dicarboxylic acid: hydrothermal syntheses and structures. CrystEngComm 12:1526–1535
35. Tranchemontagne DJ, Mendoza-Cortes JL, O'Keeffe M, Yaghi OM (2009) Secondary building units, nets and bonding in the chemistry of metal-organic frameworks. Chem Soc Rev 38:1257–1283
36. Tranchemontagne J, Ni Z, O'Keeffe M, Yaghi OM (2008) Reticular chemistry of metal-organic polyhedra. Angew Chem Int Ed 47:5136–5147
37. Perry JJ IV, Perman JA, Zaworotko MJ (2009) Design and synthesis of metal-organic frameworks using metal-organic polyhedra as supermolecular building blocks. Chem Soc Rev 38:1400–1417
38. Ulrich S (2011) Cluster-based inorganic–organic hybrid materials. Chem Soc Rev 40:575–582

39. Kong XJ, Wu YL, Long LS, Zheng LS, Zheng ZP (2009) A chiral 60-metal sodalite cage featuring 24 vertex-sharing $[Er_4(\mu_3\text{-}OH)_4]$ cubanes. J Am Chem Soc 131:6918–6919
40. Cheng JW, Zhang J, Zheng ST, Zhang MB, Yang GY (2006) Lanthanide-transition-metal sandwich framework comprising $\{Cu_3\}$ cluster pillars and layered networks of $\{Er_{36}\}$) wheels. Angew Chem Int Ed 45:73–77
41. Zhao B, Cheng P, Chen XY, Cheng C, Shi W, Liao DZ, Yan SP, Jiang ZH (2004) Design and synthesis of 3d-4f metal-based zeolite-type materials with a 3D nanotubular structure encapsulated "water" pipe. J Am Chem Soc 126:3012–3013
42. Wang RY, Carducci MD, Zheng ZP (2000) Direct hydrolytic route to molecular oxo-hydroxo lanthanide clusters. Inorg Chem 39:1836–1837
43. Tang XL, Wang WH, Dou W, Jiang J, Liu WS, Qin WW, Zhang GL, Zhang HR, Yu KB, Zheng LM (2009) Olive-shaped chiral supramolecules: simultaneous self-assembly of heptameric lanthanum clusters and carbon dioxide fixation. Angew Chem Int Ed 48:3499–3502
44. Malaestean IL, Ellern A, Baca S, Kogerler P (2012) Cerium oxide nanoclusters: commensurate with concepts of polyoxometalate chemistry. Chem Commun 48:1499–1501
45. Xu G, Wang ZM, He Z, Lu Z, Liao CS, Yan CH (2002) Synthesis and structural characterization of nonanuclear lanthanide complexes. Inorg Chem 41:6802–6807
46. Wang R, Selby HD, Liu H, Carducci MD, Jin T, Zheng Z, Anthis JW, Staples RJ (2002) Halide-templated assembly of polynuclear lanthanide-hydroxo complexes. Inorg Chem 41:278–286
47. Zheng Y, Zhang QC, Long LS, Huang RB, Müller A, Schnack J, Zheng LS, Zheng ZP (2013) Molybdate templated assembly of $Ln_{12}Mo_4$-type clusters (Ln=Sm, Eu, Gd) containing a truncated tetrahedron core. Chem Commun 49:36–38
48. Chang LX, Xiong G, Wang L, Cheng P, Zhao B (2013) A 24-Gd nanocapsule with a large magnetocaloric effect Chem Commun 49:1055–1057
49. Xu J, Raymond KN (2000) Lord of the rings: An octameric lanthanum pyrazolonate cluster. Angew Chem Int Ed 39:2745–2747
50. Kajiwara T, Wu H, Ito T, Iki N, Miyano S (2004) Octalanthanide wheels supported by p-tert-butylsulfonylcalix[4]arene. Angew Chem Int Ed 43:1832–1835
51. Huang YG, Jiang FL, Yuan DQ, Wu MY, Gao Q, Wei W, Hong MC (2008) A prototypical zeolitic lanthanide-organic framework with nanotubular structure. Cryst Growth Des 8:166–168
52. Baerlocher C, Meier WM, Olson DH (2001) Atlas of zeolite framework types. Elsevier, Amsterdam
53. Guo XD, Zhu GS, Li ZY, Chen Y, Li XT, Qiu SL (2006) Rare earth coordination polymers with zeolite topology constructed from 4-connected building units. Inorg Chem 45:4065–4070
54. Spek LA (1999) Multipurpose crystallographic tool. Utrecht University, Utrecht
55. Jhung SH, Yoon JW, Kim HK, Chang JS (2005) Low temperature adsorption of hydrogen on nanoporous materials. Bull Korean Chem Soc 26:1075–1078
56. Jhung SH, Kim HK, Yoon JW, Chang JS (2006) Low-temperature adsorption of hydrogen on nanoporous aluminophosphates: effect of pore size. J Phys Chem B 110:9371–9374
57. Hou HW, Li G, Li LK, Zhu Y, Meng XR, Fan YT (2003) Synthesis, crystal structures, and magnetic properties of three novel ferrocenecarboxylato-bridged lanthanide dimers. Inorg Chem 42:428–435
58. Huang YG, Jiang FL, Yuan DQ, Wu MY, Gao Q, Wei W, Hong MC (2009) Intricate 3D lanthanide-organic frameworks with mixed nodes nets. J Solid State Chem 182:215–222
59. Feng R, Jiang FL, Wu MY, Chen L, Yan CF, Hong MC (2010) Structures and photoluminescent properties of the lanthanide coordination complexes with hydroxyquinoline carboxylate ligands. Cryst Growth Des 10:2306–2313
60. Gschneidner KA., Eyring L, Lander GH (eds) (2001) Handbook on the physics and chemistry of rare earths, vol. 32. Elsevier, Amsterdam

61. Gai YL, Xiong KC, Chen L, Bu Y, Li XJ, Jiang FL, Hong MC (2012) Visible and NIR photoluminescence properties of a series of novel lanthanide-organic coordination polymers based on hydroxyquinoline-carboxylate ligands. Inorg Chem 51:13128–13137
62. Wu MY, Jiang FL, Zhou YF, Feng R. Chen L, Hong MC (2012) Photoluminescences and 1D chain-like structures with dinuclear lanthanide(III) units featuring bipyridine-tetracarboxylate. Inorg Chem Commun 15:25–28
63. Ma J, Jiang FL, Chen L, Wu MY, Zhang SQ, Xiong KC, Han D, Hong MC (2012) Structure and photoluminescent properties of lanthanide coordination polymers based on two isomers of iminodiacetic acid substituted isophthalate and terephthalate ligands. CrystEngComm 14:6055–6063
64. Gai YL, Jiang FL, Chen L, Bu Y, Su KZ, Al-Thabaiti SA, Hong MC (2013) Photophysical studies of europium coordination polymers based on a tetracarboxylate ligand. Inorg Chem 52:7658–7665
65. Freund C, Porzio W, Giovanella U, Vignali F, Pasini M, Destri S, Mech A, Di Pietro S, Di Bari L, Mineo P (2011) Thiophene based europium ß-diketonate complexes: effect of the ligand structure on the emission quantum yield. Inorg Chem 50:5417–5429
66. Eliseeva SV, Pleshkov DN, Lyssenko KA, Lepnev LS, Bunzli JC, Kuzmina NP (2011) Deciphering three beneficial effects of 2,2′-bipyridine-N, N′-dioxide on the luminescence sensitization of lanthanide(III) hexafluoroacetylacetonate ternary complexes. Inorg Chem 50:5137–5144
67. Sivakumar S, Reddy ML, Cowley AH, Butorac RR (2011) Lanthanide-based coordination polymers assembled from derivatives of 3,5-dihydroxy benzoates: syntheses, crystal structures, and photophysical properties. Inorg Chem 50:4882–4891
68. Gai YL, Jiang FL, Chen L, Wu MY, Su KZ, Pan J, Wan XY, Hong MC (2014) Europium and terbium coordination polymers assembled from hexacarboxylate ligands: structures and luminescent properties. Cryst Growth Des 14:1010–1017
69. Sang RL, Xu L (2013) Unprecedented infinite lanthanide hydroxide ribbons $[Ln_3(\mu_3\text{-}OH)_3]_n^{6n+}$ in a 3-D metal-organic framework. Chem Commum 49:8344–8346
70. Ke HS, Xu GF, Zhao L, Tang JK, Zhang XY, Zhang HJ (2009) A Dy_{10} cluster incorporates two sets of vertex-sharing Dy_3 triangles. Chem Eur J 15:10335–10338
71. Miao YL, Liu JL, Leng JD, Lin ZJ, Tong ML (2011) Chloride templated formation of $\{Dy_{12}(OH)_{16}\}^{20+}$ cluster core incorporating 1,10-phenanthroline-2,9-dicarboxylate. CrystEngComm 13:3345–3348
72. Bürgstein MR, Gamer MT, Roesky PW (2004) Nitrophenolate as a building block for lanthanide chains, layers, and clusters. J Am Chem Soc 126:5213–5218
73. Wang RY, Zheng ZP, Jin TZ, Staples RJ (1999) Coordination chemistry of lanthanides at "high" pH: synthesis and structure of the pentadecanuclear complex of europium(III) with tyrosine. Angew Chem Int Ed 38:1813–1815
74. Zheng ZP (2001) Ligand-controlled self-assembly of polynuclear lanthanide-oxo/hydroxo complexes: from synthetic serendipity to rational supramolecular design. Chem Commun 2521–2529
75. Kong XJ, Long LS, Zheng LS, Wang RY, Zheng ZP (2009) Hydrolytic synthesis and structural characterization of lanthanide hydroxide clusters supported by nicotinic acid. Inorg Chem 48:3268–3273
76. Zhang HJ, Wang XZ, Zhu DR, Song Y, Xu Y, Xu H, Shen X, Gao T, Huang MX (2011) Novel 3D lanthanide-organic frameworks with an unusual infinite nanosized ribbon $[Ln_3(\mu_3\text{-}OH)_2(CO_2)_6]_n^+$ (Ln=Eu, Gd, Dy): syntheses, structures, luminescence, and magnetic properties. CrystEngComm 13:2586–2592
77. Ma BQ, Zhang DS, Gao S, Jin TZ, Yan CH, Xu GX (2000) From cubane to supercubane: the design, synthesis, and structure of a three-dimensional open framework based on a Ln_4O_4 cluster. Angew Chem Int Ed 39:3644–3646

78. Li X, Sun HL, Wu XS, Qiu X, Du M (2010) Unique (3,12)-connected porous lanthanide-organic frameworks based on Ln_4O_4 clusters: synthesis, crystal structures, luminescence, and magnetism. Inorg Chem 49:1865–1871
79. McMasters OD, Gschneidner KA Jr, Brizzone G, Palenzona AJ (1971) Stoichiometry, crystal structures and some melting points of lanthanide-gold alloys. Less-common Met 25:135–160
80. Wang WH, Tian HR, Zhou ZC, Feng YL, Cheng JW (2012) Two unusual chiral lanthanide-sulfate frameworks with helical tubes and channels constructed from interweaving two double-helical chains. Cryst Growth Des 12:2567–2571
81. Shi FN, Cunha-Silva L, Trindade T, Almeida Paz FA, Rocha J (2009) Three-dimensional lanthanide-organic frameworks based on di-, tetra-, and hexameric clusters. Cryst Growth Des 9:2098–2109
82. Shi PF, Zheng YZ, Zhao XQ, Xiong G, Zhao B, Wan FF, Cheng P (2012) 3D MOFs containing trigonal bipyramidal Ln_5 clusters as nodes: large magnetocaloric effect and slow magnetic relaxation behavior. Chem Eur J 18:15086–15091
83. Lu WG, Jiang L, Feng XL, Lu TB (2009) Three-dimensional lanthanide anionic metal-organic frameworks with tunable luminescent properties induced by cation exchange. Inorg Chem 48:6997–6999
84. Yuan N, Sheng TL, Tian CB, Hu SM, Fu RB, Zhu QL, Tan CH, Wu XT (2011) Syntheses, structures and properties of three-dimensional lanthanide frameworks constructed with a trigonal anti-prismatic lanthanide cluster. CrystEngComm 13:4244–4250
85. Bernini MC, Snejko N, Gutierrez-Puebla E, Monge A (2011) From globular star-shaped molecules to self-assembled nano-spheres: a novel scandium croconate polynuclear complex. CrystEngComm 13:1797–1800
86. Fleming S, Gutsche CD, Harrowfield JM, Ogden MI, Skelton BW, Stewart DF, White AH (2003) calixarenes as aryloxides: oligonuclear europium(III) derivatives. Dalton Trans 3319–3327
87. Canaj AB, Tzimopoulos DI, Philippidis A, Kostaki GE, Millios CJ (2012) A strongly blue-emitting heptametallic $[Dy^{III}_7]$ centered-octahedral single-molecule magnet. Inorg Chem 51:7451–7453
88. Zheng XJ, Jin LP, Gao S (2004) Synthesis and characterization of two novel lanthanide coordination polymers with an open framework based on an unprecedented $[Ln_7(\mu_3\text{-}OH)_8]^{13+}$ cluster. Inorg Chem 43:1600–1602
89. Fang WH, Cheng L, Huang L, Yang GY (2013) A series of lanthanide-based cluster organic frameworks made of heptanuclear trigonal-prismatic cluster units. Inorg Chem 52:6–8
90. Blatov VA, Shevchenko AP, Serezhkin VN (2000) TOPOS3.2: a new version of the program package for multipurpose crystal-chemical analysis. J Appl Crystallogr 33:1193
91. Spek AL (2003) Single-crystal structure validation with the program PLATON. J Appl Crystallogr 36:7–13
92. Zhang MB, Zhang J, Zheng ST, Yang GY (2005) A 3D coordination framework based on linkages of nanosized hydroxo lanthanide clusters and copper centers by isonicotinate ligands. Angew Chem Int Ed 44:1385–1388
93. Huang L, Han LJ, Feng WJ, Zheng L, Zhang ZB, Xu Y, Chen Q, Zhu DR, Sy N (2010) Two 3D coordination frameworks based on nanosized huge Ln_{26} (Ln=Dy and Gd) spherical clusters. Cryst Growth Des 10:2548–2552
94. Sen R, Hazra DK, Mukherjee M, Koner S (2011) Gd_{26} cluster consisting of distorted cubane cores: synthesis, structure and heterogeneous catalytic epoxidation of olefins. Eur J Inorg Chem 2826–2831
95. Gu XJ, Xue DF (2007) Surface modification of high-nuclearity lanthanide clusters: two tetramers constructed by cage-shaped $\{Dy_{26}\}$ clusters and isonicotinate linkers. Inorg Chem 46:3212–3216
96. Sen R, Hazra DK, Koner S, Helliwell M, Mukherjee M, Bhattacharjee A (2010) Hydrothermal synthesis of dimeric lanthanide compounds X-ray structure, magnetic study and heterogeneous catalytic epoxidation of olefins. Polyhedron 29:3183–3191

97. Sen R, Hazra DK, Koner S, Helliwell M, Mukherjee M (2011) Heterogeneous catalytic epoxidation of olefins over hydrothermally synthesized lanthanide containing framework compounds. J Inorg Chem 241–248
98. Wu MY, Jiang FL, Kong XJ, Yuan DQ, Long LS, Al-Thabaiti SA, Hong MC (2013) Two polymeric 36-metal pure lanthanide nanosize clusters. Chem Sci 4:3104–3109
99. Kong XJ, RenYP LLS, Zheng ZP, Nochol G, Huang RB, Zheng LS (2008) Dual shell-like magnetic clusters containing Ni^{II} and Ln^{III} (Ln=La, Pr, and Nd) ions. Inorg Chem 47:2728–2739
100. Kostakis GE, Perlepes SP, Blatov VA, Proserpio DM, Powell AK (2012) High-nuclearity cobalt coordination clusters: synthetic, topological and magnetic aspects. Coord Chem Rev 256:1246–1278
101. Kostakis GE, Blatov VA, Proserpio DM (2012) A method for topological analysis of high nuclearity coordination clusters and its application to Mn coordination compounds. Dalton Trans 41:4634–4640
102. Wu MY, Jiang FL, Yuan DQ, Pang JD, Qian JJ, Al-Thabaiti SA, Hong MC (2014) Polymeric double-anion templated Er_{48} nanotubes. Chem Commun 50:1113–1115
103. Chen L, Guo JY, Xu X, Ju WW, Zhang D, Zhu DR, Xu Y (2013) A novel 2-D coordination polymer constructed from high-nuclearity waist drum-like pure Ho_{48} clusters. Chem Commun 49:9278–9730
104. Xiong KC, Jiang FL, Gai YL, Yuan DQ, Chen L, Wu MY, Su KZ, Hong MC (2012) Truncated octahedral coordination cage incorporating six tetranuclear-metal building blocks and twelve linear edges. Chem Sci 3:2321–2325
105. Xiong KC, Jiang FL, Gai YL, Yuan DQ, Han D, Ma J, Zhang SQ, Hong MC (2012) Chlorine-Induced assembly of a cationic coordination cage with a μ_5-carbonato-bridged Mn^{II}_{24} core. Chem Eur J 18:5536–5540
106. Xiong KC, Jiang FL, Gai YL, Zheng HG, Yuan DQ, Chen L, Hong MC (2012) Self-assembly of thiacalix[4]arene-supported nickel(II)/cobalt(II) complexes sustained by in situ generated 5-methyltetrazolate ligand. Cryst Grow Des 12:3335–3341
107. Xiong KC, Jiang FL, Gai YL, Zhou YF, Yuan DQ, Su KZ, Wang XY, Hong MC (2012) A series of octanuclear-nickel(II) complexes supported by thiacalix[4]arenes. Inorg Chem 51:3283–3288
108. Wu MY, Wei W, Gao Q, Yuan DQ, Huang YG, Jiang FL, Hong MC (2009) Hydrogen-bonded helical array, sodium-ion-mediated head-to-tail chain, and regular ionic bilayer: structural diversities of p-sulfonatothiacalix[4]arene tetranuclear cluster units. Cryst Grow Des 9:1584–1589
109. Wu MY, Yuan DQ, Huang YG, Wei W, Gao Q, Jiang FL, Hong MC (2007) Captures of copper(II)-2,2′-bpy complexes in conformation-fixed homometallic anionic dimers and heterometallic clusters. Cryst Grow Des 7:1446–1451
110. Wu MY, Jiang FL, Hong MC (2009) Inclusion of p-sulfonatothiacalix[4] arene and its metal complexes. Chem Rec 9:155–168
111. Kajiwara T, Katagiri K, Taksishi S, Tamashita M, Iki N (2006) A dodecalanthanide wheel supported by p-tert-butylsulfonylcalix[4]aren. Chem Asian J 1:349–351
112. Sanz S, McIntosh MD, Beavers CM, Teat SJ, Evangelisti M, Brechin EK, Dalgarno SJ (2012) Calix[4]arene-supported rare earth octahedral. Chem Commun 48:1449–1451
113. Liu CM, Zhang DQ, Hao X, Zhu DB (2012) Syntheses, crystal structures, and magnetic properties of two p-tert-butylsulfonylcalix[4]arene supported cluster complexes with a totally disordered $Ln_4(OH)_4$ cubane core. Cryst Grow Des 12:2948–2954
114. Gándara F, Gutiérrez-Puebla E, Iglesias M, Snejko N, Monge MA (2010) Isolated hexanuclear hydroxo lanthanide secondary building units in a rare-earth polymeric framework based on p-sulfonatocalix[4]arene. Cryst Grow Des 10:128–134
115. Xiong KC, Wang XY, Jiang FL, Gai YL, Xu WT, Su KZ, Li XJ, Yuan DQ, Hong MC (2012) Heterometallic thiacalix[4]arene-supported $Na_2Ni^{II}_{12}Ln^{III}_2$ clusters with vertex-fused tricubane cores (Ln=Dy and Tb). Chem Commun 48:7456–7458

116. Su KZ, Jiang FL, Qian JJ, Wu MY, Xiong KC, Gai YL, Hong MC (2013) Thiacalix[4]arene-supported kite-like heterometallic tetranuclear $Zn^{II}Ln^{III}_3$ (Ln=Gd, Tb, Dy, Ho) complexes. Inorg Chem 52:3780–3786
117. Kajiwara T, Iki N, Tamashita M (2007) Transition metal and lanthanide cluster complexes constructed with thiacalix[n]arene and its derivatives. Coord Chem Rev 251:1734–1746
118. Bi YF, Wang XT, Liao WP, Wang XW, Deng RP, Zhang HJ, Gao S (2009) Thiacalix[4] arene-supported planar Ln_4 ($Ln=Tb^{III}$, Dy^{III}) clusters: toward luminescent and magnetic bifunctional materials. Inorg Chem 48:11743–11747

Struct Bond (2015) 163: 185–230
DOI: 10.1007/430_2014_156

Published online: 20 September 2014

Metal-Organic Frameworks with d–f Cyanide Bridges: Structural Diversity, Bonding Regime, and Magnetism

Marilena Ferbinteanu, Fanica Cimpoesu, and Stefania Tanase

Abstract We present a selection of metal-organic frameworks based on d–f and f–f linkages, discussing their structural features and properties from experimental and theoretical viewpoints. We give an overview of our own synthetic and modeling methodologies, highlighting the complexity of the interdisciplinary approach developed. Significant experimental and computational strategies of other researchers are also reviewed. The bonding regime of lanthanide units in MOFs is similar to those encountered in mono- or polynuclear f-type coordination compounds. However, the steric demands of constructing a three-dimensional network determine specific ligand composition and topologies at the local f nodes. Due to weak interaction propensity of the inner shell f orbitals, the electronic structure treatments of lanthanide units require certain conceptual and technical subtleties. With proper handling, multiconfiguration wave function approaches as well as density functional theory (DFT) treatments can be analyzed in terms of meaningful ligand field (LF) modeling. The interplay of LF and spin–orbit (SO) effects in determining the magnetic anisotropy is illustrated, after reviewing the experimental magnetic behavior of several d–f cyanide-bridged systems.

Keywords Computational chemistry • Cyanide bridges • Lanthanide ions • Ligand field theory • Magnetic anisotropy • Prussian blue analogues

M. Ferbinteanu
Faculty of Chemistry, Inorganic Chemistry Department, University of Bucharest, Dumbrava Rosie 23, Bucharest 020462, Romania

F. Cimpoesu
Institute of Physical Chemistry, Splaiul Independentei 202, Bucharest 060021, Romania

S. Tanase (✉)
Van't Hoff Institute for Molecular Sciences, University of Amsterdam, Science Park 904, 1098 XH Amsterdam, The Netherlands
e-mail: s.grecea@uva.nl

Contents

Abbreviations

ADF	Amsterdam density functional
AO	Atomic orbital
AOC	Average of configurations
bpy	2,2′-Bipyridyl
bpym	2,2′-Bipyrimidine
CASSCF	Complete active space self-consistent field
DFT	Density functional theory
DMF	Dimethylformamide
EDA	Energy decomposition analysis
H_2mpca	5-Methyl-2-pyrazine dicarboxylic acid
HF	Hartree–Fock
hfac	1,1,1,5,5,5-Hexafluoro-pentane-2,4-dionate
HINA	Isonicotinic acid
LF	Ligand field theory
LFDFT	Ligand field density functional theory
MO	Molecular orbital
MOF	Metal-organic framework
PBAs	Prussian blue analogues
PT2	Second-order perturbation
pz	Pyrazine
pzam	Pyrazine-2-carboxamide
ROHF	Restricted open-shell Hartree–Fock
SO	Spin–orbit
terpy	2,2:6′2″-Terpyridine

1 Introduction

The large magnetic anisotropy arising from the strong spin–orbit coupling combined with their optical characteristics makes lanthanide ions very attractive components for functional molecular materials, e.g., magnetic, optical, and magneto-optical materials. Recent excellent reviews illustrate these properties [1–5]. Using

lanthanide ions in molecular-based materials is often hampered by the weak magnetic exchange interaction between the lanthanide ions and the lanthanide ion and a transition metal ion. Consequently, the magnetic phase transitions of such materials occur at very low temperature. In an attempt to increase the magnetic exchange coupling between the lanthanide ions and transition metal ions, the ability of the cyanide ion to link various metal ions has been explored. This approach afforded a great diversity of structural architectures ranging from discrete polynuclear complexes to various three-dimensional networks [6]. In these cases, the cyanide ligand in addition to its structural function also provided an important exchange path mediating the interaction between electrons localized on paramagnetic centers. Generally, the investigation of cyanide-bridged compounds is a very active research field, and it has been the subject of several excellent reviews in the last years [7–13]. Analyzing the magnetic properties of lanthanide compounds is a difficult task because of the weak magnetic interactions and not detailed enough to define correctly the magnetic dimensionality of the systems. Nevertheless, recent studies have shown that the classical ligand field theory [14] is of a great help in rationalizing the energies of the low-lying levels of both the transition metal and the lanthanide ions [15–17].

This chapter is a collection of the literature on d–f metal-organic frameworks (MOFs) containing cyanide bridges, namely, 3D assemblies. This field develops slowly as compared with other MOFs. Therefore, we will cover the synthetic strategies developed so far for designing such molecular assemblies, and we will present their magnetic properties. We will discuss in detail our own contribution in this field, by presenting synthetic methodologies and theoretical approaches for understanding the magnetism in these compounds. Using ab initio calculations and appropriate interpretations to meet the chemical intuition and physical meaning, we will discuss here case studies rationalizing the bonding regime in d–f assemblies.

2 Examples of Three-Dimensional d–f Cyanide-Bridged Frameworks

2.1 Inorganic d–f Cyanide-Bridged Frameworks

The origin of magnetic d–f cyanide-bridged compounds, also known as Prussian blue analogues (PBAs), can be traced back to 1976 when Hulliger and coworkers reported the magnetic properties of $Ln[M(CN)_6]\cdot nH_2O$ compounds (M^{III}=Fe, Co, Cr) [18, 19]. These compounds have a 3D-extended structure with hexagonal or orthorhombic symmetry, depending on the number of crystallization water molecules [18, 19]. The dominant feature of the structure is the coordination number of eight or nine for the lanthanide ions [20]. It binds to six cyanide groups and two or three water molecules. The result is a 3D structure with cubic cages which accommodate additional water molecules [20]. The isostructural compounds Sm[Fe

$(CN)_6]\cdot 4H_2O$ and $Tb[Cr(CN)_6]\cdot 4H_2O$ exhibit very interesting magnetic properties. The former behaves as a ferromagnet below 3.5 K and it has a strong coercive field, while the latter has a high critical temperature of $T_c = 11.7$ K [18].

PBAs are considered a promising class of potentially porous magnetic materials [21]. Several studies show that dehydrating PBAs can result in significant changes of the magnetic properties or induced permanent porosity [21]. Few examples are known where both microporosity and bulk magnetic ordering coexist and they were reviewed recently [21]. However, all these examples include PBAs containing only transition metal ions [21]. So far, no efforts have been dedicated to studying the magnetic properties or the eventual induced porosity of lanthanide-based PBAs upon dehydration. Most of the studies are focused on downsizing lanthanide-based PBAs [22–25]. Yonekura and coworkers studied the influence of the lanthanide ion on the PBA morphology [25]. Specifically, they showed that $Sm[Fe(CN)_6]\cdot 4H_2O$ crystallizes as asterisks which are composed of tiny assembled Fe-CN-Sm nanocrystals of approximately 10–20 nm [25]. Gao and coworkers reported the shape-controlled synthesis of nanorods and nanobelts of $Sm[Fe(CN)_6]\cdot 4H_2O$ as well as their shape-dependent behavior [23]. They showed that the shape of the nanoscale material is the dominating factor for its coercivity due to the effect of shape anisotropy (Fig. 1). Indeed, $Sm[Fe(CN)_6]\cdot 4H_2O$ nanorods have a coercive field of 275 Oe, while the coercive field is only 785 Oe in the bulk $Sm[Fe(CN)_6]\cdot 4H_2O$ microrods [23]. The flexibility of the lanthanide-based PBAs toward cationic substitutions was also studied [26, 27]. Such studies demonstrated that major structural deformations do not occur.

The octahedral clusters of type $[M'_6Q_8(CN)_6]^{4-/3-}$ (M′=Re, Mo, W, Nb; Q=S, Se, Te) are topological analogues of the hexacyanometalate ions, $[M(CN)_6]^{3-/4-}$. They can also form polymeric arrays based on cyanide-bridged interactions. Fedorov and coworkers studied the interaction of $[M'_6Q_8(CN)_6]^{4-}$ and lanthanide ions under hydrothermal conditions [28–33]. They showed that the reaction between $[Re_6Se_8(CN)_6]^{3-}$ and heavy lanthanide ions gives 3D frameworks

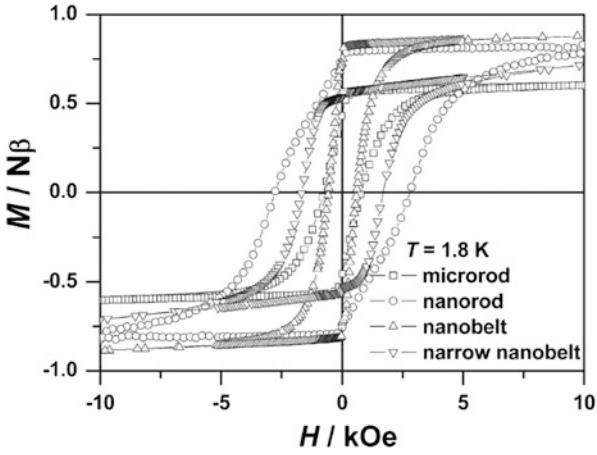

Fig. 1 The hysteresis loops for various shapes of $Sm[Fe(CN)_6]\cdot 4H_2O$. Reprinted from [23] with permission from The Royal Society of Chemistry

[33]. In these structures, the lanthanide ion is bound to five nitrogen atoms from five different cyanide clusters and three water molecules; the resulting framework has a (5,5) connectivity [33]. Notably, the structural topology of $[Ln(H_2O)_3Re_6Te_8(CN)_6]\cdot nH_2O$ (Ln=La, Nd) shows direct analogy with the PBAs of type $LnM(CN)_6\cdot nH_2O$ and $ALnM(CN)_6\cdot nH_2O$ (A=Na, K) [29]. It is a (5,5)-connected net in which the nodes are lanthanide ions in a regular triangular prismatic environment of six nitrogen atoms belonging to the cluster $[Re_6Te_8(CN)_6]^{3-}$ [29].

Designed synthesis of metal-organic frameworks using hexacyanometalate ions and lanthanide-based polyoxometalates (POMs) as building blocks was reported recently [34, 35]. The main difficulties associated with this strategy are the poor stability of the cyanometalate ions in hydrothermal synthesis as well as their negative charge. The latter makes the cyanometalates unable to overcome the charge repulsion from the negatively charged POMs. To overcome these drawbacks, Ohkoshi and coworkers built 3D multilayered structures by connecting positively charged ε-Keggin polyoxomolybdates of type $\{PMo_{12}Ln_4\}$ (Ln=La, Nd, Sm, Eu, Tb) with hexacyanoferrate ions, $[Fe(CN)_6]^{4-}$ [34, 35]. In these structures, the $\{PMo_{12}Ln_4\}$ units are assembled in 2D zigzag layers bridged by $[Fe(CN)_6]^{4-}$ (Fig. 2). Each hexacyanoferrate is connected to four different $\{PMo_{12}Ln_4\}$. The two remaining cyanide ligands are in *syn* position imposed by the bulky $\{PMo_{12}Ln_4\}$ units and form hydrogen bonds with some of the protonated oxygens from the neighboring $\{PMo_{12}Ln_4\}$. The result is $\{PMo_{12}Ln_4Fe(CN)_6\}_n$ layers which are packed together via hydrogen bonds to form a 3D framework containing 12 crystallization water molecules [34, 35]. These frameworks exhibit paramagnetism due to each Ln^{III} ion despite of the important electron delocalization on the POM structure [35].

Shore and coworkers reported the first synthetic route leading to Ln-CN-M linkages using $[M(CN)_4]^{2-}$ (M=Ni, Pt) building blocks [36]. This is a metathesis reaction between Ln^{III} salts and a cyanometalate salt, e.g., $[M(CN)_4]^{2-}$ (M=Ni, Pt), which is performed in highly polar solvents. Most of the compounds formed are 1D and 2D polymeric arrays [36]. A simple three-component metathesis reaction involving $LaCl_3$, CuCN, and KCN in DMF affords a 3D anionic lattice of type $\{[Cu_{12}(CN)_{18}]^{6-}\}$ (Fig. 3) [37]. The anionic lattice is built up of cyanide linkages between copper ions. Three cyanide groups are coordinated to each Cu^{I} in a distorted trigonal planar arrangement. The substructure of the anionic network is a twisted eight-membered ring (Fig. 3). An irregular-shaped pocket is formed by coupling five of these eight-membered rings with two ten-membered rings and one 12-membered ring. Each pocket hosts a guest $[La(DMF)_9]^{3+}$ cation and one free DMF molecule. The cation is truly encapsulated within the anionic cage since the largest pocket window (8.42×11.71 Å^2) is smaller than the width (14.72 Å) of the cation. Inhibition of the cation from leaving the pockets is assured by the strong electrostatic interactions between the cation and the anionic pocket and the smaller size of the pocket windows compared to the size of the solvated cation. Similar inclusion compounds are formed when smaller lanthanide cations (Ln=Eu, Gd, Er) are employed under the same reaction conditions [37, 38]. The only difference

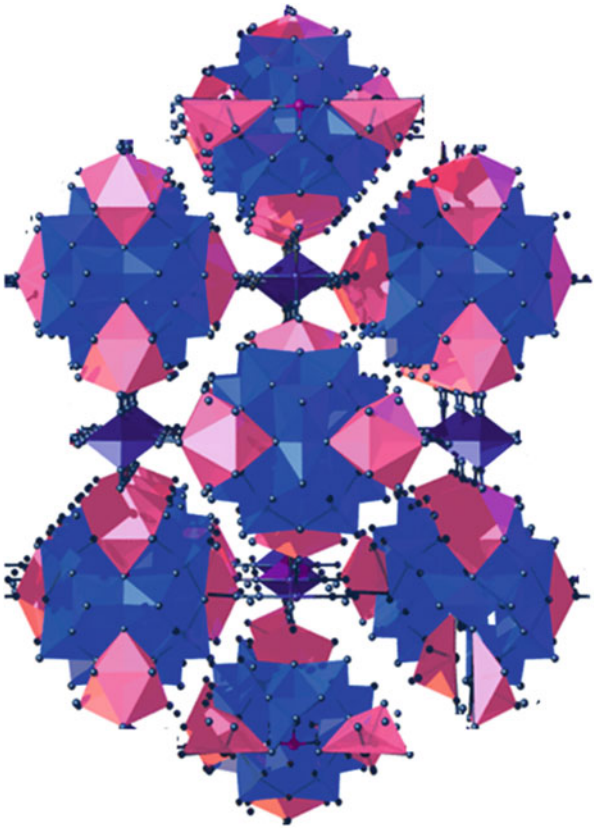

Fig. 2 The 3D packing of the $\{PMo_{12}La_4Fe(CN)_6\}_n$ metal-organic framework [34]

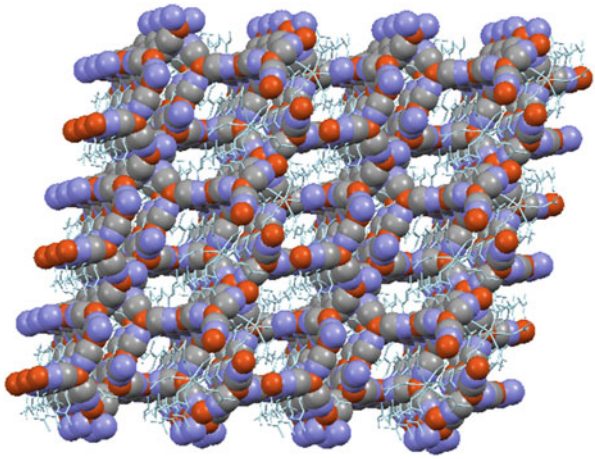

Fig. 3 3D view of $\{[La(DMF)_9]_2[Cu_{12}(CN)_{18}]\}\cdot 2DMF$ showing sequestered cations and free DMF molecules (in *blue stick style*) inside the pockets of the lattice (*spacefill*) [37]

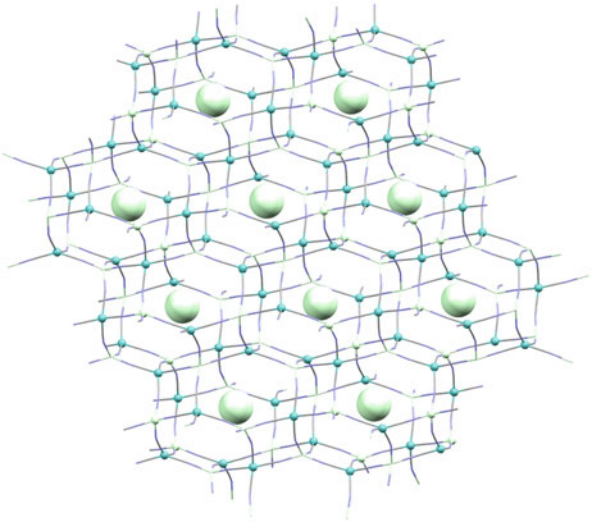

Fig. 4 3D view of the anionic $[Nd(CH_3OH)_4Mo(CN)_8]^{3-}$ framework showing the hexagonal channels and the guest $[Nd(H_2O)_8]^{3+}$ ions (*space-filling spheres*) [39]

compared to the La analogue is that the cation is eight coordinated, $[Ln(DMF)_8]^{3+}$, and therefore there are two encapsulated solvent molecules per anionic cage.

An interesting porous structure was obtained by reacting slowly Nd^{III} with $[Mo(CN)_8]^{3-}$ ions [39]. In this reaction, Mo^{V} is slowly reduced to Mo^{IV} at ambient conditions. The resulted structure has an open zeolite-like topology formed by the connection of $[Mo(CN)_8]^{4-}$ and $[Nd(CH_3OH)_4]^{3+}$ units through cyanide bridges (Fig. 4). The repeating unit is a cage composed of eight 18-membered rings (18-MRs): two of them define regular hexagonal channels (10.78×10.78 Å^2), and the other six define three ellipsoidal hexagonal channels (9.42×11.62 Å^2). These 18-MRs share their edges with each other and with six square 12-MRs (5.74×5.85 Å^2). Each cage has 14 neighbors: it shares its eight hexagonal faces with eight neighboring cages and its six square faces with six neighboring cages. One $[Nd(H_2O)_8]^{3+}$ ion and eight methanol molecule are encapsulated within the cages, being held by strong hydrogen-bonding interactions. Additionally, electrostatic interactions are established between the anionic cage and the cation $[Nd(H_2O)_8]^{3+}$. The 3D zeolite-like framework displays magnetic properties consistent with single-ion magnetic behavior for the Nd^{III} ions [39].

2.2 *Hybrid Organic–Inorganic d–f Cyanide-Bridged Frameworks*

Stepwise assembly of trinuclear $Co^{II}{}_2Ln^{III}(L)_2$ complexes (Ln=La, Gd; H_2L = 2,6-di(acetoacetyl)pyridine) and $[Cr(CN)_6]^{3-}$ ions affords isostructural 3D pillared-layer structures (Fig. 5) [40]. Four cyanide groups of the $[Cr(CN)_6]^{3-}$ ion coordinate to adjacent Co^{II} ions to form a 2D grid layer [40]. The trinuclear units are

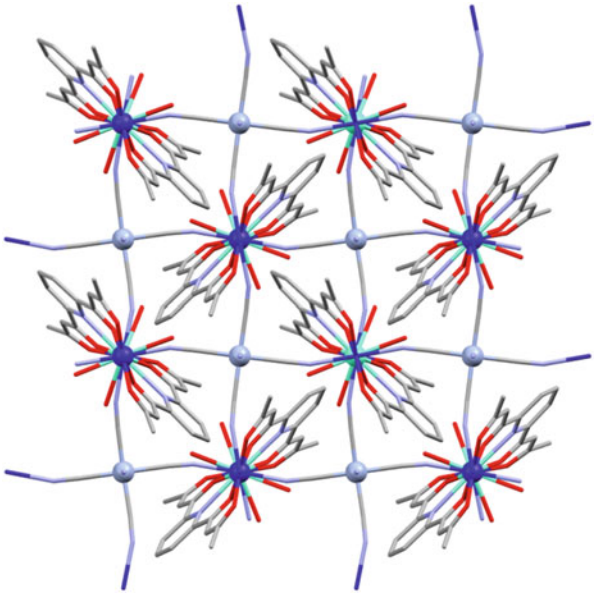

Fig. 5 Packing of $[Co_2Gd(L)_2(H_2O)_4][Cr(CN)_6]\cdot nH_2O$ along the *c*-axis [40]

arranged perpendicular to the 2D layers, and the two Co^{II} ions from the same trinuclear unit are each involved in different layers. Therefore, two types of 2D layers are aligned alternately along the *c*-axis and spliced by the $Co^{II}{}_2Ln^{III}(L)_2$ pillar affording a 3D framework with general formula $[Co_2Ln(L)_2(H_2O)_4][Cr(CN)_6]\cdot nH_2O$ [40]. Temperature-dependent magnetic susceptibility studies indicate the presence of antiferromagnetic exchange interactions in the CoLaCo units, while the exchange interaction is ferromagnetic in the CoGdCo units [40]. The magnetic exchange interaction in these units plays a key role in the overall magnetic phase (Fig. 6). The lanthanum compound shows a metamagnetic behavior ($T_c = 7.4$ K), while the gadolinium analogue shows a ferromagnetic behavior ($T_c = 15.4$ K) [40]. The latter value is one of the highest among the PBAs containing lanthanide ions.

The first truly porous compound containing cyanide-bridged Ln^{III} and $[Mo(CN)_8]^{4-}$ ions was reported by Tanase and coworkers [41]. They used the affinity of the lanthanide ions toward ligands containing hybrid oxygen–nitrogen donors, making in situ lanthanide building blocks. Then, they assembled them together with $[M(CN)_8]^{4-}$ ions to obtain highly robust porous networks of type $[Ln(mpca)_2(CH_3OH)_2Ln(H_2O)_6M(CN)_8]\cdot xCH_3OH\cdot yH_2O$ (Ln=Nd, Eu, Gd, Tb, Er; M=Mo, W) [41, 42]. These neutral 3D frameworks contain both cyanide and carboxylate bridges (Fig. 7). Each $[M(CN)_8]^{4-}$ ion is connected to three $[Ln(mpca)_2(CH_3OH)_2]^{+}$ units via cyanide bridges to form a 2D network of alternating diamond-like $Ln_2M_2(CN)_4$ features and octagonal $Ln_2M_2(CN)_4$ rings. A remarkable structural feature is the connection of the 2D networks through a second lanthanide ion. This connection occurs through the carboxylate group of one

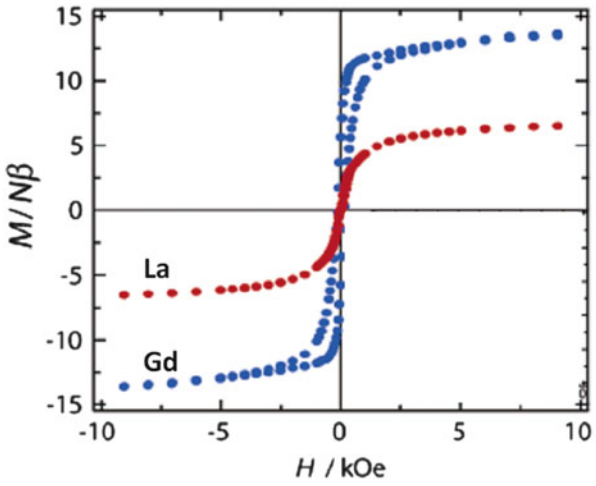

Fig. 6 Magnetic hysteresis loops for $[Co_2Ln(L)_2(H_2O)_4][Cr(CN)_6]\cdot nH_2O$. Adapted from [40] with permission from The American Chemical Society

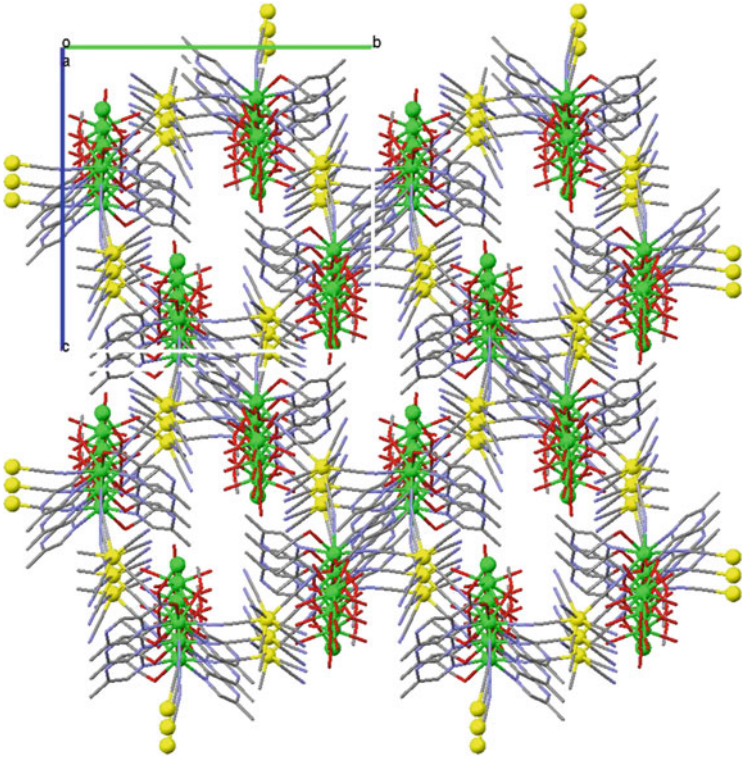

Fig. 7 The 3D structure of $[Ln(mpca)_2(CH_3OH)_2Ln(H_2O)_6M(CN)_8]\cdot xCH_3OH\cdot yH_2O$. Guest molecules were removed for clarity [41, 42]

mpca ligand. The result is a 3D structure with open channels which is further stabilized by multiple hydrogen-bonding interactions. The desolvated forms are stable up to 165°C and have moderate surface areas of 160–200 $m^2\ g^{-1}$ [42]. Notably, the Nd-containing framework exhibits a hysteresis behavior upon sorption–desorption of CO_2. This reflects a dynamic behavior due to the structural flexibility of $[M(CN)_8]^{4-}$ units. The magnetic properties show the presence of weak magnetic interactions between the lanthanide ions along the chains connecting the 2D sheets [41, 42]. Specifically, these interactions are antiferromagnetic between the Gd^{III} ions [41, 42] and ferromagnetic between the Tb^{III} ions [42]. Therefore, the ferromagnetic behavior of the Tb analogue coupled with its porosity may open exciting opportunities for developing new switchable magnetic materials.

Reacting neutral 2D layers of $[Ln(H_2O)_5W(CN)_8]$ and the pillared ligand pyrazine affords the 3D open frameworks $[Ln(H_2O)_4(pz)_{0.5}W(CN)_8]$ (Ln=La, Ce, Pr, Nd, Sm, Eu, Gd, Tb) [43, 44]. The Ln^{III} and $[W(CN)_8]^{3-}$ ions are connected through cyanide bridges in alternating manner, forming infinite 2D-corrugated layers. These layers are composed of 12-membered $Ln_2W_2(CN)_8$ squares with the Tb^{III} and W^{V} occupying the vertexes of the squares. The linear exo-bidentate pyrazine ligand acts as a pillar between adjacent layers leading to a 3D open framework (Fig. 8). The formation of this framework is highly dependent on the temperature. Below 33°C, the 2D $[Ln(H_2O)_5W(CN)_8]$ framework is highly stable, and it contains the terbium ions in nine-coordinated monocapped square antiprism geometry [44]. By heating this framework, one water molecule escapes the coordination sphere of the lanthanide ion. In the presence of an excess of pyrazine, the nine-coordinated geometry of the lanthanide ion is reestablished, resulting in the 3D framework $[Ln(H_2O)_4(pz)_{0.5}W(CN)_8]$ [44]. The magnetic properties of these compounds are dominated by the magnetic exchange interactions between lanthanide ions and W^{V}, demonstrating the minor role of the pyrazine in mediating magnetic exchange. Ferromagnetic interactions were observed between W^{V} and the Ce^{III}, Nd^{III}, Sm^{III}, and Tb^{III} ions, while antiferromagnetic interactions are operative between W^{V} and Pr^{III} and Gd^{III} ions [43, 44]. Notably, the analogues containing Ce and Sm exhibit long-range magnetic ordering below 2.8 K and 1.9 K, respectively.

CuCN is an attractive building block for constructing extended structures because the Cu^{I} ion exhibits versatile coordination features, including various coordination geometries and multiple $\{Cu_x(CN)_y\}_n$ substructures. The cyanide ion coordinated to Cu^{I} can act as a μ_1-, μ_2-, μ_3-, or μ_4-bridging ligand and therefore can form $\{Cu_x(CN)_y\}_n$ substructures with several topologies [45]. Using such building blocks, Deng and coworkers synthesized several Ln-NC-Cu frameworks with various 3D topologies [46]. Their approach is based on combining CuCN and lanthanide ions in the presence of isonicotinic acid (HINA), and it considers that both lanthanide and Cu^{I} ions possess different affinities for nitrogen and oxygen donors. The isonicotinate ion is able to bind lanthanide cations via the carboxylate groups to form lanthanide-containing motifs, and simultaneously bind to Cu^{I} via the pyridyl nitrogen atom. Thus, the isonicotinate ion is connecting the $\{Cu_x(CN)_y\}_n$ substructures with lanthanide-containing units to form 3D-extended frameworks

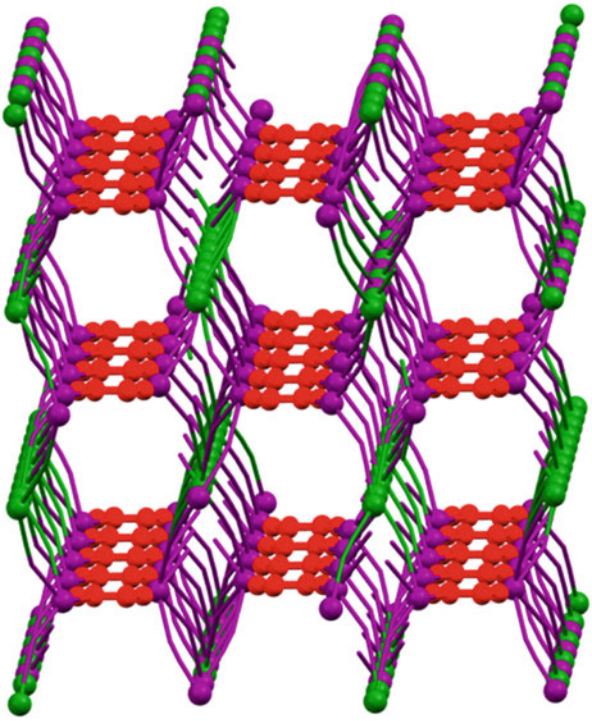

Fig. 8 2D-corrugated layers pillared by pyrazine ligands in the 3D framework of [Ln$(H_2O)_4(pz)_{0.5}W(CN)_8$] (Ln *purple*, W *green*, and pyrazine *red*) [43, 44]

[46]. Figure 9 highlights the role of the anion, pH value, and reaction temperature on the five structural topologies observed: (I) copper-inorganic entities viewed as double-stranded $\{Cu(CN)\}_\infty$ ribbons with projecting side arms, while Ln-organic motifs are zigzag chains; (II) copper-inorganic motifs are 2D $\{CuCl(CN)\}_\infty$ layers, and Ln-organic motifs are 1D chains possessing a parallel and alternating arrangement; (III) copper-inorganic motifs viewed as 2D layers, whereas the Ln-organic/Ln-inorganic motifs are fluoride-bridging 2D layers; (IV) the copper-inorganic motifs contain two unique types of 0D copper–cyanide units, and the Ln-organic counterparts are 1D chain structures linked by hydroxyl groups; and (V) the copper-inorganic motifs and the Ln-organic motifs are 2D layers that can both be topologically simplified to (4,4) networks [46].

An interesting 3D network structure based on Ru-CN-Gd bridge was obtained by reacting $Gd(hfac)_3(H_2O)_2$ and $K_4[\{Ru(CN)_4\}_2(\mu\text{-bpym})]$ in methanol solution (Fig. 10) [47]. In this framework, six cyanide ligands of the $[\{Ru(CN)_4\}_2(\mu\text{-bpym})]^{4-}$ bind six Gd^{III} centers to generate a network with square cross-sectional channels (Fig. 10). These channels are filled with ten water molecules which are involved in hydrogen-bonding interactions with each other but also with the water molecules coordinated to gadolinium.

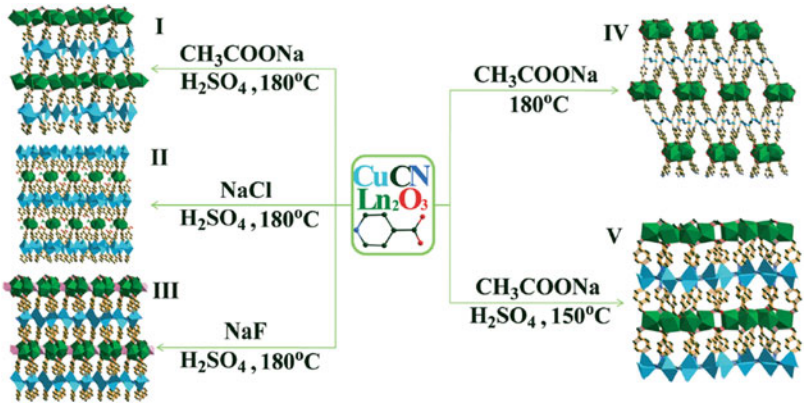

Fig. 9 Influence of the anion, reaction pH, and temperature on the topology of the Ln-NC-Cu frameworks. Reprinted from [46] with permission from The Royal Society of Chemistry

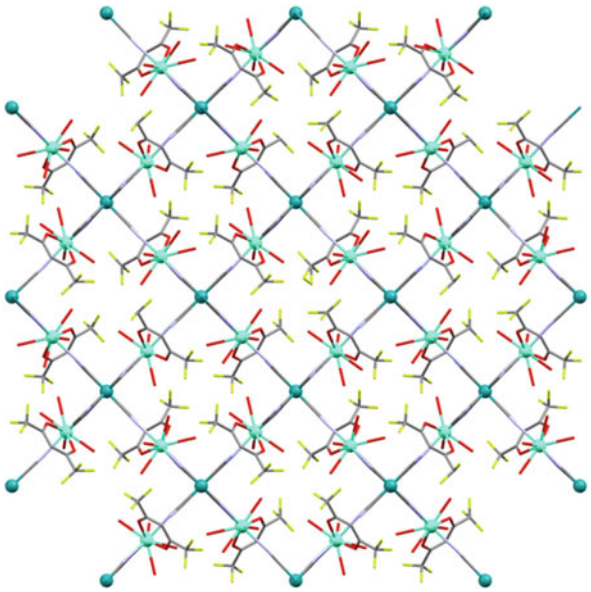

Fig. 10 The 3D structure of and $K_4[\{Ru(CN)_4\}_2(\mu\text{-bpym})][Gd(hfac)_3(H_2O)_2]_2$ showing the cross-sectional channels. The water molecules inside the channels are removed for clarity [47]

3 Experimental Studies on the Magnetism of d–f Cyanide-Bridged Assemblies

Studying the magnetic interaction in d–f assemblies is a difficult task because such interaction is usually weak and often masked by the crystal field effects on the magnetic interaction. Furthermore, the large unquenched orbital moment associated

with the f orbitals makes difficult the application of Hamiltonian schemes usually applied for the magnetism of transition metal ions. Diaz and coworkers have performed a detailed experimental analysis to ascertain the nature of the magnetic interaction between lanthanide ions and transition metal ions mediated by cyanide bridges [48–51]. They developed an experimental methodology in which the intrinsic magnetic properties of the lanthanide ion are determined by comparing the $\chi_M T$ versus T curve for two isostructural analogues (i.e., Ln-M and Ln-M′ where Ln is the lanthanide ion and M and M′ represent a paramagnetic and a diamagnetic transition metal ion) [48–51]. It was assumed that no interaction is operative if the sum of the magnetization values of the pairs containing a diamagnetic center equals that of the magnetic one. Significant deviations indicate ferro- or antiferromagnetic interactions. The approach was used to understand the magnetic exchange interaction in dinuclear and 1D Ln^{III}–Fe^{III}(low spin) and Ln^{III}–Cr^{III} systems. In the case of dinuclear compounds, this magnetic exchange is antiferromagnetic for Ln=Ce, Nd, Gd, Dy and ferromagnetic for Ln=Tb, Ho, Tm [48]. However, in several cases, this approach has likewise failed in correctly determining the strength and/or type of the d–f exchange interaction. This is because significant intermolecular magnetic interactions may hide the Ln^{III}–M^{III} intramolecular magnetic exchange at low temperature.

To overcome this drawback, Tangoulis and coworkers introduced an approach based on EPR simulations and least-square fitting of the low temperature magnetic susceptibility data [52]. Their approach uses the phenomenological spin-only exchange model. It assumes that the low temperature magnetic properties of a d–f system are determined mainly by the exchange interaction between the ground states of the lanthanide and transition metal ion. The ground state of the lanthanide ion is taken as a ground doublet with an effective spin $S = ½$, which is true for the majority of the lanthanide ions. The g parameters of the lanthanide ions are determined from low temperature EPR measurements. These values are used to simulate dual-mode EPR spectra using an anisotropic exchange model [52]. The same model is then used to fit the magnetic susceptibility and magnetization data. Using this method, it was shown that the magnetic exchange interaction between Er^{III} and Cr^{III} in the $[Er(bpy)(H_2O)_4Cr(CN)_6]\cdot nH_2O\cdot 1.5n$bpy complex is antiferromagnetic and it has a strong axial anisotropy [52]. The limitations of the approach are the assumed axial symmetry of the magnetic exchange as well as the collinearity of the g tensors of the lanthanide and transition metal ions. Detailed single-crystal EPR and magnetic studies on the series $[Ln(DMF)_4(H_2O)_3M(CN)_6]\cdot nH_2O$ (Ln=La, Ce; M=Fe^{III}, Co^{III}) were performed by Gatteschi and coworkers [16]. Using the ligand field theory, they were able to obtain a detailed picture of the low-lying levels of Ce^{III} and Fe^{III} ions and demonstrate the presence of a triplet ground state [16]. These studies showed that the interaction between Ce^{III} and Fe^{III} is indeed antiferromagnetic and its accurate description requires introduction of both symmetric and antisymmetric terms [16].

In an attempt to increase the magnetic exchange interaction in d–f assemblies, researchers turned their attention to the combination of lanthanide ions with octacyanometalate ions, $[M(CN)_8]^{3-/4-}$ [12, 53]. These building blocks profit

from the enhanced π-back-bonding superexchange efficiency resulted from the greater diffuseness and radial distribution of 4d/5d orbitals as compared with 3d orbitals. Furthermore, octacyanometalate ions can adopt different spatial configurations (antiprism, dodecahedron, or bicapped trigonal prism) depending on the metal ion and its chemical environment, and their flexibility may assist in the formation of various 3D topologies. Sieklucka and coworkers reported the first isostructural 4f–5d series, namely, $[Ln(terpy)(DMF)_4][W(CN)_8]\cdot 6H_2O$ (Ln=Ce-Dy) [54, 55]. These compounds are 1D chains consisting of $[Ln(terpy)(DMF)_4]^{3+}$ and $[W(CN)_8]^{3-}$ units. These chains are linked via π–π and hydrogen-bonding interactions to form a 2D network structure [54, 55]. The analysis of the magnetic data was made assuming that the interaction between Ln^{III} and W^{V} is much smaller than the ligand effects [55]. In this approach, the tuning of the ligand field parameters was performed considering the coordination geometry of lanthanide ions. Then, the simulated data were corrected for the presence of Ln^{III}–W^{V} coupling. Such analysis allowed to determine that the magnetic exchange interaction between the lanthanide and tungsten ions is antiferromagnetic for Ln=Ce, Pr and ferromagnetic for Ln=Nd, Tb, Dy [55].

Combining the magnetic anisotropy of the lanthanide ion with the geometrical flexibility of octacyanometalates, Hashimoto and coworkers discovered the presence of cooling-rate-dependent ferromagnetism in $[Sm(H_2O)_5W(CN)_8]$ [56]. This compound has a 2D cyanide-bridged network in which Sm^{III} and W^{V} ions are linked in alternating fashion [56]. By cooling down the sample, the temperature dependence of the magnetizations shows the presence of antiferromagnetic behavior. Heat capacity and IR measurements indicated that a structural phase transition occurs at 166 K as a result of chancing the coordination geometry of $[W(CN)_8]^{3-}$ [56]. Conversely, ferromagnetic behavior is observed when the sample is placed directly at 10 K ($T_c = 2.8$ K) [56]. This is due to the overcooling effect of the structural phase transition. The differences observed were interpreted in terms of changing the interlayer superexchange interactions [56].

Besides the magnetic properties, measuring other thermodynamic properties allows separating more reliable ligand field effects from the contributions arising from the magnetic (anisotropic) exchange coupling. Tanase and coworkers showed that low-temperature magnetic-specific measurements are powerful in determining the magnetic ground state of the lanthanide ion [57–61]. Such measurements are also valuable for estimating the strength and type of the d–f magnetic exchange interactions. Detailed magnetothermal studies were performed on the series $[Ln(pzam)_3(H_2O)Mo(CN)_8]\cdot H_2O$ (Ln=Nd, Sm, Gd, Tb, Er) which showed that their magnetic properties are mainly determined by the particular lanthanide involved [57–61]. Thus, it was found that the Nd^{III} and Mo^{V} ions are coupled ferromagnetically into magnetic chains by a *XY*-type (planar) interaction with $J_{\parallel}/J_{\perp} \approx 0.3$ and $J_{\perp}/k_B \approx 1.8$ K [61]. The interaction between Tb^{III} and Mo^{V} is ferromagnetic, but with a strong Ising-type anisotropy ($J_{\parallel}/k_B = 3.5$ K) [58]. By contrast, the noncancelation of the antiferromagnetically coupled Gd^{III} and Mo^{V} results in a ferromagnetic Heisenberg chain and long-range magnetic ordering below 0.7 K [59]. An antiferromagnetic interaction is also observed between Sm^{III}

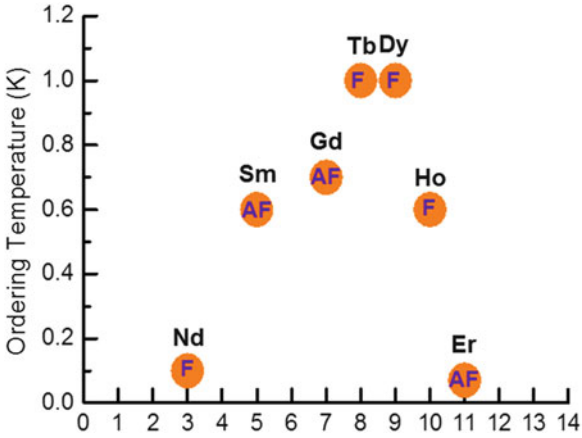

Fig. 11 Magnetic exchange interactions and long-range magnetic ordering in the series $[Ln(pzam)_3(H_2O)Mo(CN)_8]\cdot H_2O$

and Mo^V as well as Er^{III} and Mo^V, respectively [60]. The symmetry of the interaction is Ising–Heisenberg in the case of Sm^{III}, whereas the compound containing Er^{III} behaves as a pure *XY* chain [60]. Figure 11 summarizes the magnetic exchange interaction and the long-range-ordering temperature within the series $[Ln(pzam)_3(H_2O)Mo(CN)_8]\cdot H_2O$.

Replacing Mo^V with W^V in the isostructural series $[Ln(pzam)_3(H_2O)Mo(CN)_8]\cdot H_2O$ (Ln=Gd, Tb) revealed interesting properties [57, 59]. The magnetic properties of the gadolinium analogues indicate antiferromagnetic interactions for both Gd^{III}–Mo^V ($J/k_B = 0.98$ K) and Gd^{III}–W^V ($J/k_B = 1.10$ K) [59]. The strength of the magnetic exchange interaction is indeed found to increase with the radial extension of the magnetic orbitals of the transition metal ion (4d < 5d). However, substituting the Mo^V with the larger W^V in the terbium analogues causes a drastic change in the symmetry of the terbium *g* tensor. Therefore, the magnetic exchange interaction changes from Ising-type into an anisotropic *XY* exchange and a slight increase of the T_c is observed [57]. The magnetic susceptibility and specific heat data were analyzed in terms of the theoretical predictions for the 1D *XYZ* Hamiltonian, giving excellent agreement between the theoretical and experimental data ($J_x = 1.9$ K, $J_y = 2J_x$, $J_z = 0$) [57].

The magnetic anisotropy of the lanthanide ion in the series $[Ln(pzam)_3(H_2O)Mo(CN)_8]\cdot H_2O$ (Ln=Gd, Tb) was described in detail by Ferbinteanu and coworkers [17]. Multiconfiguration procedures followed by spin–orbit treatments were applied to describe the combined effects of the ligand field and spin–orbit coupling. Such studies allowed obtaining the magnetization polar diagrams for each state of the lowest multiplets of the lanthanide ions as well as the first-principles simulations of the magnetic susceptibility [17]. A remarkable match was obtained between the theoretical and experimental data [17]. Because the gallery of cyanide-bridged MOFs offers an interesting collection of coordination patterns occurring at the metal ion nodes, we will focus in the following sections on the electronic structure particularities of lanthanide sites in such networks.

4 The Bonding Regime in Lanthanide Complex Units

The nature of the chemical bonding of lanthanide nodes is similar to those encountered in other non-MOF chemical structures incorporating such ions, e.g., 0D, 1D, or 2D coordination polymers. However, the topological constraints demanded by the establishing of a MOF architecture are determining interesting new local coordination schemes. We will present below several computation experiments performed on selected f-type coordination units cut from various MOF crystal structures, in the attempt to reveal the electron structure features of such constituents.

A particularity of the lanthanide coordination is the weak interactions of the f electrons with the environment while having strong inter-electron and spin–orbit effects inside the f shell. This is understood after a glance at Fig. 12 which shows that the f-shell electron density is hidden inside the whole ionic body, hosted in atomic orbitals (AOs) with small radial extension. The maximum peak of the radial component from the f atomic orbitals is located at about 0.5 Å, smaller than the atomic radii of the lanthanide ions. The lanthanide atomic radii vary between 1.74 Å for lutetium and 1.87 Å for lanthanum [62]. Therefore, the f electrons are shielded from perturbation exerted by ligands. This contours the idea of a small nominal implication in the chemical bonding itself. However, an indirect interaction with the outskirts of the coordination sphere is possible, via empty orbitals such as 6s, 6p, 5d, or even by the 5f virtuals. For instance, the 5d and 5f show maxima of the radial profile around the atomic radii (see corresponding labeled curves in Fig. 12). In symmetries with inversion center, the d and f shells are noninteracting, having opposite parities. A weak d–f hybridization can occur in low-symmetry environments, when the interactions via the 5d overlapping are transmitted to the inner 4f shell. Besides, a mutual remixing of 4f occupied with the 5f virtual seems

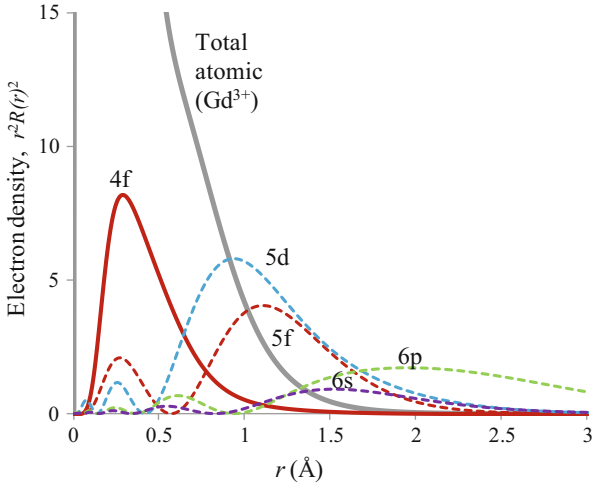

Fig. 12 Illustration of the shielded status of the f shell in the lanthanide ions, with the radial maximum of the f-type electron population engulfed by the global density of the atomic body, exemplified on the Gd^{III} case

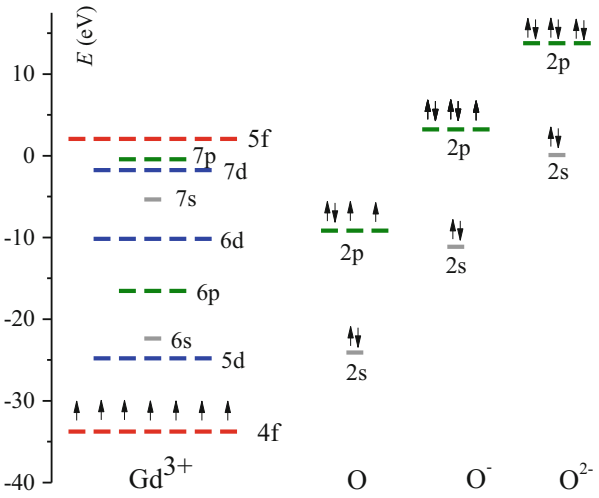

Fig. 13 Scheme of orbital energies on free lanthanide, selecting Gd^{III}, and ligand atomic species (selecting oxygen with 0, −1, and −2 charges)

possible, the latter one having maxima both in the range of atomic radius and also around the 4f internal peak. The simulation is taken for the Gd^{III} free ion, with triple zeta and polarization (TZP) basis set from a density functional theory (DFT) [63, 64] calculation with the Amsterdam Density Functional (ADF) code [65, 66].

Given the well-known affinity of the f elements to oxygen-based donors [67], we will now take a look at the orbital energies of the atomic components, selecting Gd^{III} and the oxygen. Figure 13 illustrates the relative placement of the lanthanide ion atomic orbitals with respect of oxygen atom taken with the 0, −1, and −2 charges. Since the O^{2-} side is merely hypothetical (given the negative electron affinity of the di-anion species), the situation of the oxygen donors in various molecules is mimicked by a formal tuning of the orbital scheme between the O and O^{-} panels from Fig. 13. The mutual electrostatic potentials in pro-molecule (a hypothetical state with atoms placed at the position of the molecular geometry but chemical bond not yet switched on) can move the mutual placement of the AOs entering in interaction. The repulsion exerted by the negative ligands determines upper energy shift for the electrons in the 4f, while a downward displacement occurs for the 2s and 2p nonmetal levels because of stabilizing potential from the positive lanthanide ions. Although the atomic orbitals of the free oxygen species are not completely representative for the donors in the ligand and in the whole complex, the relative placement of the occupied 2s and 2p shells with respect of partly filled 4f orbitals may suggest a non-*aufbau* situation of the complex. This is the case when unpaired f electrons are placed lower in energy than doubly occupied levels from ligands.

One may also imagine a donor–acceptor activity between the occupied levels of the ligand and the empty AOs from the lanthanide. The 5d and 6s are the lowest unoccupied orbitals to be considered. However, higher virtuals can contribute, even though these objects are not immediately resonant to the chemical intuition.

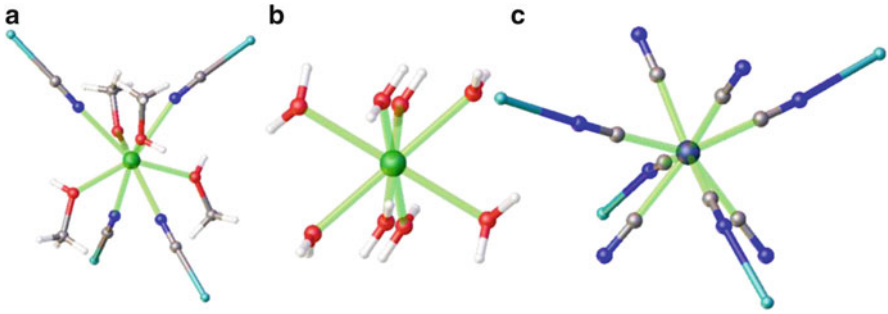

Fig. 14 Coordination units selected from the MOF in [31], having the following constitution: (**a**) antiprismatic $\{Ln(NC\text{-}Mo)_4(CH_3OH)_4\}$, (**b**) cube-like $[Ln(OH_2)_8]^{3+}$, and (**c**) antiprismatic $\{Mo^{IV}(CN)_4(CN\text{-}Ln)_4\}$

Technically speaking, the rich basis sets provide such components as useful degrees of freedom in the overall optimization of molecular orbitals.

We will discuss below several calculations on model coordination units taken at the experimental geometries from selected MOF crystal structures. A first choice is the system whose 3D packing resembles sodalite structure [39]. This example offers two interesting lanthanide coordination units. The first one (Fig. 14a) has ligands of presumed different strength: four cyanide (strong) and four methanol (weak) fragments, placed in a shape related with a $\{LnN_4O_4\}$ antiprism. The unit can also be described as the interlocking of an elongated $\{LnN_4\}$ tetrahedron with a flattened $\{LnO_4\}$ core. The explicit fragment would be $\{Ln(NC\text{-}Mo)_4(CH_3OH)_4\}$, which is connected by Ln-NC-Mo bridges to the Mo^{IV} (Fig. 14c). The octacyanomolybdate ion contains four bridged CN^- ligands (i.e., Mo-CN-Ln links) and four simple Mo-CN non-bridged contacts, the ensemble being $\{Mo^{IV}(CN)_4(CN\text{-}Ln)_4\}$. The unit represented in Fig. 14b is a beautiful, almost cubic, $\{LnO_8\}$ complex made with aqua ligands. This one is not firmly bridged with the rest of the network, but shows lots of hydrogen bonding with lattice solvent methanol molecules. For the sake of simplicity, the Li^+ ion was taken as surrogate for polarization effects exerted to a given cyanide unit by the next-neighbor ions. Although lithium ion is crude prosthetic for the bridging effect, it is an acceptable simplification for the charge polarization on the interest center. The aim is obtaining semiquantitative parameters from modeling, namely, bonding energy values that can be judged relatively between the different ligands.

Using the same simplification, the lutetium is considered as the test lanthanide ion. Because of shielded nature of the 4f shell, the lanthanides are closely similar to each other in global properties (excluding the magnetic and optical properties that depend on the given f^n configurations). Even the lanthanide contraction effect is not so important in qualitative respects, causing along the La-Lu series only about a 4% shrinkage of the Ln–ligand bond lengths [68]. Taking Lu^{III} as a common replacement for various lanthanide unit examples gives a conventional unified perspective on the coordination power of the different ligands in molecule. At this stage, the

conceptual complications related to the partly filled f shell are not considered. The model molecules are given in Fig. 14a–c, respectively, $[Lu(NC\text{-}Li)_4(CH_3OH)_4]^{3+}$, $[Lu(OH_2)_8]^{3+}$, and $[Mo^{IV}(CN)_4(CN\text{-}Li)_4]$. The calculations were done with the ADF package [65], using Becke–Perdew (BP86) functional [69–71] and the triple-zeta polarized zero-order relativistic approximation (TZP-ZORA) basis set.

The ADF suite offers convenient tools of energy decomposition analysis (EDA) implemented in ADF based on Ziegler–Rauk scheme [72, 73]. The ADF also uses a fragment-based algorithm, the coordination units being assembled from metal ion and ligand fragments, prepared in advance [74]. The total bonding energy and its components are results of computational experiments. This is imagining the relaxation of the density primarily produced from superposition of the fragments at the actual molecular geometry to the self-consistent result. The presented amounts are not directly related to thermodynamic observables. However, they offer meaningful insight into the bonding mechanisms and relative coordination strength of different ligands. The total bonding and EDA results are conventionally dependent on the choice of the fragments.

The Pauli repulsion is related to the antisymmetrization of the wave function, including the closed-shell cores, when the merged fragments are conventionally not yet perturbed by electrostatics and overlapping [75]. The electrostatic part is the classical quantity resulted from the charge distribution of the electronic clouds and nuclei, when the pro-molecule is formed from superposition of frozen fragments. The orbital effects are done by the final relaxation toward the converged MOs and densities. Therefore, it can be assimilated to the covalent effects. The orbital stabilization occurs with the help of donor–acceptor couples between occupied MOs of the ligands and empty orbitals of metal ion. Figure 12 shows that virtual AO spectrum on lanthanide ion is quite rich. The back-donation effects, involving the valence shell of lanthanide and the ligand virtual MOs, were also demonstrated as important [76]. The 4f shell does not contribute to the orbital effects due to the radial distribution shrunk inside of the atomic body (Fig. 12).

Table 1 gives computation results for the unit shown in Fig. 14a. The first line corresponds to the ligands conceived as a unique block fragment, having here two fragments: Lu^{III} and the $(NC\text{-}Li)_4(CH_3OH)_4$. The second line corresponds to the case when there are nine fragments, namely, Lu^{III}, four NC-Li, and four CH_3OH units.

Table 1 The energy decomposition analysis for several fragment definitions of the $[Lu(NC\text{-}Li)_4(CH_3OH)_4]^{3+}$ unit (see Fig. 14a). Line I corresponds to ligands merged in one fragment, while line II to individual ligand pieces. The following lines correspond to fragments based on a given ligand plus the remaining of the molecule (a complex where the considered ligand was removed). The results for chemically equivalent species are averaged

	Total bonding	Pauli repulsion	Electrostatic	Orbital energy
I	−822.4	113.6	−521.1	−414.8
II	−739.0	217.4	−704.9	−251.5
NC-Li	−66.7	33.1	−104.1	4.3
CH_3OH	−25.2	31.9	−52.7	−4.4

All the quantities are in kcal/mol

Table 2 The energy decomposition analysis for several fragment definitions of the $[Lu(OH_2)_8]^{3+}$ unit (see Fig. 14b). Lines I and II have the same meaning as in Table 1. The results are averaged over the different aqua ligands

	Total bonding	Pauli repulsion	Electrostatic	Orbital energy
I	−529.3	137.9	−345.8	−321.3
II	−472.2	235.9	−456.3	−251.7
OH_2	−29.9	35.7	−54.1	−11.5

All the quantities are in kcal/mol

In the following lines, the fragments are chosen to reflect the addition of one ligand to the remaining of the complex. Then, the line labeled NC-Li corresponds to the following fragment choice: $[Lu(NC\text{-}Li)_3(CH_3OH)_4]^{3+}$ plus NC-Li. Treating each NC-Li group from the set, there are four possible partitions of this sort, but only the averaged results are presented. Conversely, the line labeled CH_3OH contains the average of calculations based on the $[Lu(NC\text{-}Li)_4(CH_3OH)_3]^{3+}$ plus CH_3OH fragments. The first line in Table 1 shows a relatively high bonding energy, grace to a small Pauli repulsion. This is because the ligands were grouped in one block, their mutual repulsion being silenced. The Pauli component is then enhanced in the second line, having the inter-ligand repulsion included. Compared with the first line, the electrostatic energy from the second calculation shows larger absolute value. In the second line, the total bonding is almost the same as the electrostatic part. The same approximate regularity is also seen in the second line of Table 2, dedicated to the $[Lu(OH_2)_8]^{3+}$. The electrostatic component shows a relative prevalence in the lines dedicated to the bonding energy of individual ligands (Tables 1 and 2). Comparing the total bonding energies of the ligands from these tables, one infers the intuitively expected ordering in the coordination strength: NC-Li$>$ $OH_2 > CH_3OH$. The relatively large variation in the orbital parts between the first and second lines of Table 1 shows that the mutual interaction of the ligands that makes the difference plays an important role.

The first and second lines in Table 3 show that the coordination bonding is stronger in the d complexes than in the f ones. Surprisingly, the total bond energy values associated to each ligand are rather small, particularly those of the Li-NC ones. It is probably due to distortion of the realistic picture by using Li as stopper instead of a lanthanide ion over the bridge. However, it can be assumed that comparable effective ligand-bonding energies in both d and f units are a prerequisite for achieving d–f-extended structures. The Li-NC hypothetical ligand (replacement for the Ln-NC fragment) shows smaller Pauli repulsion than the NC^- because the polarization induced by the Li^+ ion contracts the clouds that are contributing to the effect. At the same time, the electrostatic stabilization is reduced, by lesser interaction with the lanthanide ion, as compared to the negatively charged cyanide. The charge polarization in the cyanide-bridged ligand is favorable to the orbital stabilization. However, the reduced electrostatic attraction decides a smaller total bonding. These results should be taken only in qualitative sense.

Table 3 The energy decomposition analysis for several fragment definitions of the $[Mo^{IV}(NC\text{-}Li)_4(CN)_4]$ unit (see Fig. 14c). The results for equivalent species (NC-Li bridging ligand and NC simple ligand) are averaged

	Total bonding	Pauli repulsion	Electrostatic	Orbital energy
I	−4,018.7	759.1	−3,240.4	−1,537.4
II	−2,342.3	1,554.2	−2,713.7	−1,182.8
Li-NC	−27.8	212.8	−160.4	−80.2
NC^-	−87.8	244.0	−278.3	−53.4

All the quantities are in kcal/mol

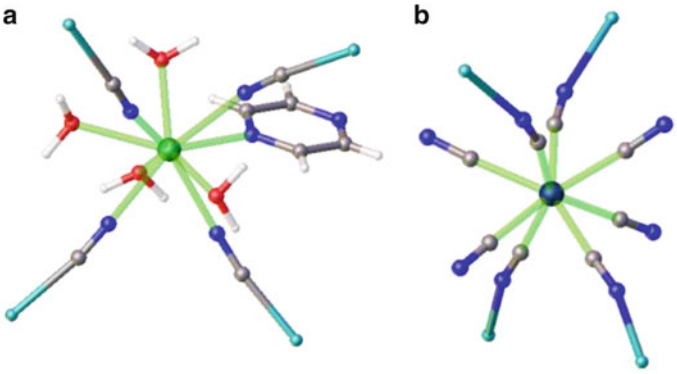

Fig. 15 Coordination units selected from the MOF in [43], having the following constitution: (**a**) $\{Ln(NC\text{-}Mo)_4(OH_2)_4(pz)\}$ and (**b**) $\{W^V(CN)_4(CN\text{-}Ln)_4\}$

The next example is taken from a neodymium-based MOF in which both cyanide and pyrazine (pz) are acting as bridging ligands [43]. The local f and d units are $\{Ln(NC\text{-}W)_4(OH_2)_4(pz)\}$ and $\{W^V(CN)_4(CN\text{-}Ln)_4\}$, respectively, with W-CN-Ln and Ln-Pz-Ln bridges (see Fig. 15 for details). Table 4 shows the results for the lanthanide unit, taking again Lu^{III} as model for estimating binding energies. Comparing with Table 1, the cyanide and aqua ligands show slightly different bonding features. However, they are in the same respective range. The pyrazine has a total bonding comparable with the aqua ligand, the similarity being understood as consequence of neutrality. The slightly higher stabilization of the water ligand can be taken as illustrating the affinity of oxygen-based donors to lanthanide ions. The higher Pauli repulsion in pyrazine than in the aqua ligand can be understood by the higher content of C-N-C moiety in atomic cores and bonding electron pairs, as compared to the H-O-H fragment, with lesser rich content in doubly occupied orbitals. We recall that the Pauli repulsion is not of electrostatic type, but of a quantum nature [75].

Although mutually comparable, the different bonding parameters retrieved for the cyanide and aqua ligands in the discussed systems, $[Lu(NC\text{-}Li)_4(CH_3OH)_4]^{3+}$, $[Lu(OH_2)_8]^{3+}$, and $[Ln(NCLi)_4(OH_2)_4(pz)]^{3+}$, show that the coordination effects are not entirely transferable. Reasonably, all sorts of energy components (Pauli

Table 4 The energy decomposition analysis for several fragment definitions of the $[Lu(NC\text{-}Li)_4(OH_2)_4(pz)]^{3+}$ unit (see Fig. 15a). Lines I and II have similar meaning as in the previous tables. The results for chemically equivalent species (cyanide, aqua, and pyrazine ligands) are averaged

	Total bonding	Pauli repulsion	Electrostatic	Orbital energy
I	−819.3	117.1	−515.9	−420.5
II	−730.3	267.0	−733.1	−264.3
NC-Li	−61.2	39.8	−105.4	4.5
OH_2	−18.2	33.7	−47.3	−4.6
pz	−17.0	47.3	−55.5	−8.9

All the quantities are in kcal/mol

Table 5 The energy decomposition analysis for several fragment definitions of the $[W^V(NC\text{-}Li)_4(CN)_4]^+$ unit (see Fig. 15b). The results for equivalent species (NC-Li bridging ligand and NC simple ligand) are averaged

	Total bonding	Pauli repulsion	Electrostatic	Orbital energy
I	−4,289.3	711.0	−1,462.5	−3,537.8
II	−3,401.6	1,651.1	−3,489.6	−1,563.1
Li-NC	−61.4	222.5	−217.1	−66.8
NC^-	−180.8	267.4	−420.2	−28.1

All the quantities are in kcal/mol

repulsion, electrostatic, and orbital parts) must show dependence from the actual topology of the remainder of the molecule. The specific placement of the other ligands determines the variation of Pauli and electrostatic energies for a given ligand in a certain complex. The geometry of the rest of the complex decides also a set of interacting orbitals. This set varies from species to species, so the orbital component of the selected ligand depends specifically on the complementary complex fragment.

Table 5 shows the d-type cyanowolframate unit from the above discussed MOF [43]. This has the same geometry of cyanide ligands, both bridging and non-bridging, as in the cyanomolybdate case shown in Fig. 14 [39]. In all the computational settings labeled I, II, Li-NC, and CN^-, the total bonding stabilization shifts are higher in the wolframate case than in the molybdate one. The Pauli repulsions are comparable in all these cases because of the similar geometry and pattern of the core orbitals. The orbital stabilization energies are sensibly larger for wolframate, pointing for a higher degree of covalence in heavier d-type coordination units.

The next examples illustrate the case of a somewhat more complicated ligand, the anionic form of the 5-methyl-2-pyrazine carboxylic acid (Hmpca) [41, 42]. The first case [41] shown in Fig. 16a contains $\{Ln(mpca)_2(NC\text{-}W)_3\}$ lanthanide coordination units (Ln=Eu, Nd) with the cyanide bridges belonging to octacyanowolframate(IV) moiety. The two mpca ligands are functioning as chelates, with one carboxylic oxygen donor and another from the aromatic amine part. The

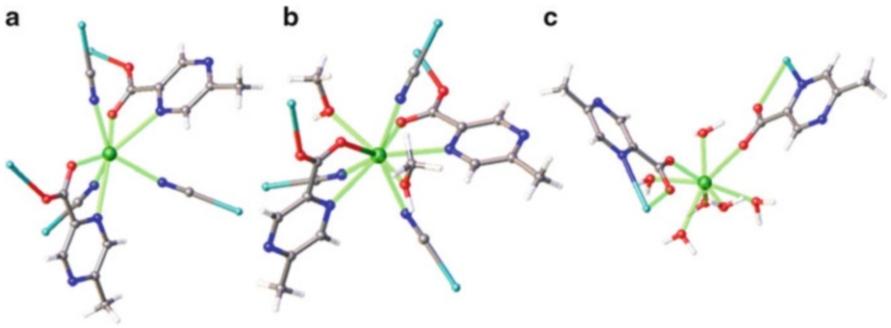

Fig. 16 Coordination units selected from the MOFs in [41, 42]: (**a**) $[Ln(mpca)_2(NC\text{-}Mo)_3]$, (**b**) $[Ln(mpca)_2(NC\text{-}W)_3(CH_3OH)_2]$, and (**c**) $[Ln(mpca)_2(OH_2)_6]$

Table 6 The energy decomposition analysis for several fragment definitions of the $[Lu(mpca\text{-}Li)_2(NC\text{-}Li)_3]^{3+}$ unit (see Fig. 16a). Lines I and II have similar meaning as in the previous tables. The results for chemically equivalent species (mpca, cyanide, methanol ligands) are averaged

	Total bonding	Pauli repulsion	Electrostatic	Orbital energy
I	−843.1	98.2	−500.6	−440.7
II	−762.6	172.5	−670.3	−264.9
NC-Li	−55.2	34.5	−100.5	10.7
mpca	−104.7	49.4	−141.0	−13.1

All the quantities are in kcal/mol

coordination number is seven, relatively small with respect of the lanthanide ion capabilities. Such unsaturated coordination enables the formation of the related species [42], where two methanol molecules are added to a frame similar to the discussed one (see Fig. 16b in comparison to 16a), having the $\{Ln(mpca)_2(NC\text{-}W)_3(CH_3OH)_2\}$ local units (Ln=Eu, Tb). This system [42] is based on octacyanomolybdate(IV) showing a lattice architecture similar to the previous system, except the supplementary coordinated methanol molecules. Both analogous MOFs [41, 42] contain another lanthanide species, $\{Ln(mpca)_2(OH_2)_6\}$, presented in Fig. 16c. The actual geometry is taken from the second crystal structure. These two nodes are connected by an mpca ligand that acts as a chelate toward the center including the cyanide ligands and monodentate against the site with aqua ligands, by the other oxygen of the carboxylate, coordinated in *anti* conformation. Thus, aside from the Ln-NC-Mo d–f links, there are *syn–anti* carboxylate f–f bridges.

Tables 6, 7, and 8 show the energy decomposition results for the coordination spheres represented in Fig. 16a–c, taken in the respective molecular models $[Lu(mpca\text{-}Li)_2(NC\text{-}Li)_3]^{3+}$, $[Lu(mpca\text{-}Li)_2(NC\text{-}Li)_3(CH_3OH)_2]^{3+}$, and $[Lu(mpca\text{-}Li)_2(OH_2)_6]^{3+}$. All molecular models are based on an mpca-Li neutral fragment, the lithium atom being taken as surrogate for the next metal ion connected in the network by the bridging metal ligand. In all tables, the second line corresponds to the making of the complex from Lu^{III} and individual fragments for each ligand. It shows the same regularity pointed previously, with the electrostatic component

Table 7 The energy decomposition analysis for several fragment definitions of the $[Lu(mpca\text{-}Li)_2(NC\text{-}Li)_3(CH_3OH)_2]^{3+}$ unit (see Fig. 16b). Lines I and II have similar meaning as in the previous tables. The results for chemically equivalent species (mpca, cyanide, methanol ligands) are averaged

	Total bonding	Pauli repulsion	Electrostatic	Orbital energy
I	−906.0	131.0	−526.9	−510.1
II	−797.0	273.3	−800.3	−270.1
NC-Li	−44.3	45.1	−102.6	13.2
mpca	−78.0	66.5	−141.0	−3.5
CH_3OH	−14.0	35.0	−51.2	2.2

All the quantities are in kcal/mol

Table 8 The energy decomposition analysis for several fragment definitions of the $[Lu(mpca\text{-}Li)_2(OH_2)_6]^{3+}$ unit (see Fig. 16c). Lines I and II have similar meaning as in the previous tables. The results for chemically equivalent species (mpca and aqua ligands) are averaged

	Total bonding	Pauli repulsion	Electrostatic	Orbital energy
I	−737.4	140.9	−476.7	−401.5
II	−679.1	254.4	−633.2	−300.4
mpca	−115.5	46.7	−139.1	−23.1
OH_2	−24.0	36.8	−54.2	−6.6

All the quantities are in kcal/mol

approximately equal to the total bonding energy. The mpca ligand shows in all the coordination spheres the highest absolute values of the total stabilization energy. One observes that the mpca and cyanide are less stabilized in the coordination sphere with two methanol molecules attached than in the pristine one. This seems primarily due to the increased steric repulsion in the more crowded coordination sphere. The electrostatic parts on both these ligands in the related units are closely comparable. The orbital stabilization component seems lower in the case of higher coordination number. Tentatively, this can be interpreted as the case of effective limited number of orbital interaction channels available for the binding of the ligands around the lanthanide ions. Therefore, the new coming ligand finds lesser donor–acceptor capabilities in a sphere with more other ligands already bonded than in a free neighborhood. Because of stronger Pauli repulsion and lesser orbital interaction routes, due the coexistence with mpca ligands, the cyanide and methanol molecules (see Table 6) are less bonded than those given for $[Lu(NC\text{-}Li)_4(CH_3OH)_4]^{3+}$ in Table 1. The coordination unit $[Lu(mpca\text{-}Li)_2(OH_2)_6]^{3+}$ is relatively relaxed from sterical point of view, having small aqua and monodentate mpca ligands. The stabilization of the aqua ligand (see Table 8) is placed between the binding energies of the same moiety in the more crowded $[Lu(NC\text{-}Li)_4(OH_2)_4(pz)]^{3+}$ unit (see Table 4) and the more relaxed $[Lu(OH_2)_8]^{3+}$ complex (see Table 2).

A numeric experiment performed on the $[Lu(mpca\text{-}Li)_2(NC\text{-}Li)_3(CH_3OH)_2]^{3+}$ fragment will be shown in the following. All the other discussed systems show

results in the same range as the selected one. We will call an ADF keyword that allows excluding selected virtual components from the fragment orbitals [77]. First, empty AOs from the Lu^{III} fragment are deleted, measuring the change in the total bonding energy. The results are the same for the settings related to lines I and II in Table 7, since the ligand fragment definitions are not affected. Thus, the total bonding energy grows by 3.1 kcal/mol by cutting all the virtual s type AOs (6s, 7s, etc.). Cutting the p, d, and f virtuals, the destabilization is about 3.2, 69.9, and 4.3 kcal/mol, respectively. The substantial role of the empty d orbitals can be observed, the energy increase being sensible when these functions are not allowed in the interaction. This emphasizes the 5d role, since keeping this shell and erasing the upper d virtuals available in the given basis set (i.e., 6d–9d) yields a negligible destabilization (≈2.4 kcal/mol). One notes the minor role of the f virtuals in the bonding, although the radial shape discussed previously may have suggested a possible implication. Removing the progressively cumulated empty shells, sp, spd, and spdf, the energy shifts are 6.3, 78.8, and 82.9 kcal/mol, respectively. The first amount equals the s + p sum, while the others are smaller (≈2 kcal/mol) than the respective s + p + d and s + p + d + f summations. The changes in total bonding at the removal of empty fragment wave functions are incorporated only in the orbital component. The Pauli and electrostatic parts remain unchanged.

The destabilization produced by removing all the virtual MOs on the block containing all the ligands is ≈266 kcal/mol. This suggests that the whole body of lanthanide ion uses the frontier MOs of the ligand for orbital and charge transfer relaxation. Since numerical experiments suspending the interaction of filled orbitals are not possible, one cannot detect which lanthanide AOs are approaching mostly the ligand virtual MOs. However, one may guess reasonably that the effect is due to the 5s–4p valence shell. Finally, removing all the possible virtuals on both lanthanide and ligand fragments, the destabilization is ≈510 kcal/mol, sensibly larger than the sum related to the elimination of spdf empty shells on lanthanide and all the ligand virtuals. This synergetic effect suggests the role of advanced mixing of all the possible components.

5 The Density Functional Theory Approach for Selected MOF Lanthanide Units

Analyses presented above are conventionally confined to the closed-shell Lu^{III} complexes, using restricted-type DFT calculations. Such calculations circumvent the issues related to the f shell itself. However, this modeling retains the interactions giving the main bonding components. These interactions are responsible for the cohesion of the complex units and of the MOFs in ensemble. In this section, we will discuss the f-shell intricacies by probing the unrestricted version of DFT calculations. The example taken is the Tb^{III} complex discussed above and represented in Fig. 16a as well as the gadolinium analogue. In the unrestricted calculations there

are independent sets of orbitals for the alpha and beta electrons. Figure 17 shows two panels corresponding to the $[Ln(mpca)_2(NC\text{-}Li)_3(CH_3OH)_2]^{3+}$ complexes (Ln=Tb and Gd). In each case, there are two columns with alpha and beta MO energies as lines, having superimposed, in each set, the ratio of f content in each MO as vertical histograms. The alpha and beta f-type populations are represented toward the positive and the negative abscissas. Having an f^7 configuration, the Gd^{III} system has seven alpha electrons distributed in rather many occupied MOs ranging between −14.5 and −13.5 eV. Among these, five functions show over 0.5 ratio of f-type AOs, three others with an f content slightly below 0.5, and several components with smaller f population. The empty beta-type orbitals are located at higher energy and grouped in a narrower window, at about −9.2 eV. The f content is almost unitary, except a couple of MOs with accidental small f traces. The fact that the alpha set does not show a compact series of seven MOs firmly identifiable as f type (by a high percentage of the corresponding AOs) is not convenient for the ligand field post-computational analysis. The situation becomes more puzzling in the case of terbium system. The f^8 configuration has seven alpha electrons and a beta one. In the free Tb^{III} ion, the beta electron can occupy any of the seven equivalent f orbitals, giving rise to the hepta-degenerate ^7F term. In the complexed Tb^{III} ion, the levels originating from the ^7F multiplet remain quasi-degenerate, because the interaction of the f electrons with the environment is weak. These levels have small gaps between successive components in the order of tens or hundreds of wavenumber units (reciprocal centimeters). Therefore, the DFT approach seems at its limits of applicability, because it is formally devised for nondegenerate states only [78, 79]. In principle, in low symmetry, one may assume that the unrestricted procedure identifies the orbital configuration corresponding to the nondegenerate ground state of the f^8 system.

The deep alpha f-type spin orbitals having energies lower than many ligand-type occupied orbitals resemble the idea of non-*aufbau* occupation, although this concept is built on a picture tacitly based on a restricted orbital scheme. The ligand-type orbitals are found in couples of alpha and beta functions mutually matching their energies and shapes. The extreme separation in energy between the alpha and beta f-type MOs may respond to certain demands of exchange–correlation mechanisms. However, it is not perfectly in line with the ligand field perspective on the f shell which assumes that the alpha and beta electrons are using the same set of orbitals. Generally, the unrestricted DFT is the method recommended for systems with unpaired electrons [64]. However, its regular form appears puzzling for f-type systems.

An innovative way to adapt the DFT to the ligand field (LF) phenomenology was developed by Daul and Atanasov. They devised the algorithm and codes called LFDFT [80, 81], applied to d-type [82, 83] and f-type [83, 84] complexes. For lanthanide systems, the so-called average-of-configuration (AOC) methodology [81, 85] is essential for retrieving good quality MOs with high f content. The procedure is based on the specific features of the Amsterdam density functional (ADF) [65, 66] code that has nonstandard leverages for handling orbital configurations [77]. Thus, in ADF, it is possible to impose non-*aufbau* configurations

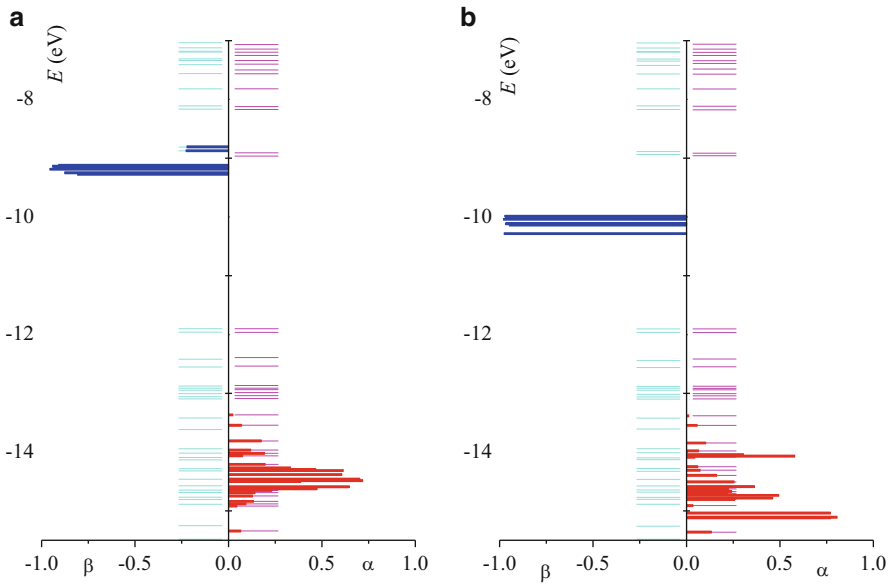

Fig. 17 The MO levels and f-type content from unrestricted calculation on (**a**) $[Gd(mpca\text{-}Li)_2(NC\text{-}Li)_3(CH_3OH)_2]^{3+}$ and (**b**) $[Tb(mpca\text{-}Li)_2(NC\text{-}Li)_3(CH_3OH)_2]^{3+}$

during the self-consistent procedure, as well as use fractional occupation numbers. The fractional orbital populations are allowed in DFT [86, 87]. These have the meaning of statistic average over configurations running integer MO populations. For a mononuclear complex with an f^n lanthanide ion, the AOC procedure consists in running a DFT calculation with a set of seven orbitals with $n/7$ on each component, provided that the converged result retrieves f-type MOs for this sequence. The AOC, as procedure of orbital optimization, is similar to the state-averaged complete active space self-consistent field (CASSCF) [88, 89] calculations. It identifies a unique set of MOs as basis for many configuration problems. This does not mean that the DFT is multiconfigurational itself, but it can, however, produce orbitals that are usable in subsequent numerical experiments. It provides ligand field parameters which can account, in separate modeling, for spectral terms [90, 91].

By the AOC-DFT route, which follows a restricted frame (i.e., with a single basis of orbitals for alpha and beta electrons), it is possible to obtain an *aufbau*-type configuration. It is fairly in contrast with the previous discussion on the Gd^{III} and Tb^{III} unrestricted calculations (see Fig. 17). Figure 18 shows the MO diagram of the $[Tb(mpca\text{-}Li)_2(NC\text{-}Li)_3(CH_3OH)_2]^{3+}$ complex calculated in AOC manner, aside to the MO stacks of the Tb^{III} ion and the $\{(mpca\text{-}Li)_2(NC\text{-}Li)_3(CH_3OH)_2\}$ block of ligands, taken as a single fragment. The main fragment contributors to a given MO from fragment orbitals are marked by lines with thickness calibrated to the relative role. One may observe that the highest occupied MOs are originating from the f shell, each having the 8/7~1.143 fractional population. The MOs related to the

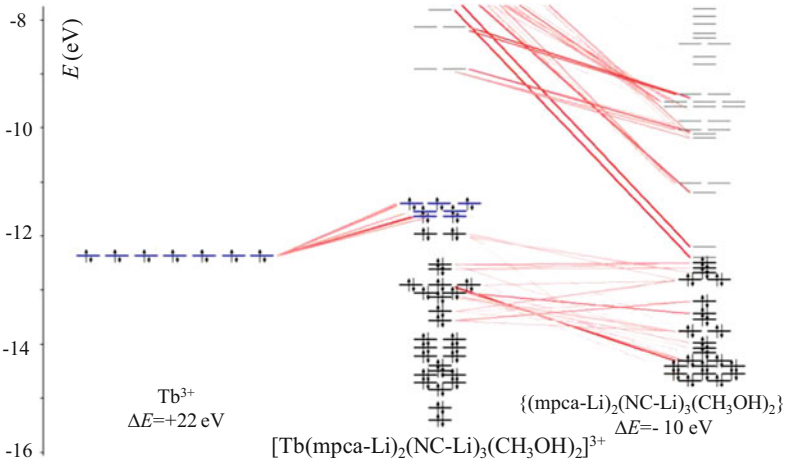

Fig. 18 The MO levels from the average-of-configurations (AOC) calculation on $[Tb(mpca\text{-}Li)_2(NC\text{-}Li)_3(CH_3OH)_2]^{3+}$ showing the parentage of MOs from Tb^{III} and ligand orbitals. The fragments levels are shifted conventionally (respectively, by +22 and −10 eV) to better visualize the matching

ligand field sequence show a high f content, with ratios between 0.93 and 0.98. Therefore, the AOC approach, with controlled population, seems to retrieve well the desired scheme. In the Gd^{III} analogue, one finds a similar scheme, with the highest orbitals having electron occupation numbers equal to 1, in the classical sense of restricted open-shell diagrams.

With appropriate ADF keywords, one may generate a series of Slater-determinant energies [73, 90]. Keeping frozen the MOs from an AOC-DFT calculation performed in advance, a series of different MO occupations can be emulated. The configurations produced in this way cannot be taken as spectral term energies, but offer useful information for retrieving LF parameters. The idea is similar to those for getting by broken symmetry (BS) [92, 93] method, the DFT estimation for the parameters from Heisenberg exchange coupling Hamiltonian. Namely, the BS configurations are not states with physical reality (being single determinants, not multiconfiguration objects as the spin eigenvectors are in general). However, the energies of these configurations can be formally equated with the parameters of interest, leading to their identification. Practically, the same situation is in the case of the LFDFT treatment [73, 81, 82, 90]. The information about the ligand field parameters can be exploited from the computed energies of various configurations. Besides, the two-electron parameters can be inferred too. Notably, the possibility to handle occupation schemes (to generate Slater determinants) and fractional occupations (to do the AOC step) is not found in all the DFT codes, the ADF being a particularly suited package [65, 66, 77].

The Tb^{III} systems are convenient for mimicking the ligand field diagrams. This implies running the beta electron of the f^8 configuration over the seven MOs obtained in preamble by the AOC procedure. Considering the parentage from the

^{7}F atomic term, the amount of two-electron effects is the same over the seven components, counting only as a uniform shift of the LF split multiplet. The LF consists in the one-electron component of the full Hamiltonian and the mentioned procedure can identify correctly this part. Even though it can be implicitly believed that the MO energies of the frontier MOs are giving the LF diagram, this is not rigorously true. It is because the MO levels contain aside the one-electron (electron–nuclear and kinetic) components also the averaged two-electron (Coulomb and exchange) effects.

Running the beta electron of the f^8 configuration, successively over the AOC orbitals of the complex $[Tb(mpca\text{-}Li)_2(NC\text{-}Li)_3(CH_3OH)_2]^{3+}$, one obtains with different functionals the following series of energies, assimilated to the LF split: LDA = {0, 156, 2,009, 2,125, 2,229, 2,356, 2,652} cm^{-1}, BP86 = {0, 261, 1,865, 2,058, 2,146, 2,205, 2,439} cm^{-1}, and B3LYP = {0, 635, 721, 774, 942, 1,875, 1,934} cm^{-1}. It seems that in this case the total gap of computed LF is overestimated, since we expect an aperture in the order of few hundreds of wavenumbers [14, 62] while obtaining a couple of thousands. However, one may also see that the gaps become smaller by passing from genuine LDA functional to the gradient-corrected one (BP86) and to the hybrid version. Besides, looking at the successive gaps inside each multiplet, one notes that while LDA and BP86 showed only the first spacing in the acceptable range of hundreds of wavenumbers, the B3LYP yielded five reasonable values. This suggests that the good result is a matter of finding the proper functional. Possibly, it may be the case to bring the long-range corrections into the calculation recipe. In simpler systems based on halide environments, where ionic interaction dominates, the LFDFT approach was proven to account well for the ligand field parameters [17, 94]. Another hypothesis on the overestimated gaps in systems with large organic ligands suggests the accidental higher content of ligand functions in the f-type MOs, leading to a nonphysical shift of the computed quantities. It may be that a percent of 93% in some MOs, as shown in the previous section, is still unsatisfactorily. The correct range is around 98–99% f-type content. Another possibility is that the imposed *aufbau*-type AOC is not the best solution, once the possibility of a non-*aufbau* pattern was foreseen.

Examining the $[Lu(mpca\text{-}Li)_2(NC\text{-}Li)_3(CH_3OH)_2]^{3+}$ orbital diagram given in Fig. 19, one notes a different pattern from those shown for the terbium congener. Namely, the MOs having preponderant f content are located much below the frontier MOs, in contrast to the terbium case where the f-type MOs were imposed as the highest occupied orbitals. The Lu^{III} complex is a simple closed-shell problem, due to the f^{14} configuration. However, it may be considered that the lanthanide ions are similar to each other, and therefore, the lutetium molecular diagram is valid to other ion complexes (at least for the previous element, Yb^{III}, with f^{13} configuration, and one unpaired electron). From this perspective, it would then seem that the paramagnetic lanthanide complexes should be non-*aufbau*. Figures 18 and 19 suggest the possibility to have a partly filled f shell placed below the occupied MOs originating from ligands or other components of the system. In principle, it is possible to catch a non-*aufbau* AOC set, but technically this is difficult in low-symmetry complexes. Given the high density of states in medium-sized or

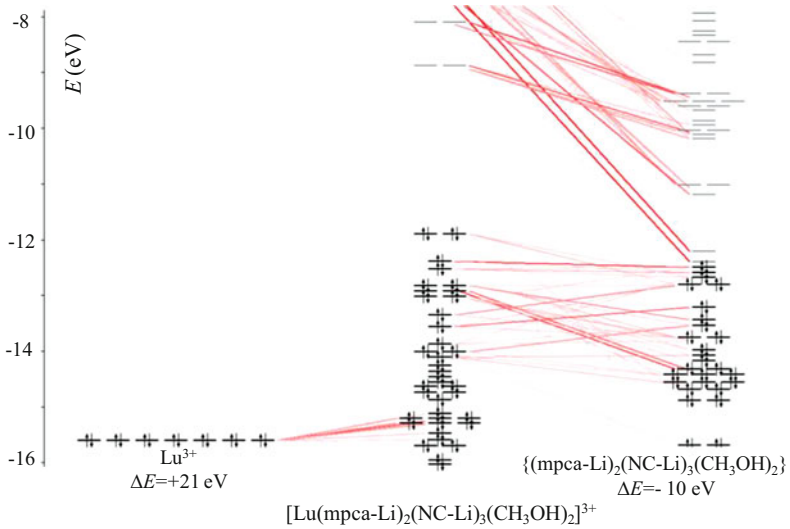

Fig. 19 The MO levels from the restricted calculation on closed-shell $[Lu(mpca\text{-}Li)_2(NC\text{-}Li)_3(CH_3OH)_2]^{3+}$ showing the parentage of MOs from Lu^{III} and ligand orbitals. The fragments levels are shifted conventionally (respectively, by 21 and −10 eV) to better visualize the matching

large ligands, the convergence is flawed by accidental mixing of MOs with close energies but having topologies not justifying a mutual interaction. In such cases, it is also difficult to predefine the position of a non-*aufbau* AOC sequence among the ordering of the many ligand-based MOs. The existence of such a different picture for different lanthanides, e.g., *aufbau* for Tb^{III} and non-*aufbau* alike toward the end of the Ln^{III} series, remains an open question.

Finally, it is important to mention that the lanthanide complexes are difficult to converge in usual restricted open-shell DFT calculations, where the control of orbital occupations is not possible (the only leverage being the molecular charge and spin projection value). The AOC procedure, smearing equally the f^n occupations over a set of targeted orbitals, is essential for obtaining a solution of formal restricted frame, compatible with ligand field concepts. The unrestricted DFT runs are easier to converge with standard procedures, but the resulted MOs are not of immediate use in LF sense.

6 The Multi-configuration Electron Structure Methods Illustrated in MOF Lanthanide Units

In this section, we will present a different approach based on complete active space self-consistent field (CASSCF) [88] and related methods. In this procedure, a set of input orbitals (active space) and a number of occupying electrons must be selected.

The calculation yields an output set of optimized canonical MOs. Simultaneously, the method accounts for all the excited states of a given spin multiplicity possible with the actual number of electrons in the orbital manifold. For lanthanide complexes, the CASSCF-optimized orbitals show always almost pure f-type shapes, with very small tails due to ligand components, provided that an appropriate starting guess was defined [57, 60, 95].

The CASSCF and subsequent spin-orbit techniques are well suited to represent the physics of lanthanide complexes. They reproduce the effect related with the quasi-degenerate status of ligand field multiplets and the corresponding optical and magnetic properties [15, 96]. The spin–orbit (SO) Hamiltonian can be called at the end of the self-consistent calculation. In a mononuclear complex, one must select an active space related with the given f^n configuration, namely, CASSCF(7,*n*), i.e., *n* electrons in seven orbitals. Besides, it is important to perform a so-called state-averaged calculation, giving equal weights to the states originating from the degenerate ground state of the lanthanide ion. This influences the nature of optimized orbitals, yielding a well-balanced set for all the states. It is in the spirit of a barycenter conceived when a ligand field split is figured with levels going up and down with respect of a conventional zero line, taken as their weighted average. Thus, the ground term is ^{7}F for the Tb^{III} ion and a terbium complex is worked with a CASSCF (7, 8) calculation averaged over seven states. The CASSCF accounts for the ligand field split of this term, the diagram being formally identical to the split of f orbitals. As discussed in the previous section, in conjuncture with LFDFT approach, the beta electron of the f^8 configuration (running on the seven active f-type orbitals) senses only the one-electron effects. The two-electron part is a common background for all the seven possible Slater determinants (considering the $S_z = 3$ spin projection). The calculation goes on the 49 states when the SO interaction is added, implied by the product of orbital and spin septets. For an Eu^{III} complex with f^6 configuration (and considering that the ground term of free ion is also ^{7}F), the state average is also on seven orbital states. In this case, the CASSCF (7, 6) calculations will yield a scheme looking like the reverse of ligand field split, since now we run a hole in an f^7 reference. It is contrary to the Tb^{III} case, where we are playing a particle over a half-filled shell. Finally, the orbital septet and corresponding seven-state averaging is considered for a Ce^{III} complex, the f^1 case where the ^{2}F-type spectral term diagram genuinely coincides with the f-type ligand field split. Conversely, the ^{2}F encountered in the Yb^{III} complexes (f^{13} configuration) is the result of a hole in the filled f^{14} reference.

For a Dy^{III} mononuclear complex, namely, a f^9 case, the CASSCF (7, 9) calculation has to be averaged over the eleven states corresponding to the high spin projection of the ^{6}H term. The SO calculation will use all the 66 terms resulted from the product of orbital and spin multiplicities. The f^9 case of Dy^{III} can be regarded as two particles (beta electrons) running over the half-filled f shell. The f^5 configuration of samarium, equivalent to two holes in the f^7 occupation, will also have an H term, and therefore, 11 states have to be averaged. Obviously, the f^2 configuration of praseodymium and the f^{12} of thulium (equivalent of two holes in

the f^{14} closed shell) will show the same orbital term and state-average pattern into the CASSCF calculations.

Another series of lanthanides are those having I-type ground term ($L = 6$) with orbital multiplicity 13 (to be considered in the state-averaged CASSCF approaches). This series occurs in the case of three particles or holes over seven orbitals. This situation occurs in the following cases: $Nd^{III} \equiv f^3$, $Pm^{III} \equiv f^4$ (three holes with respect to f^7), $Ho^{III} \equiv f^{10}$ (three particles over f^7), and $Er^{III} \equiv f^{11}$ (three holes with respect to f^{14}).

Finally, there is the trivial case of f^7 configuration of Gd^{III} which has no orbital degeneracy. In addition, there are the closed-shell diamagnetic La^{III} with f^0 configuration and Lu^{III} with f^{14}. These are in principle not objects of a CASSCF calculation. However, in the case of Gd^{III}, even though equivalent to a restricted open-shell Hartree–Fock (ROHF), the CASSCF approach converges better than under the ROHF keyword. Besides, the CASSCF becomes again legitimate in approaching the multiplets resulted from lower spin multiplicities of the f^7 case, e.g., the spin sextet series. The sextets are important in estimating the weak zero-field-splitting (ZFS) effect [95].

The above paragraphs present the state-average multiplicities to be considered along the lanthanide series. To summarize, the ground states associated with lanthanide free ions are $Ce^{III} \equiv {}^2F$, $Pr^{III} \equiv {}^3H$, $Nd^{III} \equiv {}^4I$, $Pm^{III} \equiv {}^5I$, $Sm^{III} \equiv {}^6H$, $Eu^{III} \equiv {}^7F$, $Gd^{III} \equiv {}^8S$, $Tb^{III} \equiv {}^7F$, $Dy^{III} \equiv {}^6H$, $Ho^{III} \equiv {}^5I$, $Er^{III} \equiv {}^4I$, $Tn^{III} \equiv {}^3H$, and $Yb^{III} \equiv {}^2F$. One notes the alternation of only three types of degenerate terms: F, H, and I with the corresponding 7, 11, and 13 multiplicities. For the f^7 nondegenerate configuration, the CASSCF turns into Hartree–Fock, which is the simplest electron structure method. Therefore, CASSCF does not contain enough of so-called non-dynamic correlation [97]. The electron correlation is the ingredient that would amend the average of two-electron effects imposed in the Hartree–Fock (HF) method. Namely, in HF, one electron feels the others only in a smeared manner. The method does not account well the fact that the electrons should avoid the close distance encounters. The HF methods yield higher total energies by not including such conditional probability into the wave function. The lack of electron correlation can be solved by using an extended configuration interaction (CI). Thus, all electrons and orbitals of the basis set are allowed to run all possible configurations. Then, the CASSCF is a compromise; it allows selecting a number of physically significant orbitals (the f orbitals) and occupying electrons. It does the CI over all the states in this space. The electron correlation accounted in this way is called dynamical. The non-dynamical part is then the remainder of the electron correlation, in principle up to the full CI limit.

The methods for tackling the non-dynamic correlation in wave function theory are very expensive and prone to some arbitrary choices of computational frame. For instance, the second-order perturbation increments (PT2) [98, 99], devised to be used as post-CASSCF correction, are defined in several conventions [100, 101]. The various PT2 treatments are giving different results applied to the same CASSCF. Besides, such methods are non-variational and certain properties related to the self-consistency are lost. The PT2 corrections are useful in the cases when the

limited choice of the active space does not reflect well the physics of the considered problem. However, in the case of lanthanides, most of the magnetic and optical effects are occurring inside the partly filled f shell. As discussed above, the active space confined to the f^n configuration is a perfectly reasonable choice. Cimpoesu and coworkers showed that the PT2 treatments do not change fundamentally the computed levels with respect to the CASSCF background [102, 103]. They also showed that these treatments do not add essential touches to the revealed physical meaning [102, 103]. Therefore, the CASSCF can account well the basic properties of lanthanide complexes, at the scale of realistic molecules. Besides, the CASSCF background is in line with the ligand field paradigm, which is also based on the idea of a CI performed on the f^n multiplets.

The essential step in performing ab initio calculations on lanthanides is a starting set of orbitals resembling the f AOs themselves. In all circumstances, the CASSCF needs certain predefined starting orbitals which, usually, are provided by DFT or HF routes. However, it is difficult to find a good solution in this way. To the best of our knowledge, no ab initio multiconfiguration calculations on realistic lanthanide complexes were performed prior to the pioneering work of Cimpoesu and coworkers [103, 104]. Most probably, this is because the advance was hindered in the step of obtaining starting MOs. The problem was solved in the following way: first, regular HF calculations were performed on the free lanthanide ion and ligand fragments, and then they merged the orbital blocks "by hand," with the help of auxiliary programs. In this way, one obtains a molecular-like matrix of orbital coefficients where the block between lanthanide and ligands was set to zero. This is in line with the weakly interacting nature of the lanthanides and proved to be a good choice to trigger the CASSCF calculations. It is not the only possible starting MO set, but it is very convenient, since the final CASSCF orbitals resemble much the pure f-type AOs. Another possibility is to take natural orbitals from unrestricted DFT calculations.

Next, the CASSCF approach on the $[Tb(mpca\text{-}Li)_2(NC\text{-}Li)_3(CH_3OH)_2]^{3+}$ unit will be discussed. The technical setting was reported previously [17]. The CASSCF (7,8) calculation with state average over the seven roots gives the following eigenvalues: 0, 108, 209, 263, 375, 671, and 760, all in cm^{-1}. These values represent the LF split of the ^7F term. The CASSCF yields smaller values than the previously reported approach by DFT, obeying the expected range, usual for LF on the f shell [14, 62]. Figure 20 shows the canonical MOs. It is visible that these are almost pure f shapes. For completeness, Table 9 gives the transformation coefficients of the MOs with respect to the standard f atomic orbitals (illustrated at the bottom of Fig. 20). This is a unitary transformation, the mutual mixing of pure f-type shapes into the MOs being determined by the ligand field effects.

The ligand field for d orbitals is well known by coordination and inorganic chemists, mostly at qualitative basics. The ligand field for f shell had not reached a similar level of popularity. In fact, the basic premises of ligand field are held in better conditions for the f-shell case than for the d orbitals. Namely, the fact that one may trust the physical problem at hand to a basis resembling pure AOs is better obeyed by the f shell. Figure 20 shows indeed that the rigorously computed MOs

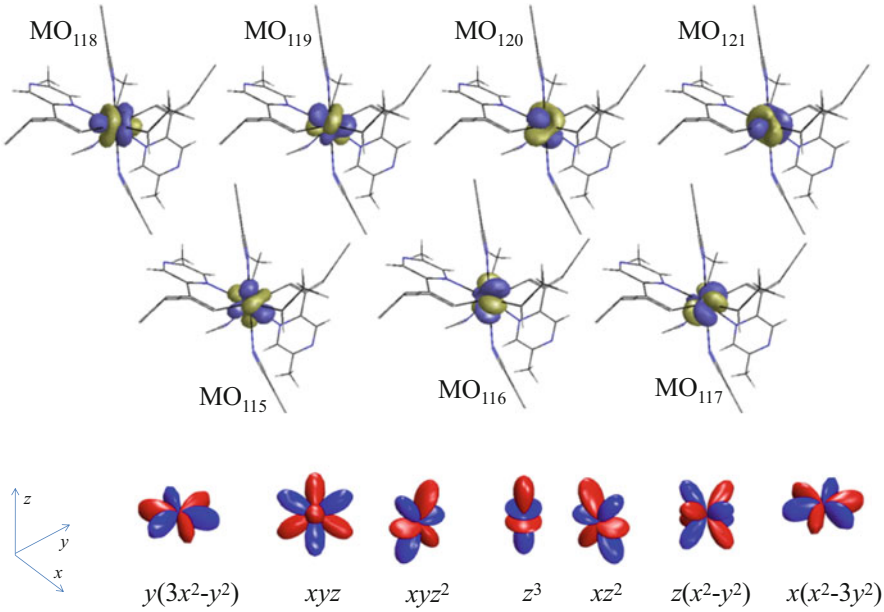

Fig. 20 *Upper part*: the shapes of canonical molecular orbitals (MO_{115}-MO_{121}) resulted from a CASSCF calculation on $[Tb(mpca\text{-}Li)_2(NC\text{-}Li)_3(CH_3OH)_2]^{3+}$. *Lower part*: the axial symmetry definition of f-type AOs

Table 9 The coefficients of the unitary transformation defining the composition of f-type canonical CASSCF orbitals (MO_{115}-MO_{121}) with respect of pure f-type AOs

	$y(3x^2\text{-}y^2)$	xyz	xyz^2	z^3	xz^2	$z(x^2\text{-}y^2)$	$x(x^2\text{-}3y^2)$
MO_{115}	−0.103	0.385	−0.115	0.780	0.290	0.302	−0.206
MO_{116}	0.157	−0.074	0.756	0.209	0.412	−0.404	0.143
MO_{117}	−0.057	−0.234	0.480	−0.171	0.022	0.820	−0.090
MO_{118}	−0.276	−0.066	−0.308	−0.307	0.802	0.087	0.279
MO_{119}	−0.478	0.701	0.286	−0.368	−0.051	−0.100	−0.221
MO_{120}	0.544	0.531	0.002	−0.107	−0.041	0.232	0.595
MO_{121}	0.600	0.111	−0.088	−0.275	0.310	−0.015	−0.668

contain an overwhelming f percentage. By contrast, the canonical orbitals for d-type problem have usually a rather high ligand-type content (≈20–30%) [80, 82]. In certain problems, like those handling the 4f–5d transitions, the lanthanides must be described in a more advanced manner, e.g., by using an extended LF Hamiltonian containing both the f and d blocks simultaneously.

The master ligand field formula for the f shell is

$$\hat{H}_{\mathrm{LF}}^{\mathrm{f}} = \sum_{k=2,4,6} \sqrt{\frac{4\pi}{2k+1}} \left(B_k^0 Y_{k,0}(\theta,\phi) + \sum_{q=1}^{2k+1} B_k^q Z_{k,q}(\theta,\phi) + i \sum_{q=1}^{2k+1} B_k^{-q} Z_{k,-q}(\theta,\phi) \right), \tag{1}$$

where $B_k{}^q$ are the nominal LF parameters, $Y_{k,q}$ spherical harmonic functions, and $Z_{k,q}$ their combination, as follows:

$$Z_{k,q}(\theta,\phi) = \left(Y_{k,q}(\theta,\phi) + (-1)^q Y_{k,-q}(\theta,\phi) \right), \tag{2}$$

$$Z_{k,-q}(\theta,\phi) = \left(Y_{k,q}(\theta,\phi) - (-1)^q Y_{k,-q}(\theta,\phi) \right). \tag{3}$$

For the $[Tb(mpca\text{-}Li)_2(NC\text{-}Li)_3(CH_3OH)_2]^{3+}$ example, the LF parameters are as follows: (1) in the $B_2{}^q$ series with q running from -2 to 2 by unit steps, the values are $\{-50.9, 138.5, 41.2, -98.9, -159.5\}$ (all in cm^{-1}); (2) in the $B_4{}^q$ set with $q = -4{:}4$ the set is $\{29.1, -33.3, -253.6, -3.3, 149.6, 394.5, 317.4, -295.8, -55.1\}$ (in cm^{-1}); and (3) for the $B_6{}^q$ series with $q = -6{:}6$ reads $\{216.0, 2.9, 54.2, -138.1, 143.2, -16.4, 36.2, 16.9, -755.3, -336.6, 49.3, -685.0, 130.7\}$ (in cm^{-1}). The $B_k{}^q$ parameters are not very transparent to the chemical intuition. In the low-symmetry case (as presented here), there are 27 independent parameters, counting $2k+1$ components for the $k = 2, 4, 6$ integers running the summation from Eq. (1). Since the spherical harmonics are well-defined expressions, Eq. (1) is nothing else than a parametric trigonometric expression. Then, it is possible to give an intuitive illustration of the LF Hamiltonian drawing the color map (conventionally represented on a sphere of arbitrary radius) of the trigonometric expression from (1) taken with the corresponding set of $B_k{}^q$ parameters.

Aside from the $[Tb(mpca\text{-}Li)_2(NC\text{-}Li)_3(CH_3OH)_2]^{3+}$ unit from actual CASSCF discussion, the simpler case of the $[Nd(H_2O)_8]^{3+}$ cubic unit is also inserted. For the simple aqua complex, one observes that, at the ligand places, the map coloring shows areas of positive values. These correspond to the perturbation exerted to the f electrons by ligand lone pairs. In between ligands, the blue color suggests negative potential. The average on all sphere is conventionally set to zero, corresponding to the LF barycenter. The map of the more complex case shown in Fig. 21b shows similar features, but it is also affected by an artificial manifestation of the LF potential, called holohedrization effect [105, 106]. The perturbations exerted from opposed parts of an axis, e.g., the A and B ligands, cannot be discriminated at their different strengths, having in turn the $(A+B)/2$ smeared perturbation, equally shared by both sides of the $A-B$ axis. Therefore, the map shows the area of high potential in zones where there is no ligand. It is because a ligand placed at the antipode of the sphere exerts a perturbation. This artificial manifestation happens because the $f \times f$ ligand field matrix includes only elements with $u \times u = g$ symmetric inversion parity and cannot mimic the asymmetric u pattern. An alternative explanation is the fact that Eq. (1) contains only even $k = 2, 4, 6$ spherical harmonics, which are all g-type. Then, the LF potential imposes an inversion center even in low-symmetry point groups. It follows that the LF mapping of the CASSCF

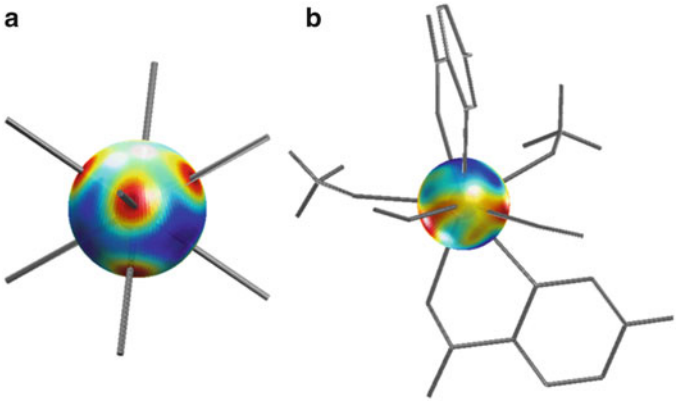

Fig. 21 The color map of the ligand field potential taken with B_k^q parameters fitted from ab initio multiconfiguration calculations. (**a**) The case of $[Nd(H_2O)_8]^{3+}$ complex from [39]; (**b**) the $[Tb(mpca\text{-}Li)_2(NC\text{-}Li)_3(CH_3OH)_2]^{3+}$ unit from [42]. The *red areas* represent zones of high ligand field perturbation, the blue ones the counterparts of low potential

results can be in certain circumstances unsatisfactory. The holohedrization effect can be cured in a two-open-shell approach [107] with f and d ligand field Hamiltonian components. Thus, it allows accounting the asymmetric terms due to the $g \times u = u$ parity of the f × d nondiagonal block.

The complete description of the lanthanide complexes demands the spin–orbit treatment. It is notorious that in f systems the SO part exceeds the LF one [14, 62]. Thus, for the free Tb^{III} ion, the computed SO multiplet energies are {0, 1,923, 3,525, 4,807, 5,769, 6,410, 6,730} (in cm^{-1}) for the respective $J = \{6, 5, 4, 3, 2, 1, 0\}$, in relatively good accordance with the experimental lines [108] {0, 2,052, 3,314, 4,292, 4,978, 5,432, 5,654} (in cm^{-1}), especially for the lowest sequence. The presented values show the respective $2J + 1$ degeneracies. Each J multiplet splits due to the LF of a given symmetry. Thus, the levels originating from ground $J = 6$ term (with the multiplicity 13) are computed in the $[Tb(mpca\text{-}Li)_2(NC\text{-}Li)_3(CH_3OH)_2]^{3+}$ unit as follows: {0.0, 1.2, 45.0, 54.0, 91.7, 128.3, 140.2, 218.4, 223.4, 349.7, 351.2, 549.2, 549.4} (in cm^{-1}). The next values are like 1,982.1 cm^{-1}, 1,989.5 cm^{-1}, etc. belonging to the higher $J = 5$ spin–orbit term. It can be observed that the LF part is encapsulated into the SO pattern. Certain couples of levels are in quasi-degenerate relationships. In the case of lanthanide ions with half integer J quantum numbers, the levels occur in rigorously degenerate levels. The combination of ligand field and spin–orbit effects determines the magnetic anisotropy. This is a characteristic necessary to make a system behaving as a molecular or nanoscale magnet [109, 110]. The spin-only magnetism is not sufficient to bring a system to be a nominal magnet, because it is isotropic and cannot impose an axis carrying the north and south poles [15, 96]. Cimpoesu and coworkers developed a useful tool for investigating the magnetic anisotropy, the so-called polar maps of state-specific magnetizations. These maps are given by the response (field derivative) of a certain state when it is perturbed by a probe field,

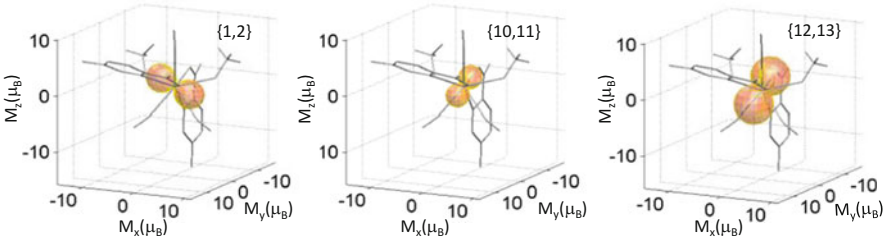

Fig. 22 The polar maps for selected state from the CASSCF-SO spectrum of the $[Tb(mpca\text{-}Li)_2(NC\text{-}Li)_3(CH_3OH)_2]^{3+}$ complex. The maps are similar for quasi-degenerate pairs of states marked in the upper-right corner of each panel ({1, 2}, {10, 11}, {12, 13}). The other states show lobes with smaller lobes

imposed from the various directions around the paramagnetic center [17, 95]. For an isotropic system, the polar maps are spheres. By contrast, in anisotropic systems, the polar maps of the $|dE_i/dB|$ derivative function for a given ith level of the CASSCF-SO spectrum (scanned on a grid of (θ, φ) angles) are taking certain shapes. Often, these shapes resemble the two-lobe pattern illustrated in Fig. 22. The orientation of the lobes indicates the magnetic axis of the given state, while its extension equals the carried magnetic moment. For a molecular magnet behavior, the magnetic anisotropy of the ground state is the important characteristic. However, this property can be defined for each state, and the extended account of this effect may be important for devising systems responding to combined stimuli, e.g., optical and magnetic.

Summary, Conclusions, and Outlook

The metal-organic frameworks can be presented as having features intermediate between coordination compounds and simple solid lattices, such as oxides and halides. The local structures have the bonding characteristics of mononuclear molecular complexes, while the 3D architecture may favor properties and applications usually reserved to solid phase. The lanthanide-based MOFs are enriching the tableau of structure–property relationships with the various manifestations tuned by the electron configuration and particular pattern of ligand field. The magnetic anisotropy is one of the interesting consequences and challenging issues. There is, nowadays, a tremendous interest for molecules behaving as magnets, the so-called single-molecule magnets (SMMs) and, more intriguingly, the single-ion magnets (SIMs) [5, 111–113]. The fascination on SMMs and SIMs can be correlated with the interest to deconstruct the complicate magnetism from solid state to the smaller and more intuitively tractable molecular case studies. Now, the MOFs offer the occasion to recompose the tableau of magnet behavior at extended scale and 3D connectivity, once the microscopic mechanisms,

(continued)

namely, the magnetic anisotropy as essential ingredient, start to be understood.

To the best of our knowledge, systematic theoretical studies on MOFs are not yet developed, given the relative novelty of the topic and a certain complexity related with size of the nodes and the periodicity of the lattice. At one hand, these systems are somewhat nonstandard for solid-state (band) electronic structure methods and, on the other hand, were not yet properly focalized from the perspective of molecular-based treatments. We compensated this lack selecting a series of MOFs with representative coordination moieties. These MOFs were treated in a unitary manner, with methods dedicated to the specifics of f-type systems. Such approaches discussed here on building blocks of MOF systems are breakthroughs and pioneering contributions in the ab initio treatment of lanthanide complexes [103, 104].

Due to electronic structure particularities of lanthanide units, the emerging properties, such as the magnetic anisotropy, are local. Then, the models obtained by proper excerpt of molecular fragments from MOF lattices are reasonable approaches. At the same time, in general concerns of bonding effects, the lanthanides are similar to each other, as ions in molecule, and the convenient closed-shell case of lutetium complexes as replacement of other congeners can be taken. The f shell is strongly contracted (as radial extension) inside the atomic body and does not contribute itself to bonding effects, determining the similarity of among the isostructural complexes along the f series. Taking lutetium complexes as representative for basic bonding features, we presented energy decomposition analysis to DFT calculations on several MOF building blocks. The treatment of paramagnetic f complexes is a subtle deal. In the frame of popular DFT methods, the routine ways cannot be followed, demanding special methodologies such as average of configuration (AOC) [81, 85] where, treating a complex with a f^n ion, n electrons are distributed over seven predefined MOs. This exploits the conceptual and technical capacity of DFT to handle fractional populations. Numeric experiments with various orbital configurations enable a description in terms of ligand field theory, with an algorithm named LFDFT [73, 81, 82, 90].

An alternative treatment is done with the help of multiconfiguration methods such as CASSCF (complete active space self-consistent field) that can enable a good description of ligand field parameters even in difficult low-symmetry cases. We showed picturesque approaches to rather complicated issues such as the ligand field modeling, drawing the potential as color map on a conventional coordination sphere. The magnetic anisotropy receives an intuitive explanation by presenting the polar maps of derivatives of energy levels with respect of a perturbing field, scanned around the coordination sphere. In other words, these maps are checking the response of a given state to a perturbation to a field applied from a certain direction.

(continued)

The direction with higher response corresponds to the so-called easy axis and the magnitude of the field derivative in this direction equals the magnetic moment carried by the given wave function component. This analysis casts a new light in the intricate problems of ligand field and magnetic anisotropy in lanthanide units, being also the key for understanding the properties of MOFs starting from the structural characterization of their metal ion nodes. The insight by theoretical methods, brought as much as possible to the transparent language of chemical intuition, is a sine qua non condition for engineering properties in a rational manner, by understanding the underlying mechanisms and choosing the relevant parameters to be used as leverage to alleviate the desired functionalities.

We foresee that further development in the field of d–f cyanide-bridged metal-organic frameworks will be in the direction of materials with coexisting properties, e.g., magneto-optical and magneto-electric materials. Recently, it was shown that MOFs can indeed show such properties [114, 115] which are mainly found in pure inorganic materials.

Acknowledgments ST thanks the Netherlands Organisation for Scientific Research (NWO) for a Veni grant. FC and MF acknowledge support from the Romania-Italy cooperation grant of Romanian Academy and PCE 14/2013 UEFISCDI research grant. We thank Dr. Alessandro Stroppa for useful discussions.

References

1. Cable ML, Kirby JP, Gray HB, Ponce A (2013) Enhancement of anion binding in lanthanide optical sensors. Acc Chem Res 46(11):2576–2584. doi:10.1021/ar400050t
2. Cui Y, Chen B, Qian G (2014) Lanthanide metal-organic frameworks for luminescent sensing and light-emitting applications. Coord Chem Rev 273:76–86. doi:10.1016/j.ccr.2013.10.023
3. Habib F, Murugesu M (2013) Lessons learned from dinuclear lanthanide nano-magnets. Chem Soc Rev 42(8):3278–3288. doi:10.1039/c2cs35361j
4. Roy S, Chakraborty A, Maji TK (2014) Lanthanide-organic frameworks for gas storage and as magneto-luminescent materials. Coord Chem Rev 273:139–164. doi:10.1016/j.ccr.2014.03.035
5. Woodruff DN, Winpenny REP, Layfield RA (2013) Lanthanide single-molecule magnets. Chem Rev 113(7):5110–5148. doi:10.1021/cr400018q
6. Tanase S, Reedijk J (2006) Chemistry and magnetism of cyanido-bridged d-f assemblies. Coord Chem Rev 250(19–20):2501–2510. doi:10.1016/j.ccr.2006.03.021
7. Beltran LMC, Long JR (2005) Directed assembly of metal-cyanide cluster magnets. Acc Chem Res 38(4):325–334. doi:10.1021/ar040158e
8. Bleuzen A, Marvaud V, Mathoniere C, Sieklucka B, Verdaguer M (2009) Photomagnetism in clusters and extended molecule-based magnets. Inorg Chem 48(8):3453–3466. doi:10.1021/ic802007g
9. Culp JT, Park JH, Frye F, Huh YD, Meisel MW, Talham DR (2005) Magnetism of metal cyanide networks assembled at interfaces. Coord Chem Rev 249(23):2642–2648. doi:10.1016/j.ccr.2005.05.011

10. Newton GN, Nihei M, Oshio H (2011) Cyanide-bridged molecular squares – the building units of prussian blue. Eur J Inorg Chem 20:3031–3042. doi:10.1002/ejic.201100407
11. Shatruk M, Avendano C, Dunbar KR (2009) Cyanide-bridged complexes of transition metals: a molecular magnetism perspective. In: Karlin KD (ed) Progress in inorganic chemistry, vol 56. Progress in inorganic chemistry. pp 155–334. doi:10.1002/9780470440124.ch3
12. Sieklucka B, Podgajny R, Korzeniak T, Nowicka B, Pinkowicz D, Koziel M (2011) A decade of octacyanides in polynuclear molecular materials. Eur J Inorg Chem 3:305–326. doi:10.1002/ejic.201001055
13. Wang S, Ding X-H, Zuo J-L, You X-Z, Huang W (2011) Tricyanometalate molecular chemistry: a type of versatile building blocks for the construction of cyano-bridged molecular architectures. Coord Chem Rev 255(15–16):1713–1732. doi:10.1016/j.ccr.2011.01.057
14. Newman DJ, Ng B (2000) Crystal field handbook. Cambridge University Press, Cambridge
15. Ferbinteanu M, Cimpoesu F (2014) Magnetic anisotropy in case studies. In: Putz M (ed) Quantum nanosystems: structure, properties and interactions. Apple Academics, Toronto, pp 254–294. ISBN 978-1-926895-90-1
16. Sorace L, Sangregorio C, Figuerola A, Benelli C, Gatteschi D (2009) Magnetic interactions and magnetic anisotropy in exchange coupled 4f-3d systems: a case study of a heterodinuclear Ce^{3+}–Fe^{3+} cyanide-bridged complex. Chem Eur J 15(6):1377–1388. doi:10.1002/chem.200801638
17. Tanase S, Ferbinteanu M, Cimpoesu F (2011) Rationalization of the lanthanide-ion-driven magnetic properties in a series of 4f-5d cyano-bridged chains. Inorg Chem 50(19):9678–9687. doi:10.1021/ic201427w
18. Hulliger F, Landolt M, Vetsch H (1976) Rare-earth ferricyanides and chromicyanides LNT (CN)6.NH2O. J Solid State Chem 18(3):283–291. doi:10.1016/0022-4596(76)90107-9
19. Hulliger F, Landolt M, Vetsch H (1976) Rare-earth cobalticyanides LNCO(CN)6.NH2O. J Solid State Chem 18(4):307–312. doi:10.1016/0022-4596(76)90111-0
20. Mullica DF, Perkins HO, Sappenfield EL, Grossie DA (1988) Synthesis and structural study of samarium hexacyanoferrate (III) tetrahydrate, SMFE(CN)6.4H2O. J Solid State Chem 74 (1):9–15. doi:10.1016/0022-4596(88)90324-6
21. Dechambenoit P, Long JR (2011) Microporous magnets. Chem Soc Rev 40(6):3249–3265. doi:10.1039/c0cs00167h
22. Uemura T, Ohba M, Kitagawa S (2004) Size and surface effects of Prussian blue nanoparticles protected by organic polymers. Inorg Chem 43(23):7339–7345. doi:10.1021/ic0488435
23. Sun HL, Shi HT, Zhao F, Qi LM, Gao S (2005) Shape-dependent magnetic properties of low-dimensional nanoscale Prussian blue (PB) analogue SmFe(CN)(6)center dot 4H(2)O. Chem Commun 34:4339–4341. doi:10.1039/b507240a
24. Guari Y, Larionova J, Corti M, Lascialfari A, Marinone M, Poletti G, Molvinger K, Guerin C (2008) Cyano-bridged coordination polymer nanoparticles with high nuclear relaxivity: toward new contrast agents for MRI. Dalton Trans 28:3658–3660. doi:10.1039/b808221a
25. Yamada M, Yonekura S (2009) Nanometric metal-organic framework of Ln Fe(CN)(6): morphological analysis and thermal conversion dynamics by direct TEM observation. J Phys Chem C 113(52):21531–21537. doi:10.1021/jp907180e
26. Mullica DF, Hayward PK, Sappenfield EL (1996) Structural analyses of two hexacyanoruthenate(II) complexes. Inorg Chim Acta 253(1):97–101. doi:10.1016/s0020-1693(96)05113-4
27. Goubard F, Tabuteau A (2003) Synthesis, spectroscopic, thermal, and structural characterization of complex ferrocyanides KLnFe((II))(CN)(6)center dot 3.5H(2)O (Ln=Gd-Ho). Struct Chem 14(3):257–262. doi:10.1023/a:1023807728378
28. Artemkina SB, Naumov NG, Virovets AV, Gromilov SA, Fenske D, Fedorov VE (2001) New polymeric structure of rhenium octahedral chalcocyanide complex: Ln(3+)-derived network with one-dimensional channels. Inorg Chem Commun 4(8):423–426. doi:10.1016/s1387-7003(01)00230-1

29. Artemkina SB, Naumov NG, Virovets AV, Fedorov VE (2005) 3D-coordination cluster polymers Ln(H2O)(3)Re6Te8(CN)(6) center dot nH(2)O (Ln=La3+, Nd3+): direct structural analogy with the mononuclear LnM(CN)(6)center dot nH(2)O family. Eur J Inorg Chem 1:142–146. doi:10.1002/ejic.200400139
30. Efremova OA, Mironov YV, Kuratieva NV, Fedorov VE (2011) Two types of coordination polymers based on cluster anions Re(4)Q(4)(CN)(12) (4-) (Q=S, Se) and cations of rare-earth metals Ln(3+): syntheses and crystal structures. Polyhedron 30(8):1404–1411. doi:10.1016/j.poly.2011.02.051
31. Tarasenko MS, Naumov NG, Virovets AV, Kim SJ, Fedorov VE (2008) Crystal structure of Cs Gd(H2O)(4)Re6Te8(CN)(6) center dot 4H(2)O. J Struct Chem 49(6):1128–1131. doi:10.1007/s10947-008-0191-4
32. Tarasenko MS, Naumov NG, Naumov DY, Kim SJ, Fedorov VE (2008) A series of three-dimensional coordination polymers with general formula {Ln(H(2)O)(n)}{Re(6)Te(8)(CN)(6)} center dot xH(2)O (Ln=Eu, Gd, Tb, Dy, Ho, Er, Tm, Yb; n=3, 4, x=0, 2.5). Polyhedron 27(11):2357–2364. doi:10.1016/j.poly.2008.04.054
33. Tarasenko MS, Naumov NG, Virovets AV, Naumov DY, Kuratieva NV, Mironov YV, Ikorskii VN, Fedorov VE (2005) New coordination polymers based on paramagnetic cluster anions Re6Se8(Cn)(6) (3-) and rare earth cations: the synthesis and structure of {Ln(H2O)(3))}{Re6Se8(CN)(6)} center dot 3.5H(2)O. J Struct Chem 46:S137–S144. doi:10.1007/s10947-006-0164-4
34. Compain JD, Nakabayashi K, Ohkoshi S (2012) A polyoxometalate-cyanometalate multilayered coordination network. Inorg Chem 51(9):4897–4899. doi:10.1021/ic300263f
35. Compain JD, Nakabayashi K, Ohkoshi S (2013) Multilayered networks built from polyoxometalates and cyanometalates. Polyhedron 66:116–122. doi:10.1016/j.poly.2013.03.004
36. Plecnik CE, Liu SM, Shore SG (2003) Lanthanide-transition-metal complexes: from ion pairs to extended arrays. Acc Chem Res 36(7):499–508. doi:10.1021/ar010050o
37. Liu SM, Plecnik CE, Meyers EA, Shore SG (2005) Two distinct Ln(III)-Cu(I) cyanide extended arrays: structures and synthetic methodology for inclusion and layer complexes. Inorg Chem 44(2):282–292. doi:10.1021/ic040113+
38. Liu SM, Meyers EA, Shore SG (2002) An inclusion complex with Gd(dmf)(8) (3+) ions encapsulated in pockets of an anionic array of {Cu-6(CN)(9)}(3-) (infinity)units; a cyanide-bridged Cu-Gd layer structure. Angew Chem Int Ed 41(19):3609–3611. doi:10.1002/1521-3773(20021004)41:19<3609::aid-anie3609>3.0.co;2-#
39. Wang ZX, Shen XF, Wang J, Zhang P, Li YZ, Nfor EN, Song Y, Ohkoshi SI, Hashimoto K, You XZ (2006) A sodalite-like framework based on octacyanomolybdate and neodymium with guest methanol molecules and neodymium octahydrate ions. Angew Chem Int Ed 45(20):3287–3291. doi:10.1002/anie.200600455
40. Shiga T, Okawa H, Kitagawa S, Ohba M (2006) Stepwise synthesis and magnetic control of trimetallic magnets Co(2)Ln(L)(2)(H2O)(4) Cr(CN)(6) center dot nH(2)O (Ln = La, Gd; H2L=2,6-di(acetoacetyl)pyridine) with 3-D pillared-layer structure. J Am Chem Soc 128(51):16426–16427. doi:10.1021/ja066434x
41. Tanase S, Prins F, Smits JMM, de Gelder R (2006) Three-dimensional Ln(III)-W-IV complexes with cyanido and carboxylato bridges. Crystengcomm 8(12):863–865. doi:10.1039/b614215j
42. Tanase S, Mittelmeijer-Hazeleger MC, Rothenberg G, Mathoniere C, Jubera V, Smits JMM, de Gelder R (2011) A facile building-block synthesis of multifunctional lanthanide MOFs. J Mater Chem 21(39):15544–15551. doi:10.1039/c1jm12789f
43. Zhou H, Diao GW, Qian SY, Yang XZ, Yuan AH, Song Y, Li YZ (2012) Lanthanide-ion-tuned magnetic properties in a series of three-dimensional cyano-bridged Ln(III)W(V) assemblies. Dalton Trans 41(35):10690–10697. doi:10.1039/c2dt30615h

44. Zhou H, Yuan AH, Qian SY, Song Y, Diao GW (2010) Efficient synthetic strategy to construct three-dimensional 4f-5d networks using neutral two-dimensional layers as building blocks. Inorg Chem 49(13):5971–5976. doi:10.1021/ic100518b
45. Bowes CL, Ozin GA (1996) Self-assembling frameworks: beyond microporous oxides. Advanced Materials 8 (1):13. doi:10.1002/adma.19960080103
46. Ma Y-Z, Zhang L-M, Peng G, Zhao C-J, Dong R-T, Yang C-F, Deng H (2014) A series of three-dimensional 3d-4f cyanide heterometallic coordination polymers: synthesis, crystal structure, photoluminescent and magnetic properties. Crystengcomm 16(4):667–683. doi:10.1039/c3ce42025f
47. Herrera JM, Baca SG, Adams H, Ward MD (2006) Syntheses and structures of two- and three-dimensional cyanide-bridged coordination networks derived from crystallization of diimine-tetracyanoruthenate anions with gadolinium(III) cations. Polyhedron 25(4):869–875. doi:10.1016/j.poly.2005.09.013
48. Figuerola A, Diaz C, Ribas J, Tangoulis V, Granell J, Lloret F, Mahia J, Maestro M (2003) Synthesis and characterization of heterodinuclear Ln(3+)-Fe3+ and Ln(3+)-Co3+ complexes, bridged by cyanide ligand (Ln(3+)=lanthanide ions). Nature of the magnetic interaction in the Ln(3+)-Fe3+ complexes. Inorg Chem 42(2):641–649. doi:10.1021/ic025669g
49. Figuerola A, Diaz C, Ribas J, Tangoulis V, Sangregorio C, Gatteschi D, Maestro M, Mahia J (2003) Magnetism of cyano-bridged hetero-one-dimensional Ln(3+)-M3+ complexes (Ln(3+)=Sm, Gd, Yb; M3+=Fe-LS, Co). Inorg Chem 42(17):5274–5281. doi:10.1021/ic034051j
50. Figuerola A, Ribas J, Casanova D, Maestro M, Alvarez S, Diaz C (2005) Magnetism of cyano-bridged Ln(3+)-M3+ complexes. Part II: one-dimensional complexes (Ln(3+)=Eu, Tb, Dy, Ho, Er, Tm; M3+=Fe or Co) with bpy as blocking ligand. Inorg Chem 44(20):6949–6958. doi:10.1021/ic050650+
51. Figuerola A, Ribas J, Llunell M, Casanova D, Maestro M, Alvarez S, Diaz C (2005) Magnetic properties of cyano-bridged Ln(3+)-M3+ complexes. Part I: trinuclear complexes (Ln(3+) = La, Ce, Pr, Nd, Sm; M3+ = Fe-LS, Co) with bpy as blocking ligand. Inorg Chem 44 (20):6939–6948. doi:10.1021/ic050648i
52. Tangoulis V, Estrader M, Figuerola A, Ribas J, Diaz C (2007) Anisotropic exchange interactions in hetero-one-dimensional Ln(3+)-M3+ systems (Ln(3+)=Er, Yb; M3+=Cr, Fe-LS): magnetometry and dual mode X-band electron paramagnetic resonance spectroscopic studies. Chem Phys 336(1):74–82. doi:10.1016/j.chemphys.2007.05.016
53. Nowicka B, Korzeniak T, Stefanczyk O, Pinkowicz D, Chorazy S, Podgajny R, Sieklucka B (2012) The impact of ligands upon topology and functionality of octacyanidometallate-based assemblies. Coord Chem Rev 256(17–18):1946–1971. doi:10.1016/j.ccr.2012.04.008
54. Przychodzen P, Lewinski K, Pelka R, Balanda M, Tomala K, Sieklucka B (2006) Ln(terpy)(3+) (Ln=Sm, Gd) entity forms isolated magnetic chains with W(CN)(8) (3-). Dalton Trans 4:625–628. doi:10.1039/b511788g
55. Przychodzen P, Pelka R, Lewinski K, Supel J, Rams M, Tomala K, Sieklucka B (2007) Tuning of magnetic properties of polynuclear lanthanide(III)-octacyanotungstate(V) systems: determination of ligand-field parameters and exchange interaction. Inorg Chem 46(21):8924–8938. doi:10.1021/ic700795q
56. Hozumi T, Ohkoshi S, Arimoto Y, Seino H, Mizobe Y, Hashimoto K (2003) Cooling-rate dependent ferromagnetism in a two-dimensional cyano-bridged Sm(III)-W(V) complex. J Phys Chem B 107(42):11571–11574. doi:10.1021/jp0356057
57. Pasca E, Roscilde T, Evangelisti M, Burzuri E, Luis F, de Jongh LJ, Tanase S (2012) Realization of the one-dimensional anisotropic XY model in a Tb(III)-W(V) chain compound. Phys Rev B 85(18). doi:10.1103/PhysRevB.85.184434
58. Prins F, Pasca E, de Jongh LJ, Kooijman H, Spek AL, Tanase S (2007) Long-range magnetic ordering in a Tb-III-Mo-V cyanido-bridged quasi-one-dimensional complex. Angew Chem Int Ed 46(32):6081–6084. doi:10.1002/anie.200701847

59. Tanase S, de Jongh LJ, Prins F, Evangelisti M (2008) Ferrimagnetic Heisenberg chains derived from M(CN)(8) (3-) (M=MOV, W-V) building-blocks. ChemPhysChem 9 (14):1975–1978. doi:10.1002/cphc.200800345
60. Tanase S, Evangelisti M, de Jongh LJ (2011) Short-range correlations in d-f cyanido-bridged assemblies with XY and XY-Heisenberg anisotropy. Dalton Trans 40(33):8407–8413. doi:10.1039/c1dt10310e
61. Tanase S, Evangelisti M, de Jongh LJ, Smits JMM, de Gelder R (2008) Crystal structure, magnetic and thermal properties of the one-dimensional complex Nd(pzam)(3)(H(2)O)Mo (CN)(8) center dot H(2)O. Inorg Chim Acta 361(12–13):3548–3554. doi:10.1016/j.ica.2008.03.026
62. Hüfner S (1978) Optical spectra of transparent rare earth compounds. Academic, New York
63. Parr RG, Yang W (1989) Density-functional theory of atoms and molecules. Oxford University Press, New York
64. Koch W, Holthausen MC (2001) A chemist's guide to density functional theory. Wiley-VCH, Berlin
65. ADF Code (2012), Scientific computing & modelling (SCM), theoretical chemistry, Vrije Universiteit, Amsterdam. http://www.scm.com
66. Guerra CF, Snijders JG, te Velde G, Baerends EJ (1998) Towards an order-N DFT method. Theor Chem Accounts 99(6):391–403. doi:10.1007/s002140050021
67. Cotton S (2006) Lanthanide and actinide chemistry. Wiley, New York
68. Cotton FA, Wilkinson G (1988) Advanced inorganic chemistry, 5th edn. Wiley, New York
69. Becke AD (1988) Density-functional exchange-energy approximation with correct asymptotic-behavior. Phys Rev A 38(6):3098–3100. doi:10.1103/PhysRevA.38.3098
70. Perdew JP (1986) Density-functional approximation for the correlation-energy of the inhomogeneous electron-gas. Phys Rev B 33(12):8822–8824. doi:10.1103/PhysRevB.33.8822
71. Perdew JP, Sahni V, Harbola MK, Pathak RK (1986) 4th-Order gradient expansion of the fermion kinetic-energy – extra terms for nonanalytic densities. Phys Rev B 34(2):686–691. doi:10.1103/PhysRevB.34.686
72. von Hopffgarten M, Frenking G (2012) Energy decomposition analysis. Wiley Interdisciplinary Rev Computat Mol Sci 2(1):43–62. doi:10.1002/wcms.71
73. Ziegler T, Rauk A (1977) Calculation of bonding energies by Hartree–Fock slater method. 1. Transition-state method. Theor Chim Acta 46(1):1–10. doi:10.1007/bf02401406
74. Dykstra CE, Frenking G, Kim KS, Scuseria GE (2005) Theory and applications of computational chemistry. Elsevier BV, Amsterdam
75. Gritsenko OV, Schipper PRT, Baerends EJ (1998) Effect of Pauli repulsion on the molecular exchange-correlation Kohn-Sham potential: a comparative calculation of Ne-2 and N-2. Phys Rev A 57(5):3450–3457. doi:10.1103/PhysRevA.57.3450
76. Ferbinteanu M, Zaharia A, Girtu MA, Cimpoesu F (2010) Noncovalent effects in the coordination and assembling of the Fe(bpca)(2) Er(NO3)(3)(H2O)(4) NO3 system. Central Eur J Chem 8(3):519–529. doi:10.2478/s11532-010-0019-x
77. te Velde G, Bickelhaupt FM, Baerends EJ, Guerra CF, Van Gisbergen SJA, Snijders JG, Ziegler T (2001) Chemistry with ADF. J Comput Chem 22(9):931–967. doi:10.1002/jcc.1056
78. Hohenberg P, Kohn W (1964) Inhomogeneous electron gas. Phys Rev 136(3):864–871. doi:10.1103/PhysRev.136.B864
79. Kohn W, Sham LJ (1965) Self-consistent equations including exchange and correlation effects. Phys Rev A 140:1133–1138. doi:10.1103/PhysRev.140.A1133
80. Atanasov M, Busche C, Comba P, El Hallak F, Martin B, Rajaraman G, van Slageren J, Wadepohl H (2008) Trinuclear {M-1}CN{M-2}(2) complexes (M-1 = Cr-III, Fe-III, Co-III; M-2 = Cu-II, Ni-II, Mn-II). Are single molecule magnets predictable? Inorg Chem 47 (18):8112–8125. doi:10.1021/ic800556c
81. Atanasov M, Daul CA, Rauzy C (2003) New insights into the effects of covalency on the ligand field parameters: a DFT study. Chem Phys Lett 367(5–6):737–746. doi:10.1016/s0009-2614(02)01762-1

82. Atanasov M, Comba P, Daul CA (2008) Combined ligand field and density functional theory analysis of the magnetic anisotropy in oligonuclear complexes based on Fe-III-CN-M-II exchange-coupled pairs. Inorg Chem 47(7):2449–2463. doi:10.1021/ic701702x
83. Atanasov M, Daul C, Gudel HU, Wesolowski TA, Zbiri M (2005) Ground states, excited states, and metal-ligand bonding in rare earth hexachloro complexes: a DFT-based ligand field study. Inorg Chem 44(8):2954–2963. doi:10.1021/ic040105t
84. Zbiri M, Atanasov M, Daul C, Garcia-Lastra JM, Wesolowski TA (2004) Application of the density orbital-free embedding potential functional theory derived to calculate the splitting energies of lanthanide cations in chloroelpasolite crystals. Chem Phys Lett 397(4–6):441–446. doi:10.1016/j.cplett.2004.09.010
85. Reinen D, Atanasov M (2004) The angular overlap model and vibronic coupling in treating s-p and d-s mixing – a DFT study. Struct Bond 107:159–178
86. Gross EKU, Oliveira LN, Kohn W (1988) Density-functional theory for ensembles of fractionally occupied states. 1. Basic formalism. Phys Rev A 37(8):2809–2820. doi:10.1103/PhysRevA.37.2809
87. Ullrich CA, Kohn W (2001) Kohn-Sham theory for ground-state ensembles. Phys Rev Lett 87 (9). doi:10.1103/PhysRevLett.87.093001
88. Jensen F (2002) Introduction to quantum chemistry. Wiley, New York
89. Roos BO (2007) The complete active space self-consistent field method and its applications in electronic structure calculations. In: Lawley KP (ed) Advances in chemical physics: ab initio methods in quantum chemistry part 2, vol 69. Wiley, New Jersey
90. Daul C (1994) Density-functional theory applied to the excited-states of coordination-compounds. Int J Quantum Chem 52(4):867–877. doi:10.1002/qua.560520414
91. Minerva T, Goursot A, Daul C (2001) Chem Phys Lett 350:147–154. doi:10.1016/S0009-2614(01)01264-7
92. Nagao H, Nishino M, Shigeta Y, Soda T, Kitagawa Y, Onishi T, Yoshioka Y, Yamaguchi K (2000) Theoretical studies on effective spin interactions, spin alignments and macroscopic spin tunneling in polynuclear manganese and related complexes and their mesoscopic clusters. Coord Chem Rev 198:265–295. doi:10.1016/s0010-8545(00)00231-9
93. Noodleman L, Peng CY, Case DA, Mouesca JM (1995) Orbital interactions, electron delocalization and spin coupling in iron-sulfur clusters. Coord Chem Rev 144:199–244. doi:10.1016/0010-8545(95)07011-l
94. Ramanantoanina H, Urland W, Garcia-Fuente A, Cimpoesu F, Daul C (2013) Calculation of the 4f(1) -> 4f(0)5d(1) transitions in Ce3+−doped systems by Ligand Field Density Functional Theory. Chem Phys Lett 588:260–266. doi:10.1016/j.cplett.2013.10.012
95. Ferbinteanu M, Cimpoesu F, Girtu MA, Enachescu C, Tanase S (2012) Structure and magnetism in Fe-Gd based dinuclear and chain systems. The interplay of weak exchange coupling and zero field splitting effects. Inorg Chem 51(1):40–50. doi:10.1021/ic1023289
96. Cimpoesu F, Dahan F, Ladeira S, Ferbinteanu M, Costes J-P (2012) Chiral crystallization of a heterodinuclear Ni-Ln series: comprehensive analysis of the magnetic properties. Inorg Chem 51(21):11279–11293. doi:10.1021/ic3001784
97. Pierloot K, Cundari T (2001) Computational organometallic chemistry. Marcel Dekker Inc., New York
98. Nakano H, Nakayama K, Hirao K, Dupuis M (1997) Transition state barrier height for the reaction H2CO->H-2+CO studied by multireference Moller-Plesset perturbation theory. J Chem Phys 106(12):4912–4917. doi:10.1063/1.473540
99. Roos BO, Andersson K, Fulscher MP, Malmqvist PA, SerranoAndres L, Pierloot K, Merchan M (1996) Multiconfigurational perturbation theory: applications in electronic spectroscopy. Adv Chem Phys 93:219–331. doi:10.1002/9780470141526.ch5
100. Andersson K, Malmqvist PA, Roos BO, Sadlej AJ, Wolinski K (1990) 2nd-Order perturbation-theory with a casscf reference function. J Phys Chem 94(14):5483–5488. doi:10.1021/j100377a012

101. Angeli C, Cimiraglia R, Evangelisti S, Leininger T, Malrieu JP (2001) Introduction of n-electron valence states for multireference perturbation theory. J Chem Phys 114 (23):10252–10264. doi:10.1063/1.1361246
102. Cimpoesu F, Dragoe N, Ramanantoanina H, Urland W, Daul C (2014) The theoretical account of the ligand field bonding regime and magnetic anisotropy in the DySc2N@C-80 single ion magnet endohedral fullerene. Phys Chem Chem Phys 16(23):11337–11348. doi:10.1039/c4cp00953c
103. Paulovic J, Cimpoesu F, Ferbinteanu M, Hirao K (2004) Mechanism of ferromagnetic coupling in copper(II)-gadolinium(II) complexes. J Am Chem Soc 126(10):3321–3331. doi:10.1021/ja030628k
104. Ferbinteanu M, Kajiwara T, Choi K-Y, Nojiri H, Nakamoto A, Kojima N, Cimpoesu F, Fujimura Y, Takaishi S, Yamashita M (2006) A binuclear Fe(III)Dy(III) single molecule magnet. Quantum effects and models. J Am Chem Soc 128(28):9008–9009. doi:10.1021/ja062399i
105. Schäffer CE (1966) A ligand field approach to orthoaxial complexes. Theor Chim Acta 4 (2):166–173
106. Schäffer CE (1967) The angular overlap model applied to chiral chromophores and the parentage interrelation of absolute configurations. Proc Roy Soc A 297:96–133. doi:10.1098/rspa.1967.0055
107. Ramanantoanina H, Urland W, Cimpoesu F, Daul C (2014) The angular overlap model extended for two-open-shell f and d electrons. Phys Chem Chem Phys 16(24):12282–12290. doi:10.1039/c4cp01193g
108. Martin WC, Zalubas R, Hagan L (1978) Atomic energy levels – the rare-earth elements. Nat 1432, Stand Ref Data Ser NSRDS-NBS 60, U.S. Gov. Printing Office, Washington
109. Aravena D, Ruiz E (2013) Shedding light on the single-molecule magnet behavior of mononuclear Dy-III complexes. Inorg Chem 52(23):13770–13778. doi:10.1021/ic402367c
110. Gatteschi D, Sessoli R (2003) Quantum tunneling of magnetization and related phenomena in molecular materials. Angew Chem Int Ed 42(3):268–297. doi:10.1002/anie.200390099
111. Sessoli R, Powell AK (2009) Strategies towards single molecule magnets based on lanthanide ions. Coord Chem Rev 253(19–20):2328–2341. doi:10.1016/j.ccr.2008.12.014
112. Wang X-Y, Avendano C, Dunbar KR (2011) Molecular magnetic materials based on 4d and 5d transition metals. Chem Soc Rev 40(6):3213–3238. doi:10.1039/c0cs00188k
113. Zhang P, Guo Y-N, Tang J (2013) Recent advances in dysprosium-based single molecule magnets: structural overview and synthetic strategies. Coord Chem Rev 257(11–12):1728–1763. doi:10.1016/j.ccr.2013.01.012
114. Di Sante D, Stroppa A, Jain P, Picozzi S (2013) Tuning the ferroelectric polarization in a multiferroic metal-organic framework. J Am Chem Soc 135(48):18126–18130. doi:10.1021/ja408283a
115. Stroppa A, Barone P, Jain P, Perez-Mato JM, Picozzi S (2013) Hybrid improper ferroelectricity in a multiferroic and magnetoelectric metal-organic framework. Adv Mater 25 (16):2284–2290. doi:10.1002/adma.201204738

Struct Bond (2015) 163: 231–264
DOI: 10.1007/430_2014_157

Published online: 13 September 2014

Transition–Lanthanide Heterometal–Organic Frameworks: Synthesis, Structures, and Properties

Wei Shi, Ke Liu, and Peng Cheng

Abstract Transition–lanthanide heterometal–organic frameworks (HMOFs) have attracted increasing interests in recent decades because of their advantageous features as potential molecular materials, such as fascinating structural topologies, and their versatile and chemically tunable properties. Since the chemical and physical properties originated from d and f electrons are totally different, it is difficult to synthesize HMOFs in contrast to homometallic MOFs and it has showed that distinguishing characteristics with regard to structures and properties are observed in HMOFs. Herein the synthetic strategy, structures, and properties of luminescence, magnetism, adsorption, etc. are reviewed in this chapter to help readers to understand various aspects of HMOFs.

Keywords Adsorption · Heterometallic MOFs · Luminescence · Magnetism · Synthetic strategy

Contents

W. Shi, K. Liu, and P. Cheng (✉)
Department of Chemistry, Key Laboratory of Advanced Energy Material Chemistry (MOE), Collaborative Innovation Center of Chemical Science and Engineering (Tianjin), Nankai University, Tianjin 300071, P. R. China

1 Introduction

As a subfamily of metal–organic frameworks (MOFs) [1, 2], transition–lanthanide heterometal–organic frameworks (HMOFs) have many features: (1) fascinating topological structures originated from the combination of metal ions with different coordination environments [3–6]; (2) versatile properties and wide potential applications such as catalysis, magnetism, gas capture/storage/separation, chemical sensing, and ion exchange [7–11]; and (3) chemically tunable properties by changing synthetic conditions, modifying organic ligand, replacing metal ions or anions, and so on [4, 12, 13]. Because the two types of metal ions in HMOFs are bridged with each other, perturbation on one of the metal ions could influence other metal ions, and thus properties of the whole material could be fine-tuned [14]. In terms of the non-paired electrons, the chemical and physical properties originated from d and f electrons are totally different. Spin carriers of d electrons, especially first-row transition-metal ions, usually show coordination environments of tetrahedron, octahedron, and so on, with relatively lower coordination number varied from 4 to 6. The orbital contribution of 3d electron is always quenched by crystal field in most cases. As a result, the properties of 3d electrons can be well predicted and calculated by crystal field theory (or ligand field theory). For lanthanide ions, the coordination number is usually as high as 8–12, which leads to various coordination environments. 4f electrons are always well shielded by the outer $5s^2 5p^6$ subshells without the quenching of orbit angular momentum, and suffer less perturbation from the ligand field [14], which results in much more complicated theoretical analysis of lanthanide ions in comparison with transition-metal ion. On the other hand, according to *hard and soft acid and base* theory, lanthanide ion is harder than transition-metal ion and prefer to coordinate with hard donors like oxygen, while transition-metal ion is likely to bond with soft donors such as nitrogen [15]. Due to these different chemical affinities of the two types of metal ions, the combination of transition-metal and lanthanide ions into a single material is difficult and full of challenge.

In general, it is necessary for elaborately selection of organic linkers with specific donors and coordination modes when rationally synthesizing HMOFs. As discussed in last paragraph, organic ligands containing both N and O donors are usually the best choices since N donor is soft and expecting to coordinate with transition-metal ion, while O donor is hard and likely to bond to lanthanides [15]. Besides, symmetry of the donors in organic ligand is believed to be another key point to build MOFs with long-range order and porosity.

In real synthetic system, it is very hard to predict in which condition both different metal ions can be combined into one material, since there are still many other factors that could influence the composition and structure of the final product besides ligands. A series of continuous experiments, as well as analysis of the unexpected results, are normally necessary and helpful to find the route to get the expected products (vide infra). In this chapter, we summarized the synthetic strategy, structural diversity, and properties (luminescence, magnetism, adsorption,

etc.) of HMOFs to illustrate the advantages of combining two different spin carriers into such intriguing porous molecular materials.

2 Synthetic Strategies

The competition between transition metal and lanthanide ions toward the same ligand always causes just one type of metal ion rather than mixed ones in the final products. Although crystal engineering or isoreticular chemistry has been well approved to be the best strategy to design and synthesize MOFs [16–18], it is not easy to use such strategy in HMOFs because of the more complicated situations of the synthetic system. Alternatively, *symmetry approach* has shown great advantages in these systems as proven by our group and other researchers. This approach needs judiciously selection of ligands with specific coordination modes, such as pyridine-2,6-dicarboxylic acid (H_2PDA) [3, 4, 10, 12, 19–24], thiophene-2,5-dicarboxylic acid (H_2TDC) [25–38], and furan-2,5-dicarboxylic acid (H_2FDA) [5, 39–41] (Scheme 1).

Since 2003, using pyridine-2,6-dicarboxylic acid (H_2PDA) as bridging ligand, a series of isostructural M^{II}–Ln^{III}–PDA ($M = Mn^{2+}$, Fe^{2+}, Co^{2+}) porous MOFs with intriguing one-dimensional channels were synthesized in our lab. HMOFs with bridging ligands similar to H_2PDA were studied as well (Scheme 2). These ligands feature special chelating and bridging coordination symmetries and all have C_2 axes in their molecular structures that is beneficial to the construction of HMOFs.

Another useful way to construct HMOFs is "using complex as ligand" approach, since many discrete complexes still have potential donors for the further coordination with second type of metal ions. The discrete complex as metalloligand used in this approach should be stable enough in the reaction solution; otherwise, the ligand may release the original metal ion and coordinate to another metal ion to form another homometallic complex. This approach is well demonstrated in d–f heterometallic complexes with interesting magnetic properties; however, examples in MOF chemistry are still limited. In 1998, Decurtins et al. reported crystal structures and magnetic properties of $\{[Ln^{III}Cr^{III}(ox)_3(H_2O)_4]_2{\cdot}H_2O\}_n$ (**1**) which were synthesized using $[Cr^{III}(ox)_3]$ as ligand to react with lanthanide salts [42]. In 2006, Guillou et al. showed that $\{La_2[Cu(pba)_3]_3(H_2O)_8 \cdot 8H_2O\}_n$ (**2**, pba = propylenebis (oxamato)) with potential porosity could be obtained by reaction of $Na_2[Cu(pba)] \cdot 2H_2O$ with $LaCl_3 \cdot 7H_2O$ [43]. In 2009, Liu et al. reported $[Cu(NTA)]^-$ (H_3NTA = Nitrilotriacetic acid) as metalloligand to react with $Sm(ClO_4)_3$ to build an interesting heterometallic framework with the formula of $\{[Na_5Cu_8Sm_4(NTA)_8(ClO_4)_8(H_2O)_{22}]ClO_4 \cdot 8H_2O\}_n$ (**3**), exhibiting interpenetrating 1D channels along the *a* and *b* axis. The uncoordinated perchlorate anions filled in the channels can be exchanged by anions of tetrafluoroborate [44]. $\{Ni(H_4L)\}$ (H_4L = 4,4′,4″,4‴-{2,2′,2″,2‴-[ethane-1,2-diylbis(azanetriyl)]tetrakis(methylene)

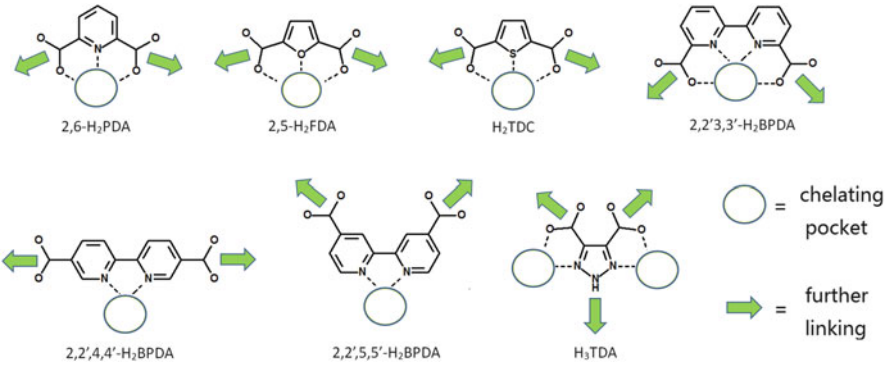

Scheme 1 Several aromatic carboxylic acid ligands with specific coordination modes

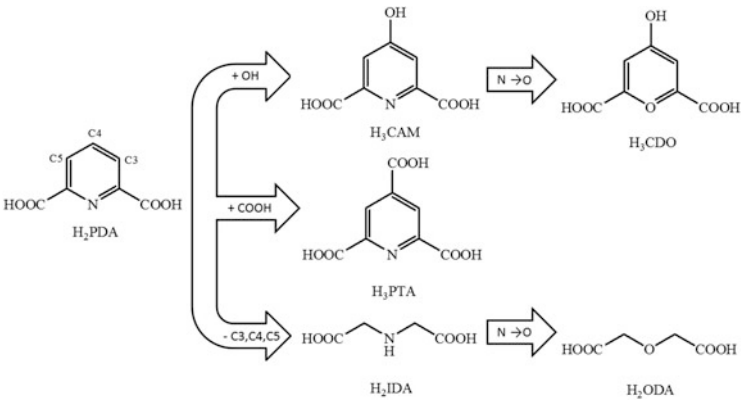

Scheme 2 Ligand H_2PDA and its derivatives

tetrakis-(1*H*-benzo-[*d*]imidazole-2,1-diyl)}tetrakis(methylene)-tetrabenzoic acid) was another interesting metalloligand. In 2013, Su et al. used this metalloligand to react with Ln^{III} ion by solvothermal method to build a series of Ni(L)-Ln_xLn_y MOFs [45]. Interestingly, one-pot synthesis and stepwise synthesis give different structures (Fig. 1). On the other hand, lanthanide metalloligands are rather rare. Very recently, our group reported using a lanthanide metalloligand [Gd$(H_2CAM)_3$] to react with $Co(NO_3)_2 \cdot 6H_2O$ to give $\{[Co_{0.5}(H_2O)_3][Gd(CAM)(HCAM)_2Co_{1.5}(H_2O)_3]\}_n \cdot 3nH_2O$ (**4**, H_3CAM = chelidamic acid) [46].

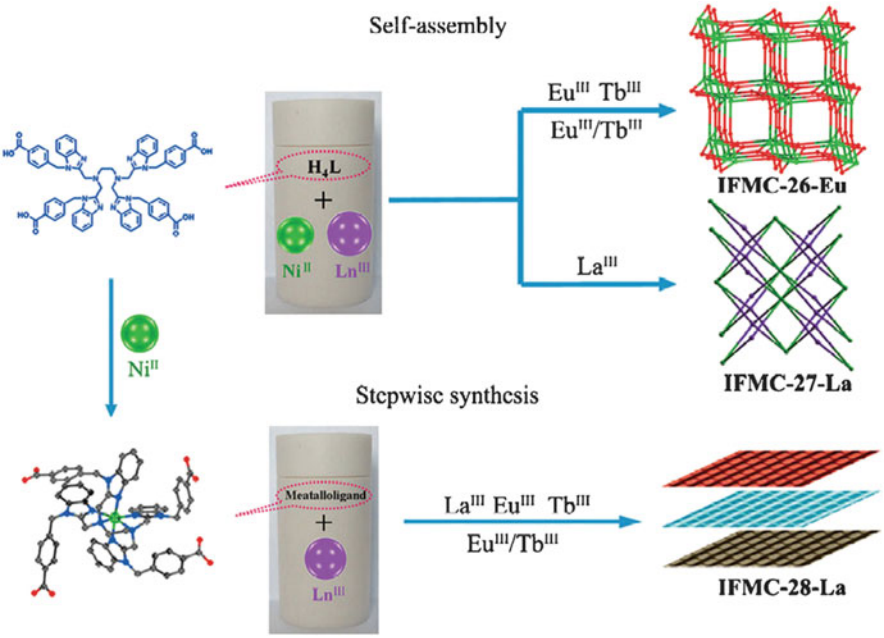

Fig. 1 Different structures of Ni(L)–Ln_xLn_y MOFs obtained by different synthetic routes. Reproduced from Zhang et al. [45] by permission of John Wiley & Sons Ltd

3 Structural Diversities

One of the most fascinating features of coordination chemistry is that even using only one ligand to react with the same metal salt, the structure and composition of the final product may vary significantly via changing reaction condition. In literature, the amount of 3d–4f heterometallic MOFs is less than that of homometallic MOFs because of the synthetic difficulty. Benefiting from the development of single-crystal X-ray technology, the studies of 3d–4f heterometallic MOFs are increasing very fast recently. In general, different organic bridging ligands will lead to different and plenty of structures. The following discussion about the structural diversity will focus on the 3d–4f MOFs obtained using selected ligands with specific coordination modes, namely, the symmetry approach with H_2PDA and its derivatives.

In 2004, a work from our group showed that the terminal ancillary ligands such as water can greatly influence the dimensionality of 3d–4f HMOFs [12]. The hydrothermal reaction at higher temperature can successfully reduce the number of terminal water molecules on Mn^{2+} in $\{[Yb(PDA)_3Mn_{1.5}(H_2O)_6]\cdot 6H_2O\}_n$ (**5**) to give a porous three-dimensional framework $\{[Yb(PDA)_3Mn_{1.5}(H_2O)_3]\cdot 1.5H_2O\}_n$ (**6**) (Fig. 2). This result suggested a new route to turn the structure of 3d–4f HMOFs, which was well demonstrated in the following work [47].

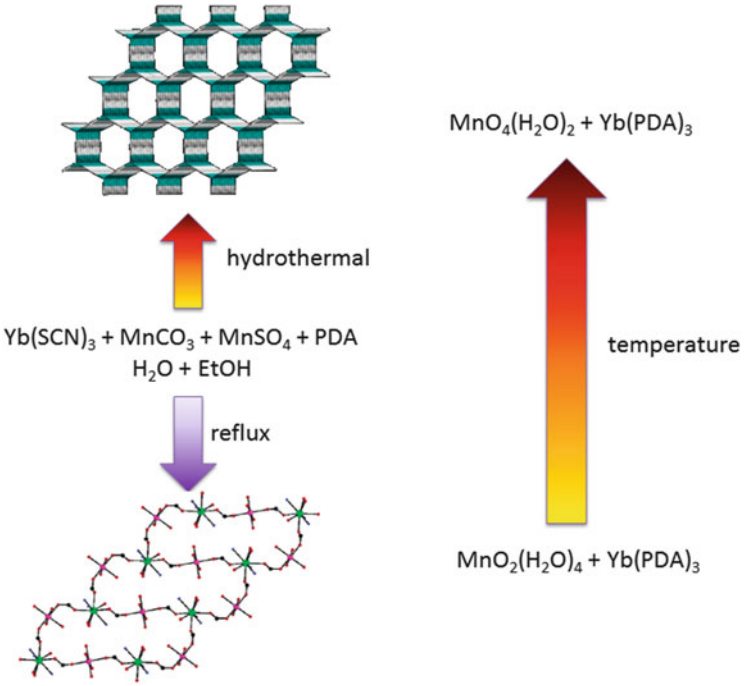

Fig. 2 The transformation from 1D molecular ladder (**5**) to nanotubular 3D framework (**6**)

Pyridine-2,6-dicarboxylic acid (H_2PDA) was firstly used as organic building block to construct HMOFs by our group. A series of porous MOFs with formula of $\{[Ln(PDA)_3 M_{1.5}(H_2O)_3] \cdot xH_2O\}_n$ ($M = Mn^{2+}$(**6**), Fe^{2+}(**7**), Co^{2+}(**8**)) were obtained and fully characterized [3, 4, 10, 12, 19–24]. Single-crystal X-ray diffraction studies revealed that they were isostructural and crystallized in high symmetric space group of *P*6/*mcc*. The interesting features of this series of HMOFs were that they not only contained large one-dimensional channels comprising 48-membered rings with about 1.8 nm diameter (Fig. 3) but also had high stabilities in air. Moreover, even under the temperature of 120°C, as well as removal of guest water molecules, the frameworks could survive as confirmed by powder X-ray diffraction patterns [3]. The wall of channels in **6–8** displayed "windows" of about 6×6 Å^2, containing transition-metal ions, lanthanide ions, and carboxyl groups, which provided a well-defined coordination environment for guest molecules and metal ions to interact with. Combining the intrinsic properties of lanthanide ions involved in the materials and the channels and windows, guest-dependent luminescent properties are expected (vide infra) [4, 10, 20].

The isostructural Fe(II)-containing MOFs were the most difficult ones in this series to obtain because in hydrothermal condition Fe(II) ions could be easily oxidized to Fe(III) ions. We successfully found a way to obtain the Fe(II)–Ln(III) frameworks without using the relatively not-easy-to-perform air-free operations by

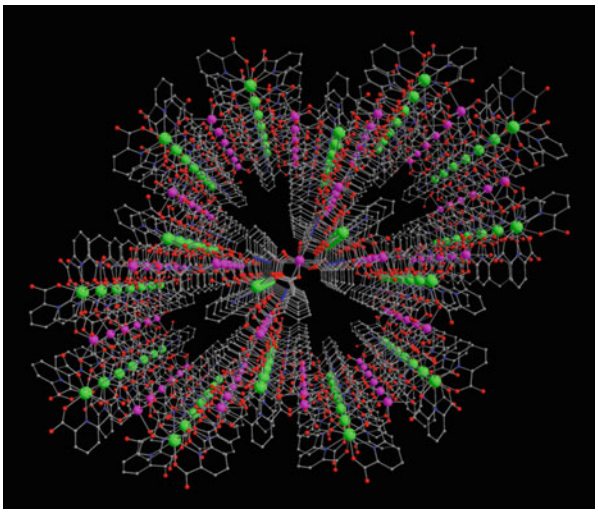

Fig. 3 The perspective of 3D framework in **6** with C_6 symmetry and 1D nanosized channels. Reproduced from Zhao et al. [4] by permission of John Wiley & Sons Ltd

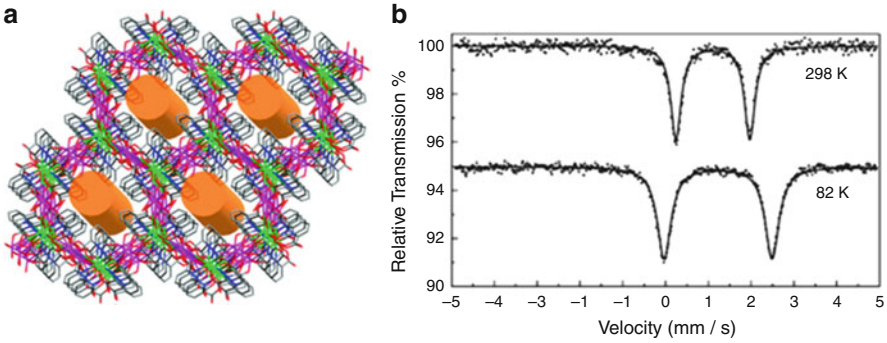

Fig. 4 Crystal structure (**a**) and Mössbauer spectrum (**b**) of **7**. Reproduced from Zhao et al. [23] by permission of The Royal Society of Chemistry

considering acetonitrile as a sacrificial oxidizing agent that could reduce the oxidation potential of Fe(II). In this way, high-spin Fe(II) ions were successfully embedded into the 3D framework of $\{[Ln(PDA)_3Fe_{1.5}(H_2O)_3]\cdot 1.5H_2O\}_n$ (**7**), which were confirmed by Mössbauer spectra and magnetic studies (Fig. 4) [23]. Nanoporous 3D frameworks containing both lanthanide and high-spin Fe(II) ions were rare. Only several examples such as discrete motif comprising lanthanide and high-spin Fe(II) ions were known [48].

Changing H_2PDA to H_2CAM, isostructural Mn^{II}–Ln^{III}–CAM (**9**) and Zn^{II}–Ln^{III}–CAM (**10**) were obtained [4, 49]. Different from the structure of **6**–**8**, they showed rare 2D honeycomb-type motif with hydrophilic cavities of ~14.4 Å

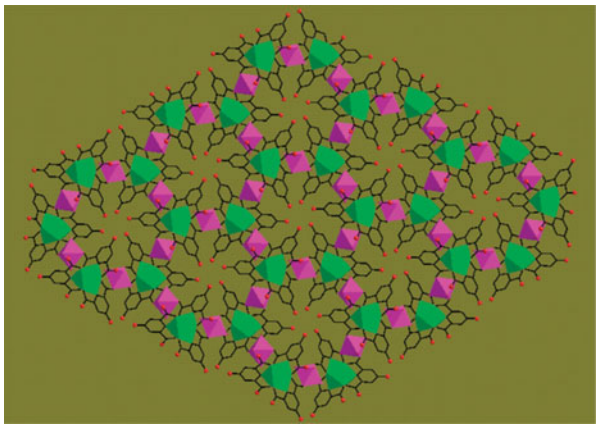

Fig. 5 Frameworks of **9**. Reprinted with the permission from Gao et al. [49]. Copyright 2008 American Chemical Society

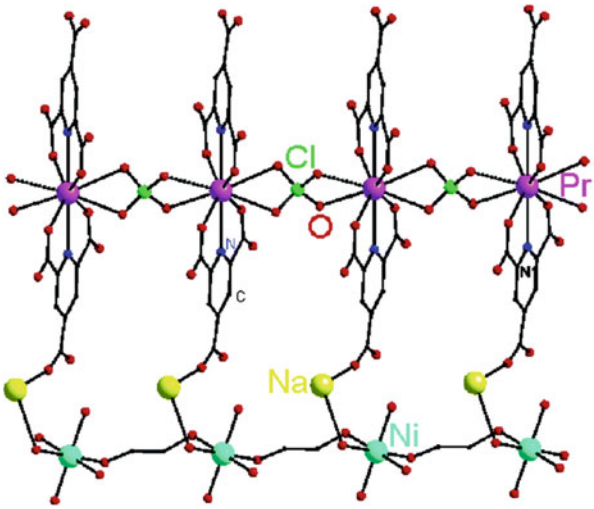

Fig. 6 Crystal structure of **11** with seven components. Reprinted with the permission from Gao et al. [50]. Copyright 2006 American Chemical Society

diameter (Fig. 5). In each cavity, six hydroxy groups directs toward the center. Compared with 3D nanoporous MOF **6**, the large difference may originate from the ligand substituent effect. The hydroxy group of CAM may enhance the steric bulk and weaken the coordinating ability of $O_{COO}-$ atoms to reduce the dimensionality, as well as the space group symmetry.

Substitution of the third carboxylic group to the 4-position of H_2PDA can give H_3PTA, which was also employed to build HMOFs. An unusual Na/Ni/Pr HMOF with formula of $\{[Na_2NiPr(\mu_4\text{-}ClO_4)(\mu_2\text{-}HOCH_2CH_2OH)(PTA)_2(H_2O)_8]\cdot 4.5H_2O\}_n$ (**11**) was obtained. More interestingly, four types of bridges involved in the framework connected Pr^{3+}, Ni^{2+}, and Na^+ into a unique 3D framework with seven components (Fig. 6) [50]. MOFs containing three different types of metal ions are rather rare, but they are promising candidates as molecular magnets or proton conductor [44, 51, 52].

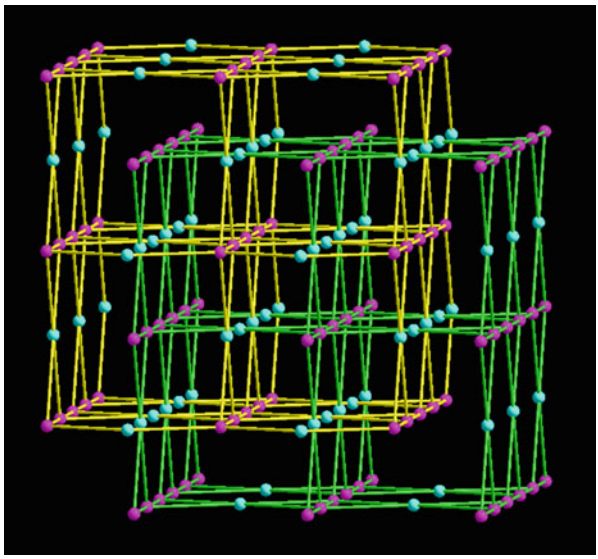

Fig. 7 Twofold interpenetrating 3D framework of **12**. Reprinted with the permission from Zhai et al. [53]. Copyright 2006 American Chemical Society

When cutting the C3, C4, and C5 off the pyridine ring without influencing the coordination groups, a flexible ligand of H_2IDA was obtained. Three-dimensional framework with formula of $\{[LnCr(IDA)_2(C_2O_4)]\}_n$ (**12**), in which $C_2O_4^{2-}$ anion came from the decomposition of H_2IDA, was hydrothermally synthesized. It showed a twofold interpenetrating 3D framework because the linkers (H_2IDA) between the metal ion nodes were so slender that allowed the interpenetrating of the frameworks (Fig. 7) [53].

O substituting N atom in H_2IDA gives H_2ODA, another interesting ligand with similar coordination groups. Reaction of Sm_2O_3, $Co(CH_3COO)_2$, and H_2ODA hydrothermally in water resulted in a cubic 3D framework $\{[Sm_2(ODA)_6Co_2][Co(H_2O)_6] \cdot 3H_2O\}_n$ (**13**), which crystallized in *Fd*3*c* space group [9]. Adjacent Sm^{3+} and Co^{2+} were bridged by carboxyl groups of in an *anti–anti* configuration (Fig. 8), and the similar framework and coordination mode were also observed in $\{[Mn(H_2O)_6][Gd_2(ODA)_6Mn_2] \cdot 6H_2O\}_n$ (**14**) [54]. Under the similar synthesis condition, $\{[Sm_2(ODA)_6Zn_3(H_2O)_6] \cdot 1.5H_2O\}_n$ (**15**) displayed a honeycomb-type 3D framework with 1D channel of about 1 nm diameter (Fig. 9) [9]. Adjacent Sm^{3+} and Zn^{2+} were bridged by carboxyl groups of ODA in a *syn–syn* mode. The two distinct ligand configurations resulted in two types of fascinating frameworks with different topologies. In 2000, Perec et al. reported a series of $\{[Cu_3Ln_2(ODA)_6] \cdot 12H_2O\}_n$, (**16**), which crystallized in *P*6/*mmc* space group and exhibited 1D columnar channel with the diameter of 0.6 nm [56]. The size of the channel was much smaller than that of M^{II}–Ln^{III}–PDA (**6**–**8**) and Co/Zn^{II}–Ln^{III}–ODA (**13**, **15**) families [4, 9]. The larger channels of **6** compared to that of **13**–**16** may benefit from the stronger rigidity of PDA with pyridine ring as the main body rather than that of ODA ligand with flexible body.

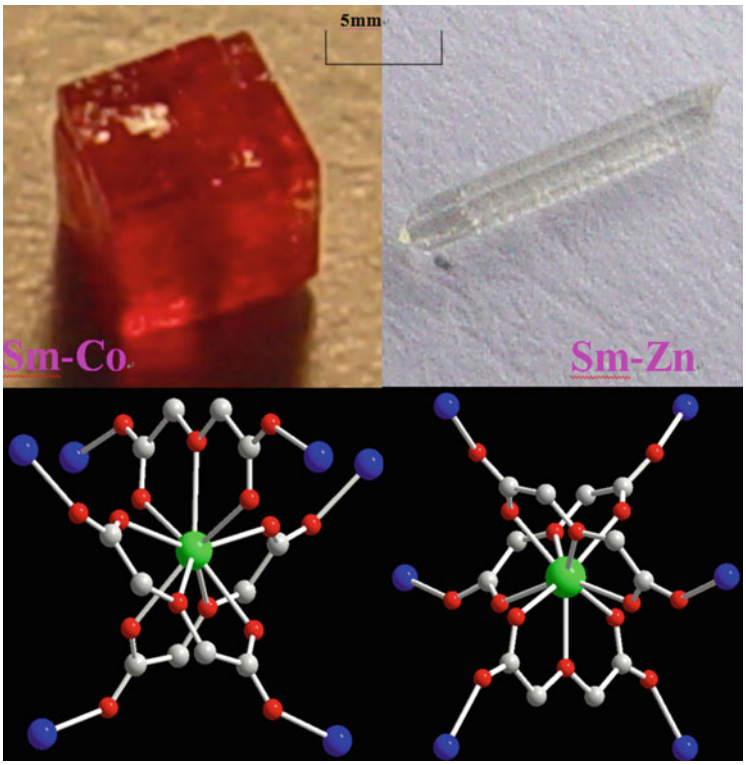

Fig. 8 Views of single crystals of **13** and **15** (*top*) and their coordination modes (*bottom*), respectively

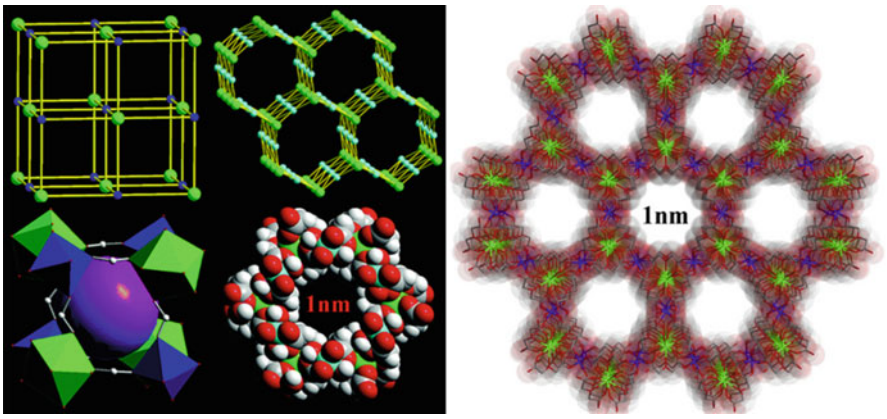

Fig. 9 Topological NaCl network and a cubic building block in **13** (*upper and lower left*) and view of nanotubes and a hexagonal aperture of **15** (*upper and lower middle* and *right*). Reprinted with the permission from Wang et al. [9]. Copyright 2007 American Chemical Society; Reprinted from Wang et al. [55]. Copyright 2010, with permission from International Association of Hydrogen Energy

4 Properties

4.1 Luminescent Properties

Luminescent properties of lanthanide-containing MOFs have received great interest due to their great potentials in many areas [57–59]. The luminescence of MOFs originates mainly from two mechanisms. The first one is ligand-based luminescence, including intra-ligand electron transfer, metal-to-ligand charge transfer (MLCT), and ligand-to-metal charge transfer (LMCT); the second one is metal-based emission, such as the emission from lanthanide ion with long excited-state lifetime. However, in principle, the f–f transitions are forbidden and always result in very weak molar absorptivity [60]. To effectively transfer energy to lanthanide ions, appropriate light-harvesting ligand(s) as antenna coordinated to lanthanide ions is important. If light could be absorbed by the ligand (S0 state) effectively, the singlet excited ligand (S1 state, short-lived) can go to the triplet excited state (T1 state, longer-lived) via intersystem crossing mechanism. Energy transfer from the T1 state of the ligand to the lanthanide ion can further populate lanthanide ion to the lowest excited state, and consequently depopulate to the ground state with characteristic emissions (Scheme 3) [59]. According to Reinhoudt's empirical rule, if the energy gap between the singlet-state and triplet-state is greater than 5,000 cm^{-1}, the intersystem crossing process will be effective [61]. In this context, the luminescent responds of porous lanthanide materials could be chemically controlled by changing the guest molecules/ions in the channels because the guests can interact with the ligand of the framework to influence the energy state via

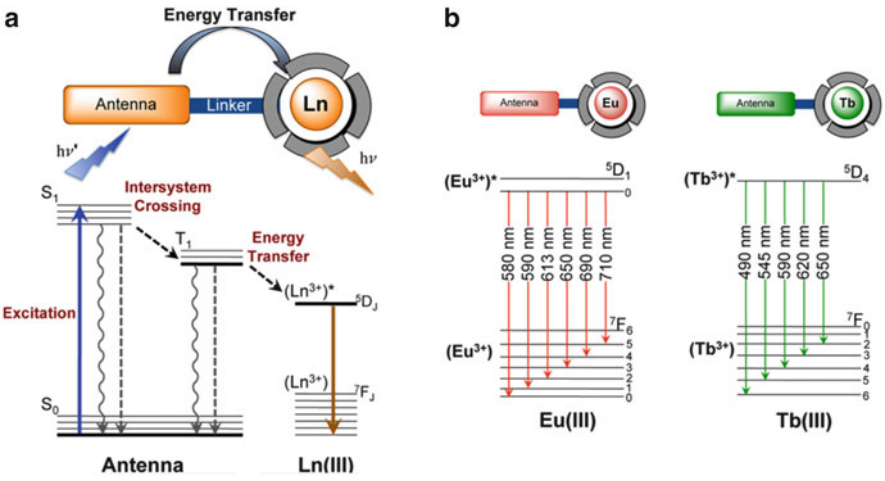

Scheme 3 (**a**) The antenna effect. (**b**) Luminescent 4f–4f transitions of Eu(III) and Tb(III) complexes and commonly observed emission wavelengths to emit red and green light, respectively. Reprinted with the permission from Heffern et al. [59]. Copyright 2014 American Chemical Society

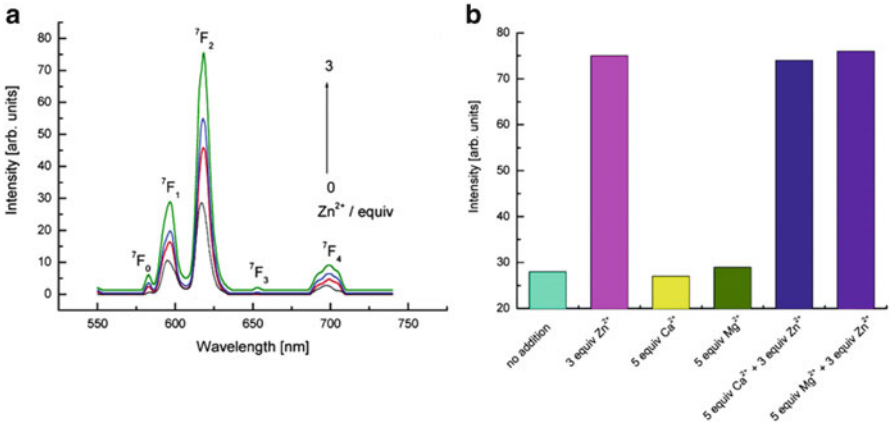

Fig. 10 (**a**)Emission spectra of **6-Eu** in DMF in the presence of 0–3 equivalents Zn^{2+} ions. *Black*, no addition; *red*, one equivalent; *blue*, two equivalents; *green*, three equivalents. (**b**) Luminescent intensity of **6-Eu** at 618 nm in DMF at room temperature upon the addition of Zn^{2+}, Ca^{2+}, or Mg^{2+} ions (excited at 287 nm). Reprinted with the permission from Zhao et al. [10]. Copyright 2004 American Chemical Society

hydrogen bonding, π–π stacking, or weak coordination bonds. Meanwhile, some guests can also influence the absorption of the light, which is another key point to the luminescence of lanthanide-containing MOFs [62].

The luminescent properties of HMOFs are mostly from the lanthanide-based emission, and the luminescent responds could be influenced by either small molecules or ions introduced into the channels of the MOFs. Several nanoporous HMOFs were firstly reported by our group as the luminescent probes of Zn^{2+} or Mg^{2+} [4, 10, 20]. For **6** (Ln = Dy, Eu, Tb), **7** (Ln = Eu, Tb), and **9**, their emissions exhibit the characteristic transitions $^5D_0 \rightarrow {}^7F_J$ ($J = 0$–4) of the Eu^{3+}, $^5D_4 \rightarrow {}^7F_J$ ($J = 6$–3) of the Tb^{3+}, and $^4F_{9/2} \rightarrow {}^6H_J$ ($J = 15/2$–13/2) of Dy^{3+}, suggesting that PDA and CAM can well sensitize the luminescence of these Ln^{3+} ions. The luminescence intensity of **6-Eu** enhanced gradually upon addition of 1–3 equivalents of Zn^{2+} (Fig. 10a). The highest peak at 618 nm is at least twice as intense as the corresponding band in the solution without Zn^{2+}. The introduction of other metal ions caused the intensity of all characteristic peaks either unchanged for Ca^{2+} and Mg^{2+} ions or weaken even quench for Mn^{2+}, Fe^{2+}, Co^{2+}, and Ni^{2+} ions (Fig. 10b) [10]. The emission intensities of **6-Tb** changed with the introduction of other metal ions in an extremely similar way as that of **6-Eu**. The results implied that these two HMOFs could monitor or recognize Zn^{2+} ion and hence can be considered as luminescent probes in biological scientific fields due to crucial roles of Zn^{2+} ion in many enzymes, transcription factors, and synaptic vesicles in excitatory nerve terminals [63]. Discrete lanthanide complex as promising luminescent sensor of Zn^{2+} ion was known [64]; however, using 3D nanoporous HMOFs as a luminescent probe of Zn^{2+} ion was firstly studied by this work. Interestingly, the emission intensity of **7-Eu** increased gradually upon addition of Mg^{2+} ions (Fig. 11), and

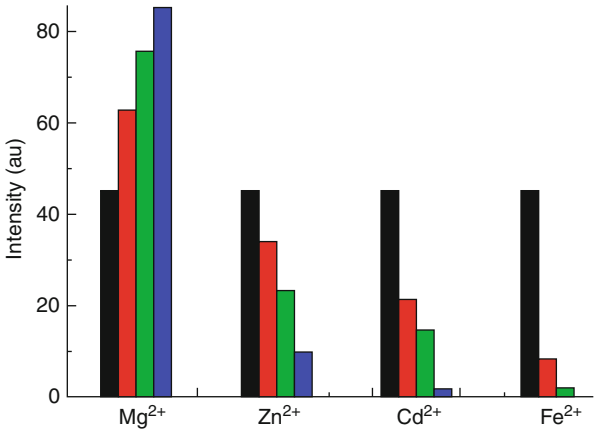

Fig. 11 Luminescent intensity of **7-Eu** at 613 nm in DMF at room temperature upon the addition of metal chloride (excited at 304 nm) with amount of 0–4 equiv. Reproduced from Zhao et al. [23] by permission of The Royal Society of Chemistry

the intensity of the highest peak at 613 nm was almost 1.9 times of magnitude larger than that of the original one [20]. Comparably, the introduction of Cd^{2+} and Zn^{2+} ions into the system resulted in the weakening of the luminescent intensities, and the addition of Fe^{2+} almost quenched the luminescence of **7-Eu**. For **7-Tb**, obvious changes were not observed with the increase of Mg^{2+} ion concentration, and the addition of other metal ions like Zn^{2+}, Fe^{2+}, Cu^{2+}, and Ni^{2+} either weakened or quenched the luminescence.

According to the structural analysis, the only difference between **6-Eu** and **7-Eu** is the type of transition-metal ions in their frameworks. The former is Mn^{2+} ion and the latter is high-spin Fe^{2+} ion, which is responsible for their different luminescent selectivity for Zn^{2+} and Mg^{2+} ions. Similarly, **6-Tb** possessed luminescent selectivity for Zn^{2+} ion, while **7-Tb** did not positively correspond to the addition of any guest metal ions. These results indicated that 3d metal ions should be considered as the second key factor in addition to the antenna effect from the ligand to influence the luminescence from lanthanide ion in HMOFs.

The luminescent intensities of **9-Dy** and **6-Dy** significantly increased on the introduction of Mg^{2+} ion (Fig. 12) [4], while the addition of other metal ions such as Ag^{+}, Zn^{2+}, and La^{3+} ions only decreased their emission intensities. The results indicated that these two HMOFs displayed excellent luminescent selectivity for Mg^{2+} ion, and both of them may be considered as luminescent probes of Mg^{2+} ion, which was the first example of nanoporous MOFs to detect Mg^{2+} ion.

In principle, the luminescent intensity of the Ln^{3+} ion relies on the efficiency of the energy transfer from the ligand to Ln^{3+} center, as mentioned before. The possible mechanism of the enhancement of emission from lanthanide ion under the presence of Mg^{2+}/Zn^{2+} ion was explored [4, 10]. **6-Dy** which was firstly considered not to fully decompose in DMF based on the optimized experiments is taken as an example to be discussed [4]. When Mg^{2+} ions were introduced into the channels of the framework, they may coordinate to O/N atoms provided by the inner surface of the nanosized channels, and one of the possible positions of Mg^{2+} may be found with reasonable Mg–O(N) bond lengths. Consequently, the energy

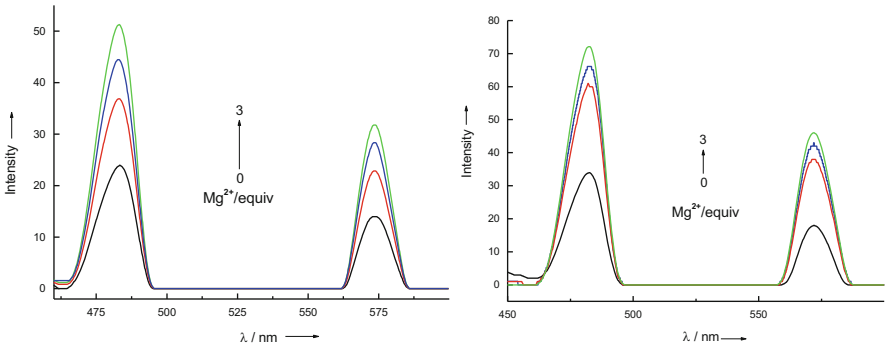

Fig. 12 Emission spectra of **6-Dy** and **9-Dy** in DMF in the presence of 0–3 equivalents of Mg^{2+}, respectively. Reproduced from Zhao et al. [4] by permission of John Wiley & Sons Ltd

matched between the excited states of both the ligand and Dy^{3+} ion may get closer, giving a more efficient energy transfer from PDA "antenna" to Dy^{3+} center. The same explanation could be applied to the similar luminescent property of **9-Dy** with the following two aspects: (a) the better energy matched between the excited states of both CAM and Dy^{3+} ion and (b) the non-radiative energy loss from thermal vibration of hydroxy groups from CAM decreased when some of the hydroxyl groups coordinated to the Mg^{2+} ions. Both the experimental results and the theoretical analysis strongly suggested that HMOFs are one of the best candidates as luminescent sensing materials.

4.2 Magnetic Properties

The magnetic behaviors for most of lanthanide ions are significantly dominated by the orbit angular momentum contribution with minor influence by ligand field due to the shield of outer $5s^25p^6$ subshells. The strong magnetic anisotropy of lanthanide ion has attracted immense interest in the construction of molecular magnetic materials [65]. One of the disadvantages of taking lanthanide ions as spin carriers to build molecular magnetic material is that the exchange interaction between inner-orbital 4f electrons is very weak. To overcome this drawback, the combination of both 3d and 4f spin carriers in one material is quite anticipated.

4.2.1 3d–4f Magnetic MOFs with Isotropic Spin Carriers

For Gd^{3+} ion, the first-order orbital moment is completely quenched. The nature of magnetic interaction between Gd^{3+} ion and 3d metal ions with negligible spin–orbit coupling can be well estimated by the $\chi_M T$ vs. T curve. According to Kahn's model, the nonzero overlapped integration of the magnetic orbits for half-filled Gd^{3+} or Mn^{2+} ion with other paramagnetic metal ion should lead to antiferromagnetic

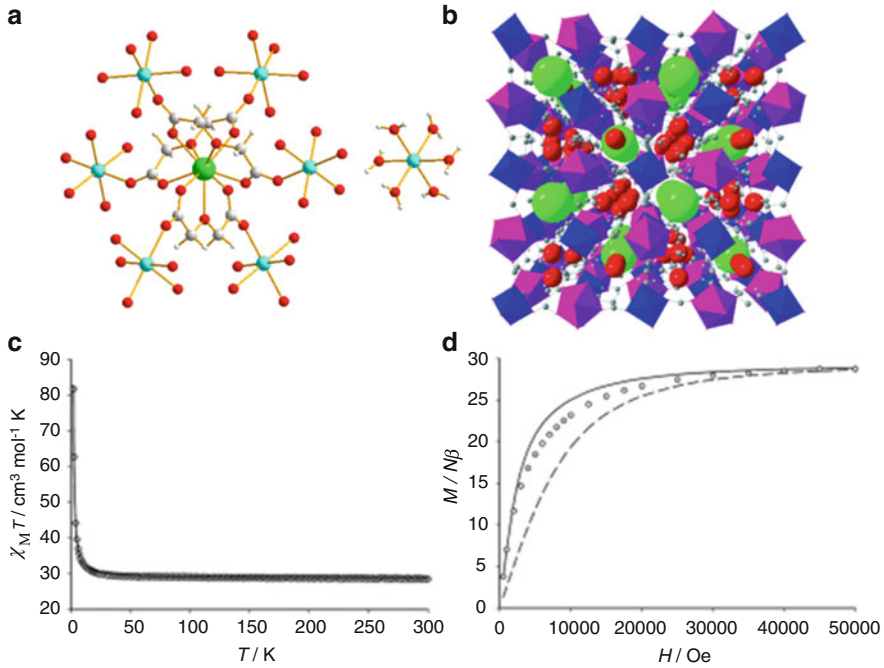

Fig. 13 (**a**) ORTEP diagram of **14**. (**b**) Perspective view along an axis of the unit cell of **14**. (**c**) Plots of $\chi_M T$ vs. T curve and the Curie–Weiss best fit. (**d**) Field dependence of the magnetization of **14** with the Brillouin function for uncoupled Gd^{3+} and Mn^{2+} ions and the Brillouin function for an $S = 24/2$ state plus an $S = 5/2$ state. Reproduced from Prasad et al. [54] by permission of John Wiley & Sons Ltd

interaction, which usually gives non-magnetic ground state [66]. However, several examples have shown contradictory magnetic properties beyond this model, suggesting new perspectives should be considered to access the magnetic interaction between 3d and 4f spin carriers. The first example that showed ferromagnetic interaction between Cu^{2+} and Gd^{3+} ions in a complex was reported by Gatteschi et al. in 1985 [67]. For MOFs, similar magnetic behavior was also observed. In **6-Gd**, $\chi_M T$ values slowly decreased while cooling, suggesting weak antiferromagnetic coupling between adjacent Gd^{3+} and Mn^{2+} ions [3]. Nevertheless, $\{[Mn(H_2O)_6][Gd_2(ODA)_6Mn_2] \cdot 6H_2O\}_n$ (**14**) (Fig. 13) exhibited unusual ferromagnetic interaction. The *anti–anti* conformation of the acetate bridge between Gd^{3+} and Mn^{2+} ions was considered to be responsible for this ferromagnetic behavior [54]. In **6-Gd**, the carboxyl bridge showed the *syn–anti* conformation, to show antiferromagnetic behavior. The result implied that the conformation of bridging ligand might significantly influence the magnetic interaction between 3d and 4f spin carriers. Quantitative analyses of this type of ferromagnetic behavior still need more examples and ab initio calculations.

4.2.2 3d–4f Magnetic MOFs with Anisotropic Spin Carriers

For other lanthanide ions with orbital contribution to the magnetic moment, the analysis of magnetic properties is more complicated. From $\chi_M T$ vs. T curve, it is hard to confirm ferromagnetic or antiferromagnetic interaction existence when $\chi_M T$ decreases upon lowering the temperature. However, if $\chi_M T$ increases upon decreasing the temperature, it is clear that there are ferromagnetic interactions. Actually, the $4f^n$ configurations of Ln(III) are split into $^{2S+1}L_J$ spectroscopic levels by interelectron repulsion and spin–orbit coupling. Each of these states is further split into Stark sublevels by crystal field perturbation. At high temperature, the Stark sublevels of the ground state are thermally populated. As the temperature is lowered, a depopulation of these sublevels leads to the decreasing of $\chi_M T$. As a result, the nature of the magnetic interactions between 3d and 4f metal ions with orbital contribution is "shielded" by the magnetic behavior of single lanthanide ion and cannot be unambiguously determined easily [14].

To solve the problem and explore the nature of the magnetic coupling between Ln^{3+} ions and the second spin carriers, Kahn et al. addressed the problem experimentally by the method of diamagnetic ion substitution [68]. Corresponding isostructural diamagnetic-ion-substitution complexes were synthesized and compared with the original complexes, based on which the trouble caused by the spin–orbit coupling of the Ln^{3+} ion may be eliminated. For example, the magnetic properties of two isostructural HMOFs, $\{[Ho_2(HCAM)_6M_3(H_2O)_{12}]\cdot mH_2O\}_n$ (M = Mn(**9-Ho**), Zn(**10-Ho**)), were studied using this method. $\chi_M T$ of **9-Ho** continuously decreased with decreasing temperature. To clearly determine the nature of magnetic interaction between Mn^{2+} and Ho^{3+}, the subtraction was employed for dc magnetic data between **9-Ho** and **10-Ho**. The difference was defined as a function of $\Delta(\chi_M T) = (\chi_M T)_{Ho-Mn} - (\chi_M T)_{Ho-Zn}$, to eliminate the crystal field contribution of Ho^{3+} ion. The result revealed that $\Delta(\chi_M T)_{Ho-Mn}$ value increased with decreasing temperature, indicative of clearly ferromagnetic interactions between Ho^{3+} and Mn^{2+} ions. Similar procedure was also applied to the isostructural **9-Er** and **10-Er** MOFs (Fig. 14) [49]. The difficulty of using this method to study the magnetic interactions between Ln^{3+} and another paramagnetic species is mainly from the synthesis of isostructural diamagnetic-ion-substitution species [69].

On the contrary, if $\chi_M T$ value increases with decreasing temperature, it is certain that the ferromagnetic coupling exists between 3d and 4f metal ions. In $\{[Tb(PDA)_3Mn_{1.5}(H_2O)_3]\cdot mH_2O\}_n$ (**6-Tb**), $\chi_M T$ slowly increased with lowering temperature and reached a maximum at 110 K, indicative of ferromagnetic coupling between Tb^{3+} and Mn^{2+} ions [10]. Similar behavior was also observed in $\{[Dy(CAM)_3Mn_{1.5}(H_2O)_6]\cdot 8.25H_2O\}_n$ (**9-Dy**), and ferromagnetic coupling between adjacent Dy^{3+} and Mn^{2+} was determined (Fig. 15) [4].

Different lanthanide spin carriers can lead to different magnetic properties at low temperatures. In 2013, using 3-hydroxypyrazine-2-carboxylic acid (H_2L) as ligand, two interesting 3D Cu(II)–Ln(III) MOFs with formula of $\{[Ln_6Cu_3L_6(\mu_3\text{-}OH)_6(\mu_6\text{-}O)$

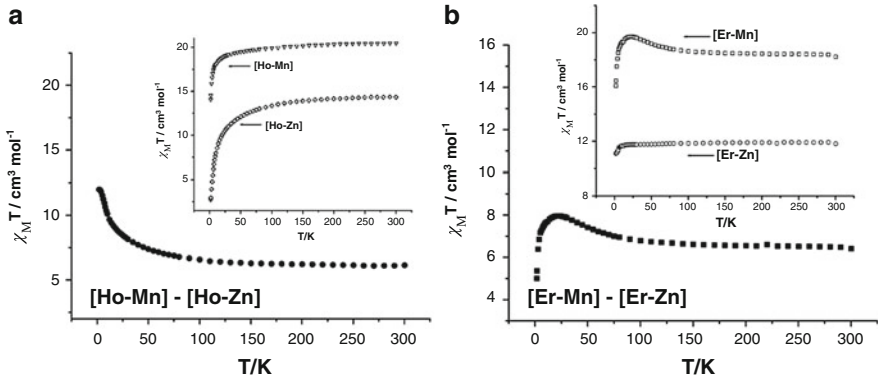

Fig. 14 The magnetic interaction between Ln^{3+} and Mn^{2+} in **9-Ho** (**a**) and **9-Er** (**b**) analyzed by diamagnetic-ion-substitution method. Inset is $\chi_M T$ vs. T plot under 1,000 Oe. Reprinted with the permission from Gao et al. [49]. Copyright 2008 American Chemical Society

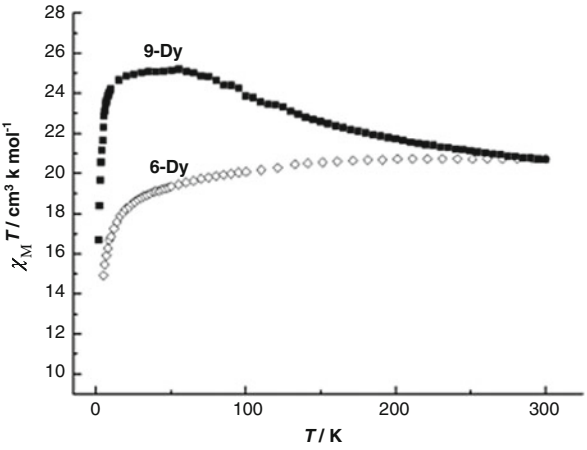

Fig. 15 Plots of $\chi_M T$ vs T of **6-Dy** and **9-Dy**. Reproduced from Zhao et al. [4] by permission of John Wiley & Sons Ltd

$(\mu_3\text{-}O)_2]\cdot 12H_2O\}_n$ (**17**, Ln = Gd, Dy) were hydrothermally obtained. The ligand H_2L was in situ formed by the nucleophilic substitution of water molecule to the amino moiety on the pyrazine ring of 3-aminopyrazine-2-carboxylic acid. Unusual $\{OLn_6\}$ cluster as building block was observed in HMOFs. The magnetic properties of the two isostructural HMOFs were totally different due to the different anisotropies spin carriers. **17-Gd** exhibited large magnetocaloric effect, with an entropy change of 35.76 J kg^{-1} K^{-1}, while **17-Dy** showed slow relaxation of the magnetization at low temperatures (Fig. 16) [70]. Zhao et al. reported two HMOFs with formula of $\{Ln_5Zn(BPDC)_3(H_2O)_{10}(\mu_3\text{-}OH)_6)](CO_3)_{0.5}(NO_3)_4\cdot mH_2O\}_n$ (**18**, BPDC = 4,4′-dicarboxylate-2,2′-dipyridine anion) that contained Ln_5 clusters as

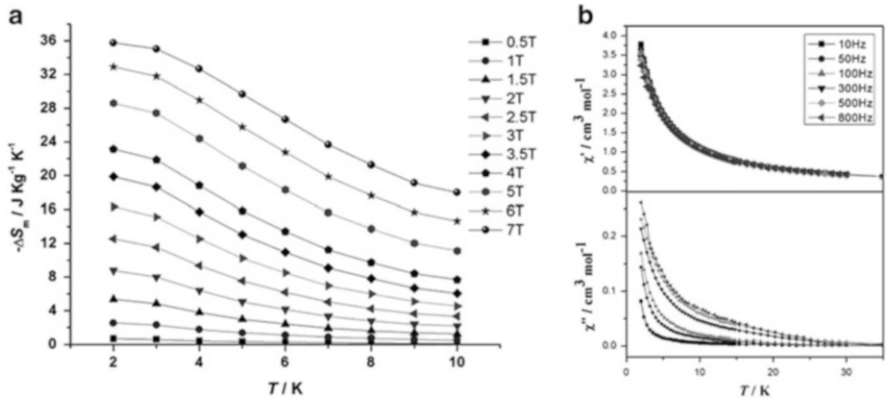

Fig. 16 (**a**) Entropy change of **17-Gd**. (**b**) Frequency-dependent in-phase and out-of-phase signals of **17-Dy** observed in ac susceptibility measurement. Reproduced from Bing et al. [70] by permission of John Wiley & Sons Ltd

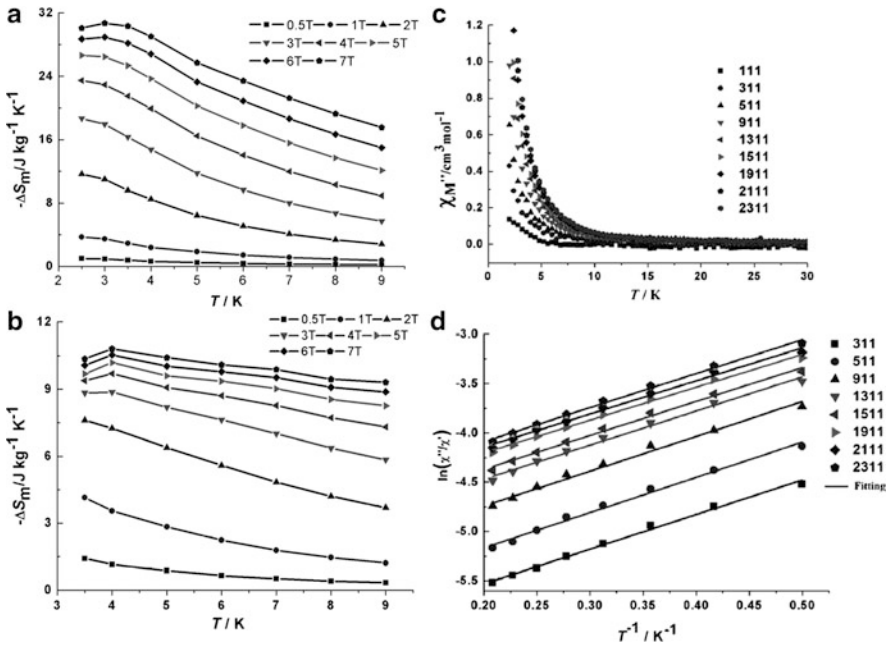

Fig. 17 The magnetic properties of **18**: entropy change of **18-Gd** (**a**) and **18-Dy** (**b**), the frequency-dependent out-of-phase signals of **18-Dy**, and the fitting results over the range 311–2,311 Hz of the plots of Ln(χ''/χ') versus 1/T for **18-Dy** (**d**). Reproduced from Shi et al. [71] by permission of John Wiley & Sons Ltd

building blocks. **18-Gd** showed large $-\Delta S_m$ value of 30.7 J kg^{-1} K^{-1} and high thermal and solvent stabilities, while **18-Dy** displayed slow magnetic relaxation behavior at low temperature (Fig. 17) [71].

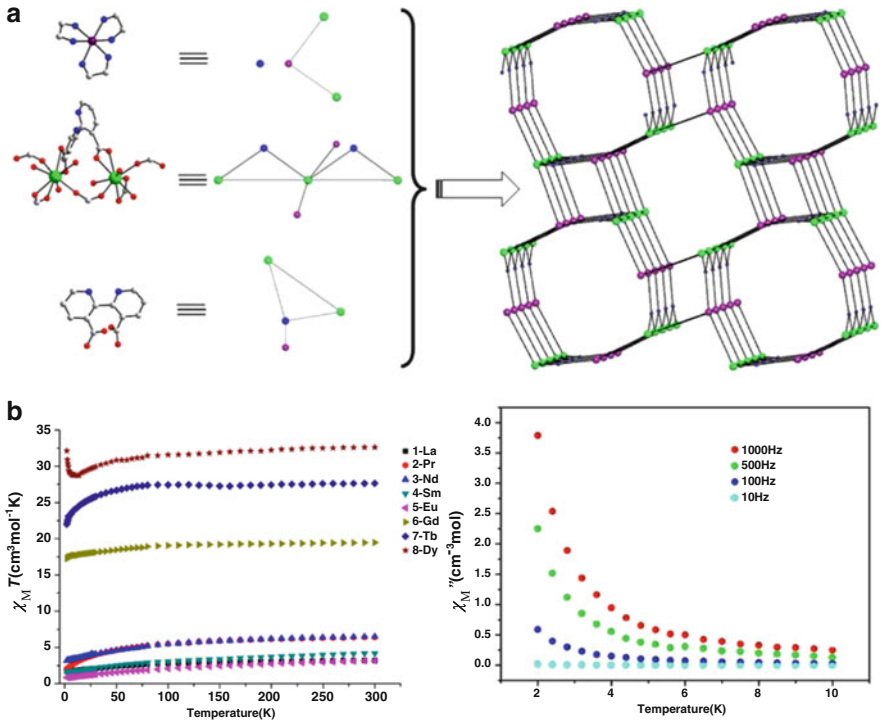

Fig. 18 (**a**) Representation of topology of **19**. (**b**) Plots of $\chi_M T$ vs. T for eight isomorphous complexes of **19** (*left*) and the frequency-dependent out-of-phase signals of ac susceptibility for **19-Dy** (*right*). Reprinted with the permission from Zhou et al. [6]. Copyright 2013 American Chemical Society

Hydrothermal reaction of 2,2′-bipyridine-3,3′-dicarboxylic acid (H_2BPDC) with $CoCl_2 \cdot 6H_2O$ and $Ln(OH)_3$ in the mixture of water and ethanol can form isostructural Co^{II}–Ln^{III}–BPDC family with formula of $\{[Ln_2Co(BPDC)_4(H_2O)_6] \cdot xH_2O\}_n$ (**19**, Ln = La, Pr, Nd, Sm, Eu, Gd, Tb, Dy). Two Ln^{3+} ions are connected via carboxyl groups to form binuclear units, which are further linked into lanthanide–BPDC chain through the bridging of $BPDC^{2-}$. The Co^{2+} ions were chelated by the bipyridine groups from three $BPDC^{2-}$ and further linked the lanthanide–BPDC chain to form a three-dimensional framework with anew topology. **19-Dy** showed slow relaxation of the magnetization at low temperature with a very small energy barrier of ~3 K (Fig. 18) [6].

1*H*-1,2,3-Triazole-4,5-dicarboxylic acid (H_3tda) containing both carboxylic and triazole groups is an interesting potential bridging ligand to build HMOFs. However, related examples are very rare. Using solvothermal method, four isostructural Co(II)–Ln(III) HMOFs, $\{[(CH_3)_2NH_2]_3[Co_3Ln(tda)_3(HCOO)_3] \cdot 2H_2O \cdot 0.75DMF\}_n$ (**20**, Ln = Eu, Gd, Tb, and Dy), were successfully synthesized [72]. Another family of HMOFs with H_3tda was $\{[Cu_2Ln(TDA)_2Cl(H_2O)_4] \cdot 2H_2O\}_n$ (**21**, Ln = Gd, Tb, Dy, Ho and Er), which was also solvothermally synthesized by the reaction of H_3tda with

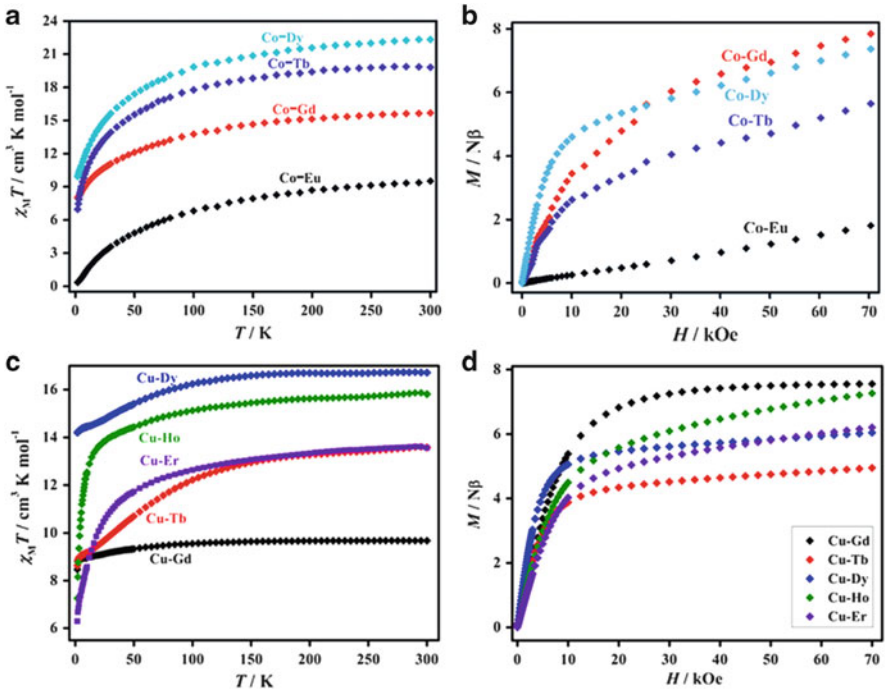

Fig. 19 Plots of $\chi_M T$ vs. T and M vs. H of a series complexes of MOF **20** (**a**, **b**) and **21** (**c**, **d**). Reproduced from Zou et al. [72] by permission of The Royal Society of Chemistry; Reproduced from Huang et al. [73] by permission of John Wiley & Sons Ltd

$CuCl_2 \cdot 2H_2O$ and $LnCl_3 \cdot 6H_2O$ in water [73]. However, the magnetic studies of these two families showed that they are paramagnetic until the temperature down to 2 K (Fig. 19).

In 2008, Gao and Hong et al. reported the synthesis and magnetic studies of four types of HMOFs with formula of $[Ln_2Co_2(2,5\text{-pydc})_6(H_2O)_4]_n \cdot 2n\,H_2O$ (**22**, Ln = Tb, Dy), $[Tb_2Co_2(2,5\text{-pydc})_6(H_2O)_4]_n \cdot 3n\,H_2O$ (**23**), $[Tb_2Co_2(2,5\text{-pydc})_6(H_2O)_9]_n \cdot 4n\,H_2O$ (**24**), and $[LaCo(2,5\text{-pydc})_3(H_2O)_2]_n \cdot 2n\,H_2O$ (**25**) using a metalloligand $Co(2,5\text{-pydc})_3^{3-}$ (2,5-H_2pydc = pyridine-2,5-dicarboxylate acid) [74]. MOF **22** showed a layer structure with well-isolated carboxylate-bridged Ln^{3+} chains. MOF **23** was a three-dimensional (3D) porous network with Tb^{3+} chains that were also well isolated and bridged by carboxylate. MOF **24** showed a layer structure based on dinuclear units, and **25** was a 3D network with boron nitride (BN) topology. All these HMOFs containing carboxylate-bridged Ln^{3+} chains exhibited ferromagnetic behavior. In addition, the two complexes of **22** showed slow relaxation of the magnetization at low temperature.

4.3 Adsorption Properties

The porous nature of MOFs provides a promising platform to study the adsorption properties for small molecules. 3d–4f heterometallic MOFs may show fascinating porous structures and unique adsorption behavior due to the combining of the two different types of metal ions. Another feature of lanthanide-containing MOFs is that the terminal ligands coordinated to lanthanide ions can be easily removed to form open metal sites, which can interact with gas molecules more strongly compared to the weak interactions between small molecules and the ligand of the framework [75, 76]. These two features may overcome the disadvantage that the density of lanthanide-containing MOFs is much heavier than that of the transition-metal-containing MOFs.

The porous nature of HMOFs makes them to be an excellent platform to study the sorption properties of small molecules. HMOFs displaying adsorption capacity for hydrogen, nitrogen, water, methanol, ethanol, methane and radical, etc. were reported [3, 4, 12, 17, 20].

The hydrogen absorption property of $\{[Sm_2(ODA)_6Zn_3(H_2O)_6]\cdot 1.5H_2O\}_n$ (**15-Sm**) was studied (Fig. 20). The result showed that it can take hydrogen up to 1.19 wt% at 77 K and 0.54 wt% at 298 K, respectively [9]. By introducing a lighter lanthanide element, isostructural $\{[Ce_2(ODA)_6Zn_3(H_2O)_6]\cdot 1.5H_2O\}_n$ (**15-Ce**) exhibited higher hydrogen storage capacity, up to 1.34 wt% at 77 K and 0.86 wt% at 298 K, respectively [55]. The density of **15-Ce** decreased by 4.7% compared with the Sm analogue; thus the hydrogen storage capacity increased by 13 and 59% at 77 and 298 K, respectively. Although the hydrogen sorption abilities of these HMOFs are not high enough for practical applications, the results showed

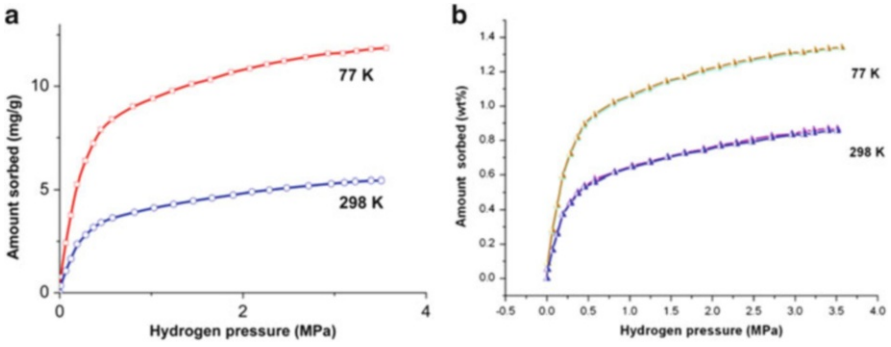

Fig. 20 (**a**) Hydrogen adsorption isotherms at 77 and 298 K of **15-Sm**. Reprinted with permission from Wang et al. [9]. Copyright 2007 American Chemical Society. (**b**) Hydrogen adsorption isotherms at 77 and 298 K of **15-Ce**. Reprinted from Wang et al. [55]. Copyright 2010, with permission from International Association of Hydrogen Energy

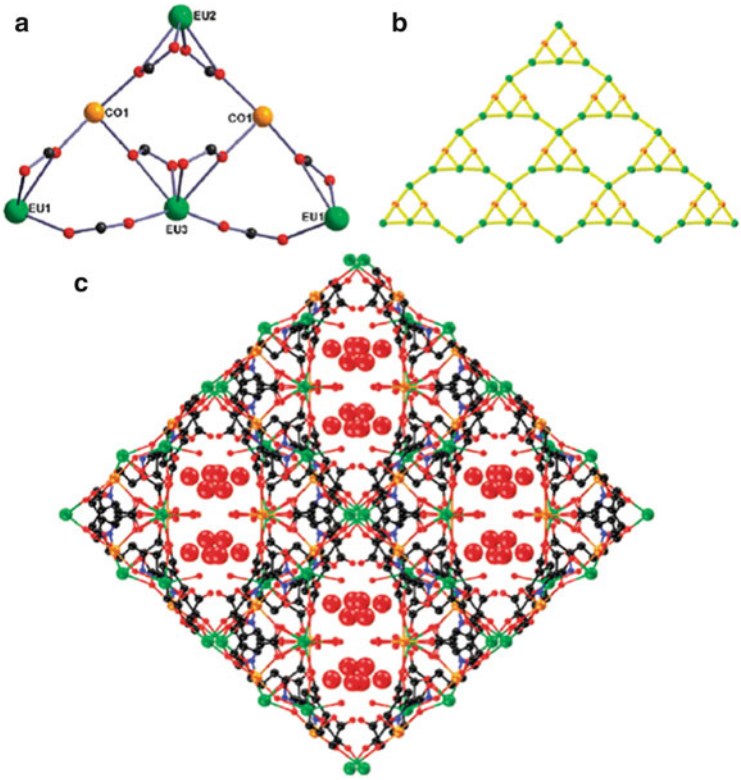

Fig. 21 (**a**) The butterfly-like $Eu_4Co_2(COO)_8$ unit and (**b**) the 2D carboxylate-bridged Eu_4Co_2 layer in **26-Eu**. (**c**) *Top view* of the 3D microporous MOF of **26**. Reproduced from Li et al. [8] by permission of The Royal Society of Chemistry

that the hydrogen molecules are likely to interact with lanthanide ion with open metal site, which need further studies to understand the mechanism for hydrogen storage in HMOFs.

In 2008, Tong et al. showed that the hydrothermal reaction of $Ln(NO_3)_3 \cdot 6H_2O$, $Co(NO_3)_2 \cdot 6H_2O$, and 2,4,6-pyridinetricarboxylic acid (H_3pyta) in distilled water gave three microporous HMOFs with formulae of $[Ln_4Co_3(pyta)_6(H_2O)_9] \cdot 5H_2O$ (**26**, Ln = Sm, Eu, Gd) (Fig. 21). Due to the size-selective effect, the three HMOFs exhibited selective adsorption abilities toward H_2/N_2 and CO_2/N_2 (Fig. 22) [8].

Selective adsorption and separation of MOFs is not only based on the adjustable pore sizes, but also regarded with surface environments and low energy cost in the separation process. Hence, removing coordination solvent molecules to obtain open metal sites is often used as a necessary activation method for most MOF materials. In 2014, a new concept was proposed by our group for enhancing the adsorption selectivity of MOFs and reducing the energy cost during the activation and regeneration processes (Scheme 4) [77]. A Eu(III)–Mn(II) HMOF {[Eu(CAM)

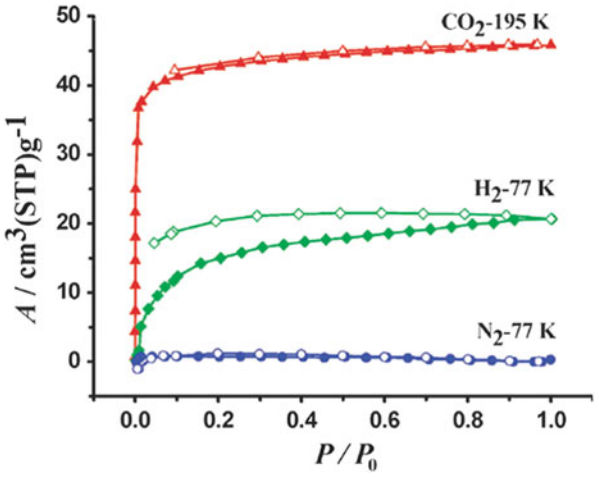

Fig. 22 Adsorption isotherms of CO_2 (*filled triangle*) at 195 K, and H_2 (*filled diamond*) and N_2 (*filled circle*) at 77 K for dehydrated **26**-**Sm**. Reproduced from Li et al. [8] by permission of The Royal Society of Chemistry

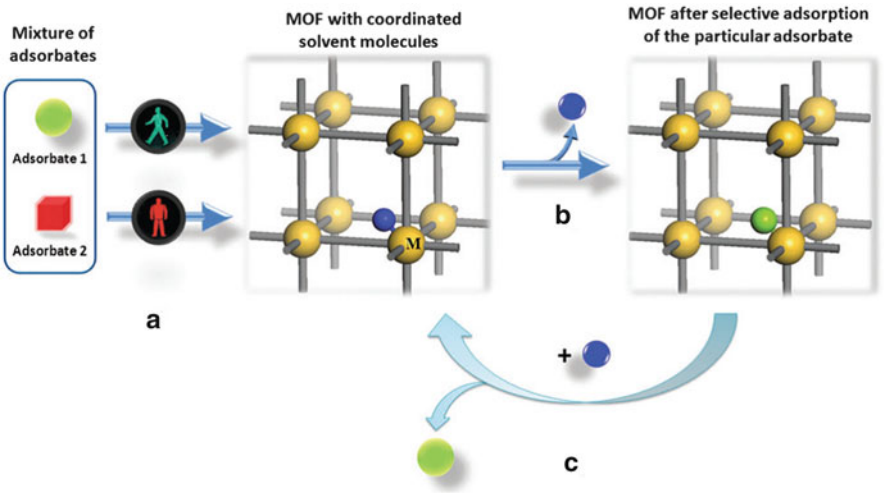

Scheme 4 Proposed process of selective separation in MOFs with the coordinated solvent. (**a**) Selective adsorption process based on the different coordination abilities of adsorbates; (**b**) exchange reaction between the coordinated molecule and the particular adsorbate; (**c**) recovery of the material under suitable conditions. Reproduced from Niu et al. [77] by permission of The Royal Society of Chemistry

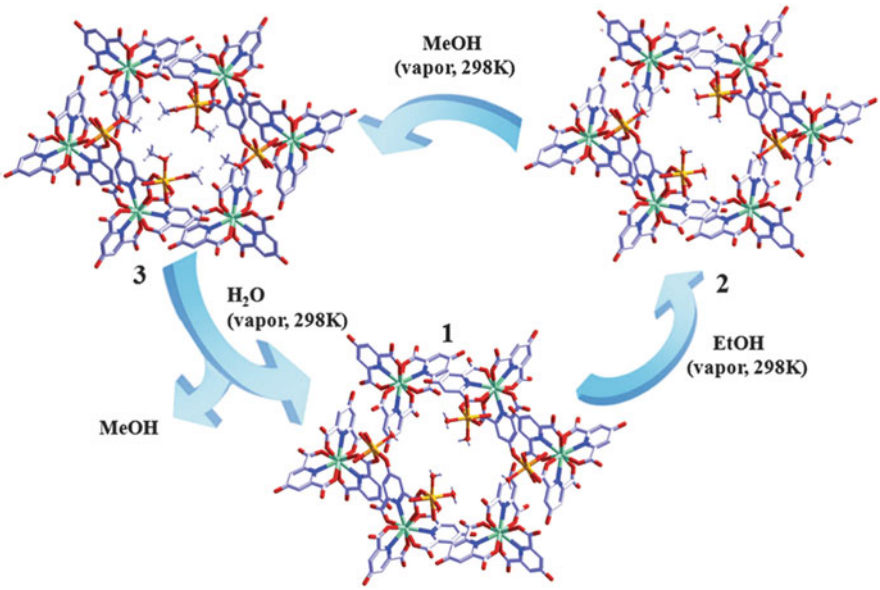

Fig. 23 The SC–SC process of exchange reactions for H_2O in **27** with EtOH and MeOH vapor. All free molecules were omitted for clarity. Reproduced from Niu et al. [77] by permission of The Royal Society of Chemistry

$(HCAM)_2Mn_2(H_2O)_7] \cdot 7H_2O\}_n$ (**27**) was prepared as a representative adsorption material and exhibited selective adsorption of MOFs toward MeOH and EtOH. The exchange reactions for H_2O in **27** with EtOH and MeOH vapor occurred in mild condition and through a single-crystal to single-crystal (SC–SC) process (Fig. 23).

Radical adsorption property was also studied in $\{[Nd_2(PDA)_6Co_3(H_2O)_6] \cdot 7H_2O\}_n$ (**8-Nd**), which can absorb both methanol and radical molecules NIT4Py (NIT4Py = 2-(4′-pyridyl)-4,4′,5,5′-tetramethylimidazoline-1-oxyl-3-oxide) [20]. The adsorbed radical in this HMOF was determined by the X-band EPR spectra (Fig. 24). The clear signal of radical at *ca.*$g = 2.0$ still remained after the sample was washed many times by distilled water to remove any NIT4Py molecules on the surface. Yaghi et al. have shown that MOFs can absorb larger molecules, such as butane, toluene, styrene, and the organic dyes [78]. In 2013, Fujita et al. reported that using soft MOFs as "platform," nanogram to microgram samples could be analyzed by X-ray single-crystal diffraction when the sample was absorbed and arranged ordered in the channels or cavities [79]. This work provided another rare example to capture large molecule such as radical in MOF, which may have potential applications in the field of biochemistry.

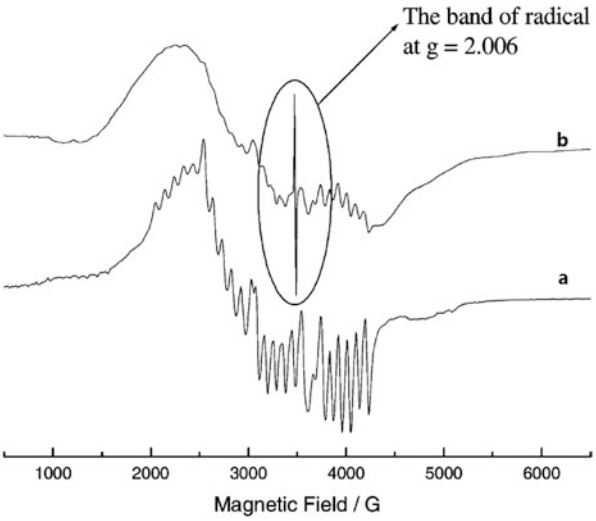

Fig. 24 EPR spectra of **9-Nd** (**a**) and the sample adsorbed with radical (**b**). Reprinted with permission from Zhao et al. [20]. Copyright 2007 American Chemical Society

4.4 Other Properties

In 2011, Kong and Long et al. reported a HMOF featuring a nanosized $Ln_6Cu_{24}Na_{12}$ (**27**, Ln = Gd, Dy) cluster as a node by the reaction of H_2ANMA (H_2ANMA = L-alanine-*N*-monoacetic acid), $Cu(NO_3)_2$, and $Ln(NO_3)_3$ with NaOH in deionized water. Magnetic studies showed that $\{[Gd_6Cu_{24}Na_{12}(ANMA)_{12}(\mu_3\text{-}OH)_{24}(\mu_5\text{-}O)_6Cl(H_2O)_{42}](NO_3)_{13}Cl_4(H_2O)_{48}\}_n$ (**27-Gd**) exhibited ferrimagnetic behavior. In addition, the electrical conductivity measurements revealed that it also behaved as a proton conductor [52].

In 2013, Su et al. reported a series of unprecedented HMOFs $\{[Ln_2Cu_5(OH)_2(pydc)_6(H_2O)_8]\cdot I_8\}$ (**28**, Ln = Sm, Eu, Gd, Tb) synthesized with iodine template. The 3D framework was constructed with the connection of paddlewheel secondary building units to six equivalent neighbors through six metalloligands, illustrating triangular helical channels accommodating linear polyiodide chains (Fig. 25). These HMOFs showed interesting photocatalytic water splitting property to produce hydrogen (Fig. 26) [80]. High framework stabilities in acid/base aqueous solutions, iodine release and recovery, and UV-light photocatalytic hydrogen evolution activities were also confirmed.

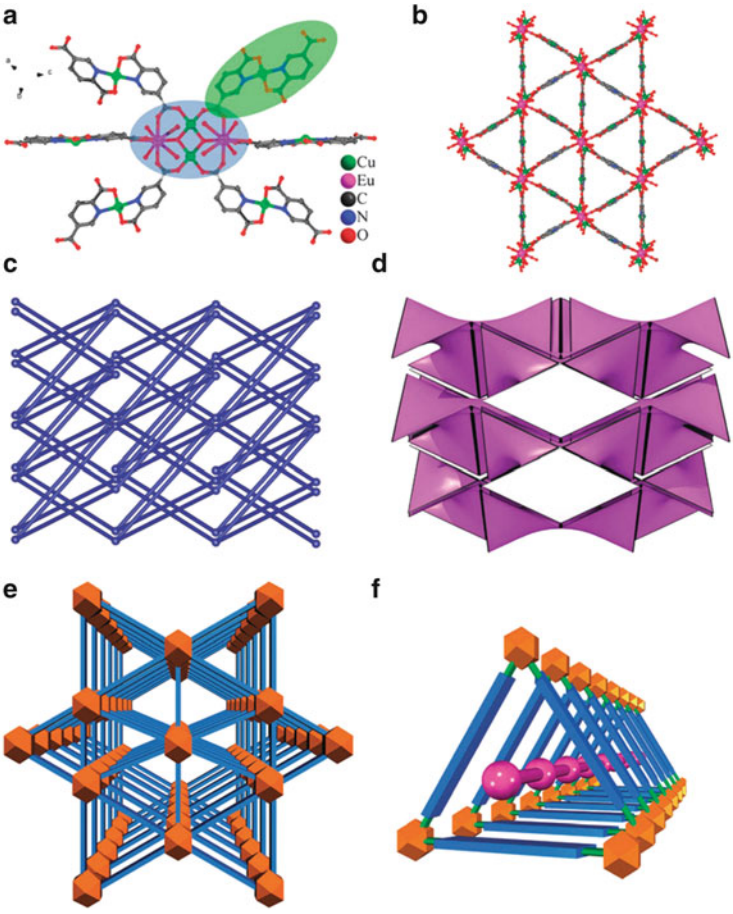

Fig. 25 (**a**) The linking mode of $[Cu_2Sm_2(\mu_3\text{-}OH)_2(H_2O)_8]$ SBU and metalloligands $[Cu(pydc)_2]$ in **28-Sm**. (**b**) Ball-and-stick representation of the expanded structure viewed from the *c* axis. (**c**) Schematic representation of the *mab* topology of **28-Sm**. (**d**) Natural tiling of *mab* topology. (**e**) 3D polyhedral presentation of **28-Sm** running along the *c* axis. (**f**) View of the 1D helical channel encapsulating the linear polyiodide chains. Reproduced from Hu et al. [80] by permission of The Royal Society of Chemistry

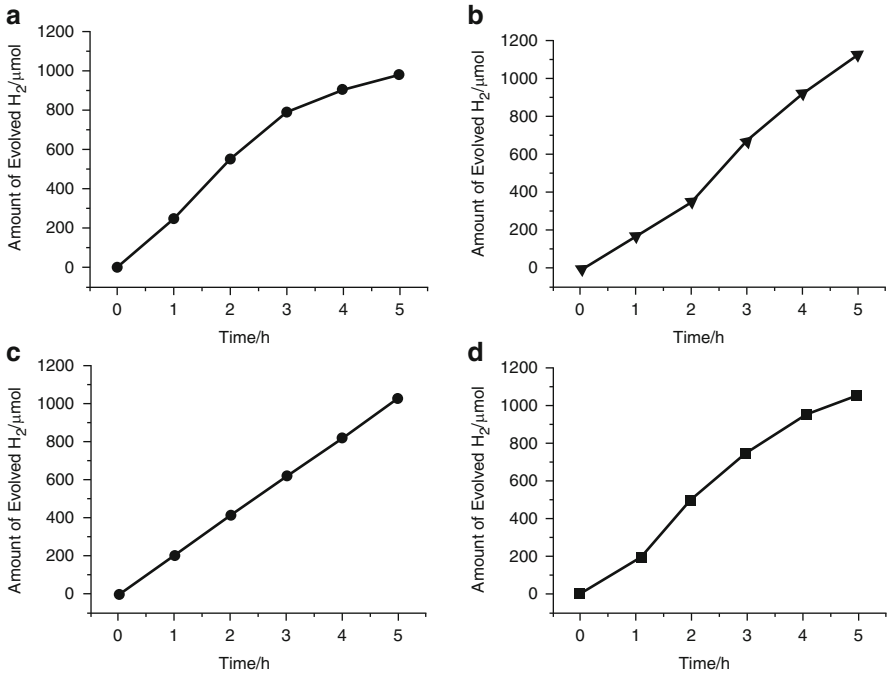

Fig. 26 Time course of H_2 evolution from **28-Sm** (**a**), **28-Eu** (**b**), **28-Gd** (**c**), and **28-Tb** (**d**) dissolved in 100 mL of 10% methanol aqueous solution under UV irradiation using a 500 W mercury lamp. Reproduced from Hu et al. [80] by permission of The Royal Society of Chemistry

In 2013, Shi et al. used 3,5-pyrazole dicarboxylic acid (H_3pdc) to obtain six new HMOFs from the reaction with lanthanide chlorides and copper hydroxycarbonate. The catalytic properties of $\{[CuEr_2(pdc)_2(Hpdc)(H_2O)_4]\cdot 2H_2O\}_n$ (**29**) were investigated, showing its activity and recyclability in the reaction of cyclopropanation of styrene [7].

Using sandwich-type $[Ln(\alpha\text{-}PW_{11}O_{39})_2]^{11-}$ polyoxoanions as the fundamental building blocks, Niu et al. showed that the hydrothermally synthesized HMOFs $[Cu(en)_2(H_2O)][Cu(en)(2,2'\text{-bipy})(H_2O)]\{[Cu(en)_2]_2(H_2O)[Cu(en)(2,2'\text{-bipy})]Er[(\alpha\text{-}HPW_{11}O_{39})_2]\}\cdot 7.5H_2O$ (**30**) containing polyoxoanions can degrade rhodamine-B (RhB) upon a 500 W Hg lamp irradiation (Fig. 27) [81].

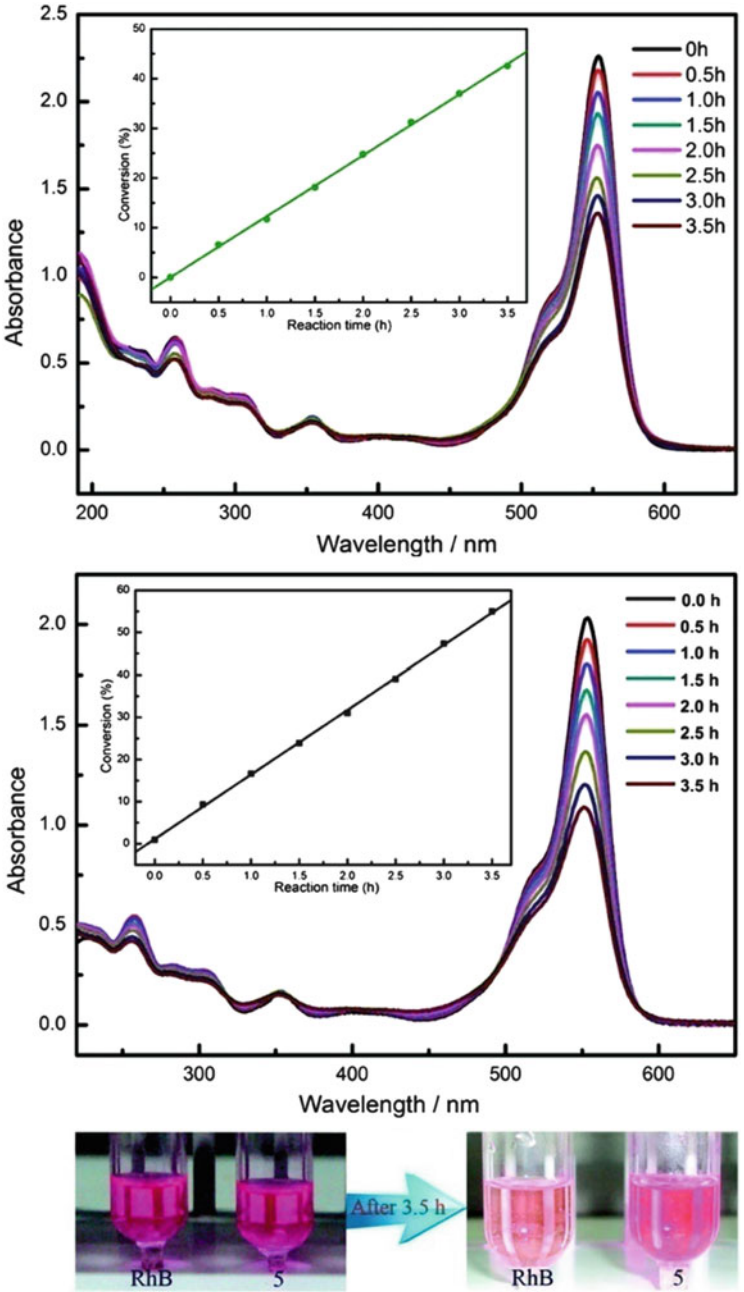

Fig. 27 (**a**) UV–vis absorption spectra vary with **26** recorded in the solution including 2×10^{-5} mol $\cdot$ L^{-1} RhB and 1.2×10^{-6} mol MOF. (**b**) Photodegradation reaction of RhB in the absence of MOF upon 500 W Hg lamp irradiation. (**c**) The color of the solution of RhB and in the presence of **6** changes as the irradiation time increases. Reprinted with permission from Niu et al. [81]. Copyright 2011 American Chemical Society

Conclusion and Perspective

In this chapter, the structural diversity and various properties including luminescence, magnetism, adsorption property, and catalysis of HMOFs were presented. The combination of two totally different metal ions (different spin carriers and coordination environments) into a singular molecular material has shown advantages compared to the homometallic molecular material, despite the difficulty in synthesis. However, symmetry approach has been well demonstrated to the construction of HMOFs efficiently when organic ligands are judiciously selected with specific coordination modes. In addition, the functional groups of organic ligands may not only effectively transfer magnetic interactions between 3d and 4f spin carriers but also act as antenna to harvest light for luminescence. Although the examples of HMOFs are not very plentiful, current results strongly suggest that HMOFs are promising multi-functional advanced materials for potential applications in luminescence, magnetism, adsorbing material, catalysis, and so on, which need further investigation on both the chemical and physical properties, as well as the structure–property correlation to fully understand this complicated but valuable system.

References

1. Zhou HC, Long JR, Yaghi OM (2012) Introduction to metal-organic frameworks. Chem Rev 112:673–674
2. Long JR, Yaghi OM (2009) The pervasive chemistry of metal-organic frameworks. Chem Soc Rev 38:1213–1214
3. Zhao B, Cheng P, Dai Y, Cheng C, Liao DZ, Yan SP, Jiang ZH, Wang GL (2003) A nanotubular 3D coordination polymer based on a 3d-4f heterometallic assembly. Angew Chem Int Ed 42:934–936
4. Zhao B, Gao HL, Chen XY, Cheng P, Shi W, Liao DZ, Yan SP, Jiang ZH (2006) A promising Mg^{II}-ion-selective luminescent probe: structures and properties of Dy-Mn polymers with high symmetry. Chem Eur J 12:149–158
5. Li HH, Shi W, Xu N, Zhang ZJ, Niu Z, Han T, Cheng P (2012) Structural diversity of four metal-organic frameworks based on linear homo/heterotrinuclear nodes with furan-2,5-dicarboxylic acid: crystal structures and luminescent and magnetic properties. Cryst Growth Des 12:2602–2612
6. Zhou JM, Shi W, Xu N, Cheng P (2013) A new family of 4f-3d heterometallic metal-organic frameworks with 2,2′-bipyridine-3,3′-dicarboxylic acid: syntheses, structures and magnetic properties. Cryst Growth Des 13:1218–1225
7. Yang TH, Silva AR, Shi FN (2013) Six new 3d-4f heterometallic coordination polymers constructed from pyrazole-bridged $Cu^{II}Ln^{III}$ dinuclear units. Dalton Trans 42:13997–14005
8. Li CJ, Lin ZJ, Peng MX, Leng JD, Yang MM, Tong ML (2008) Novel three-dimensional 3d-4f microporous magnets exhibiting selective gas adsorption behavior. Chem Commun 44:6348–6350
9. Wang Y, Cheng P, Chen J, Liao DZ, Yan SP (2007) A heterometallic porous material for hydrogen adsorption. Inorg Chem 46:4530–4534

10. Zhao B, Chen XY, Cheng P, Liao DZ, Yan SP, Jiang ZH (2004) Coordination polymers containing 1D channels as selective luminescent probes. J Am Chem Soc 126:15394–15395
11. Shi PF, Zhao B, Xiong G, Hou YL, Cheng P (2012) Fast capture and separation of, and luminescent probe for pollutant chromate using a multifunctional cationic heterometal-organic framework. Chem Commun 48:8231–8233
12. Zhao B, Cheng P, Chen XY, Cheng C, Shi W, Liao DZ, Yan SP, Jiang ZH (2004) Design and synthesis of 3d-4f metal-based zeolite-type materials with a 3D nanotubular structure encapsulated "water" pipe. J Am Chem Soc 126:3012–3013
13. Fang M, Shi PF, Zhao B, Jiang DX, Cheng P, Shi W (2012) A series of 3d-4f heterometallic three-dimensional coordination polymers: synthesis, structures and magnetic properties. Dalton Trans 41:6820–6826
14. Benelli C, Gatteschi G (2002) Magnetism of lanthanides in molecular materials with transition-metal ions and organic radicals. Chem Rev 102:2369–2387
15. Pearson RG (1963) Hard and soft acids and bases. J Am Chem Soc 85:3533–3539
16. Moulton B, Zaworotko MJ (2001) From molecules to crystal engineering: supramolecular isomerism and polymorphism in network solids. Chem Rev 101:1629–1658
17. Eddaoudi M, Kim J, Rosi N, Vodak D, Wachter J, O'Keeffe M, Yaghi OM (2002) Systematic design of pore size and functionality in isoreticular MOFs and their application in methane storage. Science 295:469–472
18. Yaghi OM, O'Keeffe M, Ockwig NW, Chae HK, Eddaoudi M (2003) Reticular synthesis and the design of new materials. Nature 423:705–714
19. Zhao B, Yi L, Dai Y, Chen XY, Cheng P, Liao DZ, Yan SP, Jiang ZH (2005) Systematic investigation of the hydrothermal syntheses of Pr(III)-PDA (PDA = pyridine-2,6-dicarboxylate anion) metal-organic frameworks. Inorg Chem 44:911–920
20. Zhao XQ, Zhao B, Ma Y, Shi W, Cheng P, Jiang ZH, Liao DZ, Yan SP (2007) Lanthanide(III)-cobalt(II) heterometallic coordination polymers with radical adsorption properties. Inorg Chem 46:5832–5834
21. Zhao XQ, Zhao B, Shi W, Cheng P (2009) Synthesis, structures and luminescent and magnetic properties of Ln-Ag heterometal-organic frameworks. Inorg Chem 48:11048–11057
22. Zhao XQ, Zhao B, Shi W, Cheng P, Liao DZ, Yan SP (2009) Self-assembly of novel 3d-4f heterometal-organic framework based on double-stranded helical motifs. Dalton Trans 38:2281–2283
23. Zhao B, Chen XY, Chen Z, Shi W, Cheng P, Yan SP, Liao DZ (2009) A porous 3D heterometal-organic framework containing both lanthanide and high-spin Fe(II) ions. Chem Commun 45:3113–3115
24. Zhao XQ, Cui P, Zhao B, Shi W, Cheng P (2011) Investigation on structures, luminescent and magnetic properties of Ln^{III}-M (M = Fe^{II}_{HS}, Co^{II}) coordination polymers. Dalton Trans 40:805–819
25. Byrnes MJ, Chisholm MH (2002) Thienyl carboxylate ligands bound to M_2 quadruple bonds involving molybdenum and tungsten. models for dimetallated polythiophenes. Chem Commun 38:2040–2041
26. Abourahma H, Bodwell GJ, Lu J, Moulton B, Pottie IR, Walsh RB, Zaworotko MJ (2003) Coordination polymers from calixarene-like $[Cu_2(dicarboxylate)_2]_4$ building blocks: structural diversity via atropisomerism. Cryst Growth Des 3:513–519
27. Byrnes MJ, Chisholm MH, Clark RJH, Gallucci JC, Hadad CM, Patmore NJ (2004) Thienyl carboxylate ligands bound to and bridging MM quadruple bonds, M = Mo or W: Models for polythiophenes incorporating MM quadruple bonds. Inorg Chem 43:6334–6344
28. Rosi NL, Kim J, Eddaoudi M, Chen B, O'Keeffe M, Yaghi OM (2005) Rod packings and metal-organic frameworks constructed from rod-shaped secondary building units. J Am Chem Soc 127:1504–1518
29. Jia HP, Li W, Ju ZF, Zhang J (2006) Synthesis, structure and magnetism of metal-organic framework materials with doubly pillared layers. Eur J Inorg Chem 15:4264–4270

30. Brown DJ, Chisholm MH, Gribble CW (2007) Substitution chemistry of MM quadruply bonded complexes (M = Mo or W) supported by the anion of 2-hydroxy-6-methylpyridine. Dalton Trans 36:1793–1801
31. Demessence A, Rogez G, Welter R, Rabu P (2007) Structure and magnetic properties of a new cobalt(II) thiophenedicarboxylate coordination polymer showing unprecedented coordination. Inorg Chem 46:3423–3425
32. Zhang J, Chen S, Wu T, Feng P, Bu X (2008) Homochiral crystallization of microporous framework materials from achiral precursors by chiral catalysis. J Am Chem Soc 130:12882–12883
33. Huang W, Wu D, Zhou P, Yan W, Guo D, Duan C, Meng Q (2009) Luminescent and magnetic properties of lanthanide-thiophene-2,5-dicarboxylate hybrid materials. Cryst Growth Des 9:1361–1369
34. Chen Z, Zhao B, Chen P, Zhao XQ, Shi W, Song Y (2009) A purely lanthanide-based complex exhibiting ferromagnetic coupling and slow magnetic relaxation behavior. Inorg Chem 48:3493–3495
35. Koh K, Wong-Foy AG, Matzger AJ (2010) Coordination copolymerization mediated by $Zn_4O(CO_2R)_6$ metal clusters: a balancing act between statistics and geometry. J Am Chem Soc 132:15005–15010
36. Takashima Y, Bonneau C, Furukawa S, Kondo M, Matsudabc R, Kitagawa S (2010) Periodic molecular boxes in entangled enantiomorphic icy nets. Chem Commun 46:4142–4144
37. Xu J, Cheng J, Su W, Hong M (2011) Effect of lanthanide contraction on crystal structures of three-dimensional lanthanide based metal-organic frameworks with thiophene-2,5-dicarboxylate and oxalate. Cryst Growth Des 11:2294–2301
38. Zhan CH, Wang F, Kang Y, Zhang J (2012) Lanthanide-thiophene-2,5-dicarboxylate frameworks: ionothermal synthesis, helical structures, photoluminescent properties, and single-crystal-to-single-crystal guest exchange. Inorg Chem 51:523–530
39. Wang JG, Huang CC, Huang XH, Liu DS (2008) Three-dimensional lanthanide thiophenedicarboxylate framework with an unprecedented (4,5)-connected topology. Cryst Growth Des 8:795–798
40. Li HH, Niu Z, Han T, Zhang ZJ, Shi W, Cheng P (2011) A microporous lanthanide metal-organic framework containing channels: synthesis, structure, gas adsorption and magnetic properties. Sci China Chem 54:1423–1429
41. Wang H, Liu SJ, Tian D, Jia JM, Hu TL (2012) Temperature-dependent structures of lanthanide metal-organic frameworks based on furan-2,5-dicarboxylate and oxalate. Cryst Growth Des 12:3263–3270
42. Decurtins S, Gross M, Schmalle HW, Ferlay S (1998) Molecular chromium(III)-Lanthanide (III) compounds (Ln = La, Ce, Pr, Nd) with a polymeric, ladder-type architecture: a structural and magnetic study. Inorg Chem 37:2443–2449
43. Guillou O, Daiguebonne C, Camara M, Kerbellec N (2006) New 3D La(III)-Cu(II)-containing coordination polymer with a high potential porosity. Inorg Chem 45:8468–8470
44. Ma JX, Huang XF, Song Y, Song XQ, Liu WS (2009) From metalloligand to interpenetrating channels: synthesis, characterization, and properties of a 2p-3d-4f heterometallic coordination polymer $\{[Na_5Cu_8Sm_4(NTA)_8(ClO_4)_8(H_2O)_{22}] \cdot ClO_4 \cdot 8H_2O\}_n$. Inorg Chem 48:6326–6328
45. Zhang SR, Du DY, Tan K, Qin JS, Dong HQ, Li SL, He WW, Lan YQ, Shen P, Su ZM (2013) Self-assembly versus stepwise synthesis: heterometal-organic frameworks based on metalloligands with tunable luminescence properties. Chem Eur J 19:11279–11286
46. Niu Z, Ma JG, Shi W, Cheng P (2014) Water molecule-driven reversible single-crystal to single-crystal transformation of a multimetallic coordination polymer with controllable metal ion movement. Chem Commun 50:1839–1841
47. Chen Z, Zhao B, Zhang Y, Shi W, Cheng P (2008) Construction and characterization of several new lanthanide-organic frameworks: from 2D lattice to 2D double-layer and to porous 3D net with interweaving triple-stranded helixes. Cryst Growth Des 8:2291–2298

48. Edder C, Piguet C, Bünzli JCG, Hopfgartner G (2001) High-spin iron(II) as a semitransparent partner for tuning europium(III) luminescence in heterodimetallic d-f complexes. Chem Eur J 7:3014–3024
49. Gao HL, Zhao B, Zhao XQ, Song Y, Cheng P, Liao DZ, Yan SP (2008) Structures and magnetic properties of ferromagnetic coupling 2D Ln-M heterometallic coordination polymers (Ln = Ho, Er; M = Mn, Zn). Inorg Chem 47:11057–11061
50. Gao HL, Yi L, Ding B, Wang HS, Cheng P, Liao DZ, Yan SP (2006) First 3D Pr(III)-Ni(II)-Na (I) Polymer and a 3D Pr(III) open network based on pyridine-2,4,6-tricarboxylic acid. Inorg Chem 45:481–483
51. Xiang SC, Hu SM, Sheng TL, Chen JS, Wu XT (2009) Structural diversity of infinite 3d-4f heterometallic cluster compounds driven by various lanthanide radii. Chem Eur J 15:12496–12502
52. Zhuang GL, Chen WX, Zhao HX, Kong XJ, Long LS, Huang RB, Zheng LS (2011) Two three-dimensional 2p-3d-4f heterometallic frameworks featuring a $Ln_6Cu_{24}Na_{12}$ cluster as a node. Inorg Chem 50:3843–3845
53. Zhai B, Yi L, Wang HS, Zhao B, Cheng P, Liao DZ, Yan SP (2006) First 3D 3d-4f interpenetrating structure: synthesis, reaction and characterization of $\{LnCr(IDA)_2(C_2O_4)\}_n$. Inorg Chem 45:8471–8473
54. Prasad TK, Rajasekharan MV, Costes JP (2007) A cubic 3d-4f structure with only ferromagnetic Gd-Mn interactions. Angew Chem Int Ed 46:2851–2854
55. Wang Y, Fang M, Li Y, Liang J, Shi W, Chen J, Cheng P (2010) A porous 3d-4f heterometallic metal-organic framework for hydrogen storage. Inter J Hydro Energy 35:8166–8170
56. Baggio R, Garland MT, Moreno Y, Peña O, Perec M, Spodine E (2000) Synthesis, structure and magnetic properties of the 2,2′-oxydiacetato-bridged Cu(II)-Ln(III) complexes $[\{Cu_3Ln_2(oda)_8(H_2O)_8\} \cdot 12H_2O]_n$ (Ln = Y, Gd, Eu, Nd, Pr). J Chem Soc Dalton Trans 29:2061–2066
57. Allendorf MD, Bauer CA, Bhakta RK, Houk RJT (2009) Luminescent metal-organic frameworks. Chem Soc Rev 38:1330–1352
58. Rocha J, Carlos LD, Filipe A (2011) Luminescent multifunctional lanthanide-based metal-organic frameworks. Chem Soc Rev 40:926–940
59. Heffern MC, Matosziuk LM, Meade TJ (2014) Lanthanide probes for bioresponsive imaging. Chem Rev 114:4496–4539
60. Valeur B (2001) Molecular fluorescence: principles and applications. Wiley-VCH, Weinheim
61. Steemers FJ, Verboom W, Reinhoudt DN, Vander Tol EB, Verhoeven JW (1995) New sensitizer-modified calix[4]arenes enabling near-UV excitation of complexes luminescent lanthanide ions. J Am Chem Soc 117:9408–9414
62. Zhou JM, Shi W, Li HM, Li H, Cheng P (2014) Experimental studies and mechanism analysis of high-sensitivity luminescent sensing of pollutional small molecules and ions in Ln_4O_4 cluster based microporous metal-organic frameworks. J Phys Chem C 118:416–426
63. Berg JM, Shi Y (1996) The galvanization of biology: a growing appreciation fro the roles of zinc. Science 271:1081–1085
64. Hanaoka K, Kikuchi K, Kojima H, Urano Y, Nagano T (2003) Selective detection of zinc ions with novel luminescent lanthanide probes. Angew Chem Int Ed 42:2996–2999
65. Sorace L, Benelli C, Gatteschi D (2011) Lanthanide in molecular magnetism: old tools in a new field. Chem Soc Rev 40:3092–3104
66. Kahn OM, Charlot MF (1980) Overlap density in binuclear complexes: a topological approach of the exchange interaction. Nouv J Chim 4:567–576
67. Bencini A, Benelli C, Caneschi A, Carlin RL, Dei A, Gatteschi D (1985) Crystal and molecular structure of and magnetic coupling in two complexes containing gadolinium(III) and copper (II) ions. J Am Chem Soc 107:8128–8136
68. Kahn M, Mathonière C, Kahn O (1999) Nature of the interaction between Ln^{III} and Cu^{II} ions in the ladder-type compounds $\{Ln_2[Cu(opba)]_3\} \cdot S$ (Ln = lanthanide element; opba = ortho-phenylenebis(oxamato), S = Solvent molecules). Inorg Chem 38:3692–3697

69. Ma BQ, Gao S, Su G, Xu GX (2001) Cyano-bridged 4f-3d coordination polymers with a unique two-dimensional topological architecture and unusual magnetic behavior. Angew Chem Int Ed 40:434–437
70. Bing YM, Xu N, Shi W, Liu K, Cheng P (2013) Two lanthanide(III)-copper(II) organic frameworks based on $\{OLn_6\}$ clusters that exhibited a large magnetocaloric effect and slow relaxation of the magnetization. Chem Asian J 8:1412–1418
71. Shi PF, Zheng YZ, Zhao XQ, Xiong G, Zhao B, Wan FF, Cheng P (2012) 3D MOFs containing trigonal bipyramidal Ln5 clusters as nodes: large magnetocaloric effect and slow magnetic relaxation behavior. Chem Eur J 18:15086–15091
72. Zou JY, Shi W, Xu N, Gao HL, Cui JZ, Cheng P (2014) Cobalt(II)-lanthanide(III) heterometallic metal-organic frameworks with unique (6,6)-connected Nia topologies with 1H-1,2,3-triazole-4,5-dicarboxylic acid: syntheses, structures and magnetic properties. Eur J Inorg Chem 23:407–412
73. Zou JY, Xu N, Shi W, Gao HL, Cui JZ, Cheng P (2013) A new family of 3d-4f heterometallic coordination polymers assembled with 1H-1,2,3-triazole-4,5-dicarboxylic acid: syntheses, structures and magnetic properties. RSC Adv 3:21511–21516
74. Huang YG, Wang XT, Jiang FL, Gao S, Wu MY, Gao Q, Wei W, Hong MC (2008) Cobalt-lanthanide coordination polymers constructed with metalloligands: a ferromagnetic coupled quasi-1D Dy^{3+} chain showing slow relaxation. Chem Eur J 14:10340–10347
75. Li HH, Shi W, Zhao KN, Niu Z, Li HM, Cheng P (2013) Highly selective sorption and luminescent sensing of small molecules demonstrated in a multifunctional lanthanide microporous metal-organic framework containing 1D honeycomb-type channels. Chem Eur J 19:3358–3365
76. Dincă M, Dailly A, Liu Y, Brown CM, Neumann DA, Long JR (2006) Hydrogen storage in a microporous metal-organic framework with exposed Mn^{2+} coordination sites. J Am Chem Soc 128:16876–16883
77. Niu Z, Fang S, Ma JG, Zhang XP, Cheng P (2014) Enhancement of adsorption selectivity for MOFs under mild activation and regeneration conditions. Chem Commun 50:7797–7799
78. Chae HK, Siberio-Pérez DY, Kim J, Go Y, Eddaoudi M, Matzger AJ, O'Keeffe M, Yaghi OM (2004) A route to high surface area, porosity and inclusion of large molecules in crystals. Nature 427:523–527
79. Inokuma Y, Yoshioka S, Ariyoshi J, Arai T, Hitora Y, Takada K, Matsunaga S, Rissanen K, Fufita M (2013) X-ray analysis on the nanogram to microgram scale using porous complexes. Nature 495:461–466
80. Hu XL, Sun CY, Qin C, Wang XL, Wang HN, Zhou EL, Li WE, Su ZM (2013) Iodine-templated assembly of unprecedented 3d-4f metal-organic framework as photocatalysts for hydrogen generation. Chem Commun 49:3564–3566
81. Niu JY, Zhang SW, Chen HN, Zhao JW, Ma PT, Wang JP (2011) 1D, 2D and 3D organic-inorganic hybrids assembled from Keggin-type polyoxometalates and 3d-4f heterometals. Cryst Growth Des 11:3769–3777

Struct Bond (2015) 163: 265–296
DOI: 10.1007/430_2014_158

Published online: 13 September 2014

MOFs of Uranium and the Actinides

Juan Su and Jiesheng Chen

Abstract Although the transition d- or 4f-block elements are the most used metals for the construction of metal–organic frameworks (MOFs), actinide cations were also involved in the elaboration of various hybrid organic–inorganic assemblies. The actinide elements with progressively filled 5f orbitals are a unique series, not only due to their radioactivity, but also because most of them have varied oxidation states. Uranium as the most important actinide element was exploited primarily to manufacture nuclear weapons due to its ability of nuclear fission. Besides its nuclear physics, the rich chemical state of this element also realizes rich chemistry and the formation of various compounds with other elements. Among the uranyl–organic frameworks (UOFs), uranyl UO_2^{2+} with the oxidation state of +6 for the metal is the most common structural unit, considering its reactivity with the different types of carboxylic acids. The construction of UOFs is always based on the coordination of organic ligands on the bipyramidal polyhedral structures of UO_2^{2+} species as primary building units. To date, multidimensional extended uranium-bearing coordination complexes have been studied, and an important library of UOFs have been developed and well defined. In this chapter, we describe efforts to synthesize MOFs of uranium and other actinides with desired structures. The basic building units and the strategies to construct different UOFs are addressed here, especially for the impact of organic ligands, structure-direct agent, and incorporation of heterometal ions. Although most of the actinide–organic frameworks are based on the uranium element due to its coordination advantages and long research history, increasing other actinide–organic frameworks with different organic ligands and structures have been developed. The typical MOFs of other actinides (actinide oxalates, actinide carboxylate, and actinide carboxyphosphonate) are also reviewed in this chapter. This work may

J. Su (✉) and J. Chen
School of Chemistry and Chemical Engineering, Shanghai Jiao Tong University, Shanghai, China
e-mail: chemcj@sjtu.edu.cn

contribute to the understanding of MOFs with actinide cations and provide a valuable reference for the development of novel MOFs materials with advanced functions.

Keywords Actinides • Metal–organic frameworks • Physicochemical properties • Uranium • Uranyl

Contents

1 Introduction

Metal–organic frameworks (MOFs) have attracted increasing attention due to their promising applications in fields such as adsorption and separation [1, 2], gas storage [3, 4], catalysis [5–7], nonlinear optics [8], sensing [9, 10], drug delivery [11], and biomedical imaging. Compared with the huge amount of transition metal–organic frameworks, the reported studies on the 5f actinide compounds with various topologies and coordination geometries are not quite common [12–27]. The actinide elements as a unique series have very large atomic/cation radii, and many of them have a large number of oxidation states. Therefore, increasing interests in the actinides have shifted from their radioactivity to their constructed complexes. From the known crystal structures in the Inorganic Crystal Structure Database (ICSD), the number of complexes from the members in the beginning and end of the actinide series is quite different. The early actinides with wide variations in oxidation states attracted more attention for studies and constructions, but the actinides after uranium possess only one thermodynamically preferred oxidation state (+3), and their solid-state studies are severely lacking [28, 29].

Among the actinides family, uranium as the heaviest naturally occurring element is the most studied metal. The radioactive uranium has been playing a major role for the exploitation of manufacturing nuclear weapons and the generation of nuclear power. In 1939, the understanding and studies of radioactive uranium were strongly promoted by the development of the Manhattan project. Extensive research has been devoted to the chemistry of uranium and its mining extraction process, waste management, and recycling/separation procedures. Besides its involvement in nuclear energy, photoluminescence [30], magnetism [31, 32], and catalytic

[33, 34] properties have also been investigated. To date, many types of inorganic or organic ligands have been coordinated with uranium, and their chemical interaction has been intensively investigated. Since the development of X-ray diffraction techniques in 1960, the crystal chemistry of uranium compounds started to be well documented with the supplied continuous structural data. Moreover, the recent expansion of uranium is correlated to the emerging and development of the porous crystalline hybrid organic–inorganic materials (MOFs) as a new research field [35–37]. The synthesis, characterization, or applications of such compounds which exhibit fascinating properties in the area of molecular storage, separation, catalysis, drug delivery, etc. [38, 39] have been reported in increasing papers. Uranium element has five different oxidation states varied from +2 to +6 in compounds or solutions. Elemental uranium is easy to be oxidized, and +6 is the most stable one, whose corresponding uranyl unit UO_2^{2+} dominates the chemistry of uranium and constructs a large number of uranium-bearing solid-state compounds (half of the single crystal X-ray structures of uranium compounds contain the uranyl dication) [40, 41]. Besides the various inorganic compounds formed by bonding inorganic ions, uranyl–organic solids are obtained from the coordination linkage of organic molecules with uranyl units. The uranyl bipyramids and polynuclear uranium structural building units are formed because the strong coordination affinity makes the uranyl ions always tend to bind oxygen, nitrogen, and fluorine atoms. Then, they may be cross-linked into various uranyl–organic coordination structures. Owing to the geometry of uranyl ions and the sterics and functionalities of the organic ligands, uranyl–organic extended structures can be designed and constructed as MOFs. A variety of uranyl–organic extended structures with varied organic ligands were successfully prepared via hydrothermal, sol–gel, solvothermal, room temperature crystallization synthetic routes, etc. A number of typical uranium compounds with various structures, such as clusters, one-dimensional (1D) chains, two-dimensional (2D) layers, and three-dimensional (3D) networks, have been synthesized [13–25]. Following the definition of MOFs, the uranium-containing organic–inorganic solids are sometimes called uranium (or uranyl)–organic framework (UOF) [35–38].

A generic terminology of "actinide–organic framework" (AnOF) was developed as similar terms (such as thorium involved in thorium–organic frameworks (TOF)) [39, 42]. Compared with the 1D and 2D structures, the 3D UOFs attracted more research interest due to their superior thermal stability and outstanding properties [13–18]. However, it is always challenging to synthesize 3D UOFs because the linear O–U–O chain with uranium (VI) usually leaves 4–6 coordination sites in the equatorial plane which favors the formation of low-dimensional (1D or 2D) structures rather than 3D ones [12–18, 43]. Meanwhile, the 3D UOFs are the most significant among these structures due to their superior thermal stability and unique properties, intriguing versatile architectures, new topologies, etc. Up to now, many synthetic strategies have been developed for 3D UOFs, and a popular one is to introduce a second functional group into ligands, by which heterometal ions as structure-directing agents have the potential to be incorporated into the structures [13, 17]. As another synthetic method, soft arylcarboxylic/aliphatic carboxylic

acids with strong hindrance are used to cross-link the uranyl moieties to form 3D networks [8, 28–30]. It is noteworthy that reaction conditions such as concentration, temperature, and pH value also play significant roles in the assembly of 3D UOFs [12, 43].

So far, the reported work of MOFs is mainly limited to the transition metal–organic frameworks, and most of the "actinide–organic frameworks" (AnOFs) are based on the uranium element due to its coordination advantages and long research history [44]. Other actinide elements are not reported in construction of MOFs, but have attracted increasing attention in this field. The actinide chemistry is very rich, and the oxidation states of actinides in aqueous solutions range from +2 (No) to +7 (Np, Pu, and Am), but some are very unstable in a solution. The reported actinides can exist as different ionic species such as M^{3+}, M^{4+}, MO^{2+}, and MO_2^{2+} (M: actinide). Many actinide-based–inorganic framework materials have been reported and exhibit possible applications to nuclear waste storage and nanotechnology [45–47]. In addition, the metal–organic frameworks exhibit important application potential in guest exchange [48, 49], gas adsorption, microporosity, or selective catalysis [50].

In this chapter, we review the recent efforts to construct multidimensional uranyl–organic complexes with an extended structure, especially for the construction of 3D frameworks which is not preferred to form. The impact of organic ligands, structure-direct agent, and incorporation of heterometal ions on the construction of UOFs are addressed in detail. In addition, as the typical MOFs of other actinides, actinide oxalates, actinide carboxylate, and actinide carboxyphosphonate are also described in this chapter.

2 MOFs of Uranium

Uranium element has a particular place and constitutes the most studied metal among the actinides family. The uranyl–organic compounds with an extended structure (1D chains, 2D layers, or 3D frameworks) and amazing properties can be constructed with five different oxidation states varying from +2 to +6. Among these valance states, uranium with +6 is the most stable one and constructs most of the uranium-bearing solid-state compounds. The most common uranium-containing structure unit is uranyl ion, UO_2^{2+}, which consists of a uranium center with a formal charge of +6 and two oxygen atoms (terminal oxygens). In some special conditions, polynuclear uranyl species, such as $U_2O_5^{2+}$ and U_3O_8, also tend to form by hydrolysis and polymerization of the uranyl cations. Thus, based on the uranyl cation and its derived structure units, various uranium-containing inorganic–organic coordination compounds were developed.

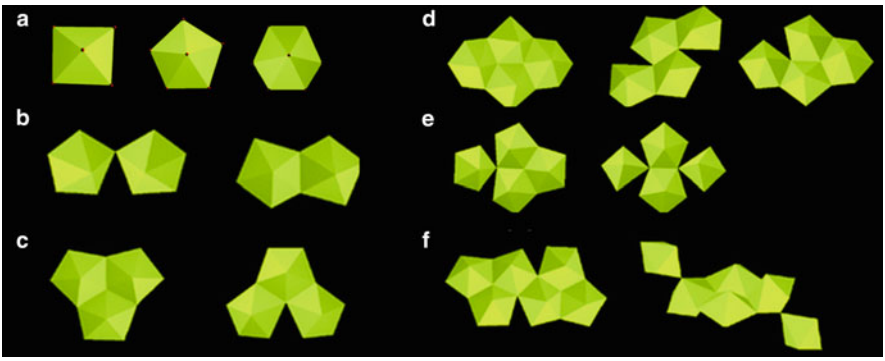

Fig. 1 Building units of UOFs: PBUs (**a**) (square bipyramid, pentagonal bipyramid, and hexagonal bipyramid); SBUs built up by corner and edge sharing the equatorial oxygen atoms of the uranyl units, including (**b**) dimers, (**c**) trimers, (**d**, **e**) tetramers, and (**f**) hexamers. Reprinted with permission from [12]. Copyright 2011, American Chemical Society

2.1 Building Units of UOFs

It has been demonstrated that isolated UO_2^{2+} cations exist in highly acidic aqueous solutions. In 1965, Rajan and Martell first proposed a dinuclear model of uranyl citrate in a solution with low pH values [51]. Trinuclear $(UO_2)_3(OH)_5^+$ complexes as another popular species may lose a water molecule to form an oxo–hydroxo-uranium polyhedral cation, $(UO_2)_3O(OH)_3^+$ under crystallization conditions. That is, the monomeric UO_2^{2+} cations always directly take part in the crystal growth under highly acidic conditions. Through EXAFS (extended X-ray absorption fine structure) technique, it was revealed that dinuclear species with uranium coordination to both hydroxyl and carboxylate groups exist in a solution with low pH values [52]. While in solutions with relatively high pH values, the uranyl cations tend to form polynuclear uranyl species (such as $U_2O_5^{2+}$ and $U_3O_8^{2+}$) via hydrolysis and polymerization and subsequently get involved in the crystallization of UOFs [53]. The formation of uranyl squarates were observed by Cahill and Rowland under ambient conditions. The building units of UOFs can be classified as follows (Fig. 1): (1) primary building units (PBUs), the uranyl species with coordination geometries such as square, pentagonal, and hexagonal bipyramids, and (2) secondary building units (SBUs), oligomeric uranyl cations ranging from dimers to hexamers formed by corner and/or edge sharing the equatorial atoms of the monomeric uranyl units [54].

The UOFs with various structures and different dimensions can be constructed based on the monomeric uranyl polyhedra, such as 1D chains, 2D layers, and 3D frameworks. A chain structure of UOFs, $UO_2(pdc)(H_2O)$ (Pdc=pyridine-2,6-dicarboxylic acid), is formed by linkage of uranyl units with pdc molecules. Through the helical arrangement of the pdc molecules and the uranyl ions, nanochannels with a diameter of about 6.4 Å and considerable adsorption capacity for water and methanol are generated [55]. In another work, various 2D layers and

3D frameworks were also built up from monomeric uranyl building units by the linkage of 1,2,3,4-butanetetracarboxylic acid (H_4BTC) and 1,2,3,4-cyclobutanetetracarboxylic acid (H_4CBTC) [56]. The dinuclear units ($(UO_2)_2O_4(\mu_2\text{-}OH)_2(H_2O)_2$) contain two uranyl cations in a 7-fold coordination. The uranyl cations are coordinated by five oxygen atoms located in a pentagonal plane. Two of them are sharing between two uranium atoms by a common edge. The dimeric uranyl units are popular SBUs in uranyl–organic extended structures. They are formed by the edge and corner sharing of two uranyl monomers [57]. In our previous work, we prepared a U–Zn–organic compound with 1D chain structure using pyridine-2,6-dicarboxylic acid as ligand. The μ_2-OH corner-sharing dinuclear uranyl clusters as a typical SBU are linked together to form the corresponding compound [55]. Trinuclear uranyl cores have proved to exist in many different minerals and uranyl–organic structures. In 1982, Lintvedt and coworkers synthesized the trinuclear core contained uranyl–organic complex with 1,3,5-triketonate ligands for the first time [58]. In this trinuclear core, the uranium atoms are in discrete triangular arrangement and are bound to another two uranium atoms with the μ_3-oxygen atom located at the center of the triangle. The trinuclear core would deviate from an ideal triangular shape if the bridging organic agent or heteroatom moiety displaces the μ_2-oxygen atoms between the uranium atoms [59]. For the tetrameric SBU, the uranium atoms are bonded by bridging μ_2- or μ_3-oxygen atoms. Many different types of tetramers with different configurations form when the μ_2-oxygen atoms are replaced by some ligands (such as acetic acid). For example, $[Zn_2(phen)_4U_4O_{10}(OAc)_2\text{-}(NA)_2\text{-}(QA)_2]$ (phen=1,10-phenanthroline; HOAc=acetic acid; HNA=nicotinic acid; H_2QA=quinolinic acid) is a previously reported tetramer-containing uranium–organic complex [60]. The two μ_2-oxygen atoms of uranyl ion was substituted by two carboxylate ligands, and thus the tetranuclear $U_4(\mu_3\text{-}O)_2(\mu_2\text{-}O)_2$ core was formed. In addition, new tetranuclear cores, $U_4(\mu_3\text{-}O)_2(\mu_2\text{-}O)_3$, $U_4(\mu_3\text{-}O)_2(\mu_2\text{-}O)_2$, and $U_4(\mu_3\text{-}O)_2$ would be obtained through the replacement of one, two, or four μ_2-oxygen atoms, respectively [61]. As reported in the literature, hexanuclear cores in some uranyl-bearing extended structures were derived from the trinuclear $U_3(\mu_3\text{-}O)(\mu_2\text{-}O)_3$ and tetranuclear $U_4(\mu_2\text{-}O)_4$ and $U_4(\mu_3\text{-}O)_2$ cores. For instance, a planar hexanuclear $U_6(\mu_3\text{-}O)_4(\mu_2\text{-}O)_4$ core was formed by the edge sharing of $U_3(\mu_3\text{-}O)(\mu_2\text{-}O)_3$ cores [27]. Another new type of hexanuclear core was obtained by the oxo-bonding of two uranium atoms to a tetrameric $U_4(\mu_3\text{-}O)_2(\mu_2\text{-}O)_4$ core [62].

Based on the abovementioned uranyl units, 1D, 2D, or 3D structures can be formed through organic chelating agents and/or heteroatoms. In some case, a uranium–organic complex may be composed of more than one type of uranyl units. Furthermore, the type of uranyl units may be varied depending on reaction conditions, such as pH. Mihalcea et al. reported a chain structure of uranyl–organic coordination polymer, $UO_2(H_2O)(1,2\text{-bdc})_3 0.32H_2O$, built up from the connection of the 7-fold coordinated uranium-centered polyhedra linked to each other with the phthalate ligands (Fig. 2a). The uranyl cation $(UO_2)O_4(H_2O)$ has a pentagonal bipyramid environment. The oxygen atoms of the double uranyl bonds are marked with O1 and O2. Uranium surrounded by seven oxygen atoms is the unique

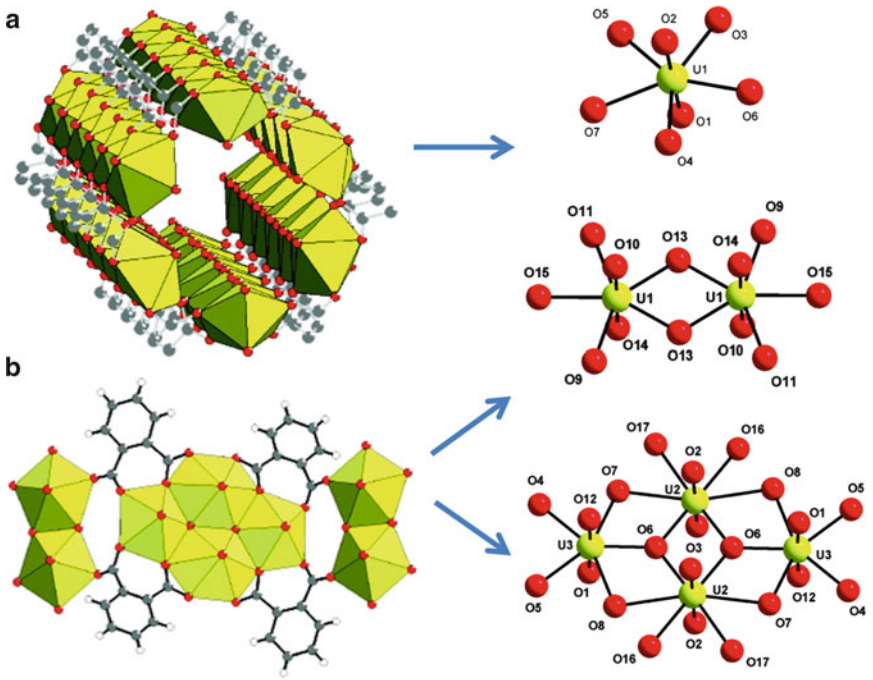

Fig. 2 View of (**a**) chain $UO_2(H_2O)(1,2\text{-bdc})_3 0.32H_2O$, building up from the connection of the 7-fold coordinated uranium-centered polyhedra; (**b**) $A(UO_2)_3O(OH)(H_2O)(1,2\text{-bdc})_2$ consisting of the 1D connection of dinuclear units $((UO_2)_2O_4(\mu_2\text{-}OH)_2(H_2O)_2)$ with tetranuclear units $((UO_2)_4(\mu_3\text{-}O)_2O_{12})$. Reprinted with permission from [63]. Copyright 2011, American Chemical Society

crystallographical site in this structure. The typical short U–O distances are associated with the uranyl bonds. Two other compounds $A(UO_2)_3O(OH)(H_2O)(1,2\text{-bdc})_2$ (A=K, NH_4) were also prepared at higher pH (1.5–3) (Fig. 2b). They consist of the 1D connection of dinuclear units $((UO_2)_2O_4(\mu_2\text{-}OH)_2(H_2O)_2)$ with tetranuclear units $((UO_2)_4(\mu_3\text{-}O)_2O_{12})$ through phthalate groups. The tetranuclear unit $(UO_2)_4(\mu_3\text{-}O)_2O_{12}$ in $A(UO_2)_3O(OH)(H_2O)(1,2\text{-bdc})_2$ (A=K, NH_4) contains two independent crystallographical uranium sites. It is constructed by two 8-fold coordinated uranium cations (U2) with a hexagonal bipyramid environment and two 7-fold coordinated uranium cations (U3) with a pentagonal bipyramid polyhedron [63].

2.2 Construction of UOFs

Uranium, apart from its nuclear physics, also shows rich structure chemistry and coordination chemistry for the construction of compounds with other elements.

Besides the inorganic–uranyl solids (such as sulfates, phosphates, silicates, and borates) [64–67], uranyl–organic coordination polymers and uranyl–organic hybrid materials are also constructed by bonding organic molecules with the uranyl moiety. Nowadays, the construction of uranyl–organic frameworks through the coordination of uranium atom centers to organic linker moieties has been the subject of considerable effort. To date, various organic ligands have been employed to isolate uranyl hybrid materials [68–83], and uranium-bearing complexes with various structures, such as clusters [84], 1D chains [85], 2D layers [86–88], and 3D frameworks [89, 90], were obtained along with versatile physiochemical properties, for example, photocatalytic performance, photoelectric conversion, and luminescence [8, 13, 26, 39, 52, 56, 84, 90]. It has been demonstrated that the structures of uranyl–organic coordination polymers and frameworks (UOFs) are extremely sensitive to the reaction conditions used. Yaghi et al. have shown that dicarboxylate groups with variable sizes and shapes would construct UOFs with different structures, and their functionality and pore size can be effectively tailored in this way [91, 92]. Thus, the modification of different organic ligands somewhat contributes to the structural variation of UOFs.

2.2.1 Impact of Organic Ligands

In the studies of nuclear waste management, extraction, and materials chemistry, carboxylates and polycarboxylates are the most commonly used organic ligands to associate with uranyl ions because of their strong affinity for the uranyl ion. This can be revealed by the sheer number of reported crystal structures of uranyl–carboxylate complexes in the Cambridge Structural Database (CSD, version 5.31, close to 400) [41]. Most of the reported carboxylate ligands used in uranyl–carboxylate coordination polymers are rigid or flexible [12]. Sun and coworkers first used isomeric ligands with semirigidity as the construction agents to prepare 3-fold interpenetrated uranyl–organic frameworks and proved that they were beneficial for the construction of new UOFs [93]. Two new uranyl–organic coordination polymers $(UO_2)(HL^1)$ and $Zn(H_2O)_3(UO_2)_2(O)(OH)(L_2)\cdot H_2O$ were constructed by using semirigid carboxylic acids, 3,3′-((2-((3-carboxyphenoxy)methyl)-2-methylpropane-1,3Diyl)bis(oxy)) dibenzoic acid (H_3L^1, Fig. 3a) and 4,4′-((2-((4-carboxyphenoxy)methyl)-2-methylpropane-1,3Diyl)bis-(oxy))dibenzoic acid (H_3L^2, Fig. 3d) [94]. The compound $(UO_2)(HL^1)$ with 1D chain structure crystallizes in the triclinic space group $P\overline{1}$, and Fig. 3b shows that its asymmetric unit is constructed by one crystallographically distinct uranyl center and one L^1 ligand. The UO_7 pentagonal bipyramid as the uranyl center was coordinated by five oxygen atoms in four carboxylate groups from three L^1 ligands equatorially (U–O length, 1.765(4) Å; U–O distances in the equatorial plane, 2.301(3) ~ 2.486(4) Å). In this asymmetric unit, one uranyl cation bridges three L^1 ligands and one L^1 ligand linked three uranyl cations. It was revealed that the carboxylate moieties of L^1 ligand feature three coordination modes: (1) didentately coordinated to two uranyl centers, (2) didentately coordinated to one uranyl center,

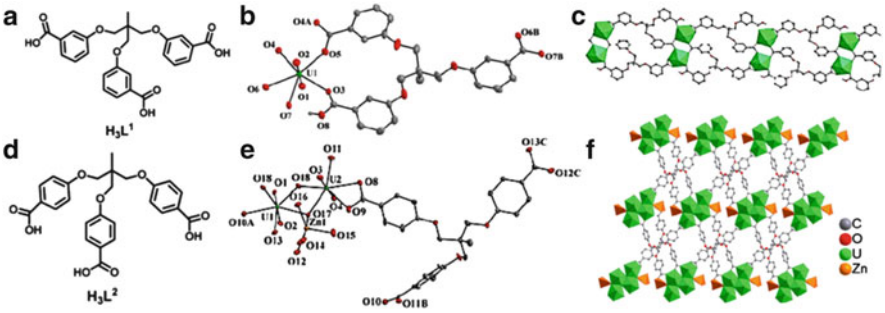

Fig. 3 View of the structure of ligand H_3L^1 (**a**), asymmetric unit (**b**), and 1D chain structure (**c**) of $(UO_2)(HL^1)$; ligand H_3L^2 (**d**), asymmetric unit (**e**), and 2D layer structure (**f**) of Zn $(H_2O)_3(UO_2)_2(O)(OH)(L_2)\cdot H_2O$. Reprinted with permission from [94]. Copyright 2013, American Chemical Society

and (3) unidentately coordinated to one uranyl center. Thus, 1D ribbonlike arrangement was produced by such a connection, and the weak π–π stacking (3.75–3.92 Å) of the ligands also contributed to the whole ribbon structures (Fig. 3c). Zn $(H_2O)_3(UO_2)_2(O)(OH)(L^2)\cdot H_2O$ with 2D structure also crystallizes in the triclinic space group $P\overline{1}$. Two crystallographically unique uranium atoms, one zinc atom, and one L^2 ligand construct its asymmetric unit, and the two uranyl centers are in the pentagonal bipyramidal geometry (Fig. 3e). Through sharing common edges, a well-known tetranuclear structural building cluster was formed by the uranyl bipyramids. In each cluster, two hydroxy groups and μ_3-oxygen donors are the common corners. The ZnO_5 trigonal pyramids are also formed in the structure by coordinating zinc atom by five oxygens (one is μ_3-oxygen shared with two uranyl centers, one is in carboxylate group, and the others are coordinated water molecules), and heterometallic hexamer was constructed by connecting two ZnO_5 trigonal pyramids with tetranuclear cluster. There are three kinds of L^2 ligand possessing different didentate coordination modes, and each L^2 ligand links three hexanuclear clusters (constructed by UO_7 and ZnO_5) which are bonded to six L^2 ligands. Thus, the whole structure of $Zn(H_2O)_3(UO_2)_2(O)(OH)(L^2)\cdot H_2O$ is packed with 3,6-connected 2D layers (Fig. 3f).

Besides carboxylates, polycarboxylates are also common among the ligands coordinated with uranyl ions in materials chemistry [1]. The variety of available polycarboxylate ligands and their possible additional ligands all offer more opportunities to construct uranyl–organic frameworks (UOFs) with novel structural features. Up to now, most of the polycarboxylic acids in UOFs are rigid. The carboxylate substituents built on the pyridyl [27, 55, 68, 95–101], pyrazyl [102, 103], pyrazolyl [104], cyclohexyl [86, 105], phenyl, and naphthalenyl [18, 26, 27, 39, 106–108] can only rotate along one axis. The polycarboxylates based on the alkyl chains with varying lengths are flexible. For example, tetracarboxylates [56], aliphatic ditartrate [89, 109], tartrate [110], and their related ligands [111–113] have been extensively investigated as flexible polycarboxylate ligands.

Interestingly, the carboxylic group connected with a rigid group through alkyl chain is in a kind of intermediate state. Several examples have been investigated before, such as the uranyl complexes with tris(2-carboxyethyl)isocyanurate [114], and with the acetate-bearing ligands 2-pyridylacetate [115], and 1,3,5-benzenetriacetate [116]. In these examples, a rigid planar platform is functionalized by one, three, or four alkylcarboxylate groups, and thus a degree of geometric freedom is introduced. Thuéry reported two acetate-bearing ligands (1,2-phenylenedioxydiacetic acid (H_2PDDA) and *trans*-1,2Diaminocyclohexane-*N*,*N*,*N*0,*N*0-tetraacetic acid (H_4DCTA)) comprising rigid phenyl- or cyclohexyl-containing platform and two to four acetate arms for the construction of novel uranyl complexes.

As an example, the complex [UO_2(PDDA)(H_2O)] with one-dimensional ribbon-like structure was successfully constructed by H_2PDDA. The complex [UO_2(PDDA)(H_2O)] was constructed by the single formula asymmetric unit, and one chelating and two bridging carboxylate groups were coordinated to the uranyl ion with the average U–O bond lengths of 2.475(5) and 2.311(10) Å, respectively (Fig. 4a). The aqua ligand was also bonded to the uranyl ion, and thus the common pentagonal bipyramidal uranium environment was obtained. Each ligand is bound to three cations, and each metal cation connects three different ligands. As shown in

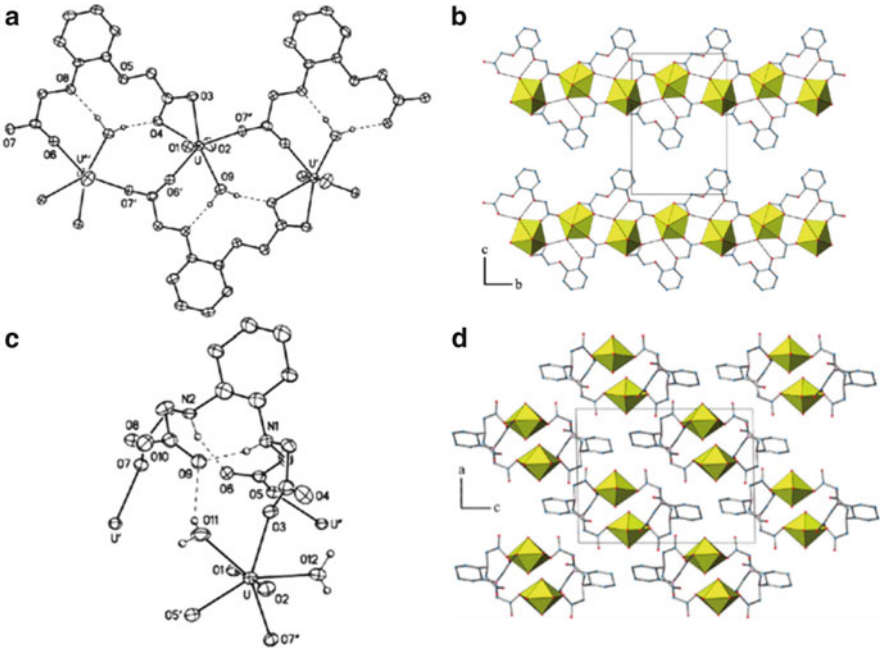

Fig. 4 (**a**) View of [UO_2(PDDA)(H_2O)]. Carbon-bound hydrogen atoms are omitted, whereas hydrogen bonds are shown as *dashed lines*. (**b**) View of the chains down the a-axis. Hydrogen atoms are omitted. Hydrogen bonds are shown as *dotted lines*. (**c**) View of [UO_2(H_2DCTA)(H_2O)$_2$] 3H_2O. Solvent molecules and carbon-bound hydrogen atoms are omitted. Hydrogen bonds are shown as *dashed lines*. (**d**) Packing of the ribbons viewed end on. Hydrogen atoms and solvent molecules are omitted. Reprinted with permission from [85]. Copyright 2011, American Chemical Society

Fig. 4b, the central row of one-dimensional arrangement is the uranyl ion which is surrounded by ligands on two sides. The complex $[UO_2(H_2DCTA)(H_2O)_2]$ $3H_2O$ with one-dimensional structure was also prepared with a polyaminopolycarboxylic acid H_4DCTA. All the nitrogen atoms in this complex were not coordinated but protonated, and the carboxylic/ate groups are monodentate. As shown in Fig. 4c, the uranyl ions in monodentate fashion is bound to three carboxylate groups, and the average U–O bond length is 2.389(8) Å. The uranyl ion is connected to three different molecules and two aqua ligands in nonadjacent positions. The topologies of the one-dimensional chains in $[UO_2(H_2DCTA)(H_2O)_2]3H_2O$ and $[UO_2(PDDA)(H_2O)]$ are similar: the number of carboxylate groups and coordination sites per ligand are identical in the two compounds. Furthermore, the overall geometries of the ligands are not very different. However, there are still obvious difference between the two complexes: the ribbon structure of $[UO_2(PDDA)(H_2O)]$ was planar, but the chain structure of $[UO_2(H_2DCTA)(H_2O)_2]$ $3H_2O$ was more expanded because the uranyl ions aligned into two rows along the side of the axis (Fig. 4d) [85].

2.2.2 Impact of Structure-Directing Agents

For the traditional organic ligands, carboxylic acid groups are always necessary as per their affinity for uranyl unit in the synthesis of UOFs [12, 93, 117–122]. Nevertheless, besides the dominant role of covalent metal–ligand bonds for the uranyl hybrid material synthesis, the noncovalent interactions are also believed to be a key factor in the construction of uranyl compounds with extended architectures [123–126]. The "terminating" sites, such as halogen atoms and nitro groups, can serve as platforms for supramolecular assembly by noncovalent interactions. Therefore, the organic ligands with a combination of covalent bonds and noncovalent interactions have been employed for the construction of UOFs with higher-dimensional structures. For example, 5-nitro-1,3-benzenedicarboxylic acid, 1,3,5-benzenetricarboxylic acid, and 4-chloro-2,6-pyridine dicarboxylic acid, all of which feature both aforementioned bonding sites and therefore are attractive organic ligands for UOFs synthesis. While the two carboxylates show direct coordination to UO_2^{2+}, the third functional moiety acts as a noncoordinating group to promote supramolecular interactions [107]. Beyond the structural role of ligands, organic species may also act as structure-directing agents to influence the complex architectures [127–131]. It was demonstrated that the formation of a given topology may be directed by the noncoordinating organic molecules in the synthesis of MOFs [132–138]. Cahill and coworkers have been working on expanding the concepts of supramolecular vs. direct coordination and exploring their influence on resulting topologies of MOFs [139]. Currently, they investigated the structure-directing influence of TEA (triethylamine) on the formation of UO_2^{2+} compounds. Double-stranded chain $[(UO_2)(C_8N_1O_6H_3)(H_2O)]\cdot H_2O$, 2D sheet $[(UO_2)_2(C_8N_1O_6H_3)2H_2O]\cdot TEA$, and 3D framework $[(UO_2)_2(OH)\text{-}(C_8N_1O_6H_3)_2]\cdot(TEAH)(H_2O)$ were synthesized by a hydrothermal method.

$[(UO_2)(C_8N_1O_6H_3)(H_2O)] \cdot H_2O$ is a chain composed of pentagonal bipyramidal uranyl monomers connected by n-bzdc ligands. The nitro functional groups beside the chains hydrogen bond to water molecules and stitch together neighboring chains, and thus a pseudo-2D sheet was formed ultimately (Fig. 5a).

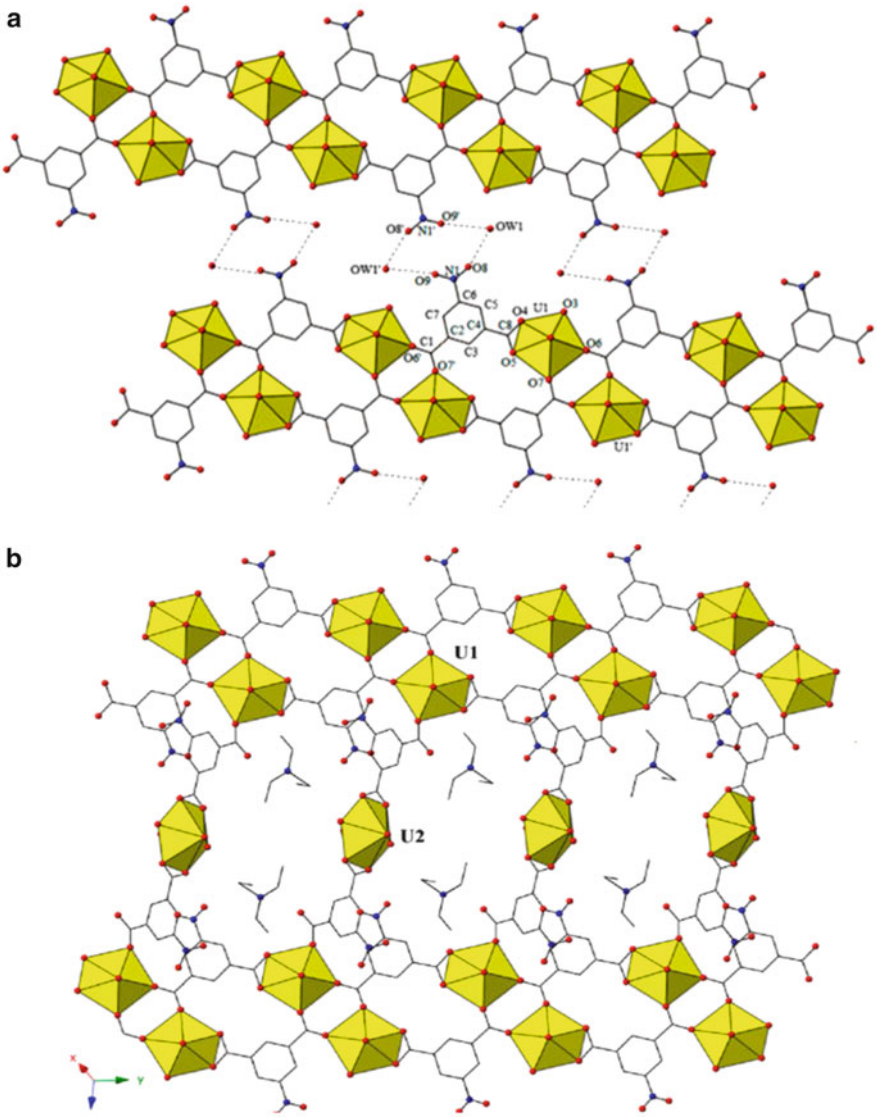

Fig. 5 Polyhedral representation of $[(UO_2)(C_8N_1O_6H_3)(H_2O)] \cdot H_2O$ (**a**) and $[(UO_2)_2(C_8N_1O_6H_3)2H_2O] \cdot TEA$ (**b**) where *yellow* polyhedra are uranium centers, *red* spheres are oxygen atoms, and *blue spheres* are nitrogen atoms. Hydrogen atoms and solvent molecules are omitted. Reprinted with permission from [139]. Copyright 2014, American Chemical Society

Besides $[(UO_2)(C_8N_1O_6H_3)(H_2O)] \cdot H_2O$, $[(UO_2)_2(C_8N_1O_6H_3)2H_2O] \cdot TEA$, and $[(UO_2)_2(OH)\text{-}(C_8N_1O_6H_3)_2] \cdot (TEAH)(H_2O)$ also contain hydrogen bonds or π-based interactions (or both) and thus realized structural connectivity. $[(UO_2)(C_8N_1O_6H_3)(H_2O)] \cdot H_2O$ was the foundation for the later two compounds. The increasing dimensionality displayed throughout the three compounds was a function of the structure-directing influence of TEA (triethylamine). $[(UO_2)_2(C_8N_1O_6H_3)2H_2O] \cdot TEA$ also contains the same chain as $[(UO_2)(C_8N_1O_6H_3)(H_2O)] \cdot H_2O$ while its chains linked by a linking unit composed of a uranyl center coordinated to an n-bzdc ligand rather than hydrogen bond. These linking units produce an infinite sheet containing TEA molecules in the interlayer (Fig. 5b). Through addition of TEA molecule in synthesis, the potential structure-directing function of TEA molecule was further confirmed. $[(UO_2)_2(OH)\text{-}(C_8N_1O_6H_3)_2] \cdot (TEAH)(H_2O)$ incorporates multiple chains connected by a dimeric uranyl linkage. TEA molecule may also act as structure-directing agent for the formation of this 3D framework because the TEA molecules residing within its channels.

2.2.3 Incorporation of Heterometal Ions

Through addition of templating species or secondary cations, the structure of UOFs is sometimes easily varied in terms of connectivity and dimensionality because of its sensitivity to the experimental conditions. This is true especially for the UOFs with polycarboxylates as ligands, whose coordinating site has different bonding modes which always result in various metal–ligand associations. It was demonstrated that the addition of d-block metal cations and neutral or protonated nitrogen-containing molecules on the uranyl complexes can obviously affect their structures [69, 128, 140, 141]. For example, in the presence of additional nickel(II) cations, uranyl ions with Kemp's triacid (*cis*,*cis*-1,3,5-trimethylcyclohexane-1,3,5-tricarboxylic acid, LH_3) [142] as ligands tend to form the architectures of nanotubular or octanuclear cage-like species [143]. The nickel (II) cations are ether associated with 2,2′-bipyridine (bipy) or alone (heterometallic uranyl–nickel nanotubules), separating from the homometallic octanuclear cages as counterions. It is hopeful that such a ligand with rigid and three-pronged geometry would favor the formation of closed or cyclic species with the uranyl ion. Therefore, incorporation of heterometal ions with strong cross-linking ability to the reaction systems is an effective approach to build up UOFs. Uranyl–heterometal–organic complexes have been constructed by uranyl species together with various metal ions, such as d-block metal ions [13, 39, 68, 98, 144], alkali [102, 103, 110], alkaline earth, and lanthanides [145].

Thuéry's group prepared a series of uranyl–heterometal–organic complexes in the presence of additional metal ions [146]. The complexes $[Hbipy][UO_2(L)] \cdot 0.5H_2O \cdot 0.25THF$ with a 2D structure and $[(UO_2)3(MeL)_2(OH)_2(H_2O)] \cdot 8MeOH$ with a 1D structure were respectively obtained in the presence of manganese nitrate and in the solution of water–THF or water–

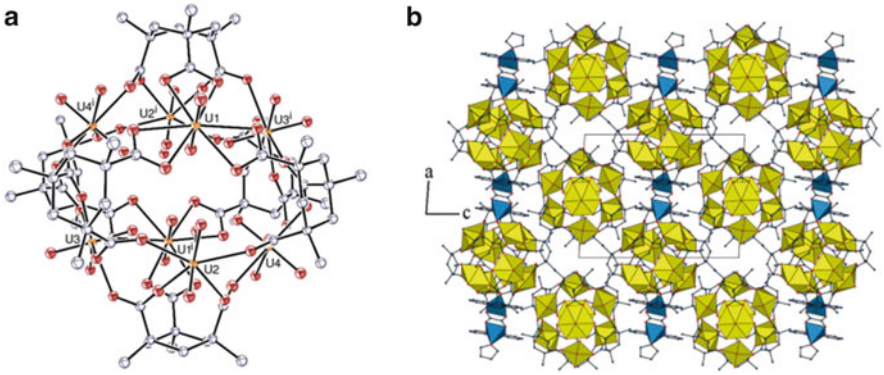

Fig. 6 View of $[Cu_2(C_2O_4)(bipy)_2(THF)_2][(UO_2)_8\{(L)_6H\}\text{-}(H_2O)_6]_2 \cdot 4H_2O \cdot 7THF$: (**a**) one of the two crystallographically independent octanuclear cages is represented; (**b**) packing of the octanuclear cages. The uranium coordination polyhedra are in *yellow* and those of copper are in *blue*. The solvent molecules and hydrogen atoms are omitted. Reprinted with permission from [146]. Copyright 2014, American Chemical Society

methanol. $[UO_2Tb\{(L)_2H\}(H_2O)_2]$, another 2D complex, was obtained in the presence of terbium(III) nitrate. In the presence of copper(II) or nickel(II) cations, the complexes $[(UO_2)_8\{(L)_6H_2\}(H_2O)_6] \cdot H_2O$, $[(UO_2)_8\{(L)_6H_2\}(H_2O)_6] \cdot 3H_2O$, and $[Cu_2(C_2O_4)(bipy)_2(THF)_2][(UO_2)_8\{(L)_6H\}\text{-}(H_2O)_6]_2 \cdot 4H_2O \cdot 7THF$ with 3D structures were obtained. All the three compounds contain the same homometallic uranyl octanuclear cage-like motif which was previously found in the complex $[Ni(bipy)(H_2O)_4]\text{-}[(UO_2)_8(L)_6(H_2O)_6] \cdot H_2O.5$. In the case of $[Cu_2(C_2O_4)(bipy)_2(THF)_2][(UO_2)_8\{(L)_6H\}\text{-}(H_2O)_6]2 \cdot 4H_2O \cdot 7THF$, one of the two crystallographically independent octanuclear cages and their packing structures are represented in Fig. 6. In addition, the complexes $[(UO_2)_8Cu_4(L)_8(H_2O)_{16}] \cdot 9H_2O$ and $[(UO_2)_{10}Cu_6(L)_{10}(OH)_2(H_2O)_7]$ were obtained together in the presence of copper(II) cations in water−THF. $[(UO_2)_8Cu_4(L)_8(H_2O)_{16}] \cdot 9H_2O$ is a dodecanuclear metallacycle comprising four $(UO_2)_2Cu$ trinuclear subunits. There are two uranyl oxo groups bonded to the central copper atom, and they are arranged in a helical geometry. $[(UO_2)_{10}Cu_6(L)_{10}(OH)_2(H_2O)_7]$ has a hexadecanuclear cage-like structure without any crystallographic symmetry. For both of the compounds, the cyclic or cage molecules tend to be formed with the topologically sufficient uranyl ions, and the hydrated copper ions are located inside. Therefore, the curved shape of the three-pronged Kemp's tricarboxylate ligand is particularly conducive to the formation of closed species (nanotubes, rings, and cages).

Our research group successfully prepared a uranyl–zinc–organic compound $(ZnO)_2(UO_2)_3(NA)_4(OAc)_2$ (HNA=nicotinic acid; HOAc=acetic acid) with 3D structure (Fig. 7). This 3D framework was assembled by $[(UO_2)_3(O)_2(CH_3CO_2)_2]_n$ chains via nicotinate ligands and Zn^{2+} cations [13]. The $[(UO_2)_3(O)_2(CH_3CO_2)_2]_n$ chains were constructed by the connection of trinuclear uranyl units through

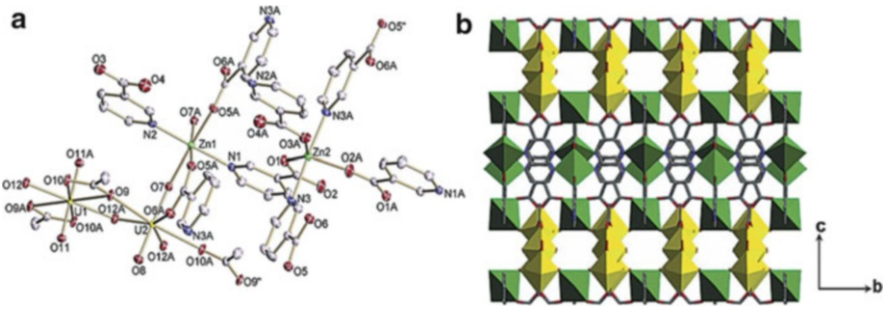

Fig. 7 View of $(ZnO)_2(UO_2)_3(NA)_4(OAc)_2$: (**a**) the Zn and U coordination environment represented by thermal ellipsoids drawn to encompass 30% of their electron density; (**b**) the three-dimensional framework viewed along the [100] direction. *Green*, ZnO_5 or ZnO_6 units; yellow, UO_7 or UO_8 units. Reprinted with permission from [13]. Copyright 2003, American Chemical Society

bridging μ_3-O atoms. The topology of inorganic U–O–Zn double sheet was further formed through the corner-linking of octahedral Zn^{2+} cations with the terminal uranyl oxygen atoms. Through the Zn^{2+} cations and tridentate nicotinate ligands, these double sheets are interconnected and finally result in the 3D sandwich uranium–zinc–organic framework. We also prepared a 3D uranium–nickel–organic compound, $[Ni_2(H_2O)_2(QA)_2(bipy)_2U_5O_{14}(H_2O)_2(OAc)_2]$ $32H_2O$(HOAc = acetic acid; bipy=4,40-bipyridine; H_2QA=quinolinic acid) in the presence of Ni (II) cations in quinolinic and acetic acids [68]. Through sharing the QA ligands, this 3D framework is constructed by the nickel metal–organic layers and polyoxouranium ribbons. The edge-sharing centrosymmetric pentanuclear U_5O cores constructed the polyoxouranium ribbons, and further constructed the 3D framework with Ni metal–organic layers through sharing QA ligands. There are two kinds of Ni atoms with different coordination structure bridged by the QA ligands to construct the 1D chain along the a-axis, which links the polyoxouranium ribbons to form 3D framework by QA ligands. Besides the d-block metal ions, alkali and alkaline earth cations with high coordination numbers were also extensively studied for the construction of 3D uranyl–organic structures [102]. They can be used as suitable additional connecting nodes not only because of their high coordination numbers (e.g., 10 for Rb^+, 9 for K^+, 6 for Na^+, and 8 for Ba^{2+}) but also because they apt to coordinate to the terminal oxygen atoms of the UO_2^{2+} moieties [103, 110]. As reported previously, the $[(UO_2)_2(C_2O_4)_2(OH)Na(H_2O)_2]$ sheets are assembled to construct the 3D framework by bonding Na^+ cations with the terminal oxygen groups of uranyl dimers. The corner-sharing dimeric uranyl structural building units leads to the $[(UO_2)_2(C_2O_4)_2(OH)Na(H_2O)_2]$ sheets with bis-bidentate oxalate and bridging hydroxide groups [110].

In the past research, among the uranyl–organic coordination frameworks, the 3D frameworks are highly desirable and widely studied due to their superior properties and stable structures. However, the 3D frameworks are proved to be less

successfully constructed compared with 1D chains [26, 147] and 2D layers [26]. This is because the coordination geometry of the uranyl ion is considerably constrained by its linear shape in the presence of the strong U–O bonds in the linear UO_2^{2+} ions [148]. The organic ligands can only bond to the center at the equatorial positions due to the inaccessibility of the uranium center in the uranyl units. Through understanding the impact of organic ligands, structure-directing agent, and heteroatom incorporation, increasing strategies for the construction of 3D uranyl–organic coordination compounds would be developed. The ligand design, heteroatom incorporation, and structure-directing agent provide the possibility for construction of 3D uranyl–organic coordination compounds. In addition, the reaction conditions (e.g., the concentration of uranyl ions, reaction temperature, etc.) also effectively affect the realization of this possibility.

3 MOFs of Other Actinides

Nowadays, increasing efforts have been devoted to synthesis of zeolite-like materials with an open-framework structure due to their applications in sorption [91, 92], separation, and heterogeneous catalysis. Interest in coordination chemistry of actinide elements is not only because a comprehensive understanding of its basic electronic structure, bonding, and properties is vital to support the development of advanced nuclear fuel cycle but is also driven by the scientific curiosity to develop advanced materials with potential applications. The actinide chemistry is very rich, and the oxidation states of actinides in aqueous solutions range from +2 (No) to +7 (Np, Pu, and Am), but some are very unstable in solution. The reported actinides can exist as different ionic species such as M^{3+}, M^{4+}, MO^{2+}, and MO_2^{2+} (M: actinide). Recently, a number of organic [149–151], metal–organic [152–154], and inorganic [155] framework materials have been constructed from molecular building units using metal–ligand coordination. Many actinide-based–inorganic framework materials have been reported, and these materials show possible applications in nuclear waste storage and nanotechnology [45–47]. In addition, the metal–organic frameworks (MOFs) exhibit important application in guest exchange, gas adsorption, microporosity, or selective catalytic activity [48–50]. However, the reported MOFs are mainly limited to those formed with the transition metals, and the "actinide–organic frameworks" (AnOFs) are mainly based on the uranium elements with coordination advantages and long research history [44]. Besides the uranyl–organic frameworks introduced above, this section would review the few reported typical MOFs of other actinides.

3.1 Actinide Oxalates

The majority of reported actinide–organic frameworks are concerned with actinyl oxalates. The precipitation of actinide oxalates was widely used as a technological

method for the purification and isolation of actinides. The oxalate ligand as a rigid bis-bidentate ligand can bridge the actinide centers. It has various coordination modes [156, 157] leading to numerous structural architectures or molecules such as linear infinite one-dimensional chains and two- or three-dimensional coordination polymers [158–169].

In 1963, Chackraburtty first reported the crystal data of plutonium oxalate decahydrate $Pu_2(C_2O_4)_3 \cdot 10H_2O$ [170]. He claimed that this compound is isostructural to $La_2(C_2O_4)_3 \cdot 10H_2O$ based on the crystal system (monoclinic) and unit cell parameters. However, 40 years later, Rundle et al. determined the structure of plutonium oxalate, whose structural formula should be $Pu_2(C_2O_4)_3 \cdot 9H_2O$ and isostructural to the series $Ln_2(C_2O_4)_3 \cdot nH_2O$ [158]. Three crystallographically independent oxalate ions and three water molecules construct the overall environment of Pu, and thus the distorted tricapped trigonal PuO_9 prism is formed. The basic building unit of 2D plutonium oxalate (3,6) networks, a $[Pu(C_2O_4)]_6$ six-membered ring, is constructed through the connection of PuO_9 (Fig. 8a). The obtained $2[\{Pu(H_2O)_3\}_2(C_2O_4)_3]$ (Fig. 8d) 2D plutonium oxalate networks are stacked in the [0 1 0] direction (Fig. 8b). Besides this plutonium (III) oxalate, the same research group also prepared a $KPu(C_2O_4)_2(OH)_3 \cdot 2.5H_2O$ with Pu (IV), which was also structurally characterized via single crystal X-ray diffraction for the first time. In contrast to the former plutonium (III) oxalate, this plutonium (IV) oxalate is a 3D network, which is constructed by $[PuO_9]$ polyhedra and $[C_2O_4]$ groups. The nine-coordinate Pu atom is bound to one oxygen atom (O_7) from a coordinated hydroxide ion and eight oxygen atoms from four bis-chelating oxalate

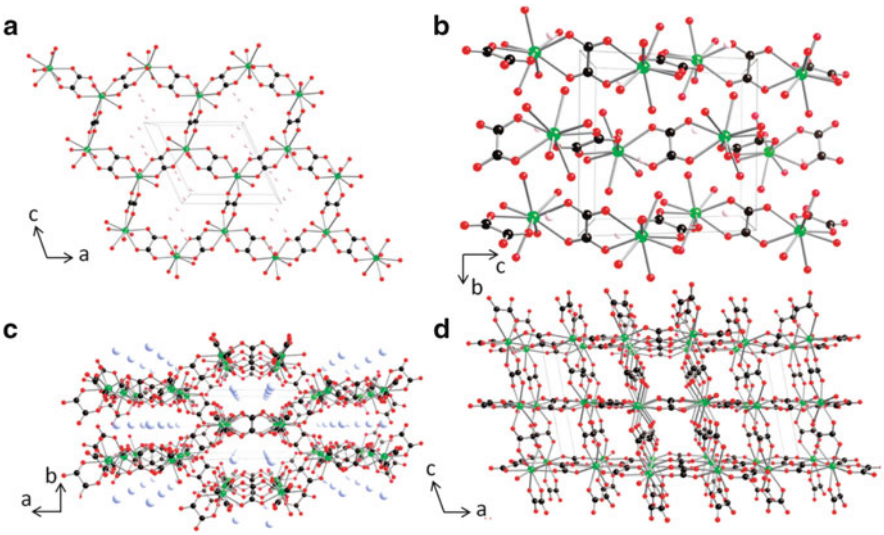

Fig. 8 Packing in $Pu_2(C_2O_4)_3(H_2O)_6 \cdot 3H_2O$, honeycomb structure along the *b*-axis (**a**) and layers in the ab plane (**b**); packing in $KPu(C_2O_4)_2(OH)_3 \cdot 2.5H_2O$, honeycomb structure along the *c*-axis (**c**) and view down the *b*-axis showing the 3D channel structure (**d**). Reprinted with permission from [158]. Copyright 2009, American Chemical Society

ligands. The Pu–Oox bond distances range from 2.454 to 2.507 Å. The Pu atom is coordinated by four oxalate groups and the hydroxide ligand lies above that base. A honeycomb structure with about 8.3 × 12.3 Å apertures is formed by the six [PuO_9] polyhedra and six oxalate ligands and filled with K atoms and water molecules (Fig. 8c). The 3D channel structures are formed with approximate dimensions of 5.5 × 4.5 Å run down the *b*-axis (Fig. 8d).

3.2 Actinide Carboxylate

The complexation of actinide ions by carboxylate organic ligands has been much investigated, particularly in the context of nuclear waste processing and management, and in decorporation studies [171–175]. Although most studies are associated with lanthanide or uranyl ions, several thorium–organic assemblies have been reported with ligands such as pyrazine-, pyridine-, and pyrazoledicarboxylates, 1,3-adamantanediacetate, 1,3,5-benzenetricarboxylate, and 4-carboxyphenylphosphonate [9, 10, 176–178].

Recently, O'Hare's research group reported a series of three-dimensionally connected thorium–organic framework solids [9, 10, 19, 20]. As described, [(Th_2F_5)-$(NC_7H_5O_4)_2(H_2O)$][NO_3] was prepared by reaction of thorium nitrate with 3,5-pyridinedicarboxylic acid in the presence of HF and DMF (*N*,*N*-dimethylformamide) [19]. Thorium oxyfluoride chain along the [010] direction and cross-linked pyridinedicarboxylate (PDC) construct the complex [(Th_2F_5)-$(NC_7H_5O_4)_2(H_2O)$][NO_3]. The thorium oxyfluoride chains are composed of thorium oxyfluoride polyhedra through corner sharing, in which the thorium is 9-coordinated and coordinated to five fluorine and four oxygen atoms in a tricapped prismatic environment. The observed Th–O distances (2.426–2.502 Å) are longer than that of Th–F bond (2.307–2.374 Å). Each thorium center is bonded to three oxygen atoms from a PDC and one water molecule, sharing one edge with another thorium through two fluoride ions, and thus the dimers are formed. The chains running along the [010] direction are constructed by the linkage of the dimers in the way of sharing corners. The three-dimensional structure is constructed from the connection of adjacent thorium fluoride chains by PDC linkers in two types (Fig. 9a). The carboxylate group on the first type of PDC linker is bound to one thorium center, and the formed chains run along the [100] direction. While, the carboxylate group on the second type of PDC linker are bound to two adjacent thorium centers each, and the formed thorium fluoride chains are linked along the [001] direction. A cavity with a width of 3.3 × 3.8 Å is created by the connectivity between the pyridine rings and the chains. The nitrate anions residing in the cavity form weak hydrogen bonds with the protonated pyridine moiety and bound water (Fig. 9b). In addition, O'Hare et al. also reported the first 1D hexagonal nanotubular thorium–organic framework, $Th[C_6H_3(CO_2)_3F]\cdot 0.3H_2O$ [20]. The eight-coordinate ThO_6F_2 polyhedra and 1,3,5-benzenetricarboxylic acid (BTC) groups

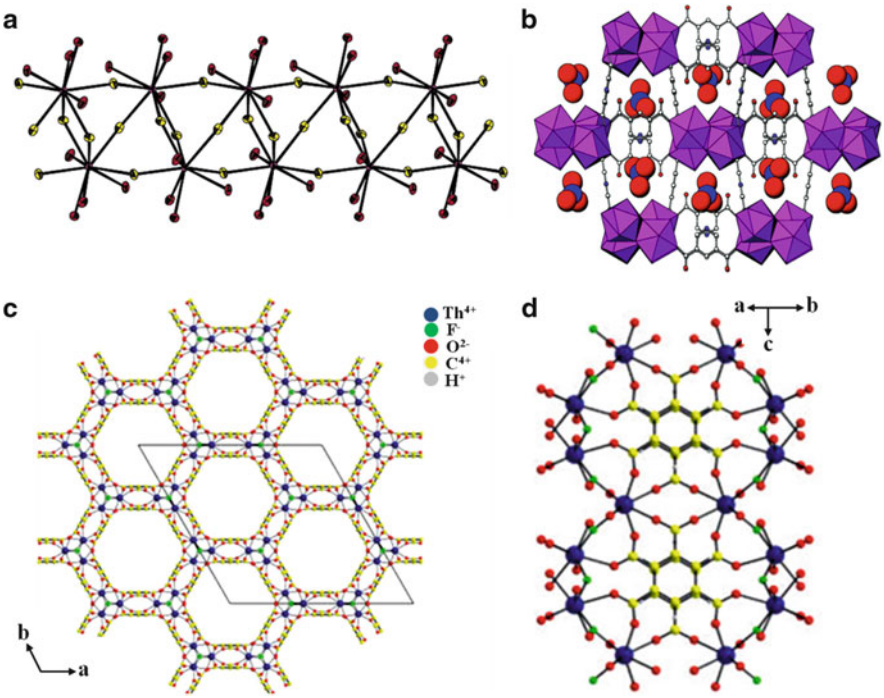

Fig. 9 (**a**) Representation of thorium backbone chain running along the [010] direction. Thorium, oxygen, and fluorine atoms are represented as *magenta*, *red*, and *yellow* colors, respectively. (**b**) Polyhedral view of the thorium-PDC framework along the [010] direction, nitrate anions (large spheres) is also represented in the framework cavity. Carbon, oxygen, and nitrogen atoms are represented as *white*, *red*, and *blue* colors, respectively. Reprinted with permission from [19]. Copyright 2003, American Chemical Society. (**c**) Ball-and-stick representation of Th $[C_6H_3(CO_2)_3F]\cdot 0.3H_2O$ revealing hexagonal channels along the *c*-axis. Occluded water molecules have been removed for clarity. (**d**) ThO_6F_2 groups form infinite one-dimensional chains along the *c*-axis and the interconnected BTC groups are in perfectly eclipsed pairs which form the walls of the tunnels. Reprinted with permission from [20]. Copyright 2008, American Chemical Society

constructed its structure through oxygen and fluorine atoms (Fig. 9c). Each Th^{4+} cation is bonded to six oxygen atoms and two fluorines. The infinite unidimensional chains are formed along the [001] direction by the connection of ThO_6F_2 group through F atoms. These chains are further interconnected by the BTC groups and thus create an unprecedented neutral hexagonal framework structure (Fig. 9d).

3.3 Actinide Carboxyphosphonate

The reactivity of phosphonic acids to the main group and the d-block elements were investigated in detail since many years ago [179–185]. Various new phosphonate

solids have been prepared by mono- or diphosphonic acids with flexible carbon-chain backbones. Some of the compounds exhibit considerable variety of structures, and some are analogous to the phosphate structures [182–184, 186–189]. One of the phosphonic acid groups in a diphosphonic acid is replaced by a carboxylic acid group, and thus the phosphonocarboxylic acids are obtained. They have attracted increasing research interest because new types of coordination behavior and structures would arise through the use of two different functional groups along with the availability of a flexible carbon backbone. Phosphonocarboxylates can be considered as the linkers of the traditional open-framework structures and MOFs. A variety of interesting compounds were constructed by exploiting the difference in the coordinating ability between the carboxylic acid and the phosphonic acid [188, 190–193]. Actinide carboxyphosphonates was firstly known and rapidly expanded in the form of uranyl carboxyphosphonates, and about 20 compounds were reported in the past few years [194–197]. Among them, phosphonoacetate is the best represented carboxyphosphonate, and 2-phosphonopropionate was reported in a smaller subset [195]. It has been previously demonstrated that the PO_3 moiety has a much stronger propensity for binding the U(VI) centers than the carboxylate group in the carboxyphosphonates [194–197], which corresponds to the study results of phosphonates and carboxylates in solution [198, 199]. Albrecht-Schmitt and coworkers prepared a thorium(IV) carboxyphosphonate compound, $ThF_2(PO_3C_6H_4CO_2H)$, through the hydrothermal reactions of thorium nitrate and uranyl acetate with carboxyphenylphosphonic acid and HF [178]. The bridging of $[ThO_4F_4]$ units and carboxyphenylphosphonate constructed the thorium oxyfluoride layers, and thus a pillared structure is built up, resulting in a three-dimensional network. $ThF_2(PO_3C_6H_4CO_2H)$ crystallizes in the monoclinic space group P21/c, and this compound is centrosymmetric. Its thorium oxyfluoride layers extend in the [ab] plane (Fig. 10a) and are linked by the carboxyphenylphosphonate ligand into a pillared structure (Fig. 10b). The thorium polyhedral unit constructed by eight-coordinate $[ThO_4F_4]$ dodecahedra is edge-shared via bridging fluoride ions, resulting in one-dimensional chains along the b-axis. As another example, Natarajan et al. developed a new phosphonoacetate hybrid framework based on the actinide element thorium, $Th(H_2O)_2(O_3PCH_2COO)(C_2O_4)_{0.5} \cdot 3H_2O$ [200]. It was built up from the connectivity between the thorium polyhedra and the phosphonoacetate/oxalate units. The thorium atom in its asymmetric unit is coordinated to nine oxygen atoms, and the resulting polyhedron exhibits tricapped trigonal prism geometry, in which the average Th–O bond distance is 2.467 Å. Three phosphonate oxygens, [O(1), O(2), O(3)], two carboxylate oxygens, [O(7), O(9)], and two water molecules [O(4), O(6)] are bonded to the central thorium atom. A two-dimensional cationic layer along the *b*-axis is formed through the connectivity between phosphonoacetate and thorium (Fig. 10c). Thus, the three-dimensional structure is constructed by bridging these two-dimensional sheets with the oxygen atoms of the oxalate moiety [O(5), O(8)]. These thorium phosphonoacetate layers are stacked in the form of *AAA*... pillared by the oxalate units (Fig. 10d).

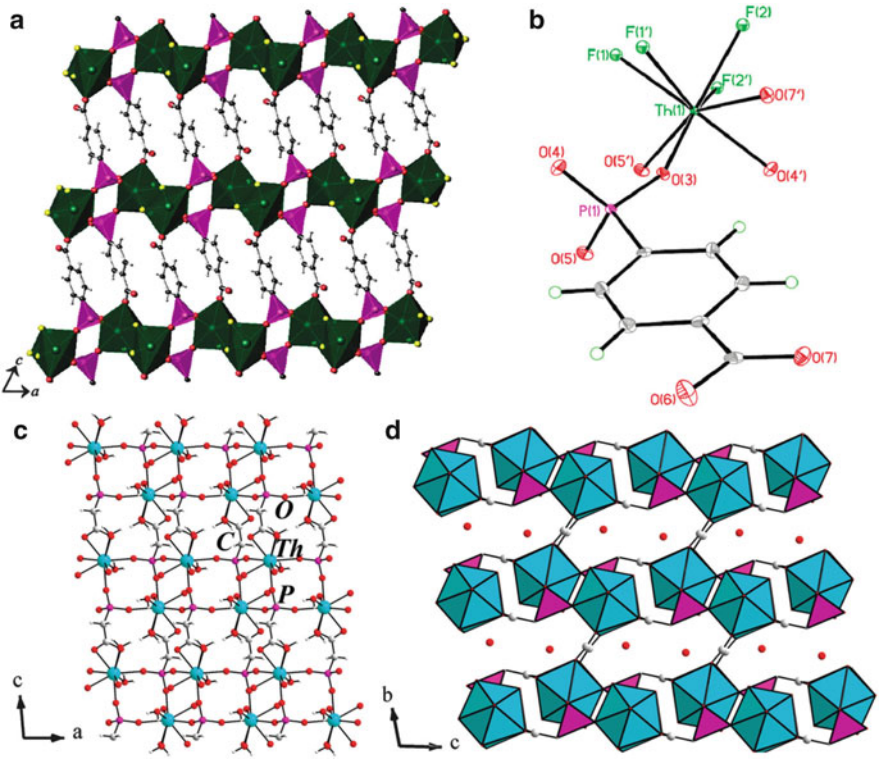

Fig. 10 (**a**) Polyhedral representation of the structure of $ThF_2(PO_3C_6H_4\text{-}CO_2H)$ viewed along the *b*-axis. The structure contains dodecahedral $[ThO_4F_4]$ units (*deep green*), oxygen (*red*), phosphorus (*magenta*), fluoride (*yellow*), carbon (*black*), and hydrogen (*white*). (**b**) Local coordination environment in $ThF_2(PO_3C_6H_4\text{-}CO_2H)$. Reprinted with permission from [178]. Copyright 2010, American Chemical Society. (**c**) View of the thorium phosphonoacetate layers in $Th(H_2O)_2(O_3PCH_2COO)(C_2O_4)_{0.5} \cdot 3H_2O$. (**d**) The three-dimensional structure of $Th(H_2O)_2(O_3PCH_2COO)(C_2O_4)_{0.5} \cdot 3H_2O$. The lattice water molecules are disordered and located in the channels. (*Cyan polyhedra*, thorium (IV) atoms in tricapped trigonal prism geometry; *Purple polyhedra*, phosphorus atoms of the phosphonoacetate ligand). Reprinted with permission from [200]. Copyright 2010, American Chemical Society

Conclusions

Actinide–organic frameworks have attracted increasing attention of synthetic chemists as they offer interesting possibilities due to the variable coordination abilities of actinides with rich oxidation states. Uranium, as the most representative actinide element, has been investigated for a long history in the nuclear fuel cycle, and this element has been devoted to construct multidimensional extended uranium-bearing coordination complexes

(continued)

because of its advantages in coordination chemistry and its structure diversities and physicochemical properties. In this chapter, we have highlighted the recent efforts to construct uranyl–organic complexes with an extended structure (such as 1D chains/tube, 2D layers, and 3D networks). To review construction strategy of uranium–organic frameworks (UOFs), the uranyl polyhedra and their oligomeric counterparts as the structural building units are first introduced. The linear UO_2^{2+} unit, which can be equatorially coordinated only, determines that the UOFs usually prefer chain/sheet arrangements to 3D structures. To obtain 3D UOFs, the cross-linking ability of both the metal centers and the organic ligands should be increased. The choice of organic ligands with multidentate points and flexible backbones or strong steric hindrance, incorporation of heteroatoms, and employment of structure direct agent would provide more opportunity to generate 3D UOFs. Compared with the reported work of UOFs, the MOFs based on other actinide elements are rare, but their rich oxidation and potential applications still inspire research enthusiasm of the chemists. As typical examples, the MOFs based on other actinide elements than uranium with oxalate, carboxylate, and carboxyphosphonate organic ligands are addressed. It is believed that this chapter would contribute to understanding the nature and construction of actinide MOFs, especially UOFs, and to developing more physicochemical properties or novel structures of MOFs.

References

1. Liu Y, Xuan WM, Cui Y (2010) Engineering homochiral metal-organic frameworks for heterogeneous asymmetric 215 catalysis and enantioselective separation. Adv Mater 22:4112–4135
2. Li JR, Kuppler RJ, Zhou HC (2009) Selective gas adsorption and separation in metal-organic frameworks. Chem Soc Rev 38:1477–1504
3. Dinca M, Long JR (2008) Hydrogen storage in microporous metal-organic frameworks with exposed metal sites. Angew Chem Int Ed 47:6766–6779
4. Rowsell JLC, Yaghi OM (2005) Strategies for hydrogen storage in metal-organic frameworks. Angew Chem Int Ed 44:4670–4679
5. Lee J, Farha OK, Roberts J et al (2009) Secondary building units, nets and bonding in the chemistry of metal-organic frameworks. Chem Soc Rev 38:1450–1459
6. Ma LQ, Abney C, Lin WB (2009) Enantioselective catalysis with homochiral metal-organic frameworks. Chem Soc Rev 38:1248–1256
7. Ma LQ, Falkowski JM, Abney C et al (2010) A series of isoreticular chiral metal-organic frameworks as a tunable platform for asymmetric catalysis. Nat Chem 2:838–846
8. Evans OR, Lin WB (2002) Crystal engineering of NLO materials based on metal-organic coordination networks. Acc Chem Res 35:511–522
9. Chen B, Xiang S, Qiang G (2010) Metal-organic frameworks with functional pores for recognition of small molecules. Acc Chem Res 43:1115–1124
10. Xie ZG, Ma LQ, Dekrafft KE et al (2010) Porous phosphorescent coordination polymers for oxygen sensing. J Am Chem Soc 132:922–923

11. Liu D, Lin WB (2011) Nanoscale metal-organic frameworks for biomedical imaging and drug delivery. Acc Chem Res 44:957–968
12. Wang KX, Chen JS (2011) Extended structures and physicochemical properties of uranyl–organic compounds. Acc Chem Res 44:531–540
13. Chen W, Yuan HM, Wang JY et al (2003) Synthesis, structure and photoelectronic effects of a uranium–zinc–organic coordination polymer containing infinite metal oxide sheets. J Am Chem Soc 125:9266–9267
14. Adelani PO, Albrecht-Schmitt TE (2010) Differential ion exchange in elliptical uranyl diphosphonate nanotubules. Angew Chem Int Ed 49:8909–8911
15. Wang S, Alekseev EV, Diwu J et al (2010) NDTB-1: a supertetrahedral cationic framework that removes TcO_4^- from solution. Angew Chem Int Ed 49:1057–1060
16. Wang S, Alekseev EV, Ling J et al (2010) Polarity and chirality in uranyl borates: insights into understanding the vitrification of nuclear waste and the development of nonlinear optical materials. Chem Mater 22:2155–2163
17. Alsobrook AN, Hauser BG, Hupp JT et al (2010) Cubic and rhombohedral heterobimetallic networks constructed from uranium, transition metals, and phosphonoacetate: new methods for constructing porous materials. Chem Commun 46:9167–9169
18. Liao ZL, Li GD, Wei X, Yu Y et al (2010) Construction of three-dimensional uranyl–organic frameworks with benzenetricarboxylate ligands. Eur J Inorg Chem 2010:3780–3788
19. Kim JY, Norquist AJ, O'Hare D (2003) $[(Th_2F_5)(NC_7H_5O_4)_2(H_2O)][NO_3]$: an actinide–organic open framework. J Am Chem Soc 125:12688–12689
20. Ok KM, Sung J, Hu G et al (2008) TOF-2: a large 1D channel thorium organic framework. J Am Chem Soc 130:3762–3763
21. Burns PC (2005) U^{6+} minerals and inorganic compounds: Insights into an expanded structural hierarchy of crystal structures. Can Mineral 43:1839–1894
22. Forbes TZ, McAlpin JG, Murphy R et al (2008) Metal-oxygen isopolyhedra assembled into fullerene topologies. Angew Chem Int Ed 47:2824–2827
23. Ling J, Qiu J, Sigmon GE et al (2010) Uranium pyrophosphate/methylenediphosphonate polyoxometalate cage clusters. J Am Chem Soc 132:13395–13402
24. Ling J, Wallace CM, Szymanowski JES et al (2010) Hybrid uranium–oxalate fullerene topology cage clusters. Angew Chem Int Ed 49:7271–7273
25. Sigmon GE, Burns PC (2011) Rapid self-assembly of uranyl polyhedra into crown clusters. J Am Chem Soc 133:9137–9139
26. Liao ZL, Li GD, Bi MH et al (2008) Preparation, structures, and photocatalytic properties of three new uranyl–organic assembly compounds. Inorg Chem 47:4844–4853
27. Zheng YZ, Tong ML, Chen XM (2005) Synthesis, structure and photoluminescent studies of two novel layered uranium coordination polymers constructed from UO(OH) polyhedra and pyridinedicarboxylates. Eur J Inorg Chem 4109–4117
28. Edelstein NM, Fuger J, Katz JJ (2006) The chemistry of the actinide and transactinide elements. Spring, The Netherlands
29. Bergerhoff G, Brown ID (1987) In: Allen FH et al. (ed) Crystallographic databases. International Union of Crystallography, Chester
30. Natrajan LS (2012) Developments in the photophysics and photochemistry of actinide ions and their coordination compounds. Coord Chem Rev 256:1583–1603
31. Baldovi JJ, Cardona-Serra S, Clemente JM et al (2013) Modeling the properties of uranium-based single ion magnets. Chem Sci 4:938–946
32. Mougel V, Chatelain L, Pécaut J et al (2012) Uranium and manganese assembled in a wheel-shaped nanoscale single-molecule magnet with high spin-reversal barrier. Nat Chem 4:1011–1017
33. Fox AR, Bart SC, Meyer K et al (2008) Towards uranium catalysts. Nature 455:341–349
34. Arnold PL (2011) Uranium-mediated activation of small molecules. Chem Commun 47:9005–9010

35. Yaghi OM, O'Keeffe M, Ockwig NW et al (2003) Reticular synthesis and the design of new materials. Nature 423:705–714
36. Kitagawa S, Kitaura R, Noro SI (2004) Functional porous coordination polymers. Angew Chem Int Ed 43:2334–2375
37. Férey G (2008) Hybrid porous solids: past, present, future. Chem Soc Rev 37:191–214
38. Zhou HC, Long JR, Yaghi OM (2012) Introduction to metal−organic frameworks. Chem Rev 112:673–674
39. Yu ZT, Liao ZL, Jiang YS et al (2005) Water-insoluble Ag-U-organic assemblies with photocatalytic activity. Chem Eur J 11:2642–2650
40. Polly LA, Jason BL, Dipti P (2009) Pentavalent uranyl complexes. Coord Chem Rev 253:1973–1978
41. Allen FH (2002) The Cambridge structural database: a quarter of a million crystal structures and rising. Acta Cryst B 58:380–388
42. Jiang YS, Yu ZT, Liao ZL et al (2006) Syntheses and photoluminescent properties of two uranyl-containing compounds with extended structures. Polyhedron 25:1359–1366
43. Walker SM, Halasyamani PS, Allen S et al (1999) From molecules to frameworks: variable dimensionality in the $UO_2(CH_3COO)_2 \cdot 2H_2O$/HF(aq)/piperazine system. Syntheses, structures, and characterization of zero-dimensional $(C_4N_2H_{12})UO_2F_4 \cdot 3H_2O$, one-dimensional $(C_4N_2H_{12})2U_2F_{12} \cdot H_2O$, two-dimensional $(C_4N_2H_{12})_2(U_2O_4F_5)_4 \cdot 11H_2O$, and three-dimensional $(C_4N_2H_{12})U_2O_4F_6$. J Am Chem Soc 121:10513–10521
44. Zhang Y, Livens FR, Collison D et al (2002) Synthesis and characterisation of uranyl substituted malonato complexes: part I. Structural diversity with dimethylmalonate and different counter-cations. Polyhedron 21:69–96
45. Bean AC, Ruf M, Albrecht-Schmitt TE (2001) Excision of uranium oxide chains and ribbons in the novel one-dimensional uranyl iodates $K_2[(UO_2)_3(IO_3)_4O_2]$ and $Ba[(UO_2)_2(IO_3)_2O_2](H_2O)$. Inorg Chem 40:3959–3963
46. Krivovichev SV, Kahlenberg V, Kaindl R et al (2005) Nanoscale tubules in uranyl selenates. Angew Chem Int Ed 44:1134–1136
47. Albrecht-Schmitt TE (2005) Actinide materials adopt curvature: nanotubules and nanospheres. Angew Chem Int Ed 44:4836–4838
48. Yaghi OM, Li GM, Li HL (1995) Selective binding and removal of guests in a microporous metal-organic framework. Nature 378:703–706
49. Kim J, Whang D, Lee JI (1993) Guest-dependent $[Cd(CN)_2]_n$ host structures of cadmium cyanide–alcohol clathrates: two new $[Cd(CN)_2]_n$ frameworks formed with Pr^nOH and Pr^iOH guests. J Chem Soc Chem Commun 1400–1402
50. Fujita M, Kwon YJ, Washzu S et al (1994) Preparation, clathration ability, and catalysis of a two-dimensional square network material composed of cadmium(II) and 4,4′-bipyridine. J Am Chem Soc 116:1151–1152
51. Rajan KS, Martell AE (1965) Equilibrium studies of uranyl complexes. III. Interaction of uranyl ion with citric acid. Inorg Chem 4:462–469
52. Bailey EH, Mosselmans JFW, Schofield PF (2005) Uranyl-citrate speciation in acidic aqueous solutions – an XAS study between 25 and 200 °C. Chem Geol 216:1–16
53. Clark DL, Conradson SD, Donohoe RJ et al (1999) Chemical speciation of the uranyl ion under highly alkaline conditions. Synthesis, structures, and oxo ligand exchange dynamics. Inorg Chem 38:1456–1466
54. Rowland CE, Cahill CL (2010) Capturing hydrolysis products in the solid state: effects of pH on uranyl squarates under ambient conditions. Inorg Chem 49:8668–8673
55. Jiang YS, Li GH, Tian Y et al (2006) Uranyl pyridine-dicarboxylate compounds with clustered water molecules. Inorg Chem Commun 9:595–598
56. Thuéry P, Masci B (2008) Uranyl-organic frameworks with 1,2,3,4-butanetetracarboxylate and 1,2,3,4-cyclobutanetetracarboxylate ligands. Cryst Growth Des 8:3430–3436

57. Masci B, Thuéry P (2005) Uranyl complexes with the pyridine-2,6-dicarboxylato ligand: new dinuclear species with μ-η2, η2-peroxide, μ2-hydroxide or μ2-methoxide bridges. Polyhedron 24:229–237
58. Lintvedt RL, Heeg MJ, Ahmad N et al (1982) Uranyl complexes of b-polyketonates. Crystal and molecular structure of a mononuclear uranyl 1,3,5-triketonate and a novel trinuclear uranyl 1,3,5-triketonate with a trigonal-planar bridging oxide. Inorg Chem 21:2350–2356
59. Szabo Z, Furo I, Csoregh I (2005) Combinatorial multinuclear NMR and X-ray diffraction studies of uranium(VI)-nucleotide complexes. J Am Chem Soc 127:15236–15247
60. Yu ZT, Li GH, Jiang YS et al (2003) A uranium-zinc-organic molecular compound containing planar tetranuclear uranyl units. Dalton Trans 2013:4219–4220
61. Borkowski LA, Cahill CL (2006) Crystal engineering with the uranyl cation II. Mixed aliphatic carboxylate/aromatic pyridyl coordination polymers: synthesis, crystal structures, and sensitized luminescence. Cryst Growth Des 6:2248–2259
62. Thuéry P, Nierlich M, Souley B et al (1999) Complexation of a hexameric uranium (VI) cluster by p-benzylcalix[7]arene. J Chem Soc Dalton Trans 1999:2589–2594
63. Ionut M, Natacha H, Thierry L et al (2011) Revisiting the uranyl-phthalate system: isolation and crystal structures of two types of uranyl-organic frameworks (UOF). Cryst Growth Des 11:1940–1947
64. Villa EM, Marr CJ, Jouffret LJ et al (2012) Systematic evolution from uranyl (VI) phosphites to uranium (IV) phosphates. Inorg Chem 51:6548–6558
65. Norquist AJ, Doran MB, O'Hare D (2005) The role of amine sulfates in hydrothermal uranium chemistry. Inorg Chem 44:3837–3843
66. Lee CS, Wang SL, Lii KH (2009) $Cs_2K(UO)2Si_4O_{12}$: a mixed-valence uranium(IV, V) silicate. J Am Chem Soc 131:15116–15117
67. Wang SA, Alekseev EV, Stritzinger JT et al (2010) Structure–property relationships in lithium, silver, and cesium uranyl borates. Chem Mater 22:5983–5991
68. Yu ZT, Liao ZL, Jiang YS et al (2004) Water–insoluble Ag–U–organic assemblies with photocatalytic activity. Chem Commun 2004:1814–1815
69. Mihalcea I, Henry N, Volkringer C et al (2012) Series of mixed uranyl–lanthanide (Ce, Nd) organic coordination polymers with aromatic polycarboxylates linkers. Cryst Growth Des 12:526–535
70. Olchowka J, Falaise C, Volkringer C et al (2013) Structural observations of heterometallic uranyl copper(II) carboxylates and their solid-state topotactic transformation upon dehydration. Chem Eur J 19:2012–2022
71. Wu HY, Yang WT, Sun ZM (2012) Tailor-made zinc uranyl diphosphonates from layered to framework structures. Cryst Growth Des 12:4669–4675
72. Yang WT, Wu HY, Wang RX et al (2012) From 1D chain to 3D framework uranyl diphosphonates: syntheses, crystal structures, and selective ion exchange. Inorg Chem 51:11458–11465
73. Diwu J, Albrecht-Schmitt TE (2012) Chiral uranium phosphonates constructed from achiral units with three-dimensional frameworks. Chem Commun 48:3827–3829
74. Yang WT, Tian T, Wu HY et al (2013) Syntheses and structures of a series of uranyl phosphonates and sulfonates: an insight into their correlations and discrepancies. Inorg Chem 52:2736–2743
75. Thuéry P (2013) Sulfonate complexes of actinide ions: structural diversity in uranyl complexes with 2-sulfobenzoate. Inorg Chem 52:435–447
76. Thuéry P (2012) Uranyl–lanthanide heterometallic assemblies with 1,2-ethanedisulfonate and cucurbit[6]uril ligands. Cryst Eng Comm 14:3363–3366
77. Tian T, Yang W, Pan QJ et al (2012) The first uranyl arsonates featuring heterometallic cation–cation interactions with U^{VI}═O–Zn^{II} bonding. Inorg Chem 51:11150–11154
78. Adelani PO, Jouffret LJ, Szymanowski JES et al (2012) Correlations and differences between uranium (VI) arsonates and phosphonates. Inorg Chem 51:12032–12040

79. Mal SS, Dickman MH, Kortz U (2008) Actinide polyoxometalates: incorporation of uranyl–peroxo in U-shaped 36-tungsto-8-phosphate. Chem Eur J 14:9851–9855
80. Miro P, Ling J, Qiu J et al (2012) Experimental and computational study of a new wheel-shaped $\{[W_5O_{21}]_3[(U^{VI}O_2)_2(\mu\text{-}O_2)]_3\}^{30-}$ polyoxometalate. Inorg Chem 51:8784–8790
81. Adelani PO, Albrecht-Schmitt TE (2011) Metal-controlled assembly of uranyl diphosphonates toward the design of functional uranyl nanotubules. Inorg Chem 50:12184–12191
82. Adelani PO, Albrecht-Schmitt TE (2009) Uranyl diphosphonates with pillared structures. Inorg Chem 48:2732–2734
83. Grohol D, Subramanian MA, Poojary DM et al (1996) Synthesis, crystal structures, and proton conductivity of two linear-chain uranyl phenylphosphonates. Inorg Chem 35:5264–5271
84. Yu ZT, Li GH, Jiang YS et al (2003) A uranium–zinc–organic molecular compound containing planar tetranuclear uranyl units. Dalton Trans 2003:4219–4220
85. Thuéry P (2011) Uranyl–organic assemblies with acetate-bearing phenyl- and cyclohexyl-based ligands. Cryst Growth Des 11:347–355
86. Knope KE, Cahill CL (2009) Homometallic uranium (VI) phosphonoacetates containing interlayer dipyridines. Inorg Chem 48:6845–6851
87. Kerr AT, Cahill CL (2011) Crystal engineering with the uranyl cation III. Mixed aliphatic dicarboxylate/aromatic dipyridyl coordination polymers: synthesis, structures, and speciation. Cryst Growth Des 11:5634–5641
88. Thuéry P (2009) Two novel uranyl–organic frameworks with cyclohexane-1,3-dicarboxylate ligands. Cryst Eng Comm 11:232–234
89. Borkowski LA, Cahill CL (2003) A novel uranium-containing coordination polymer: poly [dioxouranium (VI)-4-n-pentane-1, 5-dicarboxylato]. Inorg Chem 42:7041–7045
90. Lhoste J, Henry N, Roussel P et al (2011) An uranyl citrate coordination polymer with a 3D open-framework involving uranyl cation–cation interactions. Dalton Trans 40:2422–2424
91. Li H, Eddaoudi M, O'Keeffe M et al (1999) Design and synthesis of an exceptionally stable and highly porous metal-organic framework. Nature 402:276–279
92. Eddaoudi M, Kim J, Rossi N et al (2002) Systematic design of pore size and functionality in isoreticular MOFs and their application in methane storage. Science 295:469–472
93. Wu HY, Wang RX, Yang WT et al (2012) From 1D chain to 3D framework uranyl diphosphonates: syntheses, crystal structures, and selective ion exchange. Inorg Chem 51:3103–3107
94. Yang WT, Dang S, Wang H, Tian T et al (2013) Synthesis, structures, and properties of uranyl hybrids constructed by a variety of mono-and polycarboxylic acids. Inorg Chem 52:12394–12402
95. Immirzi A, Bombieri G, Degetto S et al (1975) The crystal and molecular structure of pyridine-2,6-dicarboxylatodioxouranium(VI) monohydrate. Sect B 31:1023–1028
96. Xie YR, Zhao H, Wang XS et al (2003) 2D chiral uranyl (VI) coordination polymers with second-harmonic generation response and ferroelectric properties. Eur J Inorg Chem 2003:3712–3715
97. Harrowfield JM, Lugan N, Shahverdizadeh GH et al (2006) Solid-state luminescence and π-stacking in crystalline uranyl dipicolinates. Eur J Inorg Chem 2006:389–396
98. Frisch M, Cahill CL (2006) Synthesis, structure and fluorescent studies of novel uranium coordination polymers in the pyridinedicarboxylic acid system. Dalton Trans 2006:4679–4690
99. Thuéry P (2009) Two uranyl–organic frameworks with pyridinecarboxylate ligands. A novel heterometallic uranyl–copper(II) complex with a cation–cation interaction. Inorg Chem Commun 12:800–803
100. Lis S, Glatty Z, Meinrath G et al (2010) Poly (isonicotinic acid N-oxide–isonicotinate-N-oxide-chloro-uranyl): the interpenetrating grids created by coordination and hydrogen bonds. J Chem Crystallogr 40:646–649

101. Cantos PM, Frisch M, Cahill CL (2010) Synthesis, structure and fluorescence properties of a uranyl-2,5-pyridinedicarboxylic acid coordination polymer: the missing member of the UO22 + -2, n-pyridinedicarboxylic series. Inorg Chem Commun 13:1036–1039
102. Masci B, Thuéry P (2008) Pyrazinetetracarboxylic acid as an assembler ligand in uranyl–organic frameworks. Cryst Growth Des 8:1689–1696
103. Masci B, Thuéry P (2008) Hydrothermal synthesis of uranyl–organic frameworks with pyrazine-2,3-dicarboxylate linkers. Cryst Eng Comm 10:1082–1087
104. Frisch M, Cahill CL (2005) Syntheses, structures and fluorescent properties of two novel coordination polymers in the U–Cu–H_3pdc system. Dalton Trans 2005:1518–1523
105. Thuéry PA (2010) Lanthanide ion-decorated uranyl–organic two-dimensional assembly with all-cis 1,2,3,4,5,6-cyclohexanehexacarboxylic acid. Cryst Growth Des 10:2061–2063
106. Kim JY, Norquist AJ, O'Hare D (2003) Incorporation of uranium(VI) into metal-organic framework solids, $[UO_2(C_4H_4O_4)] \cdot H_2O$, $[UO_2F(C_5H_6O_4)] \cdot 2H_2O$, and $[(UO_2)_{1.5}(C_8H_4O_4)_2]_2[(CH_3)_2NCOH_2] \cdot H_2O$. Dalton Trans 2003:2813–2814
107. Borkowski LA, Cahill CL (2004) A novel uranium-containing coordination polymer: poly [[aqua (benzene-1, 3, 5-tricarboxylato) dioxouranium (VI)] monohydrate]. Acta Crystallogr Sect E 60:m198–m200
108. Go YB, Wang X, Jacobson AJ (2007) (6,3)-Honeycomb Structures of Uranium (VI) Benzenedicarboxylate Derivatives: The Use of Noncovalent Interactions to Prevent Interpenetration. Inorg Chem 46:6594–6600
109. Borkowski LA, Cahill CL (2005) A novel uranium-containing coordination polymer: poly [dioxouranium (VI)-4-n-pentane-1, 5-dicarboxylato]. Acta Crystallogr Sect E 61:m816–m817
110. Thuéry P (2007) Reaction of uranyl nitrate with carboxylic diacids under hydrothermal conditions. Crystal structure of complexes with l (+)-tartaric and oxalic acids. Polyhedron 26:101–106
111. Thuéry P (2006) Uranyl ion complexation by citric and tricarballylic acids: hydrothermal synthesis and structure of two- and three-dimensional uranium–organic frameworks. Chem Commun 2006:853–855
112. Thuéry P (2007) Uranyl ion complexation by citric and citramalic acids in the presence of diamines. Inorg Chem 46:2307–2315
113. Thuéry P (2008) Novel two-dimensional uranyl–organic assemblages in the citrate and D(−)-citramalate families. Cryst Eng Comm 10:79–85
114. Liang L, Cai Y, Weng NS et al (2009) A novel uranyl complex $UO_2(tci)(C_3H_5N_2) \cdot H_2O$: synthesis, crystal structure and characterization. Inorg Chem Commun 12:86–88
115. Thuéry P (2008) One-dimensional uranium-organic framework in catena-poly[[di-μ2-hydroxido-bis[dioxouranium(VI)]]-di-μ2–2-pyridylacetato-χ3O, N:O';χ3O:O', N]. Acta Crystallogr Sect C 64:m50–m52
116. Thuéry P (2009) Uranyl–organic bilayer assemblies with flexible aromatic di-, tri- and tetracarboxylic acids. Cryst Eng Comm 11:1081–1088
117. Andrews MB, Cahill CL (2013) Uranyl bearing hybrid materials: synthesis, speciation, and solid-state structures. Chem Rev 113:1121–1136
118. Leciejewicz J, Alcock N, Kemp TJ (1995) Coordination chemistry, vol 82. Springer, Berlin, Heidelberg, pp 43–84
119. Mihalcea I, Volkringer C, Henry N et al (2012) Series of mixed uranyl–lanthanide (Ce, Nd) organic coordination polymers with aromatic polycarboxylates linkers. Inorg Chem 51:9610–9618
120. Severance RC, Vaughn SA, Smith MD et al (2011) Structures and luminescent properties of new uranyl-based hybrid materials. Solid State Sci 13:1344–1353
121. Thuéry P (2011) Uranyl ion complexation by aliphatic dicarboxylic acids in the presence of cucurbiturils as additional ligands or structure-directing agents. Cryst Growth Des 11:2606–2620

122. Loiseau T, Mihalcea I, Henry N et al (2014) The crystal chemistry of uranium carboxylates. Coord Chem Rev 266–267:69–109
123. Andrews MB, Cahill CL (2012) Utilizing hydrogen bonds and halogen–halogen interactions in the design of uranyl hybrid materials. Dalton Trans 41:3911–3914
124. Deifel NP, Cahill CL (2011) Combining coordination and supramolecular chemistry for the formation of uranyl-organic hybrid materials. Chem Commun 47:6114–6116
125. Masci B, Gabrielli M, Mortera S et al (2002) Hydrogen bonded supramolecular assemblies from uranyl ion complexes of tetrahomodioxacalix[4]arenes with various counterions. Polyhedron 21:1125–1131
126. Cantos PM, Pope SJA, Cahill CL (2013) An exploration of homo- and heterometallic UO_2^{2+} hybrid materials containing chelidamic acid: synthesis, structure, and luminescence studies. Cryst Eng Commun 15:9039–9051
127. Wu HY, Ma YQ, Zhang XW et al (2013) Syntheses, structures and luminescent properties of two organic templated uranyl phosphonates. Inorg Chem Commun 34:55–57
128. Thuéry P (2013) 2,2′-Bipyridine and 1,10-phenanthroline as coligands or structure-directing agents in uranyl–organic assemblies with polycarboxylic acids. Eur J Inorg Chem 2013:4563–4573
129. Jouffret LJ, Wylie EM, Burns PC (2013) Amine templating effect absent in uranyl sulfates synthesized with 1,4-n-butyldiamine. J Solid State Chem 197:160–165
130. Norquist AJ, Doran MB, Thomas PM et al (2003) Controlled structural variations in templated uranium sulfates. Inorg Chem 42:5949–5953
131. Krivovichev SV, Gurzhiy VV, Tananaev IG et al (2009) Full view uranyl selenates with organic templates: principles of structure and characteristics of self-organization. Russ J Gen Chem 79:2723–2730
132. Davis ME, Lobo RF (1992) Zeolite and molecular sieve synthesis. Chem Mater 4:756–768
133. de Lill DT, Bozzuto DJ, Cahill CL (2005) Templated metal-organic frameworks: synthesis, structures, thermal properties and solid-state transformation of two novel calcium–adipate frameworks. Dalton Trans 2005:2111–2115
134. de Lill DT, Gunning NS, Cahill CL (2005) Toward templated metal-organic frameworks: synthesis, structures, thermal properties, and luminescence of three novel lanthanide-adipate frameworks. Inorg Chem 44:258–266
135. Burrows AD, Cassar K, Friend RMW et al (2005) Solvent hydrolysis and templating effects in the synthesis of metal-organic frameworks. Cryst Eng Comm 7:548–550
136. Liu YL, Kravtsov VC, Eddaoudi M (2008) Template-directed assembly of zeolite-like metal-organic frameworks (ZMOFs): A usf-ZMOF with an unprecedented zeolite topology. Angew Chem Int Ed 47:8446–8449
137. Halper SR, Do L, Stork JR et al (2006) Topological control in heterometallic metal-organic frameworks by anion templating and metalloligand design. J Am Chem Soc 128:15255–15268
138. Mihalcea I, Henry N, Loiseau T (2014) Crystal chemistry of uranyl carboxylate coordination networks obtained in the presence of organic amine molecules. Eur J Inorg Chem 8:1322–1332
139. Paula M, Cantos, Christopher L et al (2014) A family of UO_2^{2+}–5-Nitro-1,3-dicarboxylate hybrid materials: structural variation as a function of pH and structure directing species. Cryst Growth Des 14:3044–3053
140. Thuéry P (2013) Uranyl–3d block metal ion heterometallic carboxylate complexes including additional chelating nitrogen donors. Cryst Eng Comm 15:6533–6545
141. Thuéry P, Rivière E (2013) Uranyl–copper(II) heterometallic oxalate complexes: coordination polymers and frameworks. Dalton Trans 42:10551–10558
142. Kemp DS, Petrakis KS (1981) Synthesis and conformational analysis of *cis*,*cis*-1,3,5-trimethylcyclohexane-1,3,5-tricarboxylic acid. J Org Chem 46:5140–5143
143. Thuéry PA (2014) Highly adjustable coordination system: nanotubular and molecular cage species in uranyl ion complexes with Kemp's Triacid. Cryst Growth Des 14:901–904

144. Wang CM, Liao CH, Kao HM et al (2005) Hydrothermal synthesis and characterization of $(UO_2)_2F_8(H_2O)_2Zn_2(4,4'\text{-bpy})_2 \cdot (4,4'\text{-bpy})$, a mixed-metal uranyl aquofluoride with a pillared layer structure. Inorg Chem 44:6294–6298
145. Cahill CL, de Lill DT, Frisch M et al (2007) Homo- and heterometallic coordination polymers from the f elements. Cryst Eng Comm 9:15–26
146. Pierre T (2014) Increasing complexity in the uranyl Ion–Kemp's triacid system: from one- and two-dimensional polymers to uranyl–copper(II) dodeca- and hexadecanuclear species. Cryst Growth Des 14:2665–2676
147. Xia Y, Wang KX, Chen JS (2010) Synthesis, structure characterization and photocatalytic properties of two new uranyl naphthalene-dicarboxylate coordination polymer compounds. Inorg Chem Commun 13:1542–1547
148. Thuéry PA (2009) Nanosized uranyl camphorate cage and its use as a building unit in a metal-organic framework. Cryst Growth Des 9:4592–4594
149. Wang X, Simard M, Wuest JD (1994) Molecular tectonics. Three-dimensional organic networks with zeolitic properties. J Am Chem Soc 116:12119–12120
150. Ghadiri MR, Granja JR, Miligan RA (1993) Self-assembling organic nanotubes based on a cyclic peptide architecture. Nature 366:324–327
151. Copp SB, Subramanian S, Zaworotko MJ (1992) Supramolecular chemistry of manganese complex $[Mn(CO)_3(.mu.3\text{-}OH)]_4$: assembly of a cubic hydrogen-bonded diamondoid network with 1,2-diaminoethane. J Am Chem Soc 114:8719–8720
152. Yaghi OM, Richardson DA, Li G et al (1994) Open-framework solids with diamond-like structures prepared from clusters and metal-organic building blocks. Mater Res Soc Symp Proc 371:15–19
153. Yaghi OM, Li G (1995) Mutually interpenetrating sheets and channels in the extended structure of [Cu(4,4′-bpy)Cl]. Angew Chem Int Ed 34:207–209
154. Hoskins BF, Robson R et al (1990) Design and construction of a new class of scaffolding-like materials comprising infinite polymeric frameworks of 3D-linked molecular rods. A reappraisal of the zinc cyanide and cadmium cyanide structures and the synthesis and structure of the diamond-related frameworks $[N(CH_3)_4][Cu^{I}Zn^{II}(CN)_4]$ and CuI [4,4′,4″,4‴-tetracyanotetraphenylmethane]$BF_4.xC_6H_5NO_2$. J Am Chem Soc 112:1546–1554
155. Ferey G (2001) Microporous solids: from organically templated inorganic skeletons to hybrid frameworks. . .ecumenism in chemistry. Chem Mater 13:3084–3098
156. Hernandez-Molina M, lorenzo-Luis PA, Ruiz-Perez C (2001) Contrasting crystal supramolecularity for $[Fe(phen)_3]I_8$ and $[Mn(phen)_3]I_8$: complementary orthogonality and complementary helicity. Cryst Eng Commun 16:1–8
157. Rao CNR, Natarajan S, Vaidhyanathan R (2004) Metal carboxylates with open architectures. Angew Chem Int Ed 43:1466–1496
158. Runde W, Brodnax LF, Goff G et al (2009) Directed synthesis of crystalline plutonium(III) and (IV) oxalates: accessing redox-controlled separations in acidic solutions. Inorg Chem 48:5967–5972
159. Favas MC, Kepert DL, Patrick JM et al (1983) Structure and stereochemistry in f-block complexes of high co-ordination number. Part 5. Ten-co-ordination: the crystal structures of tetrapotassium tetraoxalatouranate(IV) tetrahydrate(orthorhombic and triclinic phases), bicapped square antiprismatic and sphenocoronal stereochemistries. J Chem Soc Dalton Trans 1983:571–581
160. Akhtar MN, Smith AJ (1975) The crystal structure of tetrapotassium tetraoxalatothorium (IV) tetrahydrate, $K_4Th(C_2O_4)_4.4H_2O$. Acta Crystallogr B31:1361–1366
161. Imaz I, Bravic G, Sutter JP (2005) Structural and zeolitic features of a 3D heterometallic porous architecture constructed from a $\{M(oxalate)_4\}^{4-}$ building unit. Chem Commun 2005:993–995
162. Clavier N, Hingant N, Rivenet M et al (2010) X-Ray diffraction and μ-Raman investigation of the monoclinic-orthorhombic phase transition in $Th_{1-x}U_x(C_2O_4)_2 \cdot 2H_2O$ solid solutions. Inorg Chem 49:1921–1931

163. Yeon J, Smith MK, Sefat AS et al (2013) Crystal growth, structural characterization, and magnetic properties of new uranium(IV) containing mixed metal oxalates: $Na_2U_2M(C_2O_4)_6(H_2O)_4$ (M=Mn^{2+}, Fe^{2+}, Co^{2+}, and Zn^{2+}). Inorg Chem 52:2199–2207
164. Thuéry P (2011) Solid state structure of thorium(IV) complexes with common aminopolycarboxylate ligands. Inorg Chem 50:1898–1904
165. Chapelet-Arab B, Nowogrocki G, Abraham F et al (2005) U(IV)/Ln(III) unexpected mixed site in polymetallic oxalato complexes. Part I. Substitution of Ln(III) for U(IV) from the new oxalate $(NH_4)_2U_2(C_2O_4)_5 \cdot 0.7H_2O$. J Solid State Chem 178:3046–3054
166. Andreev G, Budantseva FA (2011) Moist, polymeric structure of oxalato-bridged complexes of tetravalent actinides Th, U, Np and Pu. Inorg Chem 50:11481–11486
167. Bean AC, Garcia E, Scott BL et al (2004) Structural variability in neptunium(V) oxalate compounds: synthesis and structural characterization of $Na_2NpO_2(C_2O_4)OH \cdot H_2O$. Inorg Chem 43:6145–6147
168. Sokolov MN, Gushchin AL, Kovalenko KA et al (2007) Triangular oxalate clusters $[W_3(\mu_3\text{-}S)(\mu_2\text{-}S_2)_3(C_2O_4)_3]^{2-}$ as building blocks for coordination polymers and nanosized complexes. Inorg Chem 46:2115–2123
169. Andreev GB, Budantseva NA, Tananaev IG et al (2008) Organically templated Np (IV) coordination polymer with in situ formed oxalate anion (ImidazoleH)$[Np(C_2O_4)(CH_3SO_3)_3(H_2O)_2]$. Inorg Chem Commun 11:802–804
170. Chackraburtty DM (1963) X-ray evidence of plutonium (III) oxalate decahydrate. Acta Crystallogr 16:834
171. Choppin GR, Thakur P, Mathur JN (2006) Complexation thermodynamics and structural aspects of actinide–aminopolycarboxylates. Coord Chem Rev 250:936–947
172. Cartwright AJ, May CC, Worsfold PJ et al (2007) Characterisation of thorium–ethylenediaminetetraacetic acid and thorium–nitrilotriacetic acid species by electrospray ionisation-mass spectrometry. Anal Chim Acta 590:125–131
173. Bonin L, Guillaumont D, Jeanson A et al (2009) Thermodynamics and structure of actinide (IV) complexes with nitrilotriacetic acid. Inorg Chem 48:3943–3953
174. Jeanson A, Dahou S, Guillaumont D et al (2009) A comparative study of actinide complexation in three ligand systems with increasing complexity. J Phys Conf Ser 190:012185
175. Xia Y, Felmy AR, Rao L et al (2003) Thermodynamic model for the solubility of ThO_2(am) in the aqueous Na^+-H^+-OH^--NO_3^--H_2O-EDTA system. Radiochim Acta 91:751–760
176. Frisch M, Cahill CL (2008) Thorium (IV) coordination polymers in the pyridine and pyrazinedicarboxylic acid systems. Cryst Growth Des 8:2921–2928
177. Ok KM, O'Hare D (2008) Synthesis, structure, and characterization of a new thorium–organic framework material, $Th_3F_5[(C_{10}H_{14})(CH_2CO_2)_2]_3(NO_3)$. Dalton Trans 2008:5560–5562
178. Adelani PO, Albrecht-Schmitt TE (2010) Comparison of thorium (IV) and uranium (VI) carboxyphosphonates. Inorg Chem 49:5701–5705
179. Grohol D, Clearfield A (1997) Solid-state water-catalyzed transformation at room temperature of a nonluminescent linear-chain uranyl phenylphosphonate into a luminescent one. J Am Chem Soc 119:4662–4668
180. Martin KJ, Squarttrito PJ, Clearfield A (1989) The crystal and molecular structure of zinc phenylphosphonate. Inorg Chim Acta 155:7–9
181. Zhang Y, Clearfield A (1992) Synthesis, crystal structures, and coordination intercalation behavior of two copper phosphonates. Inorg Chem 31:2821–2826
182. Clearfield A (1996) Recent advances in metal phosphonate chemistry. Curr Opin Solid State Mater Sci 1:268–278
183. Clearfield A (2002) Recent advances in metal phosphonate chemistry II. Curr Opin Solid State Mater Sci 6:495–506
184. Clearfield A (1998) Organically pillared micro-and mesoporous materials. Chem Mater 10:2801–2810

185. Clearfield A (2008) Unconventional metal organic frameworks: porous cross-linked phosphonates. Dalton Trans 44:6089–6102
186. Clearfield A (1990) Layered phosphates, phosphites and phosphonates of groups 4 and 14 metals. Comments Inorg Chem 10:89–128
187. Chen Z, Zhou Y, Weng L et al (2007) Zeolite-like zinc phosphonocarboxylate framework and its transformation into two- and three-dimensional structures. Chem Asian J 2:1549–1554
188. Maeda K (2004) Metal phosphonate open-framework materials. Microporous Mesoporous Mater 73:47–55
189. Zhang XM (2004) A microporous zinc phosphonocarboxylate with a zeolite ABW framework via the trialkyl phosphonocarboxylate route: in situ synthesis and characterization of Na $[Zn(O_3PC_2H_4CO_2)] \cdot H_2O$. Eur J Inorg Chem 3:544–548
190. Zhang XM, Hou JJ, Zhang WX et al (2006) Two mixed-valence vanadium(III, IV) phosphonoacetates with 16-ring channels: H2(DABCO)[VIVO(H2O)VIII(OH)(O3PCH2CO2)2] · 2.5H2O and H2(PIP)[VIVO(H2O)VIII(OH)(O3PCH2CO2)2] · 2.5H2O. Inorg Chem 45:8120–8125
191. Chen Z, Zhou Y, Weng L et al (2008) Mixed-solvothermal syntheses and structures of six new zinc phosphonocarboxylates with zeolite-type and pillar-layered frameworks. Cryst Growth Des 8:4045–4053
192. Stock N, Karaghiosoff K, Bein TZ (2004) Synthesis and structure of the phosphonocarboxylic acid $H_2O_3PCH_2$-NC_5H_9-$COOH \cdot 2H_2O$ and the manganese phosphonocarboxylate $Mn[O_3PCH_2$-$N(H)C_5H_9$-$COO]$. Anorg Allg Chem 630:2535–2540
193. Stock N, Frey SA, Stucky GD et al (2000) Synthesis and characterization of two manganese phosphonocarboxylates: $Mn_3(O_3PCH_2COO)_2$ and $Mn_3(O_3PCH_2CH_2COO)_2$. J Chem Soc Dalton Trans 2000:4292–4296
194. Alsobrook AN, Zhan W, Albrecht-Schmitt TE (2008) Use of bifunctional phosphonates for the preparation of heterobimetallic 5f−3d systems. Inorg Chem 47:5177–5183
195. Knope KE, Cahill CL (2008) Structural variation within homometallic uranium (VI) carboxyphosphonates: in situ ligand synthesis, directed assembly, metal–ligand coordination and hydrogen bonding. Inorg Chem 47:7660–7672
196. Alsobrook AN, Albrecht-Schmitt TE (2009) Phosphonoacetate as a ligand for constructing layered and framework alkali metal uranyl compounds. Inorg Chem 48:11079–11084
197. Knope KE, Cahill CL (2010) Synthesis and characterization of 1-, 2-, and 3-dimensional bimetallic UO_2^{2+}/Zn^{2+} phosphonoacetates. Eur J Inorg Chem 8:1177–1185
198. Nash KL (1997) f-Element complexation by diphosphonate ligands. J Alloy Cmpd 249:33–40
199. Jensen MP, Beitz JV, Rogers RD et al (2000) Thermodynamics and hydration of the europium complexes of a nitrogen heterocycle methane-1,1-diphosphonic acid. J Chem Soc Dalton Trans 18:3058–3064
200. Padmini R, Ramanath P, Srinivasan N (2010) Synthesis, structure, and solid-state transformation studies of phosphonoacetate based hybrid compounds of uranium and thorium. Inorg Chem 49:7927–7934

Struct Bond (2015) 163: 297–368
DOI: 10.1007/430_2014_167

Published online: 25 October 2014

Nanostructured and/or Nanoscale Lanthanide Metal-Organic Frameworks

Zhonghao Zhang and Zhiping Zheng

Abstract The research on metal-organic framework (MOF) compounds has developed rapidly, stimulated by not only their aesthetically pleasing structures but also diverse chemical and materials applications. The use of lanthanide-containing building blocks adds several features that are unique, fundamentally interesting, and practically significant to the construction of MOFs, due largely to the traits originated from the unique *f*-electronic configuration of these elements; these include primarily ionic metal-ligand interactions and flexible coordination geometry, line-like luminescence, and interesting magnetic properties associated with the exclusively high-spin configuration. *Nanostructured* Ln-MOFs featuring nanosized pores and channels offer even more attractive applications since when compared with their sub-nanosized analogs, a greater variety of guest species may be accommodated, either for storage or separation of guests of energy and environmental significance, sensing, or catalysis. On the other hand, reducing the physical size of MOFs to *nanoscale* imparts properties distinctly different from those of their bulk counterparts. Nanoparticles of Ln-MOFs have been shown to possess unique luminescence and magnetic properties for applications in optical and magnetic imaging as well as for drug delivery. This chapter provides an up-to-date review of the work on both nanostructured and nanoscale Ln-MOFs and ends with some personal perspectives regarding what future directions the research is heading toward.

Keywords Lanthanide clusters · Nanoporous MOFs · Nanoscale LnMOFs · Optical and magnetic imaging · Sensing by luminescence

Z. Zhang and Z. Zheng (✉)
Department of Chemistry and Biochemistry, University of Arizona, Tucson, AZ 85721, USA
e-mail: zhiping@email.arizona.edu

Contents

1 Introduction

Metal-organic framework (MOF) compounds are a class of coordination polymers synthesized from metal ions or metal clusters and organic bridging ligands and generally characterized by their porous structures. The availability of a wide variety of the metal and organic units and the ability to judiciously modify these building blocks allow for the construction of MOFs with pores whose size, shape, volume, and reactivity can be tailored for particular applications, including catalysis [1–3], gas storage [4, 5], sensing [6, 7], non-linear optical materials [8], and separation [9, 10].

Lanthanides are arguably one of the most interesting groups of metal elements, primarily due to their unique *f*-electronic configurations in addition to their large size. With a few exceptions, ions of these elements are trivalent, and the *f* electrons are shielded by 5*s* and 5*p* electrons, a direct consequence of which is the minimal overlap of the *f* orbitals with those of the ligands in lanthanide coordination compounds. A corollary is that the metal-ligand interactions are primarily ionic and any perturbation to the *f* orbitals is minimal or vibronic broadening of *f*–*f* transitions since the ligand interactions are negligibly small. As such, luminescence originated from *f*–*f* transitions is line-like with its full-width at half-maximum (FWHM) being only a few tenths of that typical of purely organic or transition metal-based luminophores. Furthermore, due to the minimal ligand-field effects, lanthanide complexes are exclusively of high-spin configurations, giving rise to interesting and tunable magnetic properties thanks to the availability of complexes with variable number of unpaired *f* electrons (from 0 in La^{3+} to 7 in Gd^{3+}). The interesting luminescence and magnetic properties are key to the potentially significant optical and magnetic applications. It is thus not surprising that the research of lanthanide-containing MOFs (LnMOFs) has attracted much recent interest and in fact developed rapidly into a subarea of its own right within the ever-expanding framework of MOF research. Synthetically, lanthanide ions are unique in that they require high-coordination numbers and are prone to hydrolysis with cluster-type,

and often nanoscopic in size, polynuclear complexes being usual products that are useful for the construction of MOFs. Combined with the use of selective organic bridging ligands, pores of nanosized dimensions can also be anticipated, allowing for the accommodation of large guest species. We refer in this chapter this type of LnMOFs as *nanostructured*, characterized either by the nanoscopic building blocks or their nanosized pores/channels.

The other class of LnMOFs to be discussed herein, related to the *nanostructured* LnMOFs by the term "nano," is characterized by their physical size in the nanoscale regardless of the dimension of the building blocks at the molecular level. They are termed *nanoscale* LnMOFs in our discussion and we note that the properties and potential applications of nanoscale materials are uniquely dependent on their size and morphology.

With the recognition of certain degree of overlap in discussion contents, these two types of LnMOFs will be treated separately, within each class, the discussions are organized into synthetic methodology, structural description, and properties and potential applications. A brief summary of the current research on nanostructured and nanoscale LnMOFs will be provided toward the end, together with some future research directions from the authors' personal perspectives.

2 Nanostructured LnMOFs

The unique coordination behaviors of lanthanide ions, namely high-coordination requirement due to their large physical size and the largely unrestricted coordination geometry as a result of the primarily ionic lanthanide-ligand interactions, position these metal ions particularly well for the assembly of complexes featuring well-defined cluster-type polymetallic core motifs. Such polynuclear complexes are not only aesthetically pleasing structure-wise, but also exhibit interesting materials properties [11–14]. A number of such cluster core motifs have also been recognized as formal building units in LnMOFs. In other words, these cluster motifs, often nanoscopic in size, can be viewed formally as secondary building units (SBUs) for the construction of MOFs despite the fact that they are not actually pre-fabricated and used subsequently as precursors to MOFs. Most of these cluster motifs are characterized by the coordination or linking between lanthanide ions by oxo and hydroxo groups within the core, but other types of lanthanide-containing clusters, those featuring the presence of non-lanthanide elements (both main group elements and transition metals) within the cluster core, have also been discovered. Together with the use of various organic bridging ligands, these SBUs are organized into a great variety of *nanostructured* LnMOFs. A related but distinct application of lanthanide oxo/hydroxo clusters is the use of such cluster complexes as ligands for the coordination of transition metal ions, resulting in MOFs with two kinds of metal-based nodes, lanthanide clusters and transition metal ions [15].

When it comes to applications of MOFs in recognition, storage, and separation of guest species of interest, as well as in catalysis, a key consideration is the pore or

channel structure, both size and functional features [7, 16, 17]. Seeking porous frameworks capable of accommodating large guests as in the original quest for synthetic zeolites has been one of the major goals in MOF research. Simulation and experimental strategies have been developed to control the size and morphology of channels/pores in transitional-metal-based MOFs, [18–22], but similar work has not been done with LnMOFs. In this chapter, our discussion also covers this distinct type of *nanostructured* LnMOFs with nanosized pores or channels. We will focus our attention on the use of specialized organic bridging ligands with the recognition that there is a certain degree of overlap with the use of the aforementioned nanostructured cluster-based SBUs.

2.1 Nanostructured LnMOFs Built from Lanthanide-Containing Clusters

2.1.1 Lanthanide Oxo/Hydroxo Clusters as SBUs

Past two decades have witnessed the development of a new area of lanthanide coordination chemistry with which a large number of polynuclear lanthanide complexes featuring structurally and compositionally well-defined cluster-type core motifs have been prepared. Nanoscopic clusters with nuclearity up to 60 have appeared in the literature. These include $\{Ln_6\}$ [23], $\{Ln_7\}$ [24], $\{Ln_8\}$ [25], $\{Ln_9\}$ [26], $\{Ln_{10}\}$ [27], $\{Ln_{12}\}$ [28], $\{Ln_{13}\}$ [29], $\{Ln_{14}\}$ [30], $\{Ln_{15}\}$ [31, 32], $\{Ln_{22}\}$ [33], $\{Ln_{24}\}$ [34], $\{Ln_{26}\}$ [35], $\{Ln_{36}\}$ [36], $\{Ln_{38}\}$ [37], $\{Ln_{48}\}$ [37] and $\{Ln_{60}\}$ [38]. The pleasing molecular structure and interesting properties of these discrete cluster complexes stimulated the synthetic efforts for MOF construction whereby the cluster motifs function formally as SBUs even though they are generally not produced in a stand-alone precursor for subsequent incorporation into the MOF, but rather an integrated component of a self-assembled framework structure.

The first LnMOFs in which lanthanide clusters have been recognized as SBUs are reported independently by Gao [39] and Zheng [40], and their respective coworkers. The MOFs feature distorted cubes of $[Ln_4(\mu_3\text{-}OH)_4]^{8+}$ bridged by glutamate or aspartate ligands whose skeletal and side carboxylate groups each serve to bridge two lanthanide atoms on the same cluster cube with the ligand linking two different cubes together, resulting in the extended framework structure (Fig. 1).

Following these pioneering work, a great variety of MOFs constructed with the formal use of larger but related lanthanide oxo/hydroxo cluster units have been obtained, the most extensive of which are based on hexanuclear clusters that actually come in different forms. The most frequently encountered hexanuclear cluster motif, formulated as $[Ln_6(\mu_6\text{-}O)(\mu_3\text{-}OH)_8]^{8+}$, features six lanthanide metal atoms centered around an interstitial μ_6-O group and occupying the vertices of a perfect octahedron with each of its triangular faces capped by a triply bridging

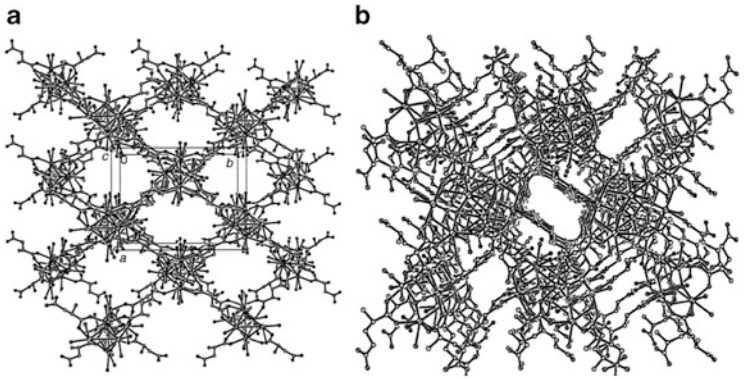

Fig. 1 (**a**) The porous frameworks of (**a**) $\{[Dy_4(\mu_3\text{-}OH)_4(asp)_3(H_2O)_8](ClO_4)_2{\cdot}10H_2O\}_n$; reproduced from [39] by permission of John Wiley & Sons Ltd. and (**b**) $\{[Er_4(\mu_3\text{-}OH)_4(Glu)_3(H_2O)_8](ClO_4)_5{\cdot}6H_2O\}_n$. Reprinted with the permission from [40]. Copyright 2001 American Chemical Society

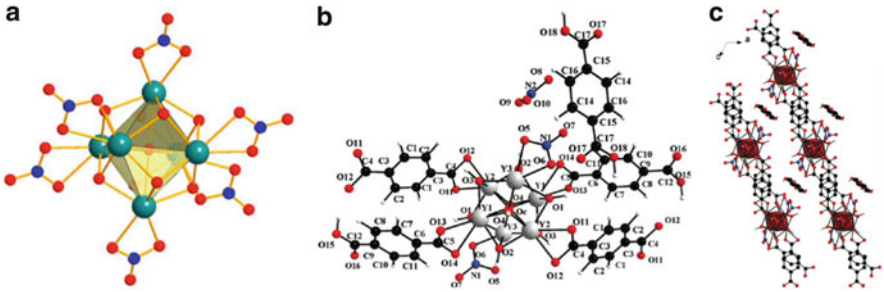

Fig. 2 (**a**) The structure of $[Ln_6(\mu_6\text{-}O)(\mu_3\text{-}OH)_8]^{8+}$ cluster with nitrate anions coordinated to Ln^{3+} (*Color codes*: O *red*; N *blue*; Ln *green*); (**b**) Coordination mode between bdc ligands and $[Ln_6(\mu_6\text{-}O)(\mu_3\text{-}OH)_8]^{8+}$ clusters; (**c**) Structure of $\{[Ln_6O(OH)_8](NO_3)_2(bdc)(Hbdc)_2{\cdot}2NO_3{\cdot}H_2bdc\}_\infty$ 1D coordination chains constructed from $[Ln_6(\mu_6\text{-}O)(\mu_3\text{-}OH)_8]^{8+}$ cluster. Reprinted with the permission from [41, 42]. Copyright 2005, 2011 American Chemical Society

μ_3-OH group (Fig. 2a). In a rare demonstration of using a pre-fabricated cluster precursor for MOF construction, Roisnel and coworkers reported the cationic cluster complex $[Ln_6(\mu_6\text{-}O)(\mu_3\text{-}OH)_8]^{8+}$ [41], and its use in making MOFs with organic ligands under hydrothermal conditions. Different from the common practice of subjecting lanthanide ions to hydrolysis in the presence of bridging organic ligands to assemble MOFs under thermodynamic control, the pre-formed SBU precursor renders feasible the production of a variety of MOFs depending on the bridging ligands used. For example, with the use of 1,4-benzenedicarboxylic acid (bdc), a one-dimensional (1D) coordination polymer with the formula $\{[Ln_6O(OH)_8](NO_3)_2(bdc)(Hbdc)_2{\cdot}2NO_3{\cdot}H_2bdc\}_\infty$ was obtained (Fig. 2b, c) [42]. Different lanthanide ions can be doped into the backbone of the polymeric chain, and intra-chain energy transfer between the lanthanide ion centers was investigated [43].

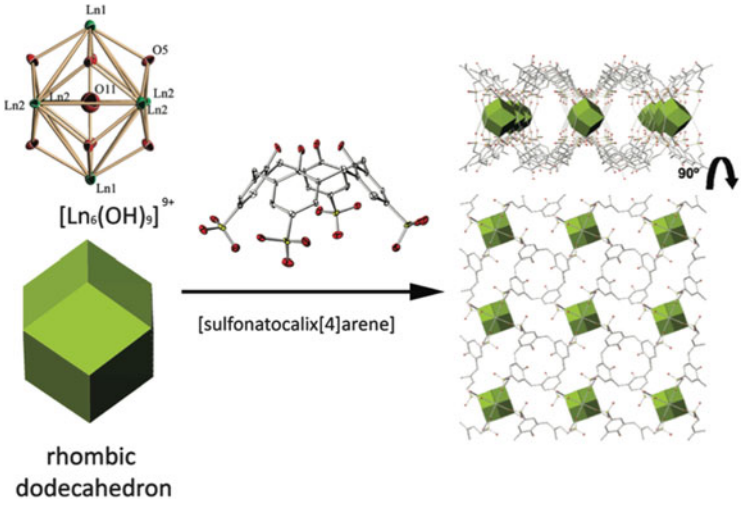

Fig. 3 The structures of $[Ln_6(OH)_9]^{9+}$ cluster core and the *p*-sulfonatocalix[4]arene ligand. (*Left*) *Side view* and *top view* of the 2D coordination layers. Reprinted with the permission from [44]. Copyright 2010 American Chemical Society

Using *p*-sulfonatocalix[4]arene as bridging ligand, Monge and coworkers succeeded in incorporating the same SBU into a 2D coordination layer within which each $[Ln_6(OH)(\mu_3\text{-}OH)_8]^{9+}$ SBU is connected to nine neighboring clusters via coordination of one of the sulfonate O atoms (Fig. 3) [44]. We note that the cluster SBU was formulated as $[Ln_6(OH)(\mu_3\text{-}OH)_8]^{9+}$; its central O atom was assigned to be from a hydroxo rather than the commonly accepted oxo group on the basis of unequal Ln–O distances.

A cluster motif closely related to the aforementioned $[Ln_6(\mu_6\text{-}O)(\mu_3\text{-}OH)_8]^{8+}$ is $[Ln_6(\mu_3\text{-}O)_2(\mu_3\text{-}OH)_6]$ with two minor differences being the absence of a central O atom and the replacement of two triply bridging hydroxo groups for two oxo groups on two of the eight triangular faces (Fig. 4a). Under hydrothermal conditions, a 3D MOF was obtained by Rocha and coworkers in which $[Pr_6(\mu_3\text{-}O)_2(\mu_3\text{-}OH)_6]$ units are connected by hydrated Pr^{3+} ions to form a 1D polymer chains (Fig. 4b) that are further linked by pyridinedicarboxylate (pydc) ligands to afford a 3D framework structure (Fig. 4c) [45]. It is interesting to note that in order to maintain the electrical neutrality of the compound, formulated as $\{Pr_{3.25}O(OH)_3(pydc)_3\}$ based on crystallographic and elemental analysis, mixed valency of the Pr centers is inferred, and hence the reported formula of $\{Pr^{III}{}_2Pr^{IV}{}_{1.25}O(OH)_3(pydc)_3\}$.

Quite distinct from the three hexanuclear cluster SBUs of octahedral symmetry is a motif of $[Ln_6(O\text{–}H\text{–}O)]^{15+}$ found in the MOF structure of $[Ln_9(NA)_{12}(O\text{–}H\text{–}O)]\cdot 6H_2O$ (Ln = Gd, Eu; NA = 2-hydroxynicotinate generated in situ from the hydrothermal decomposition of originally added 2-mercaptonicotinic acid) by Wu and coworkers [46]. In the present MOFs, the

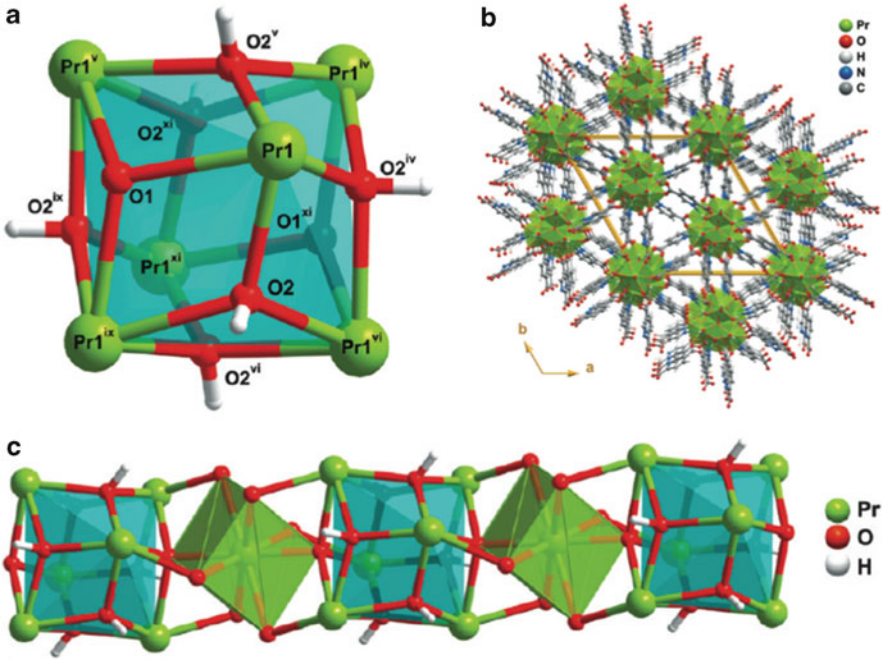

Fig. 4 (**a**) Structure of the nano scale $[Pr_6(\mu_3\text{-}O)_2(\mu_3\text{-}OH)_6]$ cluster; (**b**) Neighboring $[Pr_6(\mu_3\text{-}O)_2(\mu_3\text{-}OH)_6]$ clusters are connected together by $[Pr(H_2O)_6]$ cations to form a 1D chain; (**c**) 1D chains are further connected by pydc ligands to form a 3-D MOF. Reprinted with the permission from [45]. Copyright 2009 American Chemical Society

six lanthanide atoms are organized into a trigonal antiprism with one $[O–H–O]^{3-}$ anion situated within the body of the antiprism with each of the two O atoms capping three lanthanide atoms from inside (Fig. 5a). The O atoms of both the carboxylate and hydroxyl groups of the NA ligands are responsible for metal coordination on the exterior of the antiprism (Fig. 5b), and such individual hexanuclear cluster units are linked through the coordination of a single lanthanide ion via coordination with the NA ligands (Fig. 5c) to six identical neighbors to afford ultimately the 3D framework structure observed (Fig. 5d).

There are a couple of reports of MOFs for which heptanuclear cluster motifs of the formula $[Ln_7(\mu_3\text{-}OH)_8]^{13+}$ consisting of two $[Ln_4(\mu_3\text{-}OH)_4]^{8+}$ cubanes joined at a common metal vertex (Fig. 6a) are recognized as SBUs. This motif was first introduced into MOF as an SBU by Gao and coworkers when the controlled hydrolysis of lanthanide ions was performed in the presence of hydrolysis-limiting 1,4-naphthalenedicarboxylate ligand (1,4-NDA) [47]. The $[Ln_7(\mu_3\text{-}OH)_8]^{13+}$ units are capped by acetate ligands and bridging 1,4-NDA ligands (Fig. 6b, c) into a 3D MOF structure of the formula $[Ln_7(\mu_3\text{-}OH)_8(1,4\text{-}NDA)_6(OH)_{0.5}(Ac)_{0.5}(H_2O)_7]\cdot 4H_2O$ (Fig. 6d).

The same heptanuclear SBU is found in the MOF reported by Yang and coworkers [48], but the cluster motif is somewhat distorted into a trigonal prism

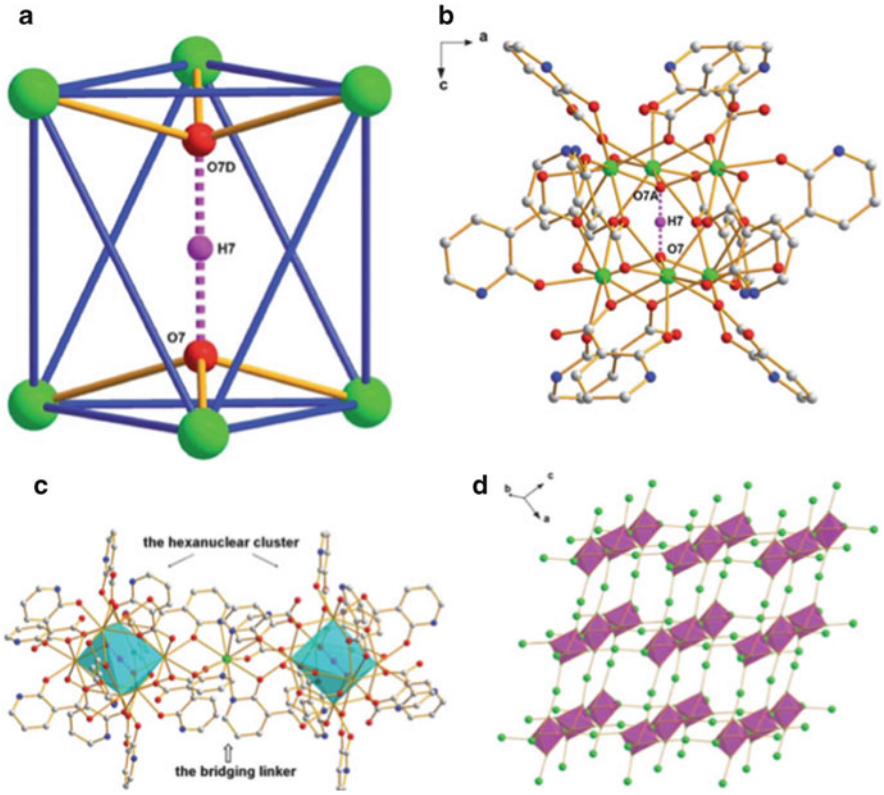

Fig. 5 (**a**) Structure of the trigonal antiprism cluster core of $[Ln_6(O–H–O)]^{15+}$; (**b**) Coordination environment between HNA ligands and $[Ln_6(O–H–O)]^{15+}$ cluster core; (**c**) The bridging mode of two neighboring $[Ln_6(O–H–O)]^{15+}$ cluster by a Ln^{3+} ion; (**d**) The backbone structure of the 3D cubic MOF constructed by the hexanuclear cluster. Reproduced from [46] by permission of The Royal Society of Chemistry

with a lanthanide atom joining the two lanthanide triangle (Fig. 7a, b). These MOFs, with the general formula $[Ln_7(\mu_3\text{-}OH)_8L_9(H_2O)_6]\cdot 4ClO_4\cdot 3HL\cdot nH_2O$ [Ln = Y, La, Gd, Yb, $n = 6$; Ln = Dy, Er, $n = 4$], were assembled under hydrothermal conditions starting with lanthanide oxide and 4-pyridin-4-ylbenzoic acid (HL) in the presence of $HClO_4$. Each cluster SBU is coordinated by the pyridinyl and carboxylate groups, extending into 2D coordination layers (Fig. 7c, e). Residing in between adjacent such layers are a different type of layers composed of hydrogen-bonded free HL ligands and water molecules (Fig. 7f). These two different types of layers are engaged in extensive hydrogen-bonding and π–π interactions, leading to a 3D framework structure (Fig. 7d).

The largest lanthanide oxo/hydroxo cluster motif so far recognized in the construction of *nanostructured* LnMOFs is the drum-shaped $\{Ln_{48}\}$ unit, first reported by Xu and coworkers [49]. Specifically, an MOF compound formulated as $K_2[Ho_{48}(IN)_{46}(\mu_3\text{-}OH)_{84}(\mu_4\text{-}OH)_4(\mu_5\text{-}O)_2(OAc)_4(H_2O)_{14}(CO_3)Br_2]\cdot 2HIN\cdot 20H_2O$

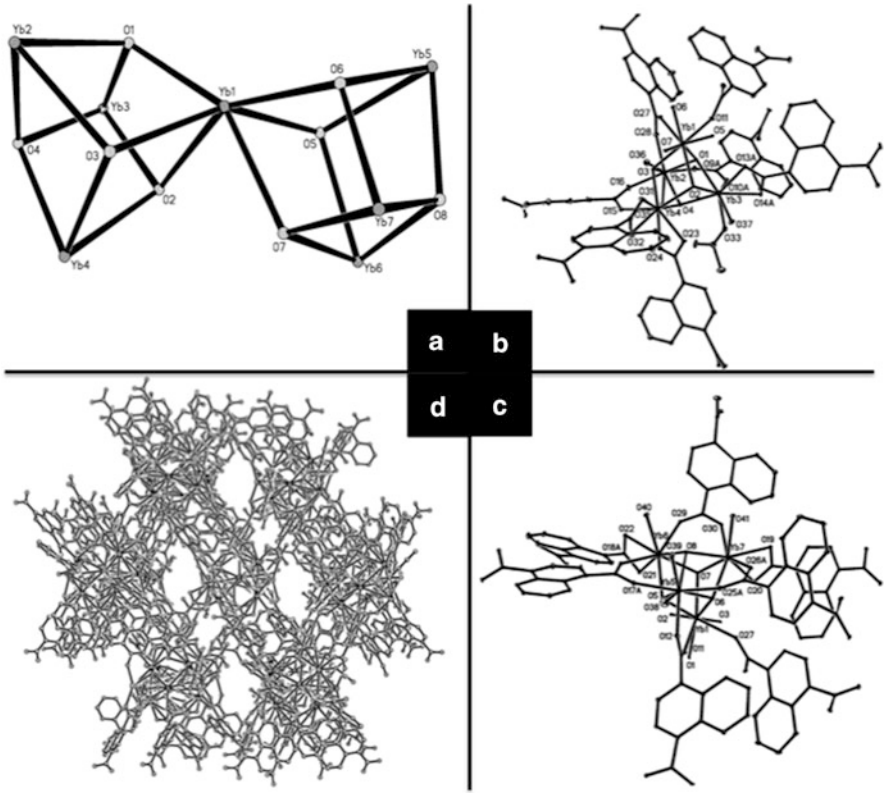

Fig. 6 (**a**) Structure of $[Ln_7(\mu_3\text{-}OH)_8]^{13+}$ cluster core (with Yb as an example); (**b**) The coordination environment around one of the two connected cubane (Yb1–Yb4); (**c**) The coordination environment around the other cubane (Yb1, Yb5–Yb7); (**d**) Structure of the 3D MOF $[Ln_7(\mu_3\text{-}OH)_8(1,4\text{-}NDA)_6(OH)_{0.5}(Ac)_{0.5}(H_2O)_7]\cdot 4H_2O$ cluster constructed from $[Ln_7(\mu_3\text{-}OH)_8]^{13+}$ clusters. Reprinted with the permission from [47]. Copyright 2004 American Chemical Society

(HIN = isonicotinic acid) was synthesized under hydrothermal conditions starting with Ho_2O_3, $Mn(OAc)_2\cdot 4H_2O$, HIN, KBr, and formic acid. There exist three types of basic cluster motifs in the $\{Ho_{48}\}$ unit, namely 12 $[Ho_4(\mu_3\text{-}OH)_4]^{8+}$ cubanes, 2 $[Ho_5(\mu_3\text{-}OH)_4(\mu_5\text{-}O)]^{9+}$ square pyramids, and 4 $[Ho_5(\mu_3\text{-}OH)_4(\mu_4\text{-}OH)]^{10+}$ square pyramids. The cubanes, organized into two identical six-membered wheels with the cubane units joined by vertex sharing, sandwich a wheel of the two kinds of square pyramids formed by sharing two opposite basal metal atoms of each of the pyramids, leading the complex yet beautiful core structure of symmetry (Fig. 8a). Inside the $\{Ho_{48}\}$ cluster, there are one carbonate anion and two Br^- acting as template, defining the formula of the $\{Ho_{48}\}$ cluster core as $[Ho_{48}(\mu_3\text{-}OH)_{84}(\mu_4\text{-}OH)_4(\mu_5\text{-}O)_2(CO_3)Br_2]^{48+}$. These $\{Ho_{48}\}$ clusters were further linked by IN ligands to form a 2-D coordination layer (Fig. 8b).

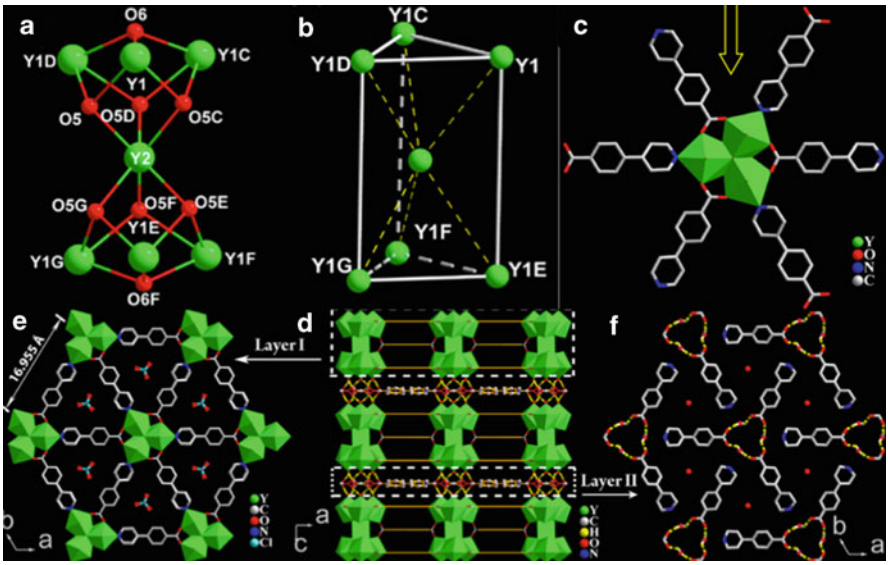

Fig. 7 (**a**) Structure of the trigonal prism $[Ln_7(\mu_3\text{-}OH)_8]^{13+}$ cluster core (with Y as an example); (**b**) A view of the trigonal prism backbone with only lanthanide ions displayed; (**c**) Coordination around the $[Ln_7(\mu_3\text{-}OH)_8]^{13+}$ cluster core; (**d**) Structure of the stacked layers; (**e**) 2D coordination layers constructed from $[Ln_7(\mu_3\text{-}OH)_8]^{13+}$ cluster; (**f**) The "glue" layer composed of free ligand and water molecules. Reprinted with the permission from [48]. Copyright 2013 American Chemical Society

Hong and coworkers reported a similar $\{Er_{48}\}$ cluster compound shortly after Xu's work [50]. The *nanostructured* MOF hydrothermally obtained starting with NaN_3, nicotinic acid (HNA), $NaNO_3$, and $ErCl_3{\cdot}6H_2O$ is formulated as $[Er_{48}(NA)_{44}(OH)_{90}(N_3)(H_2O)_{24}Cl_2(NO_3)]_6Cl_{35}{\cdot}H_2O$. Beside the use of a different lanthanide ion, the cluster unit also differs in the nature of the templating anions: In the present cluster, one nitrate anion instead of carbonate sits at the center of the cluster core, while two chloride ions take the place of the bromide ions in Xu's Ho_{48} cluster complex (Fig. 8c). Individual nanostructured $\{Er_{48}\}$ units are further linked by isonicotinate ligand and N_3^- anion, giving rise to a 2D coordination layer (Fig. 8d).

2.1.2 Coordination of Transition Metal Ions by Lanthanide Cluster Complexes Leading to Nanostructured LnMOFs

For convenience of discussion of the use of hexanuclear oxo/hydroxo lanthanide cluster SBUs for MOF construction in the previous section, we include the independent examples by Rocha [45] and Wu [46]. The construction of their MOFs is different from the others discussed above as bridging of the individual cluster units is not entirely by organic ligands. Rather, a single metal ion in between the

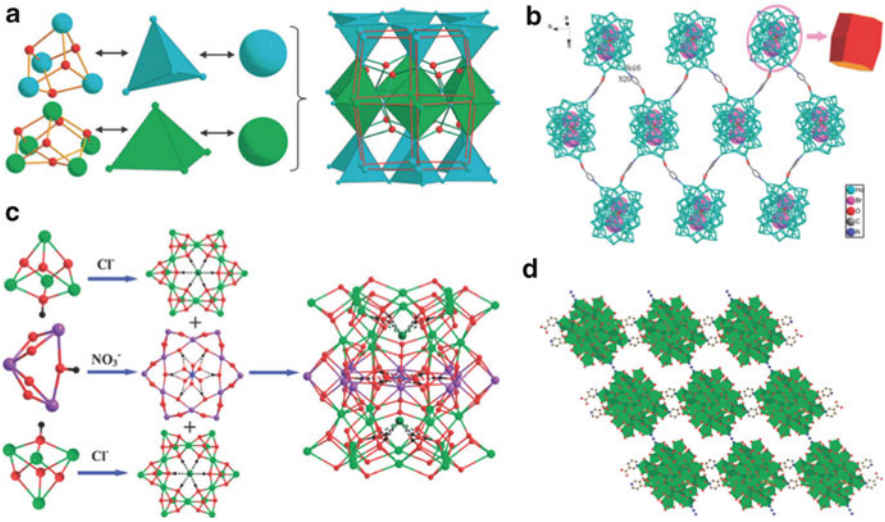

Fig. 8 (**a**) Structure of the $\{Ho_{48}\}$ cluster core (with ligands, water molecules, and template anions omitted); (**b**) The coordination mode between IN ligands and $\{Ho_{48}\}$ clusters to form a 2D coordination layer; (**c**) Structure of the $\{Er_{48}\}$ cluster core with two Cl^- and one NO_3^- as template anions; (**d**) $\{Er_{48}\}$ clusters connected by NA ligands and N_3^- to form a 2D coordination layer. Reproduced from [49, 50] by permission of The Royal Society of Chemistry

cluster-based SBUs is key to the assembly of the cluster arrays, achieved by utilizing the cluster complex as ligand for the coordination of the single metal ion. We note that this particular mode of dimensional extension, namely the use of a cluster complex as ligand for the coordination of a secondary metal ion, is actually more prevalent when the secondary metal ions are of transition metal elements. Also commonly used are ligands bearing both hard Lewis basic O atom(s) as in carboxylate and softer *N* atom as in a pyridyl moiety. The preference for O-based ligands by hard Lewis acidic lanthanide ions and the preference of a majority of transition metal ions for N-based ligands allow for creative ligand design and use, for example in creating lanthanide complexes using mostly the O-based coordinating functions and leaving N-based moiety for further coordination with transition metal ions. As such, a great variety of MOFs characterized by nanoscopic lanthanide cluster SBUs linked by transition metal complex units can be anticipated.

One early example of coordination polymers consisting of transition metal ion-linked lanthanide clusters is $\{[(DMF)_{16}Yb_6(\mu_6\text{-}O)(\mu_3\text{-}OH)_8(\mu\text{-}NC)Pd(\mu\text{-}CN)(CN)_2]^{6+}\}_\infty$ reported by Shore and coworkers [51]. The octahedral $[Yb_6(\mu_6\text{-}O)(\mu_3\text{-}OH)_8]^{8+}$ clusters are bridged linearly by the two *trans*-disposed CN ligands of $[Pd(CN)_4]^{2-}$ to form a 1D polymeric array.

The $[Ln_6(\mu_6\text{-}O)(\mu_3\text{-}OH)_8]^{8+}$ SBU is also present in the 3D MOF $[Ln_2Cu(\mu_6\text{-}O)_{1/6}(\mu_3\text{-}OH)_{2/3}(\mu_3\text{-}OH)_2(hpzc)_2(H_2O)_2]\cdot 2H_2O$ [Ln = Dy, Ho, Er; Hhpzc = 3-hydroxy-pyrazine-2-carboxylic acid derived in situ from the hydrothermal decomposition of pyrazine-2,3-dicarboxylic acid or H_2pzdc (Fig. 9d)] reported by

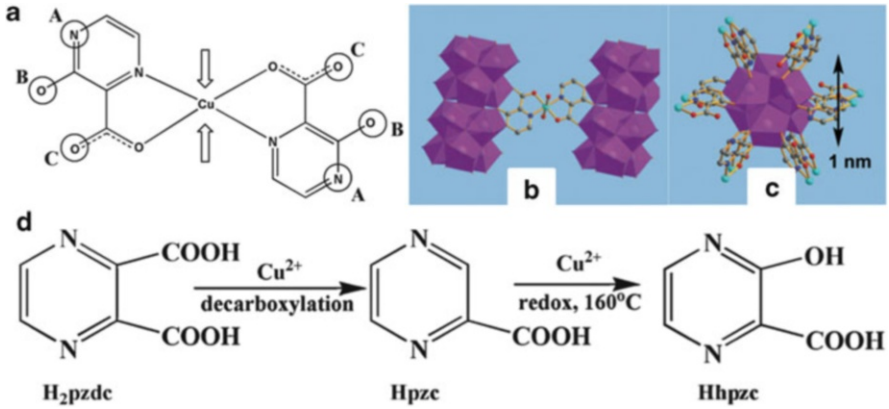

Fig. 9 (**a**) Schematic presentation of $[Cu(hpzc)_2(H_2O)_2]^{3-}$ (with water molecules abbreviated) ligand; (**b**) Presentation of neighboring lanthanide nanorod clusters bridged by $[Cu(hpzc)_2(H_2O)_2]^{3-}$ ligand; (**c**) *Top view* of lanthanide nanorod clusters with $[Cu(hpzc)_2(H_2O)_2]^{3-}$ ligands attached. The diameter of the nanorod cluster is about 1 nm; (**d**) Proposed mechanism for the formation of Hhpcz ligand from H_2pzdc ligand. Reproduced from [52] by permission of The Royal Society of Chemistry

Yao and coworkers [52]. In the extended structure, the linker is $[Cu(hpzc)_2(H_2O)_2]^{3-}$ (Fig. 20 a, b), a anionic complex of Cu^{2+} with two equatorial hpzc ligands and two axial aqua ligands. With the use of only one pyrazine *N* atom and one carboxylate O atom of each hpzc ligands, its remaining pyrazine N (**A**), hydroxyl O (**B**), and carboxylate O (**C**) atoms are poised for the coordination on the surface of the $[Ln_6(\mu_6\text{-}O)(\mu_3\text{-}OH)_8]^{8+}$ cluster (Fig. 9c). Alternatively the lanthanide cluster-transition metal combination can be viewed as assembled from the coordination of Cu^{2+} by the cluster-stabilizing hpzc ligands using one of the free pyrazine *N* atom and an unused carboxylate O atom, and the cluster complex is the ligand for the secondary (with respect to the primary coordination of lanthanide ions) complexation of Cu^{2+}. The $[Ln_6(\mu_6\text{-}O)(\mu_3\text{-}OH)_8]^{8+}$ cluster SBUs are bridged together by the **A**, **B**, **C** coordination groups from one side of the $[Cu(hpzc)_2(H_2O)_2]^{3-}$ ligands to form cluster nanorods with a diameter of about 1 nm (Fig. 9c). These nanorods are further bridged together by the $[Cu(hpzc)_2(H_2O)_2]^{3-}$ ligands to form a 3-D metal-organic framework (Fig. 9b). The MOF product was, however, rather serendipitous, made possible only because of the in situ formation of Hhpzc ligand that is critically important for the coordination of both the lanthanide cluster unit and Cu^{2+}.

A number of complexes of larger lanthanide oxo/hydroxo clusters have also been identified in nanostructured LnMOFs. For example, Fang and Yang reported two 3D MOFs formulated as $[Ln_5(\mu_3\text{-}OH)_4(\mu\text{-}H_2O)Cu_8I_8L_{11}]\cdot H_2O$ (L = 4-pyridine-4-yl-benzoate; Ln = Dy, Eu) wherein two different kinds of SBUs, one of $\{Ln_{10}\}$ cluster and the other of $\{Cu_{16}\}$ cluster, are clearly identified (Fig. 10) [53]. The $\{Ln_{10}\}$ cluster unit consists of ten Ln^{3+} ions connected by eight μ_3-OH groups

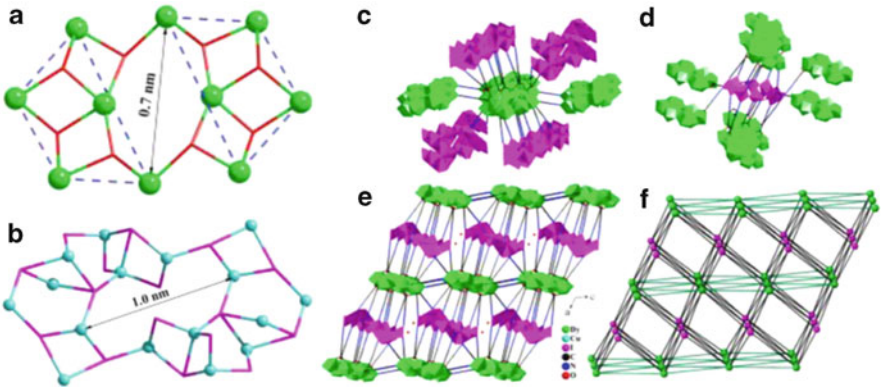

Fig. 10 The structure of $\{Ln_{10}\}$ (**a**) and $\{Cu_{16}\}$ (**b**) clusters backbone; (**c**) The coordination environment around $\{Ln_{10}\}$ clusters (*green*); (**d**) The coordination environment around $\{Cu_{16}\}$ clusters (*pink*); (**e**) Structure of the 3D MOF $[Ln_5(\mu_3\text{-}OH)_4(\mu\text{-}H_2O)Cu_8I_8L_{11}]\cdot H_2O$; (**f**) A representation of the MOF structure with $\{Ln_{10}\}$ clusters and $\{Cu_{16}\}$ clusters displayed as *green* and *pink spheres* respectively. Reprinted with the permission from [53]. Copyright 2014 American Chemical Society

(Fig. 10a), while the $\{Cu_{16}\}$ cluster building block is composed of 16 Cu^{2+} ions bridged by 16 I^- anions (Fig. 10b). These cluster SBUs are linked by the L ligands to form the 3D porous MOF structure (Fig. 10c–f).

In a series of 3*d*–4*f* coordination polymers of the general formula $[Ln_{14}(\mu_6\text{-}O)(\mu_3\text{-}OH)_{20}(IN)_{22}Cu_6C_{14}(H_2O)_8]\cdot 6H_2O$ [Ln = Y, Gd, Dy; IN = isonicotinate] reported by Yang and coworkers [54], tetradecanuclear lanthanide oxo/hydroxo cluster units have been identified. The cluster motif can be conveniently viewed as two basal face-sharing nonanuclear clusters or a hexanuclear cluster unit being sandwiched by two square pyramidal pentanuclear clusters by vertex sharing at the two opposite metal vertices of the octahedral cluster (Fig. 11a). The lanthanide cluster-capping isonicotinate ligands only use the carboxylate group for lanthanide coordination; the pyridyl *N* atoms remain free and available for the coordination of Cu^{2+} ions in a bimetallic unit of Cu_2Cl_2 (Fig. 11b), leading to the formation of the heterometallic MOF structure (Fig. 11c).

Yang and his coworkers have also reported two additional series of nanostructured heterometallic MOFs, formulated respectively as $[Ln_6(\mu_3\text{-}O)_2](IN)_{18}[Cu_8(\mu_4\text{-}I)_2(\mu_2\text{-}I)_3]\cdot H_3O$ (IN = isonicotinate; Ln = Y, Nd, Dy, Gd, Sm, Eu, Tb) [55] and $[La_6(\mu_3\text{-}O)_2(ox)_3L_{12}Cu_{11}(\mu_3\text{-}X)_6(\mu_2\text{-}X)_3]\cdot 8H_2O$ (X = Br/Cl; L = 4-pyridine-4-yl-benzonate; ox = oxalate) [56]. The IN-containing MOFs are constructed by stacking two types of 2D coordination layers, those of lanthanide and copper ions. Within the 2D lanthanide coordination layer, lanthanide ions are organized into triangular units of $[Ln_3(\mu_3\text{-}O)]^{7+}$ a centrally located triply bridging μ_3-O atom and three surrounding lanthanide ions occupying the three vertices of a triangle. Each edge of the triangle is bridged by two IN carboxylate groups, and six such triangles are linked together to form the hexagonal wheel structure of a $\{Ln_{18}\}$ cluster. By edge-sharing, these $\{Ln_{18}\}$ SBUs are further linked to form a 2D

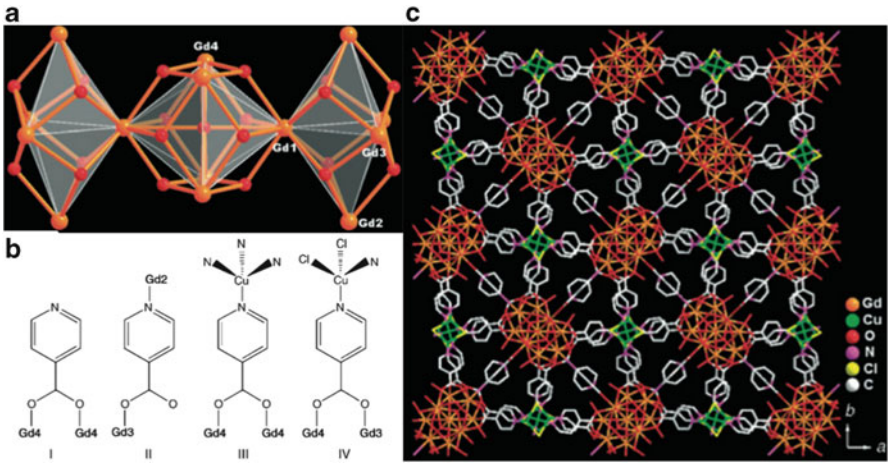

Fig. 11 (**a**) The structure of $[Ln_{14}(\mu_6\text{-}O)(\mu_3\text{-}OH)_{20}]^{20+}$ cluster core; (**b**) Coordination mode of isonicotinate ligands; (**c**) Structure of the MOF (Ln = Gd in all cases). Reproduced from [54] by permission of John Wiley & Sons Ltd.

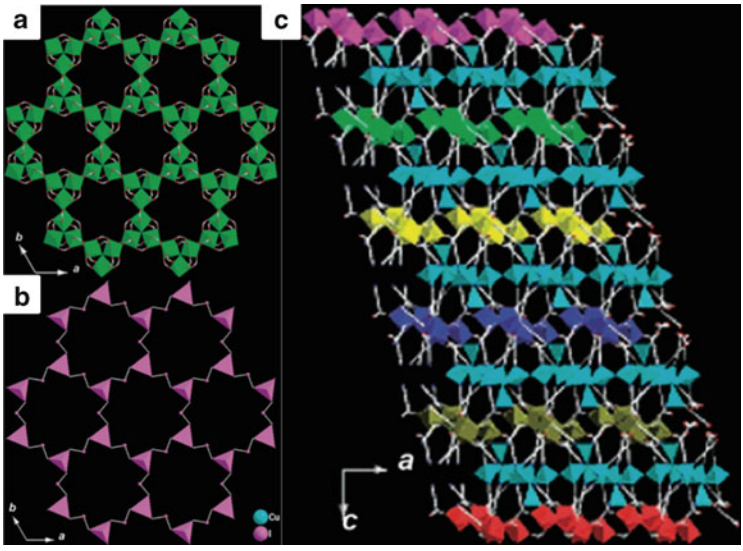

Fig. 12 The structure of the (**a**) lanthanide and (**b**) copper 2D coordination layer in MOF $[Ln_6(\mu_3\text{-}O)_2](IN)_{18}[Cu_8(\mu_4\text{-}I)_2(\mu_2\text{-}I)_3]\cdot H_3O$; (C) Lanthanide 2D coordination layer and copper 2D coordination layer stack together to form a 3D framework (Copper layers are displayed in *cyan* while other colored layers are lanthanide layers). Reproduced from [55] by permission of John Wiley & Sons Ltd.

coordination layers (Fig. 12a). In the copper coordination layer, the $\{Cu_4(\mu_4\text{-}I)\}$ building units, comprising 4 Cu atoms centered around a $\mu_4\text{-}I^-$, are bridged by μ_2-I to produce an extended coordination layer (Fig. 12b). These two different types of 2D coordination layers are stacked alternatively by connection through the IN ligands to afford the 3D MOF structure observed (Fig. 12c).

In $[La_6(\mu_3\text{-}O)_2(ox)_3L_{12}Cu_{11}(\mu_3\text{-}X)_6(\mu_2\text{-}X)_3]\cdot 8H_2O$, a similar $[La_3(\mu_3\text{-}O)]^{7+}$ cluster motif serves as the basic unit to be organized into a 2D coordination layers in a similar manner as mentioned above. The lanthanide 2D coordination layers are further connected to copper coordination layers by L ligands to give the observed 3D framework structure.

Under otherwise identical conditions but with the addition of sodium acetate and the replacement of lanthanum oxalate and CuX_2 for Ln_2O_3 (Ln = Pr, Nd, Sm, Eu) and CuX, respectively, a new series of MOF with the formula $[Ln_4(OAc)_3(H_2O)_4L_9][Cu(\mu_3\text{-}I)]@[C_{10}(\mu_3\text{-}I)(\mu_4\text{-}I)_6(\mu_5\text{-}I)_3]\cdot 7H_2O$ (Ln= Pr/Nd/Sm/Eu; OAc= acetate) rather than the above $[La_6(\mu_3\text{-}O)_2(ox)_3L_{12}Cu_{11}(\mu_3\text{-}X)_6(\mu_2\text{-}X)_3]\cdot 8H_2O$ was obtained [56] in which the 2D lanthanide coordination layers are constructed by edge-sharing wheel-like $\{Ln_{24}\}$ cluster SBUs. In the 2D lanthanide coordination layers, the basic units are triangular units of $[Ln_4(OAc)_3]^{9+}$ in which one Ln^{3+} sits in the center with the other three occupying the vertices of the triangle with three acetate ligands bridging them together. Six triangles are linked together to form the $\{Ln_{24}\}$ cluster wheel, and by sharing edges, a 2D coordination layer is resulted (Fig. 13a). Such layers are further connected with the 2D copper coordination layers (Fig. 13b) through the L ligands to produce the MOF structure as shown in Fig. 13c.

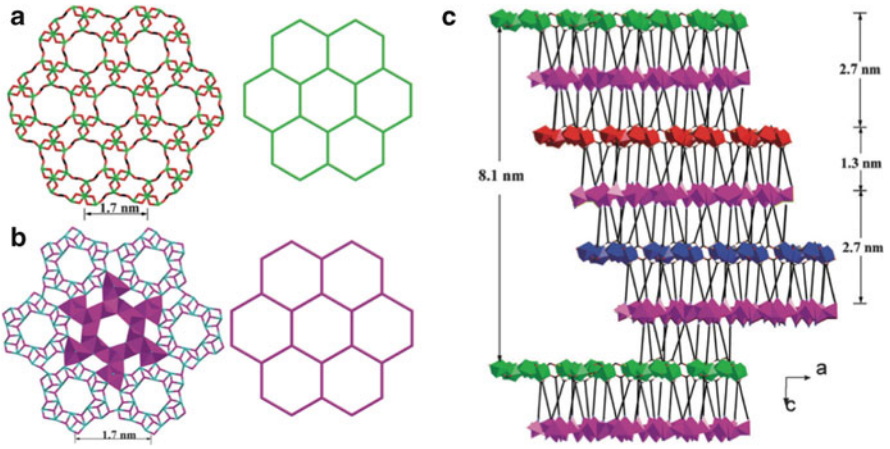

Fig. 13 Structure of (**a**) the lanthanide 2D coordination layers and (**b**) the copper 2D coordination layers in $[Ln_4(OAc)_3(H_2O)_4L_9][Cu(\mu_3\text{-}I)]@[C_{10}(\mu_3\text{-}I)(\mu_4\text{-}I)_6(\mu_5\text{-}I)_3]\cdot 7H_2O$ MOFs; (**c**) The structure of the 3D frameworks constructed by stacking lanthanide and copper 2D coordination layers. Reproduced from [56] by permission of John Wiley & Sons Ltd.

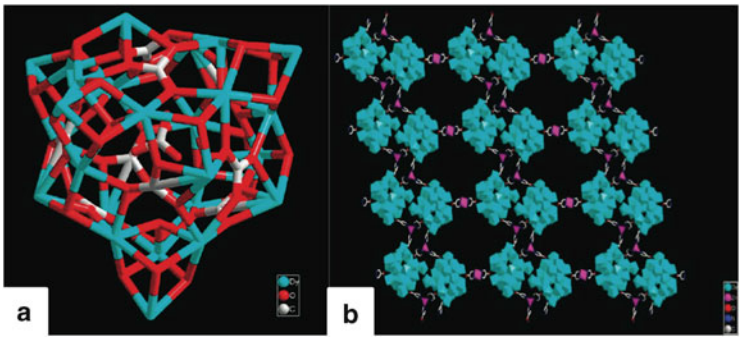

Fig. 14 (**a**) The structure of the $[Ln_{26}]$ cluster core structure with $[CO_3@Dy_{26}(CO_3)_9(OH)_{26}]$ as an example; (**b**) The 2D coordination layer constructed by $[Dy_{26}]$ clusters and Zn centers. Reprinted with the permission from [57]. Copyright 2007 American Chemical Society

Even larger lanthanide clusters have been obtained and their uses as SBUs for MOF construction have been reported. For example, individual $[Ln_{26}]$ clusters have been successfully synthesized and subsequently linked to form oligomers of the cluster units [57]. Pertinent to our discussion are the two 3D MOFs, $Zn_{1.5}Dy_{26}(IN)_{25}(CH_3COO)_8(CO_3)_{11}(OH)_{26}(H_2O)_{29}$ and $Zn_{1.5}Gd_{26}(IN)_{26}(CH_3COO)_7(CO_3)_{11}(OH)_{26}(H_2O)_{28}$, formed respectively by $[Dy_{26}]$ and $[Gd_{26}]$ clusters as SBUs linked by transition metal ions [58]. The lanthanide ions are first self-assembled into a 26-metal cluster whose formation is assisted by a carbonate ion situated in the center of the cage-like cluster. The lanthanide ions are connected by 26 hydroxo groups and 9 additional carbonate anions in the cage framework (Fig. 14a). The individual cages are then bridged by complex units of $[Zn(IN)_2(H_2O)_4]$ and $[Zn(IN)_3(H_2O)]$ complexes to form a 2-D coordination layers, which are further "stitched" together by units of $[Zn(IN)_2(H_2O)_4]$ along the crystallographic [011] direction to afford the 3D structure shown in Fig. 14b.

So far the highest nuclearity of a lanthanide cluster SBU in transition metal ion-bridged nanostructured MOFs is a wheel-like $[Er_{36}]$ reported by Yang and coworkers in 2006 [59]. The as-synthesized MOFs having a general formula of $[Er_7(\mu_3\text{-}O)(\mu_3\text{-}OH)_6(bdc)_3](ina)_9[Cu_3X_4]$ (bdc = 1,2-benzenedicarboxylate, ina = isonicotinic acid, X = Cl, Br) were obtained under hydrothermal conditions using a starting mixture containing Er_2O_3, isonicotinic acid, 1,2-benzenedicarboxylic acid, CuX_2 (X = Cl, Br), and $HClO_4$ in water. Structural analysis by single-crystal X-ray diffraction revealed units of $[Er_4(\mu_3\text{-}OH)_4]$ and $[Er_2(\mu_3\text{-}OH)_2]$ linked together by sharing the μ_3-OH group in the latter units (Fig. 15a) to form the wheel-like $[Er_{36}]$ cluster with 1,2-benzenedicarboxylate inside the wheel and coordinating to the lanthanide ions (Fig. 15b); the diameter of the wheel is about 3 nm. The $[Er_{36}]$ wheels are further incorporated into a 2D coordination layer through the sharing of the wheel edges, resulting in well-defined hexagonal pores (Fig. 15c). Linking neighboring layers by $[Cu_3Cl_4(ina)_6]$ complex units produces the observed 3D MOF structure (Fig. 15d).

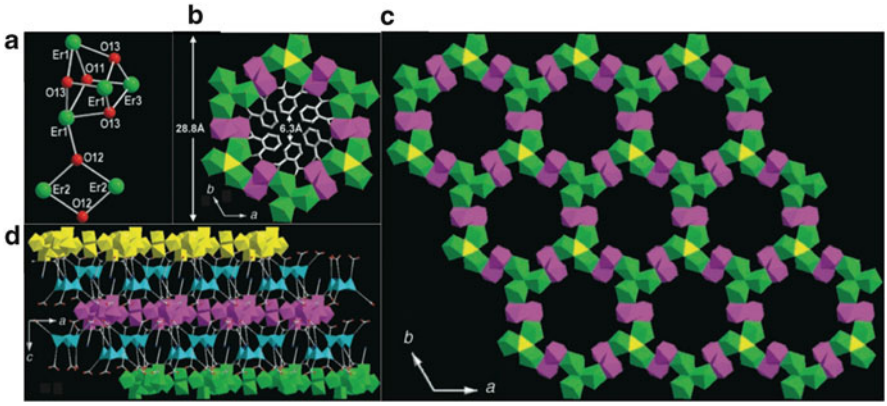

Fig. 15 (**a**) The linkage of $[Er_4]$ and $[Er_2]$ cores through μ_3-OH; (**b**) The $[Er_{36}]$ wheel composed of alternating $[Er_4]$ and $[Er_2]$ units; (**c**) 2D coordination layer composed of $[Er_{36}]$ by sharing edges (with bdc ligands omitted for clarity); (**d**) 2D coordination layers were further linked together by $[Cu_3Cl_4(ina)_6]$ complexes (in *cyan* color) to form 3D MOF. Reproduced from [59] by permission of John Wiley & Sons Ltd.

2.2 *Clusters of Lanthanide–Non-lanthanide Element as SBUs*

2.2.1 Ln–Ge Clusters as SBUs

Microporous main group metal/metalloid oxides are a kind of rigid, highly crystalline materials with diverse applications in separation, ion exchange, and catalysis. One family of such materials are germanate open frameworks [60]. Researchers have been working to incorporate other metal elements into germanate frameworks in order to introduce novel properties [61, 62]. Yang and coworkers are the first to incorporate lanthanide ions into germanate clusters and to incorporate them into 3D MOFs with the use of judiciously chosen organic ligands [63]. In their work, an organo-metalloid compound $(HOOCCH_2CH_2)_2Ge_2O_3$ ($H_2E_2Ge_2O_3$, E= $-CH_2CH_2COO^-$) was used as geranium precursor to not only overcome the poor water solubility typical of germanium precursors but also to use it as an effective ligand for the coordination of lanthanide ions by taking advantage of the carboxylate groups. The synthesis was carried out under hydrothermal conditions using a mixture of $H_2E_2Ge_2O_3$ and lanthanide oxide in an acidic aqueous solution, with or without the organic ligand 2-picolinic acid (Hpa). In the absence of Hpa, a twofold interpenetrating MOF $[Nd_8Ge_{12}(\mu_3\text{-}O)_{24}E_{12}(H_2O)_7]\cdot 13H_2O$ was obtained (Fig. 16f) in which the building block is a $[Nd_8Ge_{12}(\mu_3\text{-}O)_{24}(H_2O)_7]^{24+}$ cage (denoted as $[Nd_8Ge_{12}]$) consisting of two $[Ge_6]$ rings sandwiching one $[Nd_6]$ ring in the middle with two additional Nd^{3+} ions capping each of the open sides (Fig. 16a–e). Six of the twelve Ge groups coordinate three adjacent $[Nd_8Ge_{12}]$ cages, affording the 3D MOF with twofold interpenetration (Fig. 16e). However,

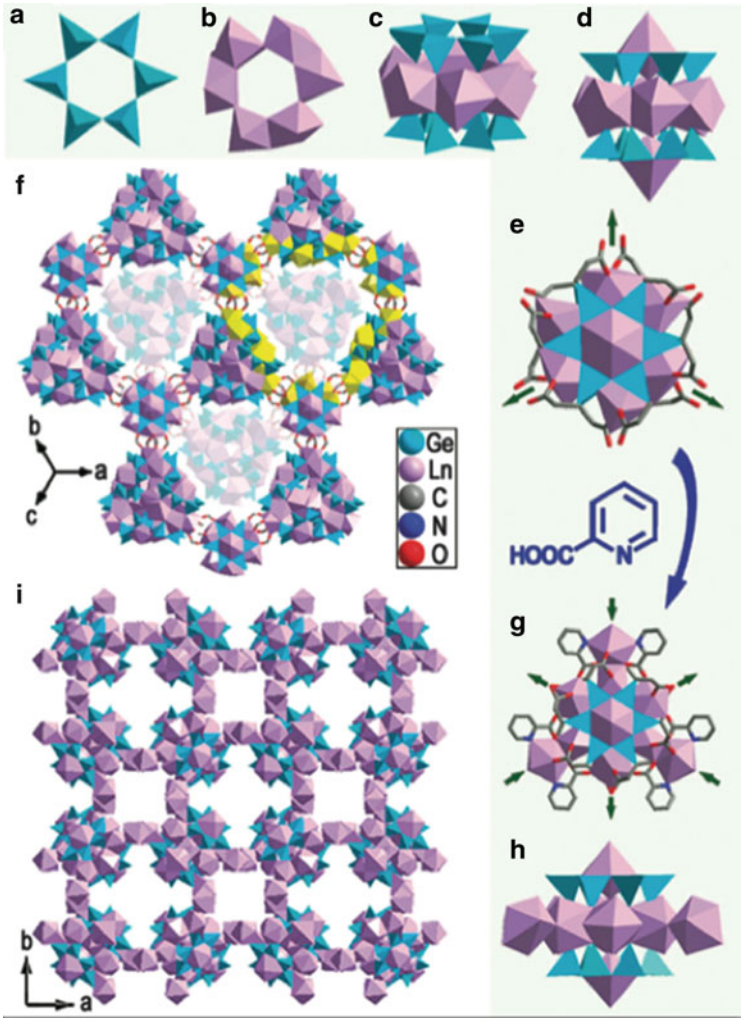

Fig. 16 (**a**–**c**) View of the Ge_6 and Nd_6 rings and the linking mode; (**d**) *Side view* of the Nd_8Ge_{12} cage; (**e**) *Top view* of the Nd_8Ge_{12} cage surrounded by 12 Ge groups with the *arrows* showing the linking modes with three adjacent Nd_8Ge_{12} cages; (**f**) Structure of the twofold interpenetrating MOF $[Nd_8Ge_{12}(\mu_3\text{-}O)_{24}E_{12}(H_2O)_7]\cdot 13H_2O$ with one of the sub-network shown lighter; (**g**) *Top view* of the $Ln_{11}Ge_{12}$ cage surrounded by 6 pa ligands and 12 Ge groups with the *arrows* showing its linking modes with six adjacent $Ln_{11}Ge_{12}$ cages; (**h**) *Side view* of the $Ln_{11}Ge_{12}$ cage; (**i**) Structure of the non-interpenetrating MOF $[Ln_{11}Ge_{12}(\mu_3\text{-}O)_{24}E_{12}(pa)_6(H_2O)_{10}]\cdot nH_2O$. Reprinted with the permission from [63]. Copyright 2009 American Chemical Society

when the rigid chelating ligand Hpa was added to the reaction under otherwise identical conditions, a series of non-interpenetrating MOFs of the general formula $[Ln_{11}Ge_{12}(\mu_3\text{-}O)_{24}E_{12}(pa)_6(H_2O)_{10}]\cdot(Cl,2OH)\cdot nH_2O$ [Ln = Pr, Nd, Eu, Gd; $n = 19$ (Pr, Nd), 15 (Eu), 14 (Gd)] were obtained (Fig. 16i). Instead of $[Ln_8Ge_{12}]$ cages as

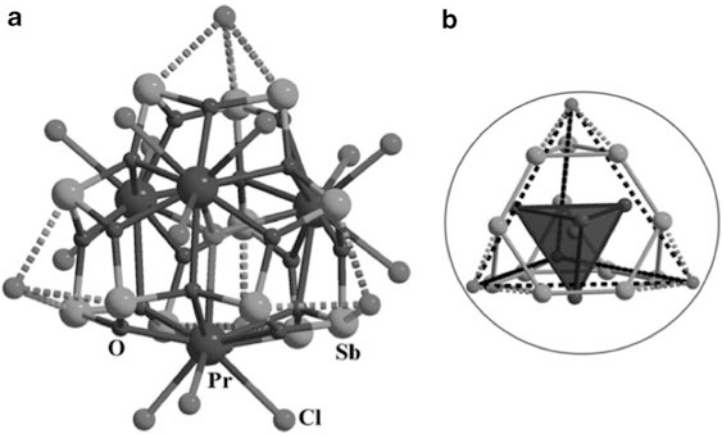

Fig. 17 (**a**) Structure of the nanoscale anionic cluster core $[Pr_4Sb_{12}O_{18}Cl_{17}]^{5-}$; (**b**) Illustration of inverted $[Pr_4]$ tetrahedron encapsulated within the truncated tetrahedral $[Sb_{12}]$ cage. Reproduced from [66] by permission of John Wiley & Sons Ltd.

SBUs, this series of MOFs are constructed using $[Ln_{11}Ge_{12}]$, a different cage-like cluster (Fig. 16g, h). The $[Ln_{11}Ge_{12}]$ cage is formally constructed from the $[Ln_8Ge_{12}]$ cluster with the presence of six pa chelating ligands that coordinate three additional lanthanide ions on the periphery. Each $[Ln_{11}Ge_{12}]$ cage is surrounded by six neighboring identical cages through 6 of the 12 Ge groups to give a 3D non-interpenetrating MOF (Fig. 16h).

2.2.2 Ln–Sb Oxohalide Clusters as SBUs

Another type of lanthanide–non-lanthanide cluster motif is that of metal oxohalides, a class of low-dimensional materials containing *d*- or *f*-block metals and a *p*-block elements oxohalide as counter anion. The existence of stereochemically active lone pair(s) in *p* orbitals is expected to lead to asymmetric coordination around the *p*-block cation, making both the active lone pair and halide ions as terminating groups to keep a low-dimensional arrangement [64]. Besides their stable existence as low-dimensional clusters, they also possess interesting properties such as magnetic frustration [64] and semiconducting [65].

The first example of cluster-type lanthanide-containing oxohalide cluster was reported by Huang and coworkers [66] in which they prepared the Pr–Sb oxohalide cluster $(2\text{-MepyH})_5[Pr_4Sb_{12}O_{18}Cl_{17}]$ (2-Mepy = 2-methylpyridine) by a hydrothermal route starting with an aqueous solution of $Pr(OAc)_3{\cdot}3H_2O$, $SbCl_3$, and 2-Mepy. The cluster core is constructed with a series of bridging and terminal Cl^- and O^{2-} ions sticking 12 Sb^{3+} and 4 Pr^{3+} cations together. The 12 Sb^{3+} ions form a large truncated tetrahedral cage while the 4 Pr^{3+} ions form an inverted tetrahedron encapsulated in the $[Sb_{12}]$ cage (Fig. 17).

Following the discovery of this beautiful and highly symmetric cluster, the authors also explored the assembly of the cluster units into higher-dimension frameworks with the assistance of certain organic linkers. For example, when 1,4-BDC was used as linker, a 2D layer with the Pr–Sb oxohalide cluster as nodes was obtained, whereas when 1,3-BDC was used, a zigzag 1D chain based on the oxohalide cluster as SBU was produced [66]. The ultimate goal of assembling these clusters into a 3D MOF was achieved when thiophene-2,5-dicarboxylic acid (H_2TDC) was utilized as the organic linker and co-directed by Fe(1,10-phen)$_3$ [67, 68]. The as-synthesized MOF, formulated as (2-MepyH)$_5$(Fe(1,10-phen)$_3$)$_{10}$[($Pr_4Sb_{12}O_{18}Cl_{13}$)$_4$($Pr_4Sb_{12}O_{18}C_{19}$)(TDC)$_{12}$]·80H_2O, is characterized to be a twofold interpenetrating network (Fig. 18a) featuring three kinds of 1D channels: the R-channels wrapped around by right-handed double-helical chain, *L*-channels wrapped around by left-handed double-helical chain, and larger achiral channels (Fig. 18b, c). The incorporated Fe(1,10-phen)$_3$ molecules, depending on their positions, are distinctly labeled as **Fe1**, **Fe2,** and **Fe3**. Encapsulated into the achiral channels and chiral channels are respectively **Fe2** and **Fe3**, with **Fe1** being buried in the pitch interspace of the helices.

Besides the detailed crystallographic analysis, the photocatalytic properties of the 3D MOF for hydrogen evolution from methanol have been explored [68].

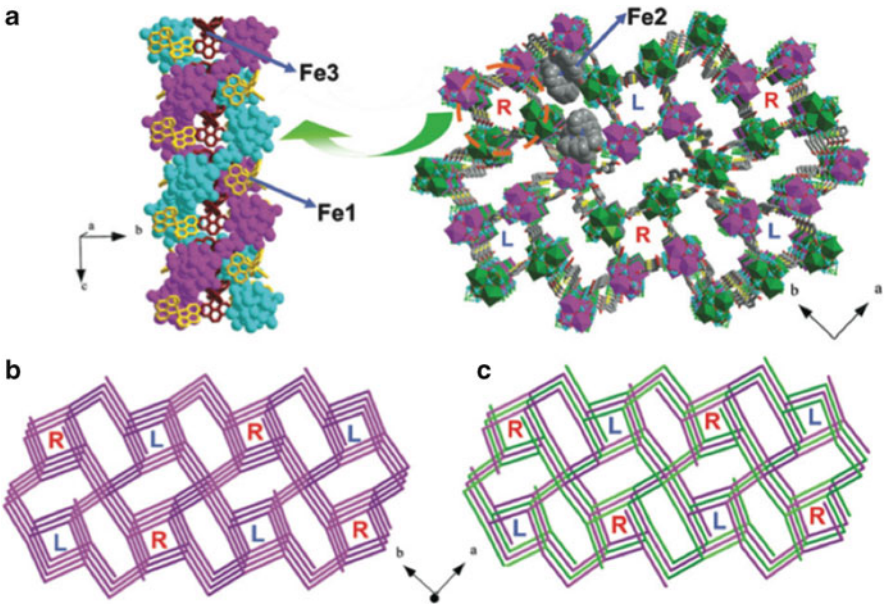

Fig. 18 (**a**) Structure of right-handed double-helical chain wrapping around the chiral channel of the MOF (*left*) and the structure of the (2-MepyH)$_5$(Fe(1,10-phen)$_3$)$_{10}$[($Pr_4Sb_{12}O_{18}Cl_{13}$)$_4$($Pr_4Sb_{12}O_{18}C_{19}$)(TDC)$_{12}$]·80H_2O MOF (*right*); (**b**) The topological view of one sub-network of the twofold self-penetrating MOF; (**c**) The topological view of the twofold self-penetrating MOF. Reproduced from [67] by permission of The Royal Society of Chemistry

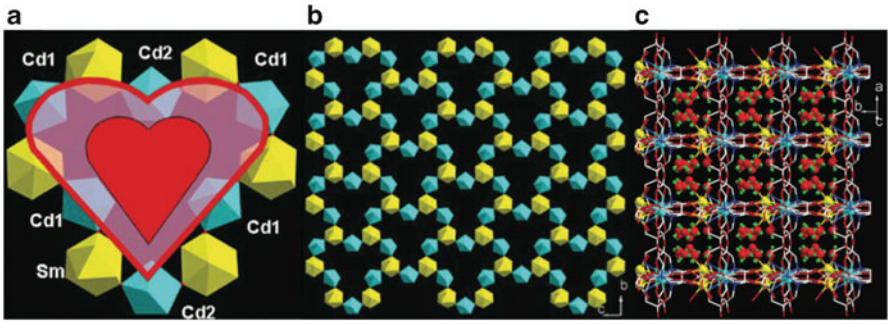

Fig. 19 (**a**) Polyhedral view of the nanoscale heart-like $Ln_6Cd_6O_{12}$ wheel cluster (with $Sm_6Cd_6O_{12}$ as an example); (**b**) Polyhedral view of layered Ln-Cd 2D coordination layer with ligands omitted for clarity (*Color code*: Ln *yellow*; Cd *cyan*); (**c**) Structure of the 2D coordination layers stacking into a 3D framework with water molecules suspended between the layers. Reproduced from [72] by permission of The Royal Society of Chemistry

2.2.3 Heterometallic 3*d*–4*f* Clusters as SBUs

Due to the disparate properties of *d*- and *f*-block metal ions, there has been interest to integrate these two rather different kinds of metal ions into the same cluster motif and to explore if such combination would lead to interesting physical properties and potentially significant applications, one of which is the environmentally friendly magnetic cooling technology [13, 69, 70]. Furthermore, by introducing transition metal ions into the lattice of lanthanide materials, the energy levels could be tuned and so could be the materials' luminescence properties [71].

Considering the attractive features of heterometallic clusters containing both lanthanide and other non-lanthanide metals, efforts have been made to build nanostructured MOFs using such clusters as SBUs with the hope of discovering novel functional materials. One such example is the series of stacked 2D lanthanide–cadmium heterometal–organic frameworks in which nanosized heart-shaped $Ln_6Cd_6O_{12}$ wheel clusters are identified [72]. In this work, the MOFs, having a common formula of $[Ln_2Cd_3(EDTA)_3(H_2O)_{11}](H_2O)_{14}$ (Ln = Sm, Eu; H_4EDTA = ethylenediaminetetraacetic acid), were synthesized by a hydrothermal route using a mixture of Ln_2O_3, $CdSO_4{\cdot}8H_2O$, and H_4EDTA as starting material. In the structure, there are alternating hepta-coordinate Cd^{2+} and deca-coordinate Ln^{3+} ions linked together via μ_2-O of the $EDTA^{4-}$ ligand, forming a heart-like $Ln_6Cd_6O_{12}$ wheel motif with a size about 2.3×2.1 nm (Fig. 19a). Each of the wheel clusters is linked to six neighboring wheels to form an Ln–Cd 2D coordination layers (Fig. 19b) that are stacked together with intercalated solvent water molecules to generate a 3D framework structure (Fig. 19c).

Although very appealing, most of the *d-f* heterometallic MOFs reported are constructed with the use of single metal ions as the metal nodes instead of nanoscale heterometallic clusters [73, 74], and the incorporation of nanoscale *d-f* heterometallic clusters as SBUs into MOFs remains a challenge and thus promises a subarea for further development.

2.3 *Ligand-Directed Assembly of LnMOFs Featuring Nanosized Pores or Channels*

LnMOFs characterized by their nanosized pores or channels are distinctly different from the nanostructured LnMOFs described above. As an example, the stunningly beautiful structure of $[Tb_{16}(TATB)_{16}(DMA)_{24}](DMA)_{91}(H_2O)_{108}$ (H_3TATB = triazine-1,3,5-tribenzoic acid and DMA = *N*,*N*-dimethylacetamide) [193] is shown in Fig. 20 with truncated tetrahedron $[Tb_{16}]$ clusters as SBUs. On each of the truncated triangular faces, there are three Tb^{3+} ions, each occupying one vertex of the triangle while an additional Tb^{3+} sits in the center of the triangle. With four truncated triangle facets on each truncated tetrahedron cluster, there are 16 Tb^{3+} ions contained in each cluster (Fig. 20a). The TATB ligands are located inside the $[Tb_{16}]$ cluster motif, bridging the 16 Tb^{3+} ions. These $[Tb_{16}]$ clusters are assembled

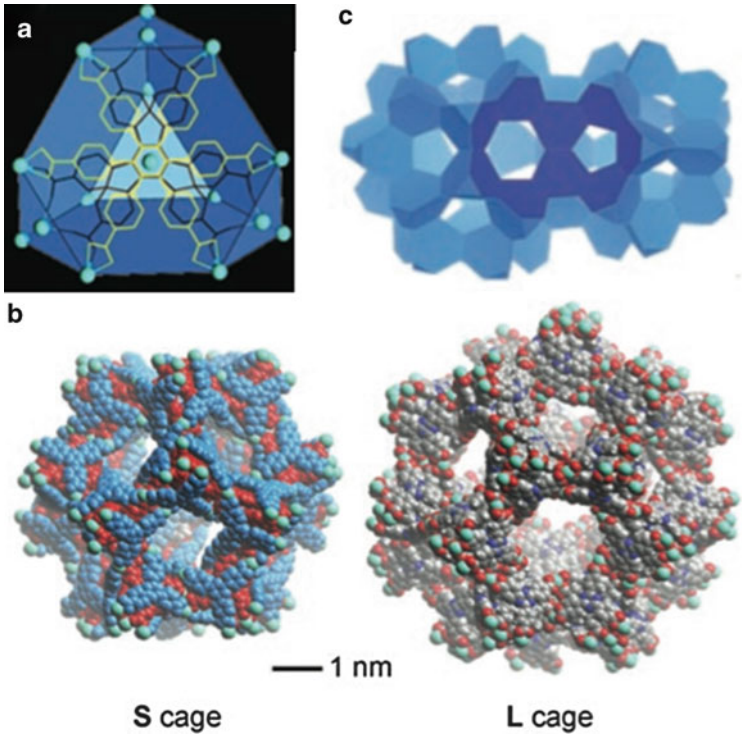

Fig. 20 (**a**) Structure of the $[Tb_{16}]$ cluster core; (**b**) Structure of the two types of cages in the MOF, smaller cage designated as **S** cage while the larger cage designated as **L** cage; (**c**) The fusion mode between S cage and L cage in the MOF. Reproduced from [193] by permission of John Wiley & Sons Ltd.

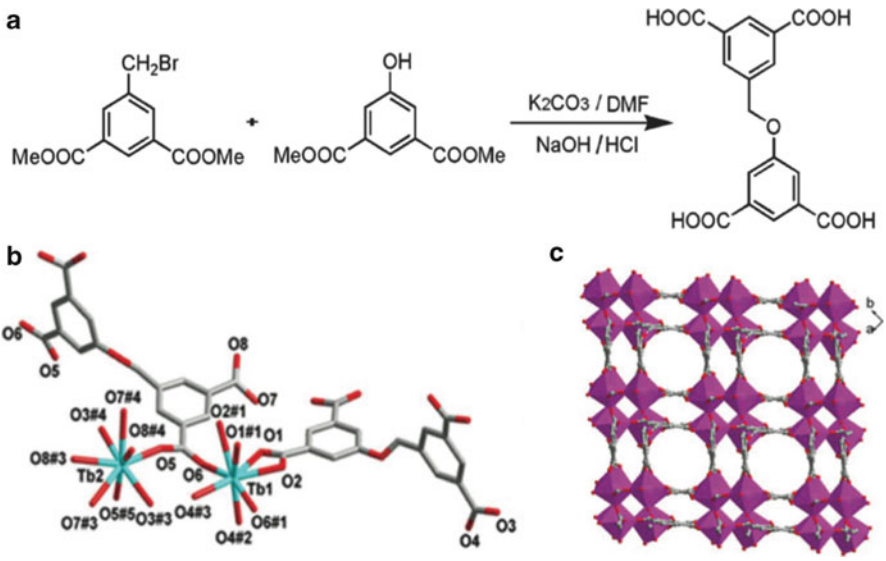

Fig. 21 (**a**) Synthetic route of the H_4L ligand; (**b**) Coordination modes between L ligands and lanthanide ions (with Tb^{3+} as an example); (**c**) Structure of the $\{[Ln_2(L)_2]\cdot(H_2O)_3\cdot(Me_2NH_2)_2\}_n$ MOF. Reproduced from [76] by permission of The Royal Society of Chemistry

into two kinds of cages by sharing the truncated triangle facets, one smaller and designated as **S** cage while the other and larger cage is designated as **L** cage. The **S** cage is constructed by 20 $[Tb_{16}]$ clusters by sharing truncated facets, with a diameter of 3.9 nm. The **L** cage is built from 28 $[Tb_{16}]$ cluster units, also by sharing truncated facets, and its diameter is 4.7 nm (Fig. 20b). These two types of cages are further fused by sharing the pentagonal windows into a 3D structure (Fig. 20c).

Using clusters as SBUs is one obvious way of constructing nanostructured LnMOFs that possess nanosized pores or channels. However, by choosing the right type of ligands, even the coordination of single lanthanide ions can also lead to the production of MOFs with similar nanostructured features. For example, a nanosized tri-carboxylic acid ligand, tris((4-carboxyl)phenylduryl)amine (H_3L), was used to synthesize LnMOFs by Zhang and coworkers [75]. These MOFs, formulated as $[Ln(L)]\cdot 1.5H_2O\cdot 0.5EtOH\cdot DMF$ (Ln = Ce, Pr, Nd, Sm), were obtained by hydrothermal method using lanthanide nitrate and H_3L ligand as reactants in a mixed solvent of water/DMF/ethanol. The as-obtained MOFs have large 1D channels along the crystallographic *c* axis with a dimension of about 1×0.8 nm.

In another example, the use of nanosized tetracarboxylic acid ligand 5-(3,5-dicarboxybenzyloxy)isophthalic acid (H_4L) (Fig. 21a) leads to the production of a series of LnMOFs of the general formula $\{[Ln_2(L)_2]\cdot(H_2O)_3\cdot(Me_2NH_2)_2\}_n$ (Ln = La, Ce, Pr, Nd, Sm, Eu, Gd, Tb, Ho, Er) [76]. The L ligands link lanthanide ions in both μ_2 bridging and η^2 coordinating modes to give 3D porous MOFs with pore size of about 0.8×0.7 nm (Fig. 21b, c).

Besides the use of purely organic ligands, nanosized transition metal complexes with macrocyclic ligands have also been utilized to construct highly porous LnMOFs. These complexes not only serve as nanosized linkers to support the formation of nanosized pores, but also prevent interpenetration from occurring as a result of the steric bulk of the macrocyclic ligands. Furthermore, the incorporation of transition metal ions introduces additional function and properties. As an example, Cao and coworkers reported the use of interconnecting transition metal complexes $[M(TETA)]^{2-}$ with TETA ligand (H_4TETA = 1,4,8,11-tetraazacyclotetradecane-1,4,8,11-tetraacetic acid); the remaining unused carboxylate groups (Fig. 22a) of the complex are perfect for the subsequent lanthanide coordination, affording $[Eu_2Zn_3(TETA)_3(H_2O)_4]\cdot 12H_2O$ and $[Gd_2Cu_3(TETA)_3(H_2O)_2]\cdot 6H_2O$, two MOFs with nanosized channels [77]. Crystallographic analysis clearly revealed the complexation of the transition metal ions within the cavity of the macrocyclic ligands, coordinated by both the backbone N atoms and one of the O atoms from each of the side-arm carboxylate groups. Each macrocyclic unit, due to the presence of four carboxylate groups, connects four lanthanide ions to give the 3D porous MOF structure (Fig. 22b) with nanosized (1.8×1.5 nm) channels (Fig. 22c).

Other structurally interesting ligands have also been used in a similar capacity. For example, Ghosh and Bharadwaj [78] reported a 3D LaMOF with the use of pyridine-2,6-dicarboxylic acid ($pdcH_2$) ligand. This MOF possesses 1D hexagon-shaped channels whose "wall" is formed by the lanthanide-pdc coordination units for which a cross-section view is shown in Fig. 23a; the hexagon is composed of six pdc ligands bridging six La(III) ions. These hexagon-shaped channels with a diameter of about 1.1 nm are further linked to afford the 3D MOF (Fig. 23b) of the formula $[La(pdc)(H_2O)_4]\cdot Cl$.

Another example of this type of ligands is 5-nitroisophthalic acid (5-H_2nip). Gao and coworkers reported a series of nanoporous LnMOFs of the formula $\{[Ln_2(5\text{-nip})_3(DMF)_4](DMF)_2\}_n$ (Ln = Nd, Dy, Ho) [79]. In the MOF structure,

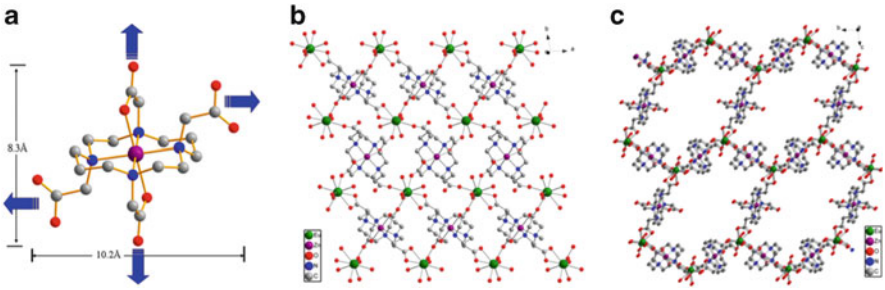

Fig. 22 (**a**) Structure of the transition metal macrocyclic complex $[M(TETA)]^{2-}$; (**b**) Coordination modes between $[M(TETA)]^{2-}$ and lanthanide ions (with $[Zn(TETA)]^{2-}$ and Eu^{3+} as an example); (**c**) A view of the nanosized 1D channels in the as-synthesized MOF. Reprinted with the permission from [77]. Copyright 2012 American Chemical Society

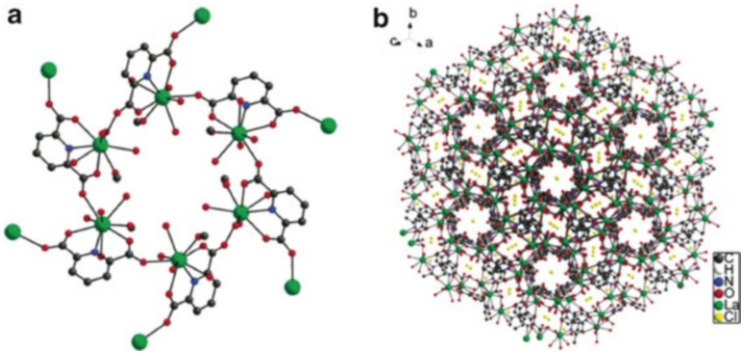

Fig. 23 (**a**) *Top view* of the cross section of hexagonal-shaped 1D channel in $[La(pdc)(H_2O)_4]\cdot Cl$. (**b**) Structure of the MOF, viewed along the direction of hexagonal-shaped 1D channels. Reprinted with the permission from [78]. Copyright 2005 American Chemical Society

the lanthanide ions are bridged together by μ_2-carboxylate groups of the nip ligands to form dinuclear lanthanide complex units that are further connected by nip ligands to form the eventual 3D MOFs with continuous and repeating rectangle-shaped pores of the dimension of 1.5×0.9 nm (Fig. 24a).

The need for high-coordination number and the flexible coordination geometry unique to the lanthanide ions often lead to dense and non-porous MOFs. If small-unit ligands are used to pre-occupy certain coordination sites, it is possible to "steer away" the otherwise more compact coordination of the organic bridging ligands, and thus, to produce LnMOFs with reasonable sized and accessible pores. This design strategy has been demonstrated in the work of Wu and coworkers in which a series of LnMOFs were obtained by 2,5-pyrazinedicarboxylate (2,5-pzdc) as the bridging ligand and oxalate as the ancillary ligand [80]. These MOFs were synthesized hydrothermally. In the absence of oxalate ligand, the MOF obtained, $[Ln(2,5\text{-pzdc})_{1.5}(H_2O)_3]\cdot 0.5H_2O$, only possesses very narrow 1D channels (Fig. 25a). In stark contrast, the addition of oxalate in the reaction mixture lead to the production of highly porous MOF of the formula $[Ln(2,5\text{-pzdc})_1(ox)_{0.5}(H_2O)_2]\cdot 4.5H_2O$ whose nanosized hexagon-shaped 1D channels (1.3 nm) are clearly shown in Fig. 25a.

In another example, Dunbar and coworkers synthesized two 3D frameworks constructed from 1D nanotubes using 2,4,6-tris(2-pyridyl)-s-triazine (tptz) as organic linker and formate as ancillary ligand for lanthanide coordination [81]. Each lanthanide ion is nonacoordinate with its coordination sphere consisting of three tptz *N* atoms and six formate O atoms. The formate ligands are also bridging, linking neighboring lanthanide ions into a hexagon, an arrangement further stabilized by π–π interactions involving the aromatic rings of the tptz ligands (Fig. 26a). The π–π interactions are extensive, extending along two directions, in the plane of the hexagon and perpendicular to it, leading to the assembly of the regular 3D porous structure as shown in Fig. 26c.

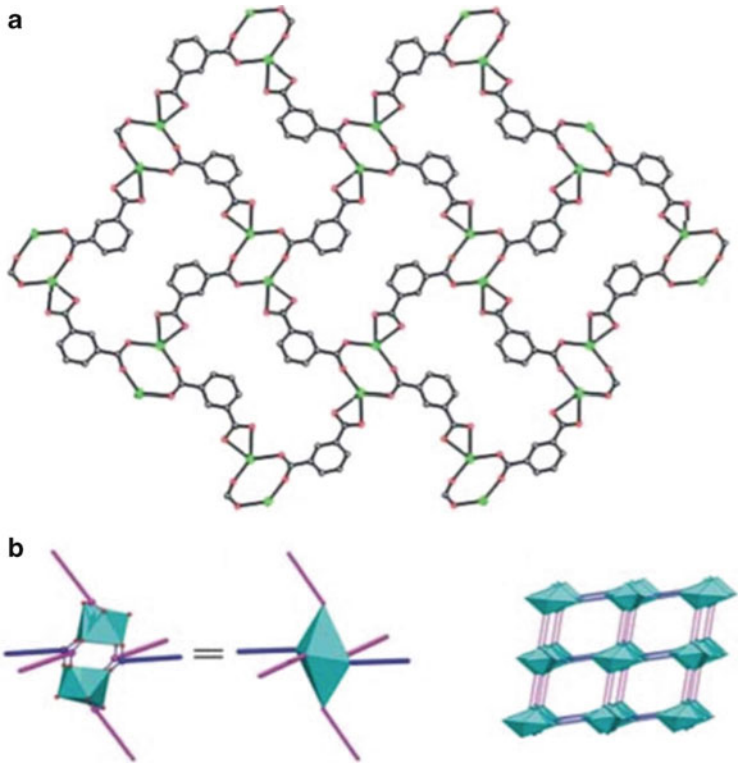

Fig. 24 (**a**) View of the nanosized pores in the $\{[Ln_2(5\text{-nip})_3(DMF)_4](DMF)_2\}_n$ MOFs (with hydrogen atoms and phenyl nitro groups omitted for clarity); (**b**) Structure of the 3D $\{[Ln_2(5\text{-nip})_3(DMF)_4](DMF)_2\}_n$ MOFs with lanthanide dimers represented as cyan octahedrons. Reproduced from [79] by permission of The Royal Society of Chemistry

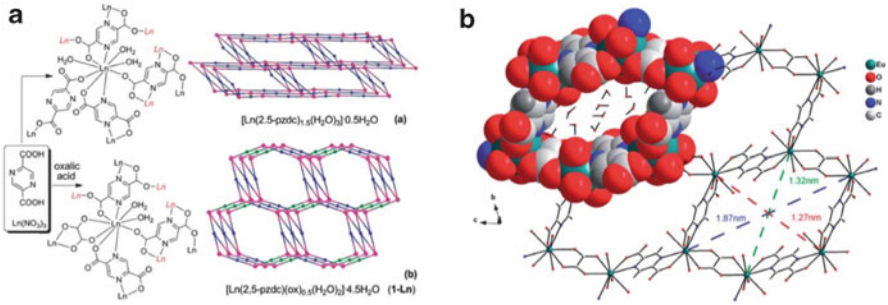

Fig. 25 (**a**) The comparison between MOF structure (viewed along the 1D channel direction) with and without adding oxalate as assistant ligands; (**b**) The channel dimension when oxalate was added as assistant ligand (with Eu as metal center). Reproduced from [80] by permission of The Royal Society of Chemistry

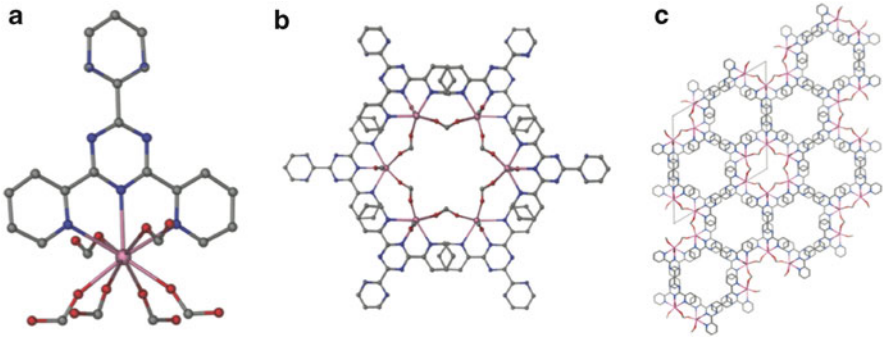

Fig. 26 (**a**) Coordination around Ln(III) metal center with tptz and formate ligands; (**b**) *Top view* of the hexagonal-shaped 1D Ln(III) nanotube. (**c**) 3D framework constructed by Ln(III) nanotubes stacking together with tptz ligands π–π interactions. Reproduced from [81] by permission of The Royal Society of Chemistry

3 Properties and Applications of Bulk Nanostructured LnMOFs

The applications of MOFs in general, envisioned or already demonstrated, are probably the main impetus for conducting such research, in addition to the initial interest in their structural aesthetics. A wide range of applications, including recognition, adsorption, storage, and/or separation of guest species of environmental [82] and energy [83, 84] significance, sensing, and drug delivery, have been reported, primarily based on the size discrimination or affinity of the pores of a particular MOF. If other functions are introduced into the framework structure, either during the synthesis by the use of building units with inherently interesting properties as in the case of LnMOFs or by post-synthesis modification, then realization of multifunctional materials becomes a reality. In the following discussion we summarize the interesting properties, many of which are originated from the presence of the unique lanthanide ions, and the potentially useful applications.

3.1 Guest Adsorption and Storage

Zhou and coworkers first studied hydrogen adsorption in $Y(BTC)(H_2O)\cdot 4.3H_2O$, a rare earth MOF [85]. Through neutron diffraction studies, details of hydrogen adsorption pattern were revealed: Hydrogen molecules are associated with the aromatic BTC liner rather than being coordinated to the open coordination sites of the metal as one would suspect [86, 87] (Fig. 27a). Besides the determination of novel hydrogen molecule adsorption pattern, the authors also provided the first structural evidence in support of the findings by other researchers that small pores with an optimal pore diameter of just slightly over twice the kinetic diameter of the

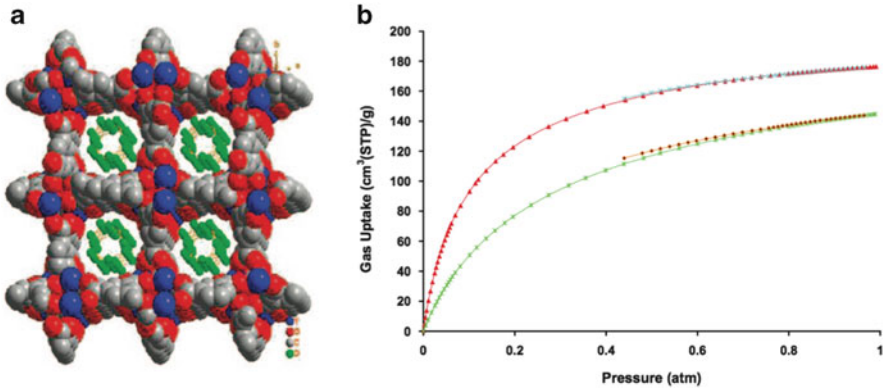

Fig. 27 (**a**) Hydrogen clusters formed inside activated Y(BTC)(H_2O)·4.3H_2O MOF lattice; (**b**) H_2 adsorption isotherms of activated Y(BTC)(H_2O)·4.3H_2O MOF lattice at 77 K (*red/light blue*), and at 87 K (*green/orange*). Reprinted with the permission from [85]. Copyright 2008 American Chemical Society

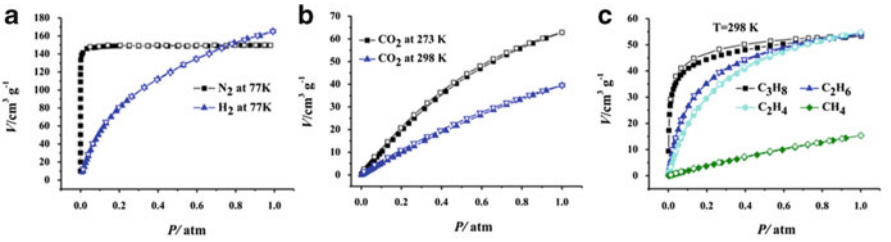

Fig. 28 Adsorption isotherms for activated [Ce(L)]·1.5H_2O·0.5EtOH·DMF MOF: (**a**) N_2 and H_2 adsorption isotherms at 77 K; (**b**) CO_2 adsorption isotherms at 273 and 298 K; (**c**) Hydrocarbons adsorption isotherms at 298 K. Reprinted with the permission from [75]. Copyright 2013 American Chemical Society

hydrogen molecules (a pore diameter around 6–7 Å) strengthen the interactions between H_2 and the pore walls. Moderate adsorption ability was observed for activated Y(BTC)(H_2O)·4.3H_2O with 176 $cm^3\ g^{-1}$ at 1 atm and 77 K (Fig. 27b).

A more comprehensive gas sorption study was done by Zhang and coworkers on a series of non-interpenetrating nanoporous MOFs constructed with the use of tris ((4-carboxyl)phenylduryl)amine (H_3L) ligand [75]. Their adsorption capacity toward H_2, N_2, CO_2, and hydrocarbons was studied (Fig. 28). With [Ce(L)]·1.5H_2O·0.5EtOH·DMF, the activated nanoporous MOF showed moderate adsorption of H_2 and N_2 (Fig. 28a). For its adsorption of hydrocarbons, a size-dependent selectivity was observed with higher adsorption abilities demonstrated for sterically more demanding hydrocarbons (Fig. 28c).

3.2 Catalysis

Arguably the most notable catalytic performance of nanostructured LnMOFs is based on the exploitation of polyoxometalates (POMs) encapsulated inside the pores of LnMOFs, abbreviated as POM-LnMOFs hereafter [88]. The first example of MOF-incorporation of POMs was provided by Duan and coworkers [89]. The authors reported the encapsulation of two different yet related POMs, $PMo_{12}O_{40}]^{3-}$ and $[SiMo_{12}O_{40}]^{4-}$, into the nanoporous MOF of $[Ln(dpdo)_4(H_2O)_3]^{3+}\}_n$ (Ln = Gd, Dy, Ho) (Fig. 29). Such entrapment of the catalytically active POMs effectively increases the concentration of the catalyst as well as the substrate as the reaction to be catalyzed now is being carried out in a confined molecular container. As such, reaction kinetics is expected to be enhanced significantly.

An added advantage of using LnMOF for the encapsulation of POMs is that lanthanide ions are Lewis acidic with high coordination numbers and fast ligand-exchange rate [90, 91], all being propitious to catalysis. Furthermore, being a weak conjugate base, the association of POMs (as counter anions) with lanthanide ions is expected to enhance the Lewis acidity of the latter and to increase the efficiency of any Lewis acid-promoted reactions [92]. On the other hand, the presence of POM in a reaction mixture may lead to POM-templated synthesis of MOFs, and the occupation of the pores by POMs would prevent interpenetration from occurring as well as restrict the coordination and activation of substrates in a certain stereo-specific fashion [93]. POM-LnMOFs have been shown to be active in photocatalysis, organic reactions, and hydrolytic cleavage of nucleases.

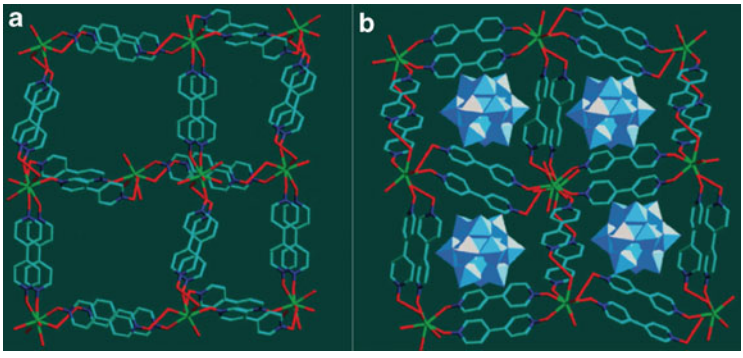

Fig. 29 (**a**) The structure of nanoporous cationic lanthanide MOF $\{[Ln(dpdo)_4(H_2O)_3]^{3+}\}_n$ backbone; (**b**) Structure of the nanoporous MOF with POM clusters incorporated. Reprinted with the permission from [89]. Copyright 2007 American Chemical Society

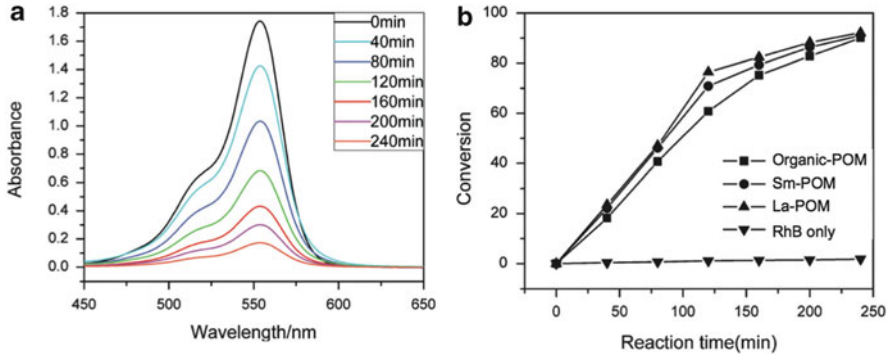

Fig. 30 (**a**) The UV–vis absorption spectra of RhB with organic-POM as photocatalyst under 175 W UV irradiation after different time; (**b**) The conversions of RhB with and without the presence of photocatalysts. Reproduced from [93] by permission of The Royal Society of Chemistry

3.2.1 Photocatalytic Properties of POM-LnMOFs

POMs are well known for their photocatalytic properties due to their similar electronic energy band gap with semiconductors such as TiO_2 [94]. Huang and coworkers reported a series of POM-incorporating nanoporous frameworks with or without lanthanide ions in the lattice and compared their photocatalytic properties on Rhodamine B (RhB) degradation [93]. The lanthanide-free framework, formulated as $[(C_5H_4NH)COOH]_3[PMo_{12}O_{40}]$ (Organic-POM), showed promising photocatalytic properties as the absorption of RhB decreased significantly in the presence of Organic-POM under UV irradiation (Fig. 30a). In comparison, the two POM-LnMOFs, formulated respectively as $\{[Sm(H_2O)_4(pdc)]_3\}\{[Sm(H_2O)_3(pdc)]\}[SiMo_{12}O_4]\cdot 3H_2O$ (Sm-POM) and $\{[La(H_2O)_4(pdc)]_4\}[PMo_{12}O_{40}]F$ (La-POM) (pdc = pyridine-2,6-dicarboxylate), exhibited enhanced photocatalytic activities as indicated by the different degree of RhB conversion using these three frameworks (Fig. 30b). The increased photocatalytic efficiency was ascribed to the fact that lanthanide ions acted as electron traps when POM clusters were excited by UV irradiation, which mitigated the recombination of electron–hole pairs and therefore increased the quantum efficiency of the photocatalytic process [95].

3.2.2 Organic Reactions Catalyzed by POM-LnMOFs

POMs are also very efficient in promoting organic transformation [96, 97]. Huang and coworkers synthesized a series of isostructural POM-LnMOFs of the general formula $Ln_4(pdc)_4[SiW_{12}O_{40}]\cdot xH_2O$ (Ln = La, Ce, Nd, Sm, Eu, Gd, Tb, Dy, Ho, Er) and studied their catalytic performance in ethyl acetate synthesis [98]. Higher degree of conversion and selectivity were observed when compared with sulfuric acid, a standard catalyst in this all important organic synthesis (Table 1). Moreover,

Table 1 Comparison of conversion efficiency and selectivity

Catalyst	Conversion (mol%)	Selectivity (mol%)
$Gd_4(C_7H_3NO_4)_4[SiW_{12}O_{40}]\cdot 13H_2O$	>99	>99
H_2SO_4	80	81
None	0	0

Reproduced from [98] by permission of John Wiley & Sons Ltd.

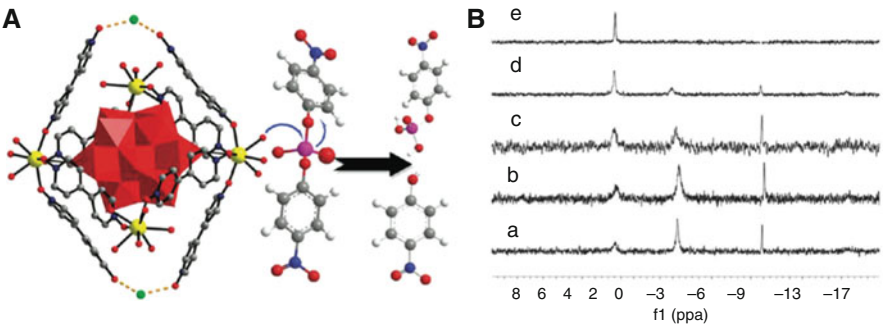

Fig. 31 (**a**) The mechanism for the cleavage of BNPP, using $\{[Eu_4(dpdo)_9(H_2O)_{16}PW_{12}O_{40}]\}(PW_{12}O_{40})_2(dpdo)_3Cl_3$ as an example; (**b**) ^{31}P NMR spectra of aqueous solution of BNPP containing $\{[Eu_4(dpdo)_9(H_2O)_{16}PW_{12}O_{40}]\}(PW_{12}O_{40})_2(dpdo)_3Cl_3$ measured after 1 day (spectrum *a*), 2 days (spectrum *b*), 4 days (spectrum *c*), 8 days (spectrum *d*), and 10 days (spectrum *e*) after mixing. Inorganic phosphate (δ 0.04), *p*-nitrophenylphosphate (δ −4.81), BNPP (δ −11.21). Reprinted with the permission from [103]. Copyright 2012 American Chemical Society

the POM-LnMOF catalysts possess high stability and recyclability with no apparent loss of catalytic activity and selectivity over ten cycles.

3.2.3 Hydrolytic Cleavage of Phosphodiesters Promoted by POM-LnMOFs

Artificial nucleases or synthetic molecules capable of catalyzing the hydrolytic cleavage of DNA or RNA are of fundamental significance and potential practical applications [99, 100]. A large number of lanthanide complexes have been studied toward the hydrolytic cleavage of phosphodiesters, model compounds of DNA, and have been shown to be very effective in some cases [101, 102]. However, simple lanthanide complex-based catalysts are usually soluble in aqueous solution and thus hard to be recycled. This drawback may be overcome by nanoporous POM-LnMOFs such as the series reported by Duan and Niu. Using 4,4′-bipyridine-N,N′-dioxide (dpdo) as organic linker, POM-LnMOFs of the general formula $Ln_2H(\mu\text{-}O)_2(dpdo)_4(H_2O)_2][PW_{12}O_{40}]\cdot 3H_2O$ were obtained and tested for their activity in the hydrolytic cleavage of bis(*p*-nitrophenyl)phosphate (BNPP), a commonly

used model compound for such experiments [92, 146]. BNPP was first cleaved into nitrophenol (NP) and nitrophenyl phosphate (NPP), (Fig. 31a) followed by the further cleavage of NPP into NP and phosphoric acid as the final products. As shown by the ^{31}P NMR spectra, 1 day after mixing BNPP with $\{[Eu_4(dpdo)_9(H_2O)_{16}PW_{12}O_{40}]\}(PW_{12}O_{40})_2(dpdo)_3Cl_3$, NPP and phosphoric acid peaks started to appear. After 10 days, all the organic phosphate was cleaved into phosphoric acid, (Fig. 31b) indicating efficient catalytic properties of the as-synthesized catalyst. The highest hydrolytic cleavage rate $1.19(\pm 0.07) \times 10^{-6}$ s^{-1} was obtained with $[Yb_2H(\mu\text{-}O)_2(dpdo)_4(H_2O)_2][PW_{12}O_{40}]\cdot 3H_2O$ as the catalyst, which was almost 10^5 higher than the rate without catalyst.

4 Nanoscale LnMOFs

Materials prepared with their physical size at the *nanoscale* exhibit properties distinctly different from those of their bulk counterparts. This unique behavior is largely due to the size effects, namely the surface and interface interactions and quantum confinement effects. When the size of a substance is reduced to the nanosized regime, its solubility has also changed dramatically as nanoparticles of otherwise insoluble bulk samples can now be dispersed in a variety of solvents. The improved solubility has significant ramifications in catalysis, drug delivery, bio-imaging, or in vivo sensing. The interest in nanoscale MOFs was stimulated by the pioneering work by Mirkin [104] and Wang [105]. Although strictly speaking the materials presented in Fig. 32 may not be considered as MOFs as they are amorphous and do not possess the well-defined structure at molecular level as commonly viewed by the community of MOF research. Nevertheless, these initial research inspired (1) much synthetic work of scaling crystalline MOF materials down to nanoparticles; and (2) the exploration of the potential applications of such nanoscale MOFs. New methodologies such as solvothermal synthesis, reverse microemulsion route, and surfactant-assisted preparation have been developed. Special attention and efforts have been paid to control the size and morphology of such nanoscale LnMOFs as well as surface modification of the nanomaterials with an eye on their niche applications. We note that excellent reviews on the synthesis [106, 107], surface modification [108], and applications of nanoscale MOFs [109, 110] exist in the literature.

4.1 Preparation of Nanoscale LnMOFs

4.1.1 Precipitation

The precipitation method was commonly utilized to produce sub-micron or *nanoscale* MOFs in early research stage because of the mild reaction condition and facile operation. Briefly, appropriate precursors, both metal salts and organic ligands, are

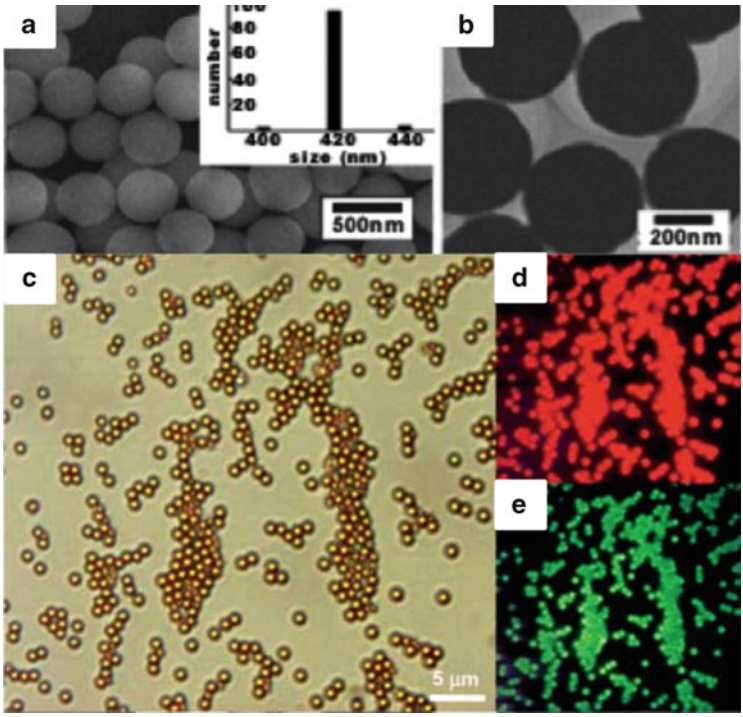

Fig. 32 (**a**) SEM image and corresponding size distribution histogram (*inset*) and (**b**) TEM image of Pt-PPD coordination polymer nano-sphere; reprinted with the permission from [105]. Copyright 2005 American Chemical Society (**c**) Optical microscopy image and (**d**, **e**) fluorescence microscopy images of M-BMSB coordination polymer nano-sphere. Reprinted by permission from Macmillan Publishers Ltd.: [104], copyright 2005

first dissolved in a solvent. During the growth process, the coordination polymer nanoparticle will precipitate out when the size reaches a critical value [111]. Addition of a less solubilizing solvent may be necessary when the coordination polymer formed remains in the original solvent [104, 112]. Mirkin proposed a cluster-fusion growth mechanism for the precipitation method based on time-resolved SEM images [104, 112] (Fig. 33). It involves nucleation in the first step, followed by oligomerization of the precursors to form seed particles, aggregations of the seeds to form initial particles, fusion of the initial particles to form larger but rough particles, and finally, annealing of the rough particles to produce nanoparticles of smooth surface [107].

The first example of nanoscale LnMOF prepared by the precipitation method was reported by Lin and coworkers in 2008 [113]. The nanoparticles were synthesized by first mixing $TbCl_3$ and (diaminedichlorodisuccinato)Pt(IV) (DSCP), an analog of the prolific anticancer drug cisplatin, in an aqueous solution followed by pH adjustment with NaOH to initiate the reaction. The nanoscale particles

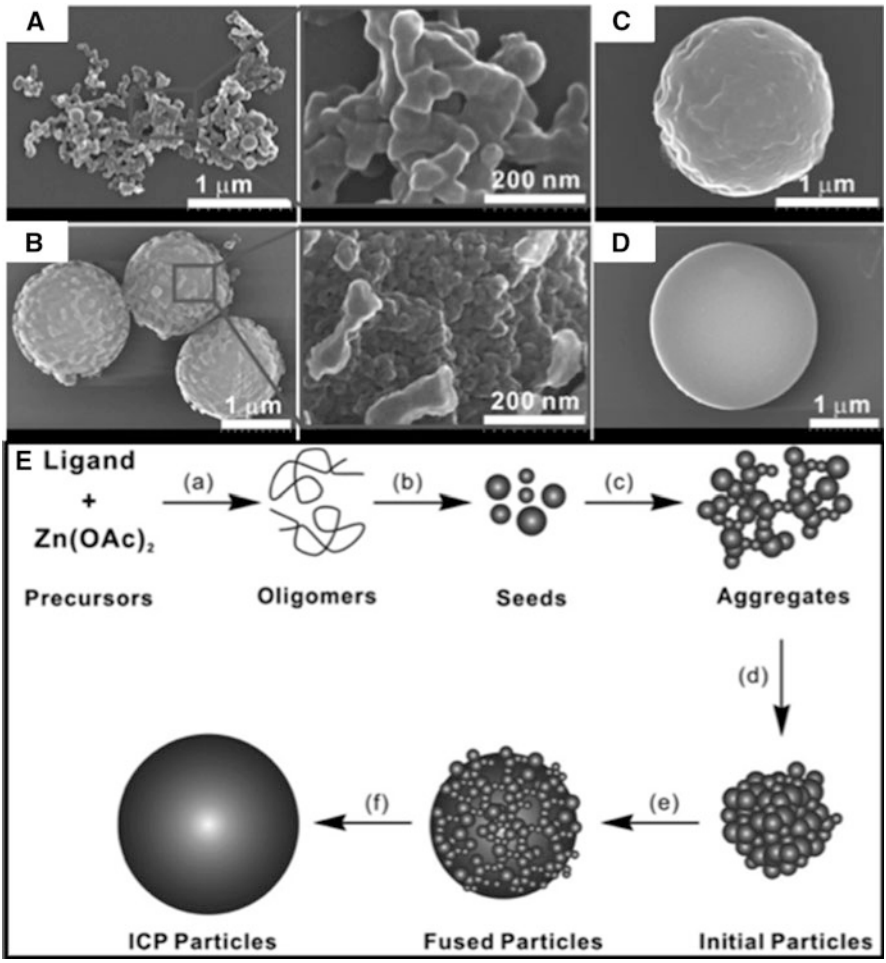

Fig. 33 Time-resolved SEM images (**a**–**d**) of the formation process of Zn-based coordination polymer nano-sphere and a schematic representation (**e**) of the proposed cluster-fusion growth mechanism. Reproduced from [112] by permission of John Wiley & Sons Ltd.

precipitated out upon addition of methanol (Fig. 34). The as-synthesized nanoparticles have a diameter of 52.8 ± 8.1 nm as evidenced by dynamic light scattering studies and transmission electron microscopy. However, the formation of nanoparticle is highly reversible by adding excess water since the final product was soluble in water. In order to make the as-synthesized nanoparticles stable enough for in vivo applications, coating with amorphous thin layer of silica by the well-established sol–gel process was performed. Also a targeting moiety c(RGDfK) was also grafted onto the surface to improve cellular uptake by tumor cells.

Another early example of amorphous nanoscale LnMOFs was reported by Kimizuka and coworkers in which the authors explored the adaptive inclusion

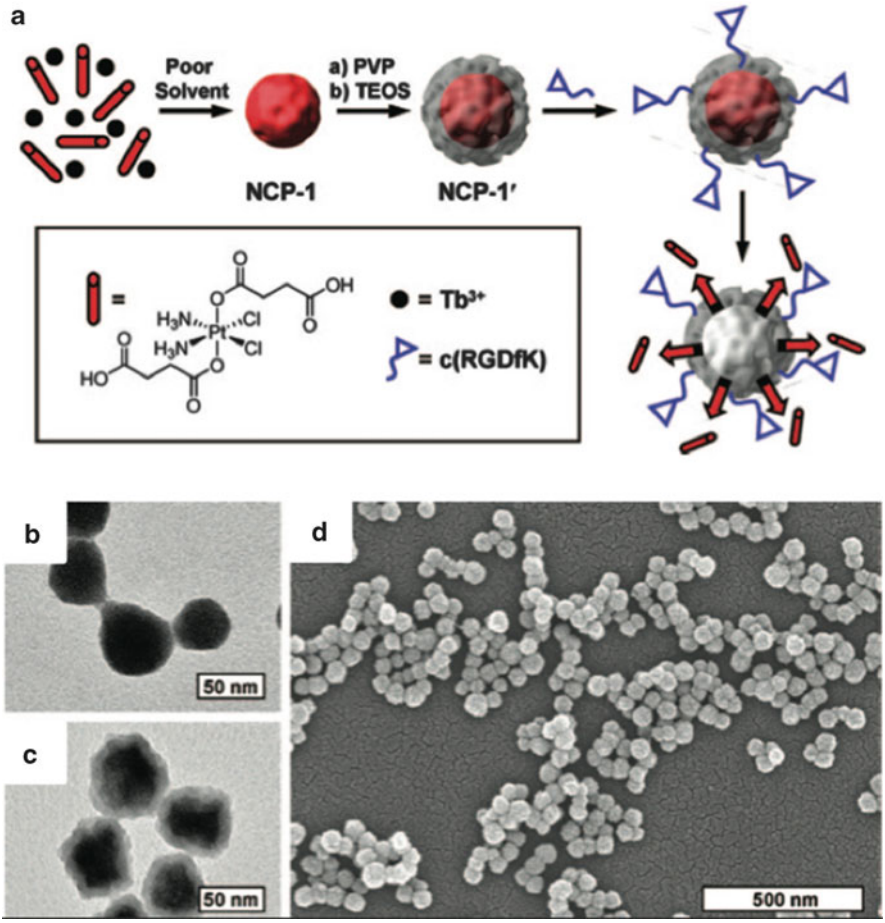

Fig. 34 (**a**) A schematic representation of the synthesis and surface modification of Tb-DSCP nanoparticle; (**b**) TEM image of the as-synthesized Tb-DSCP nanoparticle; (**c**) TEM image; and (**d**) SEM image of silica coated Tb-DSCP nanoparticle. Reprinted with the permission from [113]. Copyright 2008 American Chemical Society

properties of synthesized nanoparticles [111]. Nucleotides were utilized as the linker because they not only acted as bidentate ligands but also possessed superior biocompatibility and multiple functional groups. To prepare the nucleotide-lanthanide nanoparticles, an aqueous solution of $LnCl_3$ (Ln = Tb, Gd) was added to nucleotide HEPES buffer solution at room temperature (Fig. 35). The formed nanoparticle was collected as precipitate by centrifugation. Powder X-ray diffraction studies showed no sharp diffraction peaks, thus confirming the amorphous nature of the as-synthesized nanoparticles. Functional moieties such as dye molecules, proteins, and gold nanoparticles were incorporated in situ into the

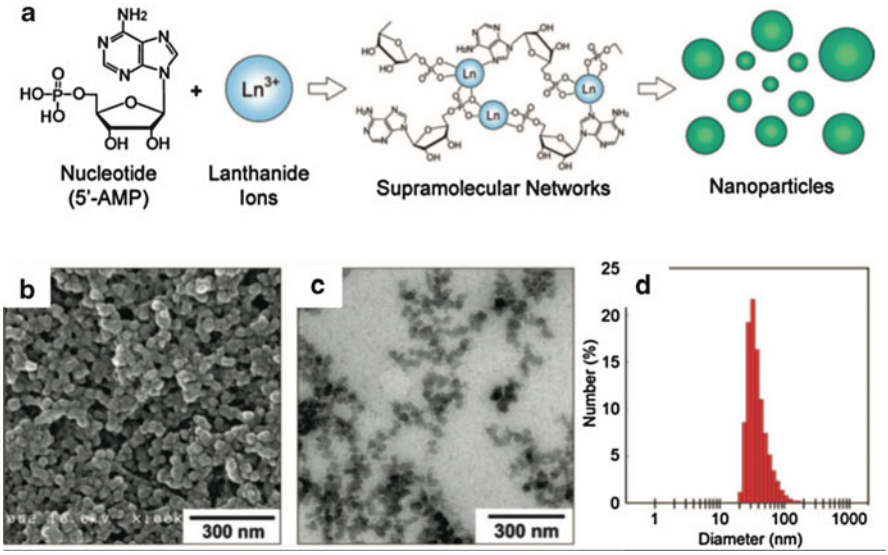

Fig. 35 (**a**) A schematic representation of the synthesis of lanthanide-nucleotide nanoparticle; (**b**) SEM image and (**c**) TEM image of 5′-AMP/Gd^{3+} nanoparticles; (**d**) Size distribution histogram obtained by DLS measurement. Reprinted with the permission from [111]. Copyright 2009 American Chemical Society

Ln-nucleotide nanoparticles, making the system promising for a variety of biomedical applications.

Later, other groups successfully utilized the precipitation method to synthesize nanocrystalline LnMOFs. The procedure is similar to the one developed for amorphous nanoscale LnMOFs. However, the reaction duration is generally much longer than in the amorphous case, allowing the seeds to grow into crystalline nanostructures. You and coworkers conducted using scanning electron microscopy a time-resolved study of the formation of the ultra-long nanobelts $Y_4(1,2\text{-BDC})_6(H_2O)_2{\cdot}5H_2O$ (1,2-BDC = 1,2-benzenedicarboxylate) [114] (Fig. 36). Small amorphous nanorods were formed initially due to oversaturation. As the reaction progressed, these amorphous nanorods grew anisotropically into crystalline ultra-long nanobelts. The as-synthesized nanobelts have a dimension of 100–150 nm in widths, 20–40 nm in thickness, and up to several hundred micrometers in length.

The same group of researchers also reported a thorough study of size/morphology control of nanocrystalline $La(1,3,5\text{-BTC})(H_2O)_6$ MOF (1,3,5-BTC = 1,3,5-benzenetricarboxylate) by monitoring the effects of changing concentration, molar ratio of precursors, and the composition of solvent [115]. It has been found that the flower-shaped nanoparticles formed at lower precursor concentrations (Fig. 37a) evolved into a more splitting, wheatear-like structure, and finally individual nanorods as the precursor concentrations increased. They rationalized this observation with a “crystal splitting” mechanism proposed by Alivisatos on the

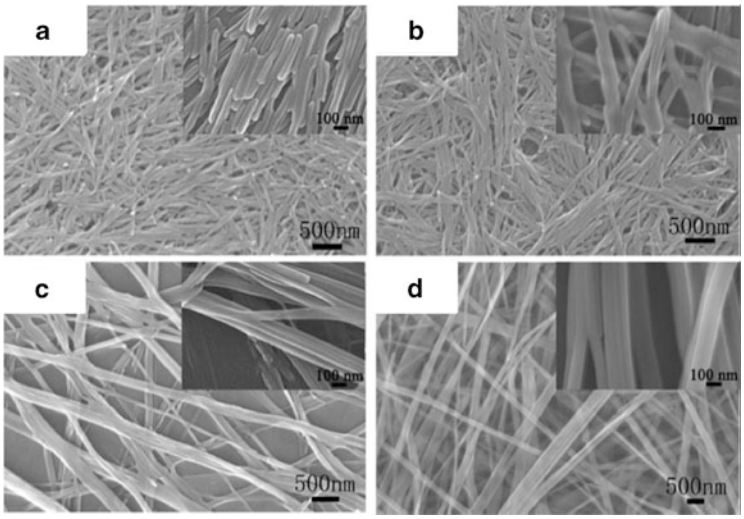

Fig. 36 SEM images of the sample $Y_4(1,2\text{-BDC})_6(H_2O)_2{\cdot}5H_2O$ at different growth stages: (**a**) 0.5 min; (**b**) 1 min; (**c**) 10 min; (**d**) 30 min. Reproduced from [114] by permission of The Royal Society of Chemistry

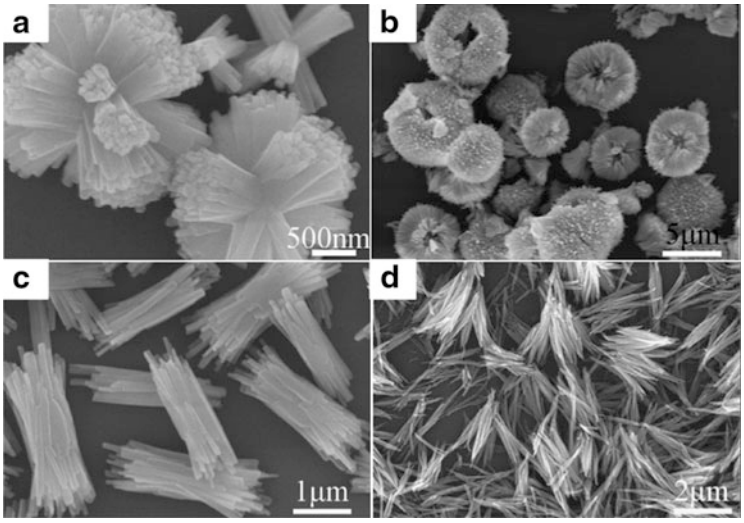

Fig. 37 (**a**) La(1,3,5-BTC)$(H_2O)_6$ MOF nano particles synthesized with La:1,3,5-BTC molar ratio 1:1 in a water:ethanol (v:v) 1:1 solvent system; (**b**) La(1,3,5-BTC)$(H_2O)_6$ MOF nano particles synthesized with La:1,3,5-BTC molar ratio 4:1 under otherwise same condition (in **a**); (**c**) La(1,3,5-BTC)$(H_2O)_6$ MOF nanoparticles synthesized when PVP was added in the reaction system; (**d**) La(1,3,5-BTC)$(H_2O)_6$ MOF nanoparticles synthesized when the solvent composition changes to water:ethanol (v:v) 3:1. Reprinted from [115]. Copyright 2010, with permission from Elsevier

formation of Bi_2S_3 nanostructures [116]. When the precursor concentration increased, crystal growth rate was enhanced, leading to crystal splitting. However, when the concentration further increased to a certain level, more crystal seeds formed during the nucleation process, and splitting growth was inhibited, in which case individual nanorods would be anticipated to form. Regarding the effect of precursor molar ratio on product morphology, when the molar ratio of La:1,3,5-BTC increased from 1:1 to 4:1, the morphology of the nanoparticles evolved from flower-like shape into sphere clusters composed of smaller nanorods (Fig. 37b). On the other hand, when the precursor molar ratio and concentration constant were kept constant, changing the solvent from water:ethanol (v:v) 1:1 to 3:1 led to the morphology change from flower-like shape to a tail-like shape (Fig. 37d).

Nanocrystalline LnMOFs of other morphologies have also been synthesized (Fig. 38). For example, Meyer and coworkers reported block-shaped particles of $[Ln_2(DHBQ)_3]\cdot 24H_2O$ (DHBQ = 2,5-dihydroxy-1,4-benzoquinone) with a {diameter around 4 μm and explored their further transformation into lanthanide oxide ceramics [117]; Wen and coworkers reported $Ln(BTC)(H_2O)_6$ (BTC = 1,3,5-benzenetricarboxylic acid) nanorods of 50–200 nm in width, 50–100 nm in thickness, and 1–2 μm in length [118]. Wong and coworkers synthesized flower-shaped $[Eu_2(bqdc)_3(H_2O)(DMF)_3]\cdot 0.5DMF\cdot H_2O$ (bqdc =

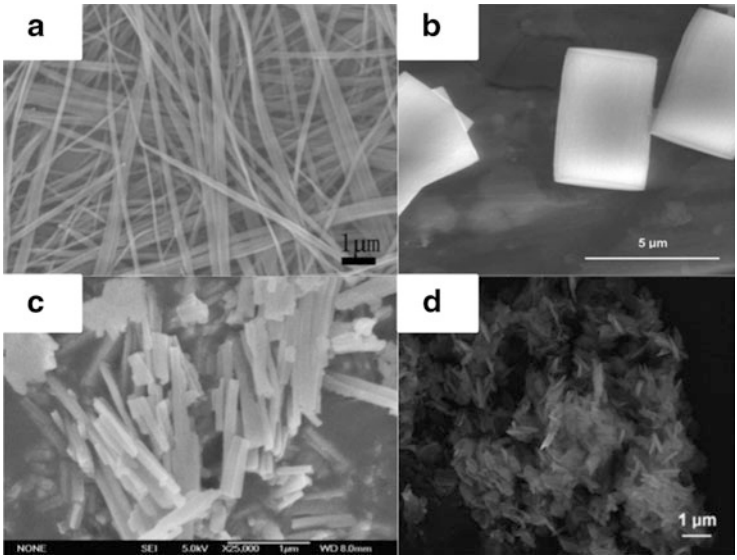

Fig. 38 SEM images of Ln nano MOFs with different morphology synthesized with precipitation method: (**a**) $Y_4(1,2\text{-BDC})_6(H_2O)_2\cdot 5H_2O$ ultra-long nanobelts; (**b**) $[Ln_2(DHBQ)_3]\cdot 24H_2O$ MOF blocks; (**c**) $Ln(BTC)(H_2O)_6$ nanorods; (**d**) $[Eu_2(bqdc)_3(H_2O)(DMF)_3]\cdot 0.5DMF\cdot H_2O$ nanoflowers. Reproduced from [114] by permission of The Royal Society of Chemistry. Reproduced from [117] by permission of John Wiley & Sons Ltd. Reprinted from [118], with kind permission from Springer Science+Business Media. Reproduced from [119] by permission of The Royal Society of Chemistry

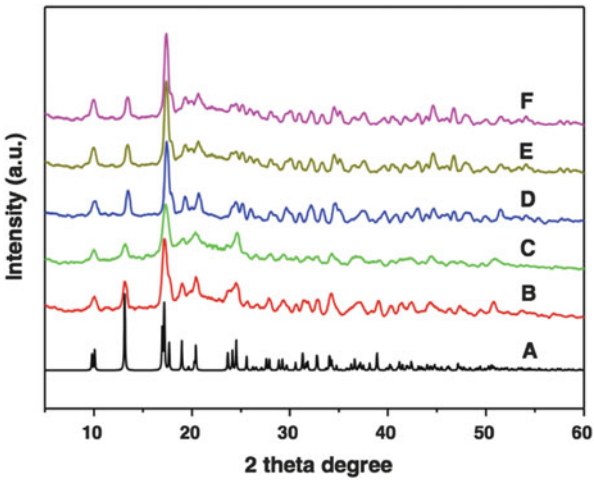

Fig. 39 Simulated powder XRD pattern (*A*) of La $(BTC)(H_2O)_6$ using single-crystal XRD data and experimental powder XRD patterns of $Ln(BTC)(H_2O)_6$, Ln = (*B*) La, (*C*) Ce, (*D*) Eu, (*E*) Gd, (*F*) Dy. Reprinted from [118], with kind permission from Springer Science+Business Media

2,2′-biquinoline-4,4′-dicarboxylate) nano MOF [119], followed by its fabrication into film deposited onto an ITO substrate for convenient sensing of Hg^{2+} based change of Eu(III)-based luminescence.

In order to determine the structure of the nanocrystalline LnMOFs at molecular level, single crystals of the MOF are first to be synthesized by traditional solvothermal method and analyzed with single-crystal XRD from which powder X-ray diffraction patters can be generated for comparison with experimentally obtained patterns for the nanocrystalline sample to verify its phase purity (Fig. 39). Due to the nanosized effects, peaks from the nanocrystalline sample are noticeably broadened when compared with the corresponding bulk solids.

The precipitation method is facile and energy-efficient with which large-scale preparation of nanoscale LnMOFs can be achieved. We also recognize the success, albeit limited, of obtaining nanocrystals by the precipitation methods, but the high likeliness of getting amorphous rather than the generally more desirable nanocrystalline samples prompted researchers to look for alternative synthetic routes. Also driving such efforts are the difficulties in controlling the size and morphology of the materials; these parameters, most significant for their properties and applications, have been found to be profoundly influenced by reaction conditions.

4.1.2 Reverse Microemulsion

Microemulsion and reverse microemulsion methods have long been developed to synthesize nanoscale materials [120]. In the former, surfactant molecules are dispersed in water to produce oil droplets, whereas in the latter, water droplets are dispersed in the bulk organic phase. Depending on the solubility of precursors (hydrophobic or hydrophilic), microemulsion (for hydrophobic precursors) or reverse microemulsion (for hydrophilic precursors) will be utilized. The droplets

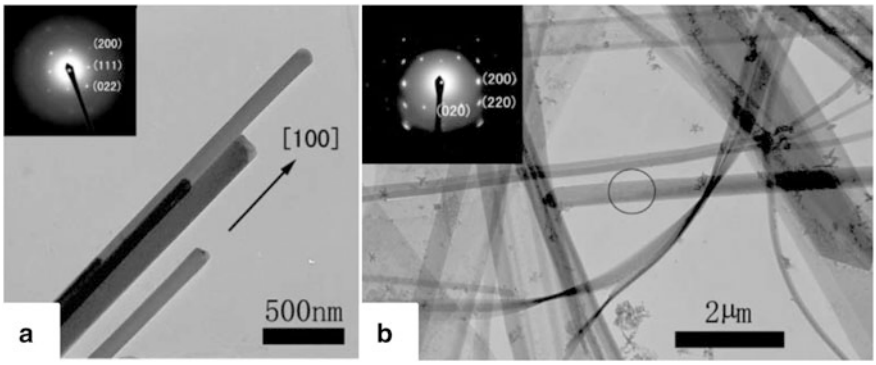

Fig. 40 (**a**) $SmFe(CN)_6{\cdot}4H_2O$ nanorods synthesized when NP-5 was used as surfactant; (**b**) $SmFe(CN)_6{\cdot}4H_2O$ long nanobelts synthesized when CTAB/*n*-hexanol was used as surfactant. Reproduced from [121] by permission of The Royal Society of Chemistry

in these suspensions are usually at nanometer scale, thus acting as a "soft template" for the growth of nanoparticles from the dissolved precursors. Since the growth of nanoparticle is highly restricted within the nanosized droplets, compared to the direct precipitation method, microemulsion or reverse microemulsion method provides a better control over size and morphology of the resulting nanoparticles through controlling the amount of surfactants used. The (reverse) microemulsion methods have been successfully applied for the preparation of nanoscale LnMOFs.

Reverse Microemulsion Synthesis of Nanoscale LnMOFs Under Ambient Conditions

Regarding the preparation of nanoscale LnMOFs using reverse microemulsion synthesis, the prototype was the synthesis of nanoscale lanthanide Prussian blue analog $SmFe(CN)_6{\cdot}4H_2O$ reported by Gao and coworkers [121]. Specifically, a reverse microemulsion system composed of cyclohexane, water, and polyoxyethylene (5) nonylphenyl ether (NP-5) as the surfactant was prepared, with $SmCl_3$ and $K_3Fe(CN)_6$ dissolved in the aqueous phase. This mixture was allowed to react at 50°C for 24 h to produce nanorods of $SmFe(CN)_6{\cdot}4H_2O$ with diameter ranging from 75 to 150 nm and an aspect-ratios of about 20–30 (Fig. 40a). On the other hand, when cetyltrimethylammonium bromide (CTAB) and *n*-hexanol were used as co-surfactants instead of NP-5, longer but thinner nanobelts with lengths up to several tens of micrometers, widths about 300 nm and thickness less than 20 nm were obtained (Fig 9b).

Shortly after the work by Gao and coworkers, Lin and coworkers reported the first synthesis of lanthanide-only nanoscale MOFs using the reverse microemulsion method [122]. In this work, a reverse microemulsion system composed of isooctane, 1-hexane and water with $LnCl_3$, and organic ligand salts dissolved in water phase was stabilized by CTAB. Precursors were allowed to react in the system for

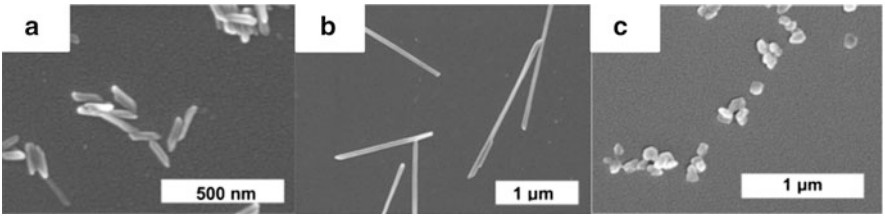

Fig. 41 SEM images of: $Gd(BDC)_{1.5}(H_2O)_2$ nanorods synthesized with $w = 5$ (**a**) and $w = 10$ (**b**); $[Gd(1,2,4\text{-BTC})(H_2O)_3]\cdot H_2O$ nanoplates. Reprinted with the permission from [122]. Copyright 2006 American Chemical Society

2 h at room temperature, followed by separating nanoparticles of the LnMOFs by centrifugation. Rod-shaped $Gd(BDC)_{1.5}(H_2O)_2$ (BDC = 1,4-benzenedicarboxylate) and irregularly shaped $[Gd(1,2,4\text{-BTC})(H_2O)_3]\cdot H_2O$ (1,2,4-BTC = 1,2,4-benzenetricarboxylate) nanoplates were synthesized (Fig. 41). The authors also explored tuning morphology of the nanoparticles by adjusting water/surfactant molar ratio (defined as w value). For example, nanorods with a dimension of 100–125 nm in length and 40 nm in diameter were synthesized when $w = 5$ (Fig. 41a), while longer nanorods of 1–2 μm in length and 100 nm in diameter were obtained with $w = 10$ (Fig. 41b).

Other researchers have used similar methods to prepare other nanoscale LnMOFs as promising functional materials. For example, Carlos and coworkers obtained the nanorods of $Tb_xEu_{1-x}(1,4\text{-BDC})_{1.5}(H_2O)_2$, a heterolanthanide MOF through reverse microemulsion method with CTAB as the surfactant and further explored the application of such materials as ratiometric luminescent nanothermometer [123]; Petoud also used similar CTAB-stabilized reverse microemulsion to obtain the nanocrystals of Yb-PVDC-3 (PVDC-3 = phenylenevinylenedicarboxylate-3), also a lanthanide-containing MOF, for potential use as fluorophore in the near-infrared imaging in living cells [124].

Reverse Microemulsion Synthesis of Nanoscale LnMOFs Under Solvothermal Conditions

Notwithstanding the initial success of reverse microemulsion synthesis at room temperature for nanoscale LnMOFs, the method is quickly found to be limited to just a few metal-ligand combination with frequent production of amorphous materials [125]. As a solution, Lin and coworkers developed reverse microemulsion synthesis at elevated temperatures and pressure, which was first proposed by geochemists as solvothermal (or hydrothermal) reaction [126]. Since the mid 1990s, solvothermal and hydrothermal syntheses have been developed rapidly for the preparation of inorganic nanomaterials, including nanoparticles of semiconducting materials, oxides, fluorides, or noble metal nanocrystals [126, 127]. The advantages of solvothermal thesis versus synthesis under ambient conditions are that crystalline

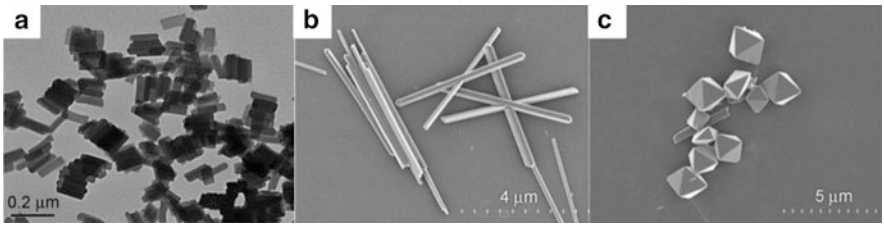

Fig. 42 (**a**) TEM image of $Gd_2(bhc)(H_2O)_6$ NMOFs; SEM images of $[Gd_2(bhc)(H_2O)_8](H_2O)_2$ NMOFs synthesized at (**b**) 60°C and (**c**) 120°C. Reproduced from [125] by permission of John Wiley & Sons Ltd.

products with well-defined structure at the molecular level are preferred due to the dominant thermodynamic control of the reaction process and the extension of reaction conditions to above the boiling point of the solvent, thus offering more opportunities to fine-tune the reaction parameters. In Lin's work, nanorods of $Gd_2(bhc)(H_2O)_6$ (bhc = benzenehexacarboxylate) were obtained in a $w = 10$ reverse microemulsion stabilized by CTAB at 120°C (Fig. 42a). In stark contrast, a reaction carried out under ambient but otherwise identical conditions yielded only amorphous materials with ill-defined morphologies, thus suggesting the advantage of conducting reverse microemulsion synthesis under hydrothermal conditions in order to obtain nanocrystalline LnMOFs. Furthermore, for the purpose of tuning particle morphology by changing reaction conditions, the authors compared the morphology of particles of $[Gd_2(bhc)(H_2O)_8](H_2O)_2$ obtained at 60 and 120°C (Fig. 42b, c). Long nanorods were obtained at 60°C, while octahedron nanoparticles were obtained at 120°C.

This method was also utilized by others. For example, Zhu and coworkers synthesized the nanorods of $Eu_2(1,3\text{-}BDC)_3(H_2O)_2$ through reverse microemulsion hydrothermal synthesis. The interesting LnMOF has been shown to be potentially useful as sensors for the detection of nitroaromatic explosive [128].

Size/Morphology Control of Nanocrystalline LnMOFs

For the works mentioned in earlier sections of reverse microemulsion synthesis, the surfactants used simply act as soft template to provide a nanoscale environment for the growth of the particles. As a result, the size/morphology of the final products is dominated by the properties of the reverse micelles; the ability to tune the properties of the product particles is thus limited.

An important lesson learned from the synthesis of colloidal inorganic nanoparticles is that different components of the reaction mixture including organic capping ligands [129], metal ions [130], and/or counter anions [131] could selectively bind to certain crystal face and therefore facilitate anisotropic growth to produce nanoparticles of various sizes and morphologies. This knowledge has been applied to the control of size/morphology for the nanoparticles of LnMOFs. For

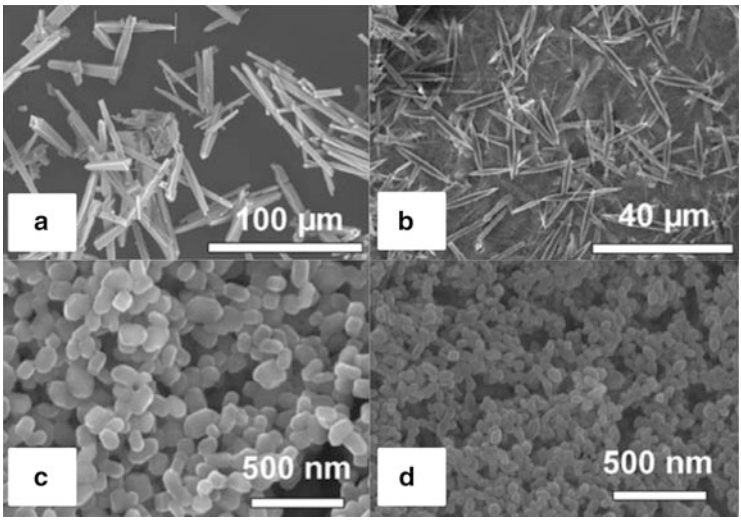

Fig. 43 SEM images of: (**a**) *Rod-shape* bulk $Eu_{1-x}Tb_x(BTC)(H_2O)$ crystals; (**b**) As-synthesized $Eu_{1-x}Tb_x(BTC)(H_2O)$ microrods when sodium oxalate was added as capping ligand; (**c**) As-synthesized *bean-shape* $Eu_{1-x}Tb_x(BTC)(H_2O)$ nanoparticles when sodium formate was added as capping ligand; (**d**) As-synthesized $Eu_{1-x}Tb_x(BTC)(H_2O)$ nanoparticles when sodium acetate was added as capping ligand. Reproduced from [132] by permission of John Wiley & Sons Ltd.

example, Zhang and coworkers reported the use of carboxylate as capping ligand to tune the morphology of $Eu_{1-x}Tb_x(BTC)(H_2O)$ nanoparticles [132]. Compared with the rod-like crystals synthesized in the absence of such ligand (Fig. 43a), much shorter and thinner rods of $Eu_{1-x}Tb_x(BTC)(H_2O)$ were obtained when oxalate was added as capping ligand (Fig. 43b). When sodium formate was added as capping ligand, bean-shaped nanoparticles with length of 125 ± 25 nm and width of 100 ± 15 nm were obtained. Even smaller particles (length and width of 90 ± 15 nm and 70 ± 10 nm, respectively) were obtained when sodium acetate was used in a similar capacity. These observations have been rationalized in terms of two competing processes during the growth of nanocrystals: metal ion complexation with the MOF-building bridging ligand(s) and coordination with the capping ligand. The effects of the competitive coordination by the capping ligand are twofold. On the one hand, the use of a capping ligand offers additional binding of the lanthanide ions, thus creating more crystallization nuclei than when such ligands are absent; crystal growth is general impeded, and smaller crystals are formed. On the other hand, the capping ligands generally have a smaller denticity than the framework linkers, and thus tend to terminate the growth of crystals by binding to the crystal's surface. Experimental observations are consistent with such analysis: The particle size of the $Eu_{1-x}Tb_x(BTC)(H_2O)$ MOF was significantly reduced when capping ligands were added. In addition, when monodentate capping ligands (formate and

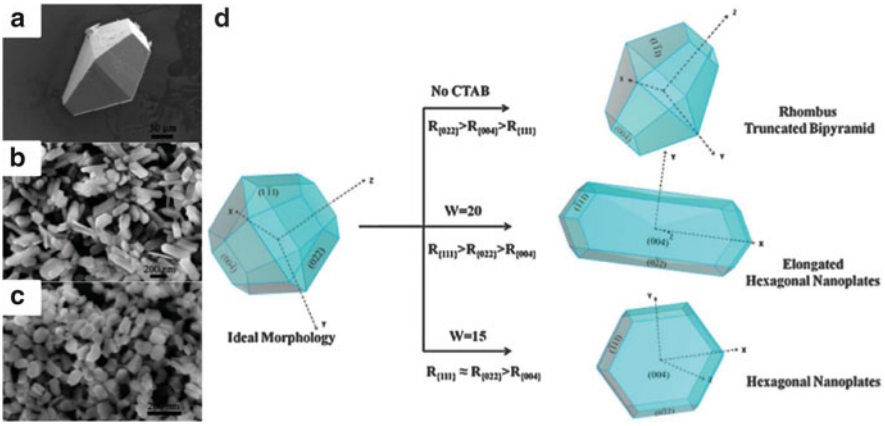

Fig. 44 (**a**) SEM image of bulk $Eu_2(FMA)_2(OX)(H_2O)_4{\cdot}4H_2O$ MOF crystal synthesized without CTAB; SEM images of $Eu_2(FMA)_2(OX)(H_2O)_4{\cdot}4H_2O$ MOF, (**b**) nanorods synthesized with CTAB at $w = 20$, and (**c**) nanoplates synthesized with CTAB at $w = 15$, (**d**) Schematic illustration of morphology control modulated by capping ligand at different w values. Reproduced from [133] by permission of The Royal Society of Chemistry

acetate) were used, the particle size was reduced with respect to when oxalate was used.

In the work by Qian and coworkers [133], the influence of capping ligand on the morphology of the nanoparticles of an LnMOF, $Eu_2(FMA)_2(OX)(H_2O)_4{\cdot}4H_2O$ (FMA = fumarate, OX = oxalate), was studied. The bulk crystal has the shape of a rhombic truncated bipyramid (Fig. 44a). When CTAB was added as capping ligand with a w value of 20, nanorods were obtained (Fig. 44b). Further increasing the amount of CTAB to $w = 15$ led to the formation of hexagonal nanoplates (Fig. 44c). To rationalize the observed change of crystal shape upon the use of capping ligand, the authors first derived the morphology of bulk crystal from its ideal crystallography morphology using Bravais–Friedel–Donnay–Harker (BFDH) method [134]. There are three possible growing facets in an ideal $Eu_2(FMA)_2(OX)(H_2O)_4{\cdot}4H_2O$ MOF crystal: {022}, {004}, and {111}. Without any interference, the growth rates of the three facets are in the increasing order of $R_{\{022\}} > R_{\{004\}} > R_{\{111\}}$. Therefore in the final crystal, the morphology was dominated by {004} and {111} facet while {022} facet disappeared due to rapid growth along the normal direction. When capping CTAB ligand was present, the preferred binding to the {022} and {004} facets to the {111} facet mitigated the growth along these two facets, giving rise to the eventual formation of the nanorod product. As the amount of CTAB increased, it started to slow down the growth along the {111} facet as it also binds to this particular facet. As a result, the morphology of the final crystal was dominated by {004}, producing the hexagonal nanoplates.

With the ability to control the size and morphology of nanoparticles, the use of surfactants also brings some problems. Most commonly used surfactants are highly toxic to aquatic organism and skin-corrosive when in direct contact due to their

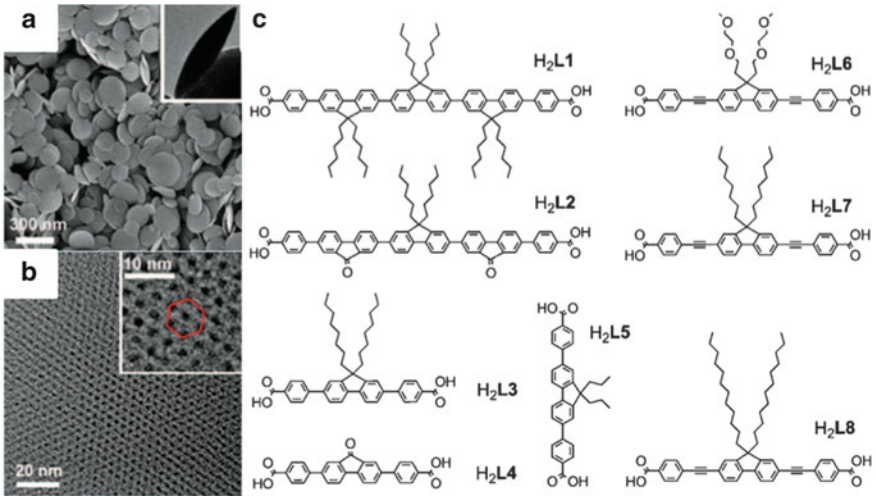

Fig. 45 (**a**) SEM and TEM (*inset*) images of Eu-**L1** MOF nanoplates; (**b**) HRTEM image of Eu-**L1** MOF nanoplates with well-resolved pores packed in hexagonal pattern; (**c**) Chemical structures of the ligands explored. Reproduced from [135] by permission of John Wiley & Sons Ltd.

similarity to lipid bilayer in cells, making waste management an expensive challenge. On the other hand, by capping surfactant molecules usually block active sites that are most critical for catalysis and sensing for which additional post-synthesis modification of the as-prepared nanoparticles is generally required.

Creatively this potential drawback of using surfactants has been addressed by grafting surfactant-like groups onto the MOF-building bridging ligands as unlike inorganic materials, MOFs are a type of inorganic–organic hybrids with organic linking group being an integral part of the molecular architecture and can be judiciously modified to suit various needs. For example, Uvdal and coworkers grafted different numbers of alkyl chains with various lengths onto phenyl dicarboxylic acid and explored their influence on the corresponding LnMOF nanoparticles [135]. In a typical synthesis, lanthanide acetate in DMF was added dropwise into heated DMF solution of alkyl chain-modified phenyl dicarboxylic acid under continuous stirring. Nanoparticles of LnMOFs, obtained as a precipitate, have been shown to be nanoplates with a diameter of around 300 nm (Fig. 45a). Large pores around 2 nm, orderly packed into a hexagonal pattern, are clearly shown in the high-resolution TEM images (Fig. 45b).

When exploring the effects of alkyl chains on the LnMOF nanoparticles, two factors were taken into consideration: the number of alkyl chains on each phenyl dicarboxylic acid ligand and the length of the alkyl chains. It has been found that longer alkyl chains and a higher number of alkyl groups per ligand produce nanoparticles of higher crystallinity and less aggregation. For example, H_2**L1** and H_2**L2** have alkyl chains of the same length, but the former possesses six chains

versus two in the latter (Fig. 45c). Powder XRD patterns and SEM images both point to the nanoparticles of Ln-**L1** MOF being more crystalline than those of Ln-**L2** MOF. When the effect of alkyl chain length was assessed, comparative studies between Ln-**L3** and Ln-**L5** MOFs showed that more crystalline nanoparticles of Ln-**L3** with the ligand equipped with longer alkyl chains were produced (Fig. 45c).

4.1.3 Sonochemical Synthesis of Nanoscale LnMOFs

Sonochemical synthesis has gain popularity in organic synthesis [136] and in the production of semiconductor materials [137] due to typically reaction duration and easy operation. Suslick and coworkers thoroughly studied the mechanisms [138–140] for which a phenomenon of "acoustic cavitation" is identified as essential. Briefly, ultrasonication produces in a liquid bubbles that go through a complete cycle of formation, growth, and collapse. During the bubble collapsing, localized hot spots with extremely high temperature (around 5,000 K), pressure (over 1,000 atm), and heating/cooling rate (around 10^{10} K/s) are generalized, leading to rapid molecular movement, bond breaking and formation, and generation of free radicals, and therefore quick reactions. With ultrasonication, reactions requiring highly demanding conditions and even those that are considered impossible under normal conditions are made possible.

Jiang and coworkers are the first to apply sonochemical synthesis for the production of nanosized MOFs [141]. Nanospheres and nanoribbons of $Zn_3(BTC)_2{\cdot}12H_2O$ were obtained in high yields by sonicating a mixture of zinc acetate and H_3BTC in water/ethanol for less than 90 min under ambient conditions; no products were obtained without sonication. In comparisons, a traditional hydrothermal synthesis using the same reaction mixture produced only bulk materials at an elevated temperature (140°C) and over a much longer reaction period (24 h).

Sonochemical synthesis of nanoparticles of LnMOFs appeared shortly after. Jhung and coworkers first reported the sonochemical preparation of nanorods of $Ln(BTC)(H_2O){\cdot}4.3(H_2O)$ (Ln-BTC) (Ln = Ce, Tb, Y) [142]. The as-synthesized samples showed comparable crystallinity to those obtained by the hydrothermal method (Fig. 46b). Based on a time-resolved powder XRD study, the authors also found that when different metal ions were utilized (Y^{3+}, Tb^{3+}, Ce^{3+}), the nucleation and crystal growth rate differ significantly in the increasing order of $Ce^{3+} \gg Tb^{3+} > Y^{3+}$. This observation was rationalized in terms of the lability of the metal ions: The more labile Ce^{3+} coordinates much more facilely with BTC ligand, causing a much faster nucleation and crystal growth.

Zhu and coworkers reported a very similar work but a much longer sonication duration was utilized (up to 140 min) [143]. The authors studied the influence of sonication time on product morphology and found that nanoparticles of $Tb(BTC)(H_2O)_6$ MOF evolved from nanorods of low crystallinity to highly crystalline nanorods, and eventually to much longer nanowires with extended sonication (Fig. 47).

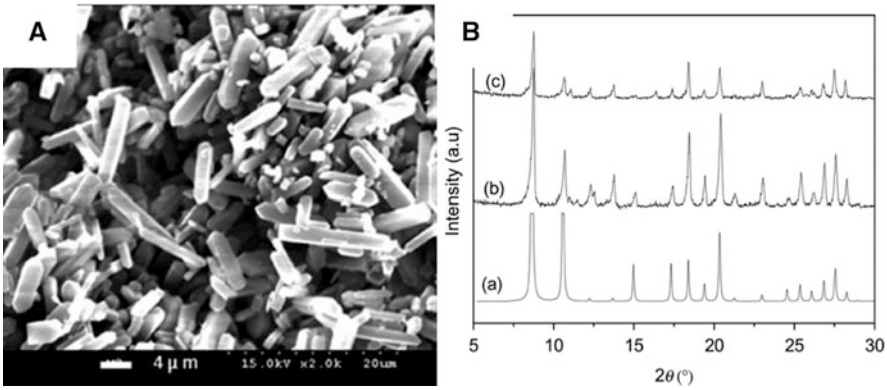

Fig. 46 (**A**) FE-SEM image of Tb-BTC MOF nanorods synthesized sonication for 20 min at room temperature; (**B**) Simulated Y-BTC powder XRD pattern (*a*), powder XRD pattern of Tb-BTC synthesized with hydrothermal method (*b*), powder XRD pattern of Tb-BTC synthesized with sonochemical method (*c*). Reproduced from [142] by permission of John Wiley & Sons Ltd.

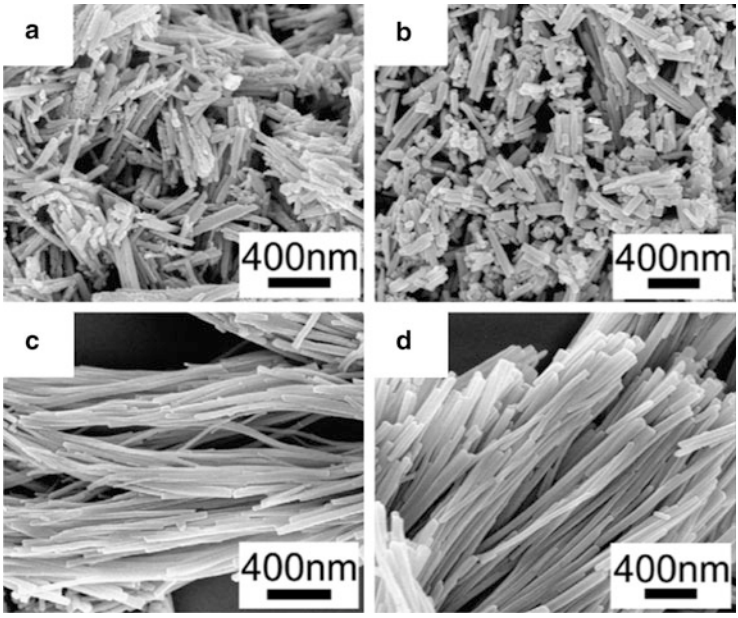

Fig. 47 SEM images of $Tb(BTC)(H_2O)_6$ MOF synthesized under sonication for: (**a**) 30 min, (**b**) 60 min, (**c**) 90 min, (**d**) 140 min. Reprinted from [143], Copyright 2012, with permission from Elsevier

Very recently, Jiang and coworkers developed a combined ultrasound-vapor phase diffusion method for the synthesis of LnMOF nanoparticles [144]. An open vial containing an aqueous solution of triethylamine (TEA) was placed in the beaker that contains a mixture of $TbCl_3$ and H_3BTC, and the whole setup was

sonicated. Nanoparticles of Tb(BTC) MOF were obtained in high yield (65.7%) after only 2 min. In comparison, in the absence of TEA and even much extended reaction time (60–90 min) but under otherwise identical conditions, the nanoparticles were obtained only in very low yield (0.6–7.2%). Apparently deprotonation of the H_3BTC ligand is the rate-determining step and with the assistance of TEA, the reaction was much facilitated. However, sonochemical synthesis of nanoparticles of LnMOF is so far limited to the sole report by Jiang [144], and much work remains to be done.

4.1.4 Incorporating Ln^{III} Ions into Nanoscale MOFs by Post-synthetic Modification

Due to the large number of coordination sites on lanthanide ions, they tend to coordinate with maximum numbers of organic ligand. Therefore lanthanide-based MOFs are usually quite dense at the molecular level, and the MOF porosity is not as high as in the MOFs constructed with the use of first-row transition metal ions. This limited porosity significantly compromises the potential applications of LnMOFs, for example, in catalysis and sensing. A possible solution is to incorporate lanthanide ions into pre-existing highly porous MOFs through post-synthetic modifications [145].

This method was successfully applied by Qian and coworkers in their recent work in which a thin film made with nanoparticles of a highly porous In-BTC MOF was soaked in a lanthanide nitrate solution to promote the diffusion of the lanthanide ions into the MOF crystal lattice and subsequent coordination by the free BTC carboxylate groups [146]. SEM images indicated that the original morphology of In-BTC nanoparticles was retained after post-synthetic modification (Fig. 48), and this lanthanide-modified thin film was shown to be an efficient sensor for the detection of thiols.

4.2 Properties and Applications of Nanoscale LnMOFs

Lanthanide-containing materials possess interesting properties and are promising for a wide of useful applications such as magnetic refrigeration [147], optical bio-imaging [148, 149], MRI imaging [150], telecommunication [151], NMR spectroscopy [152], solar cells [153], catalysis [154], information storage [155], and in organic synthesis [156]. Our discussions are limited to the properties and applications associated with the unique nanoscale LnMOFs, and readers interested in more general lanthanide-containing materials are referred to related reviews.

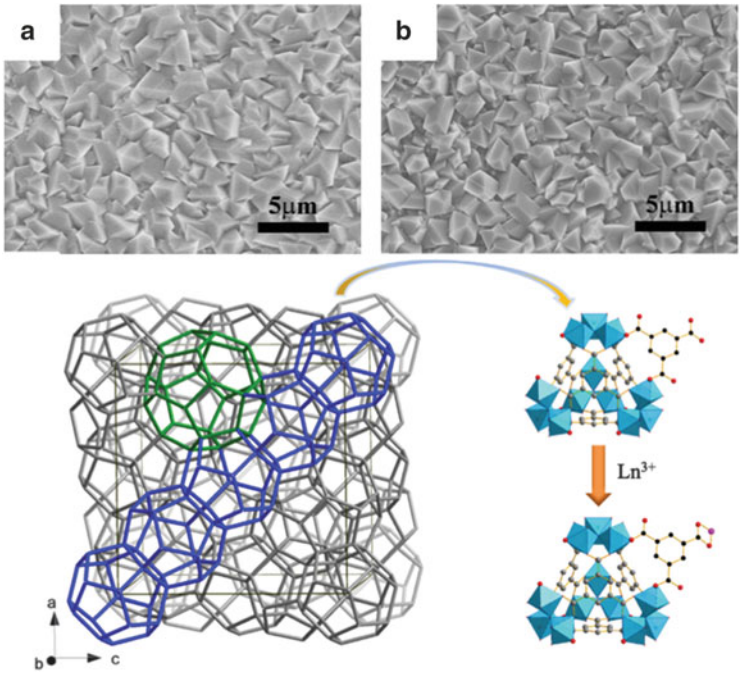

Fig. 48 SEM images of (**a**) In-BTC film and (**b**) Eu(III)-modified In-BTC film; (**c**) Schematic representation of structure of In-BTC MOF analog MIL-100 (*left*) and possible interaction mode between Ln^{3+} and BTC ligand in the MOF lattice. Reprinted from [146], Copyright 2013, with permission from Elsevier

4.2.1 Magnetic Properties and Application as MRI Contrast Agents

Magnetic resonance imaging (MRI) is one of the most widely used bio-imaging techniques. Compared with other imaging modalities such as X-ray computed tomography or optical imaging, MRI has the advantages of being non-invasive and the ability to achieve high spatial resolution with enhanced tissue penetration depth. In order to differentiate between normal and sites of interest, contrast agents which can target such sites are desired. There are two types of contrast agents, namely: $T1$ contrast agents, which are paramagnetic complexes like gadolinium chelates; and $T2$ contrast agents, which are superparamagnetic materials such as nanoparticles of iron oxide. Although "advances in MRI have strongly favored $T1$ agents" [150], nanoparticle-based $T2$ contrast agents are gaining an edge over traditional gadolinium chelate-based $T1$ agents thanks to their unique features such as easy uptake by macrophage and nonphagocytic cells and the achievement of targeted imaging made possible through surface modification by targeting functions of the nanoparticles [157]. Not surprisingly, there have been great efforts in the development of nanoparticle-based $T1$ contrast agents. This was first achieved by Lin and coworkers in the making and testing for MRI of nanorods of $Gd(BDC)_{1.5}(H_2O)_2$ [122]. These particles have been shown to possess high contrast

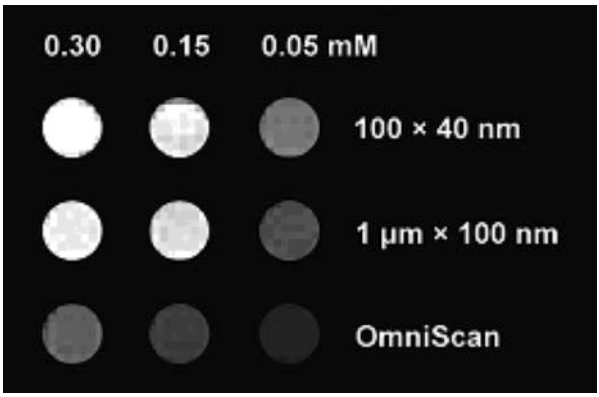

Fig. 49 The comparison of *T*1-weighted MR images between OmniScan, Gd $(BDC)_{1.5}(H_2O)_2$ MOF nanorods with dimensions of 100 × 40 nm and 1 μm × 100 nm respectively at different concentrations. Reprinted with the permission from [122]. Copyright 2006 American Chemical Society

ability. This initial stimulated additional work by both the authors and other researchers to further improve the performance of such nanoscale contrast agents through surface modification and by morphological control of the nanoparticles.

Particle Size and Contrast Ability

When proton is chosen as the nucleus for MRI imaging, one of the key factors determining the contrast ability of a *T*1 agent is the accessibility of water molecules to its paramagnetic center with greater accessibility leading to better interactions between water protons and paramagnetic metal centers which enhance local magnetic field and shorten the local proton longitudinal relaxation time, thus giving more positive enhancement of the signal. One unique feature offered by a nanomaterial is its high surface-to-volume ratio [158], which increases its accessibility to surrounding species. Therefore, smaller GdMOF nanoparticles are expected to exhibit higher *T*1 contrast ability.

This analysis was verified by the work of Lin and his coworkers [122]. By varying the water/surfactant molar ratio of the reaction mixture, nanorods of Gd $(BDC)_{1.5}(H_2O)_2$ MOF with different sizes and aspect-ratios were obtained. When compared with the clinically utilized OmniScan, a Gd(III) chelate-based *T*1 agent, all the nanorods showed a significant increase of local MR image brightness on a per mM Gd^{3+} base, with the smaller nanorods being more efficient (Fig. 49).

Surface Properties and Contrast Ability

Boyes and coworkers coated nanorods of $Gd(BDC)_{1.5}(H_2O)_2$ MOF with different RAFT polymers and conducted comparative studies of their contrast ability [159]. It has been found that nanorods coated with hydrophilic polymers possessed increased r_1 relaxivity, making them better *T*1 contrast agents, whereas those

Table 2 Experimental relaxivity data for clinical magnetic resonance imaging contrast agents, multihance, and magnevist, along with the unmodified and polymer modified gadolinium metal-organic framework nanoparticles

Contrast agent[a]	r_1 (s^{-1} mM^{-1})[b]	r_2 (s^{-1} mM^{-1})[b]	r_2/r_1
Magnevist	13.44	21.40	1.59
Multihance	19.45	30.44	1.57
Unmodified Gd MOF nanoparticles	9.86	17.94	1.82
PHPMA (5,327 g/mol) modified Gd MOF nanoparticles	17.81	25.77	1.45
PHPMA (10,281 g/mol) modified Gd MOF nanoparticles	32.94	44.85	1.36
PHPMA (19,370 g/mol) modified Gd MOF nanoparticles	105.36	129.63	1.23
PNIPAM (5,690 g/mol) modified Gd MOF nanoparticles	20.27	29.73	1.47
PNIPAM (8,606 g/mol) modified Gd MOF nanoparticles	46.99	64.10	1.36
PNIPAM (17,846 g/mol) modified Gd MOF nanoparticles	62.51	79.90	1.28
PSty (4,802 g/mol) modified Gd MOF nanoparticles	1.17	14.16	12.10
PSty (8,972 g/mol) modified Gd MOF nanoparticles	1.20	25.75	21.46
PSty (15,245 g/mol) modified Gd MOF nanoparticles	3.91	123.40	31.56
PDMAEA (15,120 g/mol) modified Gd MOF nanoparticles	37.20	54.17	1.46
PPEGMEA (19,542 g/mol) modified Gd MOF nanoparticles	59.93	81.55	1.36
PAA (10,888 g/mol) modified Gd MOF nanoparticles	21.30	31.82	1.49

Reprinted with the permission from [159]. Copyright 2009 American Chemical Society

[a]*PHPMA* poly[*N*-(2-hydroxypropyl) methacrylamide], *PNIPAM* poly(*N*-isopropylacrylamide), *PSty* polystyrene, *PDMAEA* poly-(2-(dimethylamino) ethyl acrylate), *PPEGMEA* poly(((poly) ethylene glycol methyl ether) acrylate), *PAA* poly(acrylic acid)

[b]Longitudinal relaxivity (r_1) and transverse relaxivity (r_2) values, calculated as the reciprocal values of the longitudinal relaxation time ($T1$) and transverse relaxation time ($T2$), respectively, of each of the contrast agents were determined with a 1.5 T scanner with samples diluted in deionized ultrafiltered water by acquiring signal intensity (I) measurements via region-of-interest analysis of the samples for all pulse sequences with $T1$ and $T2$ values being calculated using: $I_i = I_{o,I}\left(1 - \exp^{(-t/\mathrm{T}_i)}\right)$

coated with hydrophobic polymers showed a decrease in r_1 relaxivity but significantly increased r_2 relaxivity, making them good candidates as $T2$ agents (Table 2). The influence of water accessibility to paramagnetic metal centers on a $T1$ agent's contrast ability perfectly explained the increased r_1 relaxivity when hydrophilic polymers were utilized to coat these nanorods since hydrophilic layers had strong

water retention ability and helped improve water-metal center interactions. This explanation was also consistent with the trend of r_1 relaxivity increase along with increased molecular weight of the hydrophilic polymers; as the molecular weight of the hydrophilic polymers increased, the water retention ability increased correspondingly. For example, when the molecular weight of hydrophilic polymer PHPMA increased from 5,327 to 19,370 g/mol, the r_1 value of the coated nanorods of GdMOF increased from 17.81 to 105.36 s^{-1} mM^{-1} (Table 2).

Regarding the significantly increased r_2 relaxivity when hydrophobic polymers were utilized for coating, the authors rationalized this phenomenon with an outer-sphere dominated mechanism, that is, contrast was caused by susceptibility differences of the surroundings of the contrast agent and strongly varying local magnetic field. The hydrophobic polymer coating helped prevent interactions of water with Gd^{3+} ions, thus increasing the r_2 relaxivity, an improvement not possible with traditional Gd chelates.

4.2.2 Luminescence Properties and Related Applications

The luminescence properties of lanthanides have been studied extensively [160–162]. Compared with more familiar lanthanide-containing materials, luminescent nanoscale LnMOFs offer a number of unique features. For example, the porous structure grants target substances higher accessibility to sensing center; size/morphology control and surface tunability allow for controllable and target-specific in vivo sensing and imaging. Using selected examples of nanoscale LnMOFs, their unique luminescence-based applications are discussed below.

Nanothermometric Applications

Thermometry at the nanoscale has recently evolved into a very active field of research [163, 164]. This is due to an increasing demand of thermometry measurements at higher spatial resolution, which are not possible with traditional thermometers, for example, the measurement of intracellular temperature fluctuations and measurement of temperature in micro-electronics devices or microfluids [163]. Among all the nanoscale thermometers, responsive luminescence-based nanothermometers are most promising not only because of their ease of fabrication, quick response, accuracy, and high tolerance of interference, but also because of their versatile detection modes that make them widely applicable and compatible with a broad range of instruments [164].

Mixed-lanthanide luminescence thermometers are first introduced by Chen and coworkers [165]. They are based on temperature-dependence of phonon-assisted energy transfer from $^5D_4$ (Tb^{3+}) to $^5D_0$ (Eu^{3+}) in $Tb_{1-x}Eu_x(C_{13}H_7O_4N)(C_{13}H_8O_4N)(H_2O)_{2.5}$, a Tb^{3+}/Eu^{3+} co-doped MOF (Fig. 50a). The temperature to be measured could be calculated based on the emission intensity ratio between the $Tb^{3+5}D_4 \rightarrow {}^7F_5$ and $Eu^{3+5}D_0 \rightarrow {}^7F_2$ transitions. This ratiometric measurement

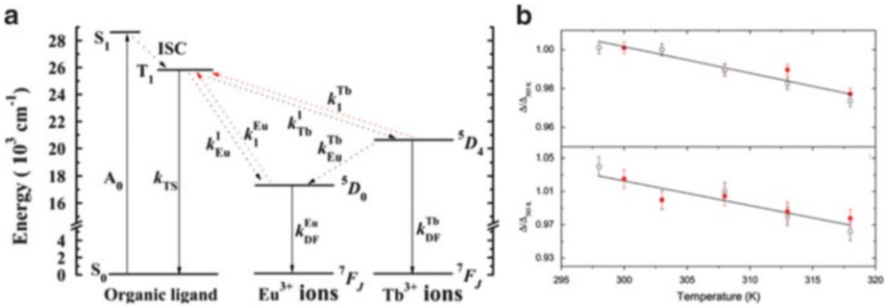

Fig. 50 (**a**) Schematic representation of energy absorption, migration, emission, and processes in luminescent mixed lanthanide MOF $Tb_{1-x}Eu_x(C_{13}H_7O_4N)(C_{13}H_8O_4N)(H_2O)_{2.5}$. (*S* singlet, *T* triplet, *A* absorption probability, ISC intersystem crossing, *k* radiative, or non-radiative transition probability. The *solid arrows* represent singlet–singlet absorption and radiative transitions; *dotted arrows* indicate non-radiative transitions.) Reprinted with the permission from [165]. Copyright 2012 American Chemical Society (**b**) Calibration curves of $Tb_{0.99}Er_{0.01}(BDC)_{1.5}(H_2O)_2$ nanorods in solid state (*top*) and in aqueous suspension (0.36 g/L, *bottom*). *Black squares* and *red circles* represent the first and second heating cycles. Reprinted with the permission from [123]. Copyright 2013 American Chemical Society

provides self-calibration and avoids variations brought by sensor concentration, instrument, or inhomogeneities. Clearly, making nanoscale LnMOF thermometers is of interest to both fundamental research and practical applications. This was first achieved by Carlos and coworkers who made nanorods of the Tb/Eu mixed-lanthanide MOF $Tb_{0.99}Eu_{0.01}(BDC)_{1.5}(H_2O)_2$ and developed a sensitive ratiometric nanothermometer in physiological temperature range (300–320 K) [123]. Temperature measurement was based on the temperature sensitive emission intensity ratio $I^{Tb^{3+}}_{^5D_4\rightarrow{}^7F_5}/I^{Eu^{3+}}_{^5D_0\rightarrow{}^7F_2}$, which is defined as Δ. The calibration curve was made with a normalized Δ value $\Delta/\Delta_{303\ K}$ (Fig. 50b). Temperature was linearly correlated with $\Delta/\Delta_{303\ K}$ value. The temperature response followed well the calibration curve over several heating cycles, indicating the good stability of the nanothermometer (Fig. 50b).

Applications for Optical Imaging

Although organic fluorophores and quantum dots based optical imaging technologies have already been well developed [166, 167], they still suffer from drawbacks such as wide emission bandwidth and short-lived emission. In comparison, lanthanide-based luminophores display long-lived and sharp line-like emissions that produce not only better signal-to-noise ratio but also allow for time-gated or time-resolved in vivo imaging [148].

Luminescence Color Tuning for Multi-Color Imaging

The desire to tune the color of luminescence of nanoscale LnMOFs is stimulated by the potential applications of such materials for in vivo bio-imaging, specifically to avoid certain spectral interference or even better, to create luminophores for simultaneous imaging of multiple targets. We note that protocols to tune the color of luminescence in bulk LnMOFs have been well developed for applications in solid-state lighting and large-panel displays [76, 168–170].

The most straightforward means of tuning the luminescence of nanoscale LnMOFs is learnt from the tuning for bulk materials, that is, by using a starting mixture containing different lanthanide ions. This is generally possible as different lanthanide ions, having very similar sizes due to lanthanide contraction, display rather similar reactivity [171]. When different lanthanide ions are co-doped into the same MOF lattice, the crystal lattice interruption is minimal and mix-lanthanide luminophores are the usual products.

You and Zhang have successfully tuned the luminescence of nanorods and nanoparticle thin films of LnMOFs from red to yellow and to green by adjusting the molar ratio Eu^{3+} and Tb^{3+} co-doped (Fig. 51) [114, 115, 132]. This color tuning protocol is mainly based on the energy transfer from Tb^{3+} to Eu^{3+} and the color mixing of red (Eu^{3+}) and green (Tb^{3+}) detailed above when the thermometric application is discussed.

UV-Vis/MRI Multimodal Imaging

In addition to possibly achieving multi-color imaging, it is also very promising to combine imaging by the luminescence of Eu^{3+} and/or Tb^{3+} with MRI based on the magnetic properties of Gd^{3+} using co-doped nanoparticles of mixed-LnMOFs. In

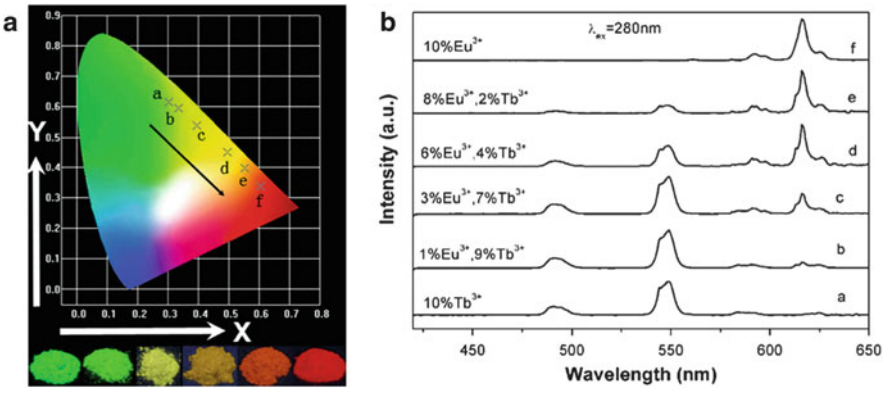

Fig. 51 (**A**) The CIE chromaticity diagram (*top*) and luminescence photograph under UV irradiation (*below*) of the Tb^{3+} and Eu^{3+} co-doped $Y_4(1,2\text{-BDC})_6(H_2O)_2{\cdot}5H_2O$ MOF nano rods: (*a*) 10% Tb^{3+}; (*b*) 1% Eu^{3+}, 9% Tb^{3+}; (*c*) 3% Eu^{3+}, 7% Tb^{3+}; (*d*) 6% Eu^{3+}, 4% Tb^{3+}; (*e*) 8% Eu^{3+}, 2% Tb^{3+}; and (*f*) 10% Eu^{3+}; and (**B**) the corresponding emission spectra. Reproduced from [114] by permission of The Royal Society of Chemistry

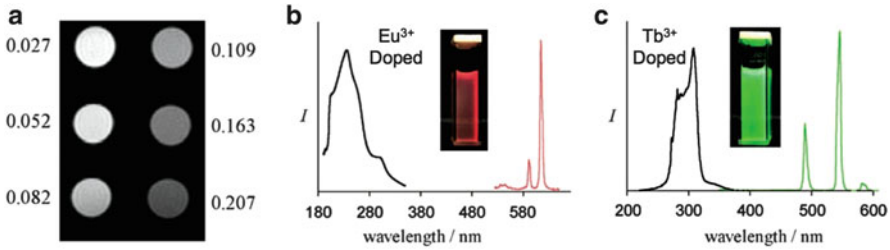

Fig. 52 (**a**) T2-weighted phantom images of $Gd_2(bhc)(H_2O)_6$ MOF nanoparticles at 9.4 T (with Gd^{3+} concentrations in mM shown next to each image); (**b**) The excitation (*black*) and emission (*red*) spectra of Eu^{3+} doped $Gd_2(bhc)(H_2O)_6$ MOF nanoparticles; (**c**) The excitation (*black*) and emission (*green*) spectra of Tb^{3+} doped $Gd_2(bhc)(H_2O)_6$ MOF nanoparticles. Reproduced from [125] by permission of John Wiley & Sons Ltd.

this context, Lin and coworkers obtained nanoparticles of Eu^{3+} and Tb^{3+}-doped Gd $(BDC)_{1.5}(H_2O)_2$ [122] and $Gd_2(bhc)(H_2O)_6$ [125] and explored their uses as multimodal imaging materials equipped with both superior *T*2 contrasting ability (Fig. 52a) and vivid green and red luminescence upon under UV excitation (Fig. 52b, c).

Near-Infrared Imaging

Near-infrared (NIR) imaging offers a number of advantages over imaging based on UV-vis-excited luminescence. These include much reduced invasiveness, reduced autofluorescence from biological molecules for better resolution, and deeper penetration for imaging of bio-tissues of interest [172]. With appropriate antenna ligands, complexes of Pr(III), Nd(III), Ho(III), Er(III), and Yb(III) can all emit NIR light with wavelengths ranging from 890 to 1,530 nm [173]. Coupled with the ability to control the size/morphology and to modify the surface of nanoscale LnMOFs, it is possible to develop a new family of probes for non-invasive and widely applicable imaging based on NIR emission properties of certain lanthanide ions.

Petoud and coworkers conducted comprehensive studies on the synthesis, stability, toxicity, and NIR imaging ability of Yb-PVDC-3 MOF nanoparticles [124]. The as-synthesized MOF nanoparticles showed a high stability in aqueous media and remained intact after soaking in water or Hepes buffer for up to 4 weeks, accompanied by reasonable cellular toxicity with IC_{50} value of 100 μg/mL, making prolonged live-cell imaging feasible. Under single excitation source, the nanoparticles exhibited two emission bands, one originated from the PVDC ligand in the visible region and centered at 500 nm while the other originated from Yb^{3+} in the NIR region and centered at 970 nm, making it a Vis/NIR dual-modal imaging luminophore (Fig. 53a–c). The excitation of Yb^{3+} was attributed to the antenna effect of PVDC ligand since Yb^{3+} has no accepting level matching the energy of excitation source (Fig. 53d).

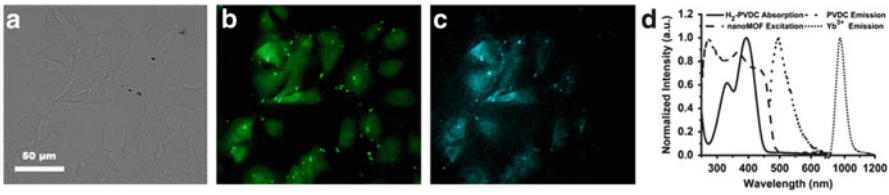

Fig. 53 Visible and NIR microscopy images of nano Yb-PVDC-3 in NIH 3T3 cells ($\lambda_{ex} = 340$ nm): (**a**) Bright-field image; (**b**) H_2-PVDC emission ($\lambda_{ex} = 377/50$ nm; $\lambda_{em} = 445/50$ nm); (**c**) Yb^{3+} emission ($\lambda_{ex} = 377/50$ nm; $\lambda_{em} =$ long pass 770 nm). (**d**) Spectroscopic characterization of Yb-PVDC-3 (30 μg/mL) nanoparticles in 0.1 M Hepes buffer (pH 7.3). Reproduced from [124] by permission of Proceedings of the National Academy of Sciences of the United States of America

Applications for Sensing

Lanthanide luminescence is highly sensitive to local chemical environment, originated from the indirect excitation by energy transfer from a ligand set to the emissive lanthanide center. This unique property of the lanthanide materials is particularly suitable for developing sensing applications as interactions with an analyte may enhance ("turn-on" mechanism) or quench ("turn-off" or "quenching" mechanism) the original luminescence. Both types of nanoscale LnMOFs have been developed.

To build a sensing system operated in the "turn-on" mode, the organic linker utilized for MOF construction should not be a good antenna in order for an incoming analyte molecule, supposedly a good antenna capable of effectively transferring its excitation energy to the potentially emissive lanthanide center, to be operative. As an example of a good "turn-on" sensor, Qian and coworkers reported the nanoparticles of $Eu_2(FMA)_2(OX)(H_2O)_4 \cdot 4H_2O$ for spore detection [133]. The material is originally optical "silent" as FMA ligand is not an effective antenna. However, dipicolinic acid (DPA), one of the major components of the bacterial endospores, serves as an antenna for the effective excitation of the Eu^{3+} ion, resulting in characteristic red emission upon relaxation of the excited states. As such, sensing of DPA and therefore, the endospores, was achieved; the detection limit in ethanol was found to be below 2 ppm of DPA (Fig. 54b). Besides its high sensitivity, this nanoscale MOF also showed highly selective sensing toward DPA as revealed by control studies using common organic compounds and inorganic anions as possible interfering species (Fig. 54a).

Albeit sensitive, such systems only provide qualitative detection. For quantitative analysis, an internal calibration is needed to identify the quantity of sensor, providing a parameter directly correlated to target substance quantity. To this end, Lin and coworkers prepared the nanorods of silica coated Eu-doped Gd $(BDC)_{1.5}(H_2O)_2$ [174] and subsequent surface-functionalization with silylated Tb-EDTA monoamide derivative (Tb-EDTM) (Fig. 55a). The Eu^{3+} ions were luminescent upon UV excitation of the BDC ligand. However, the surface-bound Tb^{3+} ions are originally optical silent because EDTM is a poor antenna and also

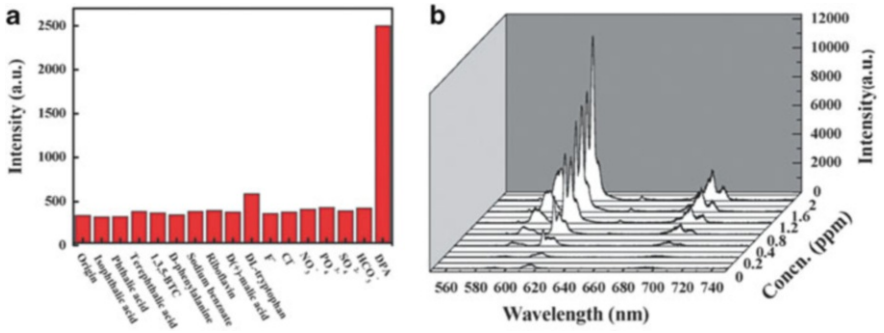

Fig. 54 (**a**) The emission intensity of $Eu_2(FMA)_2(OX)(H_2O)_4{\cdot}4H_2O$ MOF nanoparticle at 617 nm with 1 ppm of different analytes (excited at 279 nm); (**b**) The emission spectra with the addition of different concentration of DPA. Reproduced from [133] by permission of The Royal Society of Chemistry

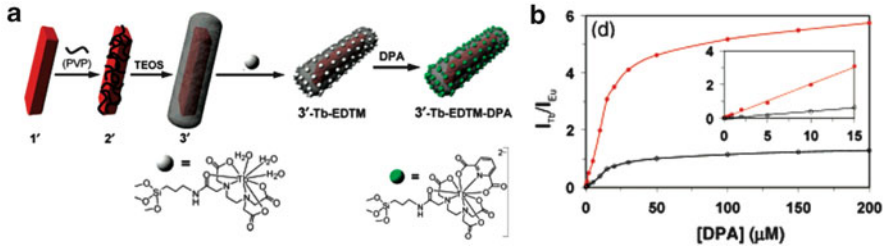

Fig. 55 (**a**) A schematic representation of the construction of Tb-EDTM modified silica coated Eu-doped $Gd(BDC)_{1.5}(H_2O)_2$ MOF nano rods; (**b**) Dependence of Tb/Eu emission intensity ratio on DPA concentration (*red* = 544/592 nm, *black* = 544/615 nm). The *inset* presents the linear relationship at low DPA concentrations. Reprinted with the permission from [174]. Copyright 2007 American Chemical Society

because of the quenching effect of the aqua ligands. Addition of DPA, an effective antenna for the excitation of Tb^{3+}, caused the replacement of the aqua ligands, both serving to enhance the green luminescence characteristic of Tb^{3+}. The Eu^{3+} ions are protected by the silica shell, and their luminescence was not influenced by DPA, making the red Eu^{3+} luminescence a good non-interfering internal calibration. The concentration of DPA could be easily quantified by Tb/Eu emission intensity ratio at 544/592 and 544/615 nm respectively, without having to consider the sensor concentration (Fig. 55b).

Alternatively, sensing can be achieved by the quenching of the sensor luminescence upon interaction with an analyte. Contrary to the design of a "turn-on" sensor, the organic linkers in an LnMOF should be good antennas for the excitation of lanthanide ions. In addition, in the presence of a target analyte, either all the emission peaks should be significantly quenched (even quenching) or be quenched at certain wavelengths (partial quenching). We note that for the detention of

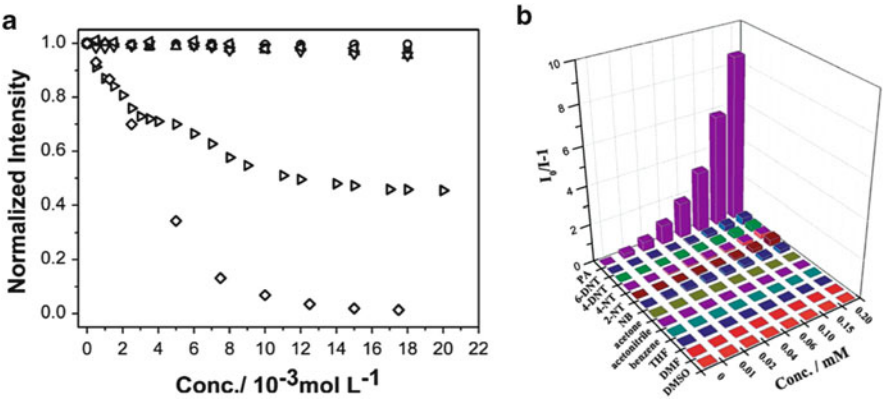

Fig. 56 (**a**) Emission intensity of $[Tb(1,3,5\text{-btc})(H_2O)_6]_n$ MOF nanorods at 548 nm in the presence of methylamine (*square*), ethylamine (*circle*), *n*-propylamine (*triangle*), *n*-butylamine (*inverted triangle*), triethylamine (*left-pointing triangle*), aniline (*right-pointing triangle*), and *p*-phenylenediamine (*diamond*) at different concentrations; reprinted from [143], Copyright 2012, with permission from Elsevier; (**b**) Luminescence quenching results of picric acid and common interferents to $[Tb(1,3,5\text{-BTC})]_n$ nanorods. Reproduced from [144] by permission of The Royal Society of Chemistry

organics, even quenching mechanism usually dominates as the absorption peaks of most organic compounds fall in the range of UV region, which overlap with the wavelengths being used to excite the antenna ligands; the competing absorption process leads to the quenching of lanthanide luminescence.

Nanoparticles of LnMOFs have been developed to detect pollutants such as organoamines [143] or picric acid [144], toxic thiols [146], and nitroaromatic explosives [128]. For example, nanorods of $[Tb(1,3,5\text{-btc})(H_2O)_6]_n$ [143] showed highly selective sensing of aromatic amines (Fig. 56a). On the other hand, nanorods of $[Tb(1,3,5\text{-BTC})]_n$ [144], a similar LnMOF, displayed highly specific responses toward picric acid against other common organic molecules (Fig. 56b).

Sensors based on even quenching mechanism are usually qualitative. However, those operating on the partial quenching mechanism, the unquenched emission peaks could serve as internal calibration, and the intensity ratio between quenched and unquenched emissions is used to quantify target substance. This mechanism has been applied to develop LnMOF sensors metal ion detection [72, 119, 175]. The polarization and concentration of a metal ion, when in close proximity to the lanthanide center, have a significant influence on the electric polarization of the emissive lanthanide ions. The change of local environment polarization significantly changes electric-dipole transitions efficiency, but has little influence on magnetic dipole transitions [176]. As such, the electric dipole/magnetic dipole transitions intensity ratio can be used to quantify metal concentration. For example, Eu^{3+}-based MOFs have been used to detect various metal ions [72, 119]. The two most intense emission peaks of Eu(III) come from the magnetic dipole transition $^5D_0 \rightarrow {}^7F_1$ (~594 nm) and the electric-dipole transition $^5D_0 \rightarrow {}^7F_2$ (~616 nm). More

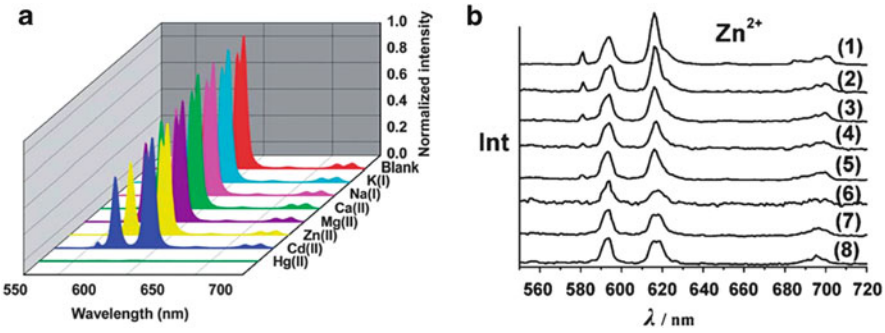

Fig. 57 (**a**) The emission spectra of $\{[Eu_2(bqdc)_3(H_2O)(DMF)_3]\cdot 0.5DMF\cdot H_2O\}_n$ MOF thin films after immersed in various 1 mM metal cation solutions; reproduced from [119] by permission of The Royal Society of Chemistry; (**b**) The emission spectra of $[Eu_2Cd_3(EDTA)_3(H_2O)_{11}](H_2O)_{14}$ MOF (with nanosized metal clusters as building blocks) in Zn^{2+} aqueous solutions of different concentrations ((*1*) 0.01 M, (*2*) 0.025 M, (*3*) 0.05 M, (*4*) 0.075 M, (*5*) 0.1 M, (*6*) 0.25 M, (*7*) 0.5 M, (*8*) 1 M). Reproduced from [72] by permission of The Royal Society of Chemistry

polarized metal ions create a more polarized local environment and tend to quench more profoundly the electric-dipole transition $^5D_0 \rightarrow {}^7F_2$ (Fig. 57a). Furthermore, the concentration of polarized metal ions also has a significant influence on the $I_{616\ nm}/I_{594\ nm}$ ratio, with a higher concentration leads to a lower $I_{616\ nm}/I_{594\ nm}$ value (Fig. 57b). Therefore, the $I_{616\ nm}/I_{594\ nm}$ value could be used to quantify the amount of metal ions analyzed.

4.2.3 Nanoscale LnMOFs for Drug Delivery

The utilization of nanoscale MOF particles to encapsulate and deliver drug in vivo is becoming a very active research field due to the advantage of facile composition and structural tuning through using different metal/ligand combinations [177]. There are two general types of drug encapsulation, non-covalent encapsulation in which drug molecules are physically trapped in the MOF channels and covalent attachment by which drug molecules are grafted onto ligands or metal centers through chemical bond [109]. The high coordination number of lanthanide ions makes nanoparticles of LnMOFs good delivery vehicles with drugs covalently attached since the large number of coordination sites around a lanthanide center permits high drug loading. On the other hand, the presence of luminescent lanthanide ions presents the opportunity to develop theranostics for simultaneous luminescence-based diagnosis and therapy by delivered drug contents. For example, dicarboxylic acid modified cis-platinum anticancer drug *c*,*c*,*t*-(diamminedichlorodisuccinato)Pt(IV) (DSCP) was used as organic linker to prepare Tb^{3+}-based MOF nanoparticles (NCP-1) [113]. These nanoparticles have been shown to release cisplatin-type drugs due to their instability in a physiological environment. Controlled drug release was achieved through silica coating, and as expected,

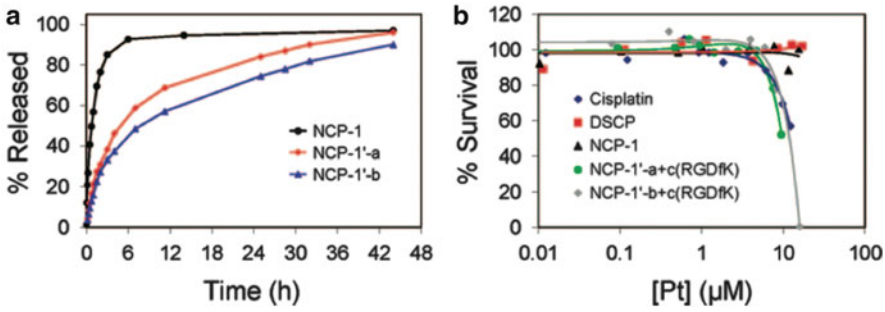

Fig. 58 (**a**) Release profiles for as-synthesized NCP-1, NCP-1′-a, and NCP-1′-b obtained by plotting the % Pt released against time; (**b**) In vitro cytotoxicity assay curves for HT-29 cells obtained by plotting the % cell viability against the Pt concentration of various samples and cisplatin control. Reprinted with the permission from [113]. Copyright 2008 American Chemical Society

the rate of drug release decreased with increased silica shell thickness. For example, NCP-1 coated with 2-nm silica shell (NCP-1′-a) showed significantly reduced release rate when compared with the uncoated NCP-1 in a control study. When the silica shell was increased to 7 nm (NCP-1′-b), the drug release rate was further reduced (Fig. 58a). The reduced drug release rate allowed sufficient time for the drug-delivery vehicle to circulate and accumulate in tumor tissue. Besides the effort to achieve controlled drug release, the researchers also explored targeted drug delivery by conjugating a cancer cell targeting peptide *c*(RGDfK) onto the surface of the drug-delivery vehicle. Studies of cancer cell viability indicated that the vehicle conjugated with *c*(RGDfK) has much enhanced therapeutic effect (Fig. 58b).

5 Perspectives and Outlooks

Despite all these fruitful results already achieved, the development of LnMOFs with nanosized pores/channels or nanoparticles of such materials remains at an early stage. Inspired by the efforts from other more developed research and by taking advantage of the intrinsically interesting properties of lanthanide elements, it appears opportunities abound, both in the preparation of such materials and more excitingly, in the exploration of their potential applications. For example, there has been an increasing amount of research on the development of lanthanide-only and 3*d*–4*f* heterometallic clusters for magnetic cooling. [147] On the other hand, a very recent trend has emerged where dense metal-organic frameworks are explored for enhanced magnetic refrigeration. [178] LnMOFs constructed by nanosized clusters as SBUs would seem to be a perfect combination, and research along this line remains to be done [41, 42, 44–50, 52–56, 58, 59, 63, 67, 72–74].

As already pointed out, one of the key considerations in improving the performance in practical applications of nanoscale LnMOFs is to tune the pore size and the size and morphology of nanoparticles. For transition metal MOFs, research in this vein has been much developed by topological analysis and molecular simulations [20–22]. However, due to the much less participation of 4*f* orbitals in coordination and demanding high coordination number requirement, protocols suitable for such control have yet to be developed. In other words, rational design of LnMOFs remains a great challenge with much more to be explored. The recent work by Freire and coworkers represented rare but much needed theoretical efforts toward the design of such materials with a better understanding of their structure–property relationship [179–181]. Increasing efforts dedicated to theoretical simulations of LnMOF are thus anticipated.

Most synthetic and characterization protocols in the research of nanoscale LnMOFs were derived from the methods well developed for inorganic nanocrystals for which we note the research on core/shell nanostructures is rapidly advancing [182]. As novel properties may arise due to the intimate core-shell interactions and in fact already demonstrated for quantum dots, it is tempting to suspect similar and possibly other new properties may also be generated if the core/shell structure can be adopted in the making of LnMOFs. In this context, the work of core/shell structured transition metal MOFs [183, 184] or inorganic nanoparticle@MOF shell hetero-nanostructures [185], albeit limited, may serve as inspiration.

A very recently emerging research field of inorganic colloid nanoparticles is the controlled assembly of nanoparticles into superlattices of higher dimensions with the showing of collective properties [186–188]. Inspired by these efforts, researchers have also explored the assembly of colloidal transition metal MOF nanoparticles into monolayers or 3D structures [108]. However, analogous efforts have yet to be known for nanoparticles of LnMOFS. Lastly, besides these inspirations learned from the research on colloidal inorganic nanocrystals, nanoparticles of LnMOFs may also be applicable to the assisted synthesis of conventional inorganic nanoparticles and modification and tuning of the resulting nanomaterials. For example, doping lanthanide ions into semiconductor nanoparticles of semiconducting materials is highly desirable due to the large number of excited electronic states for band-gap tuning and also for achieving upconverting materials for potential use in photovoltaics; a material's ability to absorb solar energy in the NIR spectral window would significantly enhance the photo-conversion efficiency, and the unique electronic states of Er^{3+} and Yb^{3+} ions position them well for this very purpose. However, examples of successful doping remain a rarity due primarily to lattice mismatch as a result of the significant disparity in ionic size and coordination requirement between the lanthanides and other metals [189]. However, it is much easier for transition metal ions and lanthanide ions to co-exist in the same MOF structure, affording a variety of 3*d*–4*f* heterometallic MOFs [190–192]. Therefore, it is promising to use nanoscale 3*d*–4*f* MOF particles as precursors to synthesize lanthanide-doped transition metal oxide and semiconducting nanoparticles since transition metal ions and lanthanide ions are pre-combined in a single-source precursor with a specific molar ratio. The work by Meyer and coworkers of using

coordination polymers as precursor to prepare doped lanthanide oxide ceramics suggests the feasibility of such a protocol [117], but no work is known for the preparation of lanthanide-doped nanoparticles using LnMOF as precursors.

Acknowledgment This work was supported by the US National Science Foundation (Grant CHE-1152609).

References

1. Lee J, Farha OK, Roberts J, Scheidt KA, Nguyen ST, Hupp JT (2009) Metal-organic framework materials as catalysts. Chem Soc Rev 38:1450–1459
2. Ma LQ, Abney C, Lin WB (2009) Enantioselective catalysis with homochiral metal-organic frameworks. Chem Soc Rev 38:1248–1256
3. Ma LQ, Falkowski JM, Abney C, Lin WB (2010) A series of isoreticular chiral metal-organic frameworks as a tunable platform for asymmetric catalysis. Nat Chem 2:838–846
4. Dinca M, Long JR (2008) Hydrogen storage in microporous metal-organic frameworks with exposed metal sites. Angew Chem Int Ed 47:6766–6779
5. Rowsell JLC, Yaghi OM (2005) Strategies for hydrogen storage in metal-organic frameworks. Angew Chem Int Ed 44:4670–4679
6. Xie ZG, Ma LQ, deKrafft KE, Jin A, Lin WB (2010) Porous phosphorescent coordination polymers for oxygen sensing. J Am Chem Soc 132:922–923
7. Chen BL, Xiang SC, Qian GD (2010) Metal-organic frameworks with functional pores for recognition of small molecules. Acc Chem Res 43:1115–1124
8. Evans OR, Lin WB (2002) Crystal engineering of NLO materials based on metal-organic coordination networks. Acc Chem Res 35:511–522
9. Liu Y, Xuan WM, Cui Y (2010) Engineering homochiral metal-organic frameworks for heterogeneous asymmetric catalysis and enantioselective separation. Adv Mater 22:4112–4135
10. Li JR, Kuppler RJ, Zhou HC (2009) Selective gas adsorption and separation in metal-organic frameworks. Chem Soc Rev 38:1477–1504
11. Kong XJ, Long LS, Zheng ZP, Huang RB, Zheng LS (2010) Keeping the ball rolling: fullerene-like molecular clusters. Acc Chem Res 43:201–209
12. Eliseeva SV, Bünzli JCG (2010) Lanthanide luminescence for functional materials and bio-sciences. Chem Soc Rev 39:189–227
13. Peng JB, Zhang QC, Kong XJ, Ren Y, Long LS, Huang RB, Zheng LS, Zheng ZP (2011) A 48-metal cluster exhibiting a large magnetocaloric effect. Angew Chem Int Ed 50:10649–10652
14. Boglio C, Lemière G, Hasenknopf B, Thorimbert S, Lacôte E, Malacria M (2006) Lanthanide complexes of the monovacant Dawson polyoxotungstate [α1-P2W17O61]10- as selective and recoverable Lewis acid catalysts. Angew Chem Int Ed 45:3324–3327
15. Du DY, Qin JS, Li SL, Su ZM, Lan YQ (2014) Recent advances in porous polyoxometalate-based metal-organic framework materials. Chem Soc Rev. doi:10.1039/c3cs60404g
16. Férey G, Mellot-Draznieks C, Serre C, Millange F (2005) Crystallized frameworks with giant pores: are there limits to the possible? Acc Chem Res 38:217–225
17. Zhao M, Ou S, Wu CD (2014) Porous metal-organic frameworks for heterogeneous biomimetic catalysis. Acc Chem Res 47:1199–1207
18. Zhao D, Timmons DJ, Yuan D, Zhou HC (2011) Tuning the topology and functionality of metal-organic frameworks by ligand design. Acc Chem Res 44:123–133

19. Furukawa H, Ko N, Go YB, Aratani N, Choi SB, Choi E, Yazaydin AÖ, Snurr RQ, O'Keeffe M, Kim J, Yaghi OM (2010) Ultrahigh porosity in metal-organic frameworks. Science 329:424–428
20. Deng H, Grunder S, Cordova KE, Valente C, Furukawa H, Hmadeh M, Gándara F, Whalley AC, Liu Z, Asahina S, Kazumori H, O'Keeffe M, Terasaki O, Stoddart JF, Yaghi OM (2012) Large-pore apertures in s series of metal-organic frameworks. Science 336:1018–1023
21. Getman RB, Bae YS, Wilmer CE, Snurr RQ (2012) Review and analysis of molecular simulations of methane, hydrogen, and acetylene storage in metal-organic frameworks. Chem Rev 112:703–723
22. Li M, Li D, O'Keeffe M, Yaghi OM (2014) Topological analysis of metal-organic frameworks with polytopic linkers and/or multiple building units and the minimal transitivity principle. Chem Rev 114:1343–1370
23. Wang R, Carducci MD, Zheng Z (2000) Direct hydrolytic route to molecular oxo-hydroxo lanthanide clusters. Inorg Chem 39:1836–1837
24. Tang XL, Wang WH, Dou W, Jiang J, Liu WS, Qin WW, Zhang GL, Zhang HR, Yu KB, Zheng LM (2009) Olive-shaped chiral supramolecules: simultaneous self-assembly of heptameric lanthanum clusters and carbon dioxide fixation. Angew Chem Int Ed 48:3499–3502
25. Xu J, Raymond KN (2000) Lord of the rings: an octameric lanthanum pyrazolonate cluster. Angew Chem Int Ed 39:2745–2747
26. Wu Y, Morton S, Kong X, Nichol GS, Zheng Z (2011) Hydrolytic synthesis and structural characterization of lanthanide-acetylacetonato/hydroxo cluster complexes – a systematic study. Dalton Trans 40:1041–1046
27. Westin LG, Kritikos M, Caneschi A (2003) Self assembly, structure and properties of the decanuclear lanthanide ring complex, $Dy_{10}(OC_2H_4OCH_3)_{30}$. Chem Commun 2003:1012–1013
28. Wang R, Selby HD, Liu H, Carducci MD, Jin T, Zheng Z, Anthis JW, Staples RJ (2002) Halide-templated assembly of polynuclear lanthanide-hydroxo complexes. Inorg Chem 41:278–286
29. Chesman ASR, Turner DR, Moubaraki B, Murray KS, Deacon GB, Batten SR (2009) Lanthaballs: chiral, structurally layered polycarbonate tridecanuclear lanthanoid clusters. Chem Eur J 15:5203–5207
30. Bürgstein MR, Roesky PW (2000) Nitrophenolate as a building block for lanthanide chains and clusters. Angew Chem Int Ed 39:549–551
31. Wang R, Zheng Z, Jin T, Staples RJ (1999) Coordination chemistry of lanthanides at "high" pH: synthesis and structure of the pentadecanuclear complex of europium(III) with tyrosine. Angew Chem Int Ed 38:1813–1815
32. Thielemann DT, Wagner AT, Rösch E, Kölmel DK, Heck JG, Rudat B, Neumaier M, Feldmann C, Schepers U, Bräse S, Roesky PW (2013) Luminescent cell-penetrating pentadecanuclear lanthanide clusters. J Am Chem Soc 135:7454–7457
33. Malaestean IL, Ellern A, Baca S, Kögerler P (2012) Cerium oxide nanoclusters: commensurate with concepts of polyoxometalate chemistry. Chem Commun 48:1499–1501
34. Chang LX, Xiong G, Wang L, Cheng P, Zhao B (2013) A 24-Gd nanocapsule with a large magnetocaloric effect. Chem Commun 49:1055–1057
35. Chen L, Huang L, Wang C, Fu J, Zhang D, Zhu D, Xu Y (2012) Hydrothermal synthesis, structure, and properties of two new nanosized Ln_{26} (Ln = Ho, Er) clusters. J Coord Chem 65:958–968
36. Wu M, Jiang F, Kong X, Yuan D, Long L, Al-Thabaiti SA, Hong M (2013) Two polymeric 36-metal pure lanthanide nanosized clusters. Chem Sci 4:3104–3109
37. Guo FS, Chen YC, Mao LL, Lin WQ, Leng JD, Tarasenko R, Orendáč M, Prokleška J, Sechovský V, Tong ML (2013) Anion-templated assembly and magnetocaloric properties of a nanoscale $\{Gd_{38}\}$ cage versus a $\{Gd_{48}\}$ barrel. Chem Eur J 19:14876–14885

38. Kong XJ, Wu Y, Long LS, Zheng LS, Zheng Z (2009) A chiral 60-metal sodalite cage featuring 24 vertex-sharing $[Er_4(\mu_3\text{-}OH)_4]$ cubanes. J Am Chem Soc 131:6918–6919
39. Ma BQ, Zhang DS, Gao S, Jin TZ, Yan CH, Xu GX (2000) From cubane to supercubane: the design, synthesis, and structure of a three-dimensional open framework based on a Ln_4O_4 cluster. Angew Chem Int Ed 112:3790–3792
40. Wang R, Liu H, Carducci MD, Jin T, Zheng C, Zheng Z (2001) Lanthanide coordination with α-amino acids under near physiological pH conditions: polymetallic complexes containing the cubane-like $[Ln_4(\mu_3\text{-}OH)_4]^{8+}$ cluster core. Inorg Chem 40:2743–2750
41. Mahé N, Guillou O, Daiguebonne C, Gérault Y, Caneschi A, Sangregorio C, Chane-Ching JY, Car PE, Roisnel T (2005) Polynuclear lanthanide hydroxo complexes: new chemical precursors for coordination polymers. Inorg Chem 44:7743–7750
42. Calvez G, Daiguebonne C, Guillou O (2011) Unprecedented lanthanide-containing coordination polymers constructed from hexanuclear molecular building blocks: $\{[Ln_6O(OH)_8](NO_3)_2(bdc)(Hbdc)_2{\cdot}2NO_3{\cdot}H_2bdc\}_\infty$. Inorg Chem 50:2851–2858
43. Natur FL, Calvez G, Daiguebonne C, Guillou O, Bernot K, Ledoux J, Pollès LL, Roiland C (2013) Coordination polymers based on heterohexanuclear rare earth complexes: toward independent luminescence brightness and color tuning. Inorg Chem 52:6720–6730
44. Gándara F, Gutiérrez-Puebla E, Iglesias M, Snejko N, Monge MÁ (2010) Isolated hexanuclear hydroxo lanthanide secondary building units in a rare-earth polymeric framework based on *p*-sulfonatocalix[4]arene. Cryst Growth Des 10:128–134
45. Shi FN, Cunha-Silva L, Trindade T, Paz FAA, Rocha J (2009) Three-dimensional lanthanide-organic frameworks based on di-, tetra-, and hexameric clusters. Cryst Growth Des 9:2098–2109
46. Yuan N, Sheng T, Tian C, Hu S, Fu R, Zhu Q, Tan C, Wu X (2011) Synthesis, structures and properties of three-dimensional lanthanide frameworks constructed with a trigonal antiprismatic lanthanide cluster. CrystEngComm 13:4244–4250
47. Zheng XJ, Jin LP, Gao S (2004) Synthesis and characterization of two novel lanthanide coordination polymers with an open framework based on an unprecedented $[Ln_7(\mu_3\text{-}OH)_8]^{13+}$ cluster. Inorg Chem 43:1600–1602
48. Fang WH, Cheng L, Huang L, Yang GY (2013) A series of lanthanide-based cluster organic frameworks made of heptanuclear tironal-prismatic cluster units. Inorg Chem 52:6–8
49. Chen L, Guo JY, Xu X, Ju WW, Zhang D, Zhu DR, Xu Y (2013) A novel 2-D coordination polymer constructed from high-nuclearity waist drum-like pure Ho_{48} clusters. Chem Commun 49:9728–9730
50. Wu M, Jiang F, Yuan D, Pang J, Qian J, AL-Thabaiti SA, Hong M (2014) Polymeric double-anion template Er_{48} nanotubes. Chem Commun 50:1113–1115
51. Liu J, Meyers EA, Shore SG (1998) An unusual cyanide bridging lanthanide-transition metal complex that contains the on-dimensional cationic array $\{[(DMF)_{16}Yb_6(\mu_6\text{-}O)(\mu_3\text{-}OH)_8(\mu\text{-}NC)Pd(\mu\text{-}CN)(CN)_2]^{6+}\}_\infty$. Inorg Chem 37:5410–5411
52. Chen LF, Zhang J, Ren GQ, Li ZJ, Qin YY, Yin PX, Cheng JK, Yao YG (2008) Nanosized lanthanide oxide rods in I^1O^3 hybrid organic–inorganic frameworks involving *in situ* ligand synthesis. CrystEngComm 10:1088–1092
53. Fang WH, Yang GY (2014) Pillared-layer cluster organic frameworks constructed from nanoscale Ln10 and Cu16 clusters. Inorg Chem 53(11):5631–5636. doi:10.1021/ic500404z
54. Zhang MB, Zhang J, Zheng ST, Yang GY (2005) A 3D coordination framework based on linkages of nanosized hydroxo lanthanide clusters and copper clusters by isonicotinate ligands. Angew Chem Int Ed 44:1385–1388
55. Cheng JW, Zhang J, Zheng ST, Yang GY (2008) Linking two distinct layered networks of nanosized $\{Ln_{18}\}$ and $\{Cu_{24}\}$ wheels through isonicotinate ligands. Chem Eur J 14:88–97
56. Fang WH, Cheng JW, Yang GY (2014) Two series of sandwich frameworks based on two different kinds of nanosized lanthanide(III) and copper(I) wheel cluster units. Chem Eur J 20:2704–2711

57. Gu X, Xue D (2007) Surface modification of high-nuclearity lanthanide clusters: two tetramers constructed by cage-shaped $\{Dy_{26}\}$ clusters and isonicotinate linkers. Inorg Chem 46:3212–3216
58. Huang L, Han L, Feng W, Zheng L, Zhang Z, Xu Y, Chen Q, Zhu D, Niu S (2010) Two 3D coordination frameworks based on nanosized huge Ln_{26} (Ln = Dy and Gd) spherical clusters. Cryst Growth Des 10:2548–2552
59. Cheng JW, Zhang J, Zheng ST, Zhang MB, Yang GY (2006) Lanthanide-transition-metal sandwich framework comprising $\{Cu_3\}$ cluster pillars and layered networks of $\{Er_{36}\}$ wheels. Angew Chem Int Ed 45:73–77
60. Zou X, Conradsson T, Klingstedt M, Dadachov MS, O'Keeffe M (2005) A mesoporous germanium oxide with crystalline pore walls and its chiral derivative. Nature 437:716–719
61. Pan CY, Liu GZ, Zheng ST, Yang GY (2008) $GeB_4O_9{\cdot}H_2en$: an organically template borogermanate with large 12-ring channels built by B_4O_9 polyanions and GeO_4 units: host–guest symmetry and charge matching in triangular-tetrahedral frameworks. Chem Eur J 14:5057–5063
62. Liu GZ, Zheng ST, Yang GY (2007) $In_2Ge_6O_{15}(OH)_2(H_2dien)$: an open-framework indate germanate with one-dimensional 12-ring channels. Angew Chem Int Ed 46:2827–2830
63. He H, Cao GJ, Zheng ST, Yang GY (2009) Lanthanide germanate cluster organic frameworks constructed from $\{Ln_8Ge_{12}\}$ or $\{Ln_{11}Ge_{12}\}$ cage cluster building blocks. J Am Chem Soc 131:15588–15589
64. Becker R, Johnsson M, Kremer RK, Klauss HH, Lemmens P (2006) Crystal structure and magnetic properties of $FeTe_2O_5X$ (X = Cl, Br): A frustrated spin cluster compound with a new Te(IV) coordination polyhedron. J Am Chem Soc 128:15469–15475
65. Cao X, Lu Z, Zhu L, Yang L, Gu L, Cai L, Chen J (2014) A new family of sunlight-driven bifunctional photocatalysts based on TiO_2 nanoribbon frameworks and bismuth oxohalide nanoplates. Nanoscale 6:1434–1444
66. Hu B, Feng ML, Li JR, Lin QP, Huang XY (2011) Lanthanide antimony oxohalides: from discrete nanoclusters to inorganic–organic hybrid chains and layers. Angew Chem Int Ed 50:8110–8113
67. Hu B, Zou GD, Feng ML, Huang XY (2012) Inorganic–organic hybrid compounds based on novel lanthanide-antimony oxohalide nanoclusters. Dalton Trans 41:9879–9881
68. Zou GD, Zhang GG, Hu B, Li JR, Feng ML, Wang XC, Huang XY (2013) A 3D hybrid praseodymium-antimony-oxochloride compound: single-crystal-to-single-crystal transformation and photocatalytic properties. Chem Eur J 19:15396–15403
69. Zheng YZ, Evangelisti M, Winpenny REP (2011) Large magnetocaloric effect in a Wells–Dawson type $\{Ni_6Gd_6P_6\}$ cage. Angew Chem Int Ed 50:3692–3695
70. Karotsis G, Evangelisti M, Dalgarno SJ, Brechin EK (2009) A calix[4]arene 3d/4f magnetic cooler. Angew Chem Int Ed 48:9928–9931
71. Cui Y, Yue Y, Qian G, Chen B (2012) Luminescent functional metal-organic frameworks. Chem Rev 112:1126–1162
72. Liu Q, Ge SZ, Zhong JC, Sun YQ, Chen YP (2013) Two novel 2D lanthanide–cadmium heterometal–organic frameworks based on nanosized heart-like $Ln_6Cd_6O_{12}$ wheel-clusters exhibiting luminescence sensing to the polarization and concentration of cations. Dalton Trans 42:6314–6317
73. Li G, Akitsu T, Sato O, Einaga Y (2003) Photoinduced magnetization of the cyano-bridged 3d-4f heterobimetallic assembly $Nd(DMF)_4(H_2O)_3(\mu\text{-}CN)Fe(CN)_5{\cdot}H_2O$ (DMF = *N*,*N*-Dimethylformamide). J Am Chem Soc 125:12396–12397
74. Zhao B, Chen XY, Chen Z, Shi W, Cheng P, Yan SP, Liao DZ (2009) A porous 3D heterometal–organic framework containing both lanthanide and high-spin Fe(II) ions. Chem Commun 2009:3113–3115
75. He YP, Tan YX, Zhang J (2013) Gas sorption, second-order nonlinear optics, and luminescence properties of a series of lanthanide-organic frameworks based on nanosized tris ((4-carboxyl)phenylduryl)amine ligand. Inorg Chem 52:12758–12762

76. Ma ML, Ji C, Zhang SQ (2013) Synthesis, structures, tunable emission and white light emitting Eu^{3+} and Tb^{3+} doped lanthanide metal-organic framework materials. Dalton Trans 42:10579–10586
77. Zhu XD, Lin ZJ, Liu TF, Xu B, Cao R (2012) Two novel 3d-4f heterometallic frameworks assembled from a flexible bifunctional macrocyclic ligand. Cryst Growth Des 12:4708–4711
78. Ghosh SK, Bharadwaj PK (2005) Coordination polymers of La(III) as bunched infinite nanotubes and their conversion into an open-framework structure. Inorg Chem 44:3156–3161
79. Chen SP, Ren YX, Wang WT, Gao SL (2010) Nanoporous lanthanide-carboxylate frameworks based on 5-nitroisophthalic acid. Dalton Trans 39:1552–1557
80. Cai B, Yang P, Dai JW, Wu JZ (2011) Tuning the porosity of lanthanide MOFs with 2,5-pyrazinedicarboxylate and the first *in situ* hydrothermal carboxyl transfer. CrystEngComm 13:985–991
81. Lopez N, Zhao H, Zhao D, Zhou HC, Riebenspies JP, Dunbar KR (2013) A porous Sm(III) coordination nanotube with hydrophobic and hydrophilic channels. Dalton Trans 42:54–57
82. Sumida K, Rogow DL, Mason JA, McDonald TM, Block ED, Herm ZR, Bae TH, Long JR (2012) Carbon dioxide capture in metal-organic frameworks. Chem Rev 112:724–781
83. Suh MP, Park HJ, Prasad TK, Lim DW (2012) Hydrogen storage in metal-organic frameworks. Chem Rev 112:782–835
84. Wu H, Gong Q, Olson DH, Li J (2012) Commensurate adsorption of hydrocarbons and alcohols in microporous metal organic frameworks. Chem Rev 112:836–868
85. Luo J, Xu H, Liu Y, Zhao Y, Daemen LL, Brown C, Timofeeva TV, Ma S, Zhou HC (2008) Hydrogen adsorption in a highly stable porous rare-earth metal-organic framework: sorption properties and neutron diffraction studies. J Am Chem Soc 130:9626–9627
86. Peterson VK, Liu Y, Brown CM, Kepert CJ (2006) Neutron powder diffraction study of D_2 sorption in Cu_3(1,3,5-benzenetricarboxylate)$_2$. J Am Chem Soc 128:15578–15579
87. Dincă M, Dailly A, Liu Y, Brown CM, Neumann DA, Long JR (2006) Hydrogen storage in a microporous metal-organic framework with exposed Mn^{2+} coordination sites. J Am Chem Soc 128:16876–16883
88. Dolbecq A, Dumas E, Mayer CR, Mialane P (2010) Hybrid organic–inorganic polyoxometalate compounds: from structural diversity to applications. Chem Rev 110:6009–9048
89. Wei M, He C, Sun Q, Meng Q, Duan C (2007) Zeolite ionic crystals assembled through direct incorporation of polyoxometalate clusters within 3D metal-organic frameworks. Inorg Chem 46:5957–5966
90. Tsang JSW, Neverov AA, Brown RS (2003) La^{3+}-catalyzed methanolysis of hydroxypropyl-*p*-nitrophenyl phosphate as a model for the RNA transesterification reaction. J Am Chem Soc 125:1559–1566
91. Belousoff MJ, Ung P, Forsyth CM, Tor Y, Spiccia L, Graham B (2009) New macrocyclic terbium(III) complex for use in RNA footprinting experiments. J Am Chem Soc 131:1106–1114
92. Dang D, Bai Y, He C, Wang J, Duan C, Niu J (2010) Structural and catalytic performance of a polyoxometalate-based metal-organic framework having a lanthanide nanocage as secondary building block. Inorg Chem 49:1280–1282
93. Chen XY, Chen YP, Xia ZM, Hu HB, Sun YQ, Huang WY (2012) Synthesis, crystal structure of α-Keggin heteropolymolybdates with pyridine-2,6-dicarboxylate based frameworks, and associated RhB photocatalytic degradation and 2D-IR COS tests. Dalton Trans 41:10035–10042
94. Hiskia A, Mylonas A, Papaconstantinou E (2001) Comparison of the photoredox properties of polyoxometallates and semiconducting particles. Chem Soc Rev 30:62–69
95. Mahapatra S, Madras G, Row TNG (2007) Structural and photocatalytic activity of lanthanide (Ce, Pr, and Nd) molybdovanadates. J Phys Chem C 111:6505–6511

96. Nishiyama Y, Nakagawa Y, Mizuno N (2001) High turnover numbers for the catalytic selective epoxidation of alkenes with 1 atm of molecular oxygen. Angew Chem Int Ed 40:3639–3641
97. Kovalchuk TV, Kochkin JN, Sfihi H, Zaitsev VN, Fraissard J (2009) Oniumsilica-immobilized-Keggin acids: acidity and catalytic activity for ethyl *tert*-butyl ether synthesis and acetic acid esterification with ethanol. J Catal 263:247–257
98. Liu X, Jia Y, Zhang Y, Huang R (2010) Construction of a hybrid family based on lanthanide-organic frameworks hosts and polyoxometalate guests. Eur J Inorg Chem 2010:4027–4033
99. Williams NH, Takasaki B, Wall M, Chin J (1999) Structure and nuclease activity of simple dinuclear metal complexes: quantitative dissection of the role of metal ions. Acc Chem Res 32:485–493
100. Weston J (2005) Mode of action of bi- and trinuclear zinc hydrolases and their synthetic analogues. Chem Rev 105:2151–2174
101. Fanning AM, Plush SE, Gunnlaugsson T (2006) Tuning the properties of cyclen based lanthanide complexes for phosphodiester hydrolysis: the role of basic cofactors. Chem Commun 2006:3791–3793
102. New K, Andolina CM, Morrow JR (2008) Tethered dinuclear europium(III) macrocyclic catalysts for the cleavage of RNA. J Am Chem Soc 130:14861–14871
103. Han Q, Zhang L, He C, Niu J, Duan C (2012) Metal-organic frameworks with phosphotungstate incorporated for hydrolytic cleavage of a DNA-model phosphodiester. Inorg Chem 51:5118–5127
104. Oh M, Mirkin CA (2005) Chemically tailorable colloidal particles from infinite coordination polymers. Nature 438:651–654
105. Sun X, Dong SJ, Wang EK (2005) Coordination-induced formation of submicrometer-scale, monodisperse, spherical colloids of organic–inorganic hybrid materials at room temperature. J Am Chem Soc 127:13102–13103
106. Lin WB, Rieter W, Taylor KML (2009) Modular synthesis of functional nanoscale coordination polymers. Angew Chem Int Ed 48:650–658
107. Spokoyny AM, Kim D, Sumrein A, Mirkin CA (2009) Infinite coordination polymer nano- and microparticle structures. Chem Soc Rev 38:1218–1227
108. Sindoro M, Yanai N, Jee AY, Granick S (2014) Colloidal-sized metal-organic frameworks: synthesis and applications. Acc Chem Res 47:459–469
109. Rocca JD, Liu D, Lin WB (2011) Nanoscale metal-organic frameworks for biomedical imaging and drug delivery. Acc Chem Res 44:957–968
110. Rocca JD, Lin WB (2010) Nanoscale metal-organic frameworks: magnetic resonance imaging contrast agents and beyond. Eur J Inorg Chem 2010:3725–3734
111. Nishiyabu R, Hashimoto N, Cho T, Watanabe K, Yasunaga T, Endo A, Kaneko K, Niidome T, Murata M, Adachi C, Katayama Y, Hashizume M, Kimizuka N (2009) Nanoparticles of adaptive supramolecular networks self-assembled from nucleotides and lanthanide ions. J Am Chem Soc 131:2151–2158
112. Jeon YM, Armatas GS, Kim D, Kanatzidis MG, Mirkin CA (2009) Tröger's-base-derived infinite co-ordination polymer microparticles. Small 5:46–50
113. Rieter WJ, Pott KM, Taylor KML, Lin WB (2008) Nanoscale coordination polymers for platinum-based anticancer drug delivery. J Am Chem Soc 130:11584–11585
114. Qiao H, Jia Y, Zheng Y, Guo N, Zhao Q, Lv W, You H (2012) Facile fabrication of Y_4(1,2-BDC)$_6$(H_2O)$_2$·5H_2O: Eu^{3+}, Tb^{3+} ultralong nanobelts and tunable luminescence properties. CrystEngComm 14:5830–5835
115. Liu K, Zheng Y, Jia G, Yang M, Song Y, Guo N, You H (2010) Nano/micro-scaled La(1,3,5-BTC)(H_2O)$_6$ coordination polymer: facile morphology-controlled fabrication and color-tunable photoluminescence properties by co-doping Eu^{3+}, Tb^{3+}. J Solid State Chem 183:2309–2316
116. Tang J, Alivisatos AP (2006) Crystal splitting in the growth of Bi_2S_3. Nano Lett 6:2701–2706

117. Demars T, Boltoeva M, Vigier N, Maynadié J, Ravaux J, Genre C, Meyer D (2012) From coordination polymers to doped rare-earth oxides. Eur J Inorg Chem 2012:3875–3884
118. Wang F, Deng K, Wu G, Liao H, Liao H, Zhang L, Lan S, Zhang J, Song X, Wen L (2012) Facile and large-scale syntheses of nanocrystal rare earth metal-organic frameworks at room temperature and their photoluminescence properties. J Inorg Organomet Polym 22:680–685
119. Zhu YM, Zeng CH, Chu TS, Wang HM, Yang YY, Tong YX, Su CY, Wong WT (2013) A novel highly luminescent LnMOF film: a convenient sensor for Hg^{2+} detecting. J Mater Chem A 1:11312–11319
120. Ganguli AK, Ganguly A, Vaidya S (2010) Microemulsion-based synthesis of nanocrystalline materials. Chem Soc Rev 39:474–485
121. Sun HL, Shi H, Zhao F, Qi L, Gao S (2005) Shape-dependent magnetic properties of low-dimensional nanoscale Prussian blue (PB) analogue $SmFe(CN)_6{\cdot}4H_2O$. Chem Commun 2005:4339–4341
122. Rieter WJ, Taylor KML, An H, Lin W, Lin WB (2006) Nanoscale metal-organic frameworks as potential multimodal contrast enhancing agents. J Am Chem Soc 128:9024–9025
123. Cadiau A, Brites CDS, Costa PMFJ, Ferreira RAS, Rocha J, Carlos LD (2013) Ratiometric nanothermometer based on an emissive Ln^{3+}-organic framework. ACS Nano 7:7213–7218
124. Foucault-Collet A, Gogick KA, White KA, Villette S, Pallier A, Collet G, Kieda C, Li T, Geib SJ, Rosi NL, Petoud S (2013) Lanthanide near infrared imaging in living cells with Yb^{3+} nano metal organic frameworks. Proc Natl Acad Sci U S A 110:17199–17204
125. Kathryn MLT, Jin A, Lin WB (2008) Surfactant-assisted synthesis of nanoscale gadolinium metal-organic frameworks for potential multimodal imaging. Angew Chem Int Ed 47:7722–7725
126. Xu B, Wang X (2012) Solvothermal synthesis of monodisperse nanocrystals. Dalton Trans 41:4719–4725
127. Shi W, Song S, Zhang HJ (2013) Hydrothermal synthetic strategies of inorganic semiconducting nanostructures. Chem Soc Rev 42:5714–5743
128. Ding SB, Wang W, Qiu LG, Yuan YP, Peng FM, Jiang X, Xie AJ, Shen YH, Zhu JF (2011) Surfactant-assisted synthesis of lanthanide metal-organic framework nanorods and their fluorescence sensing of nitroaromatic explosives. Mater Lett 65:1385–1387
129. Hua Q, Cao T, Gu XK, Lu J, Jiang Z, Pan X, Luo L, Li WX, Huang W (2014) Crystal-plane-controlled selectivity of Cu_2O catalysts in propylene oxidation with molecular oxygen. Angew Chem Int Ed 53:4856–4861
130. Li W, Zamani R, Ibáñez M, Doris C, Shavel A, Morante JR, Arbiol J, Cabot A (2013) Metal ions to control the morphology of semiconductor nanoparticles: copper selenide nanocubes. J Am Chem Soc 135:4664–4667
131. Liu B, Aydil ES (2009) Growth of oriented single-crystalline rutile TiO_2 nanorods on transparent conducting substrates for dye-sensitized solar cells. J Am Chem Soc 131:3985–3990
132. Guo H, Zhu Y, Qiu S, Lercher JA, Zhang H (2010) Coordination modulation induced synthesis of nanoscale $Eu_{1-x}Tb_x$-metal-organic frameworks for luminescent thin films. Adv Mater 22:4190–4192
133. Xu H, Rao X, Gao J, Yu J, Wang Z, Dou Z, Cui Y, Yang Y, Chen B, Qian G (2012) A luminescent nanoscale metal-organic framework with controllable morphologies for spore detection. Chem Commun 48:7377–7379
134. Buller R, Peterson ML, Almarsson Ö, Leiserowitz L (2002) Quinoline binding site on malaria pigment crystal: a rational pathway for antimalarial drug design. Cryst Growth Des 2:553–562
135. Zhang X, Ballem MA, Hu ZJ, Bergman P, Uvdal K (2011) Nanoscale light-harvesting metal-organic frameworks. Angew Chem Int Ed 50:5729–5733
136. Fillion H, Luche JL (1998) Synthetic organic sonochemistry. Plenum, New York
137. Li X, Wang X, Zhang L, Lee S, Dai HJ (2008) Chemically derived, ultrasmooth graphene nanoribbon semiconductors. Science 319:1229–1232

138. Suslick KS (1988) Ultrasound: its chemical, physical and biological effects. VCH, Weinheim
139. Didenko YT, Suslick KS (2002) The energy efficiency of formation of photons, radicals and ions during single-bubble cavitation. Nature 418:394–397
140. Flannigan DJ, Suslick KS (2005) Plasma formation and temperature measurement during single-bubble cavitation. Nature 434:52–55
141. Qiu LG, Li ZQ, Wu Y, Wang W, Xu T, Jiang X (2008) Facile synthesis of nanocrystals of a microporous metal-organic framework by an ultrasonic method and selective sensing of organoamines. Chem Commun 2008:3642–3644
142. Khan NA, Haque MM, Jhung SH (2010) Accelerated synthesis of porous isostructural lanthanide-benzenetricarboxylates (Ln-BTC) under ultrasound at room temperature. Eur J Inorg Chem 2010:4975–4981
143. Hu SM, Niu HL, Qiu LG, Yuan YP, Jiang X, Xie AJ, Shen YH, Zhu JF (2012) Facile synthesis of highly luminescent nanowires of a terbium-based metal-organic framework by an ultrasonic-assisted method and their application as a luminescent probe for selective sensing of organoamines. Inorg Chem Commun 17:147–150
144. Xiao JD, Qiu LG, Ke F, Yuan YP, Xu GS, Wang YM, Jiang X (2013) Rapid synthesis of nanoscale terbium-based metal-organic frameworks by a combined ultrasound-vapour phase diffusion method for highly selective sensing of picric acid. J Mater Chem A 1:8745–8752
145. Wang Z, Cohen SM (2009) Postsynthetic modification of metal-organic frameworks. Chem Soc Rev 38:1315–1329
146. Dou Z, Yu J, Xu H, Cui Y, Yang Y, Qian G (2013) Preparation and thiols sensing of luminescent metal-organic framework films functionalized with lanthanide ions. Microporous Mesoporous Mater 179:198–204
147. Zheng YZ, Zhou GJ, Zheng ZP, Winpenny REP (2014) Molecule-based magnetic coolers. Chem Soc Rev 43:1462–1475
148. Heffern MC, Matosziuk LM, Meade TJ (2014) Lanthanide probes for bioresponsive imaging. Chem Soc Rev 114:4496–4539
149. Wang F, Liu X (2014) Multicolor tuning of lanthanide-doped nanoparticles by single wavelength excitation. Acc Chem Res 47:1378–1385
150. Caravan P, Ellison JJ, McMurry TJ, Lauffer RB (1999) Gadolinium(III) chelates as MRI contrast agents: structure, dynamics, and applications. Chem Rev 99:2293–2352
151. Kuriki K, Koike Y, Okamoto Y (2002) Plastic optical fiber lasers and amplifiers containing lanthanide complexes. Chem Rev 102:2347–2356
152. Cockerill AF, Davies GLO, Harden RC, Rackham DM (1973) Lanthanide shift reagents for nuclear magnetic resonance spectroscopy. Chem Rev 73:553–588
153. Huang X, Han S, Huang W, Liu X (2013) Enhancing solar cell efficiency: the search for luminescent materials as spectral converters. Chem Soc Rev 42:173–201
154. Shibasaki M, Yoshikawa N (2002) Lanthanide complexes in multifunctional asymmetric catalysis. Chem Rev 102:2187–2210
155. Habib F, Murugesu M (2013) Lessons learned from dinuclear lanthanide nano-magnets. Chem Soc Rev 42:3278–3288
156. Molander GA (1992) Application of lanthanide reagents in organic synthesis. Chem Rev 92:29–68
157. Na HB, Song IC, Hyeon T (2009) Inorganic nanoparticles for MRI contrast agents. Adv Mater 21:2133–2148
158. Cui CH, Yu SH (2013) Engineering interface and surface of noble metal nanoparticle nanotubes toward enhanced catalytic activity for fuel cell applications. Acc Chem Res 46:1427–1437
159. Rowe MD, Chang CC, Thamm DH, Kraft SL, Harmon JF, Vogt AP, Sumerlin BS, Boyes SG (2009) Tuning the magnetic resonance imaging properties of positive contrast agent nanoparticles by surface modification with RAFT polymers. Langmuir 25:9487–9499
160. Sabbatini N, Guardigli M (1993) Luminescent lanthanide complexes as photochemical supramolecular devices. Coord Chem Rev 123:201–228

161. Binnemans K (2009) Lanthanide-based luminescent hybrid materials. Chem Rev 109:4283–4374
162. Bünzli JCG (2010) Lanthanide luminescence for biomedical analysis and imaging. Chem Rev 110:2729–2755
163. Brites CDS, Lima PP, Silva NJO, Millán A, Amaral VS, Palacio F, Carlos LD (2012) Thermometry at the nanoscale. Nanoscale 4:4799–4829
164. Jaque D, Vetrone F (2012) Luminescence nanothermometry. Nanoscale 4:4301–4326
165. Cui Y, Xu H, Yue Y, Guo Z, Yu J, Chen Z, Gao J, Yang Y, Qian G, Chen B (2012) A luminescent mixed-lanthanide metal-organic framework thermometer. J Am Chem Soc 134:3979–3982
166. Kim Y, Jung HY, Choe YH, Lee C, Ko SK, Koun S, Choi Y, Chung BH, Park BC, Hun TL, Shin J, Kim E (2012) High-contrast reversible fluorescence photoswitching of dye-crosslinked dendritic nanoclusters in living vertebrates. Angew Chem Int Ed 51:2878–2882
167. Gao X, Cui Y, Levenson RM, Chung LWK, Nie S (2004) *In vivo* cancer targeting and imaging with semiconductor quantum dots. Nat Biotechnol 22:969–976
168. Yang Q, Liu S, Liu Y, He D, Miao J, Wang X, Ji Y, Zheng Z (2014) Color tuning and white light emission via in situ doping of luminescent lanthanide metal-organic frameworks. Inorg Chem 53:289–293
169. Meyer LV, Schönfeld F, Müller-Buschbaum K (2014) Lanthanide based tuning of luminescence in MOFs and dense frameworks – from mono- and multimetal systems to sensors and films. Chem Commun. doi:10.1039/c4cc00848k
170. Carlos LD, Ferreira RAS, Bermudez VZ, Julián-Ĺopez B, Escribano P (2011) Progress on lanthanide-based organic–inorganic hybrid phosphors. Chem Soc Rev 40:536–549
171. Templeton DH, Dauben CH (1954) Lattice parameters of some rare earth compounds and a set of crystal radii. J Am Chem Soc 76:5237–5239
172. Piatkevich KD, Subach FV, Verkhusha VV (2013) Engineering of bacterial phytochromes for near-infrared imaging, sensing, and light-control in mammals. Chem Soc Rev 42:3441–3452
173. Bünzli JCG, Piguet C (2005) Taking advantage of luminescent lanthanide ions. Chem Soc Rev 34:1048–1077
174. Wj R, Taylor KML, Lin W (2007) Surface modification and functionalization of nanoscale metal-organic frameworks for controlled release and luminescence sensing. J Am Chem Soc 129:9852–9853
175. Yang L, Song S, Shao C, Zhang W, Zhang H, Bu Z, Ren T (2011) Synthesis, structure and luminescent properties of 3D lanthanide (La(III), Ce(III)) coordination polymers possessing 1D nanosized cavities based on pyridine-2,6-dicarboxylic acid. Synth Met 161:1500–1508
176. Foster DR, Richardson FS, Vallarino LM, Shillady D (1983) Magnetic circularly polarized luminescence spectra of Eu(β-diketonate)$_3$X$_2$ complexes in nonaqueous solution. Inorg Chem 22:4002–4009
177. Horcajada P, Gref R, Baati T, Allan PK, Maurin G, Couvreur P, Férey G, Morris RE, Serre C (2012) Metal-organic frameworks in biomedicine. Chem Rev 112:1232–1268
178. Lorusoo G, Sharples JW, Palacios E, Roubeau O, Brechin EK, Sessoli R, Rossin A, Tuna F, Mclnnes EJL, Collison D, Evangelisti M (2013) A dense metal-organic framework for enhanced magnetic refrigeration. Adv Mater 25:4653–4656
179. Filho MAM, Dutra JDL, Rocha GB, Freire RO, Simas AM (2013) Sparkle/RM1 parameters for the semiempirical quantum chemical calculation of lanthanide complexes. RSC Adv 3:16747–16755
180. Dutra JDL, Ferreira JW, Rodrigues MO, Freire RO (2013) Theoretical methodologies for calculation of Judd–Ofelt intensity parameters of polyeuropium systems. J Phys Chem A 117:14095–14099
181. Dutra JDL, Bispo TD, Freire RO (2014) LUMPAC lanthanide luminescence software: efficient and user friendly. J Comput Chem 35:772–775

182. Chaudhuri RG, Paria S (2012) Core/shell nanoparticles: classes, properties, synthesis mechanisms, characterization, and applications. Chem Rev 112:2373–2433
183. Burrows AD (2011) Mixed-component metal-organic frameworks (MC-MOFs): enhancing functionality through solid solution formation and surface modifications. CrystEngComm 13:3623–3642
184. Li T, Sullivan JE, Rosi NL (2013) Design and preparation of a core–shell metal-organic framework for selective CO_2 capture. J Am Chem Soc 135:9984–9987
185. Zhao M, Deng K, He L, Liu Y, Li G, Zhao H, Tang Z (2014) Core–shell palladium nanoparticle@metal-organic frameworks as multifunctional catalysts for cascade reactions. J Am Chem Soc 136:1738–1741
186. Guo J, Yang W, Wang C (2013) Magnetic colloidal supraparticles: design, fabrication and biomedical applications. Adv Mater 25:5196–5214
187. Nakagawa Y, Kageyama H, Oaki Y, Imai H (2014) Direction control of oriented self-assembly for 1D, 2D, and 3D microarrays of anisotropic rectangular nanoblocks. J Am Chem Soc 136:3716–3719
188. Zhang SY, Regulacio MD, Han MY (2014) Self-assembly of colloidal one-dimensional nanocrystals. Chem Soc Rev 43:2301–2323
189. Martín-Rodríguez R, Geitenbeek R, Meijerink A (2013) Incorporation and luminescence of Yb^{3+} in CdSe nanocrystals. J Am Chem Soc 135:13668–13671
190. Luo F, Yang YT, Che YX, Zheng JM (2008) Construction of Cu(II)-Gd(III) metal-organic framework by the introduction of a small amino acid molecule: hydrothermal synthesis, structure, thermostability, and magnetic studies. CrystEngComm 10:1613–1616
191. Fabelo O, Cañadillas-Delgado L, Pasán J, Díaz-Gallifa P, Labrador A, Ruiz-Pérez C (2012) Dryness sensitive porous 3d-4f metal-organic framework with unusual dynamic behavior. CrystEngComm 14:765–767
192. Hu XL, Sun CY, Qin C, Wang XL, Wang HN, Zhou EL, Li WE, Su ZM (2013) Iodine-templated assembly of unprecedented 3d-4f metal-organic frameworks as photocatalysts for hydrogen generation. Chem Commun 49:3564–3566
193. Park YK, Choi SB, Kim H, Kim K, Won BH, Choi K, Choi JS, Ahn WS, Won N, Kim S, Jung DH, Choi SH, Kim GH, Cha SS, Jhon YH, Yang JK, Kim J (2007) Crystal structure and guest uptake of a mesoporous metal-organic framework containing cages of 3.9 and 4.7 nm in diameter. Angew Chem Int Ed 46:8230–8233

Index